

AD-A241 364



DTIC

ELECTE

OCT 9 1991

(2)

**CHEMICAL  
RESEARCH,  
DEVELOPMENT &  
ENGINEERING  
CENTER**

CRDEC-SP-036

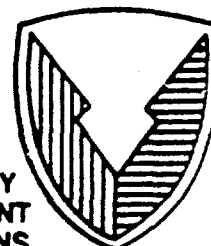
**PROCEEDINGS OF THE 1990 SCIENTIFIC CONFERENCE  
ON OBSCURATION AND AEROSOL RESEARCH**

**Elmer H. Engquist  
Deborah A. Clark**

**BATTELLE-EDGEWOOD OPERATIONS  
Edgewood, MD 21040**

**June 1991**

Approved for public release; distribution is unlimited.



**U.S. ARMY  
ARMAMENT  
MUNITIONS  
CHEMICAL COMMAND**

Aberdeen Proving Ground, Maryland 21010-5423

**91-12671**



**REPRODUCED FROM  
BEST AVAILABLE COPY**

**91 10 8 042**

#### Disclaimer

The findings in this report are not to be construed as an official Department of the Army position unless so designated by other authorizing documents.

REPORT DOCUMENTATION PAGE				Form Approved OMB No. 0704-0188	
<small>Public reporting burden for this collection of information is estimated to average 1 hour per response, including the time for reviewing instructions, searching existing data sources, gathering and maintaining the data needed, and completing and reviewing the collection of information. Send comments regarding this burden estimate or any other aspect of this collection of information, including suggestions for reducing this burden, to Washington Headquarters Services, Directorate for Information Operations and Reports, 1215 Jefferson Davis Highway, Suite 1204, Arlington, VA 22202-4302, and to the Office of Management and Budget, Paperwork Reduction Project (0704-0188), Washington, DC 20503.</small>					
1. AGENCY USE ONLY (Leave blank)		2. REPORT DATE 1991 June		3. REPORT TYPE AND DATES COVERED Final, 90 Jun - 90 Jun	
4. TITLE AND SUBTITLE Proceedings of the 1990 Scientific Conference on Obscuration and Aerosol Research				5. FUNDING NUMBERS  PR-10161102A71A	
6. AUTHOR(S)  Elmer H. Engquist and Deborah A. Clark, Compilers					
7. PERFORMING ORGANIZATION NAME(S) AND ADDRESS(ES) Battelle.- Edgewood Operations 2113 Emmorton Park Road, Suite 200 Edgewood, MD 21040				8. PERFORMING ORGANIZATION REPORT NUMBER  CRDEC-SP-036	
9. SPONSORING/MONITORING AGENCY NAME(S) AND ADDRESS(ES) CDR, CRDEC, ATTN: SMCCR-RSP-B, APG, MD 21010-5423				10. SPONSORING/MONITORING AGENCY REPORT NUMBER	
11. SUPPLEMENTARY NOTES  POC: Edward W. Stuebing, SMCCR-RSP-B, (301) 671-3089					
12a. DISTRIBUTION/AVAILABILITY STATEMENT  Approved for public release; distribution is unlimited.				12b. DISTRIBUTION CODE	
13. ABSTRACT (Maximum 200 words)  In this report, 35 papers presented at the 1990 Scientific Conference on Obscuration and Aerosol Research are included under the headings of Physical and Chemical Properties of Aerosols, Aerosol Characterization Methods, and Optical Properties of Aerosols.					
14. SUBJECT TERMS Obscurants      Aerosols      Extinction      Transmission Obscuration      Aerosol      Absorption      Infrared Scattering      Sizing      Smoke      (continued on page 2)				15. NUMBER OF PAGES 434	
				16. PRICE CODE	
17. SECURITY CLASSIFICATION OF REPORT UNCLASSIFIED	18. SECURITY CLASSIFICATION OF THIS PAGE UNCLASSIFIED	19. SECURITY CLASSIFICATION OF ABSTRACT UNCLASSIFIED		20. LIMITATION OF ABSTRACT  UL	

#### 14. SUBJECT TERMS (continued)

Electromagnetic scattering  
Millimeter wave radiation  
Submillimeter wave radiation  
Visible radiation  
Electromagnetic waves  
Spherical particles  
Mie scattering  
Rayleigh scattering  
Raman scattering  
Concentration sampling  
Particle dynamics  
Diffusive mixing  
Aerosol growth  
Nucleation  
Smoke generation  
Aerosol generation  
Photoionization  
Conductivity  
Chemical characterization  
Phosphorus smoke  
Fluorescence  
Aerosol clusters  
Spheres  
Cylinders  
Rough particles  
Irregular particles  
Nonspherical particles  
Particle aggregates  
Particle chains  
Infrared emission  
Cooperative scattering  
Dependent scattering  
Multiple scattering  
Radiative transfer  
Coagulation  
Condensation  
Liquid drop  
Drop growth  
Fog oil smoke  
Diesel oil smoke  
Particle mechanics  
Atmospheric optics  
Atmospheric dispersion  
Cloud dynamics  
Scavenging  
Aerosol collectors  
Aerosol elimination  
Aerosol characterization  
Particle sizing  
Hygroscopic smokes  
Particle size distribution  
Particle orientation distribution

Optical constants  
Optical properties  
Anomalous diffraction  
Attenuated total reflection  
Reflection spectroscopy  
ATR  
Far-infrared  
Refractive index  
Index of refraction  
Inversion  
Inversion techniques  
Gypsum  
Natural minerals  
Minerals  
Metal  
Metallic particles  
Powdered minerals  
Complex refractive index  
Effective media  
High energy laser  
Particles  
Aerosol particles  
SERS  
Surface Enhanced Raman Scattering  
Dielectric particles  
Conducting particles  
Cylindrical particles  
Fibers  
Conducting fibers  
Gas-aerosol reactions  
Transport phenomena  
Aerosol measurement  
Spheroids  
Laser pulses  
Optical pulses  
Pulse propagation  
Clouds  
Laser  
Radiation transport  
Fourier analysis  
Plume mechanics  
Light  
Plumes  
Properties



## PREFACE

The 1990 U.S. Army Chemical Research, Development and Engineering Center Scientific Conference on Obscuration and Aerosol Research was held 25 - 28 June 1990 at the Edgewood Area Conference Center of Aberdeen Proving Ground, MD. The Conference is held annually, the last full week in June, under the direction of Dr. Edward Steubing, Research Area Coordinator, Aerosol Science. This report was authorized under project number 1O161102A71A, Research in CW/CB Defense.

The Conference is an informal forum for scientific exchange and stimulation among investigators in the wide variety of disciplines required for aerosol research, including a description of an obscuring aerosol and its effects. The participants develop some familiarity with the U.S. Army aerosol and obscuration science research programs and also become personally acquainted with the other investigators and their research interests and capabilities. Each attendee is invited to present any aspect of a topic of interest and may make last minute changes or alterations in his presentation as the flow of ideas in the Conference develops.

While all participants in the Conference are invited to submit papers for the proceedings of the Conference, each investigator, who is funded by the U.S. Army Research Program, is requested to provide one or more written papers that document specifically the progress made in his funded effort in the previous year and indicating future directions. Also, the papers for the proceedings are collected in the Fall to allow time for the fresh ideas that arise at the Conference to be incorporated. Therefore, while the papers in these proceedings tend to closely correspond to what was presented at the Conference, there is not an exact correspondence.

The reader will find the items relating to the Conference itself, photographs, the list of attendees, and the agenda in the appendixes following the papers and in the indexes pertaining to them.

The use of trade names or manufacturers' names in this report does not constitute an official endorsement of any commercial products. This report may not be cited for purposes of advertisement.

Reproduction of this document in whole or in part is prohibited except with permission of the Commander, U.S. Army Chemical Research, Development and Engineering Center, ATTN: SMCCR-SPS-T, Aberdeen Proving Ground, MD 21010-5423. However, the Defense Technical Information Center and the National Technical Information Service are authorized to reproduce this document for U.S. Government purposes.

This report has been approved for release to the public.



Accession For	
NTIS OP&A1	<input checked="" type="checkbox"/>
DTIC TAB	<input type="checkbox"/>
Unannounced	<input type="checkbox"/>
Justification	
By	
Distribution/	
Availability Codes	
Dist	Avail and/or Special
A-1	

BLANK

## CONTENTS

<b>I. AEROSOL DYNAMICS</b>	<b>9</b>
MEASUREMENT OF THE MASS TRANSFER COEFFICIENT FOR THE ABSORPTION OF METHYL SALICYLATE ON FINE PARTICULATE AEROSOLS IN A VERTICAL TRANSPORT LINE IN DILUTE PHASE FLOW H. Littman and M.H. Morgan III	9
PARTICLE FORMATION BY HOMOGENEOUS NUCLEATION IN UNDEREXPANDED SONIC JETS B.J. Jurcik and J. Brock	15
A NEW STATISTICAL MEASURE OF PLUME OBSCURATION EFFECTIVENESS: MEAN WAITING TIME FOR A WINDOW J.R. Brock	23
INTERCEPTIONAL AND DIFFUSIONAL DEPOSITION OF FINE PARTICLES IN FIBROUS FILTERS M. Shapiro and H. Brenner	29
FLUCTUATIONS OF INTEGRATED CONCENTRATIONS THROUGH AN AEROSOL PLUME IN THE ATMOSPHERIC SURFACE LAYER M. Poreh, A. Hadad, and J.E. Cermak	39
<b>II. AEROSOL CHARACTERIZATION METHODS</b>	<b>47</b>
COMPARATIVE STUDIES OF BACTERIAL SHAPE AND ITS EFFECT ON THE $[S_{34}/S_{11}]^*$ ANGULAR SCATTERING PATTERN E.V. Bronk, W.P. Van de Merwe, and M. Stanley	47
INVERSION OF SINGLE SIZE PARTICLE SCATTERING DATA BY USE OF A CONSTRAINED EIGENFUNCTION EXPANSION B.P. Curry and K.H. Leong	51
LIGHT SCATTERING AND BIREFRINGENCE OF MAGNETIC BACTERIA R.G. Johnston and P.L. Jacobson	59
RAINBOWS AND PARTICLE CHARACTERIZATION R.T. Wang	73
SINGLE SCATTERING INVERSION PROBLEM P. Hu and M. Lax	87
OPTICAL PROPERTIES OF SELECTED MATERIALS IN THE ULTRAVIOLET TO MILLIMETER SPECTRAL REGION L. Newquist, R.W. Alexander, R. Vandiver, M.R. Querry, R.J. Bell, and D. Wieleczka	99

LIGHT SCATTERING FLUCTUATIONS FROM AN AEROSOL PARTICLE TRAPPED AT THE "NULL" POINT OF AN ELECTRODYNAMIC LEVITATOR	
S. Arnold, D.E. Spock, and L.M. Folan . . . . .	115
MASS SPECTROMETRY OF SINGLE PARTICLES	
J.F. Wacker . . . . .	125
MEASURING THE TEMPERATURE OF DIAMAGNETICALLY LEVITATED MICROPARTICLES	
B.R.F. Kendall and E.T. Chesworth . . . . .	131
PROGRESS IN THE DETECTION OF SINGLE MOLECULES IN LEVITATED DROPLETS	
W.B. Whitten, J.M. Ramsey, S. Arnold and B.V. Bronk . . . . .	139
THE SMOKE-ION SOURCE: THE GENERATION OF METAL AND METAL OXIDE CLUSTER IONS VIA INERT GAS CONDENSATION	
H.W. Sarkas, L.H. Kidder, J.G. Eaton, N.G. Wimer, K.M. McHugh, and K.H. Bowen . . . . .	143
PRESSURE-DEPENDENT DAMPING AND BROWNIAN MOTION OF A PARTICLE LEVITATED IN VACUUM	
L.D. Hinkle and B.R.F. Kendall . . . . .	163
MODE IDENTIFICATION OF LINEAR AND NONLINEAR OPTICAL PROCESSES IN MICRO-DROPLETS	
H.-B. Lin, J.D. Eversole, A.L. Huston, and A.J. Campillo . . . . .	165
CAVITY MODE IDENTIFICATION OF FLUORESCENCE AND LASING IN MICRO-DROPLETS	
J.D. Eversole, H.-B. Lin, and A.J. Campillo . . . . .	173
III. THE ROLE OF AEROSOLS IN ATMOSPHERIC CHEMISTRY . . . . .	187
ATMOSPHERIC CHEMISTRY ON POLAR STRATOSPHERIC CLOUD PARTICLES	
M.A. Tolbert, A.M. Middlebrook, M.A. Quinlan, C.M. Reihs, and D.M. Golden . . . . .	187
IV. NONLINEAR EFFECTS . . . . .	195
A THEORETICAL FORMULATION OF THE RESPONSE OF A DROPLET TO HIGH ENERGY RADIATION. A HYDRO DYNAMIC THEORY OF DROPLET RADIATIVE HEATING AND EXPLOSION	
D.K. Cohoon . . . . .	195

LASER INTERACTION WITH A METALLIC FILAMENT: ABLATION DYNAMICS AND PLASMA FORMATION D.R. Alexander, G.M. Holtmeier, K.-D. Song, and J.P. Barton . . . . .	211
---	-----

WAVE PROPAGATION FROM LASER-INDUCED PLASMAS IN DROPLETS J.C. Carls and J.R. Brock . . . . .	235
--	-----

## V. OPTICAL PROPERTIES OF AEROSOLS . . . . . 243

A FINITE ELEMENT SOLUTION OF THE MAXWELL EQUATIONS FOR ABSORPTION AND SCATTERING OF ELECTROMAGNETIC RADIATION BY A SPHERE L. Liebman and J. Brock . . . . .	243
--	-----

AN APPROXIMATION TO EXTINCTION EFFICIENCY FOR RANDOMLY ORIENTED SPHEROIDS G.R. Fournier and B.T.N. Evans . . . . .	249
--	-----

ELECTROMAGNETIC FIELDS FOR A BEAM INCIDENT UPON A NONSPHERICAL PARTICLE J.P. Barton and D.R. Alexander . . . . .	259
--	-----

LIGHT SCATTERING AT ZERO DEGREES BY PARTICULATE SUSPENSIONS E.S. Fry and G.G. Padmabandu . . . . .	277
--	-----

RAPID MATRIX INVERSION D.K. Cohoon . . . . .	289
---	-----

THE RESPONSE OF A CLASS OF N LAYER ELECTROMAGNETICALLY BIANISOTROPIC SPHERES TO SPATIALLY AND TEMPORALLY COMPLEX WAVES D.K. Cohoon . . . . .	299
---	-----

THE RESPONSE OF A CYLINDER WITH A THIN HIGH INDEX OF REFRACTION BIANISOTROPIC COATING TO ELECTROMAGNETIC RADIATION D.K. Cohoon . . . . .	347
---	-----

THE THERMAL RESPONSE OF AN N LAYER ELECTROMAGNETICALLY AND THERMALLY ANISOTROPIC SPHERE TO ELECTROMAGNETIC RADIATION BY AN EXACT FORMULA D.K. Cohoon . . . . .	363
---	-----

MULTIPLE SCATTERING OF ELECTROMAGNETIC WAVES FROM COATED ROUGH SURFACES E. Bahar and S.M. Haugland . . . . .	379
--	-----

**DENSITY DEPENDENCE OF THE ABSORPTION COEFFICIENT OF A  
DISPERSION OF SPHERICAL METAL PARTICLES**

E. Fucile, O.I. Sindoni, F. Borghese, P. Denti,  
R. Saija . . . . . 385

**AEROSOL SIZE DISTRIBUTION INFERRED FROM LIDAR MULTIPLE  
SCATTERING MEASUREMENTS**

A. Ben-David, Y. Benayahu and S. Fastig, and A.  
Cohen . . . . . 395

**FRACTAL ELECTRODYNAMICS: A NOVEL METHOD TO EXAMINE ROUGH  
SURFACE SCATTERING**

X. Sun and D.L. Jaggard . . . . . 407

**INDEXES FOR THESE PROCEEDINGS**

A. INDEX OF AUTHORS . . . . . 417

B. INDEX OF AUTHORS' ORGANIZATIONS . . . . . 419

**APPENDIXES FOR THESE PROCEEDINGS**

A. PHOTOGRAPH OF 1990 CONFERENCE ATTENDEES . . . . . 421

B. LIST OF 1990 ATTENDEES . . . . . 423

C. CONFERENCE AGENDA . . . . . 431

PROCEEDINGS OF THE 1990 SCIENTIFIC CONFERENCE ON OBSCURATION AND AEROSOL RESEARCH  
I. AEROSOL DYNAMICS

MEASUREMENT OF THE MASS TRANSFER COEFFICIENT FOR THE  
ABSORPTION OF METHYL SALICYLATE ON FINE PARTICULATE AEROSOLS  
IN A VERTICAL TRANSPORT LINE IN DILUTE PHASE FLOW

H. Littman and M. H. Morgan III  
Rensselaer Polytechnic Institute  
Troy, New York 12180-3590

RECENT PUBLICATIONS, SUBMITTAL FOR PUBLICATION AND PRESENTATIONS:

A) Littman, H., M. H. Morgan III, D. K. Prapas and G. O. Rubel, "An Automated System for Measuring the Mass Flowrate of Powders in Transport Lines," CRDEC-TN-013 Report January 1990, CRDEC Aberdeen, MD.

ABSTRACT

Purpose of work

In this paper, we give a method of measuring the rate of absorption of chemical agents such as methyl salicylate on fine particulate aerosols for the purpose of removing toxic vapors from the battlefield.

Experimental measurement of the mass transfer coefficient in a transport line

The rate of absorption of a gas on to a particulate aerosol in a vertical transport line is to be measured to determine the mass transfer coefficient.

Consider a dilute mixture of component A in air coflowing with fine particles vertically in a pipe. There is a short acceleration zone near the inlet to the pipe after which the flow is non-accelerating. The voidage then becomes constant as does the local pressure gradient.

Component A (methyl salicylate) is introduced in the non-accelerating region and its mass transfer to the fine particles over 10 feet of the transport line is determined by sampling the gas and chromatographically analyzing it.

To determine the mass transfer coefficient, we start with the mass balance in one dimensional flow for component A in the line.

$$\epsilon \rho_f \frac{\partial y_A}{\partial t} + \epsilon \rho_f u \frac{\partial y_A}{\partial z} + (1-\epsilon) \rho_p R_A = 0 \quad (1)$$

We assume that the flow is radially uniform and the temperature constant, and define the reaction rate as

$$R_A = \frac{N_A a M_A}{(1-\epsilon)p_p} \quad (2)$$

The rate equation for the absorption can be written in terms of the mass transfer coefficient as

$$N_{Aa} = K_G a (p_A - p_A^*) \quad (3)$$

Changing the partial pressure into mass and mole fractions

$$N_{Aa} = K_G a P \frac{M}{M_A} (y_A - y_A^*) \quad (4)$$

Combining equations 2 and 4

$$(1-\epsilon) \rho_p R_A = K_G a P M (y_A - y_A^*) = K_G a \rho_f R T (y_A - y_A^*) \quad (5)$$

Thus in the steady state, equations 1 and 5 become

$$\epsilon u \frac{dy_A}{dz} + k a (y_A - y_A^*) = 0 \quad (6)$$

Separating variables and integrating assuming that  $y_A^*$  and  $\epsilon u$  are constant, we obtain

$$k a = U \frac{\ln \left( \frac{y_{A2} - y_A^*}{y_{A1} - y_A^*} \right)}{(z_2 - z_1)} \quad (7)$$

By measuring  $y_{A1}$  and  $y_{A2}$  and the superficial gas velocity  $U$ ,  $k a$  can be measured.

#### Correlation of the mass transfer coefficient

For correlation purposes, the Colburn  $j$ -factor which has been successful in correlations of mass transfer coefficients in packed and fluidized beds will be tried so that

$$j_D \equiv \frac{k}{U} (Sc)^{2/3} = f(Re) \quad (8)$$

It is reasonable to define

$$Re = \langle d_p \rangle (u-v)/\nu \quad (9)$$



as the rate of mass transfer should be a function of the slip velocity.

The  $a$  term can be defined in terms of the average particle diameter as

$$a = \frac{6(1-\epsilon)}{\langle d_p \rangle} \quad (10)$$

#### Determination of the voidage and slip velocity

The one dimensional steady state mass and momentum equations are (1) for these fine particles

$$\epsilon u = c_1 \quad (11)$$

$$(1-\epsilon) v = c_2 \quad (12)$$

$$\rho_f \frac{d}{dz} (\epsilon u^2) = -\epsilon \frac{dP}{dz} - \beta (u-v) - F_f \quad (13)$$

$$\rho_p \frac{d}{dz} [(1-\epsilon)v^2] = -(1-\epsilon) \frac{dP}{dz} + \beta (u-v) - F_p - (1-\epsilon)(\rho_p - \rho_f)g \quad (14)$$

where  $P = p + \rho_f g z$ ,  $F_f = 2f(\rho_f U^2/D_t)$  and  $F_p = 2f_p(1-\epsilon)\rho_p v^2/D_t$ .

Combining equations 13 and 14 gives the mixture momentum equation

$$\rho_f \frac{d}{dz} (\epsilon u^2) + \rho_p \frac{d}{dz} [(1-\epsilon)v^2] = -\frac{dP}{dz} - F_f - F_p - (1-\epsilon)(\rho_p - \rho_f)g \quad (15)$$

In the non-accelerating region of the pipe the inertial terms drop out so that

$$-\frac{dP}{dz} = (1-\epsilon)(\rho_p - \rho_f)g + F_f + F_p \quad (16)$$

To calculate the voidage, equation 16 is rearranged to

$$(1-\epsilon) = \frac{-\frac{dP}{dz} - F_f - F_p}{(\rho_p - \rho_f)g} \quad (17)$$

The slip velocity is easily calculated once the voidage is known using equations 11 and 12. Thus

$$u-v = \left[ \frac{c_1}{\epsilon} - \frac{c_2}{1-\epsilon} \right] \quad (18)$$

To determine the voidage the pressure gradient in the non-accelerating region is measured in our transport line apparatus (2). The friction factor for flow in a tube without particles is then obtained from Byrd et al. (3) and  $F_f$  calculated.  $F_p$  is difficult to determine as literature correlations give vastly different estimates of the particle-wall friction factor but it is reasonable to assume in dilute phase flow this term cannot be large. As a first approximation we will neglect it.  $c_2$  is obtained by collecting the particles passing through the transport line per unit time and  $c_1$  is the measured superficial gas velocity in the line.

Once  $\epsilon$  is calculated from equation 17, the slip velocity is determined by measuring the gas and particle mass flowrates in our transport line apparatus.

#### References

1. Capes, C.E. and K. Nakamura, Can. J. Chem. Eng. 1973, 51, 31.
2. Littman, H., M. H. Morgan III, D. K. Prapas and G. O. Rubel, An Automated System for Measuring the Mass Flowrate of Powders in Transport Lines, CRDEC-TN-013 Report January 1990. CRDEC Aberdeen, MD.
3. Byrd, R.B., W.E. Stewart and E.N. Lightfoot, Transport Phenomena, J. Wiley, New York, 1960.

## Nomenclature

$a$	=	surface area of particles/unit volume of bed, $m^{-1}$
$c_1$	=	superficial velocity of gas, $m/s$
$c_2$	=	superficial velocity of particles, $m/s$
$D$	=	diffusivity, $m^2/s$
$D_t$	=	pipe diameter, $m$
$f_f$	=	friction coefficient, fluid-wall
$f_p$	=	friction coefficient, particle-wall
$F_f$	=	pressure gradient due to fluid-wall friction, $Pa/m$
$F_p$	=	pressure gradient due to particle-wall friction, $Pa/m$
$g$	=	gravitational acceleration, $m/s^2$
$j_D$	=	$\frac{k}{U} (Sc)^{2/3} = f(Re)$
$k$	=	$K_G RT$ = mass transfer coefficient, $m/s$
$K_{Ga}$	=	overall mass transfer coefficient, $kg \text{ moles } A/m^3, s, atm$
$M_A$	=	molecular weight of component A
$M$	=	molecular weight of mixture gas
$N_A$	=	rate of mass transfer, moles A transferred/surface area of particles, $s$
$p$	=	pressure, $atm$
$p_A$	=	partial pressure of component A in gas, $atm$
$p_A^*$	=	partial pressure of component A in equilibrium with absorbed gas on particulate aerosol, $atm$
$P$	=	modified pressure, $atm$
$R$	=	gas constant, $liter \text{ atm}/mole \text{ } K$
$R_A$	=	reaction rate, $kg_m \text{ } A/kg \text{ solids, } s$
$Re$	=	Reynolds number, $\langle d_p \rangle (u-v)/\nu$
$Sc$	=	Schmidt number, $\nu/D$
$t$	=	time, $s$
$T$	=	absolute temperature, $K$
$u$	=	interstitial gas velocity, $m/s$
$U$	=	$\epsilon u$ = superficial velocity, $m/s$
$v$	=	particle velocity, $m/s$
$y_A$	=	mass fraction of A in the gas, $kg_m \text{ } A/kg_m \text{ mixture}$
$z$	=	distance along transport line
$\beta$	=	fluid-particle drag coefficient, $kg/m^4$
$\epsilon$	=	voidage
$\nu$	=	kinematic viscosity
$\rho_f$	=	fluid density, $kg_m/m^3$
$\rho_p$	=	particle density, $kg_m/m^3$

BLANK

## PARTICLE FORMATION BY HOMOGENEOUS NUCLEATION IN UNDEREXPANDED SONIC JETS

B. J. Jurcik and J. Brock  
Chemical Engineering Department  
University of Texas, Austin, Texas 78712

### RECENT PUBLICATIONS, SUBMITTALS FOR PUBLICATION AND PRESENTATIONS

"Wave propagation from laser-induced plasmas in droplets" *Proceedings of the 1990 CRDEC Scientific Conference on Obscuration and Aerosol Research*, CRDEC, U. S. Army, 1990 (with J. Carls)

"Aerosol jet etching", *Aerosol Sci. Tech.*, 12, 842-856 (1990) (with Y. L. Chen and I. Trachtenberg)

"A study of low pressure impaction processes", *J. Aerosol Science* 20, 560, 1989. (with B. Jurcik and I. Trachtenberg)

"Laser-induced breakout and detonation waves in droplets: II. Model", *J. Optical Soc. America B*, In Press, 1990. (with J. C. Carls and Y. Seo)

"Distributions for moment simulation of aerosol evaporation", *In Press Journal of Aerosol Science* 1990 (with Y. Seo)

"Comparison between theory and experiment for laser-induced plasma and shock waves in droplets", *Proceedings of the 1989 CRDEC Scientific Conference on Obscuration and Aerosol Research*, CRDEC, U. S. Army, In Press, 1990 (with J. Carls)

"Statistical properties of windows in atmospheric plumes", *Proceedings of the 1990 CRDEC Scientific Conference on Obscuration and Aerosol Research*, CRDEC, U. S. Army, In Press, 1990

"Alkane oligomerization and graphite fiber formation in an electrocatalytic system", *Proceedings of the 1990 CRDEC Scientific Conference on Obscuration and Aerosol Research*, CRDEC, U. S. Army, In Press, 1990

"Particle formation by homogeneous nucleation in expanding flows", *Proceedings of the 1990 CRDEC Scientific Conference on Obscuration and Aerosol Research*, CRDEC, U. S. Army, In Press, 1990 (with B. J. Jurcik)

"A finite element solution of the Maxwell equations for absorption and scattering of electromagnetic radiation by a sphere" *Proceedings of the 1990 CRDEC Scientific Conference on Obscuration and Aerosol Research*, CRDEC, U. S. Army, In Press, 1990 (with L. Liebman)

"Aerosol jet etching of  $\text{Hg}_{1-x}\text{Cd}_x\text{Te}$ ", *Applied Physics Letters* 56 1682-1685 (1990) (with B. J. Jurcik and I. Trachtenberg)

"Particle formation by homogeneous nucleation in expanding flows" Submitted for publication (1990) (with B. J. Jurcik)

"Theory and experiment on laser assisted etching of silicon", *In Press, AIChE Symposium Series*, 1990.

"A new process for graphite fiber formation from alkane vapors", Submitted for publication, 1990.

"Wave propagation from laser-induced plasmas in droplets", Submitted for publication, 1990.

### ABSTRACT

A two dimensional simulation of particle formation by homogeneous nucleation in expanding flows is described. An exact moment method is used to describe the particle size distribution function. The model simulates the physical system of nucleation and particle growth in underexpanded sonic velocity nitrogen jets. The calculations agree with published experimental data well. It is shown that particle formation occurs initially off axis. The average particle diameter can be either on axis or off axis depending on the operating conditions.

### INTRODUCTION

In expanding free jets the vapor undergoes an isentropic expansion which results in a decrease in temperature, pressure and density. For most vapors, the saturation vapor pressure decreases with temperature more rapidly than the pressure decreases in the expansion. The vapor, therefore, approaches and crosses the saturation line and becomes supersaturated during an expansion, if the isentrope crosses the saturation line and the pressure drop in the expansion is large enough. If the cooling is rapid enough the gas or

vapor becomes quite supersaturated before any vapor condenses and small clusters or particles are formed by homogeneous nucleation. The reason the expansion does not follow the equilibrium line is that the kinetics of homogeneous nucleation and condensation are not rapid enough to maintain equilibrium. The clusters formed in an expansion also grow by a condensation mechanism. Figure 1 depicts this delay of condensation on a P - T diagram for nitrogen showing the expansion path and corresponding locations in an underexpanded sonic jet. The onset points are the conditions where condensation effects are detectable. The wave diagram of an underexpanded sonic jet is also shown in this Figure. For the sake of brevity, a description of the fluid dynamics of underexpanded jets is not presented here and the reader is referred to Adamson and Nichols (1959), Ashkenas and Sherman (1966), and Love et al. (1959).

The formation of aerosol particles in supersonic expansions has been the subject of a great many investigations (e. g. the review article of Wegener and Wu, 1977). These studies have used particle formation to study homogeneous nucleation (Abraham et al., 1981), the structure of small clusters (e. g. Mark and Castleman, 1985), and the deposition of ionized clusters (Takagi, 1986). Other practical applications that involve particle formation in an expansion are a method of Uranium 235 enrichment (Fisher, 1979) and a method for fueling fusion reactors (Moser, 1984). The formation of a condensed phase in rocket nozzle exhausts (Crowe and Willoughby, 1967), and in the sampling of gas from high pressure cylinders (Wen et al., 1987) occurs by the same mechanism but is an undesired effect.

Despite the enormous literature on systems in which nonequilibrium nucleation and condensation occur there have not been many attempts to model the flow field simultaneously with the particle formation processes. With only a single exception (Davydov, 1971) the analysis of nonequilibrium condensation has been one dimensional (Koppenwallner and Dankert, 1987). One-dimensional analysis fails to account for the two dimensional shock structure that is inherent in supersonic jets. As a result one-dimensional analysis can not show the effect of the large gradients that occur off axis. In this work a two dimensional simulation of particle formation is described. First the model is described and the numerical method for its solution is presented. Then results from the model are presented.

### Model Description

The expansions considered here are neither frozen nor equilibrium expansions. The expansions are sufficiently rapid that heterogeneous nucleation is negligible and the only mechanism for particle formation is homogeneous nucleation. Extremely large rates of homogeneous nucleation can be found at high supersaturations which, in conjunction with condensation, provides a mechanism for reaching the equilibrium line.

Obviously, the ability to simulate the expansion flows in which homogeneous nucleation and condensation occur is limited by the accuracy of the expressions used for nucleation and condensation. Stated succinctly, the expressions used are from the classical theory of homogeneous nucleation, and transfer processes to a particle in the free molecular regime (Hidy and Brock, 1970). The well known inaccuracies of classical nucleation theory are accepted, primarily because there is no other viable option. The expression used for homogeneous nucleation is:

$$J_{nuc} = \alpha \left( \frac{P_{vap}}{kT} \right)^2 v_1 \sqrt{2\sigma/\pi m_1} \exp(-\Delta G/kT) \quad (1)$$

The free energy change,  $\Delta G$ , is given by the expression:

$$\Delta G = \frac{4\pi}{3} \alpha (r^*)^2 \quad (2)$$

Where  $r^*$  is the radius of a 'critical cluster' i. e. the size of cluster formed by homogeneous nucleation. The critical cluster radius is given by:

$$r^* = \frac{2\sigma v_1}{kT \ln(P_{vap}/P_{sat})} \quad (3)$$

The rate at which mass condenses on a particle is given by the expression:

$$\frac{dm_i}{dt} = \alpha m_1 \left( \frac{P_{vap}}{\sqrt{2\pi m_1 kT}} - \frac{P_{sat}(T)}{\sqrt{2\pi m_1 kT}} \right) s_i \quad (4)$$

In these simulations the aerosol size distribution is followed exactly through the first three moments (McGraw and Saunders, 1984). The moments are defined in equations 5.

$$\mu_0 = \sum_{i=2}^{\infty} f_i \quad \mu_1 = \sum_{i=2}^{\infty} r_i f_i \quad \mu_2 = \sum_{i=2}^{\infty} s_i f_i \quad (5)$$

In these equations  $f_i$  is the number of particles with  $i$  molecules,  $\sigma$  is the surface tension,  $r_i$  is the radius of a particle with  $i$  molecules,  $s_i$  is the surface area of a particle with  $i$  molecules, and all other variables use standard notation.

Euler's equations are solved in conjunction with a conservation equation for  $\mu_0$ ,  $\mu_1$ ,  $\mu_2$ . The model of the jet uses the parabolized Navier - Stokes approach of marching in the axial direction as a time variable (Dash and Thorpe, 1981). The flow field of the underexpanded jet is mapped from the axis to the jet boundary. The boundary conditions on the jet boundary are found using a method of characteristics approach. The axial flux variables are solved for using McCormick's method. The calculation starts at the nozzle exit assuming no particles in the nozzle exit plane and assuming an isentropic expansion to sonic velocity.

## RESULTS

Dankert and Koppenwallner (1978) experimentally investigated nitrogen particle formation in underexpanded jets. Here, we simulate the experimental conditions of Dankert and Koppenwallner (1978). Figure 2 shows a calculated expansion path on the centerline in which particles are formed by nucleation and condensation. The experimentally determined onset points are those temperatures and pressures at which the effect of particles on the flow is observable. The conditions used for the model are  $P_0 = 3$  ATM,  $T_0 = 120K$ ,  $D = 0.50cm$ ,  $P_\infty = 0.01$  Torr,  $T_\infty = 120K$ . The physical properties used for nitrogen are shown in Table 1. As can be seen from Figure 2 the model determines the onset points correctly. The equation of state used for the gas phase is the ideal gas law with a constant heat capacity ratio,  $\gamma$ , equal to 1.4.

Property	Liquid phase [ $T > 63.14K$ ]	Solid phase [ $T < 63.14K$ ]
Vapor pressure [ATM]	$\ln(P_s) = 9.3996 - 723.47/T$	$\ln(P_s) = 11.034 - 826.86/T$
Density [ $gm/cm^3$ ]	0.8084	1.0265
Surface tension [dyne/cm]	$0.22 * (117.3 - T)$	18.0
$\Delta H_{vap}$ [erg/gm]	$2.148 \times 10^9$	$2.455 \times 10^9$

Table 1. Physical properties of nitrogen used in the condensing jet simulations.

The upstream stagnation conditions used by Dankert and Koppenwallner (1978) encompassed a wide range of stagnation temperatures. In the simulations of these conditions it was found that the upstream stagnation temperature,  $T_0$  had a large affect on the particle distribution properties. This effect is shown in Figures 3a, 3b, and 4a, 4b. Figure 3a and 3b show the average particle diameter in a condensing jet for a low  $T_0$  case

and a high  $T_0$  case. Figures 4a and 4b show the particle concentration in a condensing jet for the same low and high  $T_0$ 's. The low  $T_0$  case uses the same conditions as in Figure 2, while the high  $T_0$  case uses a  $T_0 = 200\text{K}$  and all other conditions are the same as in Figure 2.

The average particle diameter for the low and high  $T_0$  profiles exhibited some qualitative differences. The three dimensional profiles of average particle diameter are shown in Figure 3a for the low  $T_0$  case and Figure 3b for the high  $T_0$  case. For the low  $T_0$  jet the average diameter increased with radial distance from the axis, while the higher  $T_0$  jet has the largest average diameter on the centerline. The reason for this qualitatively different behavior is that as  $T_0$  is increased, nucleation and condensation are delayed until lower temperatures and pressures. The condensation rate for higher  $T_0$  jets is therefore lower and is not sufficiently rapid to adjust to the changes in the fluid properties. For the higher  $T_0$  jet the largest condensation rate is found on the centerline where the largest values of temperature, density and pressure are found (within the barrel shock). The largest particles are therefore found on the axis for the higher  $T_0$  jet. For the lower  $T_0$  jet the condensation rate is rapid enough throughout the flow field to adjust to the property changes during the expansion. The main factor in determining the condensation rate in the low  $T_0$  jet is the supersaturation ratio. The location where the lowest temperatures occur (and therefore highest supersaturations) therefore exhibits the largest condensation rates. As in the high  $T_0$  jet the largest temperatures are found on the axis (again, within the barrel shock) so for the low  $T_0$  jet the highest condensation rates are found off axis. The largest particles in the lower  $T_0$  jet are therefore found off axis. To summarize, at the high  $T_0$  the particle growth is limited by the collision rate because the driving force of condensation (i. e. the supersaturation ratio) has no effect on the growth rate, while for the low  $T_0$  case the flow is limited by the supersaturation ratio which determines the region of fastest growth.

The particle concentration profiles for the jets are shown in Figures 4a and 4b. The same qualitative behavior is seen in these Figures, with large particle concentrations beginning off axis downstream of the nozzle exit. The peak concentration for both conditions is found off axis near the nozzle exit during the initial burst of nucleation. The burst of nucleation is caused by the rapid cooling that occurs in the Prandtl-Meyer expansion which causes the pressure on the jet boundary to equal  $P_\infty$ . The rapid cooling that occurs in the expansion causes the gas to be supersaturated off axis, so particles are formed by homogeneous nucleation. The nucleation is delayed on the centerline because the expansion is less rapid.

## REFERENCES

- Abraham, O., Kim, S. S., and Stein, G. D. (1981). *J. Chem. Phys.*, **75** (1), 402.
- Adamson, T. C., Jr. and Nicholls, J. A. (1959). *J. Aerospace Sci.*, **26**, 16.
- Ashkenasas, H. and Sherman, F. S. (1966). *Rarefied Gas Dynamics Symposium*, Academic Press, NY, 106.
- Clarke, J. H. and Delale, C. F. (1986). *Phys. Fluids*, **29** (5), 1398.
- Crowe C. T., and Willoughby, P. G. (1967). *AIAA J.*, **5** (7), 1300.
- Dankert, C. and Koppenwallner, G. (1978). *Rarefied Gas Dynamics Symposium*, Academic Press, 1107.
- Dash S.M. and R. G.Thorpe (1981). *AIAA J.* **19** (7) 842.
- Davydov, L. M. (1971). *Fluid Dynamics - Sov. Res.*, **1** (1), 90.
- Fisher, S. S. (1979). *Phys. Fluids*, **22** (7), 1261.
- Hidy, G. M. and Brock, J. R. *The Dynamics of Aerosoloidal Systems*. Pergamon, Oxford, 1970.
- Koppenwallner, G. and Dankert C. (1987). *J. Phys. Chem.*, **91**, 2482.
- Love, E. S., C. E. Grigsby, L. P. Lee, and M. J. Woodling (1959). *NASA TR-6*.
- Mark T. D. and Castleman, A. W., Jr. (1985). *Advances in Atomic and Molecular Physics*, **20**, 65.
- McGraw, R. and Saunders, J. H. (1984). *Aerosol Sci. Tech.*, **3**, 367.
- Moser, H. O. (1984). *Rev. Sci. Instrum.*, **55** (12), 1914.
- Takagi, T. (1986). *Z. Phys. D - Atoms, Molecules and Clusters*, **3**, 271.
- Wegener, P. P. and Wu, B.J. C. (1977) *Adv. in Colloid and Interface Sci.*, **7**, 325.
- Wen, H. Y., Kasper, G. and Montgomery, D. (1987). *J. Aerosol Sci.*, **19** (1), 1988.





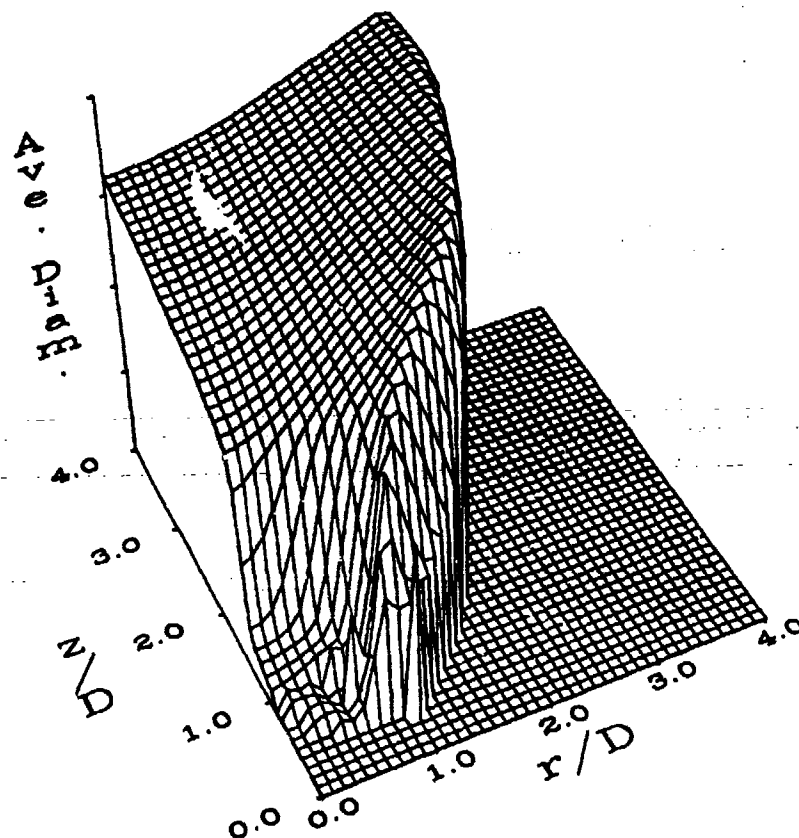


Figure 3a. Average diameter in a condensing nitrogen jet with a low  $T_o$ . The vertical axis is a linear scale from 0.0 to 1.e-5cm.

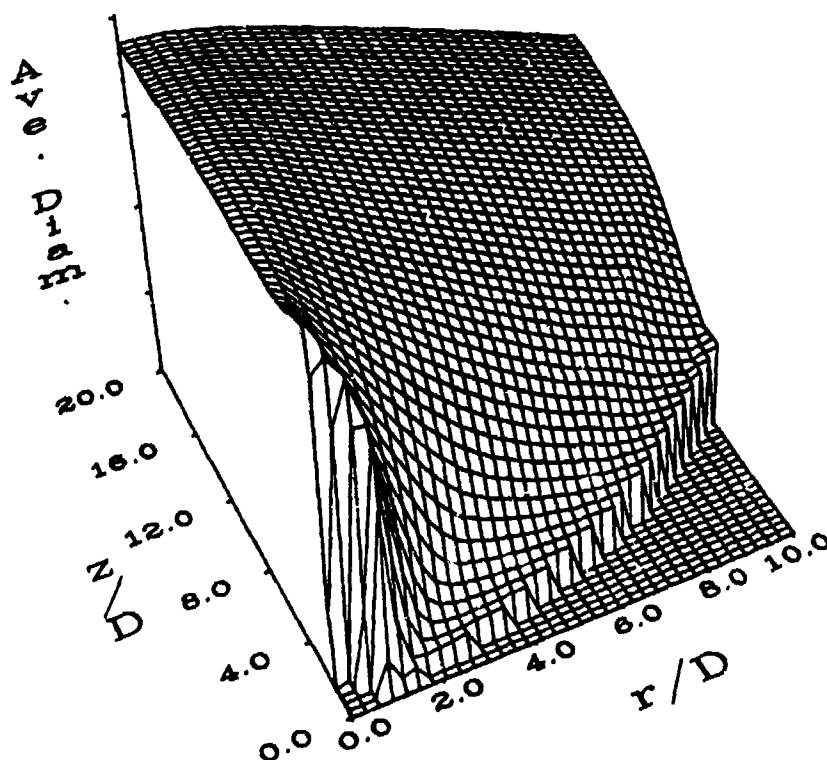


Figure 3b. Average diameter in a condensing nitrogen jet for a jet with a high  $T_o$ . The vertical axis is a linear scale from 0.0 to 1.e-6cm.

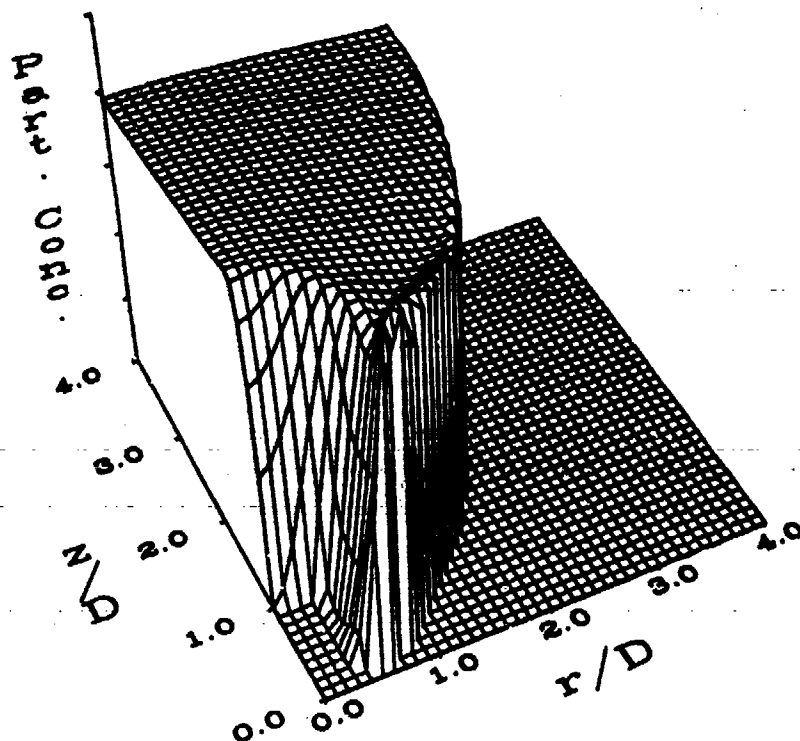


Figure 4a. Particle concentration in a condensing nitrogen jet with low  $T_o$ . Vertical axis is a log scale from  $1.0 \times 10^3$  to  $1.0 \times 10^{11}$  #/cc.

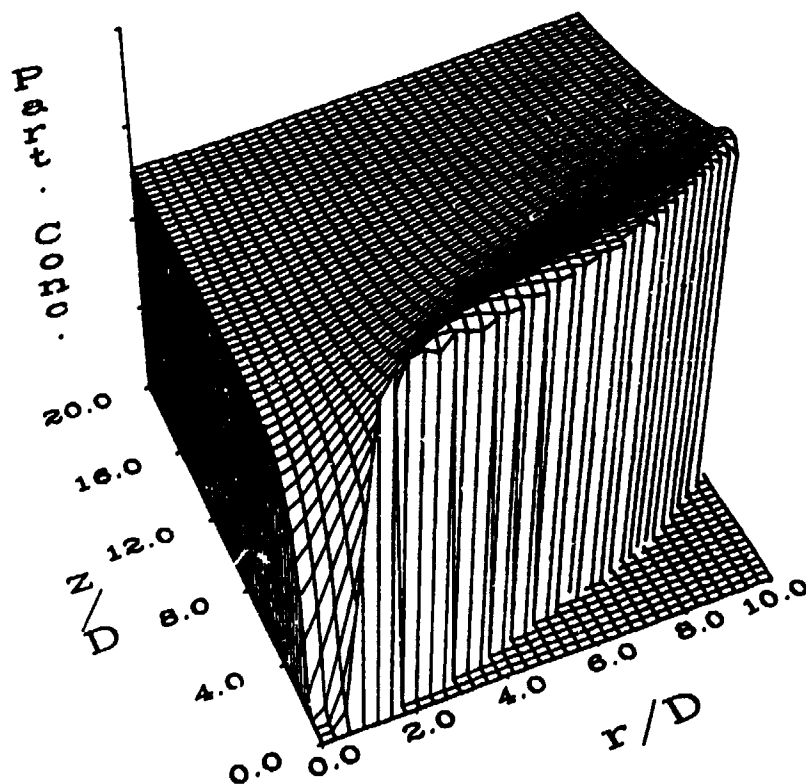


Figure 4b. Particle concentration for a condensing nitrogen jet with high  $T_o$ . The particle concentration axis is a log scale from  $1.0 \times 10^3$  to  $1.0 \times 10^{13}$  #/cc.

**BLANK**

## A NEW STATISTICAL MEASURE OF PLUME OBSCURATION EFFECTIVENESS: MEAN WAITING TIME FOR A WINDOW

J. R. BROCK  
Chemical Engineering Department  
University of Texas  
Austin, Texas 78712

### RECENT PUBLICATIONS, SUBMITTALS FOR PUBLICATION AND PRESENTATIONS

- Wave propagation from laser-induced plasmas in droplets" *Proceedings of the 1990 CRDEC Scientific Conference on Obscuration and Aerosol Research*, CRDEC, U. S. Army, 1990 (with J. Carls)
- "Aerosol jet etching", *Aerosol Sci. Tech.*, 12, 842-856 (1990) (with Y. L. Chen and I. Trachtenberg)
- "A study of low pressure impaction processes", *J. Aerosol Science* 20, 560, 1989. (with B. Jurcik and I. Trachtenberg)
- "Laser-induced breakout and detonation waves in droplets: II. Model", *J. Optical Soc. America B*, In Press, 1990. (with J. C. Carls and Y. Seo)
- "Distributions for moment simulation of aerosol evaporation", *In Press Journal of Aerosol Science* 1990 (with Y. Seo)
- "Comparison between theory and experiment for laser-induced plasma and shock waves in droplets", *Proceedings of the 1989 CRDEC Scientific Conference on Obscuration and Aerosol Research*, CRDEC, U. S. Army, In Press, 1990 (with J. Carls)
- "Statistical properties of windows in atmospheric plumes". *Proceedings of the 1990 CRDEC Scientific Conference on Obscuration and Aerosol Research*, CRDEC, U. S. Army, In Press, 1990
- "Alkane oligomerization and graphite fiber formation in an electrocatalytic system", *Proceedings of the 1990 CRDEC Scientific Conference on Obscuration and Aerosol Research*, CRDEC, U. S. Army, In Press, 1990
- "Particle formation by homogeneous nucleation in expanding flows", *Proceedings of the 1990 CRDEC Scientific Conference on Obscuration and Aerosol Research*, CRDEC, U. S. Army, In Press, 1990 (with B. Jurcik)
- "A finite element solution of the Maxwell equations for absorption and scattering of electromagnetic radiation by a sphere" *Proceedings of the 1990 CRDEC Scientific Conference on Obscuration and Aerosol Research*, CRDEC, U. S. Army, In Press, 1990 (with L. Liebmann)
- "Aerosol jet etching of  $Hg_{1-x}Cd_xTe$ ", *Applied Physics Letters* 56 1682-1685 (1990) (with B. J. Jurcik and I. Trachtenberg)
- Particle formation by homogeneous nucleation in expanding flows" Submitted for publication (1990) (with B. J. Jurcik)
- "Theory and experiment on laser assisted etching of silicon", In Press, AIChE Symposium Series, 1990.
- "A new process for graphite fiber formation from alkane vapors", Submitted for publication, 1990.

### ABSTRACT

Statistical properties of obscurant plume windows (an opening through an obscurant plume through which a target can be acquired) are estimated from limited samples of Smoke Week II data. In these samples, occurrence of windows is estimated to be a Poisson process. From the same data, a frequency function is estimated for window size (length of time a window is open). Acquisition of a target through a window is shown to be a renewal process. This permits derivation of mean waiting time for target acquisition as a function of the length of time necessary to acquire that target. Mean waiting time for a window as a measure of obscurant effectiveness appears to have some advantages over the more common average measures, such as transmission.

### INTRODUCTION

Preliminary work on this problem was described at the recent 1990 CRDEC Scientific Conference on Obscuration and Aerosols. Apparent windows were analyzed from a limited amount of Smoke Week II data. It was easily demonstrated that in two plume samples, windows had, as might be expected for rare events, a Poisson frequency, as shown in Figs. 1 and 2.

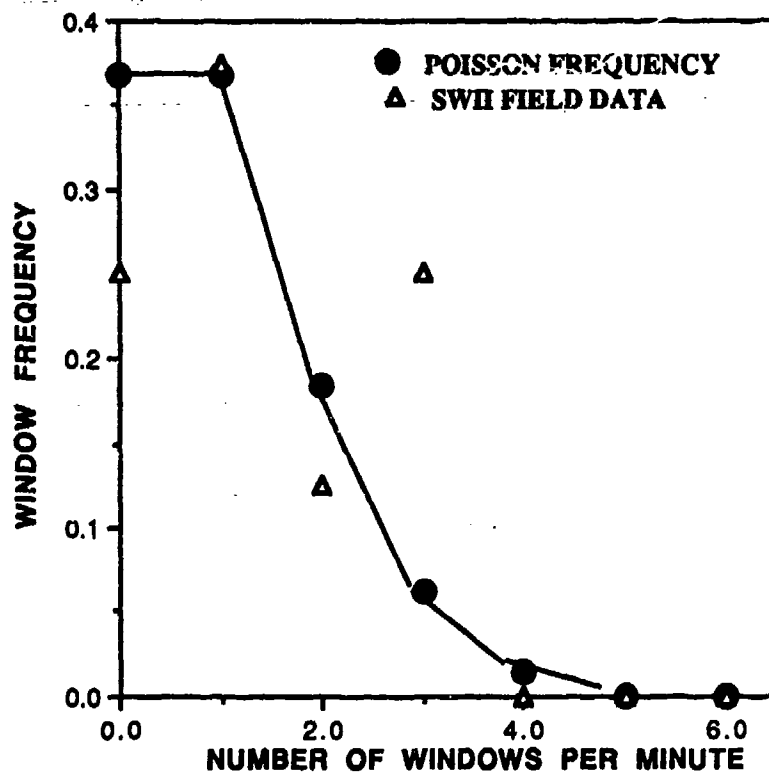


Figure 1. Demonstration of Poisson frequency for windows from SWII data for fog oil plume at  $0.6 \mu\text{m}$  radiation.

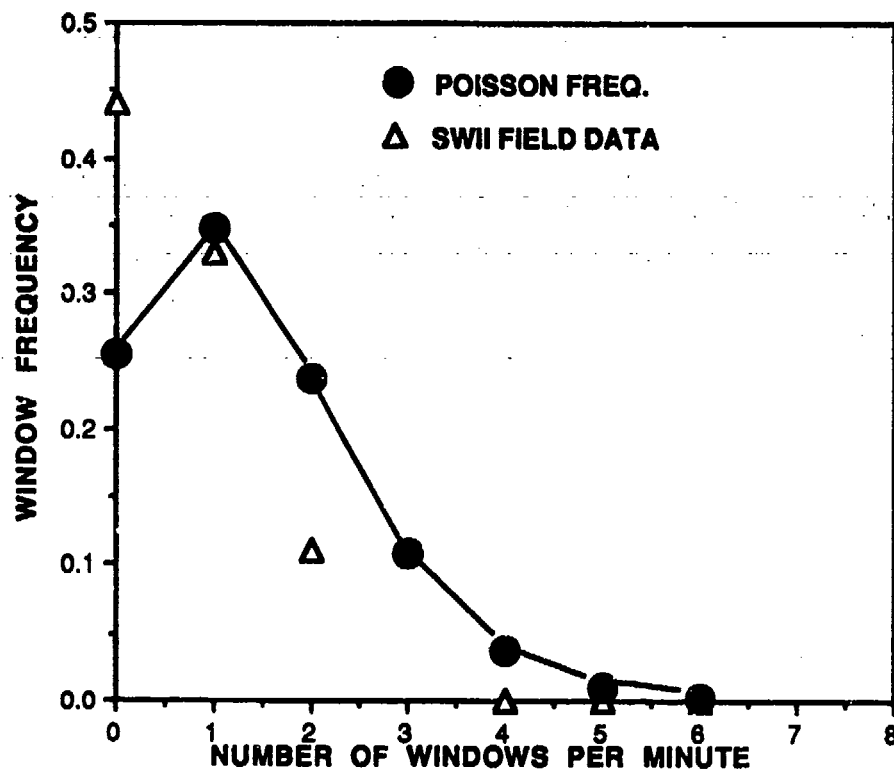


Fig. 2. Demonstration of Poisson frequency for windows from SWII data for fog oil plume at  $1.06 \mu\text{m}$  radiation.

Fig. 3 shows estimate of window size distribution based on the same SWII data for  $0.6 \mu\text{m}$  radiation. This estimate is not believed to be very reliable.

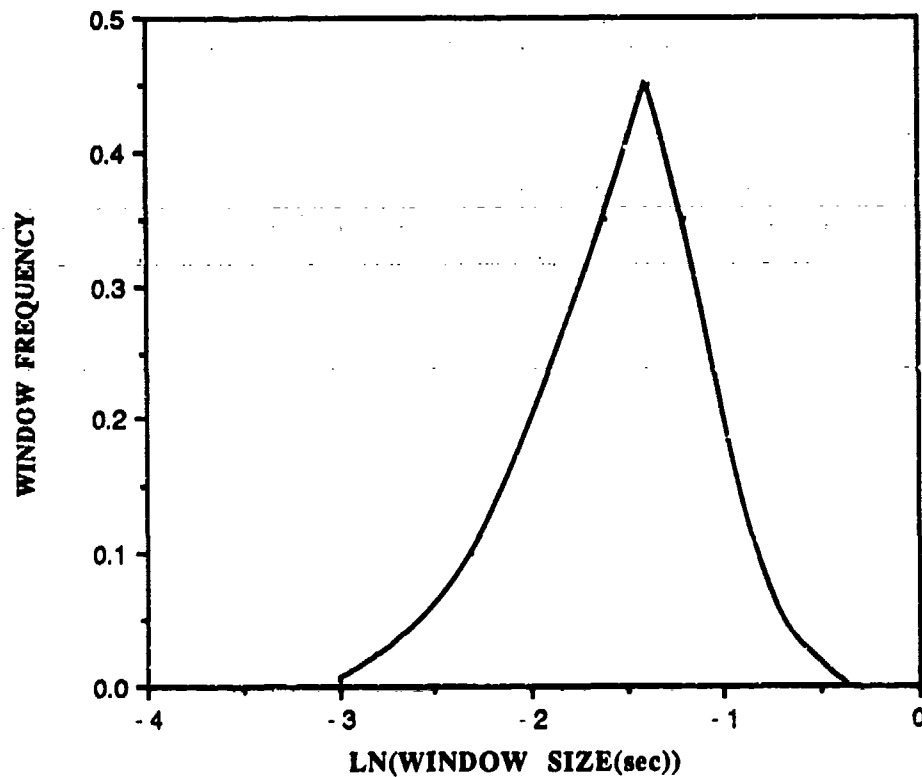


Fig. 3. Distribution of window sizes from SWII data at 0.6  $\mu\text{m}$  radiation.

With the frequencies of windows estimated in this manner and an estimate for distribution of window size, it is possible to obtain an estimate of mean waiting time for a window of a given size using well established principles in probability theory, known as renewal theory (Feller, 1950). For an exponential distribution of window size, it is easy to calculate from renewal theory the mean waiting time for a window as a function of time required for target acquisition, as indicated by Fig. 4



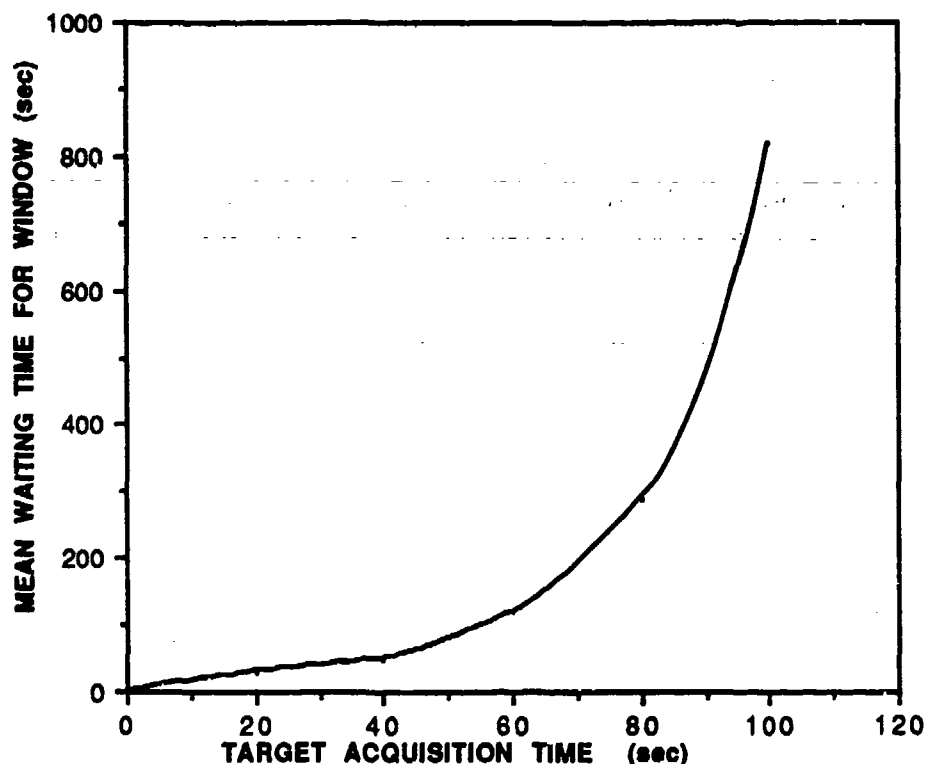


Fig. 4. Mean waiting time for a window as function of time necessary to acquire a target through a fog oil obscurant plume.

It can be seen that there is a premium on target acquisition time, because statistically a long time elapses before a sufficiently large window occurs in the obscurant plume, whereas small windows, corresponding to small target acquisition times, are relatively more frequent. We believe that a stochastic puff model could be developed starting from the usual ideas in puff models (e.g. Panofsky and Dutton, 1987). In this way a model could be constructed to give plume windows that are related to meteorological variables. This would be preferable in our opinion to an approach based on 2nd order closure models, whose application usually requires meteorological data, often not available in field investigations.

#### ACKNOWLEDGMENTS

This work has been supported by CRDEC, U. S. Army. Authors acknowledge with thanks useful discussions with Dr. Ed Stuebing and Dr. Glenn Rubel.

#### REFERENCES

- Feller, W., 1950. *An Introduction to Probability Theory and Its Applications*, John Wiley, NY.
- Panofsky, H. A. and J. A. Dutton, 1986 *Atmospheric Turbulence: Models and Methods for Engineering Applications*, John Wiley, NY.

BLANK

# INTERCEPTIONAL AND DIFFUSIONAL DEPOSITION OF FINE PARTICLES IN FIBROUS FILTERS

MICHAEL SHAPIRO

Faculty of Mechanical Engineering  
Technion - Israel Institute of Technology  
Haifa 32000 Israel  
and

HOWARD BRENNER

Department of Chemical Engineering  
Massachusetts Institute of Technology  
Cambridge, MA 02139

## RECENT PUBLICATIONS, SUBMITTALS, FOR PUBLICATION, AND PRESENTATIONS

- (i) M. Shapiro and H. Brenner, "Dispersion/reaction model of aerosol filtration by porous filters," *Proceedings of the 1989 CRDEC Scientific Conference on Obscuration and Aerosol Research*, R.H. Kohl, Ed.
- (ii) M. Shapiro and H. Brenner, "Dispersion and deposition of aerosol particles in porous filters," *J. Aerosol Sci.* **20**, 951-954 (1989).
- (iii) M. Shapiro and H. Brenner, "Dispersion/reaction model of aerosol filtration by porous filters," *J. Aerosol Sci.* **21**, 97-125 (1990).
- (iv) M. Shapiro, H. Brenner and D. Guell, "Accumulation and transport of Brownian particles at solid surfaces: Aerosol and hydrosol deposition processes," *J. Colloid Interface Sci.* **136**, 552-573 (1990).
- (v) M. Shapiro and H. Brenner, "Diffusion/reaction model of aerosol filtration by fibrous filters," *Proc. of the 23rd Israel Conference on Mechanical Engineering*, Technion-Israel Institute of Technology, Haifa, Israel (May 21-22, 1990), 4pp.
- (vi) D.A. Edwards, M. Shapiro, P. Bar-Yoseph and M. Shapira, "The influence of Reynolds number upon the apparent permeability of spatially-periodic arrays of cylinders," *Phys. Fluids A* **2**, 45-55 (1990).
- (vii) M. Shapiro, I. Kettner and H. Brenner, "Interceptional and diffusional collection of fine particles in fibrous beds. A dispersion model," *Proc. of the 3rd International Aerosol Conference*, Kyoto, Japan (September 24-27, 1990), 4pp.

- (viii) S.R. Dungan, M. Shapiro, and H. Brenner, "Convective-diffusive-reactive Taylor dispersion processes in particulate multiphase systems," *Proc. Roy. Soc. London A* **429**, 639-671 (1990).
- (ix) M. Shapiro and H. Brenner, "Taylor dispersion in the presence of time-periodic convection phenomena. Part I. Local-space periodicity," *Phys. Fluids A* (in press, 1990).
- (x) M. Shapiro and H. Brenner, "Taylor dispersion in the presence of time-periodic convection phenomena. Part II. Transport of transversely oscillating Brownian particles in a plane Poiseuille flow," *Phys. Fluids A* (in press, 1990).
- (xi) D.A. Edwards, M. Shapiro, H. Brenner and M. Shapira, "Dispersion of inert solutes in spatially periodic, two-dimensional model porous media," *Transp. Porous Media* (submitted for publication)
- (xii) L.C. Nitsche and H. Brenner, "Hydrodynamics of particulate motion in sinusoidal pores via a singularity method," *AIChE Jour.* (in press, 1990)
- (xiii) H. Brenner, "Macrotransport processes: Brownian tracers as stochastic averagers in effective-medium theories of heterogeneous media," *J. Statistical Phys.* (in press, 1990).
- (xiv) H. Brenner, "Macrotransport processes," *Langmuir* (in press, 1990).

#### ABSTRACT

Characteristic filtration lengths of fibrous filters collecting spherical submicrometer aerosol particles are calculated over a wide range of particle sizes and filtration operating parameters. The calculations were based upon the dispersion/reaction model for aerosol transport and filtration in porous filters, and were performed for spatially periodic models of fibrous arrays of circular cylinders in square arrays. Several orientations of the direction of mean air flow relative to the lattice axes were investigated. A comparison between our theoretical results, available experimental data, and the results of competitive filtration models, demonstrated the greater accuracy of our dispersion/reaction model in correlating characteristic filtration lengths of submicrometer particles possessing diameters less than 0.3-0.5 $\mu$ m. The filtration rate of larger particles, governed primarily by the interception mechanism, is shown to be sensitive to the choice of the direction of the mean air flow relative to the axes of the periodic array.

The process of aerosol filtration in porous filters occurs when an inlet air stream containing aerosol particles passes through the filter bed, depositing (a portion of the) aerosol particles upon the surfaces of the collector elements. This study is concerned with calculation of the filter efficiency

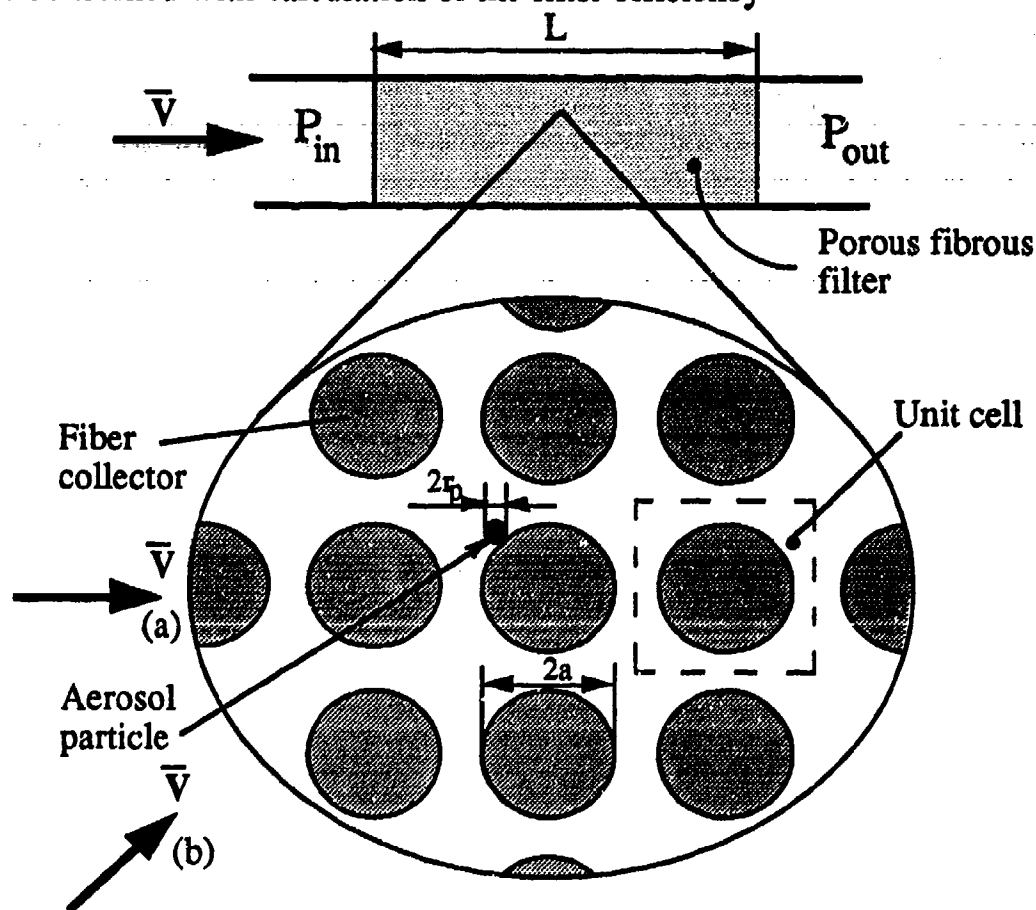


Figure 1. Spatially periodic (lattice) microstructure of a porous filter used in calculations: (a) Superficial velocity  $\bar{V}$  parallel to a principal lattice axis ("square array"); (b) Superficial velocity  $\bar{V}$  inclined  $45^\circ$  to the principal lattice axes ("staggered array").

$$\eta = 1 - P_{\text{out}}/P_{\text{in}}, \quad (1)$$

which is defined in terms of the respective inlet and outlet aerosol particle concentrations,  $P_{\text{in}}$  and  $P_{\text{out}}$  (see Fig. 1). This efficiency constitutes the main parameter of engineering interest, and is dependent upon filter dimensions, aerosol properties, and filtration operating parameters. Leers (1957) found that

the filter efficiency decays exponentially with increasing filter length  $L$  (all other things being equal), and thereby proposed the following semi-empirical formula:

$$\eta = 1 - \exp(-L/\ell_f), \quad (2)$$

wherein  $\ell_f$  (hereafter termed as the *characteristic filtration length*) is an  $L$ -independent coefficient, possessing the dimensions of length. The physical and engineering significance of this formula lies in the fact that it separates the effects of the filter's external dimension  $L$  from its intrinsic aerosol collection properties, embodied in  $\ell_f$ . The aerosol filtration length to depends upon the microstructure of the filter, the filtration operating parameters, and the aerosol particle size (Davies, 1973; Tardos *et al.*, 1978). This particle size essentially determines the physical mechanisms responsible for bringing aerosol particles to the collector surfaces, where the particles are normally trapped and retained due to the action of the short-range Van der Waals forces. Collection of fine submicrometer-sized particles, namely those possessing diameters  $2r_p \leq 0.3 \mu\text{m}$ , is governed by their Brownian diffusion towards collector surfaces. For larger particles this mechanism acts in combination with the interception mechanism, the latter being a purely geometric entrapment of those particles whose centers approach the collector surface along fluid streamlines to within a distance equal to the particle radius  $r_p$ .

This research deals with determining the characteristic filtration lengths  $\ell_f$  of fibrous filters collecting aerosol particles by diffusional and interceptional mechanisms. This problem had earlier been treated (Stechkina and Fuchs, 1966; Kirsch and Fuchs, 1968) by applying classical filtration theory (Pich, 1966), which furnished the following formula:

$$\ell_f = a/\eta_c f(\epsilon), \quad (3)$$

where  $2a$  is the collector diameter and  $\eta_c$  is the so-called unit-bed efficiency -- an essentially empirical quantity whose definition and evaluation hinge upon a chain of *ad hoc* assumptions pertaining to the filter microstructure microscale flow field, and aerosol concentration distribution prevailing within the bed;  $f(\epsilon)$  is a function dependent upon the bed porosity  $\epsilon$ , the exact functional dependence being a controversial issue. A more detailed and more carefully documented

criticism of classical filtration theory appears elsewhere (Shapiro and Brenner, 1990).

Our dispersion/reaction model of aerosol filtration by porous filters (Shapiro and Brenner, 1989; 1990) provides a precise scheme for demonstrating the existence of the characteristic aerosol filtration length  $\ell_f$  as an intrinsic,  $L$ -independent, physical quantity, as well as for computing it from the parameters characterizing the microscale problem. The model is based on a precise physicomathematical formulation of the aerosol microtransport and deposition processes throughout the *entire* filter bed (rather than within a *single* unit bed element), which bed is assumed to possess a spatially-periodic (lattice) structure. This scheme allows a precise calculation of the three Darcy-scale transport coefficients,  $\bar{U}^*$ ,  $\bar{D}^*$  and  $\bar{K}^*$ , without introducing any *ad hoc* assumptions, or using the concept of single-element efficiency, such as is done in classical filtration theory (Davies, 1973). These three coefficients are subsequently used to calculate the total filtration efficiency  $\eta$ , eschewing the *ad hoc* formula (3). In many practically important cases (Shapiro and Brenner, 1990) the characteristic filtration length is given by

$$\ell_f = \bar{U}^* / \bar{K}^*, \quad (4)$$

where  $\bar{U}^* = |\bar{\mathbf{U}}^*|$  is the aerosol's Darcy-scale mean speed and  $\bar{K}^*$  is the volumetric aerosol deposition-rate coefficient.

Figure 1 schematically represents the microscale structure and geometry of a model porous fibrous filter used in the dispersion/reaction model. Fibrous beds composed of square and staggered arrays of cylinders were used in the calculations. First, spatially periodic flow fields within these arrays were calculated by the finite element technique. An extensive description of the flow patterns thereby obtained, as well as the bed permeability data thereby derived, are summarized by Edwards *et al.* (1990).

Next, the three Darcy-scale aerosol transport coefficients were calculated for each array, which data were further used to evaluate the characteristic filtration length  $\ell_f$  via Eq. (4). These calculations necessitated numerical solutions of several eigenvalue problems formulated within a single unit cell of the spatially periodic filter bed. A detailed description of the requisite computational scheme is outlined by Shapiro and Brenner (1990).

The Darcy-scale aerosol transport coefficients depend, *inter alia*, upon the various microscale particle deposition mechanisms included in the model. Here, it was assumed that particle collection is affected only by the Brownian motion and interception mechanisms. As such, the Darcy-scale coefficients and, hence, the concomitant characteristic filtration length are functionally dependent upon the bed element Péclet number,  $Pe = 2\bar{V}a/D$ , the interception parameter  $R_p = r_p/a$ , and the bed porosity  $\varepsilon$  (as well as the collector Reynolds number  $Re = 2\bar{V}a/\nu$ , with  $\nu$  the air's kinematic viscosity).

The characteristic filtration length was found to increase with the increasing bed porosity and Péclet number. The influence of the interception parameter is shown in Fig. 2 for  $Pe=10$ . Observe that  $\ell_f$  decreases with increasing aerosol particle size, thereby leading to an enhancement of the aerosol collection rate. This effect is seen to be the most profound for highly porous filters, namely those possessing the smallest solidities  $1-\varepsilon$ . The relative influence of the interception collection mechanism is found to be more pronounced for high, rather than low Péclet numbers, corresponding to larger aerosol particles. This generally accords with experimental observations, which reveal that with increasing aerosol particle size the diffusion particle capture mechanism becomes less efficient. An extensive investigation of the effects of various filtration parameters upon the aerosol transport coefficients is presented by Shapiro *et al.* (1990).

Figure 3 compares the numerical  $\ell_f$  values derived from our dispersion/reaction model with the semi-empirical model of Stechkina *et al.* (1969), as well as with the experimental results of Lee and Liu (1977) obtained for Dacron filters of  $11\mu\text{m}$  diameter. For all calculations performed, the characteristic filtration lengths calculated for the square array were larger than for the staggered array, all other things being equal. For aerosol particles possessing diameters  $2r_p \leq 0.2\mu\text{m}$ , the experimental values of  $\ell_f$  lie between the two curves calculated for the respective square and staggered array configurations. In this submicrometer range of aerosol diameters the model of Stechkina *et al.* (1969) yields much smaller values of  $\ell_f$ , thereby significantly overestimating the aerosol filtration rate. For larger particles, where Brownian diffusion effects are weaker, and hence for which the collection process is due primarily to interception, our dispersion/reaction calculations for square arrays



overestimate  $\ell_f$ . On the other hand, the model of Stechkina *et al.* (1969) still yields smaller values of the characteristic filtration length in this range of particle diameters.

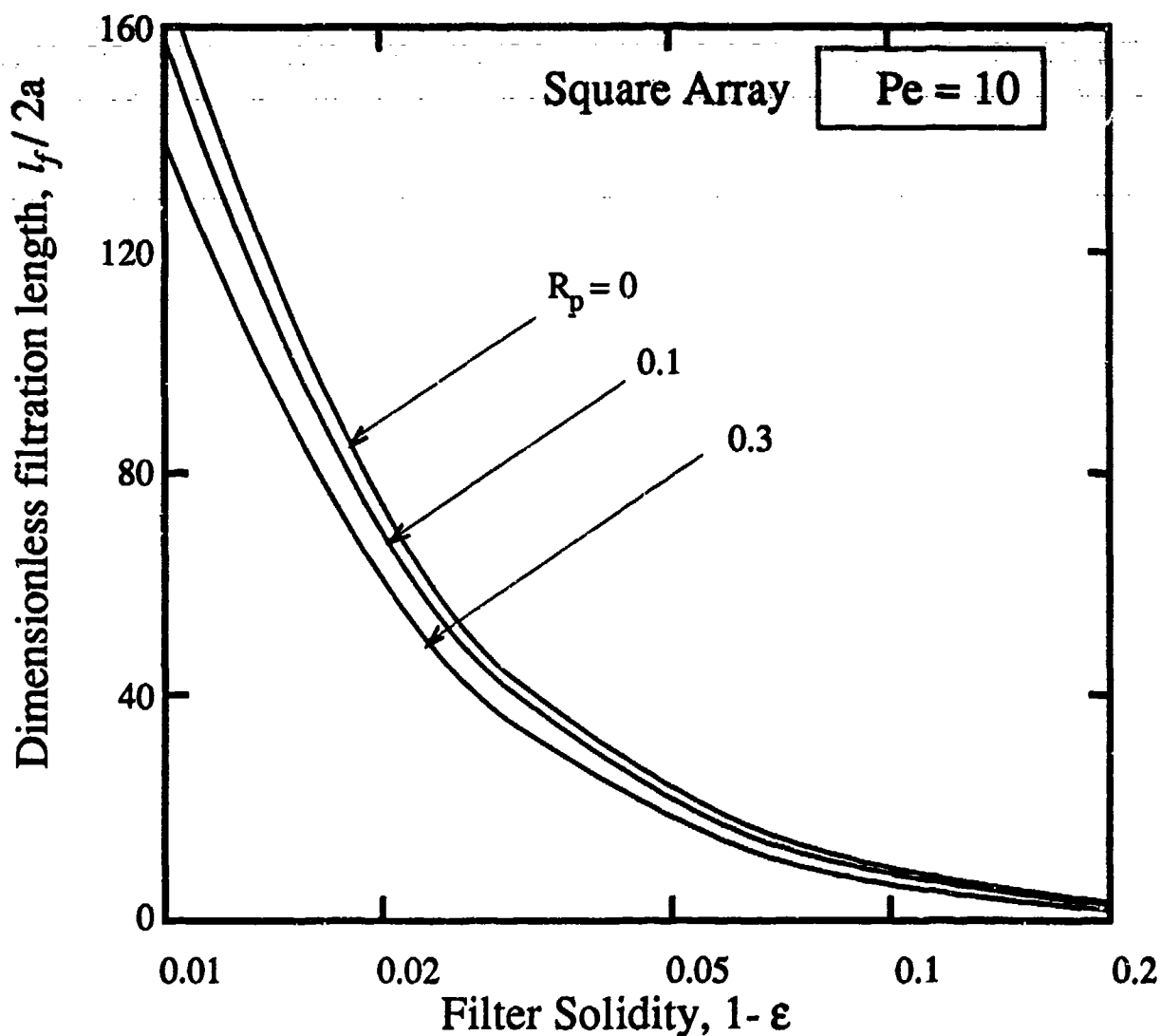


Figure 2. Dimensionless filtration length  $l_f$  vs filter bed solidity  $1 - \epsilon$

In general, the agreement between the present dispersion/reaction results and the experimental data was found to improve with the decreasing superficial air stream velocity, as well as with increasing tortuosity of the intracellular flow pattern (as embodied in the angle of the mean stream-velocity orientation of the "staggered array"). It may be inferred that more elaborate geometric lattice

models of the the filter bed (namely those containing several elements within a single cell, and hence more closely approximating the porous beds encountered in practice) would be expected to agree better with the experimental measurements.

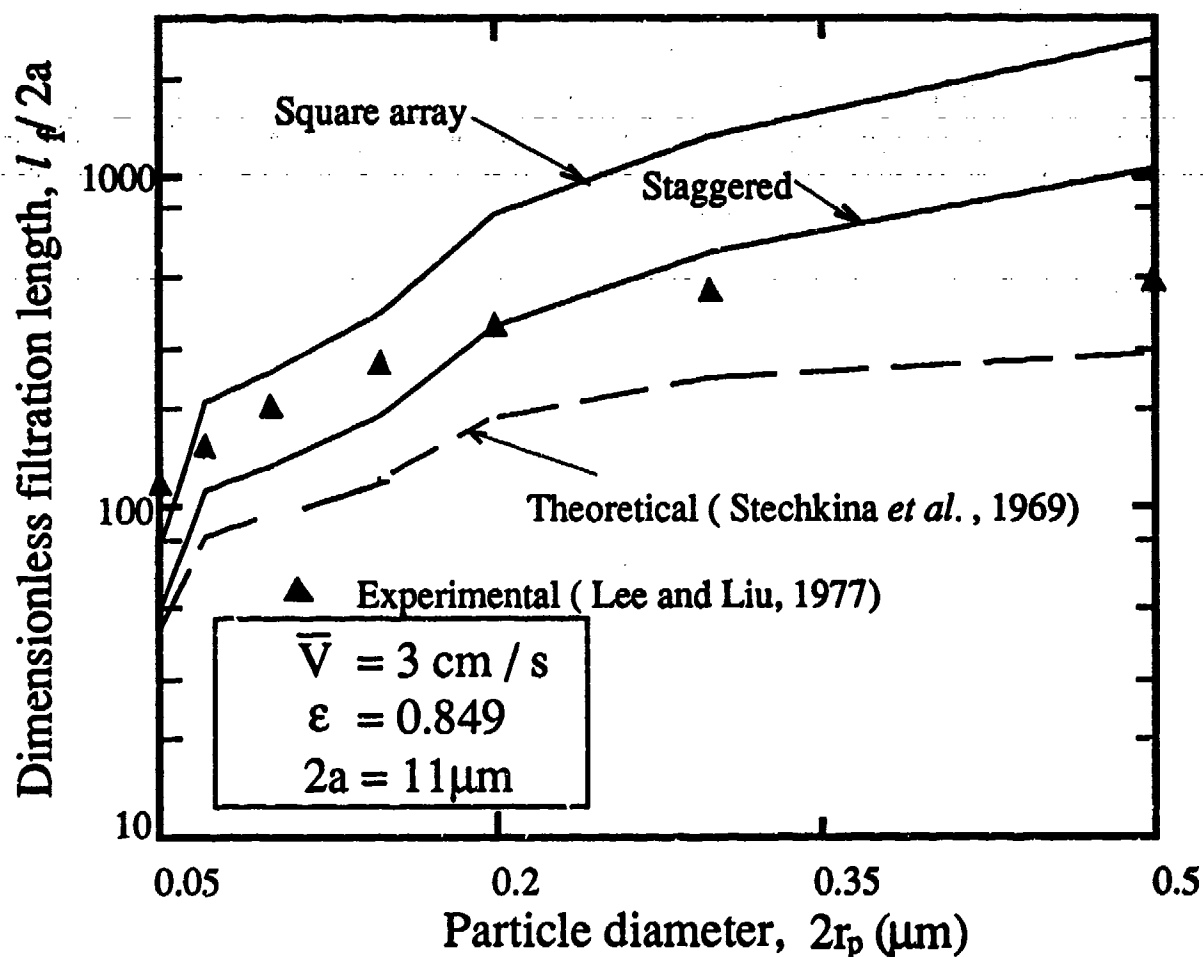


Figure 3. Characteristic filtration length vs particle diameter.

### ACKNOWLEDGEMENTS

This work was supported by and the U.S. Army Research Office (Contract No. DAAL03-87-K-0128). M. Shapiro acknowledges the support of the Basic Research Foundation administered by the Israel Academy of Science and Humanities

## REFERENCES

- Davies, C.N. *Air Filtration*. Academic Press, London (1973).
- Edwards, D.A., Shapiro, M., Bar-Yoseph, P. and M. Shapira (1990). The effect of Reynolds number upon the apparent permeability of spatially periodic arrays of cylinders. *Phys. Fluids A*, 2 45-55.
- Kirsch, A.A. and N.A. Fuchs (1966). Studies on fibrous aerosol filters - III. Diffusional deposition of aerosols in fibrous filters. *Ann. Occup. Hyg.* 11, 299-304.
- Lee, K.W. and B.Y.H. Liu (1982). Experimental study of aerosol filtration by fibrous filters. *Aerosol Sci. Technol.* 1, 35-52.
- Pich, J. (1966) Theory of aerosol filtration by fibrous and membrane filters, In "Aerosol Science" (ed. by C.N. Davies), Academic, London, pp. 223-285.
- Shapiro, M. and H. Brenner (1989). Dispersion and deposition of aerosol particles in fibrous filters. *J. Aerosol Sci.*, 20, 951-954 .
- Shapiro, M. and H. Brenner (1990). Dispersion/reaction model of aerosol collection by porous filters. *J. Aerosol Sci.*, 21, 97-125.
- Shapiro, M., Kettner, I.J. and H. Brenner (1990). Coarse-scale transport mechanics and collection of submicrometer aerosol particles in fibrous filters. (In preparation).
- Stechkina, I.B. and N.A. Fuchs (1966). Studies on fibrous aerosol filters - I. Calculation of diffusional deposition of aerosol in fibrous filters. *Ann. Occup. Hyg.* 9, 59-64.
- Stechkina, I.B., Kirsch, A.A. and N.A. Fuchs (1969). Studies on fibrous filters - IV. Calculation of aerosol deposition in model filters in the range of maximum penetration. *Ann. Occup. Hyg.* 12, 1-8.
- Tardos, G.I., Abuaf, N. and C. Gutfinger (1978). Dust filtration by granular bed filters: theories and experiments. *J. Air Poll. Contr. Assoc.* 28, 354-361.

BLANK

**FLUCTUATIONS OF INTEGRATED CONCENTRATIONS THROUGH AN  
AEROSOL PLUME IN THE ATMOSPHERIC SURFACE LAYER**

**M. Poreh, A. Hadad  
Technion-Israel Institute of Technology  
Haifa, Israel**

**and**

**J. E. Cermak  
Colorado State University  
Fort Collins, Colorado 80523**

**RECENT PUBLICATIONS, SUBMITTAL FOR PUBLICATION AND PRESENTATIONS:**

- A) M. Poreh, A. Hadad, and J. E. Cermak, "Analysis of the Fluctuations of Obscuration Through a Ground Level Aerosol Source," Proceedings of the 1989 CRDEC Scientific Conference on Obscuration and Aerosol Research, Aberdeen Proving Ground, MD, 27-30 June 1989, CRDEC-SP-026 (August 1990), pp. 9-14.
- B) M. Poreh, A. Hadad, and J. E. Cermak, "Fluctuations of Visibility Through a Ground Level Aerosol Plume," Preprint Volume, Proceedings of the Ninth Symposium on Turbulence and Diffusion, AMS, Roskilde, Denmark, 30 April-3 May 1990, pp. 141-144, CEP89-90MP-AH-JEC6.
- C) M. Poreh and J. E. Cermak, "Experimental Study of Aerosol Plume Dynamics, Part V, Measurements of Vertical Integrated Concentration Fluctuations in the Atmospheric Boundary Layer," Final Annual Report for Department of the Army, U.S. Army Armament Research and Development Command, Chemical Systems Laboratory, Aberdeen Proving Ground, MD, August 1990, 47 p., CER90-91MP-JEC6.
- D) M. Poreh and J. E. Cermak, "Fluctuations of Line Integrated Concentrations Across a CO<sub>2</sub> Plume," Summary Paper, to be presented at the Eighth International Conference on Wind Engineering, 8-12 July 1991, London, Ontario, CEP90-91MP-JEC3.

**ABSTRACT**

This paper describes new measurements of Vertical Integrated Concentrations downwind from a neutrally buoyant, ground-level, steady point source in a simulated neutrally stratified atmospheric boundary layer using a new improved IR/CO<sub>2</sub> system and summarizes findings of the CRDEC sponsored project entitled "Experimental Study of Aerosol Plume Dynamics." The work is fully described in C) listed above and in previous publications of the authors which are listed in the references.

**BACKGROUND**

Obscuration of ground objects from elevated observers by plumes of aerosols is related to the Vertical Integrated Concentration (VIC) of the aerosols along the line of vision, which is defined as

$$VIC(x,y,t) = \int_0^{\infty} C(x,y,z,t) dz .$$

The value of such integrals fluctuates with time and their statistical properties are of considerable interest (Gifford, 1959; Hanna, 1984; Robins, 1978). A novel Infrared/Carbon-Dioxide (IR/CO<sub>2</sub>) system for measuring the instantaneous value of VIC in small scale models of plumes diffusing in the atmospheric surface layer has been developed (Poreh and Cermak, 1987, 1988 and 1989). Preliminary measurements with the first prototype of the system, which had a relative high noise-to-signal ratio and a slow response, were reported in Poreh and Cermak (1987 and 1989). In a separate publication a two-coefficient semi-empirical model, which describes the Probability Density Function (PDF) of VIC was presented by Poreh, Hadad and Cermak (1989a and 1990). Recently, a new, fast response, IR/CO<sub>2</sub> system with a reduced noise level has been assembled. New measurements of VIC were made using the new system at the Meteorological Wind Tunnel at CSU (Poreh and Cermak, 1990a). A summary of the results is presented below.

### SUMMARY OF THE RESULTS

Figure 1 shows a typical time ( $T^* = tU/\delta$ ) variation of the dimensionless parameter  $VIC^* = VIC \delta U/Q$ , where  $\delta$  is the thickness of the boundary layer,  $U$  is the mean free velocity and  $Q$  is the strength of the CO<sub>2</sub> source, at an off-center location ( $y/\sigma$ ) downwind of the source. The figure demonstrates large fluctuations and intermittency of VIC. The mean value of  $VIC^*$ , denoted by  $VICM^*$ , at that location was 0.99, whereas the rms of the fluctuations was  $vic'^* = 3.28$ .

Analysis of 120 runs showed that the lateral distribution of  $VICM^*$  at each  $x$  is Gaussian and can be described by  $VICM^*(y) = VICM^*(0)\exp(-\eta^2/2)$ , where  $\eta = y/\sigma$  and  $\sigma(x)$  is the rms of the lateral displacement of the aerosols. The same Gaussian curve describes the distribution of the relative mean ground-level concentrations  $C^*$ . Figures 2 and 3 show the variation of  $\sigma(x)$  and of  $VICM^*(x,0)$  versus  $x/\delta$ . Figure 4 shows the distributions of the relative values of  $vic'^*/VICM^*$  at different locations, which are also similar, namely this ratio is a function of  $y/\sigma$  and practically independent of the distance  $x$ . The measurements of VIC were used to calculate  $P(a)$  -- the probability that the relative instantaneous value of  $VIC^*/VICM^*$  exceeds a given ratio  $a$ . No attempt was made to deduct the contribution of the noise to the value of  $P(a)$ . Figure 5 shows the measured and calculated values of  $P(a)$  at different locations along the centerline of the plume. The calculations are done using the model of Poreh et al. (1990a). The values of the two coefficients in the model were determined using the above mentioned preliminary data. Figures 6 and 7 show the distributions of  $P(a)$  at the edge of the plume. Again, an approximate similarity is found, but the new data make it possible to observe a small effect of the distance from the source particularly at  $y = 0$ . Figure 8 shows the effect of the source height  $z$  on the distributions of  $P(a)$ .

Analysis of the measurements show that the VIC fluctuations at different locations downwind of the source exhibit an approximate similarity, in the sense that dimensionless statistical variables based on the mean value of VIC at the centerline of the plume at each distance, are functions of the dimensionless off-center location  $y/\sigma$  and only slightly dependent on the distance  $x$ .

## PLANNED FUTURE STUDIES

The IR/CO<sub>2</sub> measurement system provides a unique means for acquisition of VIC statistics of plumes generated by various source configurations for a wide variety of atmospheric surface layer (ASL) types. As resources become available, VIC data for steady and instantaneous sources in simulated ASLs for surfaces of different roughness and thermal stratification will be acquired.

Development of an IR/CO<sub>2</sub> system for measurement of concentration fluctuations at a point is under consideration for future research.

## REFERENCES

1. Gifford, F. G. (1959), Statistical Properties of a Fluctuating Plume Dispersion Model, Adv. Geophys., Vol. 6, pp. 117-138.
2. Robins, A. G. (1978), Plume Dispersion from Ground-Level Sources in Simulated Atmospheric Boundary Layers, Atmospheric Environment, Vol. 12, pp. 1033-1044.
3. Hanna, S. R. (1984), Concentration Fluctuations in a Smoke Plume, Atmospheric Environment, Vol. 18, pp. 1091-1106.
4. Poreh, M. and J. E. Cermak (1984), Wind Tunnel Simulation of Diffusion in a Convective Boundary Layer, Boundary Layer Meteorology, Vol. 30, pp. 431-455. Also see: Proceedings of the 1984 CRDC Conference on Obscuration and Aerosol Research, Aberdeen Proving Ground, MD, June 1984.
5. Poreh, M. and J. E. Cermak (1984a), Criteria for Wind-tunnel Simulation of Particle Plumes in the Atmospheric Surface Layer, Proceedings of the 1984 CRDC Conference on Obscuration and Aerosol Research, Aberdeen Proving Ground, MD, June 1984.
6. Poreh, M. and J. E. Cermak (1985), Study of Neutrally Buoyant Plumes in a Convective Boundary Layer with mean Velocity and Shear, AMS Seventh Symposium on Turbulence and Diffusion, 12-15 November 1985 in Boulder, CO.
7. Poreh, M. and J. E. Cermak (1985a), Diffusion in an Atmospheric Layer with an Elevated Inversion, Proceedings of the 1985 CRDC Conference on Obscuration and Aerosol Research, Aberdeen Proving Ground, MD, June 1985.
8. Poreh, M. and J. E. Cermak (1985b), Wind-tunnel Simulation of a Particle Plume with Appreciable Settling Velocities in a Neutrally Buoyant Atmospheric Surface Layer, Proceedings of the 1985 CRDC Conference on Obscuration and Aerosol Research, Aberdeen Proving Ground, MD, June 1985.
9. Poreh, M. and J. E. Cermak (1987), Experimental Study of Aerosol Plume Dynamics, Part III: Wind Tunnel Simulation of Vertical Integrated Concentration Fluctuations, CSU Report No. CER87-88MP-JEC4.
10. Poreh, M. and J. E. Cermak (1988), Instrumentation for Measuring Fluctuations of Horizontally and Vertically Integrated Concentrations in Wind-tunnel Plumes, Fourth International Workshop on Wind and Water Tunnel

Modeling, Karlsruhe, W. Germany, October 1988, to be published in Atmospheric Environment (1990).

11. Poreh, M. and J. E. Cermak (1989), Small Scale Modeling of Line Integrated Concentration Fluctuations, Proceedings of the Sixth U.S. National Wind engineering Conference, Houston, TX, Journal of Wind Engineering and Industrial Aerodynamics, Vol. 3, Part 1, October 1990, pp. 665-673.
12. Poreh, M., A. Hadad, and J. E. Cermak (1989a), Analysis of the Fluctuations of Obscuration through a Ground Level Aerosol Source, Proceedings of the 1989 CRDC Conference on Obscuration and Aerosol Research, Aberdeen Proving Ground, MD, 27-30 June 1989, CRDEC-SP-026 (August 1990), pp. 9-14.
13. M. Poreh, A. Hadad, and J. E. Cermak, Fluctuations of Visibility Through a Ground Level Aerosol Plume, Preprint Volume, Proceedings of the Ninth Symposium on Turbulence and Diffusion, AMS, Roskilde, Denmark, 30 April-3 May 1990, pp. 141-144, CEP 89-90MP-AH-JEC6.
14. M. Poreh and J. E. Cermak, Experimental Study of Aerosol Plume Dynamics, Part V, Measurements of Vertical Integrated Concentration Fluctuations in the Atmospheric Boundary Layer, Final Annual Report for Department of the Army, U.S. Army Armament Research and Development Command, Chemical Systems Laboratory, Aberdeen Proving Ground, MD, August 1990, 47 p., CER90-91MP-JEC6.



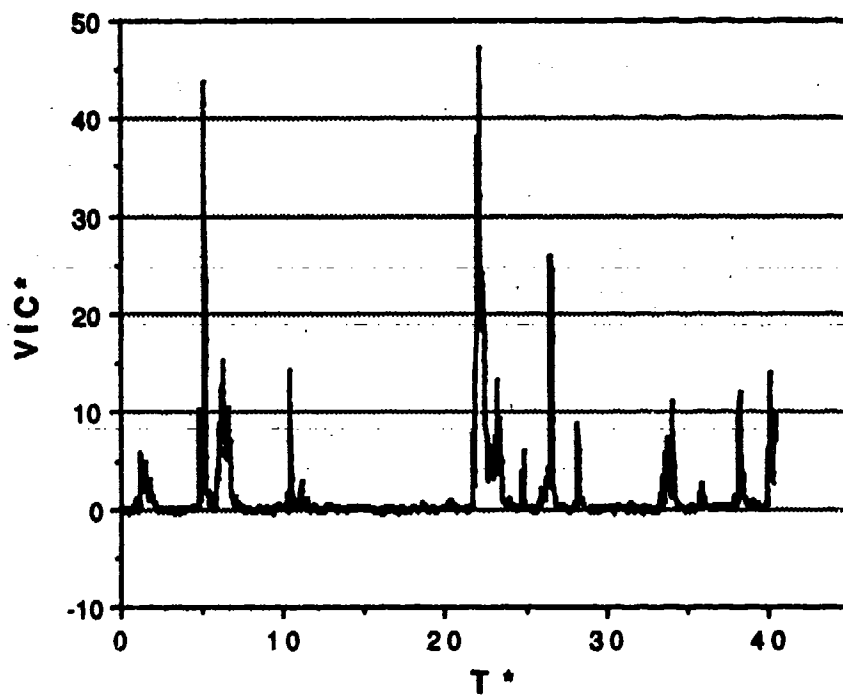


FIGURE 1. RECORDED  $VIC^*$  FLUCTUATIONS AT  $x = 50$  cm,  $y/\sigma = -2.41$  ( $VICM^* = 0.99$ ,  $vic^* = 3.28$ ,  $\gamma = 0.4$ ).

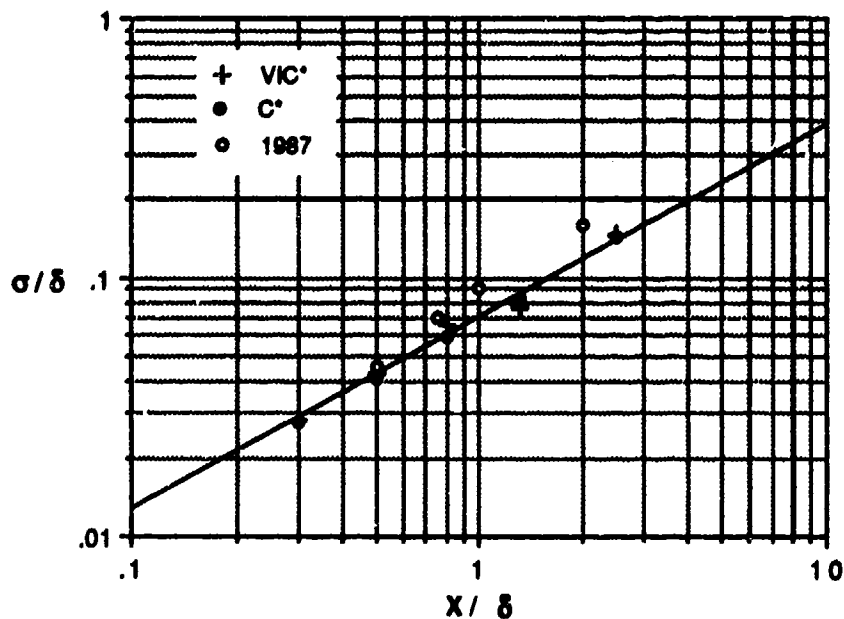


FIGURE 2. THE VARIATION OF  $\sigma/\delta$  VERSUS  $x/\delta$  ACCORDING TO THE  $VIC^*$  AND  $C^*$  MEASUREMENTS IN THE PRESENT STUDY AND IN POREH AND CERMAK (1987).

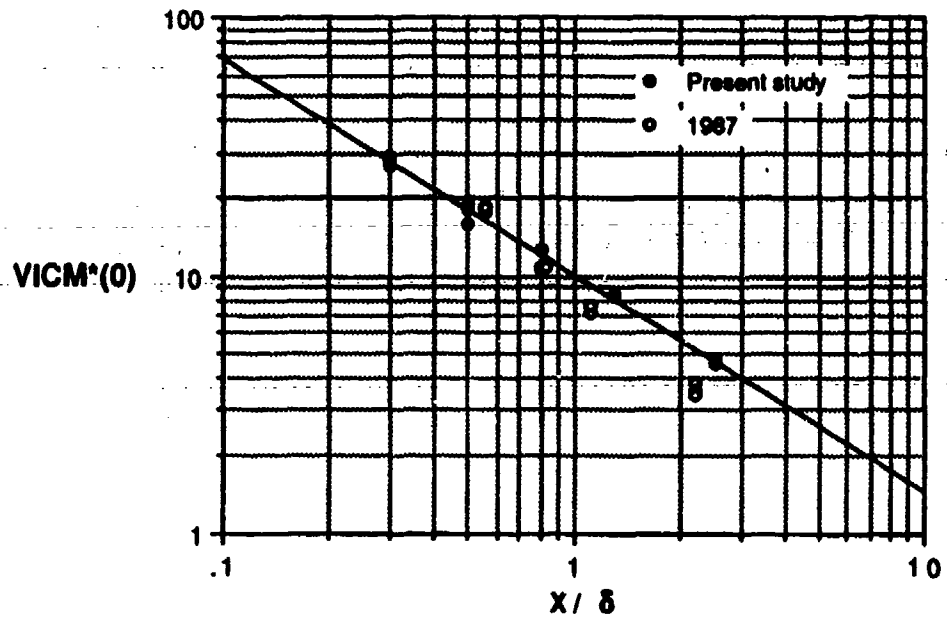


FIGURE 3. VARIATION OF  $VICM^*$  ALONG THE CENTERLINE OF THE PLUME.

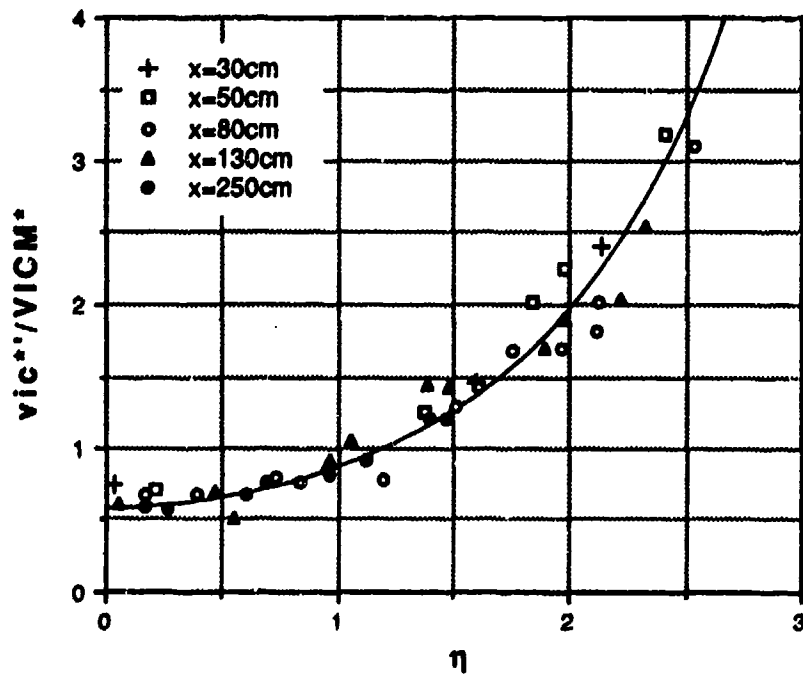


FIGURE 4. THE DISTRIBUTION OF  $vic''(\eta)/VICM^*(\eta)$ .

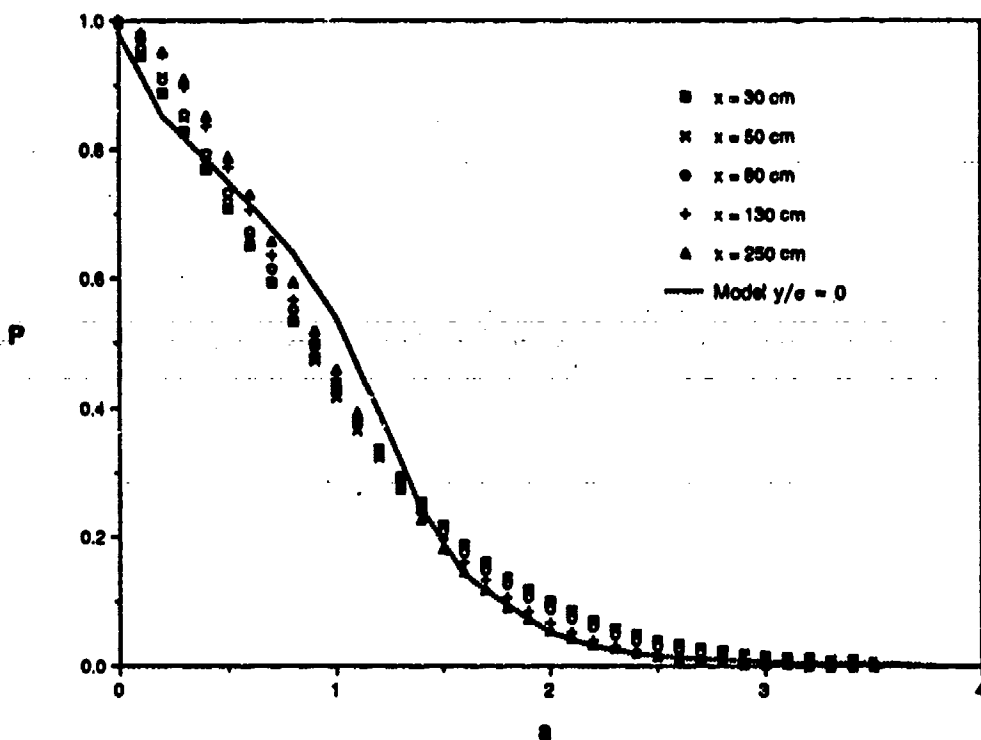


FIGURE 5. THE PROBABILITY  $P(a)$  THAT  $VIC^*/VICM^*$  EXCEEDS THE VALUE  $a$  NEAR THE CENTERLINE OF THE PLUME.

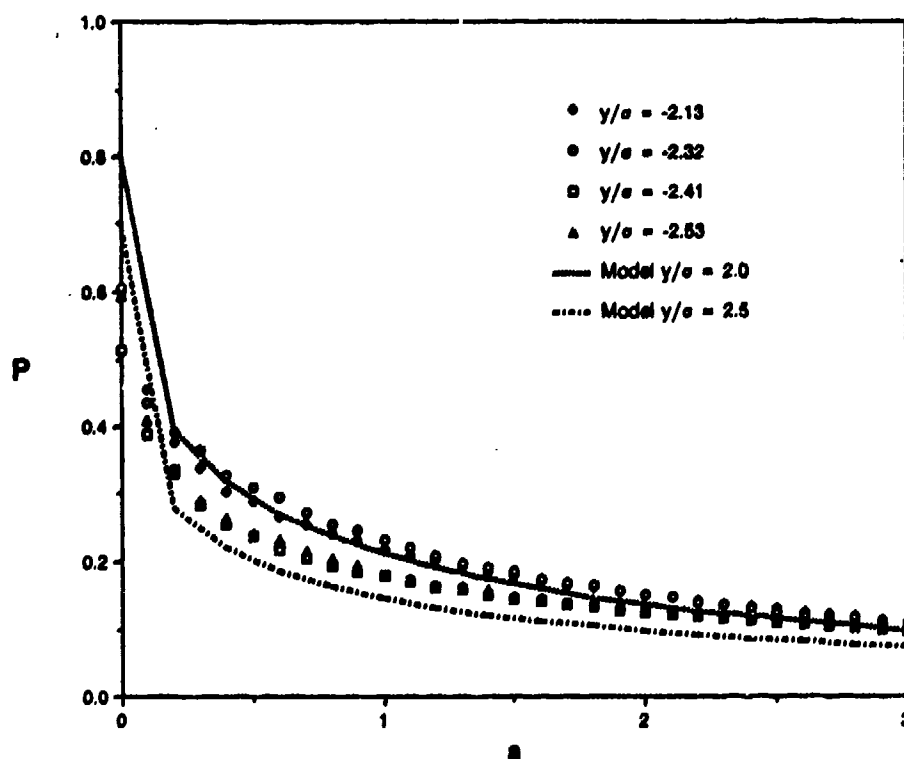


FIGURE 6. THE PROBABILITY  $P(a)$  THAT  $VIC^*/VICM^*$  EXCEEDS THE VALUE  $a$  FOR  $2.0 < y/\sigma < 2.5$ .

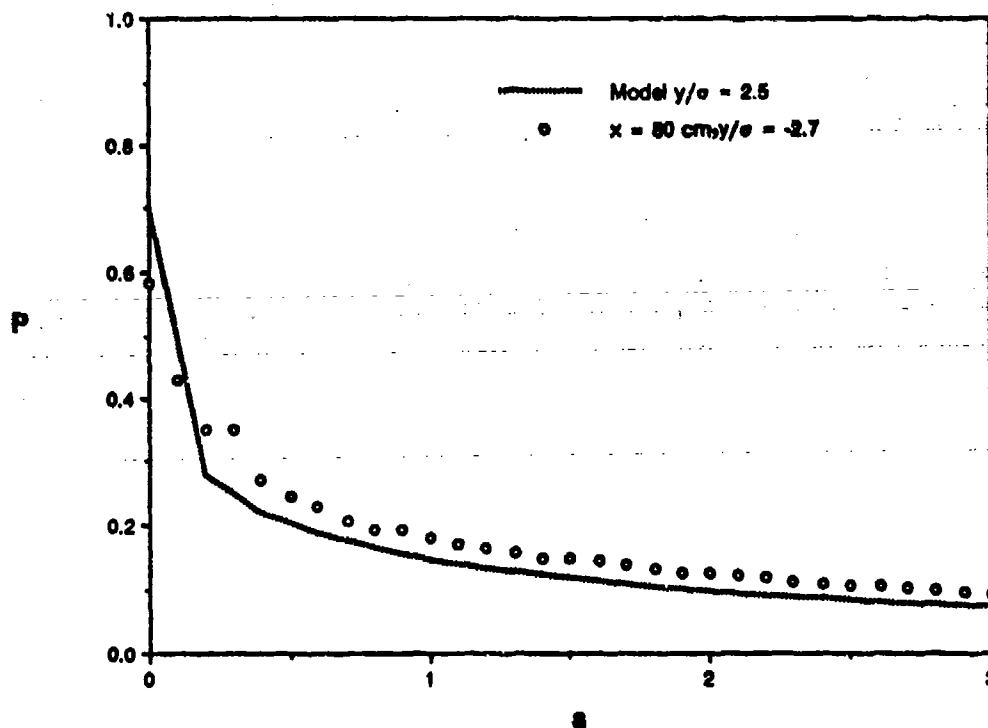


FIGURE 7. THE PROBABILITY  $P(a)$  THAT  $VIC^*/VICM^*$  EXCEEDS THE VALUE  $a$  NEAR  $y/\sigma = 2.7$ .

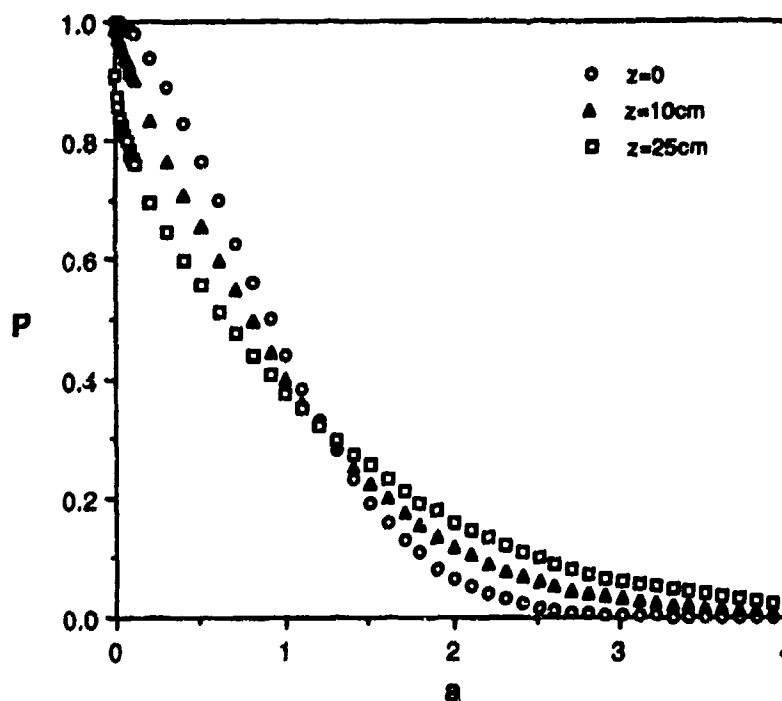


FIGURE 8. THE PROBABILITY  $P(a)$  THAT  $VIC^*/VICM^*$  NEAR  $y/\sigma = 0$  EXCEEDS THE VALUE  $a$  FOR POINT SOURCES AT DIFFERENT ELEVATIONS ( $x = 130 \text{ cm}, x/\delta = 1.3$ ).

## II. AEROSOL CHARACTERIZATION METHODS

### Comparative Studies of Bacterial Shape and Its Effect on The $[S_{34}/S_{11}]^\times$ Angular Scattering Pattern

Burt V. Bronk, Willem P. Van de Merwe\*, and Mark Stanley\*

Chemical Research Development and Engineering Center, A.P.G. Md 21010-5423

Uniformed Services University of the Health Sciences\*, Bethesda, Md 20814-4799

#### Recent Publications:

W. Van de Merwe, D. Huffman, and B. Bronk, "Reproducibility and sensitivity of polarized light scattering for identifying bacterial suspensions", *Applied Optics* 28, 5052-5056 (1989).

B. Bronk, W. Van de Merwe, D. Huffman and M. Stanley, "Relationship of Growth Conditions and Consequent Bacterial Size to the  $S_{34}/S_{11}$  Angular Scattering Pattern for Bacteria", This conference (1989).

#### Summary:

A simple preparative scheme was determined whereby bacteria could be photographed by optical microscopy in the same condition as they were prepared for light scattering experiments. An extensive series of experiments was performed in which dimensions of several representative bacteria were measured and compared with the oscillations of the polarized light scattering pattern. Both length and diameters were found to be important, but the diameters seem to predominate.

#### Introduction:

Last year we showed that changing the growth conditions for *E. Coli* bacteria led to changes in the size distribution of the bacteria as measured by electron microscopy. These changes correlated with changes in the angular scattering pattern for the combination of Mueller Matrix elements indicated by  $[S_{34}/S_{11}]^\times$ . (Here the nifty symbol after the fraction indicates that we are actually measuring the combination  $(S_{34} + S_{14})/(S_{11} + S_{31})$  but the elements suppressed in the symbol are relatively small for a randomly oriented suspension of many particles.) The angular pattern oscillates with well defined maxima and minima. It was seen that the effect of changing the particle size was analogous to the apparently much simpler effect seen when light is diffracted through a slit, in that larger particles produce more features and more crowding of the original peaks into the forward direction.

We indicated last year that simple geometrical reasoning suggests that the scattered photons should be more effected by the size of the diameter of the rod-like cells than their length, since the former dimension is sampled many more times in a randomly oriented suspension. However, the electron microscope measurements indicated that the size changes we were observing in shifting from freely growing bacteria (log phase) to starving bacteria (stationary phase) were mainly in the average length of the bacterial population with the changes in diameter much smaller. An intrinsic difficulty with such measurements is that a great deal of shrinkage of cells occurs in preparing them for electron microscopy.

Because of the clear importance of the dimensions of the bacterial cells in determining the scattering pattern for  $[S_{34}/S_{11}]^\times$ , we decided to determine the effectiveness of optical microscopy for correlating bacterial dimensions with that scattering pattern. Further, once we found this method to be practical, we embarked on an extensive series of these measurements in which we utilized several different bacterial species and conditions of growth. The preliminary analysis of some of these results is presented here.

## Methods:

It turned out that a rather simple procedure for preparing the various bacterial cells gave quite reproducible results both for optical (phase contrast) microscopy and for scattering. This consisted of spinning the cells out of the growth medium in a table top centrifuge and resuspending them in a .9% sterile NaCl solution at pH ~ 5.8. The concentration of the suspension was set with an Optical Density at 600nm of 0.05 --0.1 and an appropriately higher density for microscopy. Photographs were taken of various cells through the microscope, projected on the walls and individually measured against a calibrated standard. A rather precise recipe is required for determining the condition of growth of the cells (eg. log or stationary phase) in order to obtain reproducible size distributions. For log phase we required more than five doublings at an O.D. < 0.05 while stationary phase was arbitrarily defined to be 18 hrs after growing through an O.D. of 0.5 after passing through log phase. Further details on the methods will be given elsewhere (eg. refs (1,2))

## Results:

Since we are using our microscopic measurements near the limits of resolution imposed by optics, it was important to test the results with an easily calibrated standard. We did this by taking photographs of polystyrene beads, measuring about fifty of each size and comparing our optical determination with the determination by electron microscopy (EM) supplied by the company. For sets of beads which were sized by EM at  $1.06 \pm 0.01$  and  $0.6 \pm 0.003$  microns, we obtained  $1.03 \pm 0.02$  and  $0.59 \pm 0.01$  microns where in our case the deviation stated is a standard error of the mean. From these results and the consistency of the measurements presented below, we judge that our microscopic resolution is at least statistically somewhat better than 0.1 microns. *Bacillus Megaterium* is a spore forming bacterial species that is at the large end of the size spectrum observed for commonly occurring bacteria. We utilized a non-spore forming strain of these for our studies and illustrate the rather excellent quality of photographs which may be obtained at least for these quite large "bugs" in Figure 1.

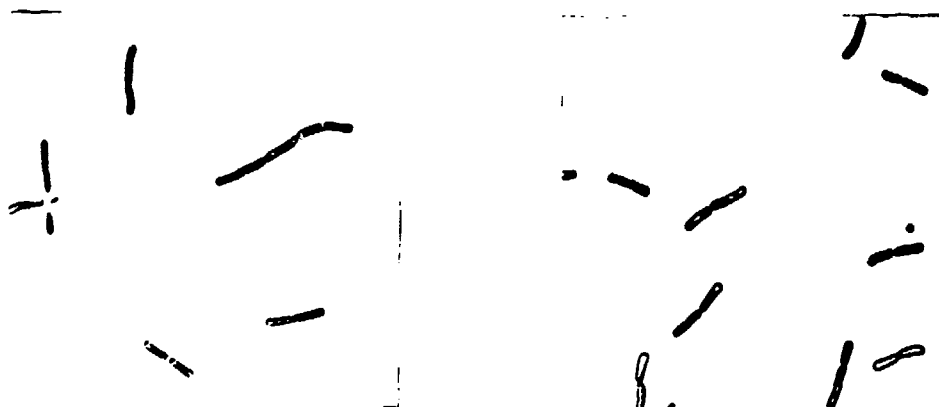


**Figure 1.** *B. Megaterium* bacteria grown in LB medium and resuspended in saline for phase contrast microscopy. The left hand photograph is of log phase cells with stationary phase cells on the right.

The log phase cells are slightly larger both in length and diameter as may be seen from the tabulation of average dimensions for the various experiments given in Table 1 below. For this tabulation, most of the chains of cells have been counted as single cells, making the average length somewhat longer than would be the case if doubles were counted as two single cells. In the case of *Staphylococcus Epidermidis* cells, which are fairly spherical in form, only one "typical" diameter was measured per cell.

**Table 1**  
**Optical Dimensions of Bacteria\***

Bacteria	Growth Stage	Medium	Diameter	Length
E. Coli B/r	Log	M1	0.77 ± 0.11	2.72 ± 0.62
E. Coli B/r	Stat	M1	0.60 ± 0.08	1.61 ± 0.32
B. Subtilis	Log	LB	0.86 ± 0.08	7.46 ± 1.9
B. Subtilis	Stat	LB	0.78 ± 0.09	3.5 ± 1.0
B. Megaterium	Log	LB	1.31 ± 0.14	10.42 ± 3.5
B. Megaterium	Stat	LB	1.41 ± 0.14	9.02 ± 3.9
S. Epidermidis	Log	M265	1.27 ± 0.10	---
S. Epidermidis	Stat	M265	1.01 ± 0.11	---
E. Coli K12	Log	LB	1.15 ± 0.11	7.40 ± 3.7
E. Coli K12	Stat	LB	0.97 ± 0.10	1.93 ± 0.34

**\* Notes:**

Lengths are group length

Error indicated is standard deviation,

Two or three hundred cells were measured in each case during at least two separate experiments.

In each case a scattering experiment to measure  $[S_{34}/S_{11}]^*$  was performed on the same afternoon and on the same cell preparation as the microscopy. All scattering for these experiments was done with the 633 line of a He-Ne laser. As shown in the references to this paper, an oscillating graph of  $[S_{34}/S_{11}]^*$  vs angle showed clearly defined maxima and minima. Plots of the peak location vs the cell width are shown in Figure 2.

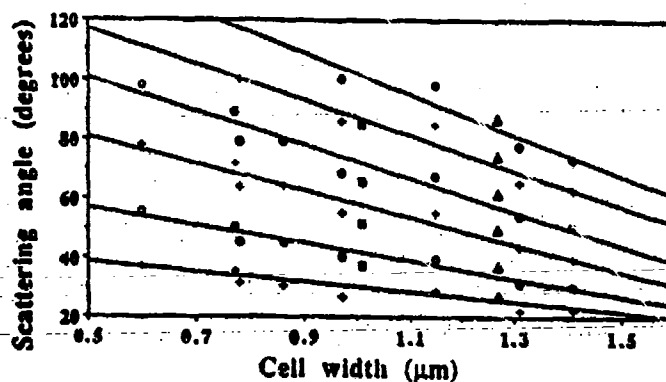


**Figure 2.** Angles of maxima (+) and minima (-) from the function  $[S_{34}/S_{11}]^{\frac{1}{2}}$  vs angle as a function of average bacterial cell diameter.

Each vertical set of points in Figure 2 represents the extrema from a scattering experiment with a cell type given by a line in Table 1. A given extremum traces a family of points at decreasing angle as the average diameter increases. The one anomalous set of points (solid squares) corresponds to stationary phase *Staphylococcus Epidermidis* cells. Our present results indicate that diameters fit into such a scheme with more regularity than cell length. In conclusion we note that additional data shows that the locations of the peaks for a given cell type are reproducible to better than a degree of angle. This fact together with the data of Figure 2 indicates that changes less than 50nm in the average diameter of a bacterial population may be rapidly and reliably detected in real time by this technique.

#### **References:**

1. See Applied Optics paper listed below title.
2. B. Bronk, W. Van de Merwe, and D. Huffman, "Polarized light scattering as a means of detecting subtle changes in microbial populations", in **Modern Techniques for Rapid Microbiological Analysis**, VCH Publishers, N.Y., editor W. Nelson, in press (1990).



# **Inversion of Single Size Particle Scattering Data by use of a Constrained Eigenfunction Expansion**

**B.P. Curry and K.H. Leong  
Argonne National Laboratory  
9700 South Cass Avenue,  
Argonne, IL 60439**

## **RECENT PUBLICATIONS, SUBMITTALS FOR PUBLICATION AND PRESENTATIONS:**

**B.P. Curry, "A Constrained Eigenfunction Expansion Method for the Inversion of Remote Sensing Data: Application to Particle Size Determination from Light Scattering Measurements," Appl. Opt. 28, 1345 (1989)**

### **Abstract**

A computer based procedure to invert the particle size and complex refractive index from angular scattering measurements of spherical particles of a single size (or nearly monodisperse narrow size distribution) is described. The procedure is intended to be used to analyze data obtained by the CRDEC multichannel nephelometers. The method is derived from a deconvolution technique for polydisperse spherical particles of known refractive index which was previously developed by one of us under CRDEC sponsorship.

### **1.0 Introduction:**

Recently the CRDEC has developed a capability to perform particle diagnostic nephelometry experiments, using two different multichannel instruments. It is desirable to develop a data analysis method to extract particle size and complex refractive index information from the data collected by these instruments. Previously, the nephelometry data have been analyzed by a variety of ad hoc techniques, but no attempt has been made to solve the formal inverse scattering problem.

We present here a restricted inverse scattering solution: determination of size and complex refractive index for single size spheres. Later extensions to nonspherical particles can be contemplated by use of techniques similar to what is involved in the inclusion of refractive indices as inversion parameters, provided one has access to computed nonspherical scattering kernels for a variety of particle shapes.

Although the present method is intended to invert single particle scattering data, the actual data obtained in the nephelometers is that of a nearly monodisperse particle size distribution, because it is necessary to add the scattering patterns for many nearly identical particles, in order to obtain good statistics. Even if all the particles were identical, variations in position as the particles traverse the laser beam would modify

the effective angular scattering pattern in the same way as slight variations in particle size. Thus the inversion technique discussed here is really one which can deconvolve a very narrow particle size distribution. The technique is intended to obtain the average particle size and the peak width of the inverted narrow size distribution, as well as the complex refractive indices of the average particle. In addition, the one-standard deviation output imprecision values for the average size and refractive indices will be obtained, corresponding to input scattering data with known variances.

## **2.0 Background:**

During the 1980's one of us enjoyed the sponsorship of the CRDEC in developing and testing computer based methods to invert the particle size distribution from laser scattering measurements from an ensemble of spherical particles. One of the ensemble deconvolution techniques developed during this period was denoted the "constrained eigenfunction expansion method."<sup>1</sup> This technique, which is the forerunner of the present inversion studies, involved expansion of the ensemble size distribution in Schmidt - Hilbert eigenfunctions of the scattering kernels, as had been previously done by Twomey and Howell<sup>2</sup> and by Capps, et. al.<sup>3</sup> The ensemble expansion coefficients were determined by the input scattering data and by a trial function through an implementation of the method of constrained linear inversion.<sup>4</sup>

Concern about the uniqueness of the recovered ensemble size distribution functions led CRDEC to acquire two unique light scattering instruments known as "multichannel nephelometers" that record the light scattering patterns produced by individual aerosol particles traversing a laser beam. Each particle is viewed simultaneously by PMT detectors positioned on a spherical surface surrounding the particle/beam intersection point.<sup>5</sup> The present inversion procedure is meant to be used with such instruments in the fashion shown in Figure 1. Initially, we are concerned only with uniform spheres. If the technique gives reliable results for spheres, than an attempt will be made to extend it to aspherical particles, beginning with spheroids. In such cases, the particle aspect ratio will be one of the inversion parameters, in addition to volumetric size and complex refractive indices.

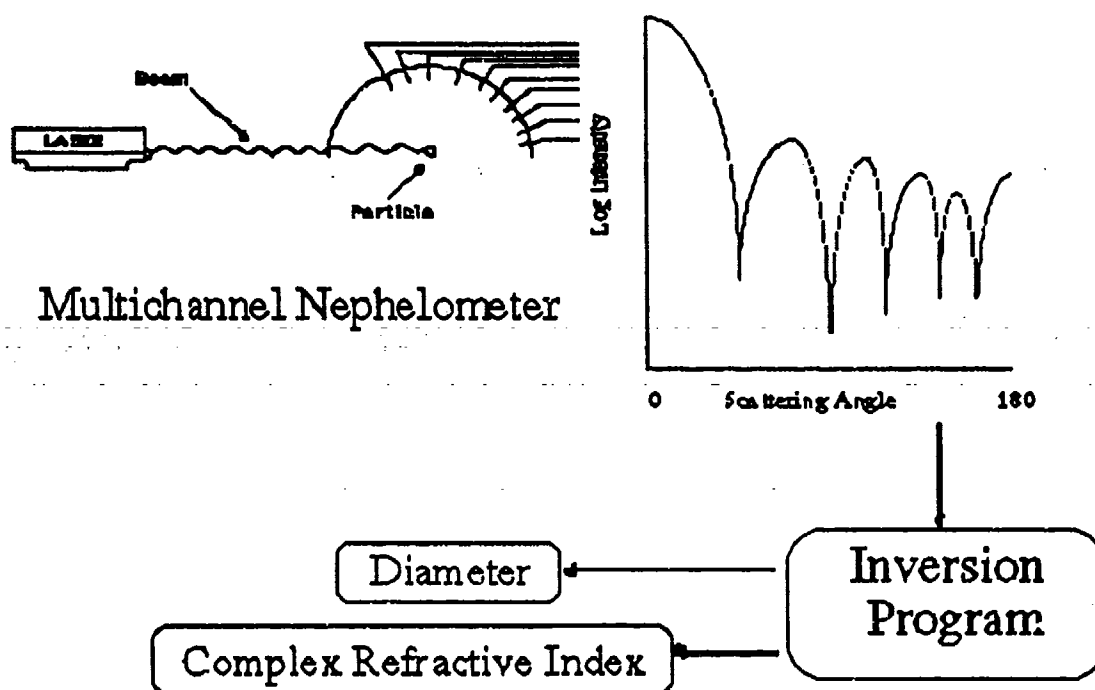


**Figure 1 Illustration of Single Particle Inversion Procedure**

### 3.0 Formalism:

The equation which describes light scattering by a single particle can be written in the form of a Fredholm equation, if the solution to the integral equation is regarded as a Dirac delta function whose argument is unknown.

$$g_i + \varepsilon_i = K(\chi, y_i, n_s, k_s) \equiv \sum_{r=1}^{N_r} \delta(r, s) \int_0^\infty \delta(x - \chi) K(x, y_i, n_r, k_r) dx \quad (1)$$

where  $\chi$  is the unknown size parameter and  $n_s, k_s$  are the unknown complex refractive index components,  $g_i$  is the "ith" measurement, and  $\varepsilon_i$  is the error in the measurement. While this equation is entirely correct for a monodispersion, it is also approximately correct for the nearly monodisperse narrow size distributions characteristic of anticipated nephelometry experiments. In practice, the product of delta functions will be replaced by an approximate expansion which, in fact, imposes a finite width in size and refractive index spaces. When solving this equation,  $n_s$  and  $k_s$  are assumed to be members of the set of refractive index components for which the kernels have been computed. Both the kernels and the measurements are assumed to represent differential scattering cross sections which have been integrated over angles subtended by the optical elements of the instrument. Note that the form of the above

equation indicates that the particle size is assumed to be a continuous variable, and the appropriate size distribution function is, thus, a Dirac delta function. In contrast, the refractive index components are treated as discrete variables; hence, the appropriate distribution function is a Kronecker delta whose argument specifies the index which locates a given value of  $n$  or  $k$  in a set of preselected values corresponding to precomputed scattering kernels. Since we are asking, in essence, for the probability of finding (among all the possible particles) a particle which has the both the size  $\chi$  and the complex refractive index pair  $(n_s, k_s)$ , the appropriate probability distribution is the product of the delta functions in the size and complex refractive index spaces.

The basis functions for the expansion of the delta function product are Schmidt - Hilbert eigenfunctions of the generalized kernel covariance matrix, which is defined below:

$$\tilde{N}_{ij} = \sum_{r=1}^{N_r} \int_0^{\cdot} K(x, y_i, n_r, k_r) K(x, y_j, n_r, k_r) dx \quad (2)$$

Note that the kernel covariance matrix has been summed over all the refractive index pairs which are included in the kernel computation set. The basis functions are obtained from the individual kernels and the generalized kernel covariance matrix by application of the Gram - Schmidt orthogonalization procedure. The result is a generalization of the Schmidt transformation used in the ensemble deconvolution procedure.

$$\Phi_i(x, n_r, k_r) = \lambda_i^{-1/2} \sum_{j=1}^N U_{ij} K(x, y_j, n_r, k_r) \quad (3)$$

where  $U_{ij}$  is an element of the matrix of eigenvectors of the generalized kernel covariance matrix,  $\lambda_i$  is an associated eigenvalue, and  $N$  is the total number of measurements. These functions are orthonormal. In addition, one can generalize sum rules for the expansion of a Dirac delta function in terms of a series of eigenfunctions (such as the arguments presented in Arfkin<sup>9</sup>) to obtain an equivalent expansion for the product of delta functions:

$$\sum_{i=1}^N \Phi_i(x, n_r, k_r) \Phi_i(\chi, n_s, k_s) = \delta(x-\chi) \delta(r,s) \quad (4)$$

Equation (4) would be an exact representation of the delta function product if the number of eigenfunctions in the expansion were infinite. However, since the number of eigenfunctions in this expansion is finite (according to Hilbert - Schmidt theory for an

Fredholm equation with a degenerate symmetric kernel) and in fact is equal to the total number of scattering inputs, equation (4) gives, at best, an approximation to the delta function product, which will have a finite spread in both size and refractive index spaces. This is all right, since the actual scattering data will consist of a superposition of the scattering patterns from many similar particles, as was previously stated. In simulations using narrow lognormal ensemble distributions to approximate the delta function, we have found that the finest resolution of the approximate Dirac delta function which can be inverted in size space is two size increments. This means that simulated scattering data corresponding to a polydispersion whose width was two of the computational size increments used to compute the kernels could be deconvolved, but a narrower size distribution could not be deconvolved.

The remainder of the formalism follows the treatment of the ensemble size distribution deconvolution procedure. The product of delta functions is first expanded in a series resembling equation (4), but the expansion coefficients contain the effect of the experimental data and of the trial functions for size and refractive indices.

$$\delta(r,s) \delta(x-\chi) = \sum_{j=1}^N C_j(\chi, n_s, k_s) \Phi_j(x, n_r, k_r) \quad (5)$$

In equation (5), the expansion coefficients are stated as functions of the unknown size  $c$  and refractive index pair  $(n_s, k_s)$ . If these were known, the expansion coefficients  $C_j(\chi, n_s, k_s)$  would simply be  $\Phi_j(\chi, n_s, k_s)$ . Instead, these coefficients are found by the method of constrained linear inversion to be

$$C_j = \frac{\sum_{k=1}^N \lambda_j^{-2} U_{j,k} g_k + \frac{\gamma}{\lambda_j} \Phi_j(x_T, n_T, k_T)}{1 + \frac{\gamma}{\lambda_j}} \quad (6)$$

where  $\gamma$  is a Lagrange multiplier and  $x_T, n_T, k_T$  are trial values of  $x, n, k$ . Equation (6) provides an approximation to  $\Phi_j(\chi, n_s, k_s)$  which should become progressively better as the iteration process proceeds. Once the solution expansion coefficients have been obtained, the inversion parameters are obtained as moments of the delta function distribution.

The recovered size parameter is obtained from

$$x_s = \frac{\sum_{i=1}^N \sum_{r=1}^{N_r} C_i \int_{x_{min}}^{x_{max}} x \Phi_i(x, n_r, k_r) dx}{A_{norm}} \quad (7)$$

where  $A_{norm}$  is a normalization factor defined as

$$A_{norm} = \sum_{i=1}^N \sum_{r=1}^{N_r} C_i \int_{x_{min}}^{x_{max}} \Phi_i(x, n_r, k_r) dx$$

Clearly, the iteration process should drive the recovered size to  $x_s = \chi$ . Similarly, the complex refractive index pair is obtained from

$$(n_s, k_s) = \frac{\sum_{i=1}^N \sum_{r=1}^{N_r} (n_r, k_r) C_i \int_{x_{min}}^{x_{max}} x \Phi_i(x, n_r, k_r) dx}{\sum_{i=1}^N \sum_{r=1}^{N_r} C_i \int_{x_{min}}^{x_{max}} x \Phi_i(x, n_r, k_r) dx} \quad (8)$$

We have also obtained equations for the uncertainties on the recovered parameters  $x_s$ ,  $n_s$ , and  $k_s$  due to one standard deviation imprecision levels of the scattering input data, assuming Gaussian distributed random errors in the data. These are analogous to similar expressions in Curry<sup>1</sup>, but are not stated here, on account of space limitations.

#### 4.0 Concluding Remarks:

This paper has presented the formalism for a computer based inversion technique to obtain the particle size and complex refractive indices from light scattering data obtained in a multichannel nephelometer. At this writing, the technique has been implemented in a triply iterative fashion. The first iteration uses an assumed size and pair of refractive index components and increases the Lagrange multiplier  $\gamma$  shown in equation (6) until an optimum value is found, as described in Curry<sup>1</sup>. The second iteration involves substituting the old solution expansion coefficients for the trial functions (the eigenfunctions in equation (6)) and repeating the first iteration. Recently, this procedure was extended for the ensemble deconvolution procedure to include fitting the recovered ensemble size distribution to a parametric distribution function and using the fitted results as a new trial ensemble distribution function, thus yielding a triply nested iteration.<sup>7</sup> A similar process is invoked for the single particle

inversion procedure. Upon convergence of the first two nested iterations, the size parameter and the refractive index pair are computed from equations (7) and (8) and compared with the trial values. If convergence is not obtained at this stage, trial parameters closest to these three parameters (within the computation set for which kernels are available) are selected and the entire process is repeated until convergence occurs. In preliminary tests we have obtained convergence on size, but recovery of the refractive index components will probably require extending the last stage of iteration to incorporate separate convergence on the size and refractive index components.

## REFERENCES

1. B.P. Curry, "A Constrained Eigenfunction Expansion Method for the Inversion of Remote Sensing Data: Application to Particle Size Determination from Light Scattering Measurements," *Appl. Opt.* **28**, 1345 (1989)
2. S. Twomey and H.B. Howell, "Some Aspects of the Optical Estimation of Microstructures in Fog and Cloud," *Appl. Opt.* **6**, 2125 (1967)
3. C.D. Capps, R.L. Henning, and G.M. Hess, "Analytic Inversion of Remote-Sensing Data," *Appl. Opt.* **21**, 3581 (1982)
4. S. Twomey, *Introduction to the Mathematics of Inversion in Remote Sensing and Indirect Measurements* (Elsevier, New York, 1979)
5. P. J. Wyatt, K. L. Schehrer, S. D. Phillips, C. Jackson, Y.-J. Chang, R. G. Parker, D. T. Phillips and J. R. Bottiger, "Aerosol Particle Analyzer," *Appl. Optics*, **27**, 217 (1988)
6. G. Arfkin, *Mathematical Methods for Physicists* (Academic, New York, 1970)
7. B.P. Curry, "A Constrained Eigenfunction Expansion Method for the Inversion of Light Scattering Remote Sensing Data," PhD Thesis, Kennedy - Western University, Agoura Hills, CA (October 1989)

**BLANK**



**LIGHT SCATTERING AND BIREFRINGENCE  
OF MAGNETIC BACTERIA**

R.G. Johnston  
Los Alamos National Laboratory  
Los Alamos, NM 87545

and

P.L. Jacobson  
Department of Physics  
Greenville College  
Greenville, IL 62246

**RECENT PUBLICATIONS, SUBMITTALS, AND PRESENTATIONS:**

A) R.G. Johnston and G.C. Salzman, "Phase Differential Scattering and Polydispersity", Proceedings of the 1988 CRDEC Conference on Obscuration and Aerosol Research.

B) R.G. Johnston, "Cytometric Applications of Zeeman Interferometry", SPIE Vol. 1063, 198 (1989).

C) R.G. Johnston, "Zeeman Interferometry", SPIE Vol. 1162, 344 (1989).

D) R.G. Johnston, "Rapid, Differential Micro-Thermometry Using Zeeman Interferometry", Applied Physics Letters 54, 289 (1989).

E) R.G. Johnston, K. Manley, and C.L. Lemanski, "Characterizing Gastrolith Surface Roughness with Light Scattering", Optics Communications 74, 279 (1990).

F) R.G. Johnston, "Zeeman Interferometry", SPIE Vol. 1319 (in press).

G) R.G. Johnston and W.K. Grace, "Refractive Index Detector Using Zeeman Interferometry", Applied Optics (in press).

H) R.G. Johnston, "Zeeman Interferometry", talk presented at the International Conference on Optics in Complex Systems, ICO-15, Garmisch-Partenkirchen, Germany, August 5-10, 1990.

I) R.G. Johnston, "Applications of Zeeman Interferometry to the Life Sciences" and "Characterizing Gastrolith Surface Roughness with Light Scattering", talks presented at the International Conference on Optics in the Life Sciences, Garmisch-Partenkirchen, Germany, August 12-16, 1990.

## ABSTRACT

The bacterium *Aquaspirillum magnetotacticum* grows its own internal single domain magnets. For a number of reasons, these magnets make the bacterium an extremely interesting scattering particle. We are engaging in light scattering and birefringence studies on *Aquaspirillum magnetotacticum*.

## INTRODUCTION

The bacterium *Aquaspirillum magnetotacticum* has the interesting property that it grows its own internal, single domain magnetite ( $\text{Fe}_3\text{O}_4$ ) particles.<sup>1-5</sup> These internal miniature magnets give each bacterial cell a magnetic dipole moment parallel to the axis of motility. The bacteria thus orient and swim along the direction of the earth's magnetic field lines.

*A. magnetotacticum* is a slightly helically-shaped bacterium. Its internal magnetite particles are usually cuboidal in shape and approximately 50 nm in size.<sup>3</sup> The average number of particles per bacterium can vary between 0 and 40, depending on the age and growth conditions of the culture. Because the magnetite particles within a given cell interact magnetically, they tend to line up inside the bacterium in a single row. These chains of magnetite are slightly helical in form due to the helical shape of the bacterial cell.

## MAGNETIC BACTERIA AS SCATTERING PARTICLES

There are a number of reasons why *A. magnetotacticum* is an interesting particle for light scattering studies:

1. The scattering particles (bacteria) can be prepared in large quantities.
2. *A. magnetotacticum* is a highly non-trivial scattering particle. Specifically, the cell has an unusual degree of internal structure. The average refractive index for most non-sporulated bacterial cells is approximately 1.38--very close to the value of 1.33 for water in the surrounding medium. *A. magnetotacticum*, however, contains magnetite particles with a large refractive index of 2.42. We thus expect the internal magnetite particles to dominate the scattering. This is in contrast to most biological cells where the exterior cell wall or membrane may be expected to dominate.
3. The bacterial orientation can be accurately measured and controlled. A strong external magnetic field can be used to give the bacterial cells any desired orientation for light scattering studies. It is thus possible to measure scattering by a **collection** of nearly identical, highly oriented particles in suspension. This avoids the experimental difficulties associated with scattering from a **single** oriented particle.

4. Multiple scattering is a factor in real-world scattering phenomena. Theoretically, however, multiple scattering is relatively intractable. With dense, oriented suspensions of magnetic bacteria it may be possible to compare multiple scattering models with experiment, without having the additional complicating factor of random particle orientation.

5. *A. magnetotacticum* should have significant form chirality due to the slight helical shape of the chain of magnetite particles within each cell. This makes the bacteria interesting for measurements of several of the Mueller scattering matrix elements, especially  $S_{14}$ .

6. Oriented magnetic bacteria can be used to study rotational diffusion coefficients<sup>4</sup> and fluctuations in Mueller scattering matrix elements.

7. *A. magnetotacticum* bacteria not only can be given any desired orientation, they can also be made to swim together in any desired direction. This offers the interesting possibility of using *A. magnetotacticum* as a kind of calibration particle for autocorrelation spectroscopy (dynamic light scattering).

8. *A. magnetotacticum* is fascinating in its own right. The ability to synthesize magnetite is of keen interest for fundamental reasons, as well as for the potential technological and environmental applications.<sup>1-5</sup>

## THEORY OF SAMPLE BIREFRINGENCE

The degree of orientation for magnetic bacteria can be determined from measurements of the sample birefringence.<sup>3</sup>

Birefringence is a difference in refractive index,  $\Delta n$ , for vertically polarized light compared with horizontally polarized light.

Let  $\mu$  be the average magnetic dipole moment for a single bacterium and  $H$  be the externally applied magnetic field. Now the birefringence of a suspension of bacteria is<sup>3</sup>

$$\Delta n = \Delta n_0 \langle P_2(\cos\phi) \rangle \quad (1)$$

where  $\langle P_2(\cos\phi) \rangle = \langle 3\cos^2\phi/2 - 1/2 \rangle$  is the expectation value for the second Legendre polynomial,  $\phi$  is the orientation angle, and  $\Delta n_0$  is the birefringence saturation value for large values of  $H$ . If  $\alpha \equiv \mu H/k_B T$  where  $T$  is temperature, and  $k_B$  is Boltzmann's constant, we can rewrite Equation (1) as<sup>3</sup>

$$\Delta n = \Delta n_0 \left( 1 - \frac{3 \coth(\alpha)}{\alpha} + \frac{3}{\alpha^2} \right) \quad (2)$$

By measuring the birefringence ratio,  $\Delta n/\Delta n_0$ , as a function of  $H$ , it is thus possible to determine the average magnetic moment,  $\mu$ . Equations (1) and (2) assume there is no magnetic interaction between the bacteria and they also ignore any randomization of bacterial orientation due to cell motility.<sup>3</sup>

## THEORY OF LIGHT SCATTERING

When a sample elastically scatters light, the Stokes parameters for the scattered light are related to the Stokes parameters for the incident light by<sup>9</sup>

$$\begin{pmatrix} I_s \\ Q_s \\ U_s \\ V_s \end{pmatrix} = k^{-2} r^{-2} \begin{pmatrix} S_{11} & S_{12} & S_{13} & S_{14} \\ S_{21} & S_{22} & S_{23} & S_{24} \\ S_{31} & S_{32} & S_{33} & S_{34} \\ S_{41} & S_{42} & S_{43} & S_{44} \end{pmatrix} \begin{pmatrix} I_i \\ Q_i \\ U_i \\ V_i \end{pmatrix} \quad (3)$$

where  $S_{hj}$  is the  $h,j$  element of the Mueller scattering matrix, the subscript  $i$  or  $s$  refers to incident or scattered light,  $k=2\pi/\lambda$ ,  $\lambda$  is wavelength, and  $r$  is the distance to the photodetector. In general,  $S_{hj}$  is a function of scattering angle  $\Theta$ . The off-diagonal matrix elements, especially  $S_{14}$  and  $S_{34}$ , are of particular interest.<sup>9</sup> They give the polarization properties of the scatterers and depend strongly on particle size, morphology, chirality, and optical constants.

## EXPERIMENTAL METHODS AND RESULTS

We constructed a Helmholtz coil box for generating magnetic fields in 3 orthogonal directions simultaneously.

This can be used to cancel the earth's magnetic field and generate any desired additional H vector. When the sample is placed inside the box, we can thereby give the bacteria any desired orientation. Slots were cut into the Helmholtz box to allow light transmitted and scattered by the bacterial sample to exit the box.

The magnetic field inside the Helmholtz box was measured with a 3-axis magnetometer (Applied Physics Systems). The field strength could be measured simultaneously along 3 orthogonal axes with a resolution of 1 micro-Oersted ( $1 \mu\text{Oe}$ ).

The sample birefringence was measured using a Zeeman effect laser. This interferometric technique is discussed in detail in references 6-9.

Figure 1 shows typical birefringence data for our Zeeman laser measurements of birefringence as a function of magnetic field strength. From these types of measurements, we found the average magnetic moment of our bacterial cells to be  $\mu = 3.7 \times 10^{-13}$  emu. The value of  $\mu$  varies by  $\pm 50\%$  depending on the culture age and growth conditions. This value for  $\mu$  is in fairly good agreement with measurements made by others workers using dissimilar techniques:  $1.2 \times 10^{-13}$  emu in reference 3,  $(2.6 \pm 1.7) \times 10^{-13}$  emu in reference 4, and  $2.2 \times 10^{-13}$  to  $5.0 \times 10^{-13}$  emu in reference 5.

Figure 2 is a schematic of the experimental set-up, as viewed from above, for making scattered irradiance measurements on suspensions of the magnetic bacteria. The scattering plane was horizontal. The polarizer (POL) was used to choose the incident polarization--horizontal or

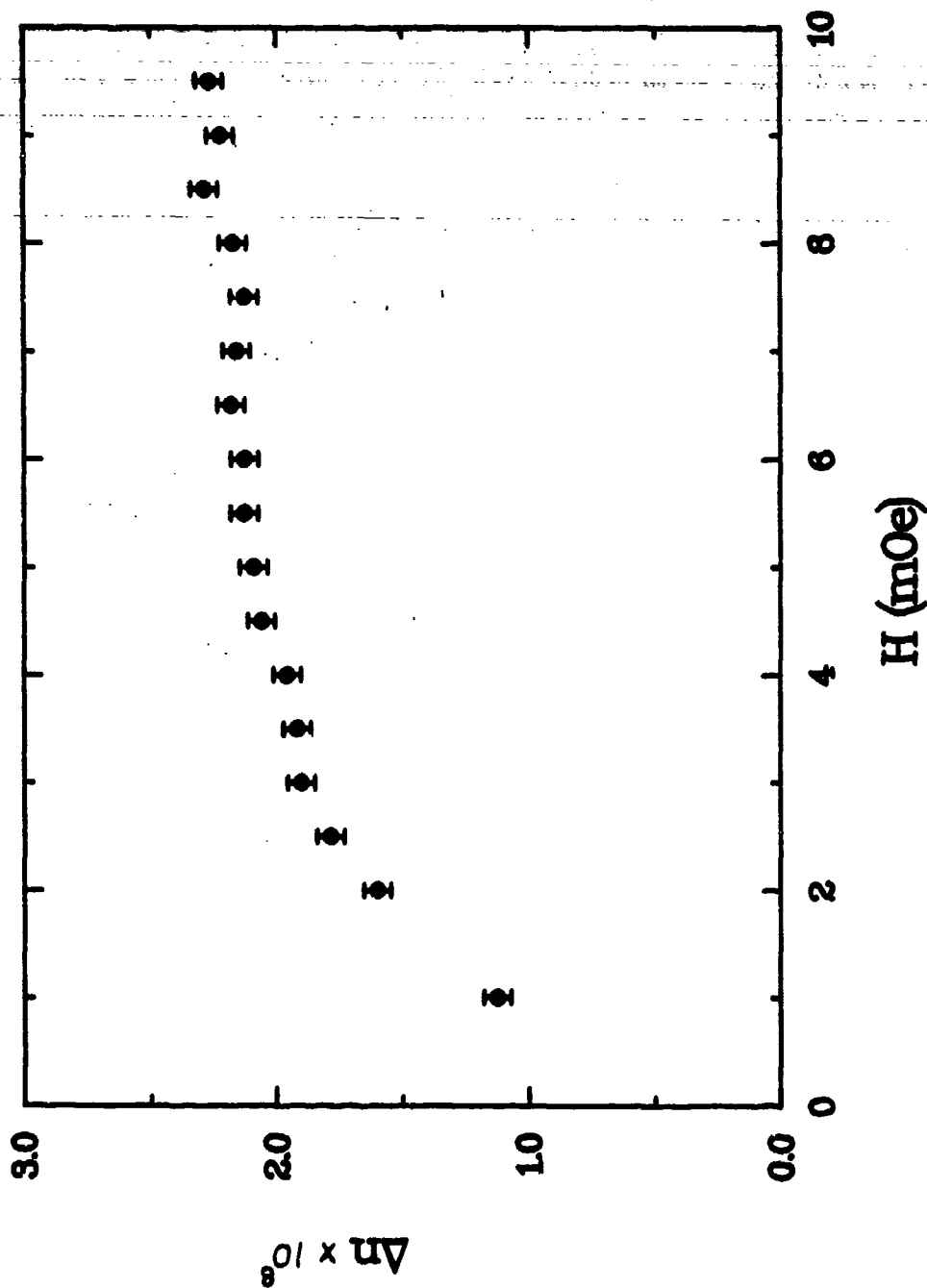


Figure 1. TYPICAL BIREFRINGENCE MEASUREMENTS ON ORIENTED BACTERIA. Birefringence is shown plotted as a function of magnetic field strength, H. At low values of H, Brownian motion tends to disrupt perfect orientation. The saturation birefringence compared to non-saturated measurements can be used to calculate the average bacterial magnetic dipole moment. These measurements were made using a Zeeman interferometric technique developed by the authors.



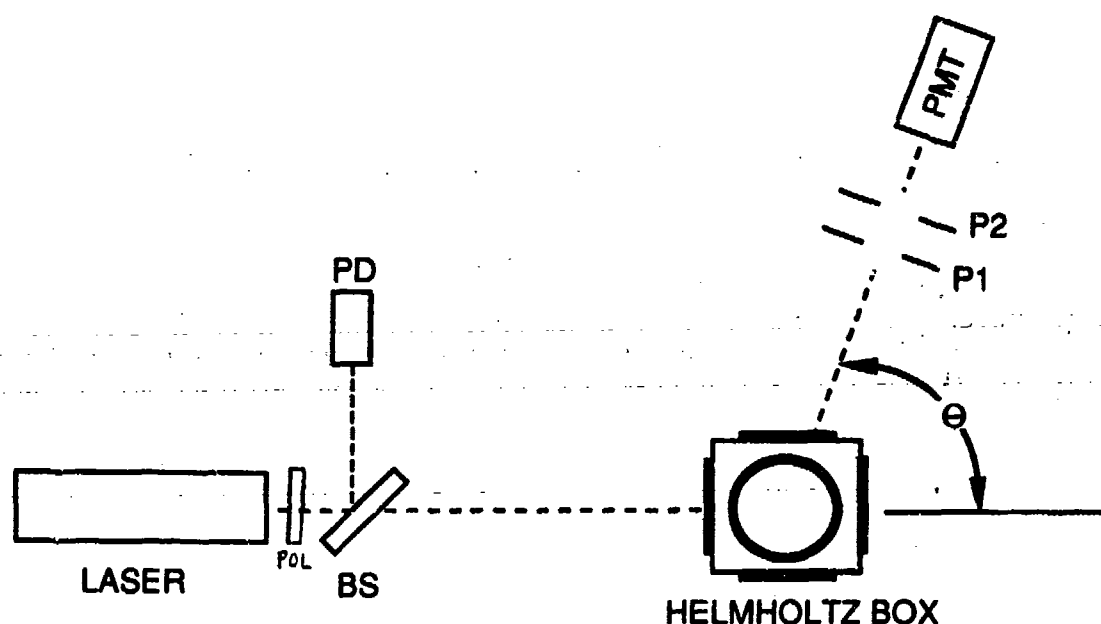


Figure 2. A SCHEMATIC OF THE APPARATUS USED TO MEASURE SCATTERING FROM ORIENTED MAGNETIC BACTERIA. The light source (LASER) was an argon-ion laser operated at a wavelength of 515 nm. A beam splitter (BS) allows a reference photodiode (PD) to monitor the laser intensity and correct for any fluctuations in the laser power. The sample of magnetic bacteria was placed inside the HELMHOLTZ BOX. The bacteria could be given any orientation by adjusting the strength of the magnetic fields in each of 3 orthogonal directions. P1 and P2 are pin holes used to define the scattering volume. A photomultiplier tube (PMT) collected the scattered light as a function of scattering angle ( $\theta$ ). For S14 or S34 measurements, a single photoelastic modulator must be added.

vertical.

Figures 3 and 4 show experimental scattering data for vertical (s) and horizontal (p) incident polarizations, respectively.  $S_{xx}$  is plotted as a function of scattering angle where  $S_{xx} = S_{11} \pm S_{12}$ . The 4 different orientations are:

45° in SP = the bacterial optic axis is in the horizontal scattering plane and oriented at  $\Theta = 45^\circ$ ,

90° in SP = the bacterial optic axis is in the horizontal scattering plane and oriented at  $\Theta = 90^\circ$ ,

45° in PP = the bacterial optic axis is in the vertical (perpendicular) plane and oriented at 45° to the vertical,

90° in PP = the bacterial optic axis is vertical.

The variation in scattered intensity shown in figures 3 and 4 for suspensions with different bacteria orientations can be understood by considering the total bacterial cell geometric cross-section viewed by the incident laser beam and the incident polarization (s or p).

The curves in figures 3 and 4 are spline fits to the experimental points. Data points around  $\Theta = 125^\circ$  and  $\Theta = 50^\circ$  are missing because the corners of the Helmholtz box block the scattered light at those angles. Additional measurements (not shown) made with a rotated Helmholtz box indicate there is no significant fine structure in the scattering curves around those scattering angles.

For measurements of  $S_{14}$  and  $S_{34}$ , it is necessary to add a single photoelastic modulator<sup>9</sup> to the set-up shown in figure 2. These measurements are still in progress.

# VERTICAL INCIDENT POLARIZATION

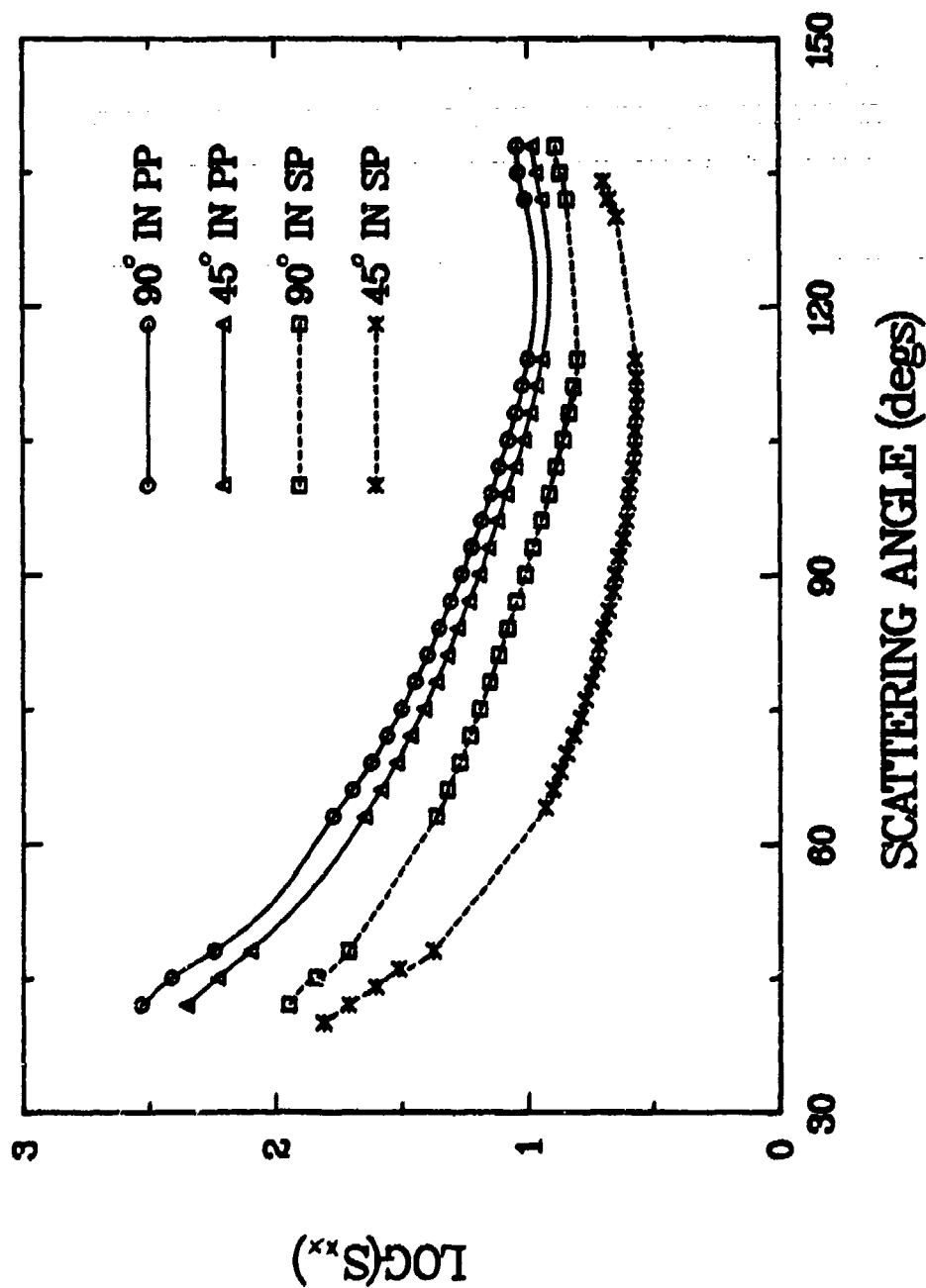


Figure 3. SCATTERING FROM ORIENTED MAGNETIC BACTERIA FOR INCIDENT s POLARIZATION.  
 $S_{xx} = S_{11} - S_{12}$ .

# HORIZONTAL INCIDENT POLARIZATION

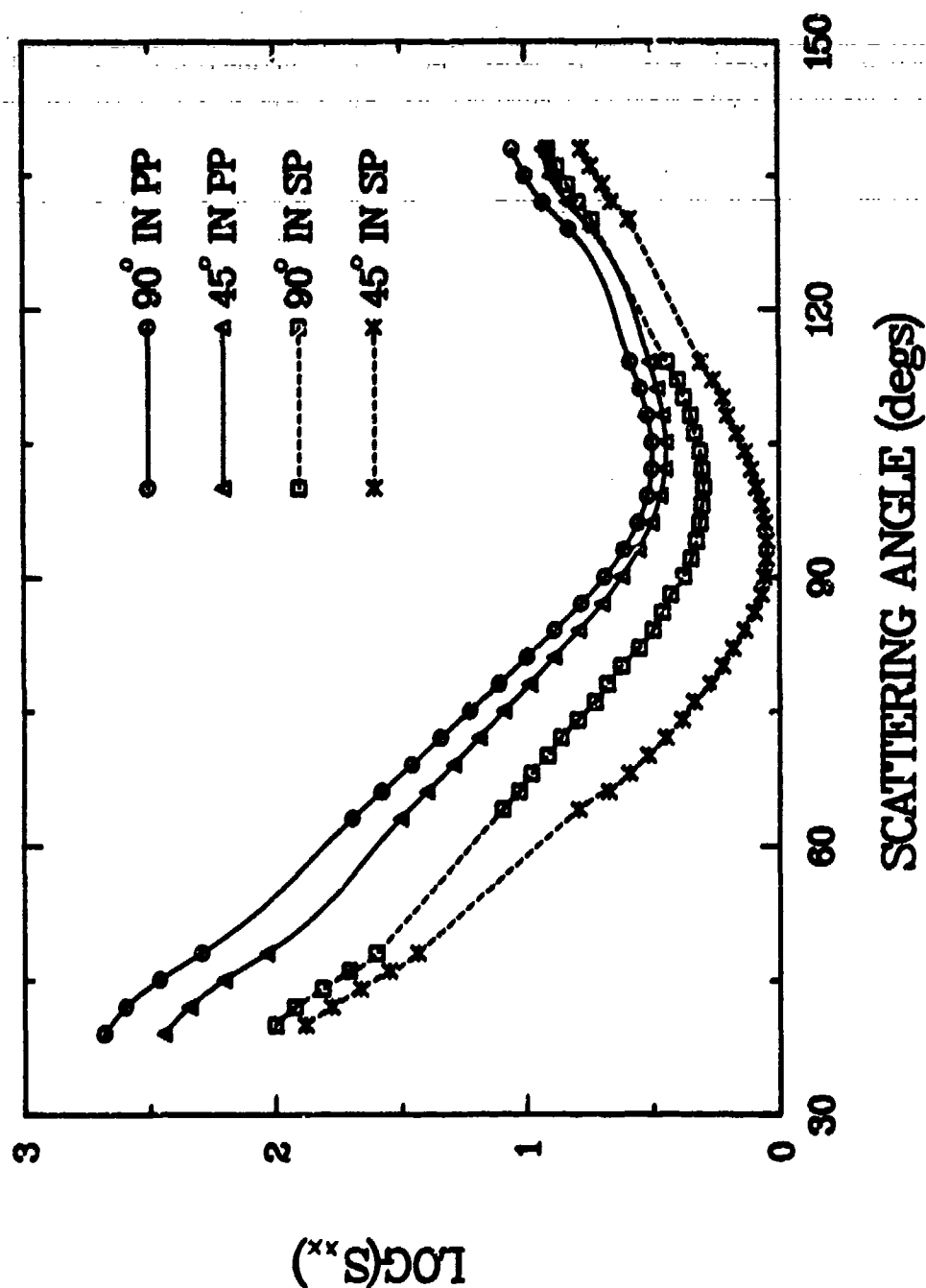


FIGURE 4. SCATTERING FROM ORIENTED MAGNETIC BACTERIA FOR INCIDENT p POLARIZATION.  
 $S_{xx} = S_{11} + S_{12}$ .

## ACKNOWLEDGEMENTS

This work was performed under the auspices of the U.S. Department of Energy and was supported in part by NIGMS Grant GM38287. Cheryl Lemanski prepared the cultures. Richard and Nancy Blakemore kindly provided *A. magnetotacticum* samples and advice on culturing protocols. Kevin Grace assisted with the mechanical design. Richard Maginn assisted with computer data acquisition.

## REFERENCES

1. R.P. Blakemore, "Magnetotactic Bacteria", *Science* 190, 377 (1975).
2. R.B. Frankel, R.P. Blakemore, and R.S. Wolfe, "Magnetite in Freshwater Magnetotactic Bacteria", *Science* 203, 1355 (1979).
3. C. Rosenblatt, F.F. Torres de Araujo, and R.B. Frankel, "Birefringence Determination of Magnetic Moments of Magnetotactic Bacteria", *Biophysics Journal* 40, 83 (1982).
4. C. Rosenblatt, R.B. Frankel, and R.P. Blakemore, "A Birefringence Relaxation Determination of Rotational Diffusion of Magnetotactic Bacteria", *Biophysics Journal* 47, 323 (1985).
5. C. Rosenblatt, F.F. Torres de Araujo, and R.P. Frankel, "Light Scattering Determination of Magnetic Moments of Magnetotactic Bacteria", *J. Applied Physics* 53, 2727 (1982).
6. R.G. Johnston, "Cytometric Applications of Zeeman Interferometry", *SPIE Vol. 1063*, 198 (1989).
7. R.G. Johnston, "Zeeman Interferometry", *SPIE Vol. 1162*, 344 (1989).
8. R.G. Johnston, "Zeeman Interferometry", *SPIE Vol. 1319* (in press).
9. R.G. Johnston, S.B. Singham, and G.C. Salzman, "Polarized Light Scattering", *Comments on Molecular and Cellular Biophysics* 5, 171 (1988).

**BLANK**

## **RAINBOWS AND PARTICLE CHARACTERIZATION**

**R.T. WANG**

**Space Astronomy Laboratory, Institute for Space Science & Technology, Inc.  
Gainesville, FL 32609**

### **RECENT PUBLICATIONS, SUBMITTALS FOR PUBLICATION AND PRESENTATIONS:**

A) R.T. Wang, "A new algorithm for exact scattering calculations using ratios", submitted to Proceedings of the 1988 CRDEC Conference on Obscuration and Aerosol Research (in press).

B) R.T. Wang and H.C. van de Hulst, "Rainbows: Mie computations and the Airy approximation", to appear in Applied Optics, **29**, Dec. 1990.

C) H.C. van de Hulst and R.T. Wang, "Glare points", Proc. of the 2nd International Congress on Optical Particle Sizing, E.D. Hirtleman, ed., Arizona State Univ. Press, Tempe, AZ pp. 40-49 (March 1990). A revised version of this paper was also submitted to Applied Optics, June 1990.

### **ABSTRACT**

This paper extracts some topics from the joint work with Prof. H.C. van de Hulst of the Leiden Observatory, the Netherlands (papers B) and C) shown above), and add a few which may be useful in particle characterization. Rainbow seen at a large distance, and at a finite distance with a lens are discussed with the aid of graphs. For the former the classical Airy theory, which we generalized to rainbows of arbitrary order, was found very useful even for smaller particles than were previously thought. For the latter a royal road to Mie theory calculation has to be taken, and we performed the Fourier transform of Mie field over the lens aperture. A few such Mie glare point images, nicely in accord with the classical geometrical optics, are shown. This article deals with single particles only. But a further step on scattering by size-distributed particles has already been taken, aiming toward inverse problems. Extension to a more elusive phenomenon, the backscatter glory, is also planned.

## 1. Introduction

Rainbows are ubiquitous phenomena resulting from the play of light in transparent spherical drops whose size is very large compared to the wavelength. The beauty of the display by water drops in the atmosphere following a rainfall is so familiar to us, and has inspired analytical studies over 7 centuries. We can only cite a few recent literature [Refs. 3-5, 7-11] and discuss here only a few practical topics related to characterizing a particle.

We first remark that the same rainbow phenomenon gives different appearances depending on whether (1) we see the collective effect at a large distance from a number of contributing drops, or (2) we see at a finite distance from a single drop with a lens focused on the drop surface. The familiar colored circular arcs we see around the anti-solar direction for atmospheric rainbows constitute a good example of case (1). For case (2), we see instead a few brighter or fainter glare spots, often colored, whose positions change in the field of view as the lens' angular position is varied [Refs. 7,10,11]. If, however, only a detector without lens is employed, as in many light-scattering experiments, the detector registers only the integrated scattered light over its aperture and the glare spots are not seen.

The time-honored Lorenz-Mie theory [Refs. 2,6,9] renders detailed explanation of such phenomena, but its numerical evaluation is rather time-consuming even by a computer with an efficient computational algorithm [Ref. 12], especially when the drop size parameter

$$x = 2\pi a / \lambda \quad (1.1)$$

is large. Here  $2a$  denotes the drop diameter, and  $\lambda$ , the wavelength. Through extensive comparisons with the Mie results, however, we found the classical Airy approximation, which we generalized to rainbows of arbitrary order  $p-1$  ( $p-1$ =number of internal reflections), was very useful in particle characterization under the case (1) and part of case (2). Section 2 summarizes some useful Airy formulae, depicts a few Mie-Airy rainbow profile comparisons, and explains the use in particle characterization. Section 3 deals with the glare points under case (2) and discuss their interpretation. Sec. 4 gives the summary.

## 2. Particle characterization via the Airy's Theory of Rainbows

This classical theory of rainbow preceded the Lorenz-Mie theory by more than half a century [Ref. 1]. Applying the Huygens' diffraction theory on the cubic wavefront formed by



emerging rainbow rays from a drop, it successfully approximated the positions and intensities of the main rainbow ( $p=2$ ) and its supernumerary bows. This was then a significant improvement over the famous Descartes' theory of rainbow based on the geometrical optics (G.O.). Airy approximation has been widely discussed, employed, and even modified in several forms in many rainbow articles to this date. Contrary to what has often been thought, however, our extensive comparison with Mie results shows the Airy approximation starts to be useful at a relatively small drop size  $x$  where laboratory levitation of the particle is also feasible. The lower bound for  $x$  appears to go even lower as the refractive index  $m$  increases, as long as the 1st primary rainbow ( $p=2$ ) peak is of interest. Since the Airy-Mie comparison was made both on the angular position and the absolute-magnitude of intensity, our finding could also be stated as: Airy theory can be employed for the quick absolute-magnitude calibration of intensity in a light scattering experiment by measuring the primary rainbow.

After the above brief outline we list a few useful Airy formulae as extracted from [Ref. 12] which are also valid for rainbows of arbitrary order. Notations by van de Hulst [Ref. 9] and also by Humphreys [Ref. 5] are employed.

(A) Scattering angle positions (in radians) of Airy maxima/minima

First Airy maximum ( $K=0$ ):

$$\theta_{\text{max},0} = \theta_0(p,m) - q \cdot 1.087376 \left[ h\pi^2/12 \right]^{1/3} x^{-2/3} \quad (2.1)$$

Supernumerary Airy maxima ( $K \geq 1$ ):

$$\theta_{\text{max},K} = \theta_0(p,m) - qh^{1/3} [3\pi(K-1/4)/2]^{2/3} x^{-2/3} \quad (2.2)$$

All Airy minima ( $K \geq 0$ ):

$$\theta_{\text{min},K} = \theta_0(p,m) - qh^{1/3} [3\pi(K+3/4)/2]^{2/3} x^{-2/3} \quad (2.3)$$

where  $\theta_0(p,m)$  is the rainbow angle by geometrical optics [Ref. 9, p.229] and

$$q = -1 \quad \text{if } \theta_0(p,m) \text{ is a minimum deviation angle (e.g. } p=2, 5, 6, 9, \text{ etc)} \quad (2.4)$$

$$q = +1 \quad \text{if } \theta_0(p,m) \text{ is a maximum deviation angle (e.g. } p=3, 4, 7, 8, \text{ etc)}$$

$$h = \left[ (p^2 - 1)^2 / (p^2(m^2 - 1)) \right] \cdot [(p^2 - m^2) / (m^2 - 1)]^{1/2} \quad (2.5)$$

$h$  is related to the curvature of cubic wavefront [Ref. 5, p.470].

(B) Scattering intensity  $(S_{11})_{\text{Airy}}$  for unpolarized incident light

$$(S_{11})_{\text{Airy}} = (\epsilon_1^2 + \epsilon_2^2) \{81/(16\pi^2 h^4)\}^{1/6} \cos \tau_p x^{7/3} f^2(z) / \sin \theta_0(p, m) \quad (2.6)$$

where

$$f(z) = \int_0^\infty \cos[\pi(z t - t^3)/2] dt = \text{Airy integral}$$

$$z = (-q) \left[12/(h\pi^2)\right]^{1/3} x^{2/3} (\theta - \theta_0(p, m)) \quad (2.7)$$

$$\tau_p = \tan^{-1} \left[ (m^2 - 1) / (p^2 - m^2) \right]^{1/2}$$

$$\epsilon_i = (1 - r_i^2) (-r_i)^{p-1} \text{ where } i=1 \text{ or } 2 \text{ and } p \geq 2$$

$r_i$  = Fresnel's reflection coefficient for polarization  $i$  (Ref.9, p204)

Unlike the time-consuming Mie scattering calculation whose computer CPU time increases linearly with  $x$  and the number of scattering angles, the evaluation of Airy intensity, (2.6), is practically independent of the drop size  $x$ , thus making it a very efficient tool in laboratory use. Figs. 1 and 2 show the direct Mie-Airy rainbow profile comparisons with  $x$  fixed at  $x=241.661$  and  $x=120.83$ , respectively, and with 4 typical refractive indexes. Both Mie and Airy theory calculations were made by our laboratory-oriented DECLAB PDP11/23 computer, using only 7-digits single-precision arithmetics. The respective drop sizes are  $2a=36.5\mu\text{m}$  (Fig. 1A),  $2a=50\mu\text{m}$  (Fig. 1B),  $2a=52.2\mu\text{m}$  (Fig. 1C) and  $2a=38.5\mu\text{m}$  (Fig. 1D); while in the corresponding Figs. 2A-2D, all the drop sizes are halved. The selected particles are thus typical for those employed in light scattering experiments for their manageable levitation. We cannot reproduce here a far greater number of Mie-Airy comparison graphs covering the drop size to  $2a \sim 6.2\text{ mm}$ , but we found as  $x$  increased the Mie/Airy rainbow profiles matched progressively better. Indeed, at  $2a \sim 0.4\text{ mm}$  the match already came to almost exact for water drops, as long as only the rainbow peak positions and intensities were concerned.

We summarize a few interesting findings through Figs. 1 and 2: (a) The angular positions of rainbows depend most critically on the refractive index  $m$  and the number of internal reflections  $p-1$  ( $p=2$ : primary rainbow;  $p=3$ : secondary rainbow; etc.), but to a lesser degree also on the size  $x$ . (b) Eq. (2.1) can be employed to scan the primary ( $p=2$ ) rainbow peak position for quick particle characterization. (c) For the  $p=2$  first peak, Mie and Airy theories agree rather well both in position and intensity, even for such small drop sizes. The agreement improves as the refractive index  $m$  and/or the size  $x$  increases, which is also accompanied by the increase in intensity but decrease in width of this main peak, i.e., the primary rainbow becomes more and more prominent. Thus, analyzing the primary rainbow profile via Airy theory will be a feasible approach to characterizing a particle. (d) Whenever we go to the supernumeraries for  $p=2$  or to rainbows of higher order ( $p \geq 3$ ), the agreement between Mie and Airy theories becomes less impressive or is virtually lost at the drop sizes of Figs. 1 and 2.

### 3. Mie Glare Point Images

In sec. 2 we assumed that both the small light source and observation aperture were located very far from the scattering particle. We now turn into the problem of imaging a particle with a lens located at a finite distance  $r$  from it, over various angular positions of  $\theta$  (Fig. 3 illustrates the geometry). This corresponds to the case (2) in sec. 1. Since the lens subtends an appreciable half angle  $b/r$  with respect to the particle, the interferences between all rays over the lens aperture have to be assessed. This will result in brightness variation over the particle image formed on the plane  $Q$  of Fig. 3. We shall see such an image contains several glare points, the images of the exit points of those rays strongly reflected or refracted into the observing direction. The calculation requires the Mie theory for integrating the contributions of wavelets across the lens aperture. This is the direct application of the Huygens' diffraction principle, and we call it the Fourier transform of Mie field.

For simplicity the incident light is assumed polarized perpendicular to the scattering plane, and we further assume  $r$  is large enough so that the complex scattering amplitude before entering the lens is given by [Refs. 2,6,9]

$$S_1(\theta) = \sum_{n=1}^{n_{\max}} \frac{2n+1}{n(n+1)} \left\{ a_n \pi_n(\cos \theta) + b_n \tau_n(\cos \theta) \right\} \quad (3.1)$$

The amplitude of the received field at  $Q$  can then be derived and is proportional to [Refs. 7,10]

$$A_1(w) = \int_{\theta_0 - b/r}^{\theta_0 + b/r} S_1(\theta) \exp[-ixw(\theta - \theta_0)] d\theta \quad (3.2)$$

where  $\theta_0$  is the angular position of the lens center, and  $w$  denotes the dimensionless image position,  $w=+1$  corresponding to the image position of one particle edge, while  $w=-1$ , to the opposite edge.

We first remark that a glare point is not necessarily be the image of a particular order rainbow. Whenever the intensity of light rays is very much strengthened at an exit point of the particle surface, that point is focused by the lens to produce a glare point image. Besides rainbow-forming rays, others such as directly reflected rays ( $p=0$ ) or those emerging after transmission and/or internal reflections ( $p \geq 1$ ) can also be responsible for it. In the  $x \rightarrow \infty$  geometrical optics limit, one can construct a map (Fig. 4) showing for each  $p$  the image position  $w$  as a function of the lens position  $\theta_0$  [cf also Ref. 9, p.229]. Such a map is convenient in identifying the rays producing a given glare point image for a very large particle. It is very sensitive to the refractive index  $m$  of the particle. Fig. 4 is for  $m=1.331$ , that of water at  $\lambda=0.65 \mu\text{m}$ , and shows for  $p$  from  $p=0$  to  $p=6$ .

We next state an important remark that such a glare point experiment can be performed only when  $x$  is very large, for the resolution criterion deduced from a fundamental diffraction consideration [Ref. 10]

$$\Delta\theta_0 \cdot \Delta w \sim \frac{1}{x} \quad (3.3)$$

This means we cannot simultaneously measure with infinite precision the angular position  $\theta_0$  and the image position  $w$ . Choosing a big lens helps define  $w$  but spoils the accuracy of  $\theta_0$ . Choosing a small lens does the opposite effect. For this reason we chose here a water drop of  $x=10,000$  or  $x=20,000$  at  $\lambda=0.65 \mu\text{m}$  with  $b/r=0.01$ , corresponding to, say, placing a  $b=1 \text{ cm}$  lens at a distance of  $r=100 \text{ cm}$ .

Fig. 5 shows the Mie glare point image for the test sample  $x=10,000$ ,  $m=1.331 - i 1.3 \text{ E-}8$  and  $b/r=0.01$ .  $\log |A_1(w)|$  from eq. (3.2) was plotted against  $w$  over  $-1.25 \leq w \leq 1.25$ , which cover

a little beyond both geometrical optics image boundaries  $w=\pm 1$  in order to see also the spill-overs/surface-waves, if any, occurring at the particle edges, near which most rainbows are also produced. Fig. 4 was very useful in tracing the sources of rays responsible for the glare points, the positions, heights and widths of which are very sensitive to particle parameters (and also to  $b/r$ ). Thus, the glare point imaging technique would be very important not only for particle characterization, but also for understanding the basic physics of light interacting with a large particle.

A glare point image is accompanied by many diffraction side lobes of the lens spaced uniformly on both sides, as can be seen in Fig. 5 at each prominent peak. Similar phenomenon is also experienced by an optical astronomer as nuisance when he finds his faint star image is ringed. He then apodizes the lens to suppress the unwanted sidelobes at the cost of a slight widening and decrease in intensity of the main peak, by coating the lens with an absorbing material whose thickness increases as one goes toward the lens limb. Similar techniques can be applied to a microwave antenna, a process known as tapering. Fig. 6 shows some examples by using the apodization factors:

$$\begin{aligned} g(z) &= 1 - (90z)^2 \\ g(z) &= \cos^2(110z) \\ g(z) &= \exp [-(140z)^2] \end{aligned} \tag{3.4}$$

where  $z$  is proportional to the distance of a point on the aperture from its center, taking the value  $b/r$  at its edge. These multiplication factors are then placed in the integrand of eq. (3.2) to perform the Fourier transform. In Fig. 6 we employed  $x=20,000$ ,  $m=1.331 - i 1.3E-8$  and  $b/r=0.01$ . The lens position is at  $\theta_0 = 127.61^\circ$ , the  $p=6$  Airy rainbow angle evaluated by eq. (2.1). As seen, besides the  $p=6$  rainbow itself many faint glare peaks become more discernable by increasing the degree of apodization. A large number of similar graphs has been compiled to study also the edge phenomena, where most rainbows also take place.

#### 4. Summary

- Rainbows, either seen at a large distance (case (1)), or at a finite distance with a lens (case (2)), can be explained in detail through the Lorenz-Mie theory.

- For the case (1), the classical Airy approximation was found more useful than had often been thought. For  $m \geq 1.4$ , for example, the Airy theory can be employed to analyze the primary rainbow ( $p=2$ ) for particles as small as  $2a \sim 0.02$   $\mu\text{m}$ . The Mie-Airy rainbow profiles match better for the  $p=2$  rainbow as  $m$  and/or  $x$  increases.
- The numerical evaluation of Airy theory is much less time-consuming than Mie calculation. Thus the Airy theory may be employed for absolute-magnitude calibration in light scattering experiments, by analyzing the primary rainbow.
- The glare point images pack a lot of more information than merely observing rainbows at a distance, for they contain detailed pictures on the behavior of light rays inside the scattering particle. There would be many interesting problems for which the glare point imaging technique prove to be a powerful tool, including the particle characterization.

### Acknowledgments

The author is indebted to and very pleased to work with Prof. H.C. van de Hulst, a man with extraordinary insights. Thanks are due to Prof. J.L. Weinberg, President of the ISST, for supporting our collaboration. Information related to the glare points from Prof. J.A. Lock, along with his critical review on Ref. 12, are highly appreciated. Special thanks are due to Mrs. Joye Dunlop for artistic typings. This work was supported in part by the U.S. Army Research Office under contract DAAL03-86-K0021 to the University of Florida, where this work was initiated.

### References

1. Airy, G.B., On the intensity of light in the neighborhood of a caustic, Trans. Cambridge Phil. Soc. 6, 379-402 (1838).
2. Bohren, C.F. and Huffman, D.R., Absorption and Scattering of Light by Small Particles (Wiley, New York 1983).
3. Boyer, C.B., The Rainbow: From Myth to Mathematics (Yoseloff, New York, 1959).
4. Greenler, R., Rainbows, halos and glories (Cambridge Univ. Press, N.Y. 1980).
5. Humphreys, W.J., Physics of the Air (McGraw-Hill, New York, 1929).
6. Kerker, M., The Scattering of Light and other Electromagnetic Radiation, (Academic Press, New York 1969).

7. Lock, J.A., Theory of the observations made of high-order rainbows from a single water droplet, *Appl. Opt.* **26**, 5291-5298 (1987).
8. Nussenzveig, H.M., Complex angular momentum theory of the rainbow and the glory, *J. Opt. Soc. Am.* **69**, 1068-1079 (1979).
9. van de Hulst, H.C., Light Scattering by Small Particles (Wiley, N.Y. 1957).
10. van de Hulst, H.C. and Wang, R.T., Glare points, submitted to *Appl. Opt.* (June 1990).
11. Walker, J.D., How to Create and Observe a Double Rainbow in a Single Drop of Water, *Sci. A.* **237**, 138 (July 1977); Mysteries of Rainbows, Notably their Rare Supernumerary Arcs, *Sci. Am.* **242**, 147 (June 1980).
12. Wang, R.T. and van de Hulst, H.C., Rainbows: Mie computations and the Airy approximation, to appear in *Appl. Opt.* **29** (Dec. 1990).

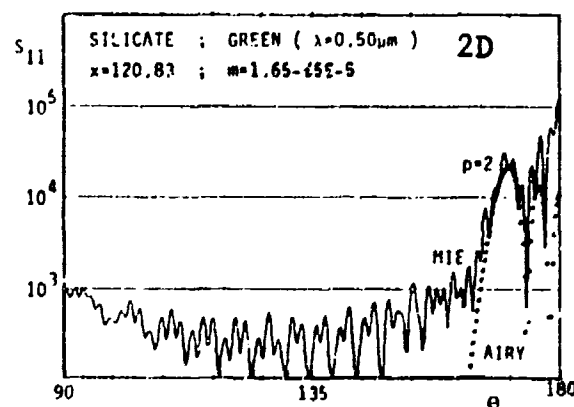
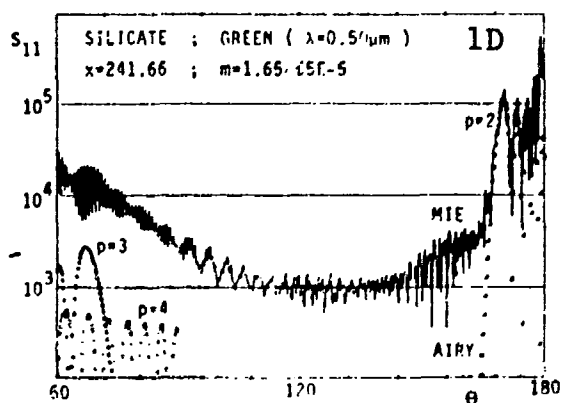
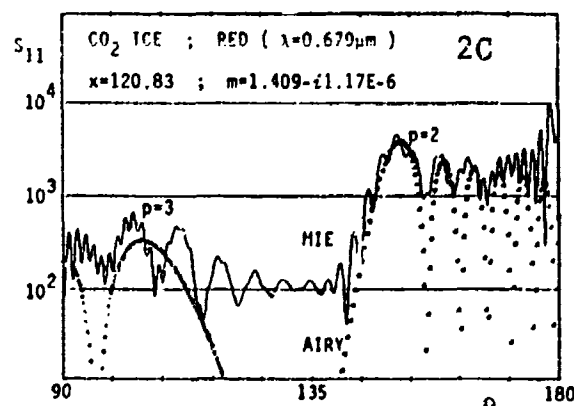
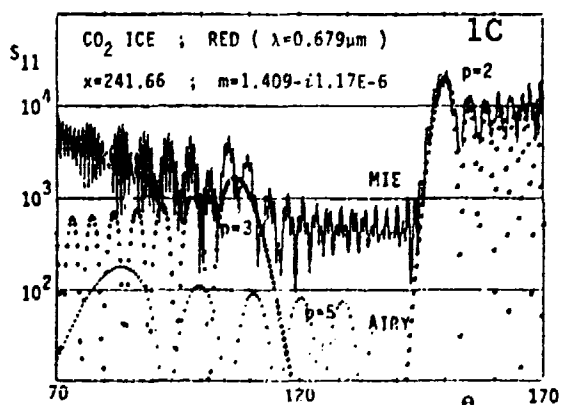
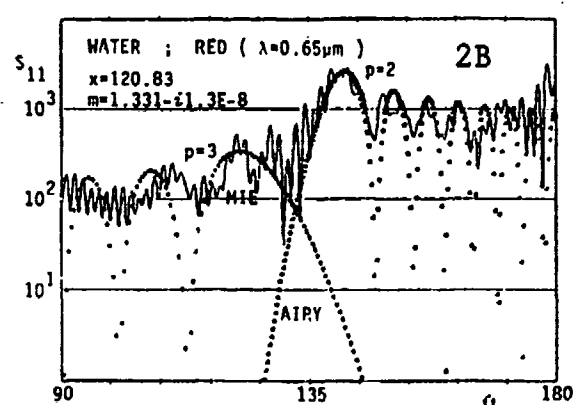
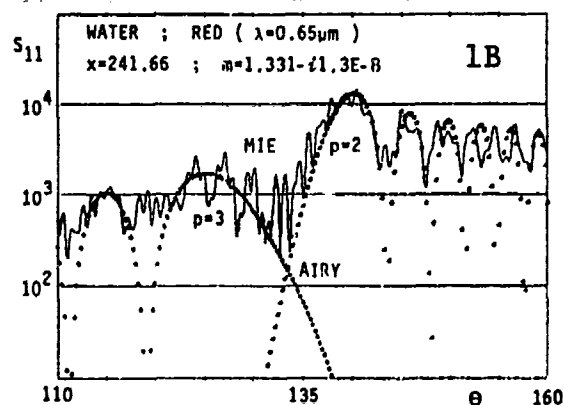
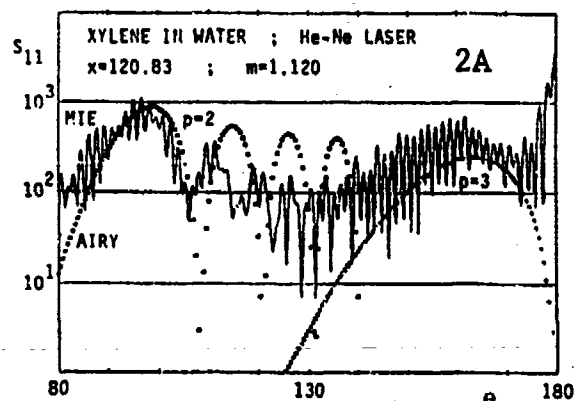
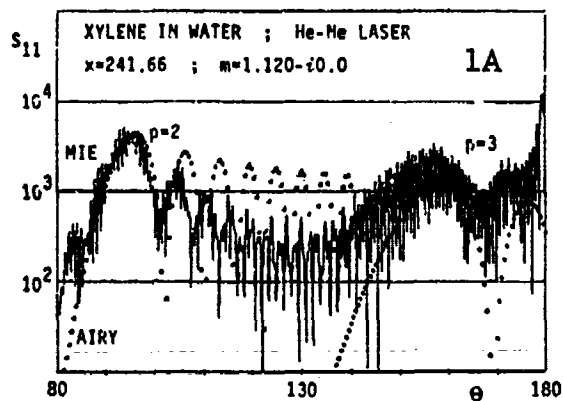


Fig. 1 Mie & Airy Rainbow Intensity Profiles.  
 $x=241.66$ . See sec. 2.

Fig. 2 Mie & Airy Rainbow Intensity Profiles.  
 $x=120.83$ . See sec. 2.



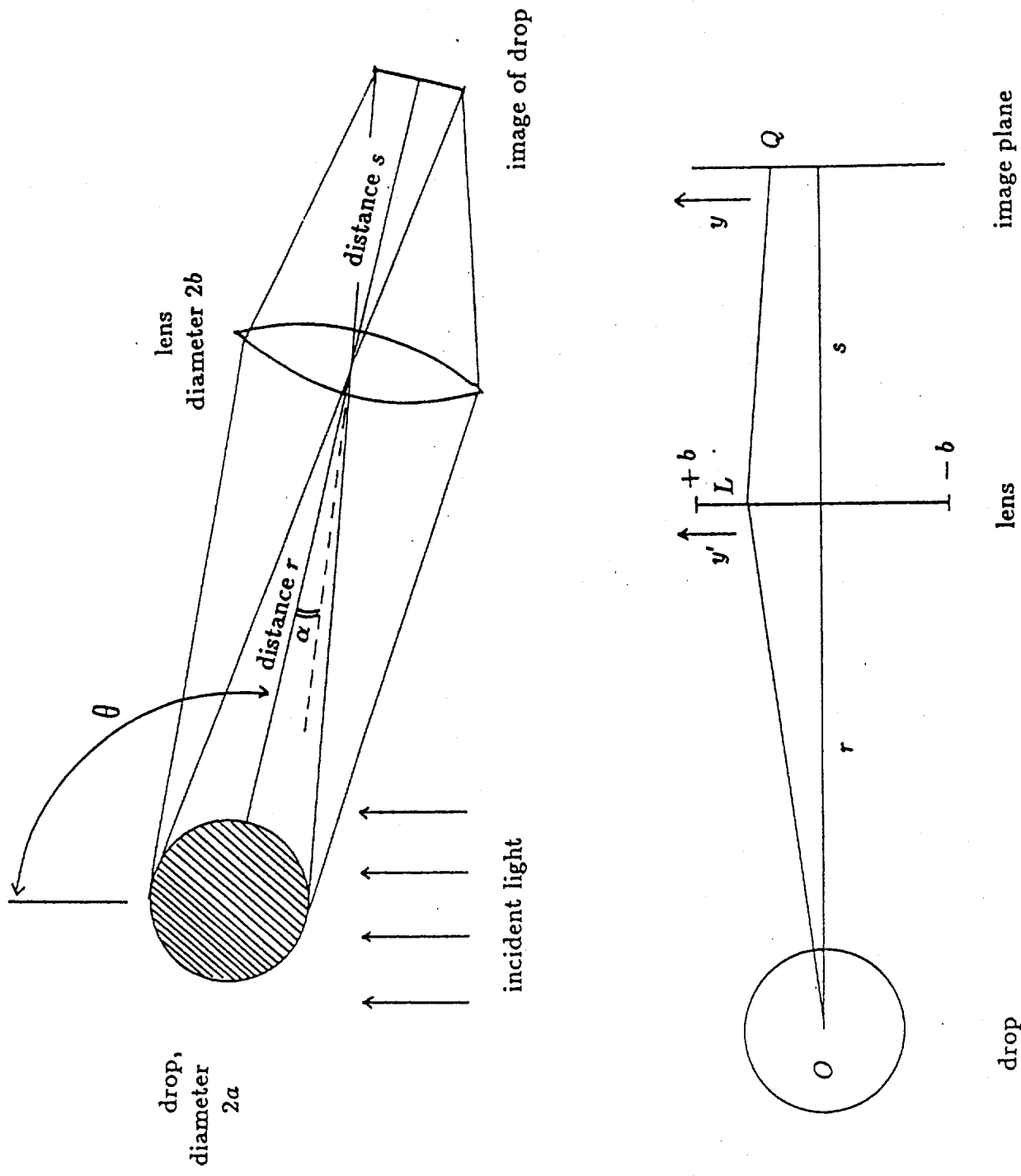


Fig. 3 Geometry of imaging glare points by a lens.

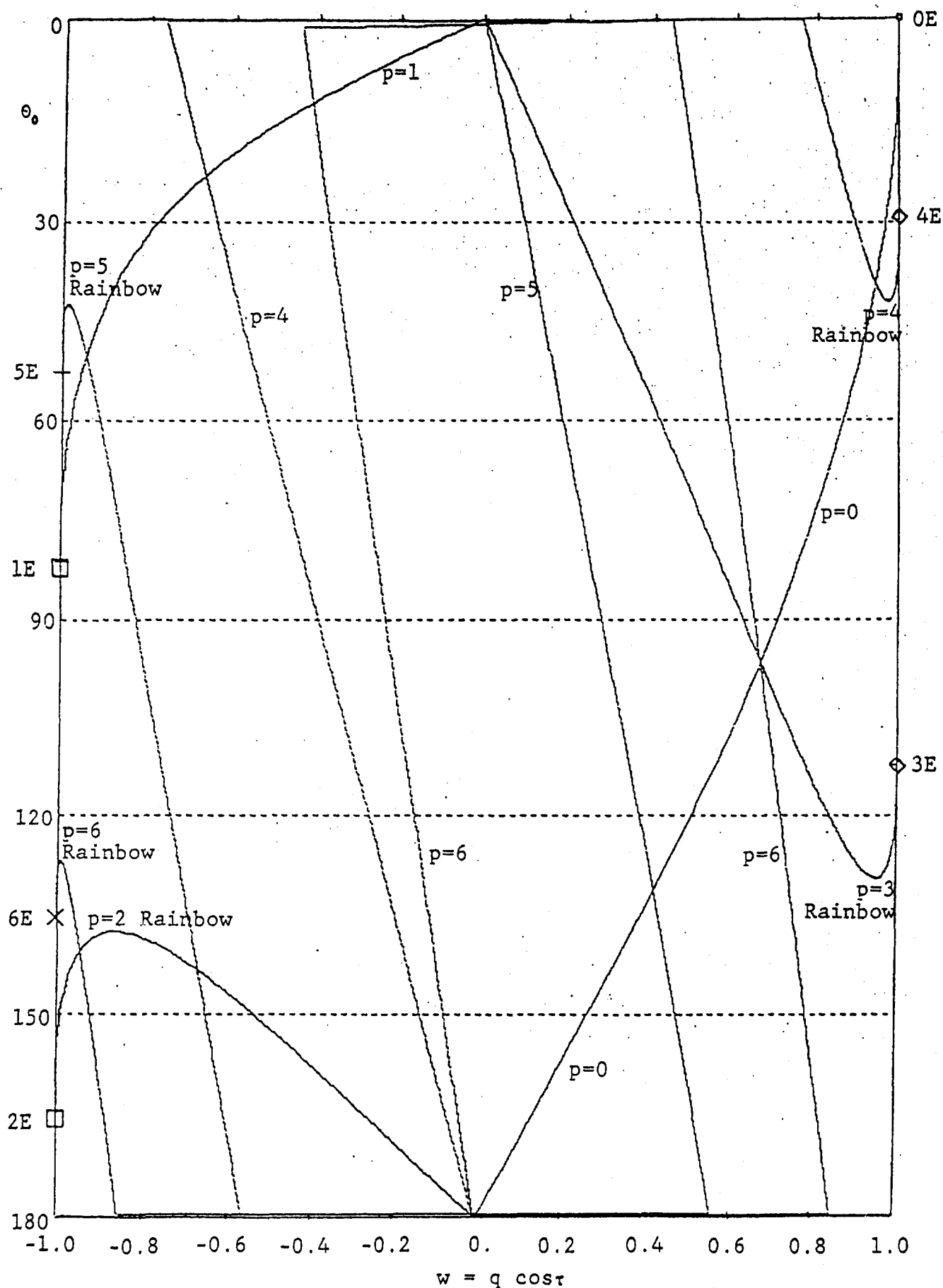


Fig. 4. Geometrical Optics Road Map

$x=\infty$ ,  $m=1.331$ . E denotes edge ray, e.g., 2E is the image position of the edge ray for  $p=2$ . See sec.3.

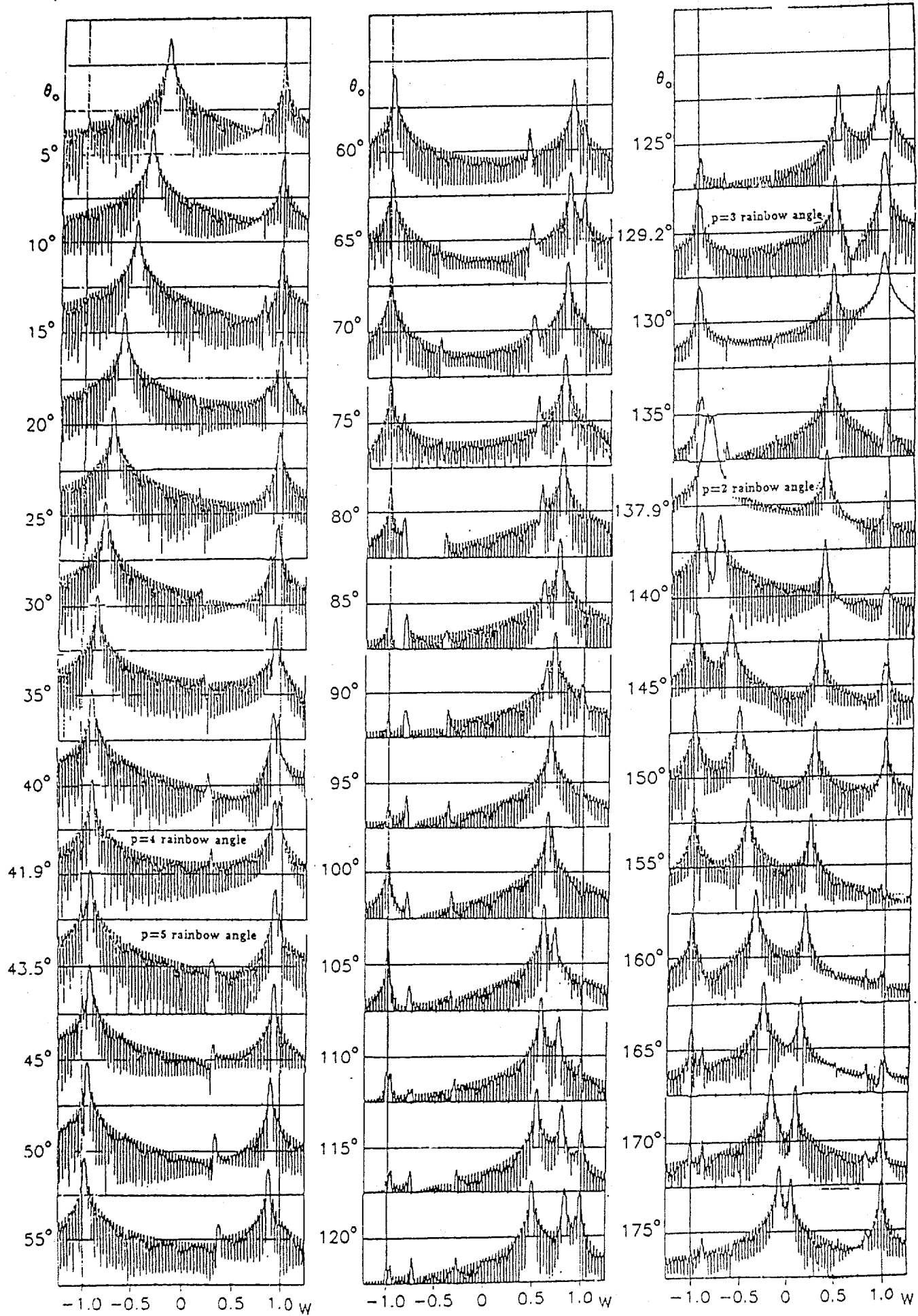


Fig. 5 Mie Theory Glare Point Images for  $x=10,000$ ,  $m=1.331-i1.3E-8$ , and  $b/r=0.01$ . See sec. 3.

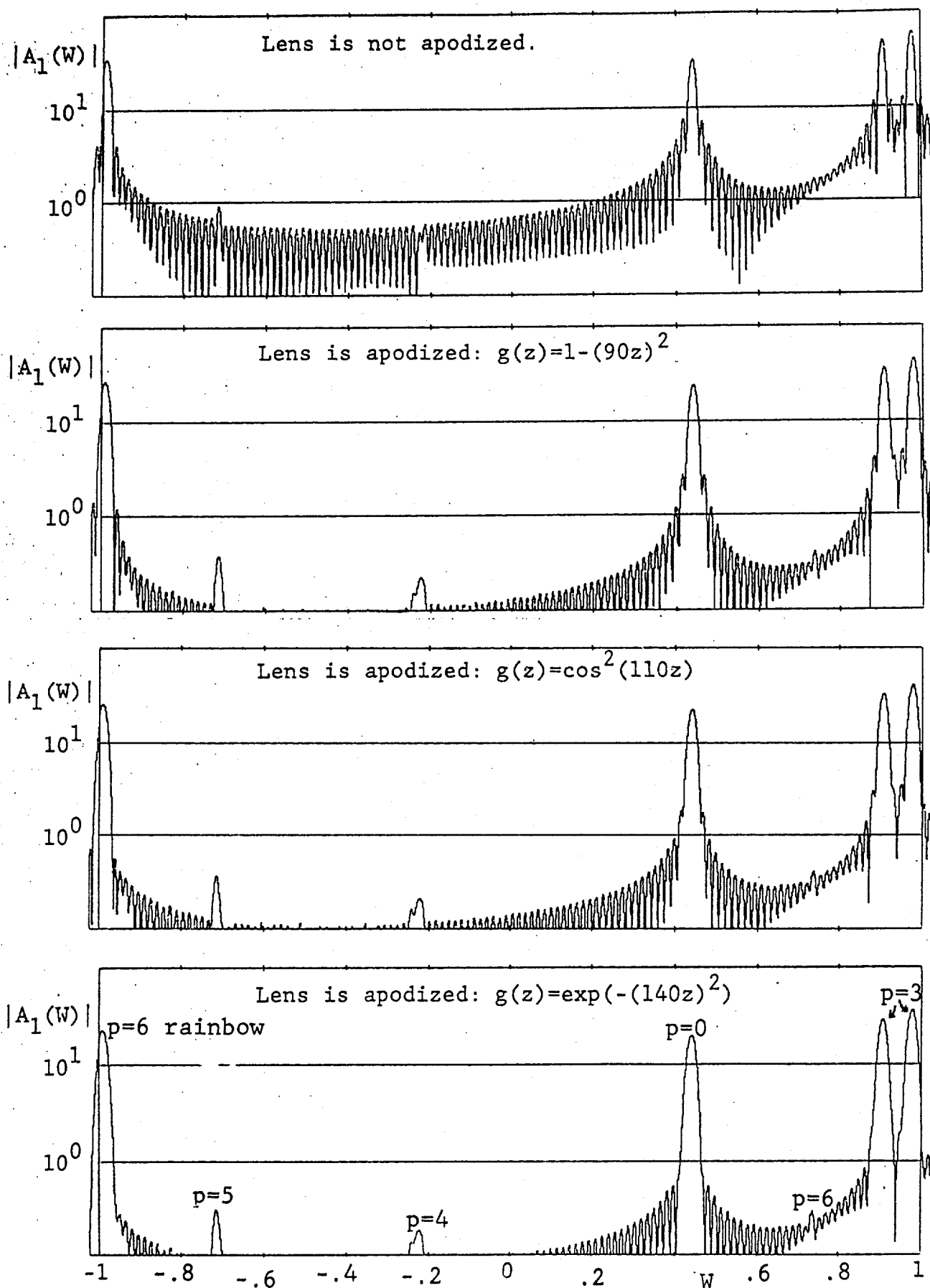


Fig. 6 Mie Theory Glare Point Image for  $x=20,000$ ,  $m=1.331-i1.3E-8$ ,  $b/r=0.01$ , and  $\theta_0=127.61^\circ$  ( $p=6$  Airy rainbow angle).

# SINGLE SCATTERING INVERSION PROBLEM

Po Hu and M. Lax  
Physics Department, City College of New York  
New York, New York 10031

## RECENT PUBLICATIONS, SUBMITTAL FOR PUBLICATION AND PRESENTATIONS:

- <sup>1</sup>B. Yudanin, P. Hu, M. Lax, "Numerical Solution of the Riemann Problem in the Presence of an External Energy Source", in Proceedings of the 1988 CRDEC Scientific Conference on Obscuration and Aerosol Research.
- <sup>2</sup>B. Yudanin, M. Lax, "POST Adaptation for a Numerical Solution of the Spherically-Symmetric Riemann Problem," J. of Computational Physics, (submitted).
- <sup>3</sup>B. Yudanin, M. Lax, "Hydrodynamical Response to Uniform Laser Absorption in a Droplet," in Proceedings of the CRDC 1985 Scientific Conference on Obscuration and Aerosol Research, edited by R. H. Kohl and D. Stroud (1985).
- <sup>4</sup>M. Lax, B. Yudanin, "Early-Time Hydrodynamic Response to Pulsed Laser Radiation," Digest - Intl. Conf. on Optical and Millimeter Wave Propagation and Scattering in the Atmosphere, Florence, Italy, 1986.

## ABSTRACT

It is proposed to apply the techniques of statistical decision theory to the problem of inverting scattering information from a single scatterer to determine if the scatterer has a shell-like structure. We shall start with a spherical scatterer with an index of refraction varying from 1.33 to 1.55. and compare it with a spherical core of 1.33 surrounded by a shell of index 1.55. We assume that the outer radius of the sphere is fixed at 2.5 microns, and the inner radius (when present) can vary from 1.76 to 2.2 microns.

## 1. Decision Problem

From a set of experimental light scattering data by a spherical scatterer, we wish to make a decision concerning the nature of the scatterer. We assume, initially, that the structure of the scatterer is restricted to be one of the following two cases. In case (hypothesis) 1, the scatterer is assumed to be a uniform sphere with radius 2.5 microns and a refraction index between from 1.33 to 1.55. In the case (hypothesis) 2, the scatterer is a layered sphere with varying inner radius from 1.76 to 2.2 microns and a core index 1.33 and shell index 1.55, the outer radius is assumed to be the same as the case 1. The wave length of the light is assumed to be .4416 microns. We need to decide which case it is with minimum probability of an incorrect guess. (Case 1 is a uniform sphere with a permitted range of index of refraction. Case2 is a layered sphere with a permissible range of inner radii. In both cases, in this note, the outer radius is fixed.)

The method of examining the experimental data to decide between these two cases (called hypotheses by statisticians) is a classical problem in decision theory solved by Neyman and Pearson in 1933<sup>1</sup>. The results are expressed in terms of "maximum likelihood ratios". An excellent overview is given by Kendall and Stuart<sup>2</sup>. A readable description of the Bayes theorem approach to the same problem is given by van Trees<sup>3</sup>. The close connection between these two approaches is touched on by Middleton<sup>4</sup> in his section on binary detection systems, although I believe that this is well understood in both the statistics and communications literature. For convenience, a brief summary of these ideas will be presented in an appendix.

## 2. The Method

Suppose the experimental data have been taken at the scattering angles  $\theta_i$  and  $\phi=0$ , the intensity of the scattering light per unit solid angle is denoted as  $i_{\text{exp}}(\theta_i)$ . We indicate the numerically calculated intensity for each case as  $i_{1,2}(\theta_i, \eta_{1,2})$ , where  $\eta_1$  is the varying parameter (refraction index) for the case 1 and  $\eta_2$  is the varying parameter (inner radius) for the case 2. In order to make a decision, we need to compare the experimental data with the calculated data for the two cases. Therefore we consider the following minimized deviation

$$v_k = \min_{\eta_k} \sum_i \left[ i_{\text{exp}}(\theta_i) - i_k(\theta_i, \eta_k) \right]^2 \quad (1)$$

by varying the parameter  $\eta_k$  for the case  $k$ . A simple thought is that one can choose the correct hypothesis by comparing two minimum values  $v_1$  and  $v_2$  and say that scatterer belongs to case 1 or case 2 depending on whether  $v_1$  is smaller or larger than  $v_2$ . This is true only when there is no any noise involved in the experimental data. When we consider a real experiment, noise is always involved. We can not separate the noise from the experimental data. The noise is assumed to have a known distribution. If the noise level is relatively high, it will mix the two cases so badly that we can not distinguish them. The noise level depends on the experimental apparatus, the environment and the kind of data taken. For a given apparatus and environment, one should measure such data so that the relative noise level is minimized. To understand the noise properties, we shall do some numerical simulation and find out what kind data should be measured to minimize the relative noise level. Although this is an important minimization process, we will not discuss it here and assume the experimental data have been already taken at a set of appropriate angles  $\theta_i$ .

Let  $H_1$  and  $H_2$  denote the two hypotheses, case 1, the sphere, and case 2, the layered sphere, respectively. The statistic we shall use to decide between these cases can be chosen as

$$R = \log_{10}(v_1/v_2) . \quad (2)$$

Suppose the conditional probability density  $P(R | H_k)$  of obtaining  $R$  under case  $k$  is known. In the language of radar detection, the Neyman-Pearson is equivalent to minimizing the probability  $P_M$  of a miss (choosing the null hypothesis  $H_1$  when there is a signal, i.e.  $H_2$  is true) subject to a fixed probability  $P_F$  of a false alarm (declaring that a signal  $H_2$  exists, when there is none, i.e.  $H_1$  is true). The constraint is:

$$P_F = \alpha = \int_{\lambda}^{\infty} P(R | H_1) dR \quad (3)$$

where  $\lambda$  is the threshold above which a "hit" is chosen. After finding the threshold,  $\lambda$  from the specified value of  $\alpha$ , the Neyman-Pearson decision criterion is simply:

$$\text{if } \Lambda(R) > \lambda \quad \text{choose } H_2 \quad (4)$$

$$\text{if } \Lambda(R) < \lambda \quad \text{choose } H_1 \quad (5)$$

where  $\Lambda(R)$ , the likelihood ratio, is defined to be:

$$\Lambda(R) = P(R | H_1) / P(R | H_2). \quad (6)$$

A proof is supplied in the appendix.

### 3. Numerical simulation

First we generate uniformly distributed random numbers in the range of variation of the parameter  $\eta_k$  for case  $k$  and then use these parameters to calculate the intensity. Secondly, we generate Gaussian distributed random numbers with magnitude of 5% of the intensity and then add them to the intensity calculated in the first step, we will refer to these results as test data  $i_{\text{test}}(\theta_i)$ . Thirdly, we use the minimizing formula Eq. (1) above to find the distribution  $P(R | H_k)$ . Finally, using the Neyman-Pearson criterion, we then can make a decision.

Numerical results are given in Fig. 1. From Fig.1, we see a slight overlap of the two sets of data near region  $R=0$ . From this figure, we can almost always tell which case is correct from the value of  $R$ . When  $R$  falls in the region to the left of the overlap region we can choose case 1, and when it falls in the right of the overlap region we can choose case 2. In the overlap region, we need to use the Neyman-Pearson criterion. The dots and  $\Delta$  in Fig.1 can be used as conditional probability densities  $P(R | H_1)$  and  $P(R | H_2)$ , respectively. Given an  $\alpha$ , we can use Eqs. 4-6 to make a decision.

### 4. Another Apriori Distribution (Stuebing's Choice)

In this section, we want to distinguish the following two cases. Case 1: the scatterer is a uniformed sphere with a index 1.33 and a wide varying radius from .1 to 10 microns. Case 2: the scatterer is layered with the inner radius being .9 times the outer radius. The latter, however, can vary over the wide range from .1 to 10 microns. This uncertainty makes the

decision problem much more difficult even though we maintain the core index at 1.33 and the shell index at 1.55. The wave length is the same as in the previous example (.44 microns). Because  $ka = 2\pi a/\lambda$  can be large, the intensity of Mie scattering as function of the outer radius has hundreds of oscillations. In order to find the true minimum of Eq. 1, we must cut the outer radius into hundreds pieces to find the local minima. Then finally we must compare these minima to find the global minimum.

The computer results for 100 tries for each case are displayed in Fig. 2.

### 5. The Probability of Errors of Both Kinds

Neyman and Pearson recognized that there were two possibilities of error: choosing hypothesis  $H_1$  when  $H_2$  is correct and vice-versa. A decision making process must assign (probably different) costs to these two errors. Such criteria will be dealt with in our discussion of the Bayes approach in the appendix. Here, we recognize that minimizing one error will increase the other. For simplicity, we can require that these errors be equal, and adjust the parameters to minimize that error.

The Neyman-Pearson criterion applies to any single test, i.e. when we obtain the value  $R$  we compare the densities of probability for the two cases and then make a decision.

If we choose  $H_1$  when  $R \geq \lambda$ , and  $H_2$  when the opposite is true, how can we select the decision threshold,  $\lambda$ , so that both errors are equal? Let us denote

$$\alpha_1(\lambda) = \int_{\lambda}^{\infty} P(R | H_1) dR = \text{probability of an incorrect guess of } H_1 \quad (7)$$

and

$$\alpha_2(\lambda) = \int_{-\infty}^{\lambda} P(R | H_2) dR = \text{probability of an incorrect guess of } H_2 \quad (8)$$

$\alpha_1$  and  $\alpha_2$  are the total probability of a wrong guess for case 1 and case 2 with the boundary  $R = \lambda$ . In general, the importance of a "miss" is different from that of a false alarm, and the threshold should be adjusted accordingly. When there is a clean separation between the two cases, as in Fig.1, the threshold should be close to  $\lambda = 0$  in any case. In the absence of other information, we can choose to make the two errors equal. The decision threshold for the equal error case is given by:

$$\alpha_1(\lambda) = \alpha_2(\lambda). \quad (9)$$

Let us now define

$$F(\lambda) = \left[ \alpha_1(\lambda) - \alpha_2(\lambda) \right]^2 \quad (10)$$

Then the boundary value  $\lambda$  can be found at the minimum of the function  $F$ . For the data of Fig.1 and 2, function  $F(R)$  is plotted in Fig.3 and 4 respectively. We see that for the case of equal errors, the threshold based on the Monte Carlo data of Figs. 1,2 is not at the noise-free value of zero, but is slightly negative. The meaning of the threshold  $\lambda$  means that we can globally make a decision knowing only that  $R$  is larger or smaller than the threshold.



## 6. Two-parameter tries

In this section, we consider a scatterer with two varying parameters. For the layered sphere, the parameters are the inner radius and outer radius in the range of

$$4 < R_{in}/\lambda_L < 5; \quad 5.5 < R_o/\lambda_L < 6;$$

Here  $R_{in}$  and  $R_o$  are the inner radius and outer radius, respectively, and  $\lambda_L$  is the wave length of the light. Although there is only one independent parameter in the uniform sphere ( $q = mR_o/\lambda_L$ ) for a fixed wave length, for convenient in comparing with the layered sphere, we still chose the two varying parameters as  $R_o$  and  $m$ , where  $m$  is the refraction index.

1000-pair random numbers for these parameters in the specified region are generated and are plotted in Figs 6-7 for both cases. Horizontal and vertical polarized scattering intensities at five angles,  $\theta = 45, 50, 55, 60$  and  $65$ , are assumed to be detected. We use Gaussian distributed random numbers to generate computer simulated experimental data. The distributions of these random numbers are plotted in Figs. 8-9 for both cases. In Fig. 5, the number of tries as function of  $R = \log(v_1/v_2)$  is given. The left profile is due to the hypothesis  $H_1$ , the uniform sphere, while the right one is for the layered sphere  $H_2$ .

### Appendix: The Binary Decision Problem<sup>3</sup>

The problem of detecting a layered sphere (as opposed to a uniform one) is analogous to that of distinguishing a plane from a radar signal (as opposed to noise from other objects). Statisticians refer to  $H_1$  as the hypothesis that the object of interest (e.g. the plane) exists, and  $H_0$  as the small hypothesis (e.g. the noise). It is, of course, possible to deal with a set of hypotheses  $H_i$ , but we are mainly concerned here with the binary decision problem.

There are two principal methods of dealing with the binary decision problem (referred to as detection by electrical engineers):

#### (a) The Bayes Method

The first method uses the statistical ideas employed by Bayes. The Bayes method assumes that an apriori probability  $P_i$  exists for the occurrence of  $H_i$ , and assigns a cost  $C_{ji}$  of guessing that  $H_j$  has occurred when, in fact,  $H_i$  has occurred. If we denote the conditional probability

$$P(H_j | H_i) = P_r(\text{choose } H_j | \text{if } H_i \text{ is true}) \quad (\text{A1})$$

then the average cost is given by

$$C = \sum_{i,j} C_{ji} P(H_j | H_i) P_i \quad (\text{A2})$$

Let us assume that a set of objects are measured, which we can describe as a vector  $\mathbf{R}$  in some multi-dimensional space  $Z$ . We shall assume the existence of a decision rule of the form:

$$\text{Choose } H_j \text{ if } \mathbf{R} \text{ is in subspace } Z_j \quad (\text{A3})$$

Our problem is to choose the domains  $Z_j$  in such a way as to minimize the cost, Eq. (A2). With this decision rule, our cost, Eq. (A2) can be written in the form

$$C = \sum_{ij} C_{ji} \int_{Z_j} P(\mathbf{R} | H_i) d\mathbf{R} P_i \quad (\text{A4})$$

We also have the normalization conditions:

$$\int P(\mathbf{R} | H_i) d\mathbf{R} = 1 \quad (\text{A5})$$

In the binary case, normalization permits an integral over  $Z_1$ , to be expressed as an integral over  $Z_0$ :

$$\int_{Z_1} P(\mathbf{R} | H_j) d\mathbf{R} = 1 - \int_{Z_0} P(\mathbf{R} | H_j) d\mathbf{R} \quad (\text{A6})$$

As a result, it is possible to reexpress the cost, in the binary case, in the form

$$C = C_{10} P_0 + C_{11} P_1 + \int_{Z_0} [(C_{01} - C_{11}) P(\mathbf{R} | H_1) P_1 - (C_{10} - C_{00}) P(\mathbf{R} | H_0) P_0] d\mathbf{R} \quad (\text{A7})$$

But the cost of a wrong decision must be taken greater than that of a correct decision. This we must have:

$$C_{10} > C_{00} ; C_{01} > C_{11} \quad (\text{A8})$$

Thus aside from the first, fixed cost, term we have a difference of two positive terms. We can therefore minimize the risk by choosing the region  $Z_0$  to be such that the argument in braces is always negative in that region, or conversely, any point  $\mathbf{R}$  for which the argument in brackets is positive is chosen to be in  $Z_1$ .

Thus we choose  $Z_1$  whenever

$$(C_{01} - C_{11}) P(\mathbf{R} | H_1) P_1 \geq (C_{10} - C_{00}) P(\mathbf{R} | H_0) P_0 \quad (\text{A9})$$

or

$$\Lambda(\mathbf{R}) = \frac{P(\mathbf{R} | H_1)}{P(\mathbf{R} | H_0)} > \frac{(C_{10} - C_{00}) P_0}{(C_{01} - C_{11}) P_1} = \lambda \quad (\text{A10})$$

Thus the multidimensional statistic  $\mathbf{R}$  is replaced by a one-dimensional quantity  $\Lambda(\mathbf{R})$ , the "likelihood ratio". The latter is to be compared with a parameter  $\lambda$  which is fixed. The handling of the data is thus confined to computing the maximum likelihood ratio  $\Lambda(\mathbf{R})$  even though the costs or the apriori probabilities  $P_0$  and  $P_1$  or costs may not be known.

#### (b) The Neyman-Pearson Method

The Neyman-Pearson test arrives at the identical result by considering the problem of minimizing the probability  $P_M$  of a miss (choosing  $H_0$  when a "real target"  $H_1$  is true) subject to the constraint of a fixed probability of a false alarm  $P_F$  (choosing a "real target"  $H_1$  when  $H_0$  is true). In this case, one chooses  $C_{00} = C_{11} = 0$ ,  $C_{01} = C_M$ ,  $C_{10} = C_F$ . One minimizes  $P_M$  subject to a fixed false alarm ( $P_F = \alpha$ ) by minimizing

$$F = P_M + \lambda [P_F - \alpha] \quad (\text{A11})$$

where  $\lambda$  is a Lagrange multiplier.

$F$  can be rewritten as

$$F = \int_{Z_0} P(\mathbf{R} | H_1) d\mathbf{R} + \lambda \left[ \int_{Z_1} P(\mathbf{R} | H_0) d\mathbf{R} - \alpha \right] \quad (\text{A12})$$

If we constrain  $P_F = \alpha$ , the second term vanishes, and minimizing the first term,  $P_M$ , is equivalent to minimizing  $F$ . In view of the normalization conditions, Eq. (A5), Eq. (A12) can be rewritten as

$$F = \lambda(1 - \alpha) + \int_{Z_0} [P(\mathbf{R} | H_1) - \lambda P(\mathbf{R} | H_0)] d\mathbf{R} \quad (\text{A13})$$

Assume that  $\lambda$  is positive. To minimize  $F$ , we choose the domain  $\mathbf{R}$  to include all points for which the bracket is negative. Thus if

$$\Lambda(\mathbf{R}) = \frac{P(\mathbf{R} | H_1)}{P(\mathbf{R} | H_0)} < \lambda \text{ choose } H_0 \quad (\text{A14})$$

Again, the decision is based on the "likelihood ratio",  $\Lambda(\mathbf{R})$ . This criterion is equivalent to that used by the Bayes method, except that the costs and apriori probabilities are unknown. Instead of Eq. (A13),  $\lambda$  is chosen by the originally specified constraint:

$$P_F = \int_{\lambda}^{\infty} P(\Lambda | H_0) d\Lambda = \alpha \quad (\text{A15})$$

All that is needed, is a knowledge of the conditional probabilities  $P(\mathbf{R} | H_j)$ .

<sup>1</sup>J. Neyman and E. S. Pearson, "On the Problem of the Most Efficient Tests of Statistical Hypotheses," *Philosophical Trans. A*, 231, 289 (1933)

<sup>2</sup>M. G. Kendall and A. Stuart, *The Advanced Theory of Statistics, Volume 2* Hafner Publishing Co, New York (1967)

<sup>3</sup>H. L. Van Trees, *Detection, Estimation, and Modulation Theory, Part I*, John Wiley and Sons, (1968)

<sup>4</sup>David Middleton, *Introduction to Statistical Communication Theory*, McGraw-Hill (1960)

Fig.1.  $N(R)$ , number of tries falling into a interval of  $dR=0.1$  is plotted. The dots are for the case of uniform sphere with a varying refraction index 1.33 to 1.55.  $\Delta$  are for the case of the layered sphere with core index 1.33 and shell index 1.55 and a varying inner radius from 1.76 to 2.2 micron. The outer radius is fixed at 2.5 micron for both cases. The total number of tries is 1000 for each case. The intensity of one scattered light of one polarization at  $\theta=45,50,55,60,65$  and  $\phi=0$  are used.

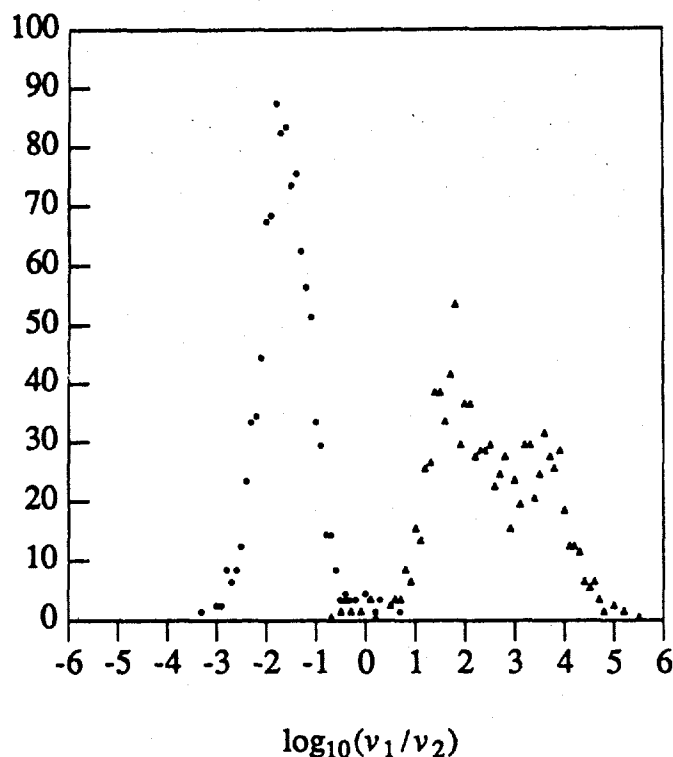


Fig.2.  $N(R)$ , the number of tries falling into a interval of  $dR=0.1$ , is plotted. The dots are for the case of the uniform sphere with a refraction index 1.33. The  $\Delta$  are for the case of a layered sphere with core index 1.33, shell index 1.55 and inner radius 0.9 times outer radius. The outer radius can vary from 0.1 to 10 microns for both cases (wide varying range). The total number of tries is 100 for each case. Intensity of one polarization of scattering light at the angles  $\theta=45,50,55,60,65$  and  $\phi=0$  are used.

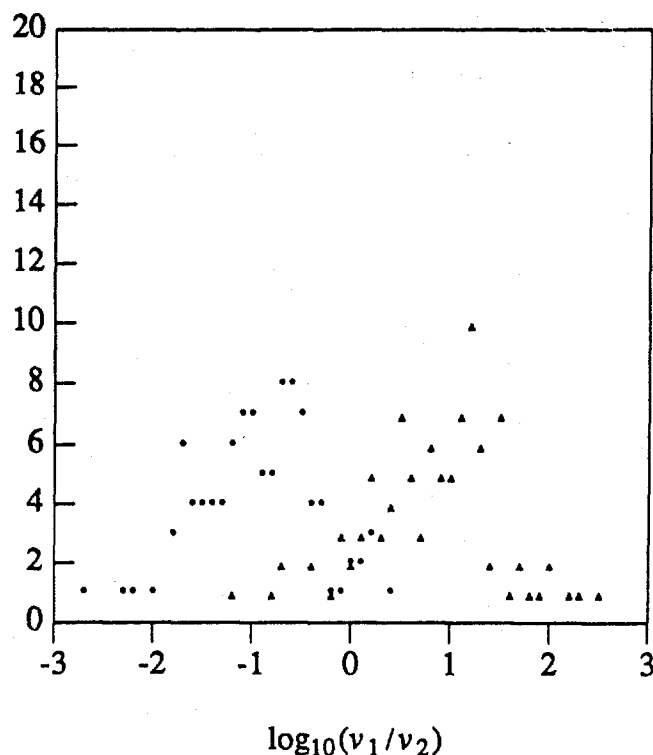


Fig.3. Plot of function  $F$  for the data from Fig.1. The minimum is at  $\lambda = -0.1$  with the EPOWG of 1%.

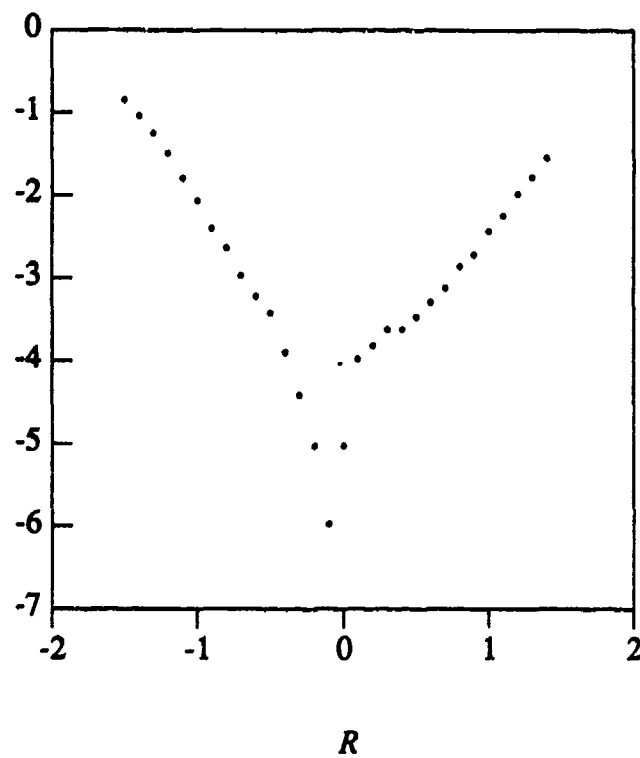


Fig.4. Plot of function  $F$  for the data from Fig.2. The minimum is at  $\lambda = -0.1 \sim 0.2$  with the EPOWG of 8%.

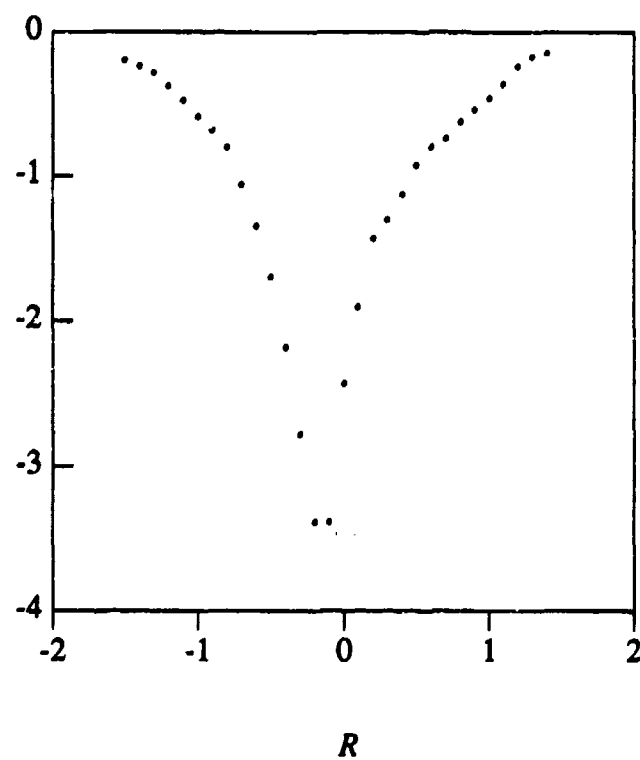


Fig.5. Two parameter plot. Number of tries is plotted as function of  $R=\log_{10}(v_1/v_2)$ . For the case of uniform sphere, the two parameters are a refraction index in the range of 1.33 to 1.55 and radius in the range of 2.43 to 2.64 microns. For the layer structured sphere, the core index 1.33 and shell index 1.55 are fixed. The two varying parameters are the inner radius in the range of 1.76 to 2.2 microns and outer radius in the range of 2.43 to 2.64 microns. The total number of tries is 1000 for each case. The intensities for two polarized lights at  $\theta=45,50,55,60,65$  and  $\phi=0$  are used.

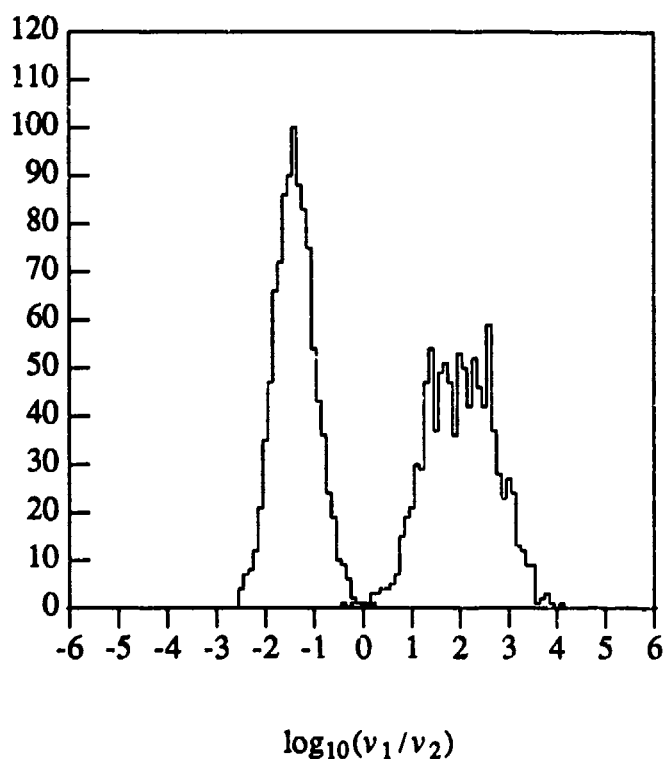


Fig.6. 1000-pair random numbers are generated for the two varying parameters of uniform sphere. The two parameters are the refraction index in the range of 1.33 to 1.55 (the horizontal axis) and radius in the range of 2.43 to 2.64 microns (the vertical axis).

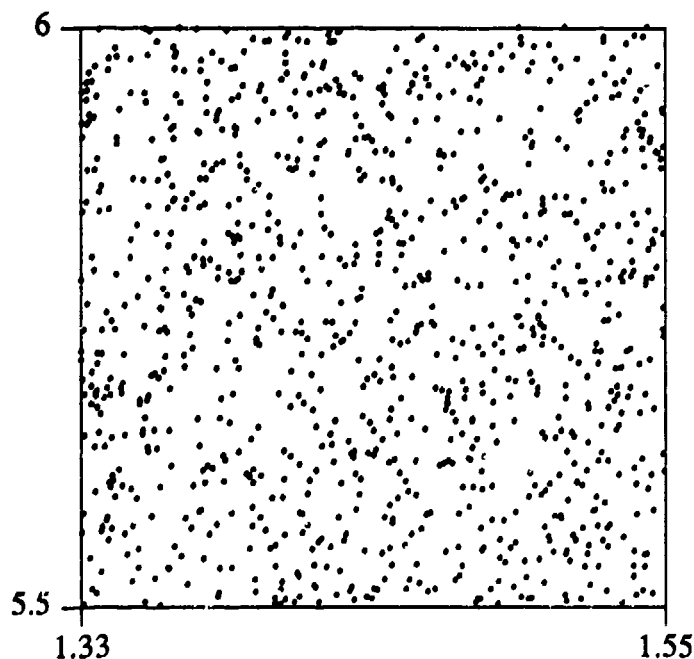


Fig.7. 1000-pair random numbers are generated for the two varying parameters of layer structured sphere. The two parameters are the inner radius in the range of 1.76 to 2.2 microns (the horizontal axis) and the outer radius in the range of 2.43 to 2.64 microns (the vertical axis). for two polarized lights at  $\theta=45,50,55,60,65$  and  $\phi=0$  are used.

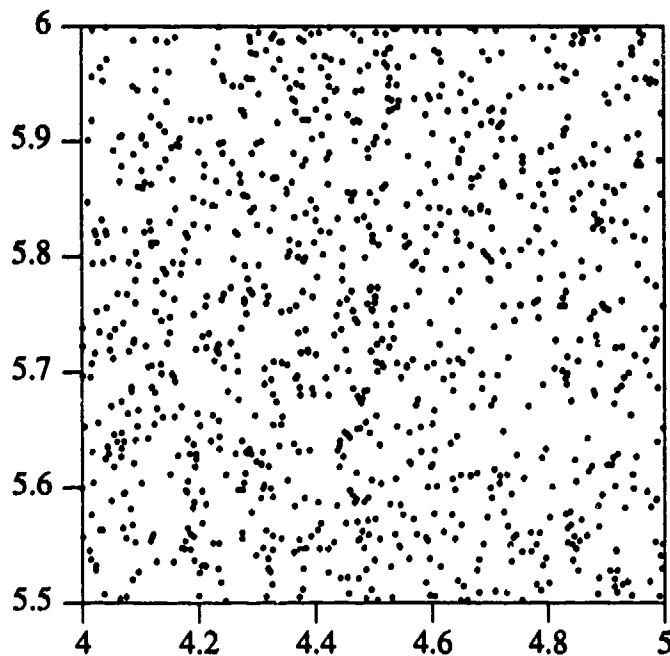


Fig.8. Plot of the 10000 gaussian random numbers which are added to the intensity of scattering light for the uniform sphere.

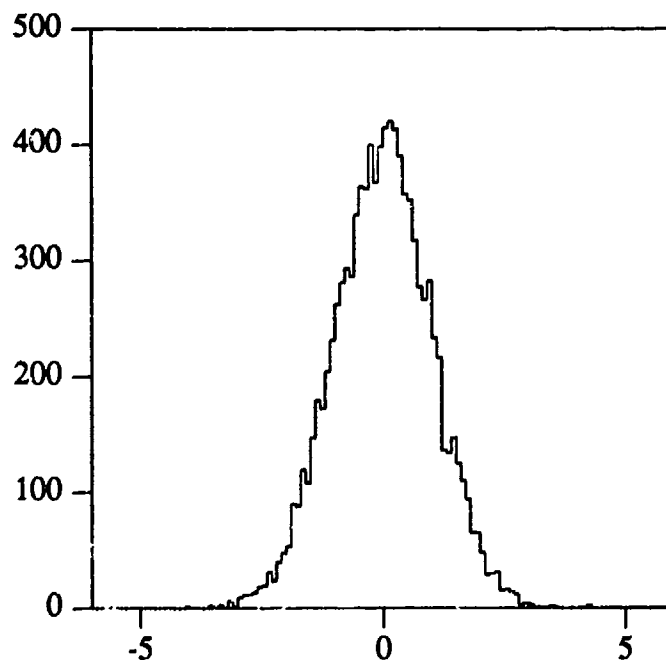
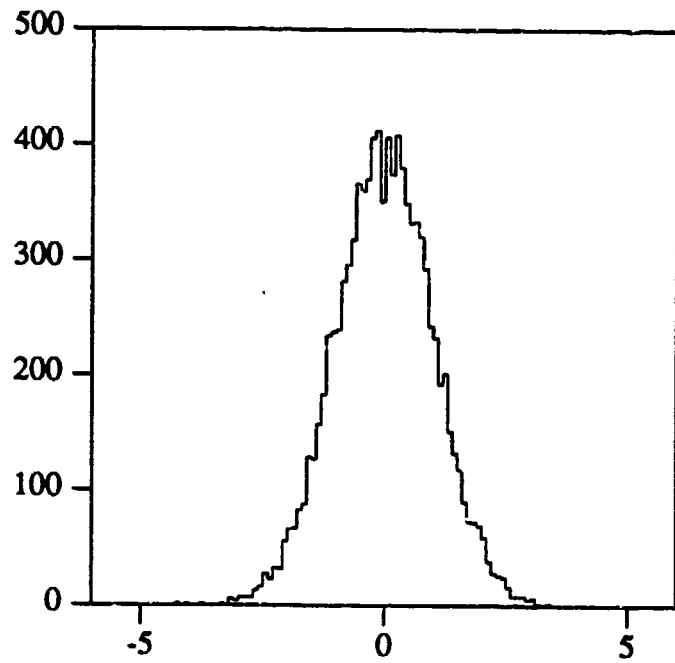


Fig.9. Plot of 10000 gaussian random numbers which are added to the intensity of scattering light for the layer structured sphere.





**OPTICAL PROPERTIES OF SELECTED MATERIALS IN THE ULTRAVIOLET  
TO MILLIMETER SPECTRAL REGION**

Lawrence Newquist, Ralph W. Alexander, Jr.  
Ray Vandiver, and Robert J. Bell  
University of Missouri - Rolla  
Rolla, MO 65401

and

Marvin R. Querry, David Wielszczka  
Physics Department  
University of Missouri - Kansas City  
Kansas City, MO 64110

**RECENT PUBLICATIONS, SUBMITTAL FOR PUBLICATION AND PRESENTATIONS:**

A) Lawrence Newquist, R. W. Alexander, Jr., David Wielszczka, Ray Van Diver, Marvin R. Querry and R. J. Bell, "Optical Properties of Selected Materials in the Ultraviolet to Millimeter Spectral Region", Final Report, CRDEC SSP 88-22, in preparation.

**ABSTRACT**

The reflectance of a graphite fiber sample (Hercules IM6), type 316L stainless steel, two samples of iron fibers, rutile and terephthalic acid were measured from 10 to 50,000 wavenumbers. Kramers-Kronig analysis or oscillator analysis was used to extract the complex refractive index from the measured reflectance. Work is continuing on Hercules C3X graphite fibers.

## INTRODUCTION

The work described in this report was carried out at the University of Missouri-Kansas City and at the University of Missouri-Rolla. Reflectance measurements at infrared, visible and ultraviolet wavelengths were made at the University of Missouri-Kansas City Optics Laboratory and measurements at longer wavelengths were made at the Far Infrared Spectroscopy Laboratory at the University of Missouri-Rolla. The far infrared reflectance measurements were made using a modified Beckman-RIIC Far Infrared Fourier Transform Spectrometer with a Golay cell detector. The near-infrared and visible measurements were made with Carey and the ultraviolet reflectance measurements were made with a Perkin-Elmer instrument.

Individual samples and results are discussed below, but here we outline the general techniques used and the type of results obtained. Most of the samples to be measured were in the form of powders or metal fibers. These materials were pressed into pellets. The reflectance,  $R$ , of these pellets was measured from the far infrared to the ultraviolet. For the crystalline powders, namely rutile and terephthalic acid, the measured reflectance was fit with an independent oscillator model. From the oscillator parameters, the real part of the refractive index,  $n(\omega)$  and the imaginary part of the refractive index,  $k(\omega)$ , can be calculated as a function of the frequency,  $\omega$ . Tables of the data can be found in the report referenced above or obtained from Mr. Merrill Milham at the United States Army Chemical Research, Development and Engineering Command at Aberdeen, Maryland.

The metal fiber and graphite powder samples were also pressed into pellets. The stainless steel fiber sample did not make a satisfactory pellet and so a bulk sample of the same kind of stainless steel was measured. Again for all these samples, reflectance was measured from the far infrared to the ultraviolet. For the bulk stainless steel, measurements were made with a non-resonant cavity in the far infrared. For these samples an oscillator fit doesn't describe the sample correctly and so we performed a Kramers-Kronig analysis of the data to obtain  $n(\omega)$  and  $k(\omega)$ . Again the results are tabulated in our contract final report and were transmitted to Mr. Milham at Aberdeen.

## TEREPHTHALIC ACID

The terephthalic acid powder used was obtained from the Kodak Chemical Company. Using an hydraulic press and standard 13 mm diameter die, pellets were pressed. An excellent smooth, shiny finish was obtained on the surface of these pellets. Figure 1 shows the measured reflectance for a pellet of terephthalic acid.

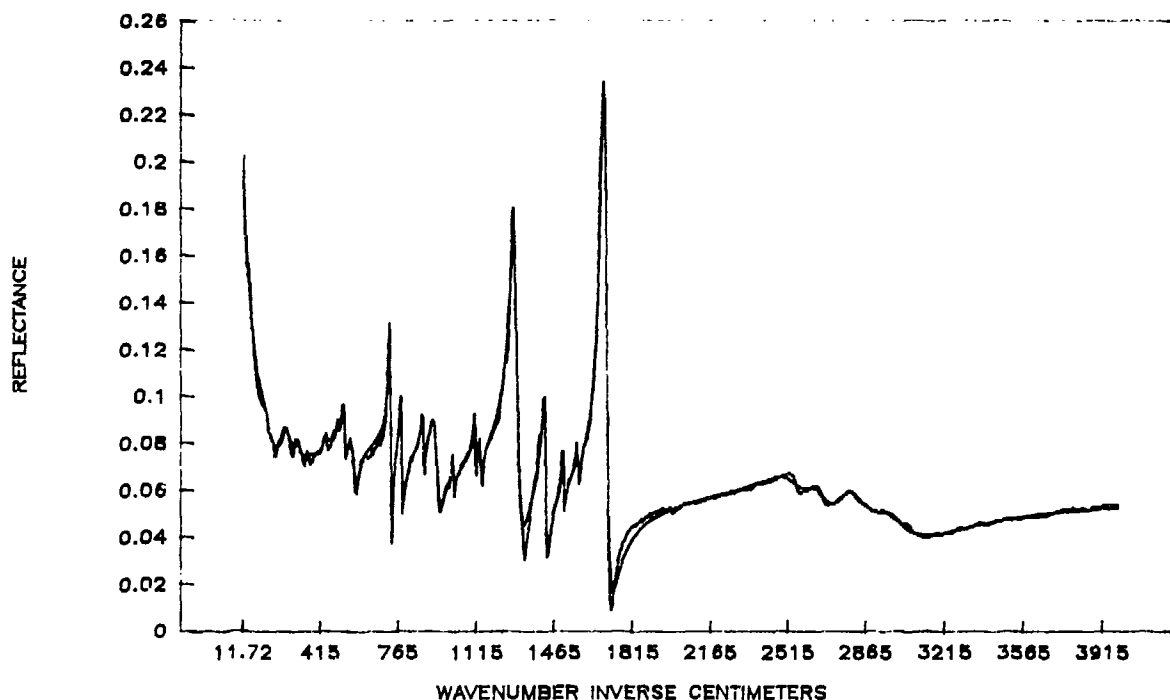


FIGURE 1: MEASURED REFLECTANCE FOR TEREPHTHALIC ACID (solid line). Calculated reflectance for terephthalic acid from Eq.(1) using the fit parameters from Table I (dotted line).

The measured reflectance was fit to a four parameter oscillator fit. The form of the four parameter oscillator is

$$\epsilon = \epsilon_1 + i\epsilon_2 = \epsilon_\infty + \pi \frac{\Omega^2}{jL\Omega - \omega^2 - i\gamma} \frac{jL\Omega \omega}{jT\Omega - \omega^2 - i\gamma} \quad (1)$$

$$\epsilon = (n + ik)^2$$

This equation is taken from Gervais and Piriou<sup>1</sup> and gave a better fit to the measured reflectance than did the usual three parameter fit. A simplex routine was written to find the parameters in Eq. (1) from the measured reflectance. The parameters of the fit to Eq. (1) are given in Table I. It required 26 oscillators to fit the measured reflectance. Figures 2 and 3 show the calculated  $n(\omega)$  and  $k(\omega)$  using the parameters of Table I. Because the sample was a powder, we cannot determine the axial orientation of the oscillators.

TABLE I. OSCILLATOR FIT PARAMETERS FOR TEREPHTHALIC ACID

Epsilon Infinity = 2.672731E+00

Omega LO	Omega TO	Gamma LO	Gamma TO
3.412226E-01	1.134454E+00	3.141359E+01	1.136635E+01
1.963044E+02	1.961179E+02	6.610109E+01	6.069158E+01
2.872253E+02	2.869526E+02	2.975464E+01	2.878901E+01
3.426134E+02	3.427794E+02	2.340949E+01	2.375019E+01
4.346661E+02	4.351035E+02	2.432366E+01	2.335594E+01
4.973356E+02	4.972266E+02	1.171355E+01	1.096206E+01
5.254370E+02	5.246458E+02	1.233165E+01	1.094883E+01
5.378671E+02	5.380323E+02	1.286756E+01	1.296866E+01
5.797212E+02	5.787125E+02	2.056138E+01	2.384116E+01
7.360277E+02	7.334085E+02	6.815039E+00	8.284336E+00
7.852258E+02	7.831400E+02	1.163604E+01	1.185021E+01
8.861681E+02	8.851940E+02	1.217681E+01	1.326811E+01
9.455857E+02	9.390853E+02	4.057190E+01	4.136718E+01
1.019547E+03	1.019199E+03	1.135041E+00	6.669838E-01
1.119379E+03	1.118974E+03	4.854231E+00	4.953890E+00
1.142040E+03	1.141491E+03	7.789229E+00	8.624388E+00
1.306162E+03	1.288753E+03	4.370269E+01	3.604603E+01
1.431583E+03	1.426795E+03	1.649779E+01	1.707556E+01
1.509321E+03	1.508815E+03	1.351949E+00	1.684685E-01
1.580776E+03	1.580365E+03	8.825333E+00	9.519658E+00
1.709666E+03	1.687345E+03	2.825751E+01	2.513271E+01
2.557554E+03	2.547019E+03	2.046527E+02	2.051552E+02
2.666428E+03	2.661515E+03	1.229304E+02	1.176768E+02
2.804322E+03	2.802767E+03	1.389001E+02	1.263177E+02
2.995279E+03	2.993081E+03	1.444847E+02	1.366910E+02
3.052491E+03	3.035247E+03	5.195965E+02	5.825635E+02

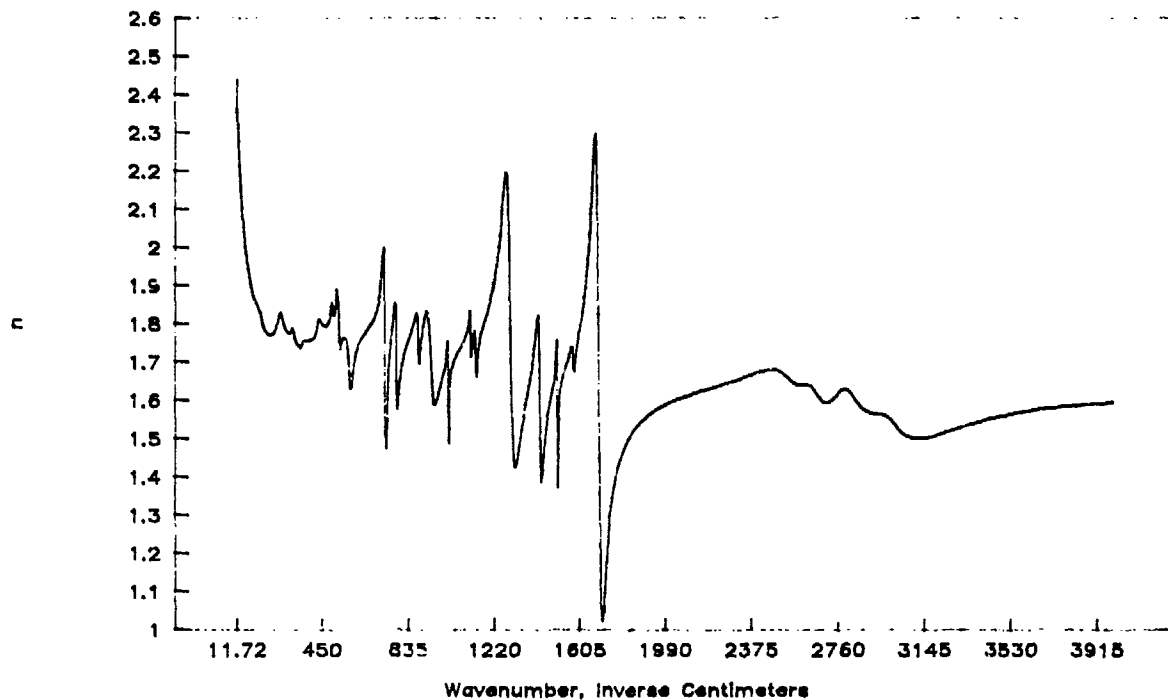


FIGURE 2: REAL PART OF THE COMPLEX REFRACTIVE INDEX,  $n$ , FOR TEREPHTHALIC ACID calculated from the oscillator fit.

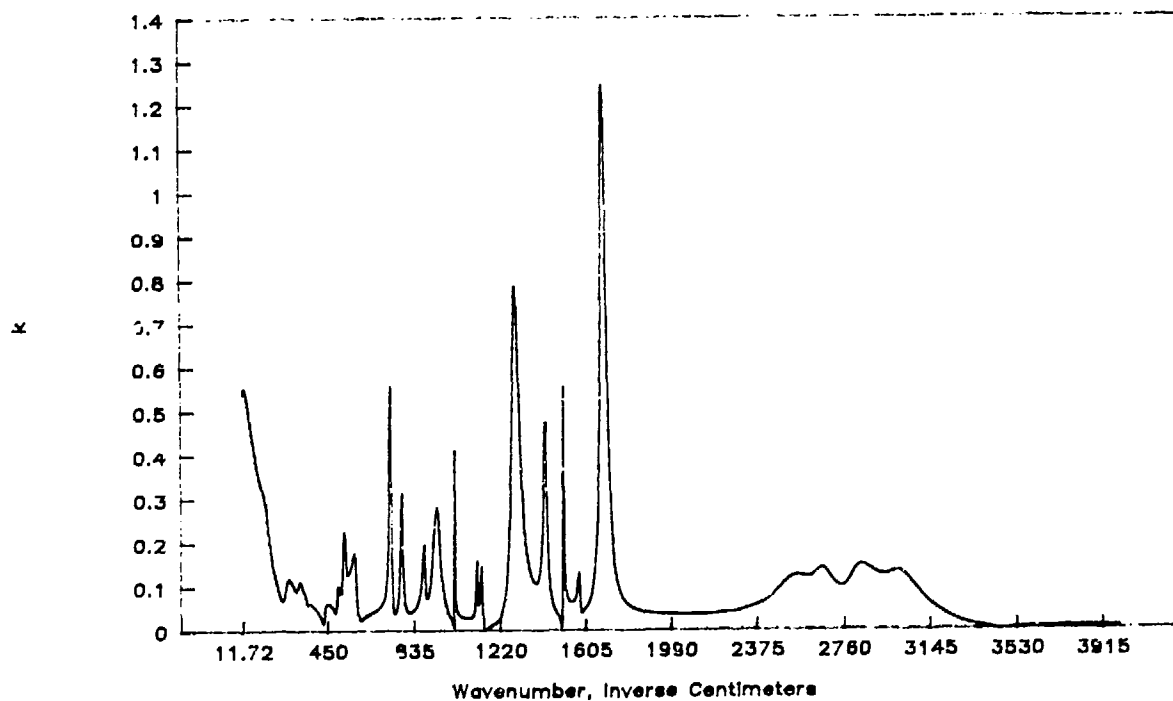


FIGURE 3: IMAGINARY PART OF THE COMPLEX REFRACTIVE INDEX,  $k$ , FOR TEREPHTHALIC ACID calculated from the oscillator fit.

## RUTILE

Rutile ( $\text{TiO}_2$ ) powder was purchased from Kodak Chemical Company. Despite the fact that rutile is quite hard, we were able to press satisfactory pellets in the hydraulic press with good surface finish. Again, the reflectance was measured as a function of wavelength. The parameters of Eq. (1) were again determined by fitting the measured reflectance. Figure 4 shows the measured reflectance,  $R(\omega)$ . Table II shows the oscillator parameters determined from the fit to the measured reflectance. Figures 5 and 6 show  $n(\omega)$  and  $k(\omega)$  calculated from the oscillator fit.

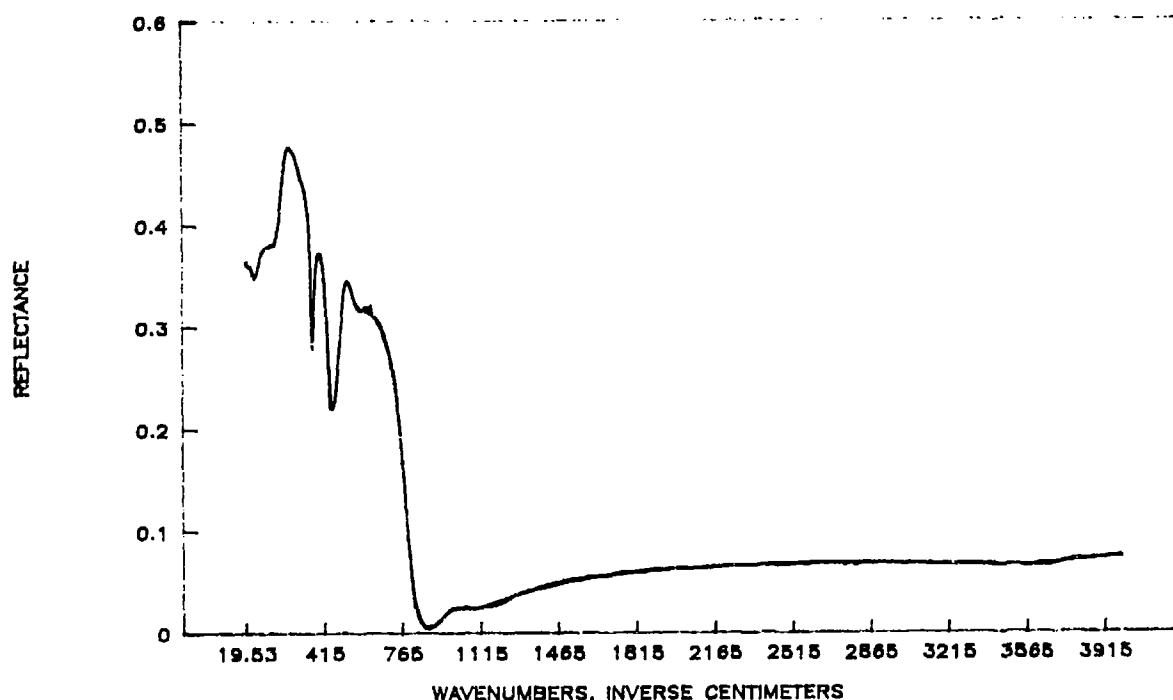


FIGURE 4: MEASURED REFLECTANCE OF RUTILE POWDER versus frequency in  $\text{cm}^{-1}$ .

TABLE II: OSCILLATOR FIT PARAMETERS FOR RUTILE

Epsilon Infinity = 3.27			
Omega LO	Omega TO	Gamma LO	Gamma TO
6.272781E+01	6.433150E+01	2.697446E+01	2.983328E+01
3.661339E+02	2.446405E+02	1.554678E+01	2.843664E+02
1.777941E+02	1.927793E+02	9.955939E+01	8.522772E+01
7.866856E+02	3.693307E+02	6.456564E+01	2.327765E+01
5.194609E+02	5.045944E+02	9.641367E+01	7.032333E+01
4.104109E+02	4.289806E+02	2.522783E+02	9.298299E+01
4.399180E+02	5.546226E+02	5.164677E+01	3.121541E+02
1.003910E+03	9.959520E+02	1.757303E+02	1.335943E+02
3.684361E+03	3.717502E+03	9.654258E+02	1.050955E+03

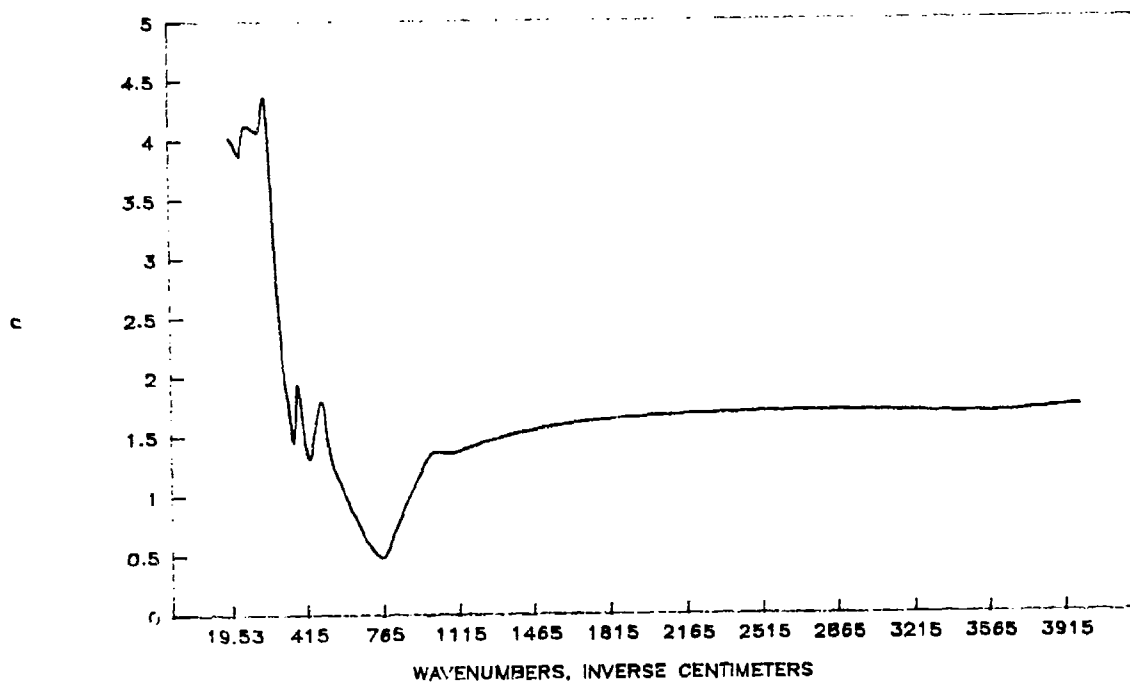


FIGURE 5: REAL PART OF THE COMPLEX REFRACTIVE INDEX,  $n$ , for rutile calculated from the oscillator fit.

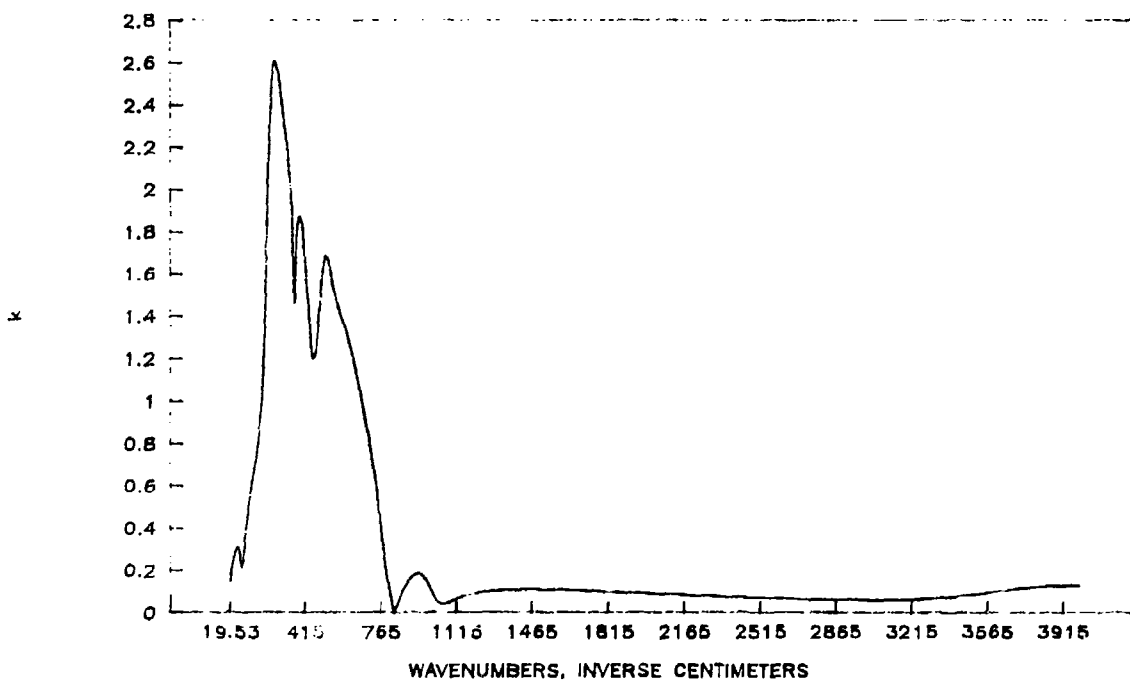


FIGURE 6: IMAGINARY PART OF THE COMPLEX REFRACTIVE INDEX,  $k$ , for rutile calculated from the oscillator fit.

## STAINLESS STEEL

Stainless steel fibers of type 316L stainless steel were obtained from Bekaert Steel Wire Corporation, Irving, Texas. The fibers were 2 micrometers in diameter and were woven into a mesh. The fibers were coated with polyvinyl alcohol. The mesh was chopped up and the fibers washed to remove the polyvinyl alcohol. We then attempted to press pellets from the fibers. We were unable to do this. Hence we used bulk type 316L stainless steel and measured its reflectance as a function of frequency from the far infrared to the ultraviolet. Better results were obtained at far infrared wavelengths using a non-resonant cavity.<sup>2</sup> The measured reflectance,  $R(\omega)$ , is shown in Figure 7 and the real part of the surface impedance,  $r_s(\omega)$  in the far infrared (measured using the non-resonant cavity) is shown in Figure 8.

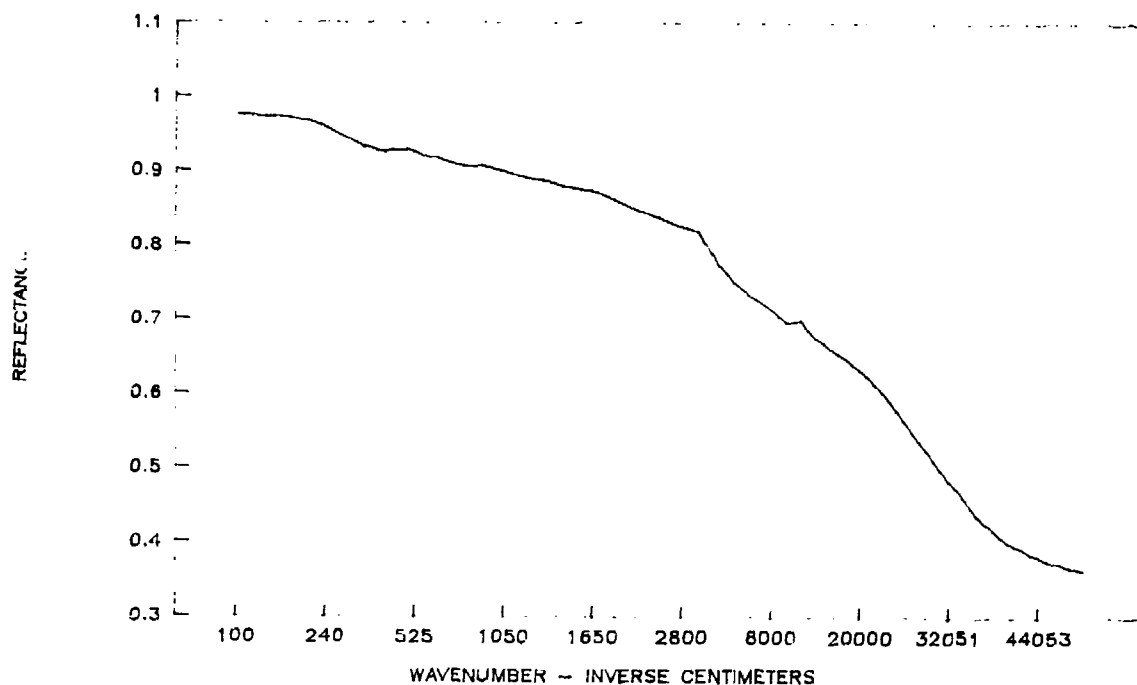


FIGURE 7: MEASURED REFLECTANCE OF TYPE 316L STAINLESS STEEL versus frequency in  $\text{cm}^{-1}$ .

Using  $r_s(\omega)$ , we calculated  $R(\omega)$  assuming that the stainless steel was a good conductor. This  $R(\omega)$ , calculated in the far infrared ( $100\text{cm}^{-1}$  to  $400\text{ cm}^{-1}$ ) was combined with the measured  $R(\omega)$  for the near infrared, visible and ultraviolet to use in a Kramers-Kronig analysis to determine  $n(\omega)$  and  $k(\omega)$  for the type 316L Stainless Steel. The resulting  $n(\omega)$  and  $k(\omega)$  are plotted in Figures 9 and 10 as a function of wavenumber.



A Drude model fit was made to the  $n(\omega)$  and  $k(\omega)$  at long wavelengths where one expects the Drude model to hold. Table III gives the Drude model parameters determined from the fit. The Drude model fits the data well from  $50 \text{ cm}^{-1}$  to about  $400 \text{ cm}^{-1}$ .

TABLE III: DRUDE MODEL PARAMETERS FOR 316L SS AND IRON FIBERS

Metal	$\omega$	$\omega$
Stainless Steel 316L	23500	478
Fe pellet	15900	226

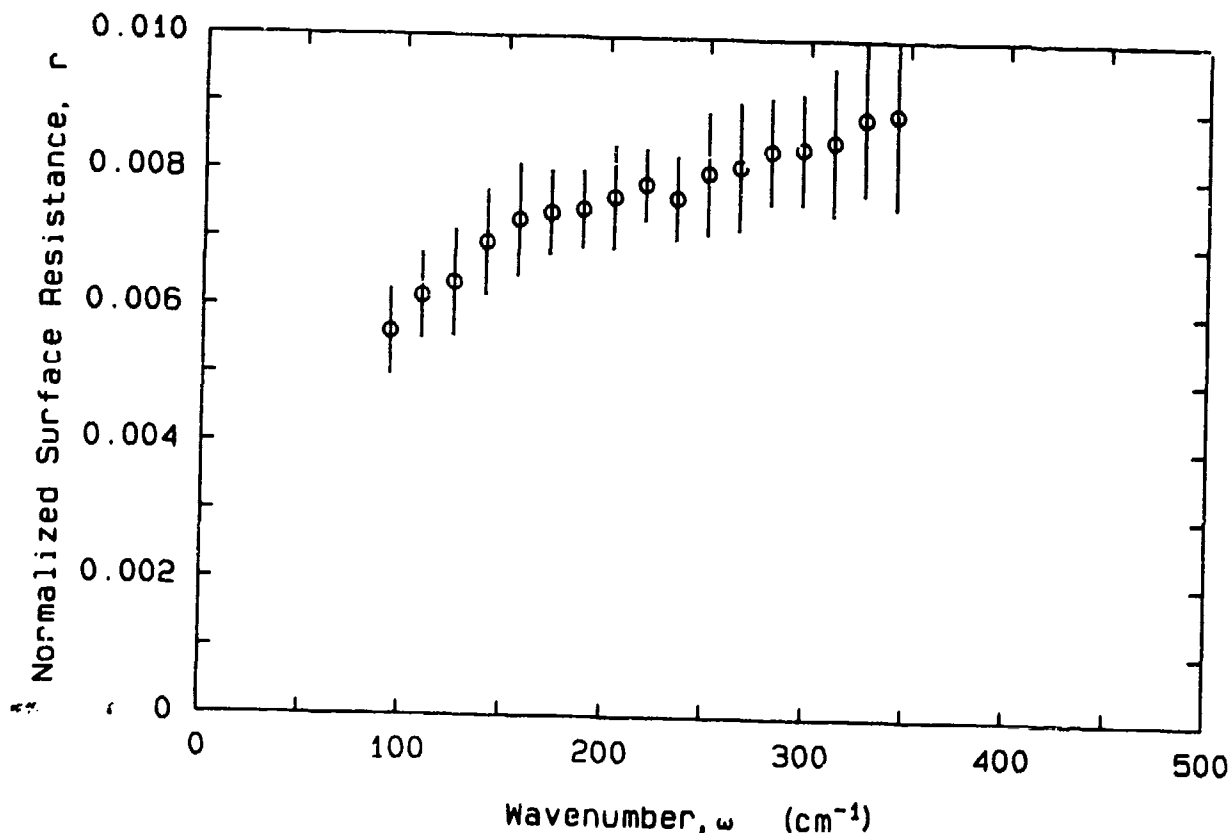


FIGURE 8: REAL PART OF THE SURFACE IMPEDANCE,  $r_s$ , versus frequency in  $\text{cm}^{-1}$  for type 316L stainless steel as measured with a non-resonant cavity.

Two different samples of iron fibers were supplied by the U.S. Army Chemical Research, Development and Engineering Command. These samples were not further identified so we call them sample 1 and sample 2 which is the way they were labelled when delivered. The iron fibers were soft enough to press into pellets with a surface quality sufficient to allow measurements in the infrared.

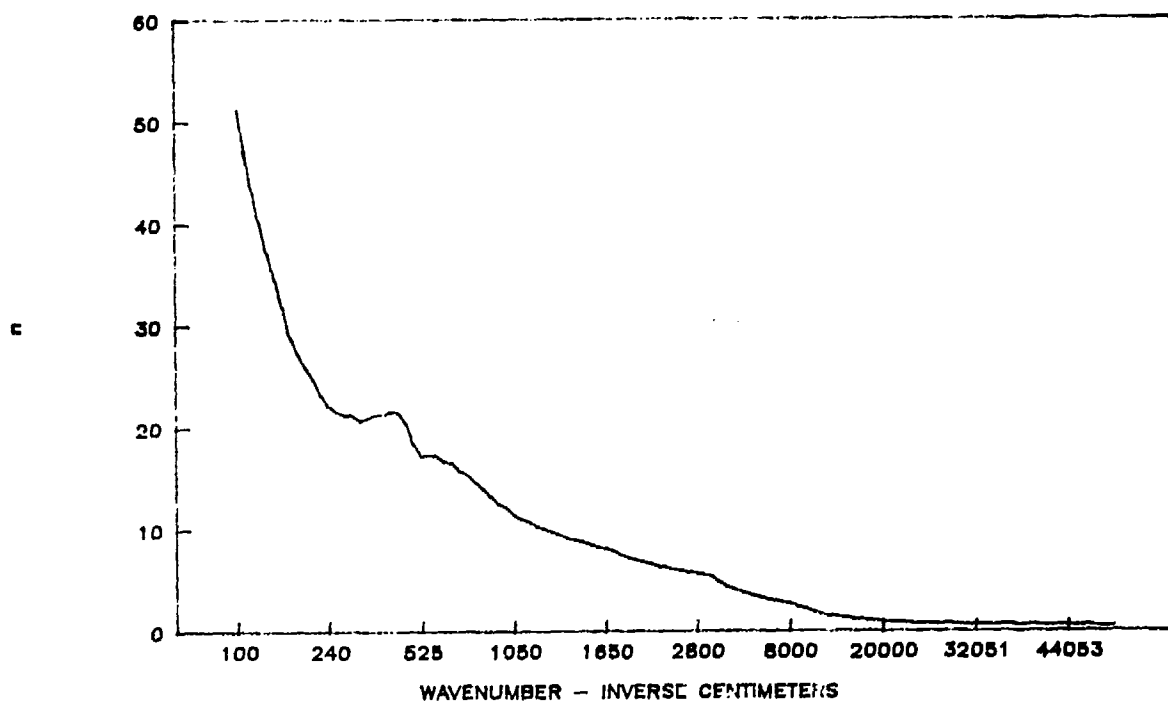


FIGURE 9: REAL PART OF THE COMPLEX REFRACTIVE INDEX,  $n$ , for type 316L stainless steel versus frequency in  $\text{cm}^{-1}$  determined from a Kramers-Kronig analysis of the reflectance.

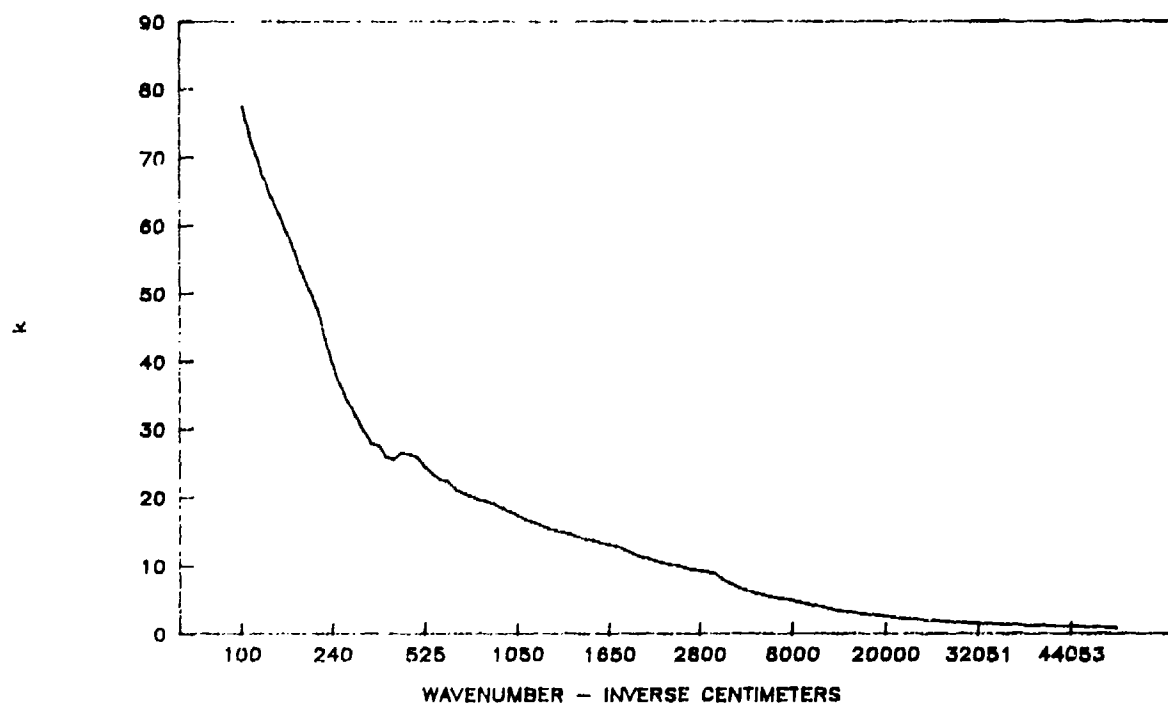


FIGURE 10: IMAGINARY PART OF THE COMPLEX REFRACTIVE INDEX,  $k$ , for type 316L stainless steel versus frequency in  $\text{cm}^{-1}$  determined from a Kramers-Kronig analysis of the reflectance.

In the far infrared, the reflectance of the iron fiber pellet was measured, the pellet was then vacuum plated with a gold film and remeasured. The gold plated sample was the reference for the iron sample and was corrected for the known reflectance of gold. The measured reflectance from  $50 \text{ cm}^{-1}$  to  $400 \text{ cm}^{-1}$  is shown in Figure 11. A Drude model fit should be appropriate to a metal at these wavelengths and it was made. From the Drude model fit,  $n(\omega)$  and  $k(\omega)$  were calculated. The Drude model parameters are given in Table III (above) and the calculated values of  $n(\omega)$  and  $k(\omega)$  are plotted versus wavenumber in Figure 12 and 13. NO DIFFERENCE was found between the two samples of iron fibers and so the data given applies both to sample 1 and sample 2 of the iron fibers.

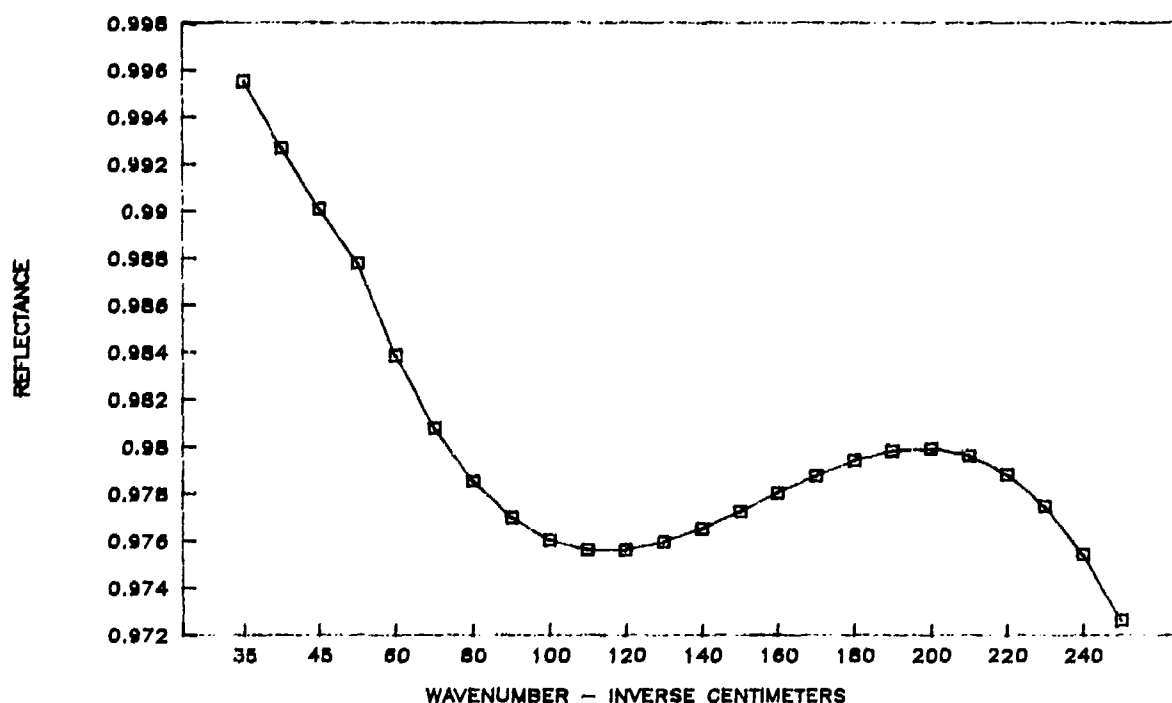


FIGURE 11: MEASURED REFLECTANCE OF IRON FIBERS versus frequency in  $\text{cm}^{-1}$ .

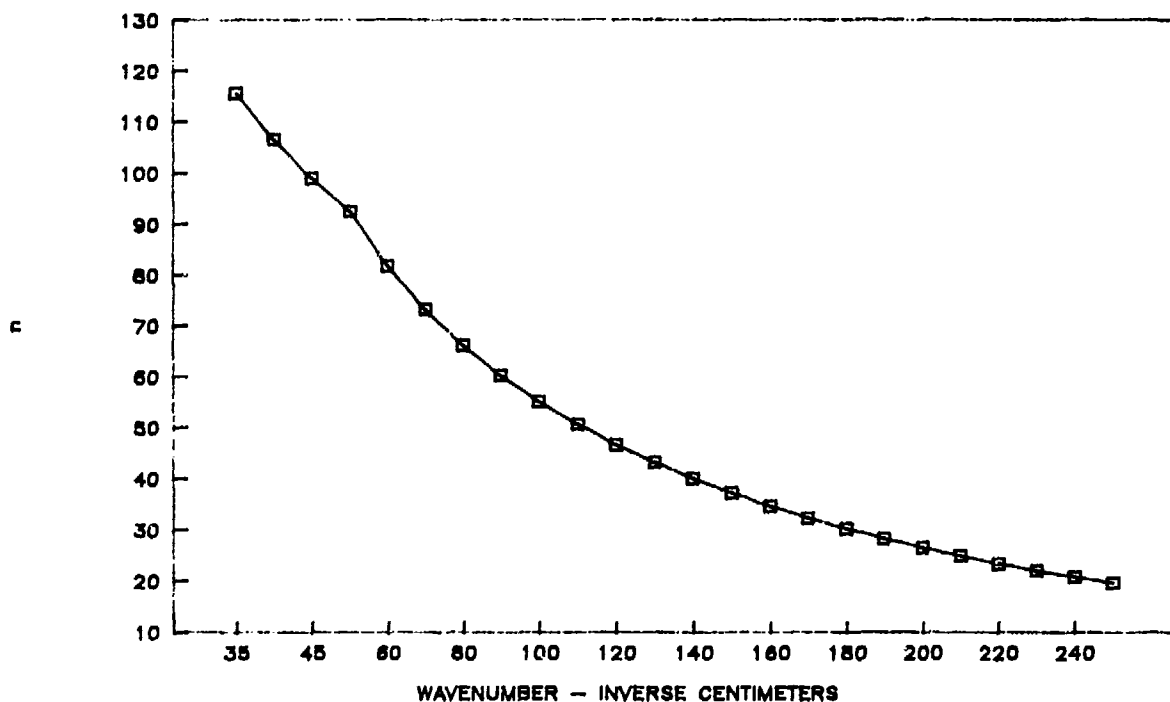


FIGURE 12: REAL PART OF THE COMPLEX REFRACTIVE INDEX,  $n$ , for iron fibers versus frequency in  $\text{cm}^{-1}$  determined from a Drude model fit to the measured reflectance.

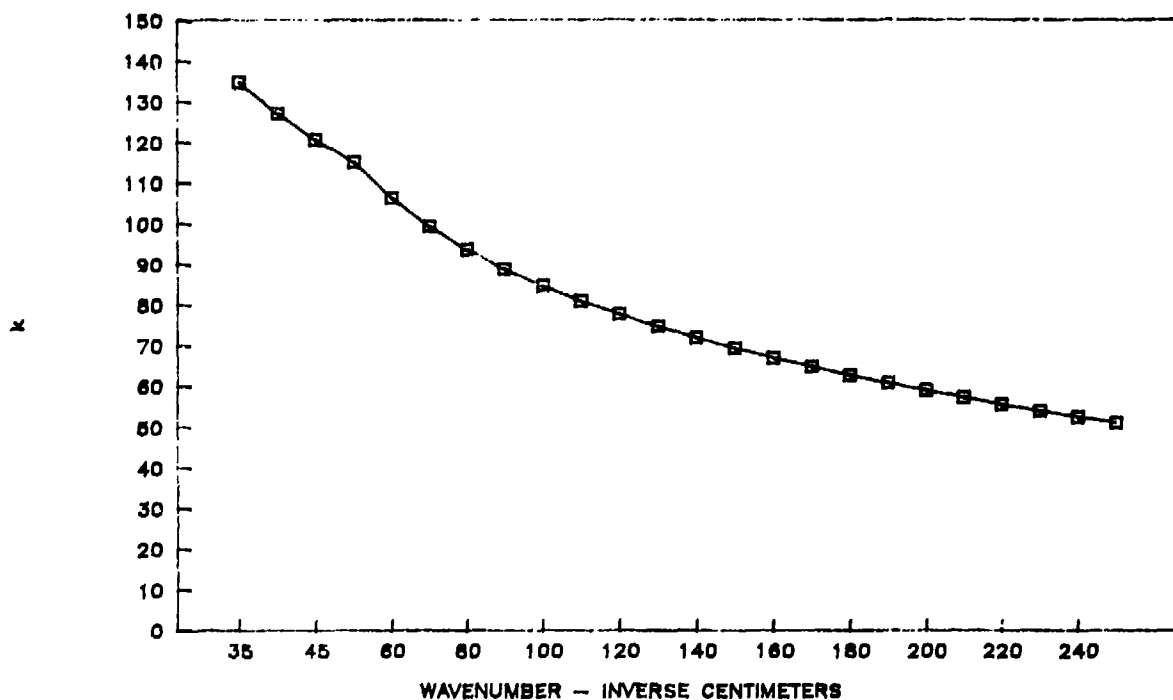


FIGURE 13: IMAGINARY PART OF THE COMPLEX REFRACTIVE INDEX,  $k$ , for iron fibers versus frequency in  $\text{cm}^{-1}$  determined from a Drude model fit to the measured reflectance.

## GRAPHITE

The contract called for the analysis of two types of graphite fibers. The first was Hercules C3X. This powder was not available from Hercules because it was a single experimental batch that had been made for the U.S. Army Chemical Research, Development and Engineering Command and Hercules had delivered the entire batch to them. A sample was finally located at CRDEC and measurements will be made on it and reported later.

The second graphite sample was IM6 Magnamite obtained from Hercules also. This material was in the form of a fabric woven from graphitized fiber. In order to measure the optical properties of the graphite in these fibers, the fibers were separated from the fabric and then ground into a very fine powder. Pellets were pressed with great difficulty from this powder.

Figure 14 shows the measured reflectance of a pressed pellet of IM6 Magnamite in the far infrared region of the spectrum. To determine the optical constants, a Drude model fit to the reflectance was attempted. We were unable to make a satisfactory fit, which indicates that the free carrier concentration in this material is sufficiently low that it does not dominate the optical properties. Instead, a Kramers-Kronig analysis was performed on the measured reflectance and  $n$  and  $k$  determined this way is shown in Fig. 15 and 16.

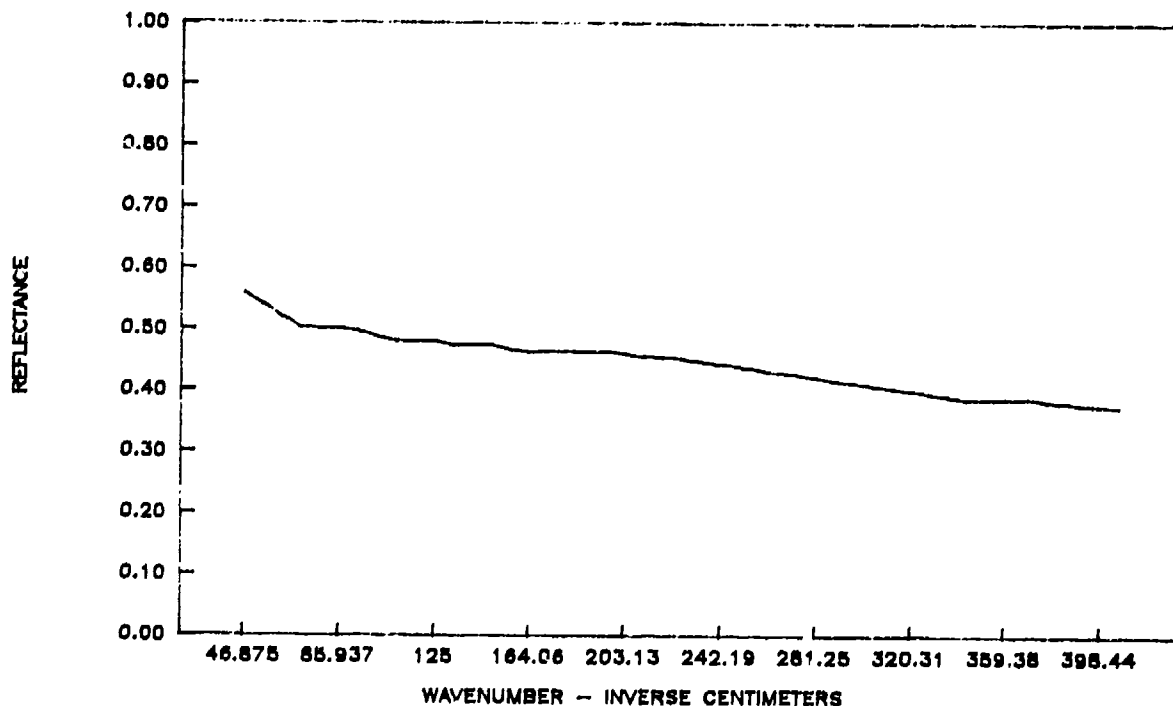


FIGURE 14: MEASURED REFLECTANCE OF A PRESSED PELLET OF IM6 MAGNAMITE graphite versus frequency in  $\text{cm}^{-1}$ .

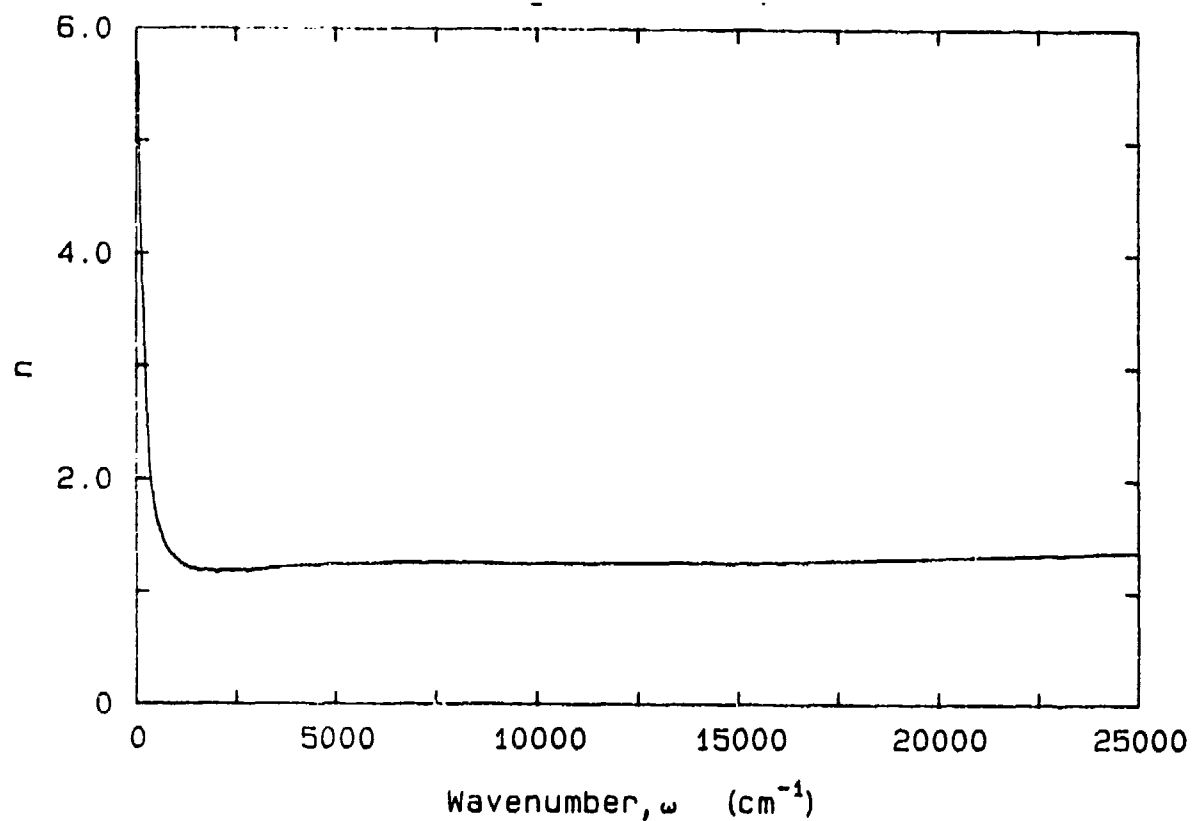


FIGURE 15: REAL PART OF THE COMPLEX REFRACTIVE INDEX,  $n$ , for IM6 magnamite graphite.

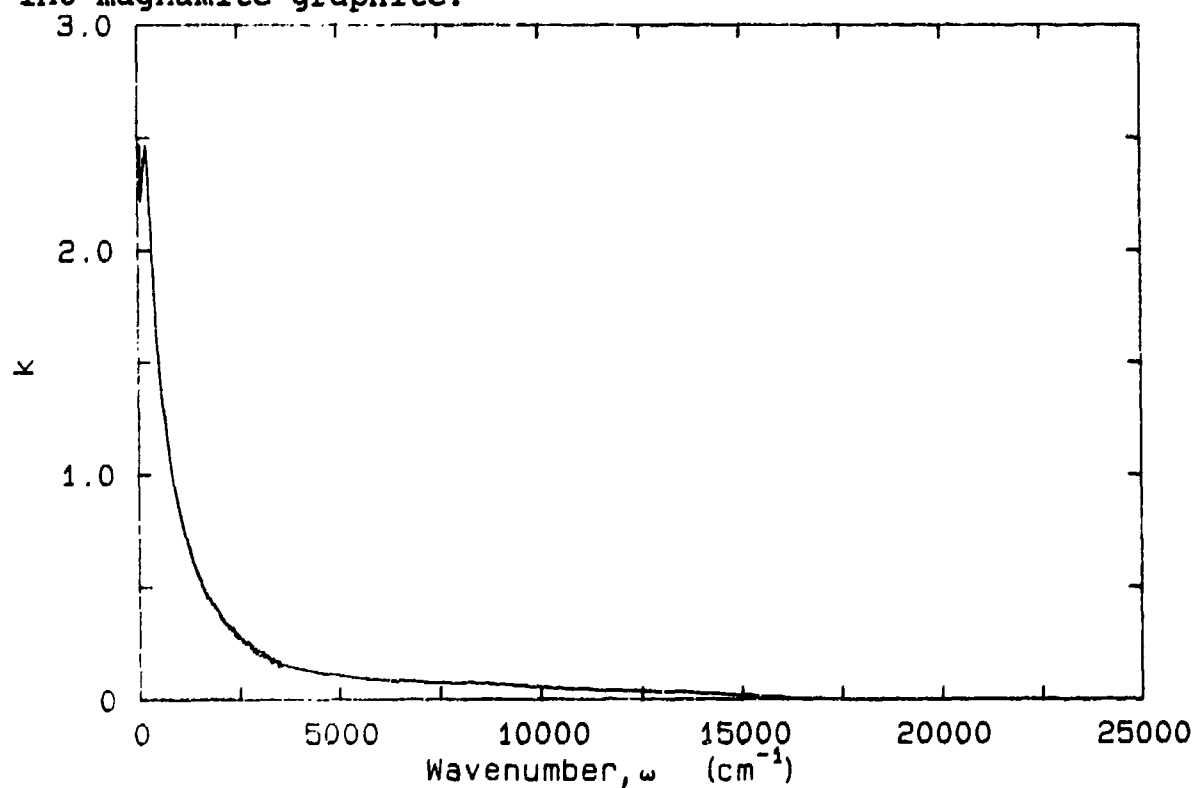


FIGURE 16: IMAGINARY PART OF THE COMPLEX REFRACTIVE INDEX,  $k$ , for IM6 magnamite graphite.

#### REFERENCES

1. Gervais, F. and Piriou, B.. "Temperature dependence of transverse- and longitudinal- optic modes in  $\text{TiO}_2$ ", Phys. Rev. B10, 1642-54 (1974).
2. Ordal, M. A., Bell, R. J., Alexander, R. W., Newquist, L. A., and Querry, M. A., "Optical properties of Al, Fe, Ti, Ta, W, and Mo at submillimeter wavelengths, Appl. Opt. 27, 1203-09 (1988).
3. Brandli, G. and Sievers, A. J., Absolute measurement of the far-infrared surface resistance of Pb," Phys. Rev. B5, 3550 (1972).

BLANK



Light Scattering Fluctuations from an Aerosol Particle Trapped at the "Null" point of an  
Electrodynamic Levitator

S. Arnold\*  
Infrared Sciences Department  
Chemistry and Physics Laboratory  
The Aerospace Corporation  
P.O. Box 92957, Los Angeles, CA 90009

D.E. Spock and L.M. Folan  
Microparticle Photophysics Laboratory (MP<sup>3</sup>L)  
Department of Physics  
Polytechnic University  
333 Jay St., Brooklyn, N.Y. 11201

RECENT PUBLICATIONS, SUBMITTALS FOR PUBLICATION AND PRESENTATIONS

- A) S. Arnold, D.E. Spock and L.M. Folan, " Electric Field Modulated Light Scattering Near a Morphological Resonance of a Trapped Aerosol Particle" , (submitted, Feb.,1990).
- B) S. Arnold, T.R. O'Keeffe, K.M. Leung, L.M. Folan, T. Scalese and A. Pluchino  
"Optical Bistability of an Aqueous Aerosol Particle Detected through Light Scattering:Theory and Experiment" Appl. Opt.(in press).
- C)S. Arnold and L.M. Folan,"Energy Transfer and the Photon Lifetime within an Aerosol Particle, Opt.Lett.13 1(1989).
- D)L.M. Folan and S. Arnold, "Determination of Molecular Orientation at The Surface of an Aerosol Particle by Morphology Dependent Photoselection", Opt.Lett.13 1(1988).

ABSTRACT

We report electric field induced fluctuations in the elastic scattering near optical resonances of a spherical aerosol particle trapped at the "null" point of an electrodynamic levitator. The particle is apparently driven into a quadrupolar distortion by the electro-mechanical stress at its surface. Our results coupled with recent theory indicate that, (1) the effect is principally due to a modulation in the frequencies of individual optical resonances, (2) a coherent distortion smaller than a part in  $10^5$  ( $\sim 1\text{\AA}$ ) is detected in this manner, and (3) the effect may be used for a continuous probe of surface tension and bulk viscosity.

\* Permanent Address: Department of Physics, Polytechnic University, Brooklyn, NY 11201

The spectroscopy of microparticles levitated and trapped in electric fields is now quite extensive.<sup>1</sup> It has always been assumed that the influence of the electric field is confined to levitation and trapping. In fact, we will show that a time varying electric field having quadrupole symmetry and an amplitude  $\sim 10$  V/cm at the particle surface leads to an easily measured fluctuation in optical scattering. The particle is apparently driven into a quadrupolar distortion by the electro-mechanical stress at its surface. Our results coupled with recent theory<sup>2</sup> indicate that, (1) the effect is principally due to a modulation in the frequencies of individual optical resonances, (2) a coherent distortion as small as a part in  $10^5$  ( $\sim 1$  Å) is detected in this manner, and (3) the effect may be used for a continuous probe of surface tension and bulk viscosity. In what follows we describe our experimental setup, display the results, and present a model for understanding these results.

The experimental apparatus is shown in Fig.1. In addition to the usual trapping field provided by a supply at amplitude  $V_1$  and frequency  $\omega_1$  ( $2\pi \times 60$  Hz) from the center electrode to each of the hyperboloids of revolution, there is an additional set of hollow cylindrical electrodes (1/8 in. in diam. and separated by 0.145 in.) insulated from the hyperbolic electrodes and driven by another supply at amplitude  $V_2$  and frequency  $\omega_2$  (with switches S closed). These cylindrical electrodes create an additional time varying potential near the center of the apparatus which is also of quadrupole symmetry (to 1st order), but which is driven at a higher frequency (3 kHz-16 kHz). The dc levitation field is provided by a battery supply attached between the cylinders.

A charged glycerol particle  $\sim 40$   $\mu\text{m}$  in diameter is generated on demand, charged and "loaded" into the center of the apparatus by injecting<sup>3</sup> it through the top cylinder with switches S opened. Once the particle is captured by the low frequency field, switches S are closed with  $V_2$  set to zero and the particle is balanced by adjusting the battery supply. Now  $V_2$  is turned up to a few hundred Volts, however, this field has no noticeable effect on the trapping process; this is to be expected since the trapping force on a micron-sized particle at atmospheric pressure follows an inverse power law with frequency<sup>4</sup>. The more important effect as we will show is on elastic scattering.

Light from a dye laser is directed upward along the symmetry axis in Fig.1.

The laser beam is polarized in the plane of scattering. Light scattered by the particle is collected at right angles through an F/6 aperture and detected by two photomultipliers.

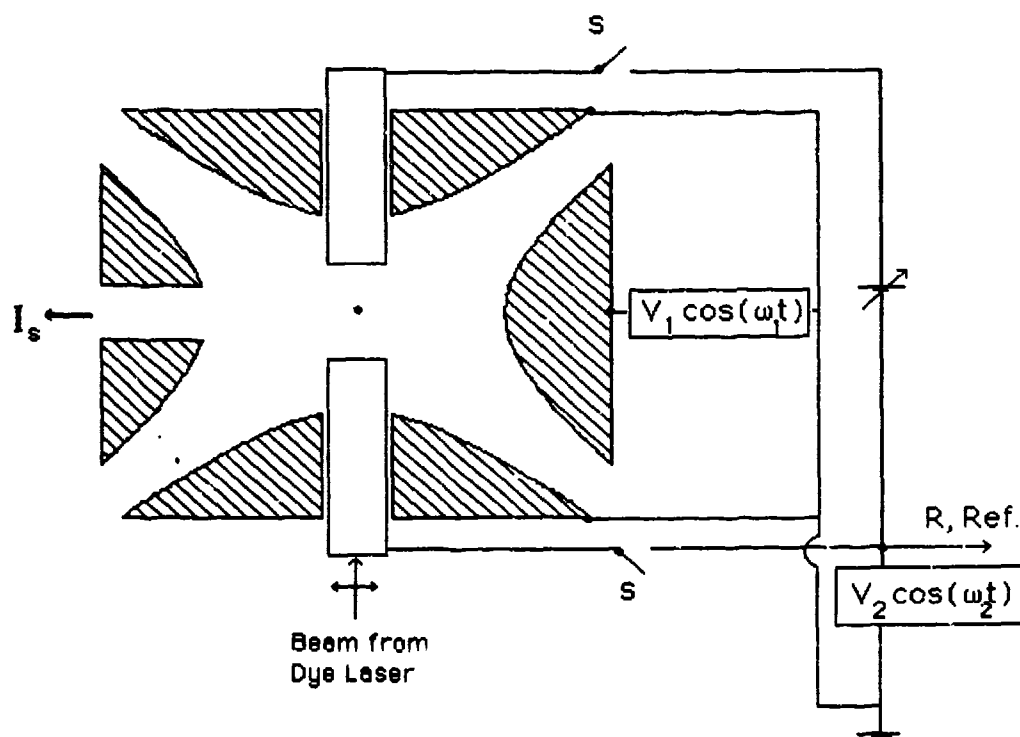


Fig.1 Experimental Apparatus.

The output from the first phototube, S, is conditioned by a low-pass filter(3db at 10 Hz), while the signal from the second phototube,  $S_{\omega_2}$ , is fed into a Lock-In amplifier operating as a vector voltmeter. The reference for this phase sensitive detector was proportional to the ac potential on the cylinders. Both conditioned signals were recorded simultaneously as two "Y" inputs to an X-Y recorder.

Spectra were principally obtained as a function of wavelength, with the particle size approximately constant, however, similar effects were seen as a function of time with the wavelength fixed but the particle size changing slowly through evaporation. Each of these methods allows the optical size (circumference/wavelength) of the particle to continuously change so that the particle is brought in and out of optical resonance. Fig.2a shows the time averaged scattering S as a function of dye laser wavelength for a

glycerol particle  $24.0\mu$  in radius. Below this spectrum is the corresponding r.m.s fluctuation  $|S_{\omega_2}|$  produced by placing a potential  $V_2 = 355$  Volts at  $\omega_2 = 2\pi \times 3$  kHz on

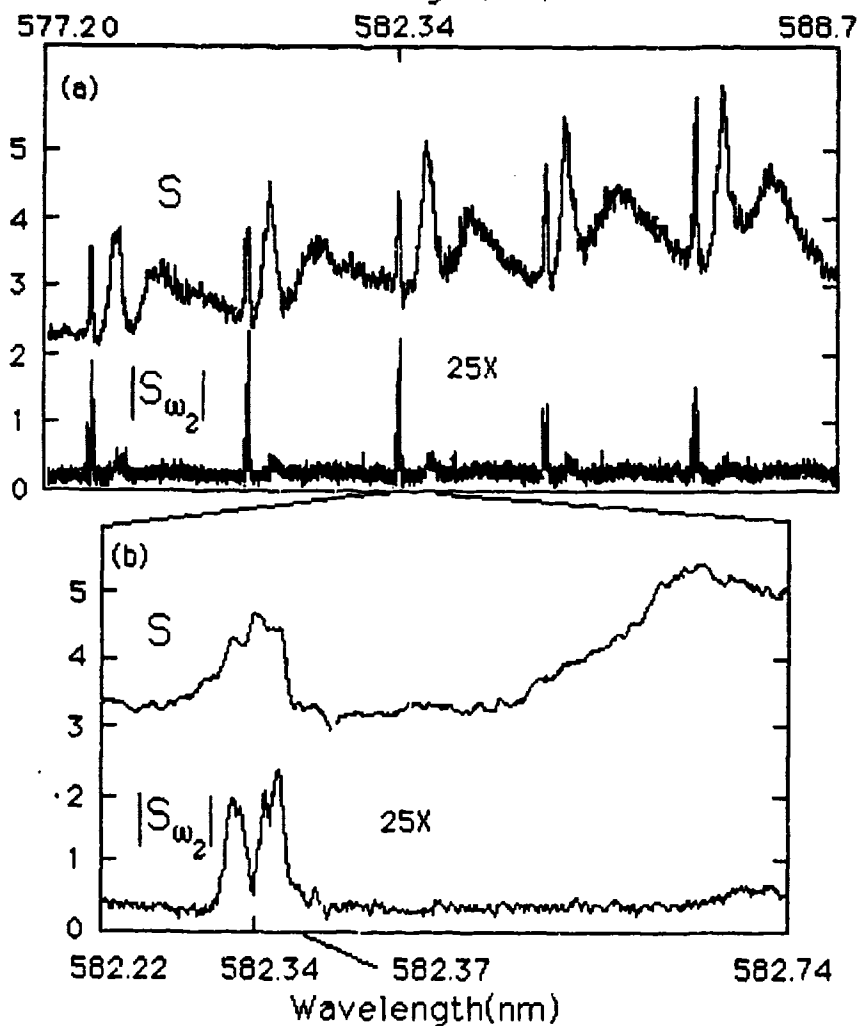


Fig. 2 Time averaged scattering  $S$  and electric field induced fluctuation  $|S_{\omega_2}|$  spectra of a glycerol particle  $24.0\mu\text{m}$  in radius.  $\omega_2$  and  $V_2$  are  $2\pi \times 3$  kHz and 355 Volts, respectively.

the cylindrical electrodes in Fig.1. As one can see the spectrum of  $|S_{\omega_2}|$  is (1) considerably different than  $S$  with signal only appearing near positions of the narrowest resonances in  $S$ , and (2) weaker than  $S$  with the largest peak only  $\sim 1.5\%$  of the largest

amplitude in the time averaged scattering. In addition, each of the features in the  $|S_{\omega_2}|$  spectrum appears to be split as illustrated by the expanded spectrum of the region around 582.34nm(Fig.2b). Fig.3 demonstrates the same effect at a considerably broader resonance of another particle 14.7 $\mu$ m in radius.

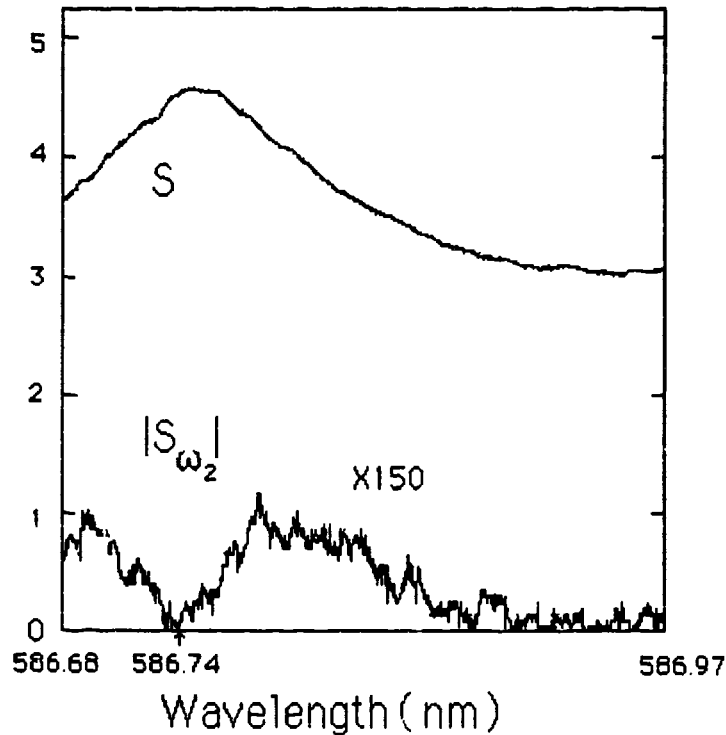


Fig. 3 Spectra of a glycerol particle 14.7 $\mu$ m in radius.  $\omega_2$  and  $V_2$  are  $2\pi \times 4$  kHz and 450 Volts, respectively.

We note that the fluctuation amplitude is markedly reduced. In order to further understand the mechanism for the  $|S_{\omega_2}|$  spectra we isolated a given peak and observed the dependence of the peak height on drive voltage  $V_2$  and frequency  $\omega_2$ . The height of the peak was found to be proportional to  $V_2$  and approximately inversely proportional to  $\omega_2$  (with the measurement taken from  $2\pi \times 4$  kHz to  $2\pi \times 10$  kHz).

The most likely mechanism for the light scattering fluctuation spectrum in Figs.2 and 3 is an electro-mechanical distortion of the particle from its spherical shape due to the stress caused by the external field on excess charge on the particle surface. In what

follows we briefly describe how this interaction can lead to the observed fluctuation.

Any static distortion may be modeled in terms of a sum of spherical harmonics  $Y_{LM}$ . However, since the external stress is axisymmetric ( $M=0$ ) with quadrupole symmetry ( $L=2$ ), and varies at frequency  $\omega_2$  [i.e. the potential produced by the external electrodes near the "null" point has an angular dependence which varies as  $P_2(\theta)$ ], the surface distortion must select this symmetry, and the angular dependence of the particle radius is approximately

$$r(\theta, t) = a \left[ 1 + P_2(\theta) \operatorname{Re} \left( \frac{\Delta}{a} e^{i\omega_2 t} \right) \right], \quad (1)$$

where  $\Delta$  is the complex distortion (i.e.  $\Delta = |\Delta| e^{i\phi}$ ) along the axis of symmetry (vert. axis), and  $a$  is the radius of the undistorted sphere.<sup>5</sup> One might expect such a distortion to perturb the optical Morphological Dependent Resonances (MDRs) of the particle. In fact Lai et al<sup>2</sup> have recently theorized that for a plane wave incident along the axis of symmetry of a slightly eccentric spheroid (i.e.  $|\Delta|/a \ll 1$ ) having axial distortion  $\Delta$ , the MDRs which are stimulated are shifted in wavelength by  $\delta\lambda_r = (1/4) (\Delta/a) \lambda_r$ . Thus one can picture each resonance in the dynamic case as shifting back and forth in wavelength at frequency  $\omega_2$  with an amplitude  $|\delta\lambda_r|$ . As a laser with zero linewidth is tuned slowly through such a feature the rms fluctuation in scattering will be proportional, to first order, to the derivative of the scattering spectrum,  $|S_{\omega_2}| = (1/2) |(\partial S / \partial \lambda)_\lambda| |\delta\lambda_r|$ . One can now understand, in a qualitative manner, the shape of the fluctuation spectrum in comparison with the scattering spectrum. The fluctuation spectrum will be most pronounced where the derivative of the scattering spectrum is greatest (near narrow resonances) and every peak in  $S$  will appear to be split since there are two wavelengths within a given peak for which the absolute derivative is maximum. One can estimate the amount of distortion from the ratio of the fluctuation amplitude to the scattering amplitude,

$$\frac{|\Delta|}{a} = \frac{4\sqrt{2}}{\beta_\lambda \lambda_r} \frac{|S_{\omega_2}|}{S}, \quad (2)$$

where  $\beta_\lambda = |(\partial S / \partial \lambda)_\lambda| / S$ . Since the actual laser linewidth ( $\sim 0.3 \text{ nm}$ ) is  $\sim 1/3$  of the width of the narrow resonance in Fig.2b, to avoid rather uncertain deconvolution, we will apply

Eqn.2 to the data in Fig.3 where the larger breadth of the scattering feature makes the need for such a deconvolution relatively unimportant. For the peak at the right in the pair centered at 586.74nm,  $|S_{\omega_2}|/S$  is  $(1.7 \pm 0.2) \times 10^{-3}$ ,  $\beta_\lambda$  is  $(2.7 \pm 0.1) \text{ nm}^{-1}$ , and  $|\Delta|/a$  turns out to be  $(6 \pm 1) \times 10^{-6}$ . Therefore our hypothesis for the fluctuations suggests the ability to detect a periodic distortion of amplitude less than 1 Å. This hypothesis may be further supported by comparing our experimentally estimated distortion with a direct calculation using dynamical elasticity theory.

The entire calculation will be presented elsewhere, however, a summary of the key results are given here for the sake of completeness. The observation that the effect is proportional to  $V_2$  indicates that it is first order in the local field. The largest first order effect in the Maxwell stress at the surface may be identified as being due to the interaction of the local field  $\underline{E}$  (in the absence of excess charge) with the excess charge density  $\sigma_e$  (at the surface). In the radial direction this interaction leads to a pressure  $\sigma_e E_r(a, \theta) e^{i\omega_2 t}$ . Since  $E_r(a, \theta)$  has quadrupole symmetry it maps perfectly onto the quadrupole capillary oscillation of the sphere with the resulting distortion

$$\frac{\Delta}{a} = \left[ \frac{-1}{\left(1 - \frac{\omega_2^2}{\omega_0^2}\right) + i \frac{\omega_2 \gamma}{\omega_0^2}} \right] \left[ \frac{5K}{2(3+2K)} \right] \left( \frac{a}{g_0} \right)^2 \frac{\sigma_e V_2}{\sigma_s}, \quad (3)$$

where  $\omega_0$  is the resonant frequency of an undamped quadrupole capillary oscillation,  $\gamma$  is the damping rate,  $K$  is the static dielectric constant,  $g_0$  is the characteristic length associated with the external electric potential [i.e. the external potential far from the particle is taken to be  $(r/g_0)^2 P_2(\theta) V_2 e^{i\omega_2 t}$ ],  $\sigma_e$  is the excess surface charge density, and  $\sigma_s$  is the surface tension. Eqn.3 indicates that in order to obtain an approximate inverse dependence on  $\omega_2$ , in agreement with experiment (Fig.3),  $\gamma \gg \omega_0$ ; the system must be overdamped.  $\omega_0$  and  $\gamma$  may be estimated for the quadrupole mode using  $\omega_0^2 = 8\sigma_s/(\rho a^3)$  and  $\gamma = 10\eta/(a^2\rho)$ , where  $\eta$  and  $\rho$  are the particle viscosity and density, respectively.<sup>6</sup> Using these expressions we find  $\gamma \sim 89\omega_0$  for a glycerol particle 14.7  $\mu\text{m}$  in radius, at room temperature, consistent with overdamping. To further check the validity

of our mechanism we can estimate the distortion corresponding to the data in Fig.3 using Eqn.3 and the expressions for  $\omega_0$  and  $\gamma$ . In the overdamped limit the distortion is given by

$$\frac{|\Delta|}{a} \sim \left[ \frac{1}{a\eta\omega_2} \right] \left[ \frac{2K}{(3+2K)} \right] \left( \frac{a}{g_0} \right)^2 \sigma_e V_2. \quad (4)$$

Since the size and density of the particle are known, the particle's mass is known. Given the mass, the charge on the particle may be obtained from the levitating field (which is determined from the dc levitation potential and the electrode geometry); using an equation similar to Millikan's balance equation. For the particle used in Fig.3,  $\sigma_e$  is found to be  $71 \mu\text{C}/\text{m}^2$ . Using this charge density, handbook values for the dielectric constant  $K$  and viscosity  $\eta$  for glycerol, taking  $g_0$  to be 1.8mm (approx. half separation between the cylindrical electrodes), and  $V_2 = 450$  Volts, we find  $|\Delta|/a$  for the particle in Fig.3 to be  $6.8 \times 10^{-6}$ . This is consistent with the value for  $|\Delta|/a$  of  $(6 \pm 1) \times 10^{-6}$  obtained by applying Eqn.2 to the experimental data in Fig.3. Thus the basic hypothesis appears to be reasonable.

Although surface tension drops out of the analysis for the overdamped case, by combining Eqns.2 and 3, one clearly sees that a spectrum of  $S_{\omega_2}$  vs.  $\omega_2$  can give both surface tension and viscosity. In cases where  $\omega_0 \gg \gamma$  (e.g. water, methanol, etc.) the line shape of  $S_{\omega_2}$  vs.  $\omega_2$  near a quadrupole capillary resonance provides this information without specific reference to the spectrum of  $S$ .

Aside from the utility which such a technique provides for determining  $\sigma_e$  and  $\eta$ , the ability to generate a small distortion of known amplitude should go a long way in increasing our understanding of the orders of magnitude disparity which has been found<sup>7</sup> between the photon lifetime within a microparticle as determined from Mie theory and experiments.<sup>7,8,9</sup> Recent theory by Lai et al<sup>10</sup> suggests that thermal fluctuations at the surface of a liquid particle are  $\sim 1\text{\AA}$ , and that such an amplitude can reduce the  $Q$  in a glycerol particle from  $10^9$  (based on Mie theory) to  $\sim 10^6$ . Consequently it would be interesting to investigate the effect which the electric field induced fluctuations have on processes which are thought to be sensitive to  $Q$ ,<sup>11</sup> such as intermolecular energy transfer within a microparticle<sup>12</sup>. Such experiments are currently underway at the MP<sup>3</sup>L.

We are grateful for the cooperative support for the experiments at the



Polytechnic by the National Science Foundation and the Chemical Research Development and Engineering Center of the Army through ATM-89-05871. We are also grateful for support from the US Joint Services Electronics Contract No. F49620-82-C-0084. S.A. was supported while on sabbatical leave by the Aerospace Sponsored Research Program.

## REFERENCES

1. S. Arnold, in *Optical Effects Associated with Small Particles*, P.W. Barber and R.K. Chang, eds.(World Scientific, Teaneck, N. J., 1988), Chap.2.
2. H.M. Lai, P.T. Leung and K. Young, *Phys.Rev.A* 41, 5187(1990).
3. S. Arnold and L.M. Folan, *Rev.Sci.Inst.*57, 2250(1986).
4. S. Arnold and N. Hessel, *Rev. Sci. Inst.*56, 2066(1985); *Rev. Sci. Inst.*57, 993(1986).
5. Eqn.1 is only volume preserving to 1st order in  $(\Delta/a)$ .
6. H. Lamb, *Hydrodynamics*, Sec.275 and 355, (Dover, New York, 1945).
7. S. Arnold and L.M. Folan, *Opt. Lett.* 14, 387(1989)
8. R.G. Pinnick, A. Biswas, P. Chylek, R.G. Armstrong, H. Latifi, E. Creegan, V. Srivastava, M. Jarzembski, and G. Fernandez, *Opt.Lett.*13, 494(1988).
9. Jian-Zhi Zhang, D.L. Leach, and R.K. Chang, *Opt. Lett.* 13, 270(1988).
10. H.M. Lai, P.T. Leung and K. Young, *Phys.Rev.A* 41, 5199(1990).
11. P.T. Leung and K. Young, *J. Chem. Phys.* 89, 2894(1988).
12. L.M. Folan, S. Arnold, and S.D. Druger, *Chem. Phys. Lett.*118, 322(1986).

BLANK

## MASS SPECTROMETRY OF SINGLE PARTICLES

John Wacker

Battelle  
Pacific Northwest Laboratory  
P.O. Box 999, Mailstop P7-07  
Richland, WA 99352

### RECENT PUBLICATIONS, SUBMITTAL FOR PUBLICATION AND PRESENTATIONS:

J.F. Wacker, "Mass spectrometric analysis of individual particles using particle-inlet mass spectrometry," *Amer. Assoc. Aerosol Res. 1989 Annual Meeting*, abs. 1P28.

J.F. Wacker and A.F. Stewart, "A multiple anode microchannel plate ion detector for use in magnetic sector mass spectrometers," In Preparation for submission to *Rev. Sci. Instrum.*

J.F. Wacker and A.F. Stewart, "A dual electron multiplier ion detector for isotope ratio measurements," In Preparation for submission to *Rev. Sci. Instrum.*

### ABSTRACT

#### INTRODUCTION

We are developing particle-inlet mass spectrometry (PIMS) for analyzing the elemental or isotopic composition of single particles from aerosol and particulate samples, without isolating particles of interest. With PIMS, particles are dispersed and resuspended in a gas at atmospheric pressure and admitted directly into the ion source of a mass spectrometer. Particles are measured individually by sequential admission into the mass spectrometer. Both real-time and off-line measurements of aerosol particles are possible. Of particular importance is the measurement of isotope ratios in single particles, which improves the detection of elements and is useful for monitoring the release of radioactive pollutants into the environment and for isotopic tracer studies. PIMS is based on the method developed by Davis [1,2] and can be applied to a variety of particle and aerosol analysis problems.

#### EXPERIMENTAL METHODS

The PIMS instrument is a single-focusing, 60°, 15-cm-radius, magnetic sector mass spectrometer, equipped with a multi-channel, pulse-counting ion detector and a thermal-ionization ion source [3]. A specially designed aerosol inlet, containing a nozzle-skimmer system, forms the basis of the PIMS technique. The inlet reduces the pressure in the aerosol and directs the particles into an oven in the mass spectrometer ion source. A rhenium-foil oven traps the particles, vaporizes them, and thermally ionizes the vapor. The ions are extracted, focused, and accelerated into the mass spectrometer for analysis. Ions are measured using a multi-channel ion detector, equipped with a microchannel plate.

The PIMS instrument accepts samples in aerosol form. To generate aerosols from collected particulate samples, the sample is loaded onto a filter and then vacuumed from the surface using the airflow entering the inlet of the PIMS instrument. The vacuum is sufficient to dislodge  $\mu\text{m}$ -sized particles from the filter surface and draw them up through a tube and into the inlet; better than 90% of the particulate mass is removed from the filter using this process. An automated sample introduction system has been built that scans filters past a tube connected to the PIMS inlet.

The analysis of an aerosol sample consists of admitting particles into the PIMS instrument and monitoring the resultant ion signals. Ion counts are acquired over a series of 200 msec integration steps (steps from 5 msec to 6 sec are possible). Mass spectra, reflecting the average composition of a population of particles, are obtained by scanning the magnetic field during data collection. For example, the uranium isotope ratio in single particles can be measured by tuning the magnetic field so that  $^{235}\text{UO}$

and  $^{238}\text{UO}$  are focused on the ion detectors. Particles containing U (such as mineral grains) produce ion bursts that typically covers several 200-msec steps. Isotope ratios are calculated as

$$R = (C_1 - Nx B_1)/(C_2 - Nx B_2)$$

where R is the isotope ratio,  $C_1$  and  $C_2$  are the total ion counts on isotopes 1 and 2 during the ion burst, N is the number of steps covering the ion burst, and  $B_1$  and  $B_2$  are the average backgrounds per step for each isotope.

## RESULTS

Typical results for an environmental sample are shown in Fig. 1, which is a scan of the 1- to 300-amu mass region taken during admission of ~0.5 mg of an airborne dust sample. Many elements can be identified in Fig. 1, including alkalis, alkaline earths, rare earths, Re, Ta, U, and Th. PIMS easily detects both uranium and thorium in the sample (which contains 5.5 ppm U and 7.4 ppm Th) as the ion signals due to  $\text{ThO}^+$ ,  $\text{UO}^+$ , and  $\text{UO}_2^+$  were  $10^3$  to  $10^4$  times greater in the sample than in the background. Our results show that  $\text{UO}_2$  particles larger than 1.5  $\mu\text{m}$  diameter (containing 19 pg of  $\text{UO}_2$ ) can be detected, based on measuring a  $^{235}\text{UO}/^{238}\text{UO}$  ratio of 0.0072.

Results of measuring  $^{235}\text{UO}$  and  $^{238}\text{UO}$  ions simultaneously in single particles are shown in Fig. 2, which is data from a sample of  $\text{TiO}_2 + 0.1\% \text{UO}_2$ . Ion bursts occur simultaneously at both  $^{235}\text{UO}$  and  $^{238}\text{UO}$ , with individual bursts having a  $^{235}\text{U}/^{238}\text{U}$  ratio that was, to within 10 to 50% errors, consistent with a ratio of 0.0072. Similar measurements made with  $^{238}\text{UO}$  on one detector channel and no isotope peak on the other channel (corresponding to mass 257) gave ratios much lower than when both uranium isotopes were analyzed. These results clearly demonstrate the capability of using PIMS to measure isotope ratios in single particles.

As an example of the sensitivity of PIMS, Fig. 3 shows a scan of the uranium mass region during admission of reagent-grade  $\text{TiO}_2$ , which contains 50 ppb U. Both isotopes of uranium were detected. Note that the ThO signal is smooth (it is a background peak in the PIMS instrument), whereas the UO signals show prominent spikes, which are ion bursts produced by individual particles.

## CONCLUSIONS

The PIMS technique has been developed to analyze single aerosol particles with minimal preparation. Our results demonstrate the capability of PIMS to detect trace constituents in heterogeneous materials, as shown by the detection of U and Th in airborne dust and reagent grade  $\text{TiO}_2$ . Multi-isotope analysis allows measurement of isotope ratios in single particles so that specific elements can be identified and discriminated from interfering elements by measuring diagnostic isotope ratios. Moreover, real-time background corrections to the ion burst data can be made. Our development work has emphasized uranium, partly because of the promising applicability of PIMS to real-time detection of airborne radioactivity (PIMS can detect uranium at picogram levels without interferences from other species, e.g., radon and its progeny), and because of the low background in the uranium mass region. PIMS can measure aerosols either in real-time or off-line as collected aerosol particles. Measurement of collected samples gives added flexibility as the PIMS instrument need not be near the aerosol source, and allows samples to be taken from gas volumes too large to be sampled quickly at the PIMS gas inlet flow.

This paper is based on work sponsored by the U.S. Department of Energy, under Contract DE-AC06-76RLO-1830.

## REFERENCES

- [1] Davis W.D., *Environ. Sci. Tech.*, **11**, 587-592 (1977). [2] Davis W.D., *Environ. Sci. Tech.*, **11**, 593-596 (1977). [3] Stoffels, J.J., *Int. J. Mass Spectrom. Ion Phys.*, **40**, 217-222 (1981).

## Airborne Dust at 2100°C

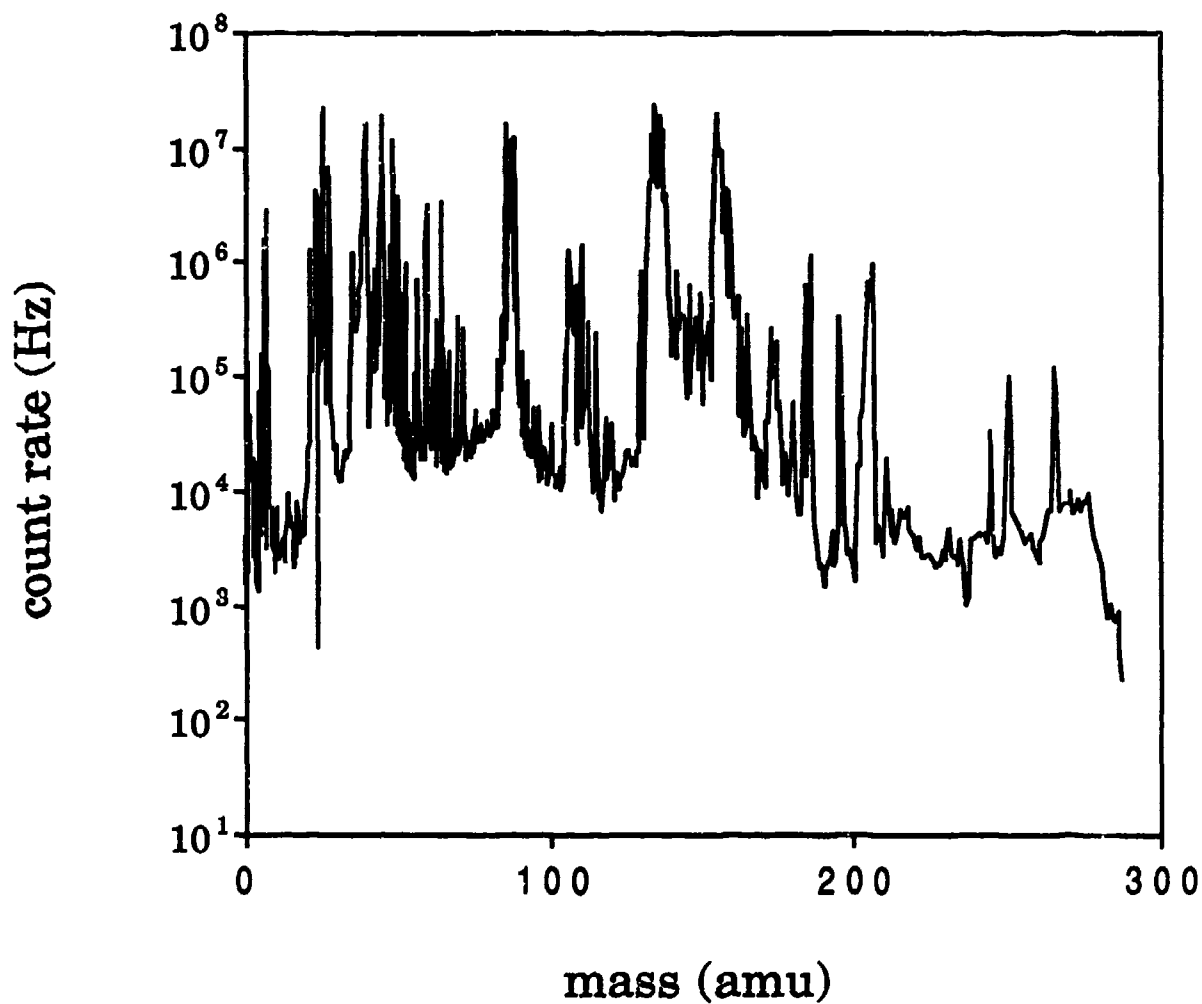
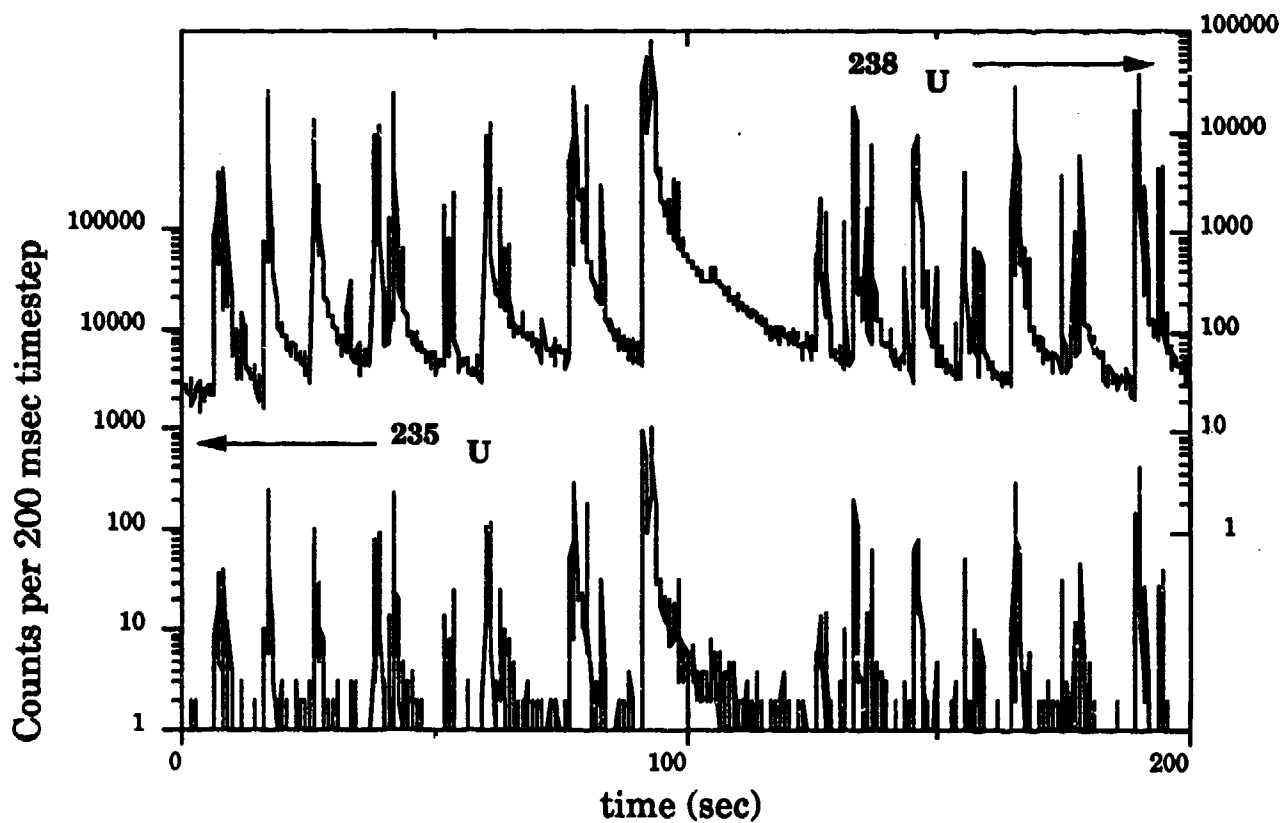


Figure 1. The mass spectrum from 1 to 300 amu was scanned during the admission of ~0.5 mg of airborne dust (National Institute of Standards and Technology, Standard Reference Material 1648 -- urban particulates). Oven temperature was 2100°C. The three peaks at ~250 amu are ThO, UO, and UO<sub>2</sub> -- masses 248, 254 and 270, respectively.

## Uranium Ion Bursts from Single Particles



**Figure 2.** Uranium ion bursts are shown for  $^{238}\text{U}$  on top (scale on the right) and  $^{235}\text{U}$  on the bottom (scale on the left). Good correlation is seen between the two isotopes, giving a  $^{235}/^{238}$  isotopic ratio consistent with the natural value of 0.0072.

## Trace Uranium in TiO<sub>2</sub> Particles

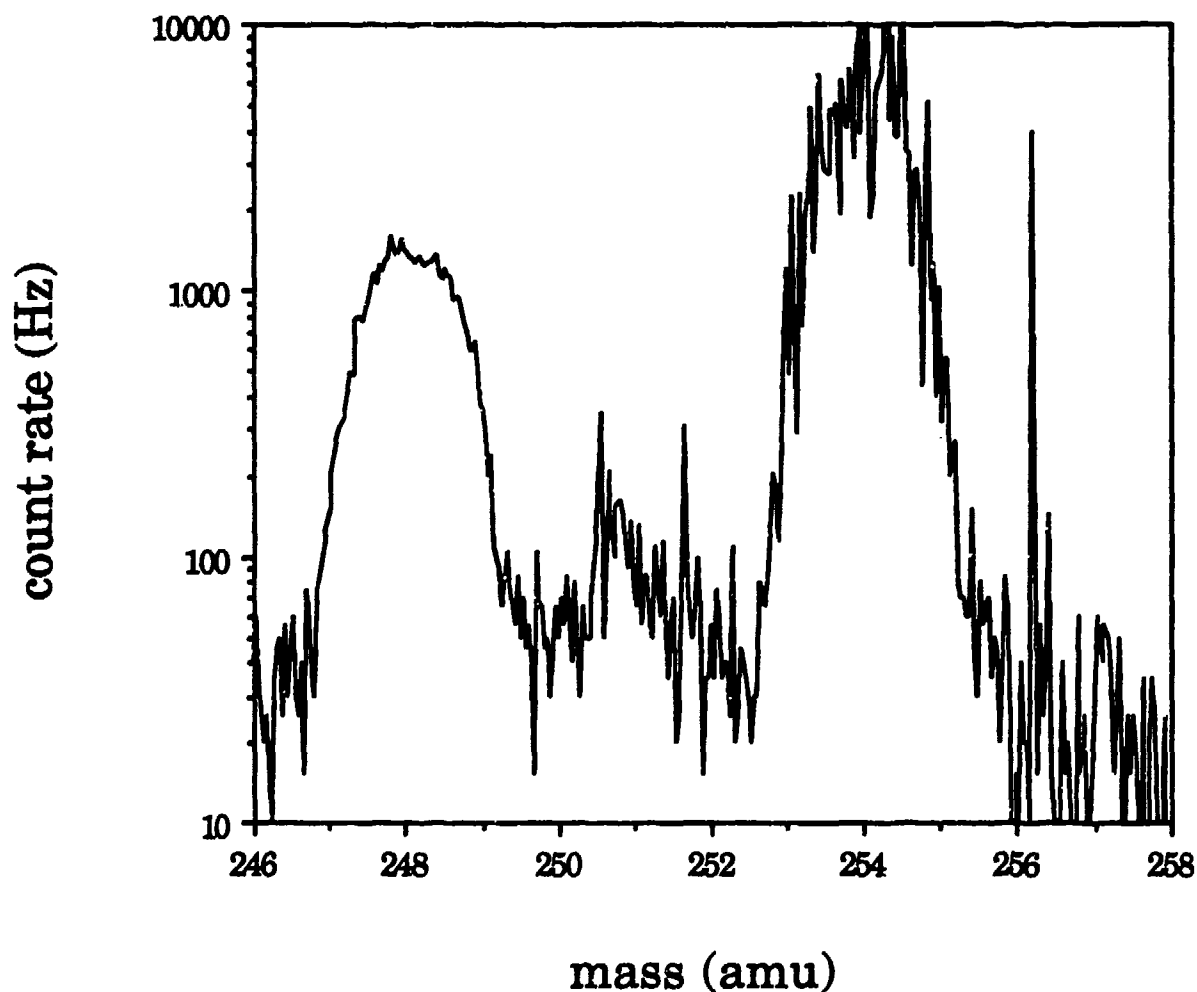


**Figure 3.** Reagent-grade TiO<sub>2</sub> contains 50 ppb of uranium, which is detectable using PIMS. The data were taken by admitting TiO<sub>2</sub> into the PIMS instrument while scanning the magnetic field across the mass region from 246 to 258 amu. The uranium signals (<sup>238</sup>UO at 254 amu, <sup>235</sup>UO at 251 amu) show pulses that are produced by individual particles. In contrast, the peak at 248 amu (ThO) is steady, showing that it is due to background Th in the PIMS instrument. Approximately ~0.1 mg of TiO<sub>2</sub> powder was drawn into the PIMS instrument during the scan.

BLANK



# MEASURING THE TEMPERATURE OF DIAMAGNETICALLY LEVITATED MICROPARTICLES

B. R. F. Kendall

Department of Physics

The Pennsylvania State University

University Park, PA 16802

and

E. Thomas Chesworth

Seven Mountains Scientific, Inc.

P. O. Box 650

Boalsburg, PA 16827

## INTRODUCTION

Appropriately shaped static magnetic fields can be used to trap and levitate diamagnetic materials.<sup>1-6</sup>

The lifting force  $\vec{\Delta F}$  on a small volume of magnetic material  $\Delta v$  is given by

$$\vec{\Delta F} = \frac{\chi}{2\mu_0} \text{grad} (B^2) \Delta v \quad (1)$$

where  $\mu_0$  is the magnetic permeability constant of free space,  $\chi$  the magnetic volume susceptibility (negative for diamagnetic materials), and  $B$  the magnitude of the magnetic induction.

Several field configurations can be used to provide the necessary levitation and centering forces for stable suspension in the Earth's gravitational field. One example is shown in Figure 1. Although the magnetic fields themselves are approximately horizontal, the field gradient (and hence the lifting force) is vertical.

The advantage of diamagnetic levitation is that it requires neither the position sensing and feedback circuits needed in active systems, nor the alternating fields employed in dynamic systems. The necessary fields can be produced by permanent magnets so that permanent trapping of a particle is possible in a system which consumes no power.

Because the lifting force per unit volume is constant in a given system at a given field strength, particles or groups of particles from millimeter to submicron dimensions can be levitated with equal ease. Figure 2 shows a relatively large particle of graphite permanently suspended between poles approximately 2mm apart.

This form of levitation is normally used with graphite or bismuth samples but is potentially applicable to many other materials, including glasses and organic solids and liquids, which exhibit diamagnetic behavior.

#### TEMPERATURE MEASUREMENT

Because the diamagnetic volume susceptibility  $\chi$  is temperature dependent, a magnetic levitation system can be used as a temperature-sensitive balance. The procedure is summarized in Figure 3.

The magnetic induction is first adjusted at ambient temperature  $T_1$ , using an electromagnet or a booster winding on a permanent magnet, to a value  $B_1$  which brings the suspended particle to some convenient reference level as viewed through a microscope. The particle is then allowed to take up the temperature  $T_2$  which is to be measured. In our experiments the heating was by laser illumination. The particle typically drops in the field of view as the temperature rises. The magnetic induction is then increased to the value  $B_2$  needed to return the particle to the reference mark.

We define  $\chi$  so that

$$B_2 = B_1 (1 + \chi) \quad (2)$$

We also have, from an extension of equation (1),

$$mg = (\text{const})\chi_1 \text{ grad } (B_1^2) = (\text{const}) (\chi_2) \text{ grad } (B_2^2) \quad (3)$$

where  $mg$  is the weight of the particle and  $\chi_1, \chi_2$  the magnetic susceptibilities at  $T_1$  and  $T_2$ , respectively.

We can define  $y$  as a fractional temperature coefficient of susceptibility so that

$$\chi_2 = \chi_1 [1+y(T_2-T_1)]. \quad (4)$$

From (3) we obtain, because the geometry of the system remains unchanged,

$$B_2^2/B_1^2 = \chi_1/\chi_2$$

or, for small changes in  $x$  and  $y$ ,

$$2x \approx -y (T_2-T_1) .$$

Thus the temperature change above ambient is given by

$$(T_2-T_1) = \frac{-2x}{y} . \quad (5)$$

Values of  $y$  are available from Tables. For graphite a typical value is  $-8 \times 10^{-4} \text{K}^{-1}$ .

If frequent temperature measurements are required, the vertical scale of the microscope can be calibrated in terms of temperature. This is done by recording the vertical positions of the particles after heating but prior to the field increase and relating them to the subsequently calculated temperatures. The resulting plot of vertical position vs. temperature is typically somewhat nonlinear but quite reproducible.

#### RESULTS AND DISCUSSION

This temperature-sensing technique has so far been used primarily on graphite particles in vacuum using a low-powered laser for heating up to 30K above ambient. Temperature variations of 1K are easily detected.

The method is particularly suited to the measurement of small temperature changes around ambient, in contrast to the more conventional optical methods used at high temperatures.<sup>7,8</sup>

#### ACKNOWLEDGEMENTS

The valuable assistance of R. S. Butler, S. Rossnagel, and R. Friesenhahn during the early stages of this work is gratefully acknowledged. The use of a magnetic bridge element to enhance the lift force from a horizontal magnetic field was suggested and developed by R. Friesenhahn. The work was supported in part by the National Bureau of Standards under Grant No. 70-NANB5H0563 and by the National Institute of Standards and Technology under Grant No. 70-NANB9H0969.

#### REFERENCES

1. W. Braunbek, Z. Phys. 112, 753 (1939).
2. W. Braunbek, Z. Phys. 112, 764 (1939).
3. A. H. Boerdijk, Philips Res. Rep. 11, 45 (1956).
4. E. Evrard and G. A. Boutry, J. Vac. Sci. Technol. 6, 279 (1969).
5. R. S. Butler, B. R. F. Kendall, and S. M. Rossnagel, Vacuum 27, 589 (1977).
6. B. R. F. Kendall, M. F. Vollero and L. D. Hinkle, J. Vac. Sci. Technol. A5, 2458 (1987).
7. M. C. Lee (ed.), "Noncontact Temperature Measurement," NASA Conf. Pub. 2503 (1988).
8. E. R. Monazam, D. J. Maloney, and L. O. Lawson, Rev. Sci. Instrum. 60, 3460 (1989).

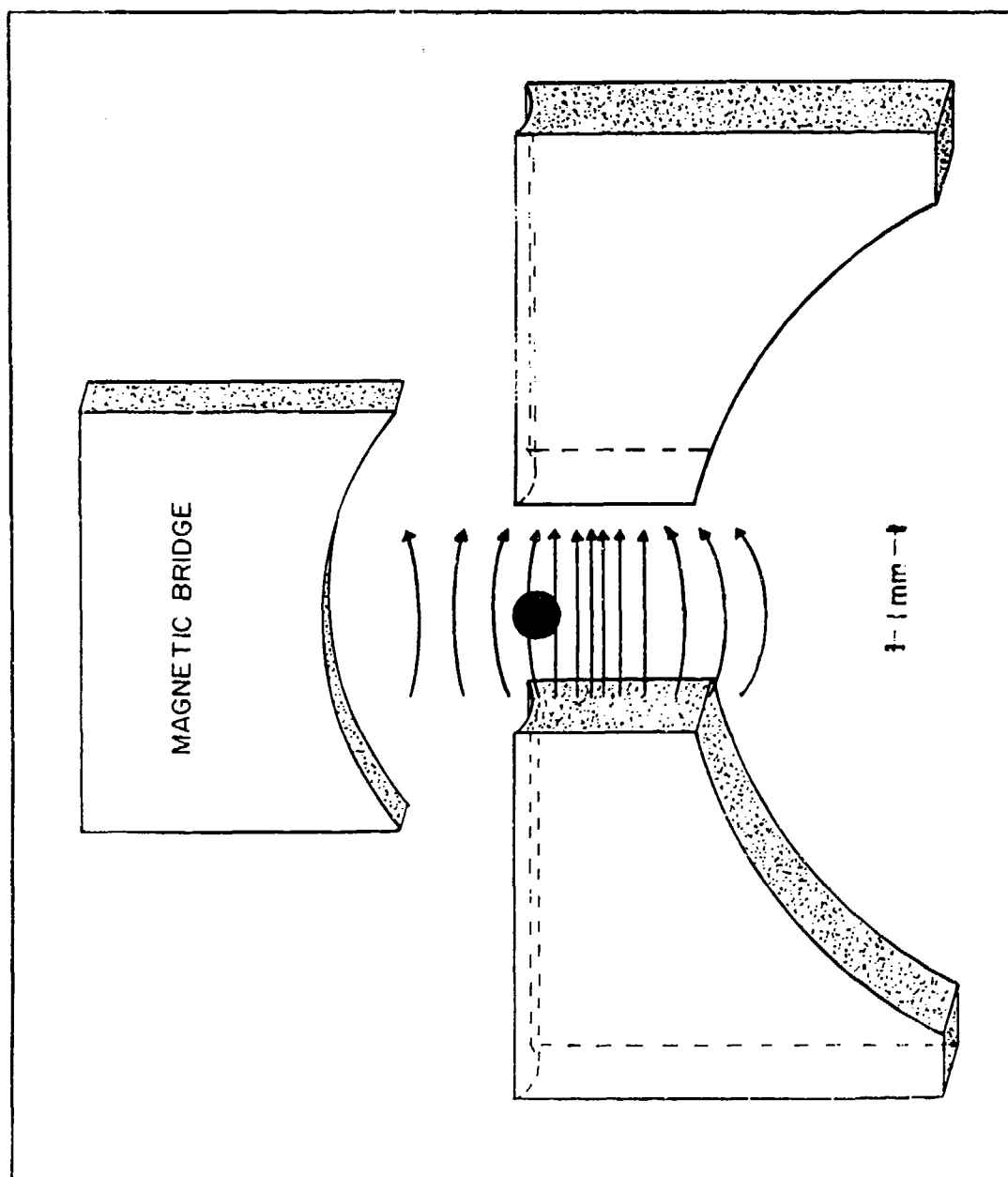


Figure 1. One of several possible field configurations suitable for stable diamagnetic levitation.  
Polarity of main magnet can be reversed without affecting operation.

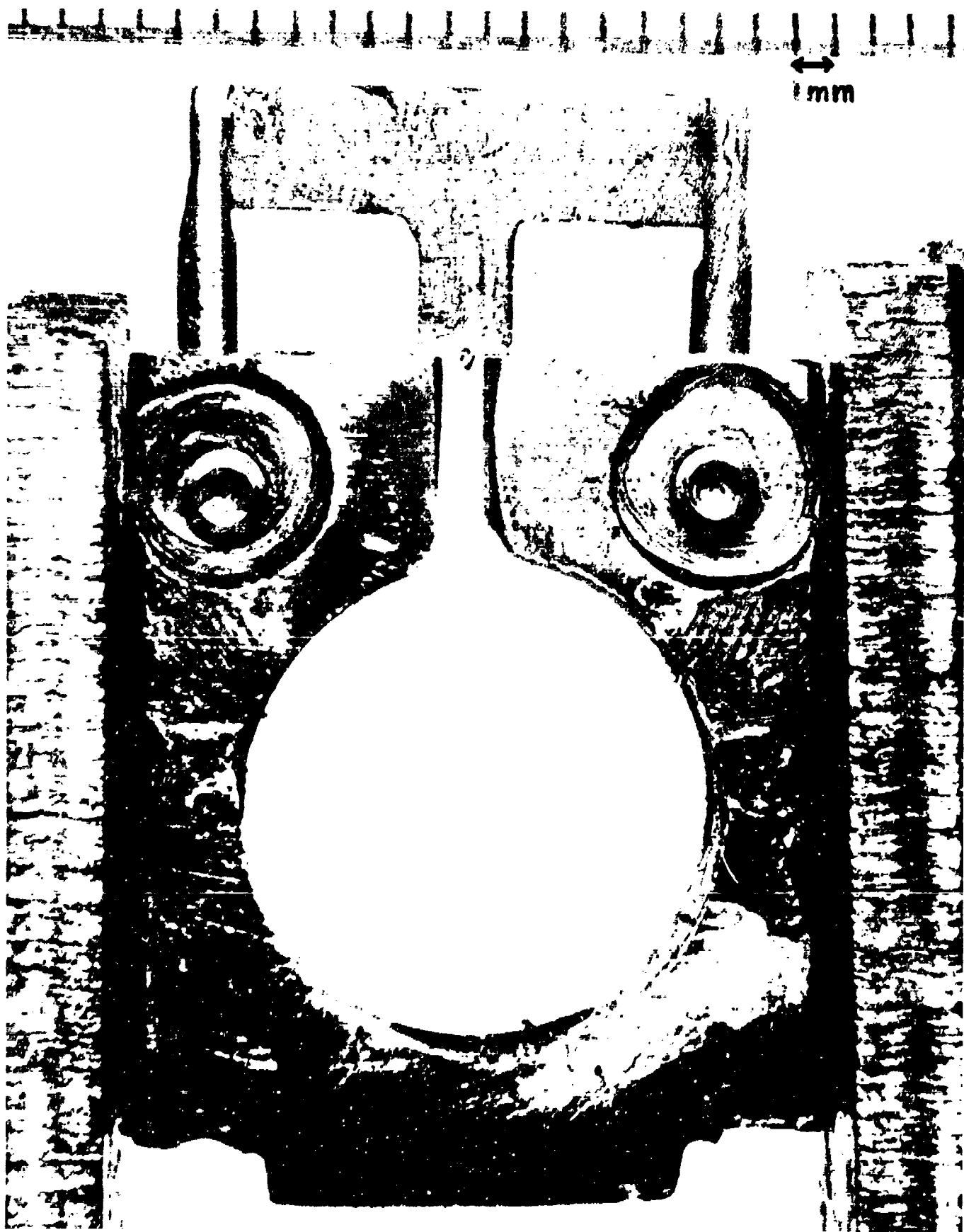
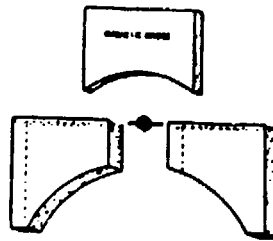
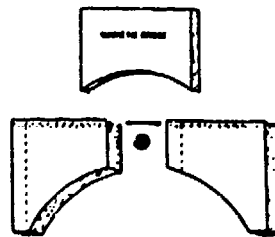


Figure 2. Large diamagnetic particle in suspension. Particles and clusters down to submicron sizes can be permanently trapped in such systems until forcibly removed.

- 1) Adjust B to bring particle to a reference level.



- 2) Heat particle using, for example, a laser



- 3) Adjust B to bring particle back to the reference level.

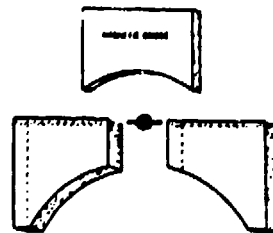


Figure 3. Temperature measuring procedure, based on temperature dependence of  $\chi$ . Vertical movement of particle is exaggerated for clarity.

BLANK



**PROGRESS IN THE DETECTION OF SINGLE MOLECULES  
IN LEVITATED DROPLETS**

W. B. Whitten, J. M. Ramsey  
Oak Ridge National Laboratory  
Oak Ridge, Tennessee 37831-6142

S. Arnold  
Polytechnic Institute of New York  
Brooklyn, NY 11201

B. V. Bronk  
U.S. Army CRDEC  
Aberdeen, MD 21010

**RECENT PUBLICATIONS, SUBMITTALS FOR PUBLICATION, AND PRESENTATIONS**

- A) W. B. Whitten, J. M. Ramsey, S. Arnold, and B. V. Bronk, "An Approach to the Ultimate Detection Limit by Fluorescence Measurements in Microdroplets", Proceedings of the 1989 CRDEC Scientific Conference on Obscuration and Aerosol Research, in preparation.
- B) "New Applications Underscore Analytical Importance of Lasers", Chem. and Eng. News 67 (41), 21 (1989).
- C) J. M. Ramsey, "Spectrochemical Analysis in Electrodynamic Traps: Particles, Neutrals, and Ions", Dept. of Chemistry, University of Tennessee, Knoxville, TN. Oct. 26, 1989 (invited).
- D) J. M. Ramsey and W. B. Whitten, "Fluorescence Analysis of Microdroplets: An Approach to Single Molecule Detection", Laser Applications to Chemical Analysis, Incline Village, NV. Feb. 7, 1990.
- E) J. M. Ramsey, "Optical Spectroscopy in Electrodynamic Traps", Department of Chemistry, Michigan State University, East Lansing, MI. April 12, 1990.
- F) J. M. Ramsey and W. B. Whitten, "Looking for Single Molecules in Levitated Microdroplets", Analytical Chemistry Division Information Meeting, ORNL, Oak Ridge, TN. June 14, 1990.
- G) J. M. Ramsey, "Approaching Single Molecule Detection in Condensed and Gas Phase Measurements Using Electrodynamic Traps", Department of Chemistry, University of British Columbia, Vancouver, British Columbia, June 18, 1990.
- H) W. B. Whitten and J. M. Ramsey, "Laser Analysis in an Electrodynamic Trap", Sixth Interdisciplinary Laser Science Conference, Minneapolis MN. Sept. 18, 1990.
- I) W. B. Whitten, J. M. Ramsey, S. Arnold, and B. V. Bronk, "Single Molecule Detection in Levitated Microdroplets", in preparation.

## ABSTRACT

Fluorescence detection limits for molecules in solution are historically limited to concentrations of  $\sim 10^{-13}$  M by solvent background. We are trying to detect single molecules in solution within this limit by reducing the volume of the sample to the pl range. This is achieved by sampling the solution as levitated microdroplets about 10  $\mu\text{m}$  in diameter. With excitation from an argon-ion laser at 514.5 nm, we detect fluorescence photons from glycerol-water droplets containing as few as 11 molecules of rhodamine-6G. Our present detection limit, due to impurities in the blank determinations, is  $\sim 0.4$  molecules.

We are trying to detect single molecules of rhodamine-6G in levitated (1) glycerine-water droplets by optical fluorescence. A typical analyte molecule can undergo on the order of  $10^6$  excitation-fluorescence cycles before photolyzing (2). It is fairly easy to collect from  $10^3$  to  $10^4$  of these photons as counts from a detector. Thus, from 10 to 1000 photocounts should be observable per molecule, clearly sufficient for single molecule detection. It is the noise in the solvent background that limits the sensitivity of detection. In our report last year, we described the basic principles of the measurement technique. Several improvements have been made since then. The more important of these include changing to a hyperbolic electrodynamic trap for droplet levitation and reduction of the laser intensity. These two changes reduce the photophoretic displacement of the droplet when the laser is turned on. Droplets of glycerol-water containing a small quantity of rhodamine-6G dye are produced by a Uniphoton Systems droplet generator and suspended in the quadrupole trap. Horizontally polarized light at 514.5 nm from an argon-ion laser is focused on the droplet at the beginning of a measurement. Elastic scattering from the droplet in the direction of the photomultiplier is substantially reduced with this arrangement. The laser intensity is  $100 \text{ W cm}^{-2}$ . Fluorescence from the droplet is collected by a GRIN lens and 20X microscope lens, focused through a 0.15 mm aperture, filtered by an interference filter with 26-nm bandwidth at 575 nm and a Corning 3-66 glass filter, and detected by a cooled C31034 photomultiplier. Photocounts are collected by a gated photon counter and stored on a laboratory computer.

The volume of the trapped droplets is needed to calculate the number of analyte molecules being observed. We estimate the droplet diameter from a microscopic examination of the droplet at 90 degrees from the laser excitation. Ashkin and Dziedzic (3) have shown that the scattered light in the far field consists of two main spots, one a reflected ray scattered from the face of the sphere, the other a refracted ray that emerges tangentially from the opposite edge of the sphere. The two spots are separated by approximately 1.7  $\lambda$ . The microscope body is extended for these measurements so that the spot separation can be measured to an accuracy of about 10%.

For greater precision in droplet diameter, the positions of structural resonances in Mie scattering are measured as the droplet evaporates with fixed laser frequency. The resonances are identified by matching the experimental curves with calculations made with the Fortran program given by Bohren and Huffman (4), averaged over the appropriate range of azimuthal angles and the droplet diameter calculated from the size parameter and the glycerol refractive index.

In a typical measurement, after verifying with the HeNe laser that the particle is centered in the trap, the photon counters are initiated and the argon laser beam switched on. With a laser intensity of  $100 \text{ W cm}^{-2}$ , the fluorescence from the sample or blank decays in about 20 s to background. Mie scattering photons are recorded in a second channel of the photon counter for droplet size determination. The separation of the reflected and refracted spots is measured visually at the conclusion of the measurement.

The data for a pair of experiments on sample and blank of similar size are shown in Fig. 1. The sample was a 13- $\mu\text{m}$  droplet of 16-pM concentration of R-6G in glycerol-water, the blank of the same diameter with no R-6G deliberately added. The upper curve is the detected fluorescence as a function of time after the laser beam is unblocked. Most of the signal decays in a few seconds as the R-6G is photolyzed. The signal remaining after about 20 s is believed to be mainly fluorescence from the filters or the black paint in the trap excited by the elastic scattering from the droplet. The initial fluorescence from the blank droplet, lower curve, shows a photolyzable component presumably due to impurities in the solvent. Variations in the size of this component from droplet to droplet limit the ultimate detection we can achieve.

The results of six determinations, three for droplets with 16-pM concentration of R-6G in glycerol, and three for blanks, are presented in Table I. The probable number of R-6G molecules in each sample droplet is calculated from the concentration in glycerol and the measured diameter. All of the water is assumed to have evaporated. An average of 340 photocounts per R-6G molecule is calculated for the three droplets with R-6G. The equivalent concentration of R-6G molecules in the blank droplets would be 0.5 R-6G  $\text{pL}^{-1}$  or 0.8 pM. Twice the noise in the integrated blank photocounts is 140 counts  $\text{pL}^{-1}$ , equivalent to 0.4 R-6G  $\text{pL}^{-1}$ . This value can be taken to be our present detection limit, with the main source of noise being photolyzable impurities in the solvents.

The above results show that detection of a single R-6G molecule should be achievable by this method. It is the poor reproducibility of the blank determinations that is presently limiting our sensitivity. Even so, our detection limit of  $\sim 0.4$  molecules is the lowest that has been reported to date for condensed phase determinations.

#### ACKNOWLEDGEMENTS

This research was sponsored by the U.S. Department of Energy, Office of Energy Research, under Contract DE-AC05-84OR21400 with Martin Marietta Energy Systems, Inc., and by the U.S. Army Chemical Research Development and Engineering Center.

#### REFERENCES

1. S. Arnold and L. M. Folan, *Rev. Sci. Instrum.* **57**, 2250 (1986).
2. E. P. Ippen, C. V. Shank, and A. Dienes, *IEEE J. Quant. Electron.* **QE-7**, 178 (1971).
3. A. Ashkin and J. M. Dziedzic, *Appl. Opt.* **20**, 1803 (1981).
4. C. F. Bohren and D. R. Huffman, *Absorption and Scattering of Light by Small Particles*, Wiley, New York, 1983.

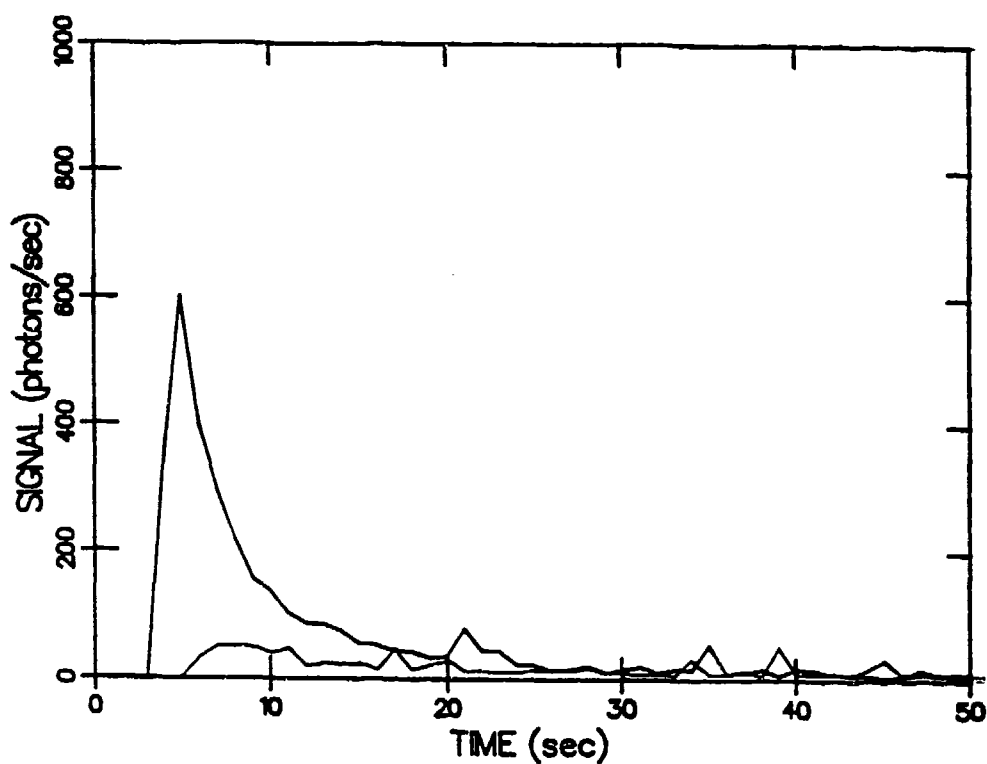


Figure 1. Fluorescence vs time for 13- $\mu$ m sample and blank droplets. Upper curve, 16-pM sample; lower curve, blank.

Table I. Results for Blank, 16 pM R6G Droplets

<u>Net Photons Counted</u>	<u>Droplet Vol (pL)</u>	<u>#R6G Molecules</u>	<u>Counts/Molecule</u>	<u>#R6G Equiv. in Blank</u>
382	1.2	--	--	1.1
1908	11.5	--	--	5.6
669	4.2	--	--	2.0
11295	2.6	25	460	--
2630	1.2	11	240	--
8451	3.0	29	290	--

average: 340 counts/R6G molecule

equivalent blank concentration: 0.5 R6G/pl. = 0.8 pM

2 x noise on blank: 140 counts/pl. = 0.4 R6G/pl.

THE SMOKE-ION SOURCE: THE GENERATION OF METAL AND METAL OXIDE  
CLUSTER IONS VIA INERT GAS CONDENSATION

H.W. Sarkas, L.H. Kidder, J.G. Eaton, N.G. Wimer, K.M. McHugh, and K.H. Bowen

Department of Chemistry, Johns Hopkins University,

Baltimore, MD 21218

RECENT PUBLICATIONS, SUBMITTAL FOR PUBLICATION AND PRESENTATION:

A) K.M. McHugh, H.W. Sarkas, J.G. Eaton, C.R. Westgate, and K.H. Bowen,  
"The Smoke Ion Source: A Device for the Generation of Cluster Ions via Inert  
Gas Condensation" Z. Phys D-Atoms Molecules and Clusters, 12, 3 (1989).

B) K.H. Bowen, presented at the "Workshop on Structural and Electronic  
Properties of Systems with Reduced Size and Dimensions," Virginia Commonwealth  
University, Richmond, Virginia, May, 1990.

C) K.H. Bowen, in "An Evaluative Program for Assessing the Utility of Cluster  
Ions in Semiconductor Processing," Report to the Semiconductor Research  
Corporation, 1990.

D) K.H. Bowen, presented at the "5th International Symposium on Small  
Particles and Inorganic Clusters," Konstanz, Germany, Septemeber, 1990.

## ABSTRACT

We report on the further development and mass spectrometric characterization of our Smoke-Ion Source. This ion source is capable of generating intense, continuous beams of both positive and negative cluster ions of metals, metal oxides, and other relatively high temperature materials. This device is the result of the marriage of the inert gas condensation method for generating metal smokes with techniques for injecting electrons directly into expanding jets. Intense cluster ion beams have been generated from metal smokes of lead, lithium, sodium, magnesium, and from mixed lithium-magnesium smokes. In addition, metal oxide cluster ions of lithium and of magnesium have also been generated. Future studies will focus on mass spectral studies involving new materials and on probing, via negative ion photoelectron spectroscopy and photoabsorption experiments, the electronic energy levels of size-selected cluster ions generated with this source .

## BACKGROUND

We report on the continuing development and characterization of a source for generating intense, continuous beams of metal and metal oxide cluster ions. This device<sup>1</sup> is the result of combining the inert gas condensation method with techniques for injecting electrons directly into expanding jets. Inert gas condensation is a proven approach for generating strong beams of large neutral clusters comprised of relatively high temperature materials.<sup>2-9</sup> In inert gas condensation cells, an oven evaporates the material of interest into a bath of cool inert gas. The evaporated material supersaturates in this cool environment and nucleates to form a dilute smoke composed of ultrafine particles and clusters. The inert gas, along with its entrained smoke, then exits the cell through a small aperture into a high vacuum region where it forms a beam. The injection of low energy electrons directly into the high density region of supersonic expansions has been shown to be a highly efficient method for generating beams of both positive and negative cluster ions.<sup>10-12</sup>

Several investigators had previously generated positive cluster ions from inert gas condensation cells, usually in the course of mass spectrometric characterization studies. In each case, this was accomplished well downstream of the cells' exit apertures by subjecting the neutral cluster beams to either electron bombardment ionization or to photoionization.<sup>4-9</sup> In the present work however, electrons from a biased filament are injected in a close-coupled manner directly into the weak jet expansion of the smoke-containing inert gas as it leaves the condensation cell, allowing the generation of intense beams of large positive and negative cluster ions. We refer to the unique union of these two techniques as the Smoke-Ion Source. Below, we describe the Smoke-

Ion Source along with its associated apparatus, and present the results of mass spectrometric investigations involving cluster ions of lead, lithium, sodium, and magnesium; mixed cluster ions of lithium and magnesium; and cluster ions of lithium oxide and magnesium oxide.

## EXPERIMENTAL

A schematic diagram of the Smoke-Ion Source is presented in Figure 1. The material of interest is evaporated from a heat shielded crucible (capable of achieving temperatures to 2,300 K) by direct resistive heating. The assembly containing the crucible is separated from the inert gas condensation cell by a water-cooled copper box which thermally isolates the cool inert gas from the high temperature environment of the crucible region. Vapor effusing from the crucible enters the condensation cell, which typically contains from 0.5 to 10 torr of helium and can be maintained at constant temperatures between 77 K and 285 K by a coolant reservoir. The cool inert gas thermally quenches the vapor, causing supersaturation with subsequent nucleation and cluster growth. Metal oxide cluster formation is accomplished by doping the inert gas with a small percentage (0.5-2.5 %) of reactant gas (typically  $O_2$ ). The condensation cell is coupled to high vacuum by a small (1.0-2.5 mm diameter) aperture, creating a flow of helium which entrains the clusters and transports them into the high vacuum region via a weak jet expansion. A negatively biased hot filament injects low energy electrons into the smoke-containing helium flow immediately as it exits the aperture. The presence of axial magnetic fields in the expansion region greatly enhances cluster ion production. The entire source is electrically floated at either  $\pm 500$  V or



$\pm 1$  kV with respect to ground potential. This electron injection configuration is used to generate both positive and negative cluster ions.

The resulting beam of cluster ions and accompanying neutrals is skimmed before entering the remaining part of the apparatus. Briefly, this consists of an ion optical beam line, an ExB mass separator (Wien filter) and a Faraday cup for ion detection. The Wien filter can be operated at a high electrostatic field where it achieves normal mass resolution over a limited mass range, or at a low electrostatic field where it exhibits poor resolution but over a much larger mass range. The latter mode is particularly useful for detecting very large cluster ions.

#### GENERATION OF METAL AND METAL OXIDE CLUSTER IONS

(1) Lead: Cluster ions of lead were generated under two different sets of source conditions.<sup>1</sup> The first set employed a source aperture diameter of 1.0 mm, a helium pressure of 6.0 torr maintained at 195 K, and a crucible temperature of 1,460 K. Figure 2 presents mass spectra for both positive and negative lead cluster ions recorded under these conditions. In order to obtain these spectra, the Wien filter was operated in its high mass range mode. Both spectra exhibit a progression of unresolved cluster ion peaks ranging from approximately 40-400 atoms per cluster ion, and for both ion polarities, the intensity maximum in the size distribution corresponds to ~200 atoms per cluster ion. Assuming these cluster ions are spherical in shape, their diameters can be estimated through the expression  $D = 2 Z^{1/3} R_s$ , where  $D$  is the cluster diameter,  $Z$  is the total number of valence electrons in the cluster, and  $R_s$  is the Wigner-Seitz radius of the bulk metal. These lead cluster ions are estimated to range in size from ~15-30 Å in diameter with the

peak of the size distribution at  $\sim 20$  Å. In the anion spectrum, an ion current of 600 pA was observed at this maximum. If average currents of cluster anions are compared, this is about five orders of magnitude more intense than those available via laser vaporization techniques.<sup>13</sup> In the cation mass spectrum, a series of low mass peaks due to  $\text{Pb}^{++}$  and  $\text{Pb}_{n=1-3}^{+}$  was observed in addition to the high mass distribution. Interestingly, these low mass peaks were absent in the anion spectrum, suggesting the small lead cluster cations may have resulted from fragmentation. However, the similarity between the high mass distributions in the cation and anion spectra may indicate that they reflect the neutral cluster distribution.

In an effort to explore the source's ability to access different cluster ion size distributions, a second set of source conditions was selected. This set utilized a source aperture diameter of 1.5 mm, a helium pressure of 1.6 torr at 273 K, and a crucible temperature of 1,460 K. Figure 3 shows the resultant lead cluster anion mass spectrum with the Wien filter operating in its low mass range mode. A variety of small lead cluster anions was observed demonstrating the ability to shift the cluster ion size distribution by manipulating source conditions.

(2) Lithium: Negatively and positively charged clusters of lithium were generated utilizing a 2.0 mm diameter source aperture, 1.5 torr of He at 273 K, and a crucible temperature of 1,100 K. Figure 4 presents a typical mass spectrum of lithium cluster anions generated under these conditions. This set of source conditions produced lithium cluster ion distributions that ranged from 650-2,800 atoms per cluster ion ( $D \cong 30$ -50 Å). The intensity maximum in the size distribution corresponded to about 1,200 atoms per cluster ion ( $D \cong 35$  Å). By utilizing slightly higher He pressures in the condensation

cell (3-5 torr), cluster anions comprised of 11,500 lithium atoms ( $D \approx 80 \text{ \AA}$ ) have been generated.

(3) Sodium: Cluster anions of sodium were generated utilizing a 2.0 mm diameter source aperture, 1.9 torr of He at 273 K, and a crucible temperature of 785 K. Figure 5 presents the mass spectrum of sodium cluster anions generated using these conditions. A sodium cluster anion distribution that ranged from 700 ( $D \approx 35 \text{ \AA}$ ) to well beyond 1,750 ( $D \approx 50 \text{ \AA}$ ) atoms per cluster anion was observed. The intensity maximum in the size distribution corresponded to about 1,250 atoms per cluster anion ( $D \approx 45 \text{ \AA}$ ).

(4) Magnesium: Cluster anions of magnesium were generated utilizing a 2.0 mm diameter source aperture, 1.2 torr of He at 273 K, and a crucible temperature of 975 K. The resultant magnesium cluster anion distribution ranged from 150-850 ( $D \approx 20\text{-}35 \text{ \AA}$ ) atoms per cluster anion, with the intensity maximum in the size distribution at 375 atoms per cluster anion ( $D \approx 25 \text{ \AA}$ ).

(5) Lithium-Magnesium: Mixed lithium-magnesium cluster anions were generated by evaporating lithium and magnesium metals from separate chambers in a single crucible at a temperature of 1,015 K. The evaporation rates per unit area of each metal were controlled so that the ratio of Mg to Li atoms in precondensed metal vapor would be 3:1. Other source conditions used included 1.2 torr of He maintained at 273 K and a 2.0 mm diameter source aperture. The mass spectrum of mixed lithium-magnesium cluster anions recorded under these conditions is presented in Figure 6. The  $(\text{Li}_x\text{Mg}_y)^-$  cluster anions observed ranged in mass from ~2,000 amu to well over ~20,000 amu with the intensity maximum of the mass distribution at ~7,000 amu. The ion current at this maximum measured approximately 1 nA.

(6) Metal Oxides: Oxides of lithium and magnesium cluster anions were generated under essentially the same source conditions used to generate pure metal cluster anions, but a small percentage of  $O_2$  was added to the helium inert gas. In the case of the lithium-oxygen system, 1.5 %  $O_2$  in helium was used in the condensation cell. The resultant mass spectrum, presented in Figure 7, shows a series of unresolved  $(Li_xO_y)^-$  cluster anions as well as  $O^-$  and  $O_2^-$ . For the formation of  $(Mg_xO_y)^-$  anions, 1.0 % oxygen in helium was used in the condensation cell. The resultant mass spectrum, presented in Figure 8, was recorded with the Wien filter operating in its low mass range mode. Peaks corresponding to  $(Mg_xO_y)^-$  cluster anions of various stoichiometries are evident along with  $O_2^-$  and  $O^-$ . In both cases, the addition of small amounts of oxygen to the condensation cell dramatically lowered the sizes of the particles produced in the source.

## CONCLUSION

We have shown the Smoke-Ion Source to be a powerful and versatile tool for generating intense beams of positive and negative cluster ions comprised of metals and metal oxides. Future experiments with the Smoke-Ion Source fall into one of two categories. The first category will involve the generation of cluster ions from additional materials, and these experiments shall primarily be mass spectrometric in nature. The second category involves probing the electronic energy levels of the clusters and cluster ions produced by this source. Negative ion photoelectron spectroscopy performed on size-selected cluster anions will reveal the ground and low-lying excited electronic state structure of a cluster anion's corresponding neutral (at the anion geometry). In addition, photodestruction and photodissociation experiments will be

performed on size-selected beams of positive and negative cluster ions to examine Mie-like resonances and other photoabsorption processes in these systems.

#### ACKNOWLEDGEMENTS

We are grateful to A. Yokozeki, K. Sattler, T. P. Martin, W. Schulze, J. L. Gole, E. Recknagel, S. J. Riley, and the late G. D. Stein for helpful discussions. The development of this ion source was supported by the Semiconductor Research Corporation under contract #83-01-034 and by the National Science Foundation under grant #CHE 8511320. Some of this work was also supported by ARCO Chemical Company.

## REFERENCES

1. K. M. McHugh, H. W. Sarkas, J. G. Eaton, C. R. Westgate, and K. H. Bowen, *Z. Phys. D* **12**, 3 (1989)
2. A. Yokozeki and G. D. Stein, *J. Appl. Phys.* **49**, 2224 (1978)
3. D. M. Mann and H. P. Broida, *J. Appl. Phys.* **44**, 4950 (1973)
4. T. P. Martin, *J. Chem. Phys.*, **81**, 4426 (1984)
5. J. Mühlbach, P. Pfau, K. Sattler, and E. Recknagel, *Z. Phys. B.* **47**, 233 (1982)
6. F. Frank, W. Schulze, B. Tesche, J. Urban, and B. Winter, *Surf. Sci.* **156**, 90 (1985)
7. S. J. Riley, E. K. Parks, C. R. Mao, L. G. Pobo, and S. Wexler, *J. Phys. Chem.* **86**, 3911 (1982)
8. A. E. T. Kuiper, G. E. Thomas, and W. J. Schouten, *J. Cryst. Grow.* **51**, 17 (1981)
9. R. W. Farley, P. J. Ziemann, R. G. Keesee, H. Funasaka, and A. W. Castleman, Jr., to be published
10. H. Haberland, H. G. Schindler, and D. R. Worsnop, *Ber. Bunsenges. Phys. Chem.* **88**, 270 (1984)
11. J. V. Coe, J. T. Snodgrass, C. B. Freidhoff, K. M. McHugh, and K. H. Bowen, *J. Chem. Phys.* **84**, 618 (1986)
12. M. L. Alexander, M. A. Johnson, N. E. Levinger, and W. C. Lineberger, *Phys. Rev. Lett.* **57**, 976 (1986)
13. O. Cheshnovsky, C. L. Pettiette, and R. E. Smalley, in *Ion and Cluster Ion Spectroscopy and Structure*, ed. J.P. Maier (Elsevier, Amsterdam, 1989), p. 373

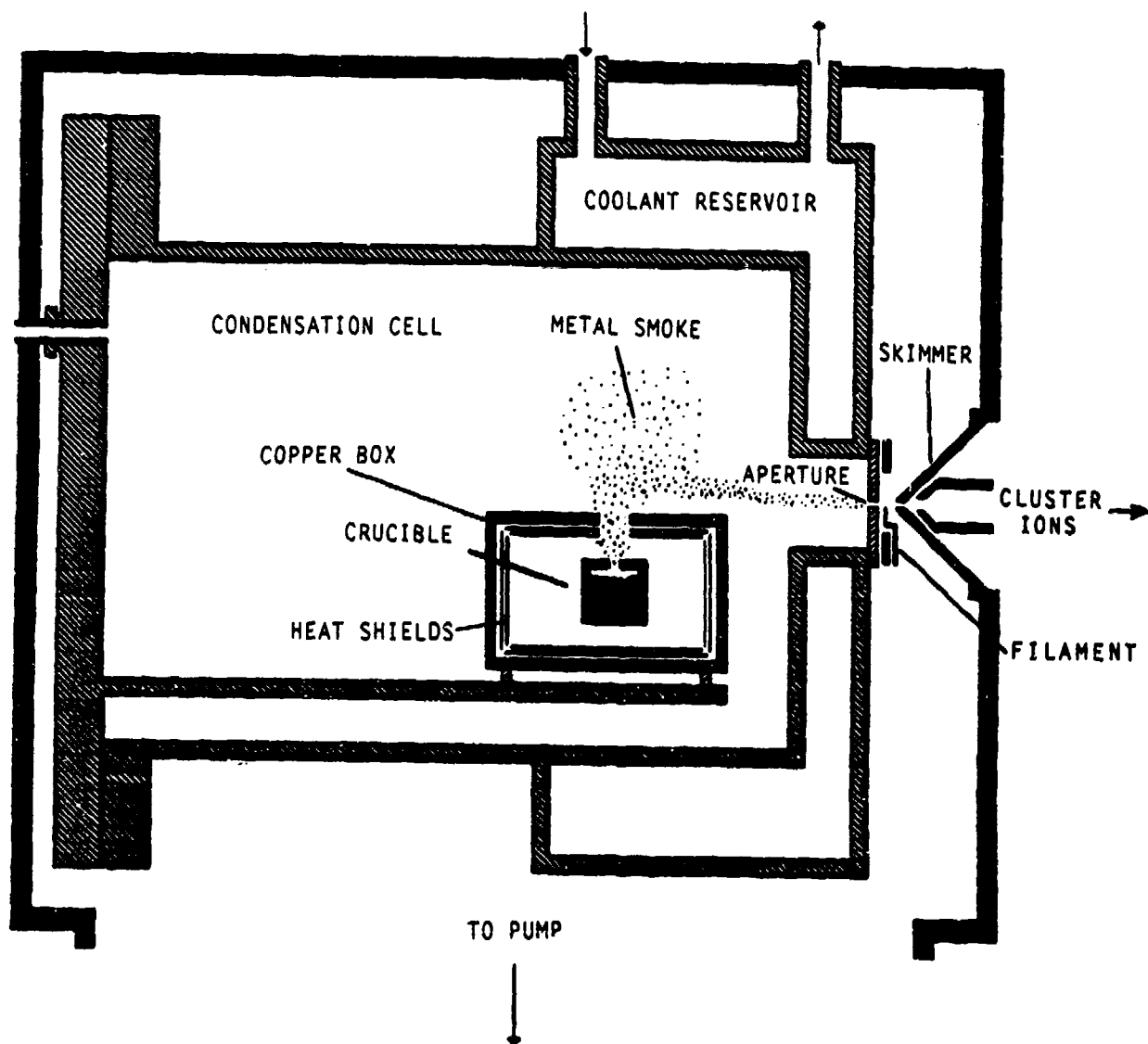


FIGURE 1. SCHEMATIC DIAGRAM OF THE SMOKE-ION SOURCE



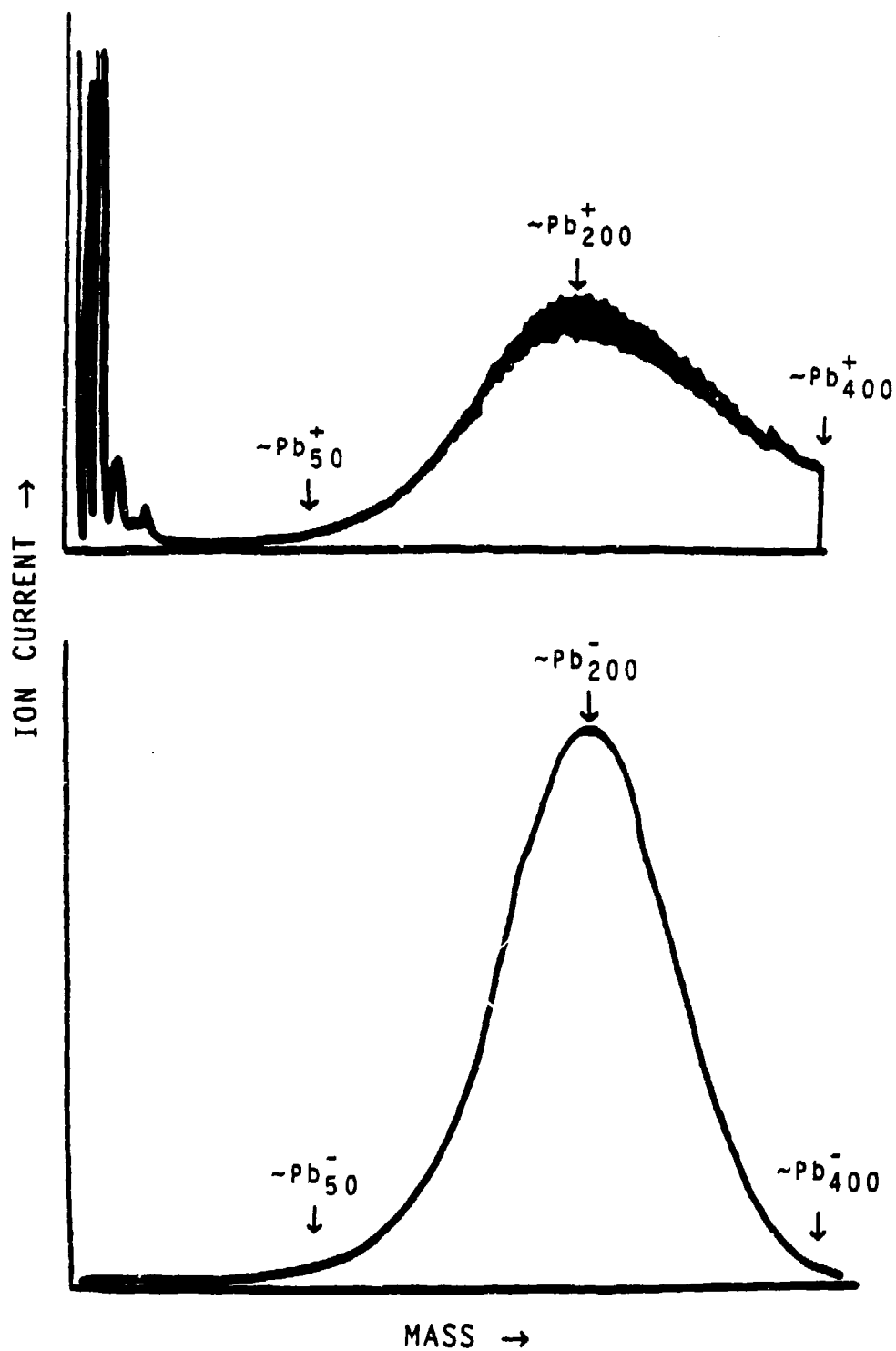


FIGURE 2. MASS SPECTRA OF LARGE POSITIVE AND NEGATIVE CLUSTER IONS OF LEAD GENERATED BY THE SMOKE-ION SOURCE

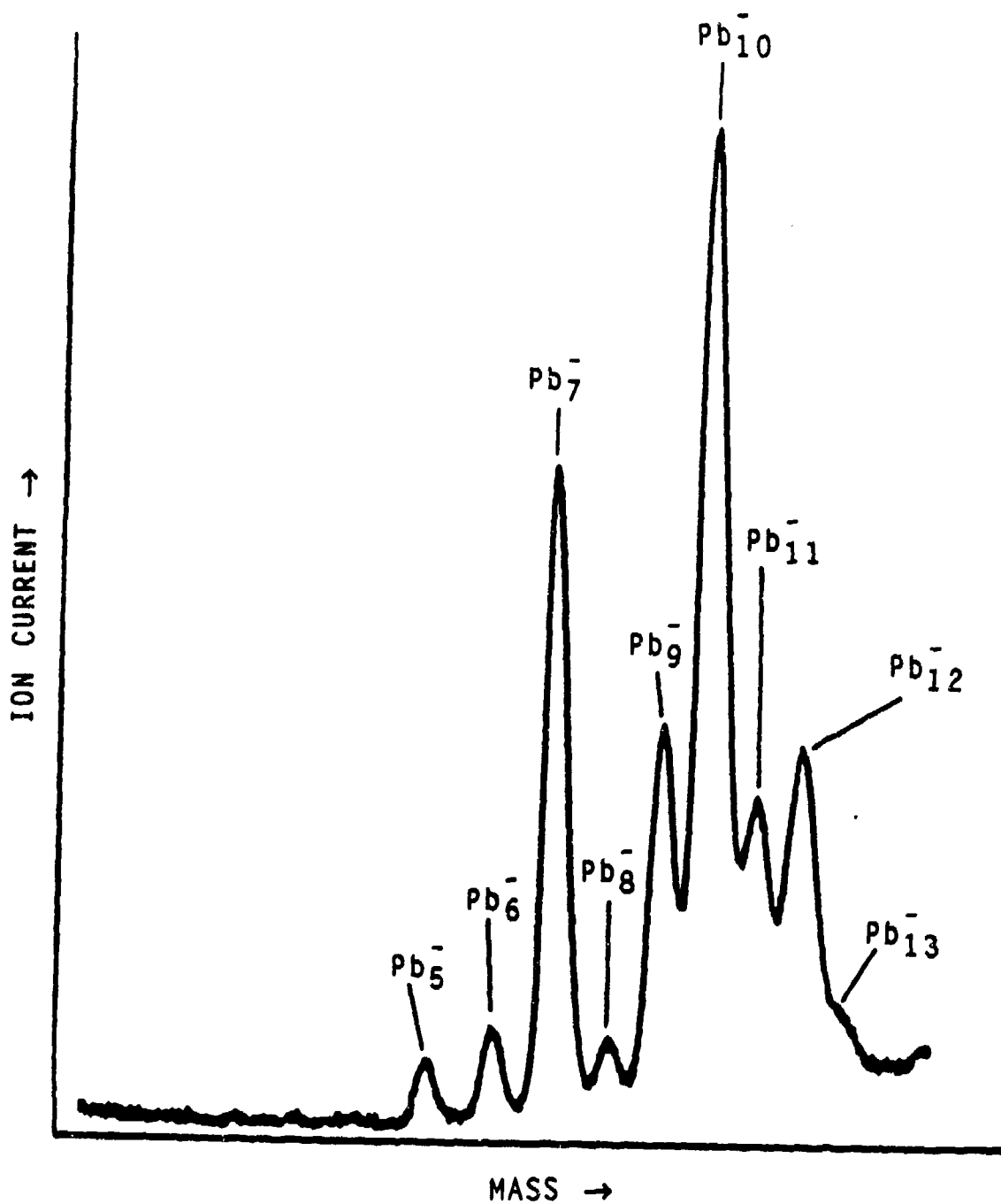


FIGURE 3. MASS SPECTRUM OF SMALL LEAD CLUSTER ANIONS GENERATED USING THE SMOKE-ION SOURCE

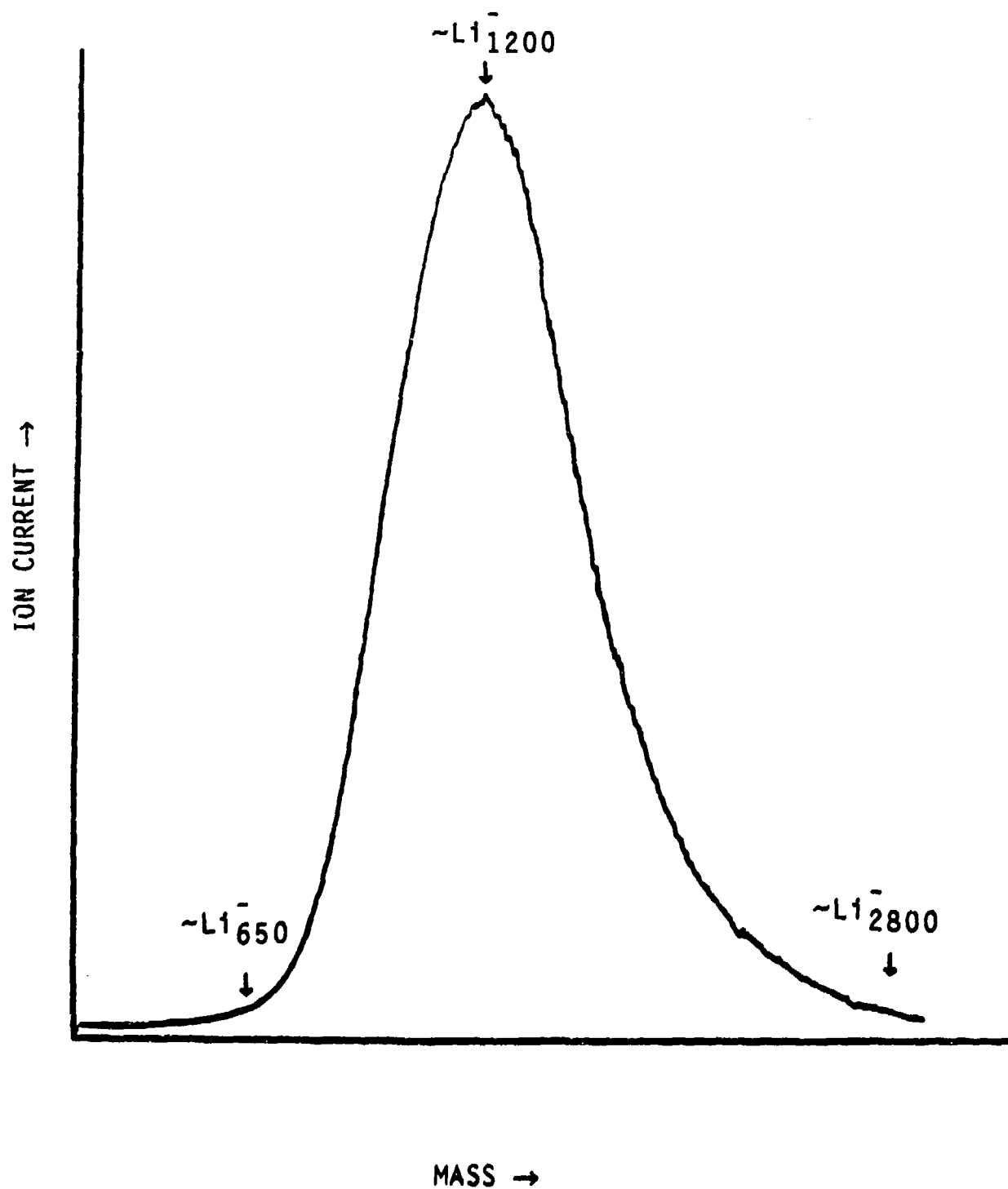


FIGURE 4. MASS SPECTRUM OF LARGE NEGATIVE CLUSTER IONS OF LITHIUM GENERATED BY THE SMOKE-ION SOURCE.

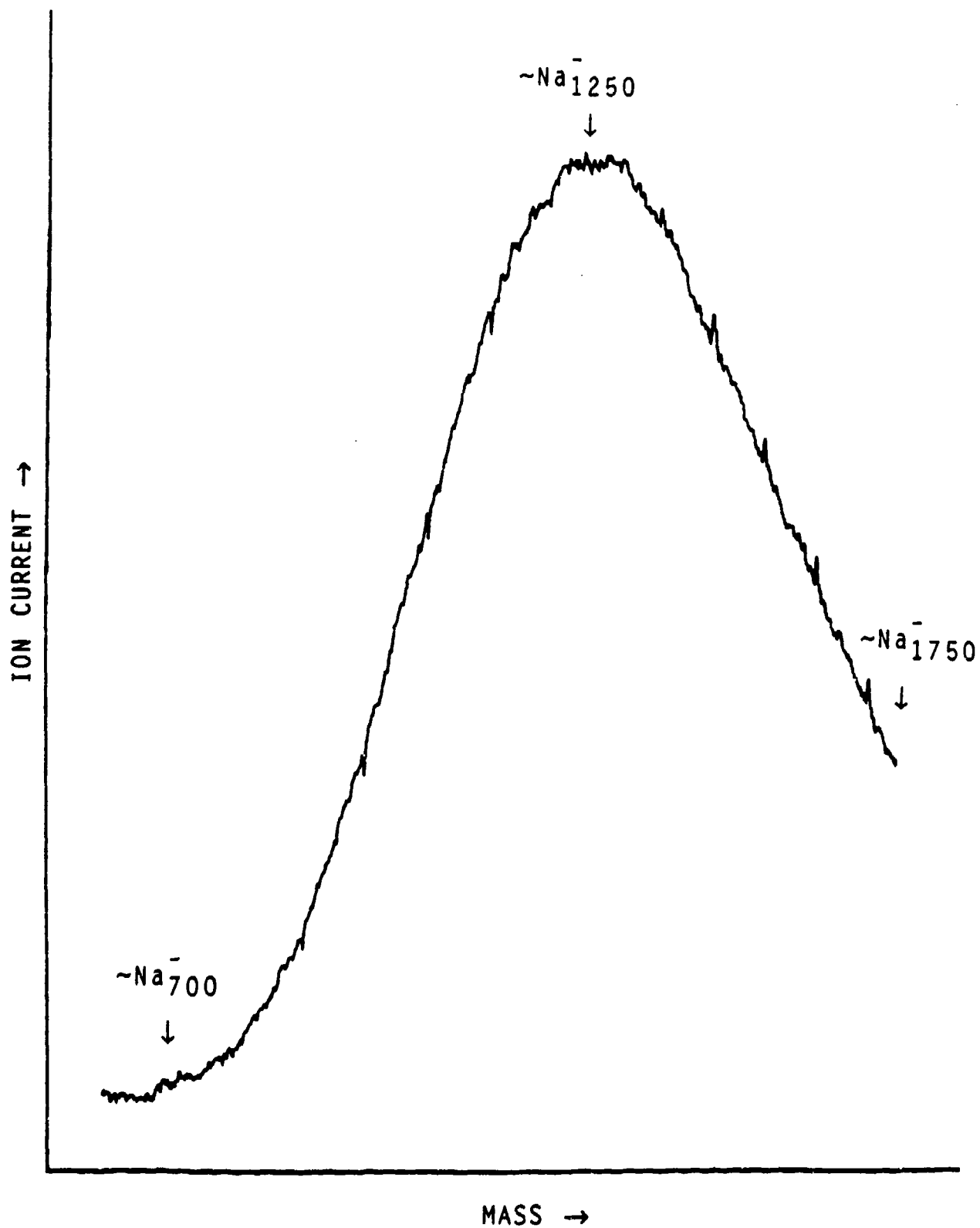


FIGURE 5. MASS SPECTRUM OF LARGE NEGATIVE CLUSTER IONS OF SODIUM GENERATED BY THE SMOKE-ION SOURCE

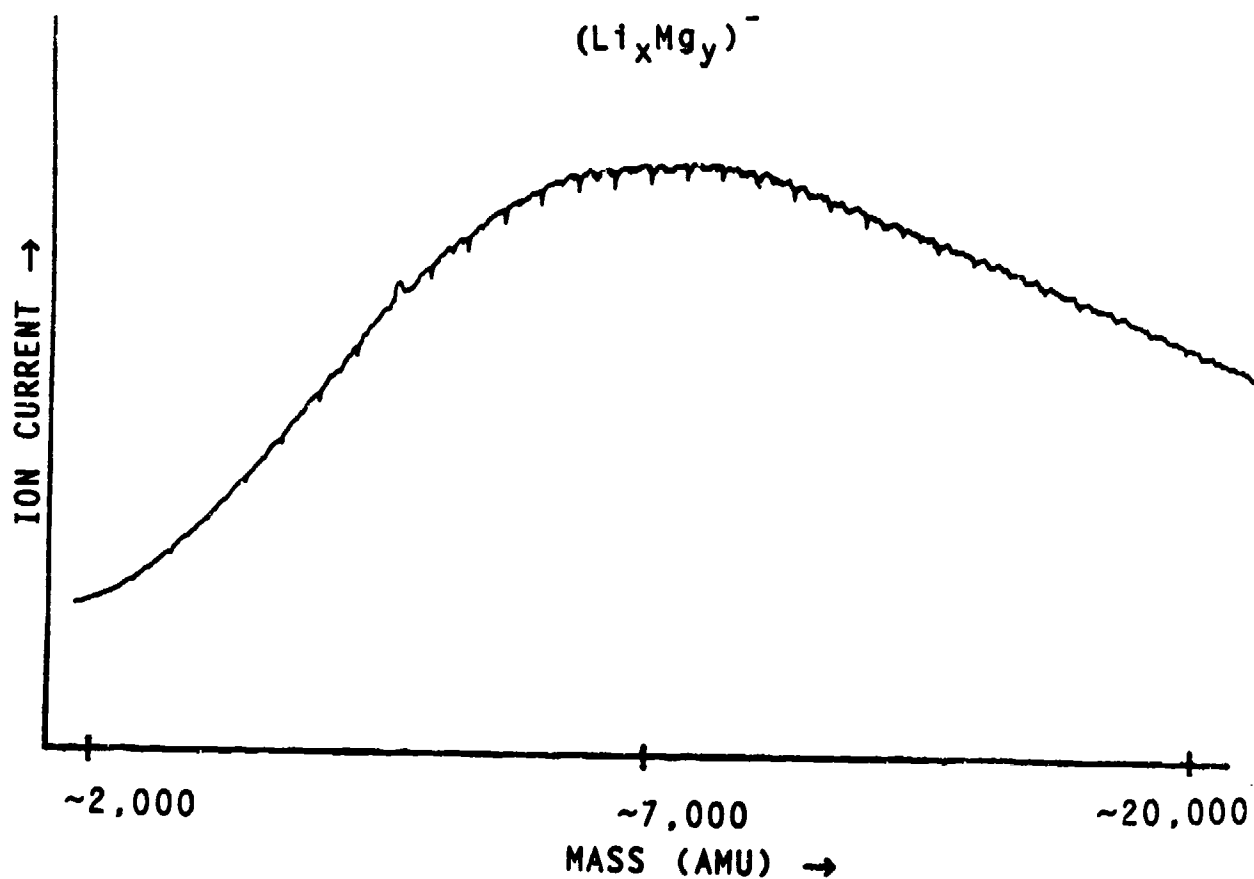


FIGURE 6. MASS SPECTRUM OF LARGE LITHIUM-MAGNESIUM CLUSTER ANIONS GENERATED BY THE SMOKE-ION SOURCE

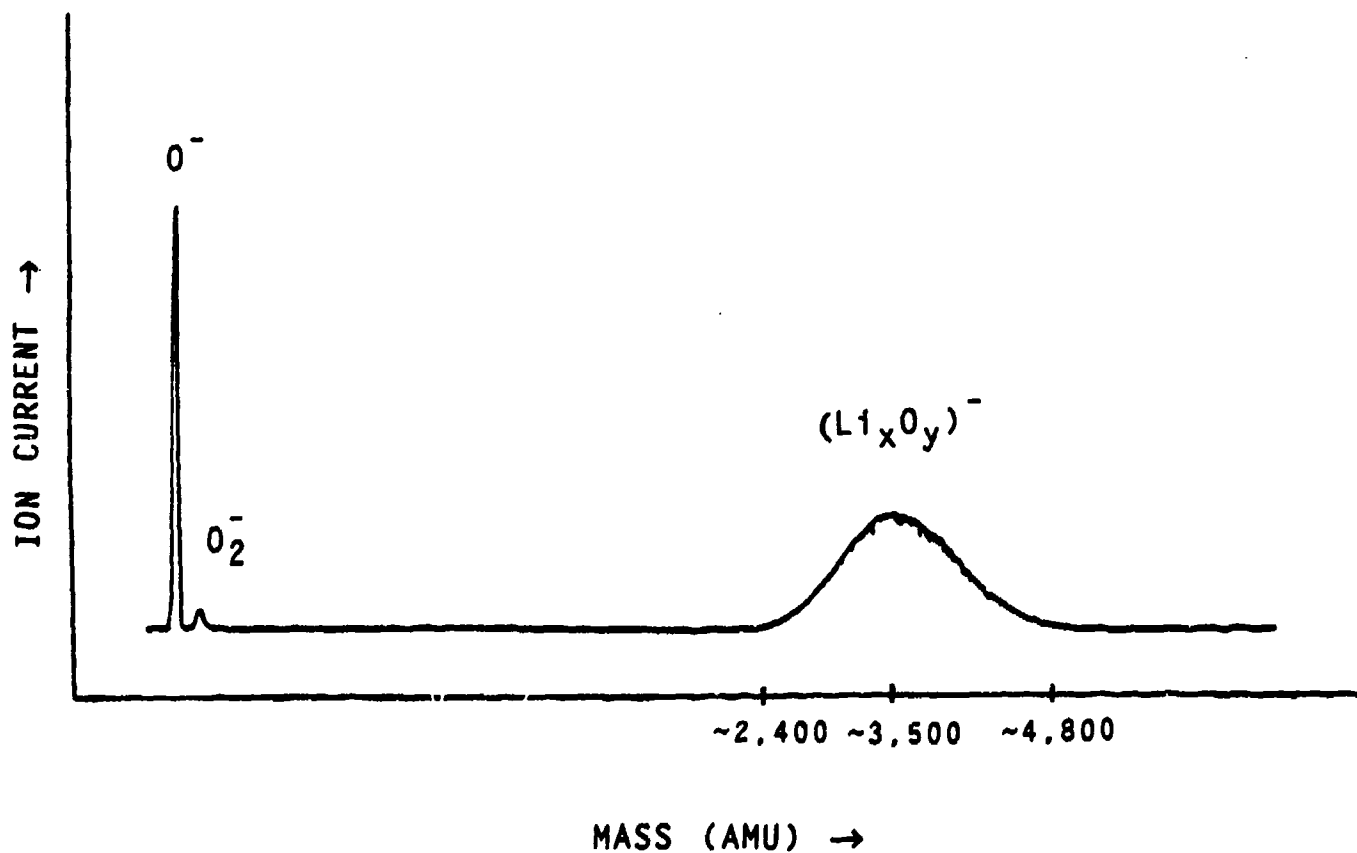


FIGURE 7. MASS SPECTRUM OF LARGE  $(Li_xO_y)^-$  CLUSTER ANIONS, ALONG WITH  $O_2^-$  AND  $O^-$ , GENERATED USING THE SMOKE-ION SOURCE

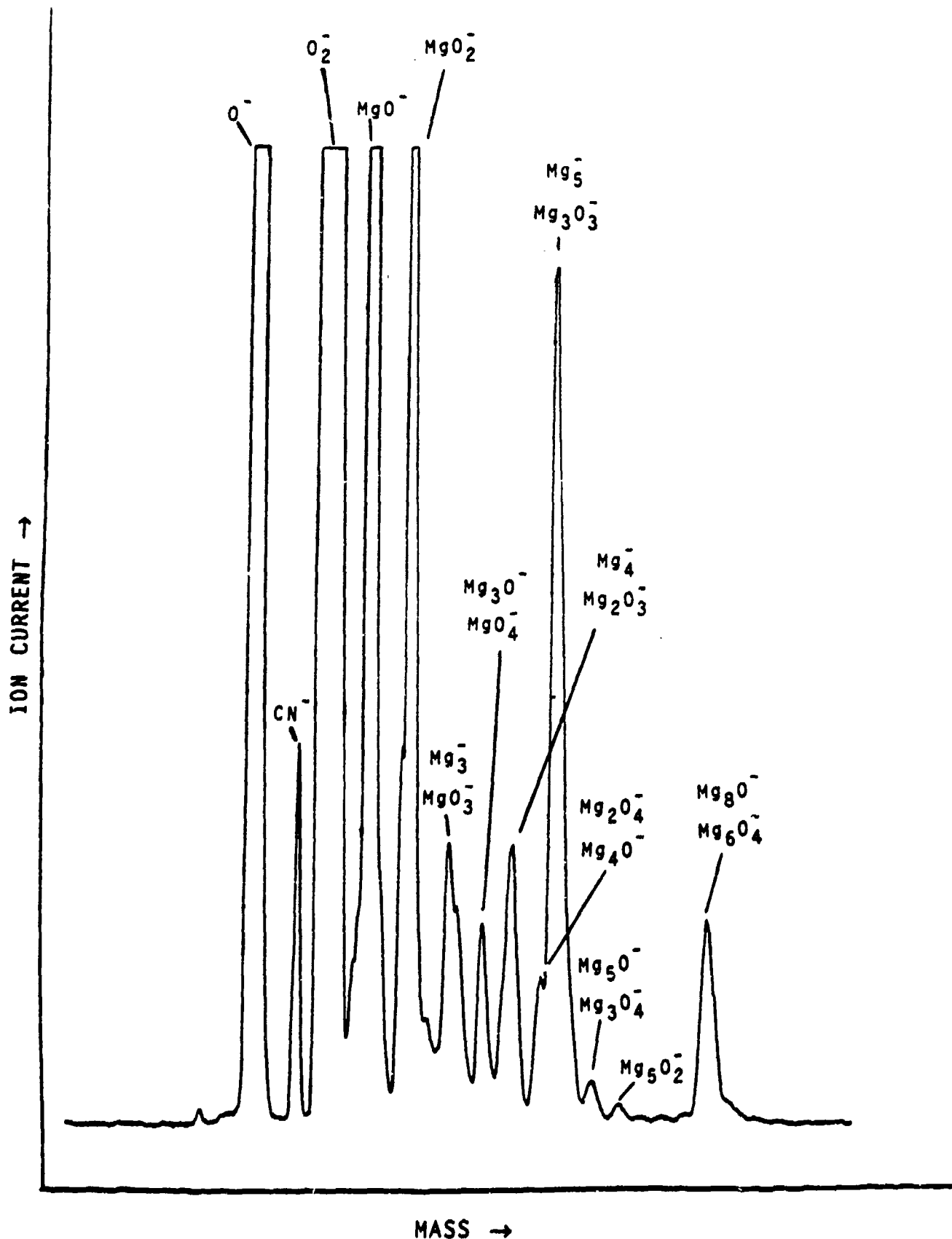


FIGURE 8. MASS SPECTRUM OF SMALL  $(Mg_xO_y)^-$  CLUSTER ANIONS, ALONG WITH  $O_2^-$  AND  $O^-$ , GENERATED USING THE SMOKE-ION SOURCE

BLANK



PRESSURE-DEPENDENT DAMPING AND BROWNIAN MOTION OF A PARTICLE  
LEVITATED IN VACUUM

L. D. Hinkle\*, B. R. F. Kendall  
Department of Physics,  
The Pennsylvania State University  
University Park, PA 16802

A novel method of levitation, using an actively controlled electric field, launches, captures, and stably suspends a microscopic ( $\sim 15 \mu\text{m}$ ) particle in high vacuum. While held to within one diameter in the vertical direction, the particle is allowed to oscillate nearly freely in the horizontal plane under the influence of a central restoring force. The damping of horizontal oscillations was measured over the pressure range from  $10^{-2}$  Torr to  $10^{-8}$  Torr. The damping was observed to be proportional to pressure down to less than  $10^{-8}$  Torr, where residual (pressure-independent) damping became significant. An absolute high vacuum gauge based on the pressure-dependent damping observed with this apparatus could operate linearly throughout at least a six decade range. A prototype gauge design is suggested.

The Brownian motion of the particle was observed and quantified by successive measurements of the oscillation amplitude in a horizontal axis. Brownian motion was exhibited throughout the pressure range from  $10^{-3}$  Torr to  $7 \times 10^{-6}$  Torr. The upper limit of pressure was determined by the gauging on the vacuum system. At pressures below  $7 \times 10^{-6}$  Torr, the Brownian motion was obscured by residual (pressure-independent) fluctuations in amplitude.

The statistical behavior of the oscillation amplitude is consistent with the theoretical prediction for Brownian motion in a low pressure gas. These measurements constitute the first evidence of Brownian motion of a levitated particle below 1 Torr. In addition to the experimental verification of low pressure Brownian motion theory, this work serves as an important step in the development of a standardizing high vacuum gauge.

\*Current address: MKS Instruments, Andover, MA 01810

Related Publications

1. B. R. F. Kendall, *Vacuum* 20, 540 (1970).
2. R. S. Butler, B. R. F. Kendall, and S. M. Rossnagel, *Vacuum* 27, 589 (1977)
3. B. R. F. Kendall, M. F. Vollero and L. D. Hinkle, *J. Vac. Sci. Technol. A* 5, 2458 (1987).
4. B. R. F. Kendall, D. J. Manzi, L. D. Hinkle, and M. F. Vollero, *J. Vac. Sci. Technol. A* 5, 3224 (1987).
5. L. D. Hinkle, "Brownian Motion in Low-Pressure Gas: The Behavior of Particles Levitated in a Vacuum," Ph.D. Thesis, The Pennsylvania State University, 1989.

BLANK

# MODE IDENTIFICATION OF LINEAR AND NONLINEAR OPTICAL PROCESSES IN MICRO-DROPLETS

H.-B. LIN, J.D. EVERSOLE\*, A.L. HUSTON, and A.J. CAMPILLO

U.S. Naval Research Laboratory,  
Optical Sciences Division, code 6546  
Washington, D.C. 20375 U. S. A.

## ABSTRACT

A recently developed aerosol generator provides 10-80  $\mu\text{m}$  droplets sufficiently stable and monodisperse to allow identification and detailed analysis of experimental results from stimulated optical processes, cavity quantum electrodynamic effects, and cw nonlinear optical phenomena. We report here results of our study on double resonance stimulated Raman scattering and cavity quantum electrodynamic enhanced spontaneous and stimulated emission in 20-mm ethanol droplets.

## INTRODUCTION

There has recently been a great deal of interest in the optical behavior of microspheres in the 10 to 100  $\mu\text{m}$  diameter size range. Total internal refraction in transparent droplets of this size allow them to act as high Q cavities in the presence of light. Lorenz-Mie scattering theory for the case of a sphere predicts a dense spectrum of such resonances spaced throughout the visible. Since these resonances are a function of particle size, shape and index of refraction, they are often referred to as morphology dependent resonances (MDRs) in the literature. In general,

resonances are characterized by a mode number,  $n$ , and order number,  $l$ , and both TE and TM mode resonances exist. These modes provide the necessary feedback mechanism for coherent processes such as stimulated Raman scattering (SRS), lasing, and other coherent nonlinear optical mixing. The MDRs also account for the ripple structure observed in elastic light scattering as well as sharp spectral peaks observed in fluorescence, spontaneous Raman, and radiation pressure. They may also lead to strong cavity quantum electrodynamic effects, e.g., fluorescence and absorption rate enhancement and inhibition.

Recently, we have developed a special purpose vibrating orifice droplet generator which has achieved a short term monodispersity with instantaneous diameter fluctuation of less than  $2 \times 10^{-5}$  and a long term drift rate of  $10^{-5}/\text{min}$ . It will be demonstrated that this degree of size precision is sufficient to correctly identify particular MDRs that are observed in experimental fluorescence, spontaneous Raman, and stimulated processes. Mode identification is usually very difficult because of uncertainties in particle size and index of refraction and the density of modes. Our development has allowed determination of both droplet size and refractive index and, subsequently, the first unambiguous assignment of specific modes observed in stimulated processes. In this paper, we report the mode identification of MDRs for the double resonance stimulated Raman scattering case and the spontaneous and stimulated process of R6G dye molecules in 20- $\mu\text{m}$  ethanol microdroplets.

## VARIATIONAL DROPLET SIZE SPECTROSCOPY

The droplet source is a modified Berglund-Liu vibrating orifice aerosol generator (VOAG). Figure 1 shows the essential components of the highly monodisperse vibrating aerosol generator and the optical configuration for sizing. Sample liquid is direct pressure fed to a 10- $\mu\text{m}$  vibrating orifice by the retained pressure of a 40-liter ballast tank pre-filled to nominally 30 psi with  $\text{N}_2$  gas. Size stability was achieved through the use of a programmable frequency synthesizer (HP3335A) to drive the orifice. Droplet size determination was made possible by ramping the VOAG frequency to induce a controlled size variation while simultaneously recording the elastic light scattering measurements from either a He-Ne or excitation laser. The frequency synthesizer is programmed to sweep between two operating frequencies of the vibrating orifice. As the frequency changes the scattering light displays a variational "frequency spectrum" (see Fig.2) due to induced size changes that has similar features to those displayed by wavelength spectra. Indeed, both radius and wavelength spectra are simple

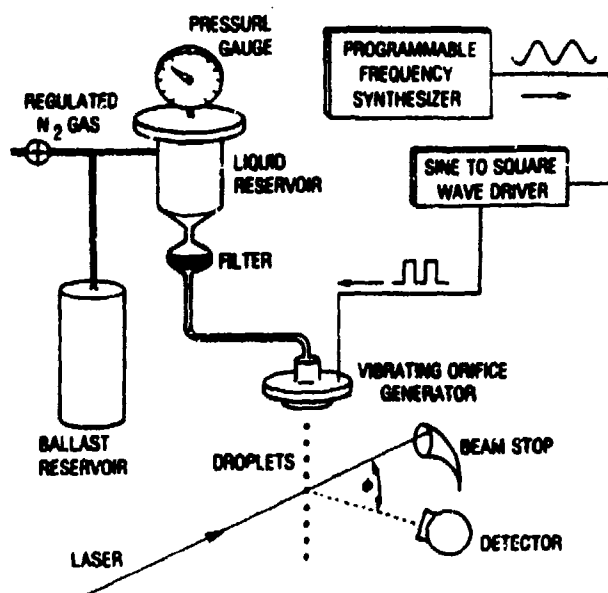


Fig.1 Schematic of the experimental apparatus.

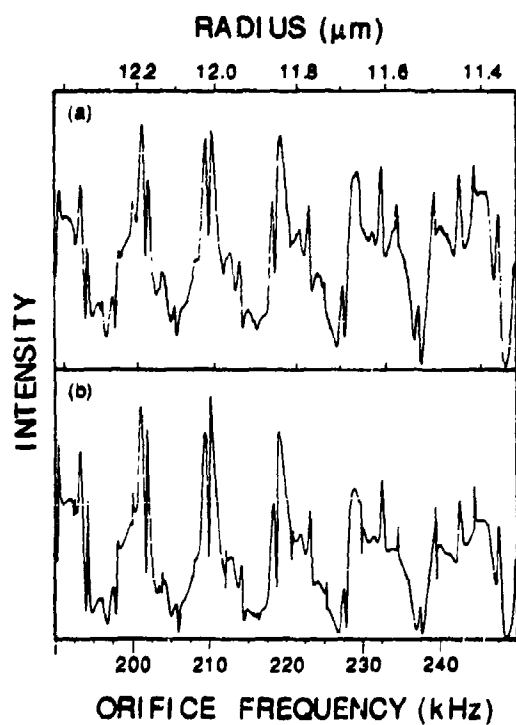
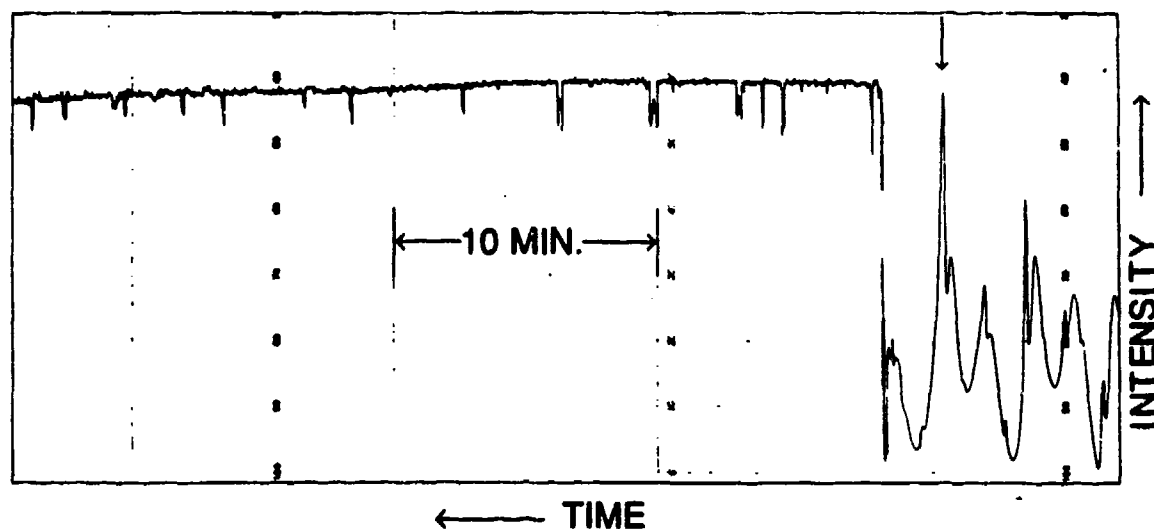


Fig.2 Variational size elastic scattering spectra. (a) is an ethanol spectrum obtained by ramping the orifice frequency from 190.0 to 250.0 kHz at 632.8 nm. (b) is calculated from Lorenz-Mie theory assuming an index of refraction of 1.362.



**Fig.3** Elastic scattering test of the size stability of a typical monodisperse aerosol stream. Time proceeds from right to left. The size of the droplets has been adjusted at the right by setting the vibrating orifice frequency to bring a morphology dependent resonance into coincidence with a 632.8 nm laser. The minimal decrease in scattering intensity after 30 minutes, corresponding to a droplet size drift of only 1 part in  $10^5/\text{min.}$ , allows considerable confidence to be placed in the subsequent MDR assignments.

transformations of each other and of size parameter. A typical 632.8 nm elastic scattering pattern obtained while ramping the frequency of the VOAG vibrating orifice is shown in Fig. 2(a). Fig. 2(b) shows the scattered light spectrum of a homogeneous sphere calculated from Lorenz-Mie theory. Matching computed spectra to the observed spectra was accomplished by iteration of the input parameters over their respective ranges of uncertainty or experimental error.

In an effort to quantify the drift in the position of features, the scattering curve displayed in Fig. 3 was taken. Time proceeds from right to left. Initially, the orifice frequency is ramped over a 20 kHz range and the precise frequency noted of the sharp feature indicated by the arrow in the figure. At the end of the scan, this frequency was imposed on the vibrating orifice, resulting in the droplet being forced into resonance with a  $\text{TE}_6$  mode having a  $Q$  of  $3 \times 10^3$ . The orifice frequency is then held constant as a test of the size drift. After 30 minutes, the scattering is still 90% of its peak height, implying an experimentally observed size drift of 1 part in  $10^5/\text{min.}$  Superimposed on the drift are several types of short term fluctuations.

## DOUBLE RESONANCE STIMULATED RAMAN SCATTERING

Since our VOAG permits the diameter of a linear stream of monodisperse droplets to be varied in a predetermined manner and, when desired, to force the droplet into resonance with a fixed frequency input beam, it allows us to maintain an input resonance condition for the study of SRS in a controlled and repeatable way. By ramping the frequency of the vibrating orifice and monitoring the total SRS output

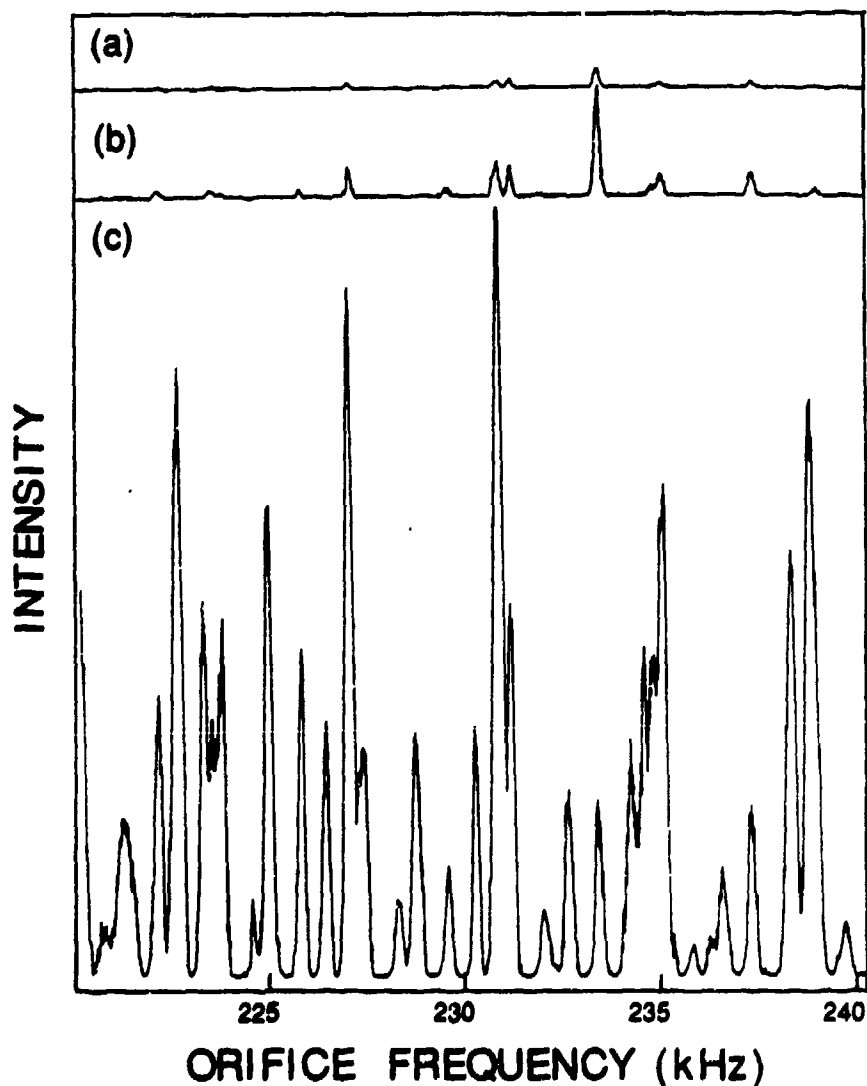
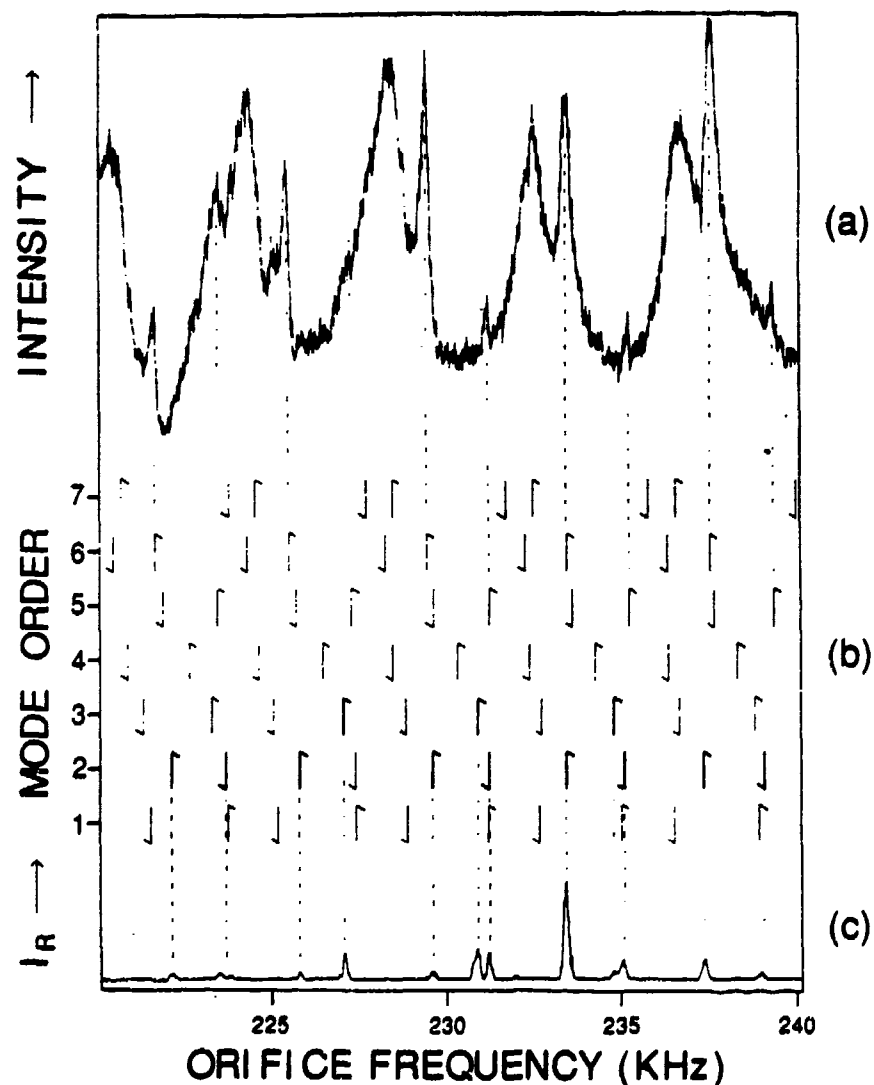


Fig.4 Variational size SRS spectra obtained using a high repetition rate Q-switched and mode-locked 532 nm source having intensities of (a) 0.3 GW/cm<sup>2</sup>, (b) 0.75 GW/cm<sup>2</sup> and (c) 1.5 GW/cm<sup>2</sup> and a frequency ramped VOAG. The peaks correspond to input resonances at 532 nm that are normally hidden in elastic scattering.



**Fig.5** (a) The 532 nm elastic scattering spectrum is shown with the corresponding calculated MDR placement. (b) is all MDRs of order 1 through 7. Arrows up (down) refer to TE (TM) modes. The variational size SRS spectra of Fig.4-(b) is reproduced in (c). The observed peaks align well with the calculated placement of  $TM^2$ ,  $TE^2$ , and  $TE^3$  modes.

intensity, we are able to generate novel variational size spectra of SRS showing many input resonances (see Fig. 4 ) which are not observed in elastic scattering. Figure 4 shows three such spectra of SRS output versus orifice frequency (droplet size) taken sequentially with increasing pump beam intensity (from top to bottom). As shown in Fig. 5, simultaneous elastic scattering measurements during size ramping provided a fiducial spectrum marking certain resonance positions and allowing unambiguous identification of the participating input modes. SRS spectra (Fig. 5(c)) display resonances corresponding to narrow low



order ( $l = 2$  to  $4$ ) modes in a size range (refer to Fig. 5(b)) where broader  $l = 5$  and  $6$  modes dominate elastic scattering (Fig. 5(a)). Our mode identification is consistent with a simple physical picture in which the highest  $Q$  modes ( $l = 2$ ) will exhibit the lowest threshold intensities, as we observe.

## CAVITY QUANTUM ELECTRODYNAMIC (QED) ENHANCEMENT

The capability of unambiguous identification of the various cavity modes enables quantitative study of QED cavity enhanced effects in a fluorescent droplet, since depending on what mode they correspond to, resonances will have different  $Q$  values, mode volumes, degeneracies and emission enhancements. Droplets of a constant size and containing a low concentration ( $\sim 10^{-5}$  M) of Rhodamine 6G dye were directed through a focused 514.5 nm cw laser beam. The fluorescence from the droplets was then detected by a photomultiplier and scanning monochromator. Figure 6 shows typical resulting fluorescing spectra and also mode assignments made on the basis of concurrent elastic scattering measurements as previously described. Mode lifetimes, or  $Q$  values calculated from Lorenz-Mie theory are found to be consistent with observed fluorescence linewidths for the experimentally resolvable  $l = 4$  modes. Typical predicted and measured values ranged from  $10^3$  for  $l = 4$  modes to  $10^7$  for  $l = 1$  modes. High quantum efficiency fluorescing dyes have emission bands so broad that they encompass regions of both enhanced and inhibited cavity emission. Mode and energy conservation arguments lead to the interpretation that droplet fluorescence spectra (see Fig. 6) mimic plots of the cavity modulated density of states (or alternatively, the  $A$  or  $B$  coefficient) vs wavelength. Both calculated and measured linewidths confirmed that  $Q$ 's of only  $10^3$  were sufficient to observe sizeable enhancements in the  $A$  coefficient.

Lasing was observed to occur at very low pumping thresholds in this study. Modes of  $l = 1$  near the peak of the fluorescence band showed a nonlinear intensity dependence even at the lowest pumping levels. Figure 7 shows fluorescent intensity for three pump intensities (increasing from bottom to top). Comparison of calculated  $Q$  values and the measured onset of lasing for the  $l = 3$  modes revealed that the gain was typically enhanced by  $10^3$ . This is not a subtle effect whose possible misinterpretation is subject to small experimental errors. Note that even if all R6G molecules in a typical droplet were assumed excited at peak pump intensities, the calculated gain using the conventional R6G cross-section (ca.  $2 \times 10^{-16}$  cm<sup>2</sup>) would still be below threshold for certain  $l = 3$  and  $4$  modes by factors of 10 and 100, respectively. The presence

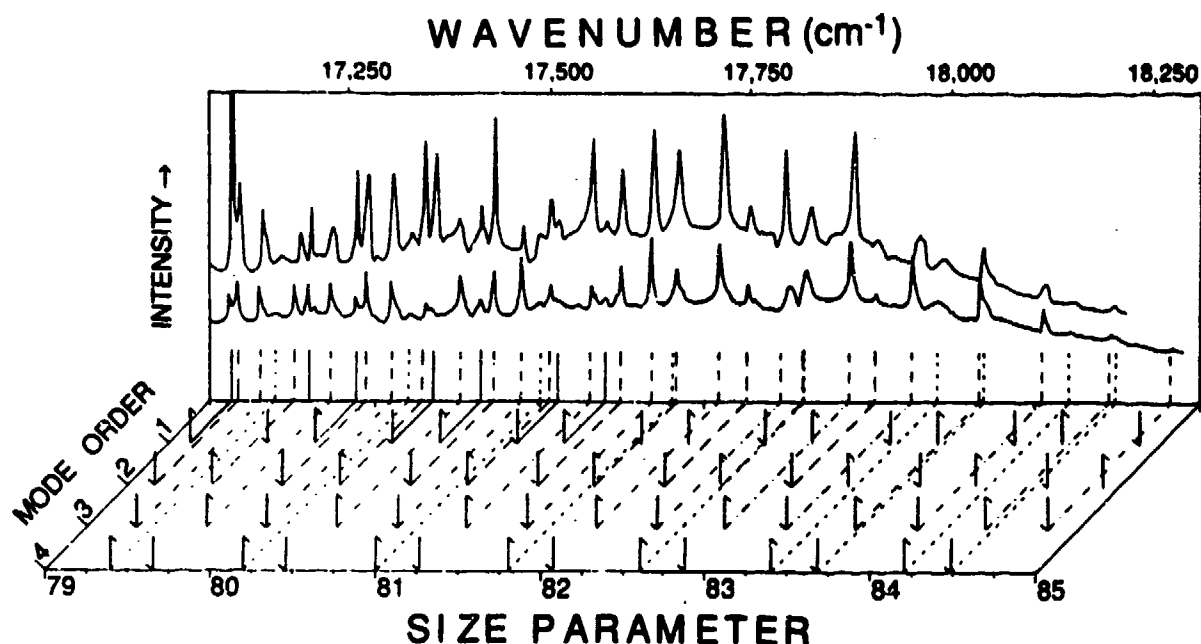


**Fig.6** Fluorescence spectrum observed from R6G in ethanol droplets. Spectral peaks correlate well with predicted spherical cavity resonance wavelengths. Arrows up(down) refer to TE(TM) modes.

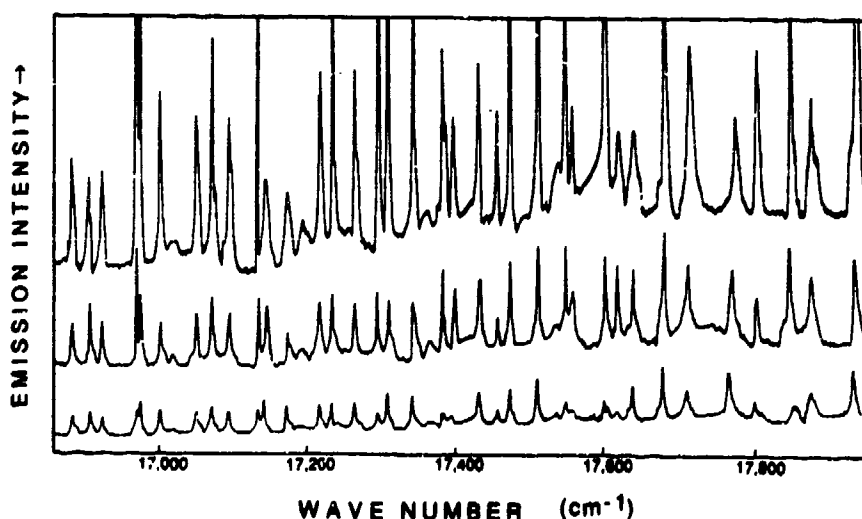


**Fig.7** Nonlinear intensity dependence of emission showing presence of lasing pumping intensities vary from 360 (lower trace) to 600 W/cm<sup>2</sup> (upper trace).

of lasing in these modes can only be explained by cavity QED enhancement.

# **Cavity Mode Identification of Fluorescence and Lasing in Micro-Droplets**

**J. D. Eversole**  
**Potomac Photonics, Inc.**  
**Lanham, MD 20706**

**H-B. Lin, and A. J. Campillo**  
**Optical Sciences Division, Code 6546**  
**Naval Research Laboratory**  
**Washington, D. C. 20375**

## **ABSTRACT**

Recent advances in an aerosol generation technique with droplet diameters from 10 to 80 micrometers permit the precise identification of optical resonance mode features as a function of size parameter. In particular, fluorescence and lasing in dye-doped spherical particles of this size range, although previously observed, can now be analyzed and spectral features assigned to specific spherical cavity modes. Such assignments provide insight to the mechanisms of droplet optics and permits the beginning of a general theory of droplet lasing.

## **Introduction**

When a transparent droplet or spheroidal particle which contains a low concentration of dye is illuminated in the dye absorption spectral region, one might naively expect a fluorescence spectrum from the droplet which mimics the spectrum of bulk solutions under similar external conditions. However, as originally reported by Chang and co-workers<sup>1</sup>, such particle spectra actually display relatively fine structure superimposed on the broad fluorescence band, consisting of narrow peaks of varying height. In that paper it was also speculated that the fluorescence peaks were

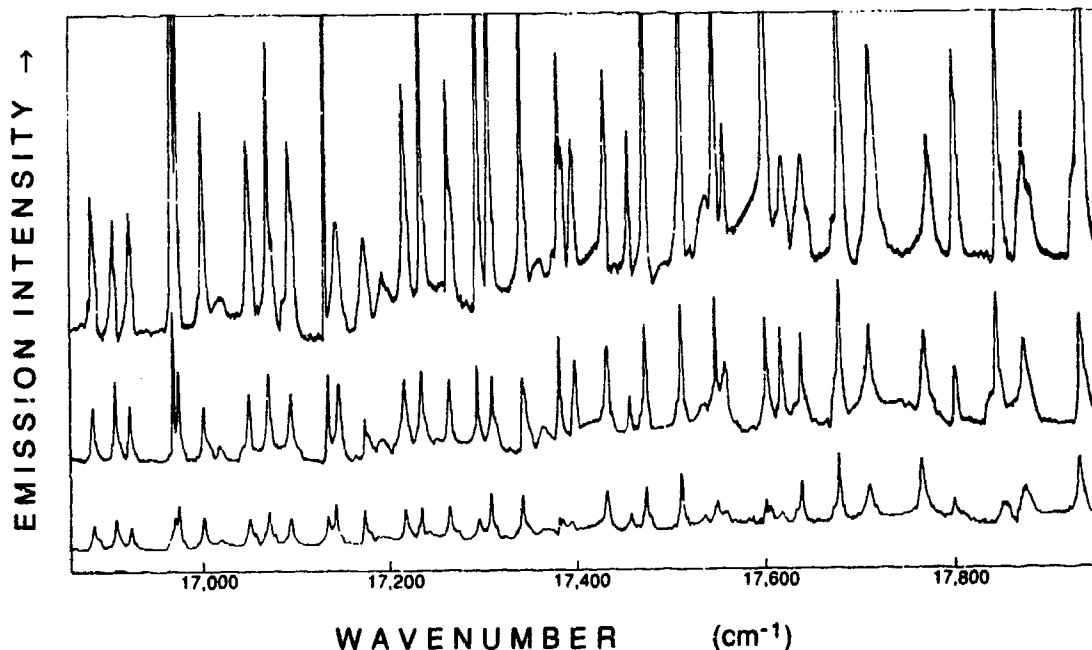


Figure 1. Typical fluorescence spectra from  $14\mu\text{m}$  diameter droplets of ethanol/R6G excited with a cw  $\text{Ar}^+$  514.5nm laser. Laser pump intensity is increased by  $\sim 2\text{X}$  for each spectrum from bottom to top.

caused by morphology dependent resonances (MDR's) which are readily predicted and observed features in elastic scattering from such particles. In the intervening decade, a number of papers have reported observation of individual particle fluorescence and, more recently, lasing. To illustrate the richness and complexity of single particle fluorescence, Fig. 1 shows typical spectra, recently obtained from  $\sim 14$  micrometer diameter ethanol droplets doped with rhodamine 6G, and pumped with a cw  $\text{Ar}^+$  laser. Three spectra are displayed showing the effect of increasing pump intensity (from bottom to top) with all other conditions held constant. The connection between elastic scattering MDR's, and such fluorescence structure, although widely accepted, has not been previously demonstrated conclusively. For the special case of a spherical particle, MDR's are the resonances which occur in the Lorenz-Mie partial-wave expansion of the internal and scattered electromagnetic fields and are also referred to as spherical cavity modes. The remainder of this paper will be divided into three parts: (1) a brief description of spherical cavity modes, (2) an overview of the general experimental technique, and (3) analysis and discussion of experimental results.

## Spherical Cavity Modes

Optical properties of spheres are conveniently described in terms of the dimensionless size parameter  $x = 2\pi a/\lambda$ , where  $a$  is the sphere radius and  $\lambda$  is the optical wavelength. The only other physical parameter necessary to describe the particle is the index of refraction  $m$  which may be complex to include absorption. Although a geometric optics representation is not strictly appropriate for particles in this size range ( $\approx 10 \leq x \leq \approx 200$ ), physical insight is gained by imagining a ray which is just captured at grazing incidence by a sphere.<sup>2</sup> The angle of the ray interior to the sphere is therefore the critical angle, and at each successive encounter with the sphere-air interface the ray is totally internally reflected. If, after a number of bounces, the ray folds back on itself in phase then it constitutes a standing wave or cavity resonance mode similar to wave guides. While this model is approximate, it immediately suggests two aspects that are accurate: (1) that different resonances may be designated by an integer (number of bounces) and (2) that the intensity associated with a resonance should be concentrated near the surface of the particle rather than its center.

A complete background and description of cavity modes, even for just the case of a perfect spherical boundary, is well beyond the scope of this paper (an excellent review is provided by Benner and Hill<sup>3</sup>). To briefly summarize the spherical case, the field equations are separable resulting in a general series solution for the electric and magnetic components, each term of which is the product of a Ricatti-Bessel function of the radial variable, a spherical harmonic function of the two angular variables, and an expansion coefficient determined by the boundary conditions.<sup>4-6</sup> In rigorous terms, cavity mode resonances occur whenever the real part of the denominator of the partial-wave expansion coefficients becomes zero. While this analysis originated from consideration of plane wave elastic scattering, it can be shown (for examples, see refs. 7-9) that the denominators of the expansion coefficients for generalized optical fields (including point dipole radiators interior to the sphere) have the same zeros as those of the familiar  $c_n$  and  $d_n$  (or  $a_n$  and  $b_n$ )

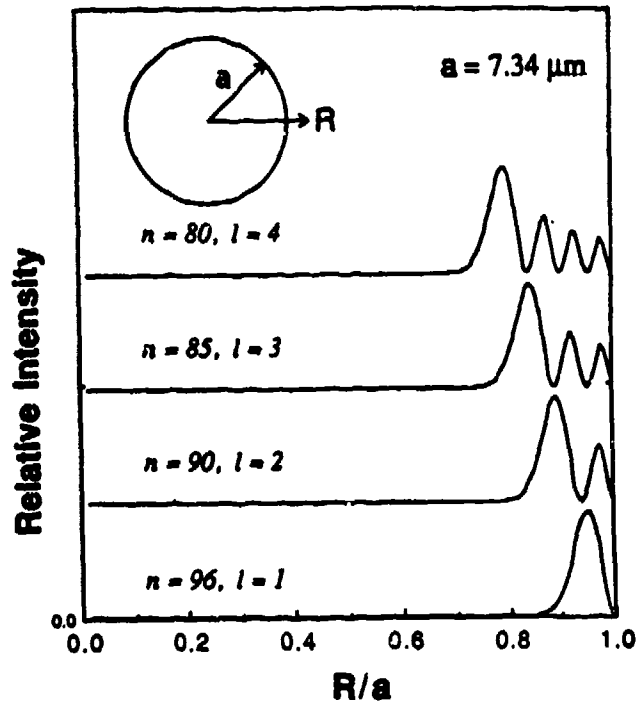


Figure 2. Calculated radial distributions of relative angle-averaged intensities for 4 different TE modes are plotted.

elastic scattering coefficients. Here  $n$  is an integer denoting that term of the expansion which multiplies the appropriate spherical Bessel function of order  $n$ . Cavity modes are either TM or TE in character and are designated by two integers:  $n$  and  $l$ . In physical terms  $n$  is a circumferential standing wave,  $n$  represents the number of maxima in the wave as the angular variable  $\theta$  (the scattering angle between the  $z$  axis and the radial vector) ranges between 0 and  $\pi$  radians, while  $l$  is the number of radial maxima. Figure 2 illustrates calculated relative intensities (integrated over the angular coordinates) for four different modes of a sphere with  $a = 7.34 \mu\text{m}$  and  $m = 1.362$  as a function of the radial coordinate ( $R$ ). These modes illustrate the dependence of the intensity distribution over  $l$  and  $R$ , and show that virtually all of the intensity of the mode is concentrated near the circumference of the droplet, but moves further towards the interior as the number of radial maxima,  $l$ ,

becomes larger. These four modes all occur for values of  $x$  close to each other ( $\approx 73.55 \pm 0.15$ ).

## Experimental Technique

In these experiments monodisperse aerosol droplets were generated using a modified Berglund-Liu vibrating orifice aerosol generator (VOAG)<sup>10</sup> recently described by Lin et al.<sup>11</sup>. This is a well-established aerosol generation technique whose basic principles are schematically shown in Fig. 3. Constancy in the droplet size  $D$  is determined by the stability of the fluid flow rate  $F$ , and of the orifice vibration frequency  $f$ . Improvements in the stability and precision of these two experimental parameters has lead to dramatic reduction in the drop-to-drop size variation in the droplet stream. As illustrated by Fig. 4, liquid ethanol sample is direct pressure fed to a 10- $\mu\text{m}$  vibrating orifice by the retained pressure of a 40 l ballast tank pre-filled to nominally 30 psi with  $\text{N}_2$  gas. Size stability (instantaneous size fluctuations of less than 3 parts in  $10^5$  and a size drift of less than one part in  $10^5/\text{minute}$ )<sup>11</sup> was achieved through the use of a frequency synthesizer (HP3335A) to drive the

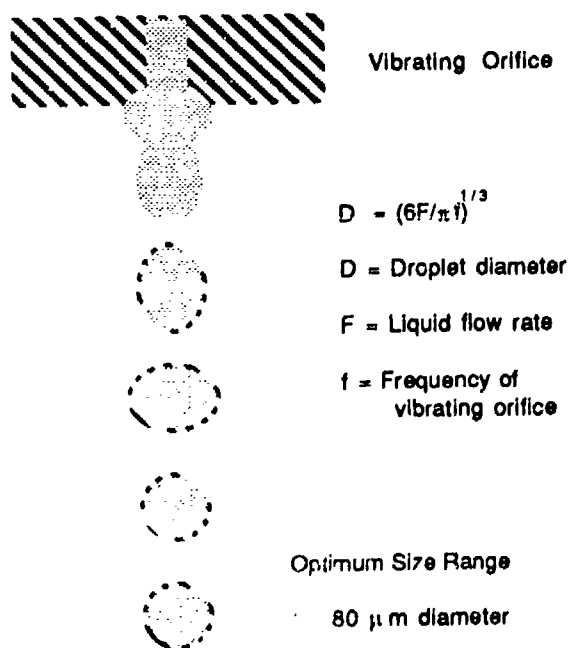


Figure 3. Schematic representation of the operation of the vibrating orifice aerosol generator

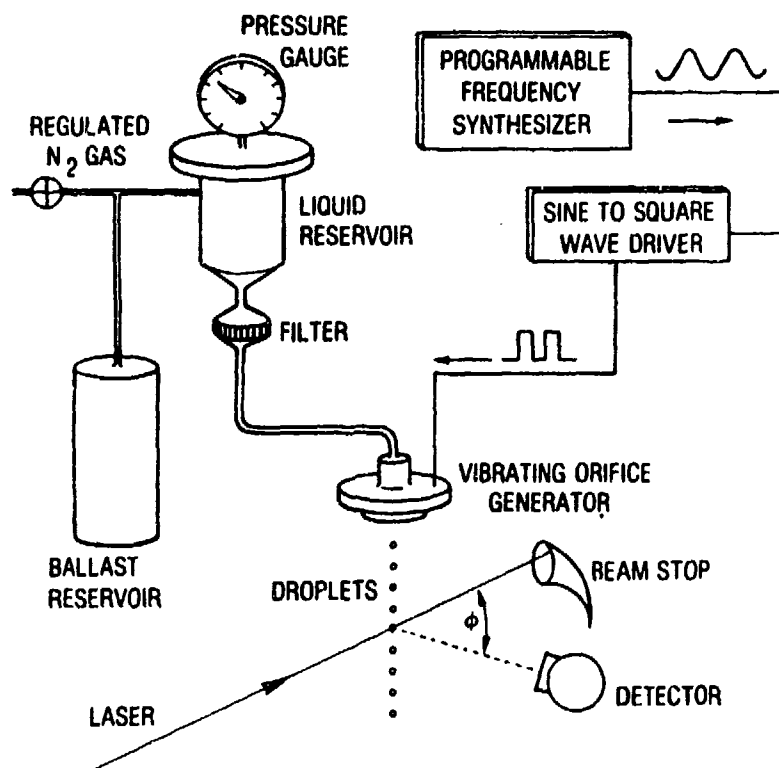


Figure 4. Schematic drawing of the experimental apparatus.

piezoelectric transducer (PZT) mounted in the orifice. Droplet size determination was made possible by ramping the VOAG frequency to induce a controlled size variation while simultaneously recording elastic light scattering measurements. Elastic scattering from the particles was observed at an angle near  $90^\circ$  using both He-Ne (632.8 nm) and cw Ar<sup>+</sup> (514.5 nm) laser light as probes. The frequency synthesizer was typically programmed to sweep between two operating frequencies of the vibrating orifice and the elastic scattered light was detected via photomultiplier and displayed as a function of VOAG frequency using an x-y recorder (see, for example, Figure 5(a)). The resulting variational frequency spectrum, due to induced size changes, has features similar to those displayed by wavelength spectra. Elastic scattering spectra such as these provide unique fingerprints of the droplet morphology and allow both  $a$  and  $m$  to be determined by comparing the experimental curve to Lorenz-Mie theory. The structure shown in the elastic scattering spectra are the original MDR's discussed earlier. Such spectra can be calculated



# SCATTERING INTENSITY

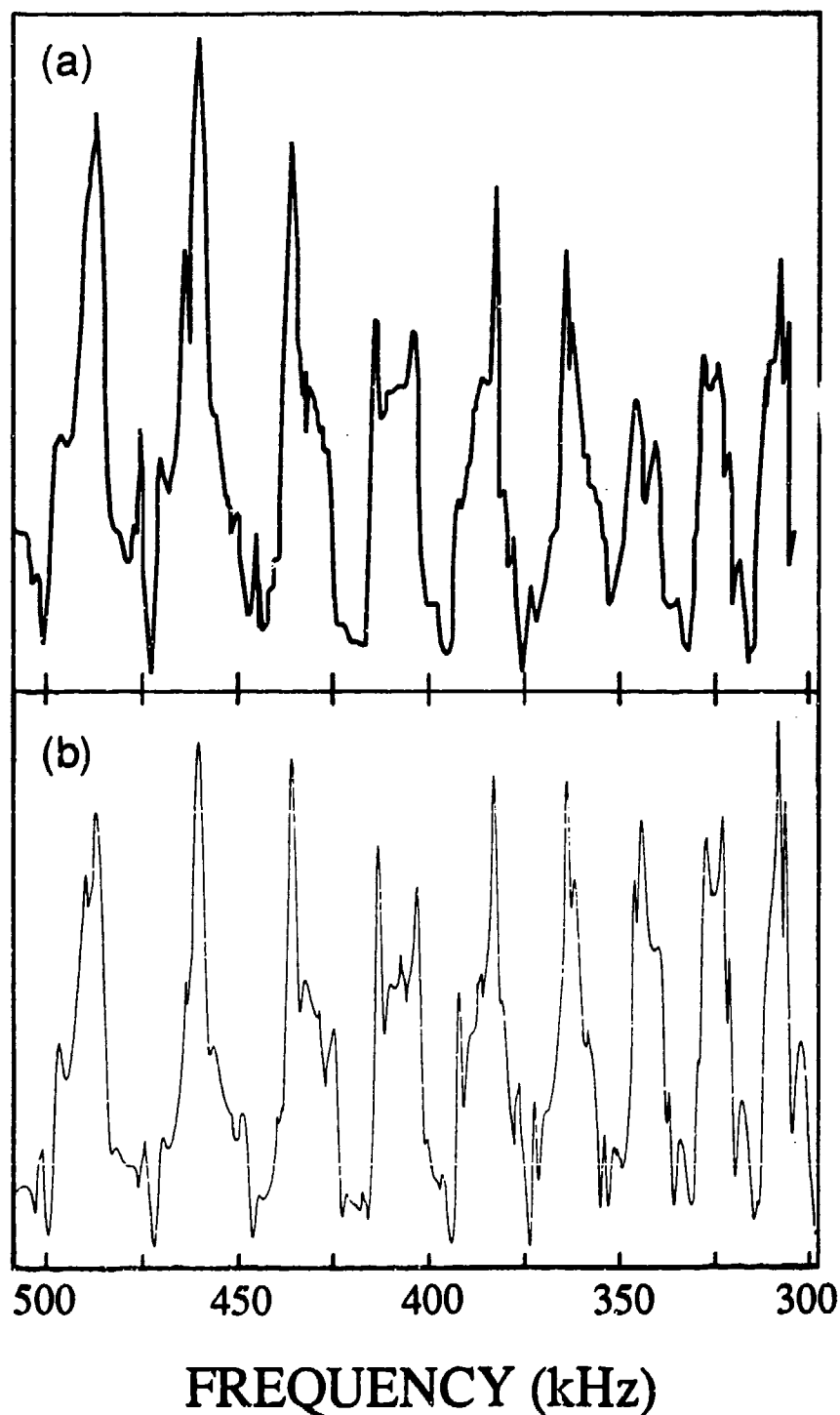


Figure 5. Elastic scattering "size spectra" are plotted as a function of the vibrating orifice frequency from 500 to 300 kHz. The upper spectrum is experimental data obtained with 514.5 nm light at a scattering angle near  $90^\circ$ . the lower spectrum was calculated from Lorenz-Mie theory for  $\theta = 90.8^\circ$  and  $m = 1.364$ .

as a function of  $x$  for given  $m$  and  $\theta$ , and then plotted versus  $\alpha$  for a fixed (laser)  $\lambda$ .<sup>12,13</sup> Additionally, using the relations shown in Fig. 3 (where  $D = 2a$ ), the scattered light intensity can be plotted as a function of orifice frequency for direct comparison to the experimental results as shown in Fig. 5(b). The procedure for matching the computed spectra to the data is basically iterative and somewhat tedious since the complex structure in the spectrum is quite sensitive to small changes in the input parameters  $m$  and  $\theta$ . A detailed description of the matching procedure is provided elsewhere.<sup>13</sup> It should be noted here that precise determination of resonance positions and the refractive index is limited at some point by other considerations. Eventually one part of the spectrum can be better matched only by sacrificing the quality of another part. Every feature in the experimental spectrum is accounted for in the computational plot over an extensive range in  $f$  (200 kHz). Although differences in relative heights do exist the overall match is optimized. More importantly, our objective is not to determine absolute droplet size and refractive index to the highest possible accuracy, but to assign spectral features, and for this task there is ample information available in the experimental data, as will be shown.

## Results and Discussion

Figure 5(a) shows elastic scattering for a fixed wavelength and angle as the droplet size is monotonically increased via changing the orifice frequency. Within minutes of the collection of the elastic scattering data, the orifice frequency was tuned to a value which makes the excitation laser light close to an input resonance, and fluorescence data was collected using  $\sim f/8$  optics centered at  $90^\circ$  to the incident laser beam, dispersed by a scanning double monochromator and detected with a photomultiplier tube. Figures 1 and 6 show examples of the observed R6G fluorescence spectrum recorded as a function of wavenumber. Since the fixed size of the droplets was known from analysis of the elastic scattering, it is possible to

compute the position of all spherical cavity modes as a function of wavenumber. Figure 6 is therefore a composite plot showing both experimental fluorescence spectra and computed cavity mode resonance positions. Since the spectra are so rich in detail the Fig. 6 has been split into two parts (a) and (b) showing the longer and shorter wavelength regions of the total spectrum respectively. The two experimental fluorescence spectra plotted with a vertical offset were taken consecutively with all conditions held constant except the laser excitation intensity was increased for the second (upper) spectrum. These spectra took about 40 minutes to record, and aside from where an occasional glitch or temporary fluctuation in the droplet stream occurs, the two spectra exactly reproduce each others' features within experimental resolution. This illustrates the stability and reproducibility of the experimental arrangement. It should be noted that the three fluorescence lines which leave the top of the figure for the upper spectrum have increased much more than the  $\approx 2.5 \times$  increase in the pump intensity and are in fact lasing. Many other lines are clearly close to threshold.

Because of the large number of possible cavity modes, it was necessary to plot their positions in a pseudo-3-dimensional horizontal plane with the experimental spectra in a vertical back plane. Modes with the same  $l$  value (mode order) are plotted as horizontal rows across this plane, with  $l$  increasing as one moves away from the vertical back-plane. Positions of TE (TM) modes are indicated by arrows pointing up (down). Broken lines are used to indicate the projection of the mode position onto the vertical back-plane with a slightly different style for each of the 4 different orders to help distinguish them. It is readily apparent that the projected positions of the modes line up quite well with the peaks of the experimental spectra. All of the fluorescence peaks expressed in the longer wavelength region (Fig. 6(a)) are assignable to modes of orders 1-3. Orders 4 and larger do not participate in the fluorescence in this region. However, as the spectra move towards larger wavenumber (Fig 6(b)) order 4 resonances begin to appear, weakly at first, but increasing in strength as the size parameter increases. Additionally, the order 4 resonances display a wider line width than

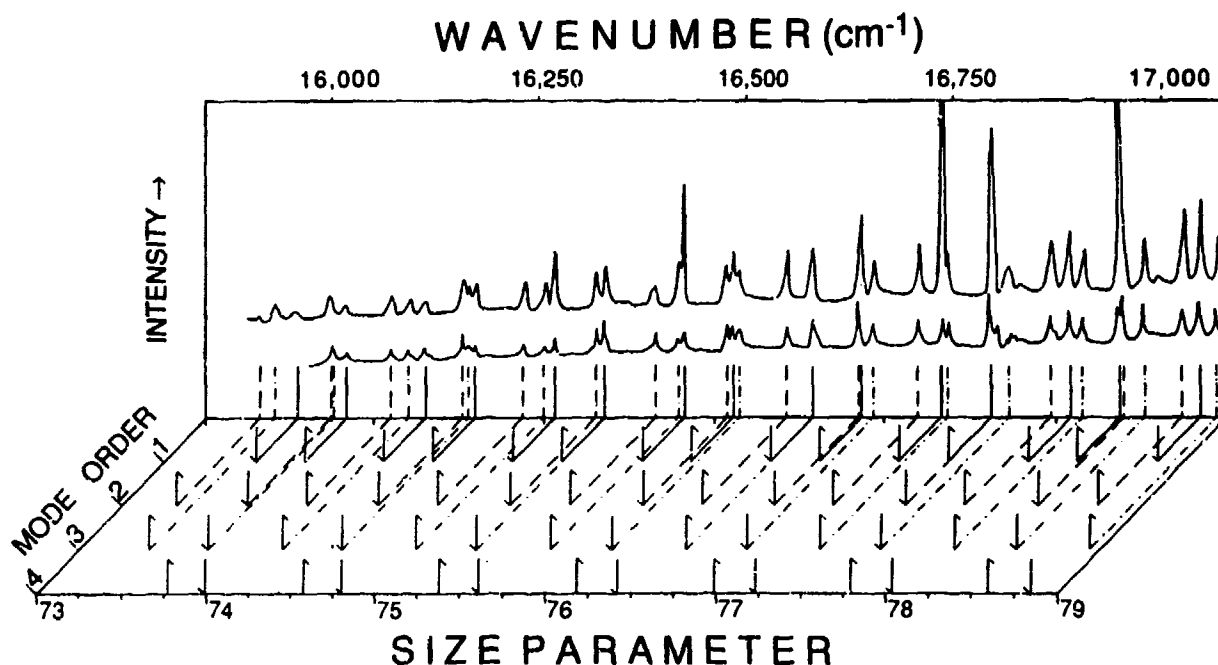


Figure 6(a) Shows the long wavelength region of the ethanol/R6G droplets fluorescence. Two experimental spectra shown in the upper part of the figure were taken under identical conditions except that the excitation intensity was changed. Calculated cavity mode positions are indicated in horizontal plane of the 3-D plot and then projected into the vertical plane of the spectra for comparison.

the other modes. Lower order modes have high Q's and the fluorescence lines displayed are essentially determined by the instrumental resolution. However, mode Q's decrease with increasing mode order, and the order four modes have linewidths large enough to be experimentally resolved. Order 1 modes should have the highest Q's, and therefore are the first to cross the lasing threshold as the pump intensity was increased. However, they begin to drop out as the spectrum moves toward shorter wavelengths. This is understood in terms of the increasing absorption occurring as the absorption band of the R6G dye is approached. Although the total absorption is small (typical dye concentration was about  $10^{-5}$  molar), it is sufficient to make the first order modes disappear.

Time does not permit further discussion of the implications of the fluorescence data for the feedback and gain of the lasing modes,

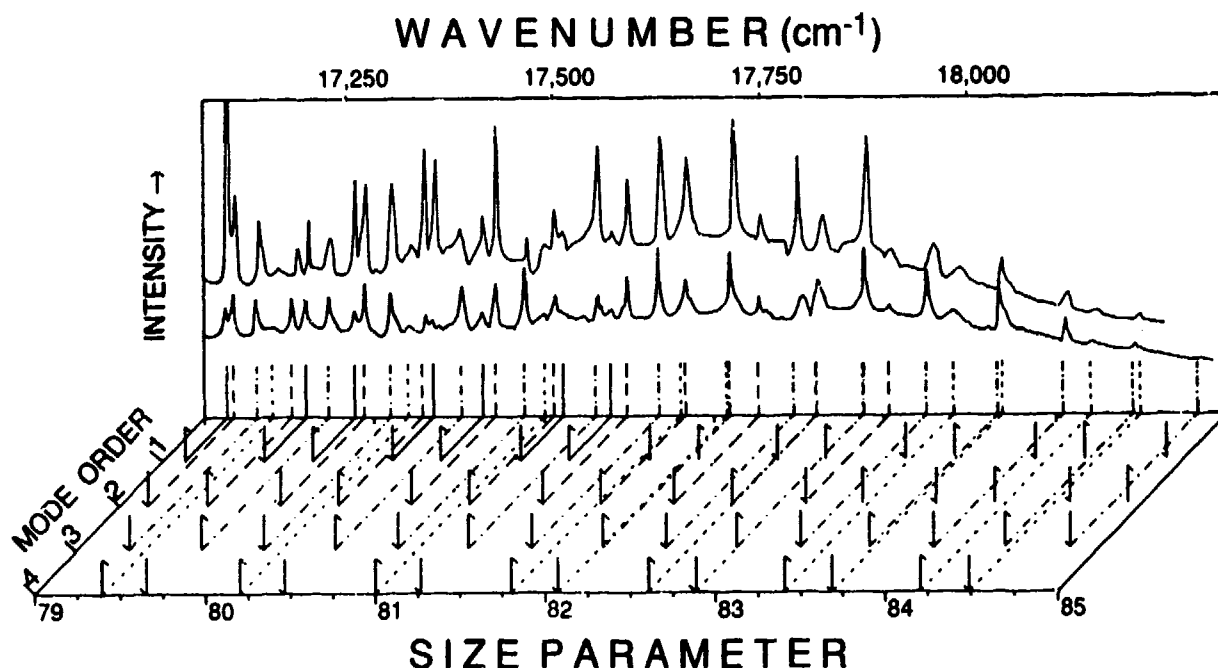


Figure 6(b) Shows the shorter wavelength region of the ethanol/R6G droplets. As in Fig. 6(a) the two experimental spectra are continued in the upper part of the figure while the calculated cavity mode positions are indicated in horizontal plane of the 3-D plot and then projected into the vertical plane of the spectra for comparison.

or the QED enhancement of the absorption and emission that takes place in confined structures such as these droplets. Instead, we close by addressing the issue of correct mode assignment of the fluorescence peaks. The exercise of matching the elastic scattering is a valid technique, which has been and can be applied to many experiments involving the optical properties of droplets. However, in the case of fluorescence data it is almost redundant. By cataloging the wavenumbers at which the fluorescent peaks occur, a set of numbers is extracted for which one can now attempt matching calculated mode positions. If the number of peaks is large, then the probability of having more than one possible assignment becomes small. For the longest spectrum recorded in this experiment, 104 distinct peaks were observed. Uncertainties in the refractive index or droplet size will change the scale by which the mode positions are converted to wavenumber. Therefore one can iterate on these two parameters to generate sets of mode positions and then compare

those to the peak data set by essentially performing a cross-correlation of the calculated set with the measured set. Figure 7 shows a 3-D plot of the cross-correlation of the 104 experimental fluorescence peaks with computed mode positions. In the horizontal plane the mode positions are either incrementally translated (to account for errors in absolute wavelength calibration), or incrementally compressed (by changing the computational droplet size). The compression is denoted in the figure as the Delta R coordinate, while the translation is denoted as the Delta X coordinate. Over a broad range of possible values only one major peak appears which corresponds to the mode assignments indicated in Fig. 6. This confirms that the mode assignment is unique and therefore correct.

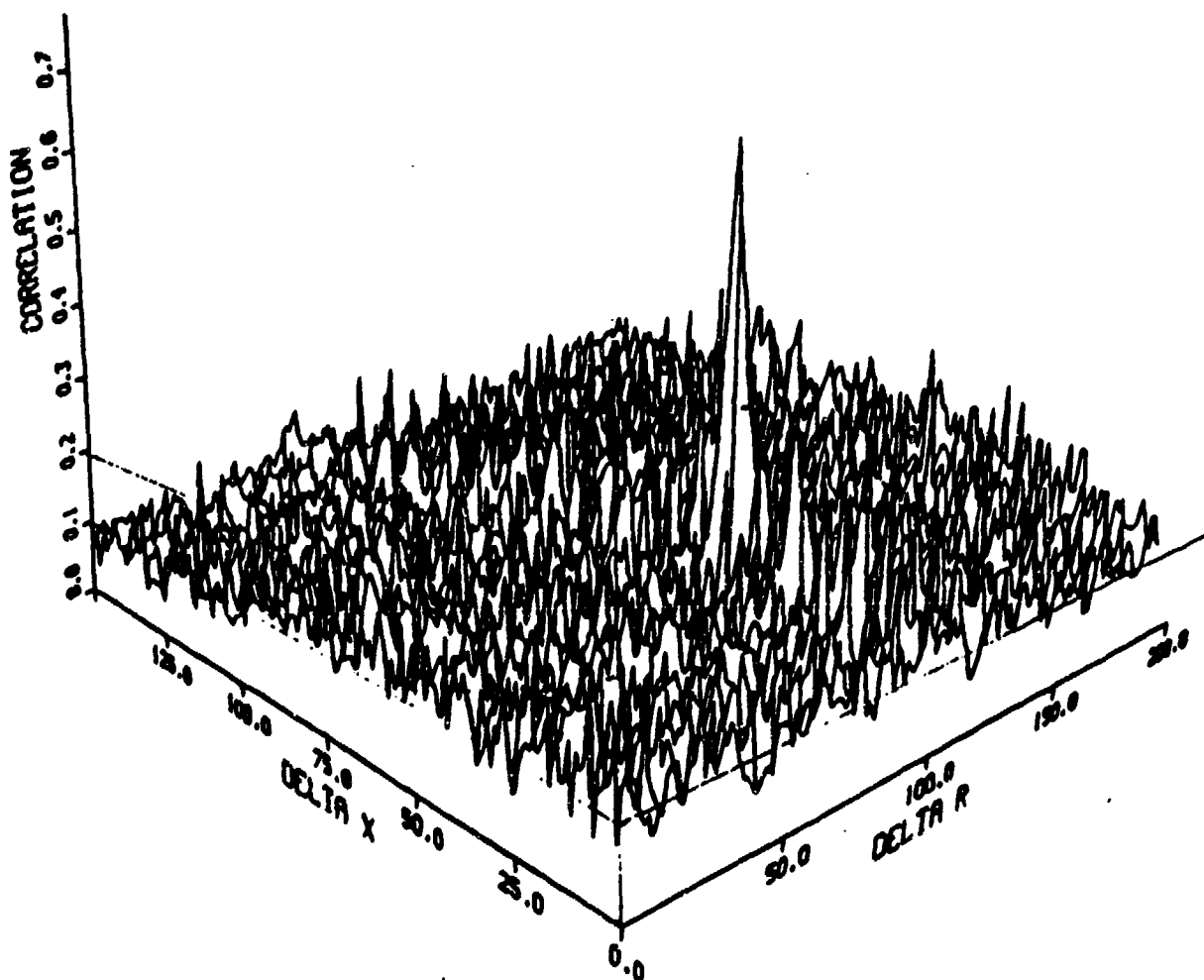


Figure 7 Crosscorrelation of a very large number of coomputed possible mode assignments with the measured fluorescence peaks results in only one possible assignment of cavity modes for the experimental data.

## References

1. R. E. Benner, P.W. Barber, J. F. Owen, and R. K. Chang, *Phys. Rev. Lett.* **44**, 475 (1980).
2. Khare and Nussenzweig, *Phys. Rev. Lett.* **38**, 1279 (1977).
3. S. C. Hill and R. E. Benner, "Morphology-Dependent Resonances," in *Optical Effects Associated with Small Particles*, P. W. Barber and R. K. Chang, eds. (World Scientific, New Jersey, 1988) p.3-61.
4. H.C. van de Hulst, *Light Scattering by Small Particles*, (Dover Publications, Inc. New York, 1981).
5. M. Kerker, *The Scattering of Light and Other Electromagnetic Radiation*, (Academic Press, New York, 1969).
6. C. F. Bohren and D. R. Huffman, *Absorption and Scattering of Light by Small Particles*, (Wiley-Interscience, New York, 1983).
7. H. Chew, P. J. McNulty, and M. Kerker, "Model for Raman and fluorescent scattering by molecules embedded in small particles", *Phys. Rev. A* **13** 396 (1976).
8. H. Chew, "Radiation and lifetimes of atoms inside dielectric particles", *Phys. Rev. A* **38** 3410 (1988).
9. J. P. Barton, D. R. Alexander, and S. A. Schaub, "Internal and near-surface electromagnetic fields for a spherical particle irradiated by a focused laser beam", *J. Appl. Phys.* **64** 1632 (1988).
10. R. N. Berglund and B. Y. H. Lui, "Generation of monodisperse aerosol standards" *Environ. Sci. & Tech.* **7**, 147-53 (1973).
11. H.-B. Lin, J. D. Eversole, and A. J. Campillo, "Vibrating Orifice Droplet Generator for Precision Optical Studies," *Rev. Sci. Instrum.* **61**, 1018-23 (1990).
12. H.-B. Lin, A. L. Huston, J. D. Eversole, and A. J. Campillo, "Double Resonance Stimulated Raman Scattering in Micrometer Sized Droplets," *JOSA B* **7** 2079 (1990).
13. J. D. Eversole, H.-B. Lin, and A. J. Campillo, "Spherical Cavity Mode Assignments of Optical Resonances in Microdroplets Using Elastic Scattering", *JOSA A* (scheduled for Dec. 1990 publication).

BLANK



### III. THE ROLE OF AEROSOLS IN ATMOSPHERIC CHEMISTRY

## Atmospheric Chemistry on Polar Stratospheric Cloud Particles

M. A. Tolbert, A. M. Middlebrook, M. A. Quinlan, C. M. Reihs, and D. M. Golden

*Department of Chemical Kinetics  
SRI International, Menlo Park, CA 94025*

#### RECENT PUBLICATIONS AND SUBMITTAL FOR PUBLICATION:

- A) M. A. Quinlan, C. M. Reihs, D. M. Golden and M. A. Tolbert, "Heterogeneous Reactions on Model Polar Stratospheric Cloud Surfaces: Reaction of  $\text{N}_2\text{O}_5$  on Ice and Nitric Acid Trihydrate," *J. Phys. Chem.*, **94**, 3255-3260, 1990.
- B) C. M. Reihs, D. M. Golden and M. A. Tolbert, "Nitric Acid Uptake by Sulfuric Acid Solutions Under Stratospheric Conditions: Determination of Henry's Law Solubility," *J. Geophys. Res.*, in press.
- C) M. A. Tolbert and A. M. Middlebrook, "FTIR Studies of Model Polar Stratospheric Cloud Surfaces: Growth and Evaporation of Ice and Nitric Acid/Ice," submitted to *J. Geophys. Res.*, May, 1990.

#### ABSTRACT

Heterogeneous reactions on the surfaces of polar stratospheric clouds (PSCs) over Antarctica are now recognized to play a central role in the photochemical mechanism responsible for the dramatic yearly occurrence of the Antarctic ozone 'hole' [Solomon, 1988]. PSCs are characterized as type I or type II depending on their composition. Type II PSCs, composed of water ice, form only at very low temperatures in the stratosphere. Type I PSCs are much more abundant and their composition and chemical properties have been the subject of intensive research. Field measurements [Fahey *et al.*, 1989], laboratory studies [Hanson and Mauersberger, 1988a,b] and model calculations [Turco *et al.*, 1989] have suggested that type I PSCs are nitric acid trihydrate (NAT) crystals (or solid solutions of nitric acid in ice) which form in the stratosphere at temperatures 5-7 °C higher than the ice frost point. Because they can form at warmer temperatures, type I PSCs may also form in the Arctic stratosphere where temperatures are rarely low enough to support pure ice formation. Heterogeneous reactions on NAT may therefore be relevant for considerations of Arctic as well as Antarctic ozone.

Several recent studies have shown that reactions 1-4 occur readily on laboratory ice surfaces representative of type II PSCs [Molina *et al.*, 1987; Tolbert *et al.*, 1987, 1988; Leu, 1988a,b]:



Reactions 1-3 convert the stable chlorine reservoir species ( $\text{ClONO}_2$  and  $\text{HCl}$ ) into more active forms ( $\text{HOCl}$ ,  $\text{Cl}_2$ ,  $\text{ClNO}_2$ ) which photolyze readily to provide  $\text{Cl}$  for catalytic ozone destruction cycles. All of the above heterogeneous reactions result in the formation of nitric acid. Laboratory studies on ice surfaces at  $-85^\circ\text{C}$  have shown that the nitric acid formed as a result of reactions 1-4 is retained in the condensed phase.

Removal of nitric acid from the stratosphere, so-called denitrification, is required for efficient ozone destruction. Denitrification prevents the sequestering of active chlorine via reaction 5:



Severe denitrification has been observed in both the Antarctic and Arctic stratospheres. There are numerous theories of how this observed denitrification occurs [Toon *et al.*, 1990]. All theories require that  $\text{HNO}_3$  be permanently removed via sedimentation of PSCs, but the theories differ in whether type I or type II PSCs are involved. For example, slow cooling may favor preferential growth of a relatively small number of NAT particles, which may then grow large enough to fall out of the stratosphere [Salawitch *et al.*, 1989]. Another denitrification mechanism [Wofsy *et al.*, 1990] suggests that falling ice from higher altitudes may sequester  $\text{HNO}_3$ , forming a layer of NAT on the ice. This NAT coating may prevent ice from evaporation even when the temperature is above the ice frost point. This scenario allows  $\text{HNO}_3$  to be permanently removed from certain regions of the stratosphere without requiring the formation of large pure NAT particles.

To better understand both the formation of PSCs and the role of PSCs in denitrification, fundamental investigations of the interactions between ice and nitric acid under stratospheric conditions are needed. We have used FTIR surface studies to probe the microphysical properties of NAT and ice films representative of type I and II PSCs, respectively. The infrared spectra of ice, NAT and nitric acid monohydrate (NAM) are obtained by dosing calibrated mixtures of water and nitric acid onto a low temperature support. The infrared spectra obtained for ice, NAT and

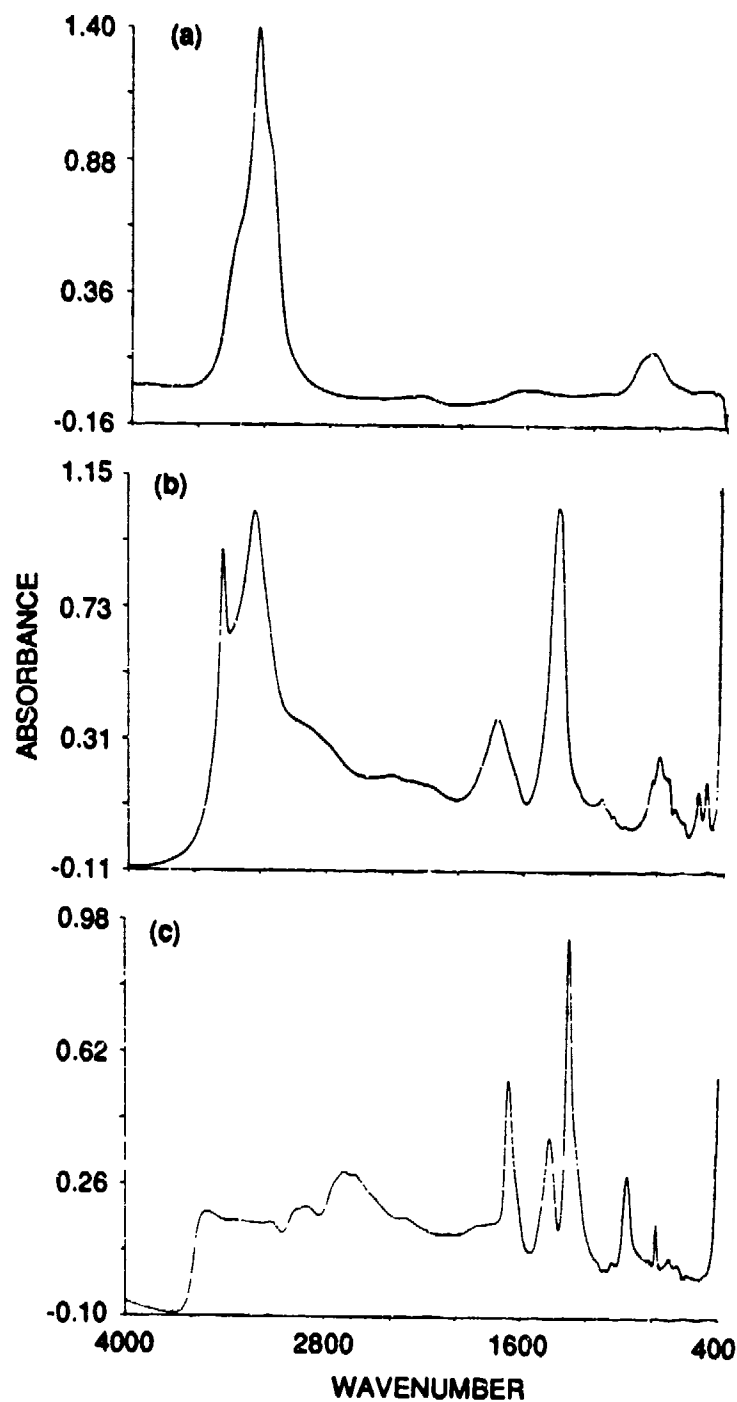
NAM at -90 °C are shown in Figure 1. These spectra are used to monitor growth, transformation, and evaporation of ice and NAT films under a variety of conditions.

Under conditions approaching those found in the stratosphere, NAT is observed to grow at temperatures around 5 °C higher than the ice frost point. The infrared spectra obtained while cooling the support from -60 °C to -90 °C in the presence of HNO<sub>3</sub> and excess H<sub>2</sub>O are shown in Figure 2. The spectra shown in parts a-d are separated by 87 second intervals, or approximately 3 °C intervals. The onset of film growth begins near -77 °C with a spectrum resembling that of NAT (part a). The characteristic NAT spectrum with a single peak for NO<sub>3</sub><sup>-</sup> at 1384 cm<sup>-1</sup> is clearly evident by -80 °C (part b), well before ice growth begins. As the temperature is reduced below -83 °C (part c), ice growth starts to occur and by -86 °C (part d), ice growth overwhelms NAT growth. This general observation of NAT growth before ice growth is in agreement with the conclusions drawn by *Hanson and Mauersberger* [1988a,b] from vapor pressure studies of ice and NAT solids.

Because NAT forms at warmer temperatures than ice under stratospheric conditions, heterogeneous reactions 1-4 may be important on NAT particles in the atmosphere. To compare the reactivity on type I vs. type II PSCs, we are performing laboratory studies of the reaction efficiencies on ice and nitric acid/ice surfaces. Recent work has focused on reaction 4 where measurements were made of the uptake efficiency for N<sub>2</sub>O<sub>5</sub> on model PSC surfaces. The uptake efficiency,  $\gamma$ , is defined by equation 6:

$$\gamma = \frac{\text{\# reactant molecules lost to surface (molec/cm}^2\text{s)}}{\text{\# gas-surface collisions (coll/cm}^2\text{s)}} \quad 6$$

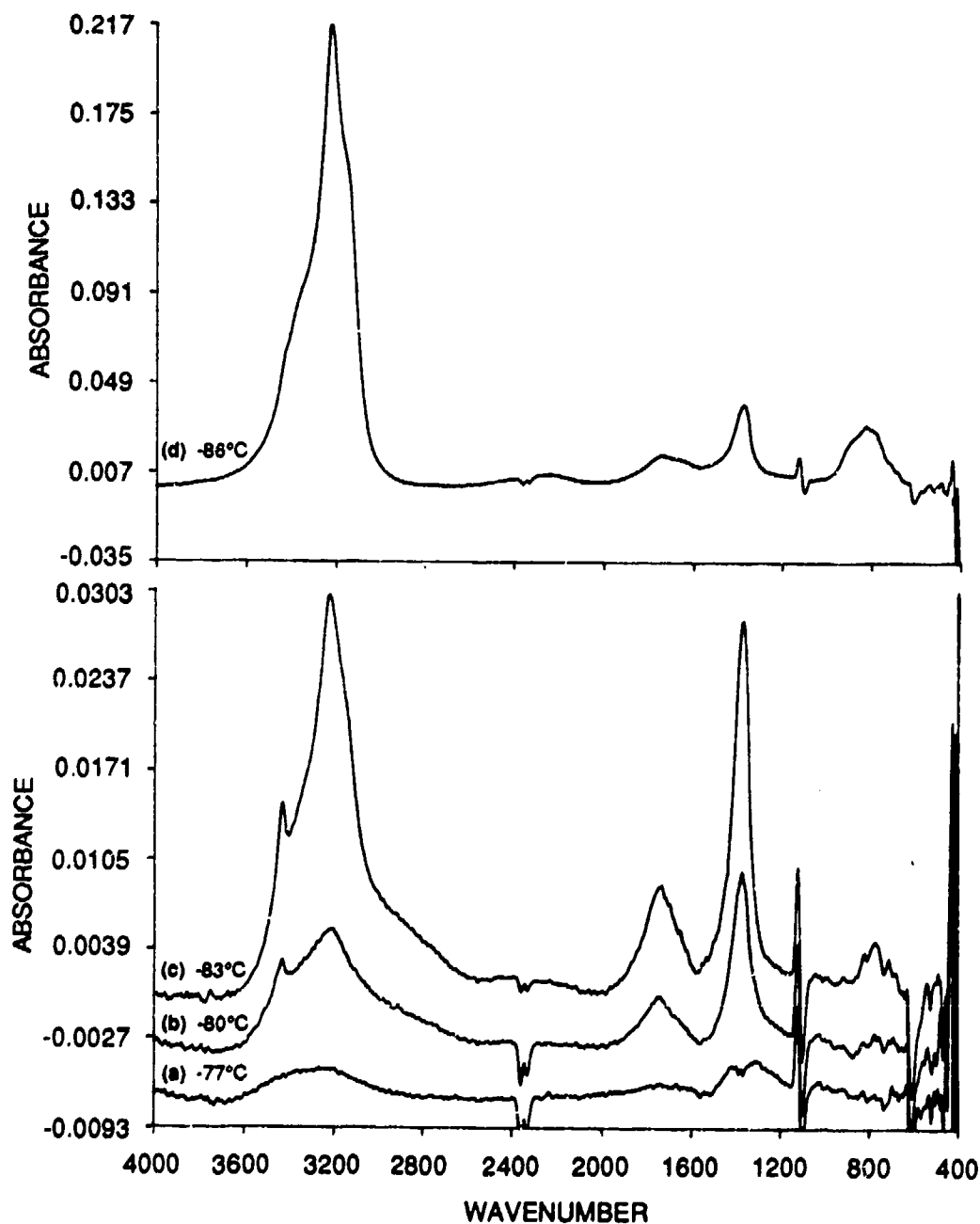
Laboratory measurements of the uptake efficiency for N<sub>2</sub>O<sub>5</sub> on ice and NAT surfaces are shown in Figure 3. Overall, N<sub>2</sub>O<sub>5</sub> appears to be somewhat less reactive on NAT than on ice. However, while  $\gamma$  for N<sub>2</sub>O<sub>5</sub> on NAT is constant in time,  $\gamma$  on ice varies considerably over the same time period. We interpret the slow rise in  $\gamma$  for N<sub>2</sub>O<sub>5</sub> on ice as being due to an acid-catalyzed surface reaction. The slow fall in  $\gamma$  at longer times is interpreted as being due to slow conversion of the top surface ice layers into layers of NAT due to the reaction. The complex reactivity observed for N<sub>2</sub>O<sub>5</sub> suggests that the details of surface structure and composition may be quite important in determining the overall reaction efficiencies for heterogeneous processes on PSCs. Future work will include FTIR studies of the condensed species during heterogeneous reactions to address the complex relationship between the structure and reactivity of PSC surfaces.



CA-320583-508

Figure 1. IR spectra of ice, NAT, and NAM.

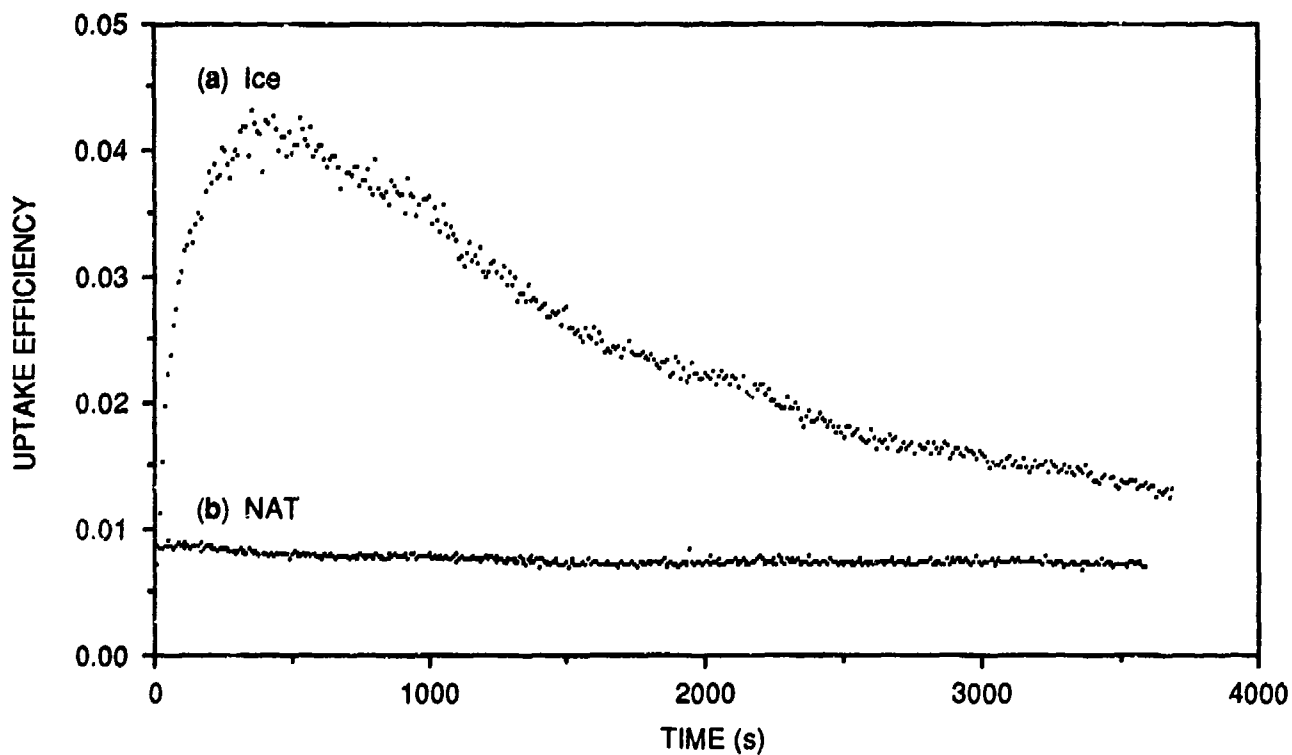
Infrared spectra obtained after calibrated flows of  $\text{H}_2\text{O}$  and  $\text{HNO}_3$  were dosed onto silicon at  $-90^\circ\text{C}$ . Calibrated flows of (a)  $\text{H}_2\text{O} = 9.3 \times 10^{16}$  molec/sec, (b)  $\text{H}_2\text{O} = 1 \times 10^{17}$  molec/sec,  $\text{HNO}_3 = 3 \times 10^{16}$  molec/sec and (c)  $\text{H}_2\text{O} = 4.6 \times 10^{16}$  molec/sec and  $\text{HNO}_3 = 5.0 \times 10^{16}$  molec/sec were used.



RA-6863-88

Figure 2. Film growth.

Infrared spectra obtained during film growth at a cooling rate of 2°C/minute as the temperature is ramped from -60 to -90°C. Partial pressures used are  $1.1 \times 10^{-5}$  torr  $H_2O$  and  $1.8 \times 10^{-6}$  torr  $HNO_3$ . Parts (a), (b), and (c) are all shown on the same absolute absorption scale, but shifted for clarity. Part (d) is shown on a much less sensitive absorption scale.



RAM-320522-191B

Figure 3. Uptake efficiency for  $N_2O_5$ .  
Comparison of the uptake efficiencies for  $N_2O_5$  on (a) bulk ice versus (b) bulk NAT at  $-85^\circ\text{C}$ .  
For both curves, water vapor was added to account for water removed from the surface due to pumping through the escape orifice.

## REFERENCES

- Fahey, D. W., K. K. Kelly, G. V. Ferry, L. R. Poole, J. C. Wilson, D. M. Murphy, M. Loewenstein, and K. R. Chan, In situ measurements of total reactive nitrogen, total water and aerosol in a polar stratospheric cloud in the Antarctic, *J. Geophys. Res.*, **94**, 11,299-11,315, 1989.
- Hanson, D. and K. Mauersberger, Vapor pressures of  $\text{HNO}_3/\text{H}_2\text{O}$  solutions at low temperatures, *J. Phys. Chem.*, **92**, 6167-6170, 1988a.
- Hanson, D. and K. Mauersberger, Laboratory studies of the nitric acid trihydrate: implications for the south polar stratosphere, *Geophys. Res. Lett.*, **15**, 855-858, 1988b.
- Leu, M.-T., Laboratory studies of sticking coefficients and heterogeneous reactions important in the Antarctic stratosphere, *Geophys. Res. Lett.*, **15**, 17-20, 1988a.
- Leu, M. -T., Heterogeneous reactions of  $\text{N}_2\text{O}_5$  with  $\text{H}_2\text{O}$  and  $\text{HCl}$  on ice surfaces: implications for Antarctic ozone depletion, *Geophys. Res. Lett.*, **15**, 851-854, 1988b.
- Molina, M. J., T.-L. Tso, L. T. Molina, and F. C.-Y. Wang, Antarctic stratospheric chemistry of chlorine nitrate, hydrogen chloride, and ice: release of active chlorine, *Science*, **238**, 1253-1257, 1987.
- Salawitch, R. J., G. P. Gobbi, S. C. Wofsy and M. B. McElroy, Denitrification in the Antarctic stratosphere, *Nature*, **339**, 525-527, 1989.
- Solomon, S., The mystery of the Antarctic ozone 'hole', *Rev. Geophys.*, **26**, 131-148, 1988.
- Tolbert, M. A., M. J. Rossi, R. Malhotra, and D. M. Golden, Reaction of chlorine nitrate with hydrogen chloride and water at Antarctic stratospheric temperatures, *Science*, **238**, 1258-1260, 1987.
- Tolbert, M. A., M. J. Rossi, and D. M. Golden, Antarctic ozone depletion chemistry: reactions of  $\text{N}_2\text{O}_5$  with  $\text{H}_2\text{O}$  and  $\text{HCl}$  on ice surfaces, *Science*, **240**, 1018-1021, 1988.
- Toon, O. B., R. P. Turco and P. Hamill, Denitrification mechanisms in the polar stratospheres, *Geophys. Res. Lett.*, **17**, 445-448, 1990.
- Turco, R. P., O. B. Toon and P. Hamill, Heterogeneous physicochemistry of the polar ozone hole, *J. Geophys. Res.*, **94**, 16,493-16,510, 1989.
- Wofsy, S. C., R. J. Salawitch, J. H. Yatteau, M. B. McElroy, B. W. Gandrud, J. E. Dye, and D. Baumgardner, Condensation of  $\text{HNO}_3$  on falling ice particles: mechanism for denitrification of the polar stratosphere, *Geophys. Res. Lett.*, **17**, 449-452, 1990.

BLANK



A THEORETICAL  
FORMULATION OF THE RESPONSE  
OF A DROPLET  
TO HIGH ENERGY RADIATION. A  
Hydrodynamic Theory  
of Droplet Radiative Heating and Explosion

D. K. Cohoon

Department of Mathematics

West Chester University

West Chester, PA 19383

August 2, 1990

In this paper we consider the problem of the detailed description of an exploding droplet. We consider equations describing the conservation of mass, momentum, and energy coupled by an equation of state. droplet

## 1 INTRODUCTION

We use this concept of a material derivative and fluxes of mass, momentum, kinetic energy, internal energy, temperature, and radiation to express the conservation of mass, momentum, and energy in a droplet irradiated by a high energy source. Initially there are more dependent variables than there are equations. However, these equations are coupled by an equation of state which enables one to develop a semigroup formulation which will predict pressure, density, velocity, and temperature distributions in the interior of the droplet.

The material derivative of a function  $f$  is defined by

$$\frac{Df}{Dt} = \frac{\partial f}{\partial t} + \frac{\partial f}{\partial x} \frac{\partial x}{\partial t} + \frac{\partial f}{\partial y} \frac{\partial y}{\partial t} + \frac{\partial f}{\partial z} \frac{\partial z}{\partial t} \quad (1.1)$$

Thus, the material derivative is, if we define,

$$\vec{v} = \frac{\partial x}{\partial t} \vec{e}_x + \frac{\partial y}{\partial t} \vec{e}_y + \frac{\partial z}{\partial t} \vec{e}_z \quad (1.2)$$

given by

$$\frac{D}{Dt} = \frac{\partial}{\partial t} + (\vec{v} \cdot \text{grad}) \quad (1.3)$$

where  $\vec{v}$  is the velocity of a point in the fluid.

We assume that the droplet material is bianisotropic, a material more general than a chiral material. The Maxwell equations are, for time harmonic radiation, given by

$$\text{curl}(\vec{E}) = -i\omega\bar{\mu}\vec{H} - \bar{\alpha}\vec{E} \quad (1.4)$$

and

$$\text{curl}(\vec{H}) = (i\omega\bar{\epsilon} + \bar{\sigma})\vec{E} + \bar{\beta}\vec{H} \quad (1.5)$$

The radiation source term which drives the droplet explosion is given by

$$\begin{aligned} \left( \frac{\partial}{\partial t} \right) Q_{in} = & \\ (1/2) Re \{ & \vec{E}^* \cdot (i\omega \vec{\epsilon} + \vec{\sigma}) \vec{E} + \vec{E} \cdot \vec{\alpha}^* \vec{H}^* - \\ & \vec{H} \cdot (i\omega \vec{\mu}^* \vec{H}^*) + \vec{H} \cdot (\vec{\beta}^* \vec{E}^*) + \\ & \chi_{\partial\Omega}(r) \sigma_s | \vec{E}_{tangential} |^2 \} \end{aligned} \quad (1.6)$$

where if  $\partial\Omega$  is the surface containing the impedance sheet, then

$$\int_{\Omega} \chi_{\partial\Omega} \sigma_s | \vec{E}_{tangential} |^2 dv = \int_{\partial\Omega} \sigma_s | \vec{E}_{tangential} |^2 dA \quad (1.7)$$

is the characteristic function of the surface supporting the impedance sheet. We consider non plane wave sources such as tightly focused laser beams interacting with droplets ([13], [45], [14], [33], [7], [6]) and use the energy densities to as a source term in the energy equation to determine the future state of the droplet.

## 2 Continuity Equation

Assuming that in the droplet interior that the rate at which mass is created or destroyed is given by  $Q_M$  and that the flux of mass across a surface is given by  $\rho \vec{v}$  we see that

$$\frac{\partial \rho}{\partial t} + \text{div}(\rho \vec{v}) = Q_M \quad (2.1)$$

or if  $Q_M = 0$  that

$$\text{div}(\rho \vec{v}) = -\frac{\partial \rho}{\partial t} \quad (2.2)$$

## 3 Momentum Equation

In this section we derive the conservation of momentum by equating the rate of change of momentum to the work done by the fluid pressure and the viscous forces and the body forces and the flux of momentum across the boundaries of test volumes. We define the velocity as

$$\vec{v} = u \vec{e}_x + v \vec{e}_y + w \vec{e}_z \quad (3.1)$$

An important identity involving the dyadic product of two vectors  $\vec{A}$  and  $\vec{B}$  is

$$\text{div}(\vec{A}\vec{B}) = \text{div}(\vec{A})\vec{B} + (\vec{A} \cdot \text{grad})\vec{B} \quad (3.2)$$

The momentum flux is the dyad  $\rho\vec{v}\vec{v}$  and using the concept of conservation of mass or equation (2.2) and equation (3.2) we see that

$$\begin{aligned} \text{div}(\rho\vec{v}\vec{v}) &= \text{div}(\rho\vec{v}) + \rho(\vec{v} \cdot \text{grad})\vec{v} \\ &= -\frac{\partial \rho}{\partial t}\vec{v} + \rho(\vec{v} \cdot \text{grad})\vec{v} \end{aligned} \quad (3.3)$$

If  $p$  is the pressure, then the total stress tensor  $\Pi$  is given by

$$\bar{\Pi} = -p(\vec{e}_x\vec{e}_x + \vec{e}_y\vec{e}_y + \vec{e}_z\vec{e}_z) + \bar{\tau} \quad (3.4)$$

The viscous stress tensor is given, using equation (3.1) for velocity, by the rule,

$$\begin{aligned}
\bar{\tau} = & \mu \left( 2 \frac{\partial u}{\partial x} \right) \bar{e}_x \bar{e}_x + \mu \left( \frac{\partial v}{\partial x} + \frac{\partial u}{\partial y} \right) \bar{e}_y \bar{e}_x + \\
& \mu \left( \frac{\partial w}{\partial x} + \frac{\partial u}{\partial z} \right) \bar{e}_z \bar{e}_x + \mu \left( \frac{\partial u}{\partial y} + \frac{\partial v}{\partial x} \right) \bar{e}_x \bar{e}_y + \\
& + \mu \left( 2 \frac{\partial v}{\partial y} \right) \bar{e}_y \bar{e}_y + \mu \left( \frac{\partial w}{\partial y} + \frac{\partial v}{\partial z} \right) \bar{e}_z \bar{e}_y + \\
& \mu \left( \frac{\partial u}{\partial z} + \frac{\partial w}{\partial x} \right) \bar{e}_x \bar{e}_z + \mu \left( \frac{\partial v}{\partial z} + \frac{\partial w}{\partial y} \right) \bar{e}_y \bar{e}_z + \\
& + \mu \left( 2 \frac{\partial w}{\partial z} \right) \bar{e}_z \bar{e}_z - \frac{2}{3} \mu \left( \frac{\partial u}{\partial x} + \frac{\partial v}{\partial y} + \frac{\partial w}{\partial z} \right) \bar{e}_x \bar{e}_x \\
& - \frac{2}{3} \mu \left( \frac{\partial u}{\partial x} + \frac{\partial v}{\partial y} + \frac{\partial w}{\partial z} \right) \bar{e}_y \bar{e}_y \\
& - \frac{2}{3} \mu \left( \frac{\partial u}{\partial x} + \frac{\partial v}{\partial y} + \frac{\partial w}{\partial z} \right) \bar{e}_z \bar{e}_z
\end{aligned} \tag{3.5}$$

We have seen that the total stress tensor, equation (3.4) is given in terms of the pressure  $p$  and the viscous stress (3.5). The momentum equation is given by

$$\begin{aligned}
\frac{\partial}{\partial t}(\rho \vec{v}) &= -\text{div}(\rho \vec{v} \vec{v}) \\
\rho \vec{f} + \text{div}(\bar{\Pi}) &
\end{aligned} \tag{3.6}$$

Using equation (3.3) we see that equation (3.6) and equations (3.4) and (3.5) we see that

$$\begin{aligned}
\rho \frac{\partial \vec{v}}{\partial t} + \rho(\vec{v} \cdot \text{grad}(\vec{v})) &= \\
\rho \vec{f} - \text{grad}(p) + \text{div}(\bar{\tau}) &
\end{aligned} \tag{3.7}$$

Using the concept of material derivative, equation (1.1) and assuming that  $\vec{f}$  is the zero vector, equation (3.7) reduces to

$$\frac{D\vec{v}}{Dt} = -\frac{1}{\rho} \text{grad}(p) + \frac{1}{\rho} \text{div}(\bar{\tau}) \tag{3.8}$$

## 4 Energy Equation

There is internal energy, kinetic energy, work done by the viscous forces (equation 3.5), pressure, and work done by the external body forces. The energy is transferred from one region of the heated droplet to another by thermal conduction, kinetic energy flux, and radiation conduction processes, and by the external radiative power source. Using equation (3.5) we define the viscous dissipation function  $\Phi$  by the rule,

$$\begin{aligned} \Phi = \mu \left[ 2 \left\{ \left( \frac{\partial u}{\partial x} \right)^2 + \left( \frac{\partial v}{\partial y} \right)^2 + \left( \frac{\partial w}{\partial z} \right)^2 \right\} + \right. \\ \left. \left( \frac{\partial v}{\partial x} + \frac{\partial u}{\partial y} \right)^2 + \left( \frac{\partial w}{\partial y} + \frac{\partial v}{\partial z} \right)^2 \right. \\ \left. \left( \frac{\partial u}{\partial z} + \frac{\partial w}{\partial x} \right)^2 - \frac{2}{3} \left( \frac{\partial u}{\partial x} + \frac{\partial v}{\partial y} + \frac{\partial w}{\partial z} \right)^2 \right] \end{aligned} \quad (4.1)$$

In these terms the energy equation is given by (Anderson, Tannehill, and Pletcher [1], pages 188-189).

$$\begin{aligned} \frac{\partial}{\partial t} \left\{ \rho e + \frac{\rho \vec{v} \cdot \vec{v}}{2} \right\} = \\ -div(\rho e \vec{v}) + \vec{f} \cdot \vec{v} + \\ div(\vec{\Pi} \cdot \vec{v}) - div\left(\left(\frac{\rho \vec{v} \cdot \vec{v}}{2}\right) \vec{v}\right) + \\ div(\vec{K} grad(T)) + \left(\frac{\partial}{\partial t}\right) Q_{in} + \left(\frac{\partial}{\partial t}\right) Q_{out} \end{aligned} \quad (4.2)$$

We define the enthalpy  $h$  as (see Anderson [1], p 188)

$$h = e + \frac{p}{\rho} \quad (4.3)$$

where

- $e$  = the internal energy including quantum states,
- $p$  = the pressure, and
- $\rho$  = the density.

To telescope the terms in the energy equation we make use of the vector identity

$$\begin{aligned} \text{grad}(\vec{A} \cdot \vec{B}) &= \vec{A} \times \text{curl}(\vec{B}) + \vec{B} \times \text{curl}(\vec{A}) + \\ &(\vec{B} \cdot \text{grad})\vec{A} + (\vec{A} \cdot \text{grad})\vec{B} \end{aligned} \quad (4.4)$$

to observe that

$$\begin{aligned} \rho \vec{v} \cdot \text{grad} \left( \frac{\vec{v} \cdot \vec{v}}{2} \right) &= \\ \rho \vec{v} \cdot \{ \vec{v} \times \text{curl}(\vec{v}) + \vec{v} \cdot \text{grad}(\vec{v}) \} \end{aligned} \quad (4.5)$$

Interchanging the dot and cross product in equation (4.5) we see that since for an arbitrary vector field  $\vec{v}$

$$\vec{v} \cdot (\vec{v} \times \text{curl}(\vec{v})) = (\vec{v} \times \vec{v}) \cdot \text{curl}(\vec{v}) = \vec{0} \quad (4.6)$$

it follows that

$$\rho \vec{v} \cdot \text{grad} \left( \frac{\vec{v} \cdot \vec{v}}{2} \right) = \rho \vec{v} \cdot \{ (\vec{v} \cdot \text{grad})(\vec{v}) \} \quad (4.7)$$

We can then collapse terms in equation (4.2) by observing that the momentum equation implies that

$$\begin{aligned} \vec{v} \cdot \rho (\vec{v} \cdot \text{grad})\vec{v} &= \\ -\rho \frac{\partial \vec{v}}{\partial t} \cdot \vec{v} \\ + \rho \vec{f} - \text{grad}(p) \cdot \vec{v} + \text{div}(\vec{\tau}) \cdot \vec{v} \end{aligned} \quad (4.8)$$

Thus, using equation (1.1) and equations (4.7) and (4.8) the energy equation (4.2) may be rewritten in the form,

$$\begin{aligned} \rho \frac{Dh}{Dt} &= \frac{Dp}{Dt} + \\ \left( \frac{\partial}{\partial t} \right) Q_{in} &+ \left( \frac{\partial}{\partial t} \right) Q_{out} + \\ \Phi &+ \text{div}(\vec{K} \text{grad}(T)) \end{aligned} \quad (4.9)$$

where  $(\partial/\partial t) Q_{in}$  is given by equation (1.6) and  $\Phi$  is the dissipation function representing the work done by the viscous forces of the fluid. The term representing the transfer by radiation from one part of the fluid to another is given by (Siegel and Howell [48], page 689)

$$\left( \frac{\partial}{\partial t} \right) Q_{out} = \text{div} \left( \frac{16\sigma T^3}{3a_R} \cdot \text{grad}(T) \right) \quad (4.10)$$

This equation may be interpreted as providing a radiation flux across a surface defined by

$$k_r = \frac{16\sigma T^3}{3a_R}, \quad (4.11)$$

where  $a_R$  is the Rosseland mean absorption coefficient (Siegel [48], p 504 and Rosseland) and where  $\sigma$  (Siegel [48], page 25) is the hemispherical total emissive power of a black surface into vacuum having a value of

$$\sigma = 5.6696 \times 10^{-8} \text{ Watts / (meters}^2 \text{ }^\circ K) \quad (4.12)$$

Using equation (4.10) and equation (4.2) we see that

$$\begin{aligned} \rho \frac{De}{Dt} = & \left( \frac{\partial}{\partial t} \right) Q_{in} + \left( \frac{\partial}{\partial t} \right) Q_{out} + \\ & (-p \operatorname{div}(\vec{v})) + \operatorname{div}(\bar{K} \operatorname{grad}(T)) + \Phi \end{aligned} \quad (4.13)$$

where  $\Phi$  is the viscous dissipation function given by equation (4.1)

## 5 EQUATION OF STATE

In the energy equation (4.13) the perfect fluid assumption ([1], p 189) would yield

$$e = c_v T, \quad (5.1)$$

where  $c_v$  is the specific heat at constant volume, and if we define

$$\gamma = \frac{c_p}{c_v} \quad (5.2)$$

where  $c_p$  is the specific heat at constant pressure, then the pressure  $p$ , the internal energy  $e$  and the density  $\rho$  are related by ([1], p 189)

$$p = (\gamma - 1)\rho e \quad (5.3)$$



## 6 SUMMARY

Using the definition of velocity (equation 3.1) and the equation of state (5.3) we see that the number of equations is 5, allowing 3 equations for the three components of the momentum, and while the initial variables are  $\rho$ ,  $u$ ,  $v$ ,  $w$ ,  $p$ ,  $e$ , and  $T$ , we see that since the temperature  $T$  is related to  $e$  and since pressure is a function of  $\rho$  and  $e$ , we see that there are now exactly 5 unknowns. This means that locally within the droplet we can describe the future state of the droplet as a semigroup (Temam [51], p 16) acting on the conditions at time  $t_0$ . If we want to know the value at time  $t$  and  $S$  is defined so that the solution at time  $t$  is given by  $S(t - t_0)$  acting on the values at  $t = t_0$  of the density  $\rho$ , the velocity components  $u$ ,  $v$ , and  $w$ , and the temperature  $T$ . The semigroup relation,

$$\begin{pmatrix} \rho(t) \\ u(t) \\ v(t) \\ w(t) \\ T(t) \end{pmatrix} = S(t - t_0) \begin{pmatrix} \rho(t_0) \\ u(t_0) \\ v(t_0) \\ w(t_0) \\ T(t_0) \end{pmatrix} \quad (6.1)$$

tells us how to get future values of the density  $\rho$ , the three velocity components, and the temperature at time  $t$  when the values at time  $t_0$  are known.

## References

- [1] Anderson, Dale A. *Computational Fluid Mechanics and Heat Transfer* New York: McGraw Hill (1984).
- [2] Armstrong, Robert L. and Andrew Zardecki. "Propagation of High Energy Laser Beams Through Metallic Aerosols" *Applied Optics. Volume 29, Number 12* (April 20, 1990) pp 1786-1792
- [3] *Explosions in Air* Austin, Texas: University of Texas Press (1973)

- [4] Barton, J. P., D. R. Alexander, and S. A. Schaub. "Internal fields of a spherical particle illuminated by a tightly focused laser beam: focal point positioning effects at resonance." *Journal of Applied Physics*. Volume 65 No. 8 (April 15, 1989) pp 2900-2906
- [5] Barton, J. P., D. R. Alexander, and S. A. Schaub. "Internal and near surface electromagnetic fields for a spherical particle irradiated by a focused laser beam" *Journal of Applied Physics*. Volume 64, no 4 (1988) pp 1632-1639.
- [6] Barton, J. P., D. R. Alexander, and S. A. Schaub. "Internal fields of a spherical particle illuminated by a tightly focused laser beam: focal point positioning effects at resonance." *Journal of Applied Physics*. Volume 65 No. 8 (April 15, 1989) pp 2900-2906
- [7] Barton, J. P., D. R. Alexander, and S. A. Schaub. "Internal and near surface electromagnetic fields for a spherical particle irradiated by a focused laser beam" *Journal of Applied Physics*. Volume 64, no 4 (1988) pp 1632-1639.
- [8] Belts, V. A., O. A. Volkovitsky, A. F. Dobrovolsky, E. V. Ivanov, Y. V. Nasedkin, L. N. Pavlova. "Intensive  $CO_2$  laser pulse transmission through droplet and ice crystal fogs" *IN Kaye, A. S. and A. C. Walker. Gas flow and chemical lasers. 1984. Proceedings of the Fifth International Symposium Oxford, England: Gas Flow and Chemical Laser Symposium (August, 1984) pp 20-24*
- [9] Benedict, Robert P. *Gas Dynamics* New York: John Wiley (1963)
- [10] Birkhoff, Garrett. *Hydrodynamics. A Study in Logic Fact, and Similitude* New York: Dover (1950)
- [11] Biswas, A., H. Latifi, R. L. Armstrong, and R. G. Pinnick. "Time resolved spectroscopy of laser emission from dye doped droplets" *Optics Letters*. Volume 14, No. 4 (February 15, 1989) pp 214-216
- [12] Bloembergen, N. *Nonlinear Optics* New York: W. A. Benjamin (1965)

- [13] Caledonia, G. E. and J. D. Teare. "Laser beam hygroscopic aerosol interactions" *Transactions of the ASME Journal of Heat Transfer. Vol 99* (May, 1977) pp 281-286.
- [14] Carls, J. C. and J. R. Brock. "Explosive vaporization of single droplets by lasers: comparison of models with experiments." *Optics Letters. Volume 13, No. 10* (October, 1988) pp 919-921
- [15] Chang, Randolph and E. James Davis. "Knudsen Aerosol Evaporation" *Journal of Colloid and Interface Science. Volume 54, No. 3* (March, 1976) pp 352-363.
- [16] Chow, S. N., J. Mallet-Paret, and J. A. Yorke. Finding zeros of maps: homotopy methods that are constructive with probability one. *Math. Comp. Volume 32* (1978) pp 887-889.
- [17] Chevaillier, Jean Phillipe, Jean Fabre, and Patrice Hamelin. "Forward scattered light intensities by a sphere located anywhere in a Gaussian beam" *Applied Optics, Vol. 25, No. 7* (April 1, 1986) pp 1222-1225.
- [18] Chevaillier, Jean Phillippe, Jean Fabre, Gerard Grehan, and Gerard Gousbet. "Comparison of diffraction theory and generalized Lorenz-Mie theory for a sphere located on the axis of a laser beam." *Applied Optics, Vol 29, No. 9* (March 20, 1990) pp 1293-1298.
- [19] Chylek, Petr, Maurice A. Jarzembski, Vandana Srivastava, and Ronald G. Pinnick. "Pressure Dependence of the Laser Induced Breakdown Thresholds of Gases and Droplets" *Applied Optics Volume 29, Number 15* (May 20, 1990) pp 2303-2306
- [20] Cross, L. A. "High repitition rate, high resolution back lit, shadow, and schlieren photography of gaseous and liquid mass transport phenomena and flames" *International Congress on Instrumentation in Aerospace Simulation Facilities Dayton Ohio 1981* Dayton, Ohio: ICIASF 1981 Record (September 30, 1981)
- [21] Davis, E. James and Asit K. Ray. "Determination of diffusion coefficients by submicron droplet evaporation"

- [22] Eringen, A. Cemal, and S. Suhubi S. Erdogan. *Elastodynamics. Volume I. Finite Motions* New York: Academic Press (1974)
- [23] Eringen, A. Cemal, and S. Suhubi S. Erdogan. *Elastodynamics. Volume II. Linear Theory* New York: Academic Press (1975)
- [24] Eyring, Henry, and Mu Shik Jhon. *Significant Liquid Structures* New York: John Wiley and Sons (1969)
- [25] Fisher, I. Z. *Statistical Theory of Liquids* Chicago: The University of Chicago Press(1961)
- [26] Garcia, C. B. and W. I. Zangwill. *Pathways to Solutions, Fixed Points, and Equilibria.* Englewood Cliffs, NJ: Prentice Hall(1981)
- [27] Glickler, S. L. "Propagation of a 10.6  $\mu$  laser through a cloud including droplet vaporization" *Applied Optics, Volume 10, No. 3* (March, 1971) pp 644-650
- [28] Hochstadt, Harry. *The Functions of Mathematical Physics.* New York: Dover(1986).
- [29] Hörmander, Lars. *Linear Partial Differential Operators* New York: Academic Press (1963)
- [30] Hsu, Yih-Yun, and Robert W. Graham. *Transport Processes in Boiling and Two Phase Systems* New York: McGraw Hill(1976)
- [31] Incropera, Frank P. and David P. Dewitt. *Fundamentals of Heat Transfer* New York: John Wiley and Sons (1981)
- [32] Kogelnik, H. and T. Li. "Laser beams and resonators" *Applied Optics. Volume 5, Number 10* (October, 1966) pp 1550-1566
- [33] Kozaki, Shogo. "Scattering of a Gaussian Beam by a Homogeneous Dielectric Cylinder" *Journal of Applied Physics. Volume 53. No. 11* (November, 1982) pp 7195-7200

- [34] Liou, K. N., S. C. Ou Takano, A. Heymsfield, and W. Kreiss. "Infrared transmission through cirrus clouds: a radiative model for target detection" *Applied Optics. Volume 29, Number 13* (May 1, 1990) pp 1886-1896
- [35] Luikov, A. V. and Yu A. Mikhailov. *Theory of Energy and Mass Transfer* New York: Pergamon Press (1965)
- [36] Mackowski, D. W., R. A. Altenkirch, and M. P. Menguc. "Internal absorption cross sections in a stratified sphere" *Applied Optics, Volume 29, Number 10* (April 1, 1990) pp 1551-1559
- [37] Majda, Andrew. *The Stability of Multi Dimensional Shock Fronts* Providence, Rhode Island: Memoires of the AMS. Volume 41, Number 275 (January, 1983)
- [38] Monson, B., Vyas Reeta, and R. Gupta. "Pulsed and CW Photothermal Phase Shift Spectroscopy in a Fluid Medium: Theory" *Applied Optics. Volume 28, No. 13* (July, 1989) pp 2554-2561.
- [39] Mugnai, Alberto and Warren J. Wiscombe. "Scattering from nonspherical Chebyshev Particles. I. Cross Sections, Single Scattering Albedo, Asymmetry factor, and backscattered fraction" *Applied Optics, Volume 25, Number 7* (April 1, 1986) pp 1235-1244.
- [40] Park, Bae-Sig, A. Biswas, and R. L. Armstrong. "Delay of explosive vaporization in pulsed laser heated droplets" *Optics Letters. Volume 15, No. 4* (February 15, 1990) pp 206-208
- [41] Pinnick, R. G., Abhijit Biswas, Robert L. Armstrong, S. Gerard Jennings, J. David Pendleton, and Gilbert Fernandez. "Micron size droplets irradiated with a pulsed CO<sub>2</sub> laser: Measurement of Explosion and Breakdown Thresholds" *Applied Optics. Volume 29, No. 7* (March 1, 1990) pp 918-925
- [42] Pinnick, R. G., S. G. Jennings, Petr Chylek, Chris Ham, and W. T. Grandy. "Backscatter and Extinction in Water Clouds" *Journal of Geophysical Research. Vol 88, No. C11* (August 20, 1983) pp 6787-6796

- [43] Richardson, C. B., R. L. Hightower, and A. L. Pigg. "Optical measurement of the evaporation of sulfuric acid droplets" *Applied Optics*. Volume 25, Number 7 (April 1, 1986) pp 1226-1229
- [44] Rosseland, S. *Theoretical Astrophysics: Atomic Theory and the Analysis of Stellar Atmospheres and Envelopes* Oxford, England: Clarendon Press (1936)
- [45] Schaub, S. A., D. R. Alexander, J. P. Barton, and M. A. Emanuel. "Focused laser beam interactions with methanol droplets: effects of relative beam diameter" *Applied Optics*. Volume 28, No. 9 (May 1, 1989) pp 1666-1669
- [46] Schiffer, Ralf. "Perturbation approach for light scattering by an ensemble of irregular particles of arbitrary material" *Applied Optics*, Volume 29, Number 10 (April 1, 1990) pp 1536-1550
- [47] Siegel, R. "Radiative Cooling Performance of a Converging Liquid Drop Radiator." *Journal of Thermophysics and Heat Transfer*. Volume 3, Number 1 (January, 1989) pp 46-52.
- [48] Siegel, Robert, and John R. Howell. *Thermal Radiation Heat Transfer* New York: Hemisphere Publishing Company (1981)
- [49] Smoller, Joel. *Shock waves and reaction diffusion equations* New York: Springer Verlag (1983)
- [50] Svetlyurov, D. E. "State of transfer of radiant energy accompanied by evaporation of a disperse medium" *Soviet J. Quantum Electronics* Volume 3, No. 1 (July August, 1973) pp 33-36
- [51] Temam, Roger. *Infinite Dimensional Dynamical Systems in Mechanics and Physics*. *Applied Mathematical Sciences* 68 New York: Springer Verlag (1988).
- [52] Tsai, Wen Chung and Ronald J. Pogorzelski. "Eigenfunction solution of the scattering of beam radiation fields by spherical objects" *Journal of the Optical Society of America*. Volume 65. Number 12 (December, 1975) pp 1457-1463.

- [53] Trefil, J. S. *Introduction to the Physics of Fluids and Solids* New York: Pergamon Press, Inc. (1975)
- [54] Tzeng, H. M., K. F. Wall, M. B. Long, and R. K. Chang. "Laser emission from individual droplets at wavelengths corresponding to morphology dependent resonances" *Optics Letters. Volume 9, Number 11* (1984) pp 499-501
- [55] Volkovitsky, O. A. "Peculiarities of light scattering by droplet aerosol in a divergent  $CO_2$  laser beam" *Applied Optics. Volume 26, Number 24* (December 15, 1987) pp 5307-5310
- [56] von Mises, Richard, Hilda Geiringer, and G. S. S. Ludford. *Mathematical Theory of Compressible Fluid Flow* New York: Academic Press (1958)
- [57] Wasow, Wolfgang. *Asymptotic Expansions for Ordinary Differential Equations* New York: John Wiley (1965)
- [58] Whittaker, E. T. and G. N. Watson. *A Course of Modern Analysis* London: Cambridge University Press (1986).
- [59] Zardecki, A. and J. David Pendleton. "Hydrodynamics of water droplets irradiated by a pulsed  $CO_2$  laser." *Applied Optics. Volume 28, No. 3* (February 1, 1989) pp 638-640
- [60] Zel'dovich, Ya B. and Yu P. Raizer. *Physics of Shock Waves and High Temperature Thermodynamic Phenomena* New York: Academic Press (1966)

BLANK



## **LASER INTERACTION WITH A METALLIC FILAMENT: ABLATION DYNAMICS AND PLASMA FORMATION**

D.R. Alexander, G. M. Holtmeier, Kyo-Dong Song, and J. P. Barton

Center for Electro-Optics

College of Engineering

University of Nebraska

Lincoln, NE 68588-0656

### **RECENT PUBLICATIONS, SUBMITTALS FOR PUBLICATION, AND PRESENTATIONS:**

A.) J.P. Barton, D.R. Alexander, and S.A. Schaub, "Electromagnetic field calculations for a tightly-focused laser beam incident upon a spherical particle," Proceedings of the 1989 U.S. Army CRDEC Scientific Conference on Obscuration and Aerosol Research, Aberdeen, Maryland, 1989.

B.) D.R. Alexander, J.P. Barton, and S.A. Schaub, "Laser induced breakdown of H<sub>2</sub>O droplets and solid wires at 0.248  $\mu\text{m}$ ," Proceedings of the 1989 U.S. Army CRDEC Scientific Conference on Obscuration and Aerosol Research, Aberdeen, Maryland, 1989.

C.) J.P. Barton, D.R. Alexander, and S.A. Schaub, "Theoretical determination of net radiation force and torque for a spherical particle illuminated by a focused laser beam," Journal of Applied Physics, Vol. 66, pp. 4594-4602, 1989.

D.) J.P. Barton and D.R. Alexander, "Fifth-order corrected electromagnetic field components for a fundamental Gaussian beam," Journal of Applied Physics, Vol. 66, pp. 2800-2802, 1989.

E.) J.P. Barton, D.R. Alexander, and S.A. Schaub, "Internal fields of a spherical particle illuminated by a tightly-focused laser beam: focal point positioning effects at resonance," Journal of Applied Physics, Vol. 65, pp. 2900-2906, 1989.

F.) J.P. Barton, W. Ma, S.A. Schaub, and D.R. Alexander, "Theoretical determination of the electromagnetic fields for a laser beam incident upon two adjacent spherical particles of arbitrary arrangement," Proceedings of the 2nd International Congress on Optical Particle Sizing, Tempe, Arizona, 1990.

G.) J.P. Barton, W. Ma, S.A. Schaub, and D.R. Alexander, "Electromagnetic fields for a beam incident upon two adjacent spherical particles," submitted to Applied Optics, May, 1990.

H.) J.P. Barton and D.R. Alexander, "Electromagnetic fields for an irregularly-shaped, near-spherical particle illuminated by a focused laser beam," submitted to the Journal of Applied Physics, August, 1990.

I.) D.R. Alexander, S.A. Schaub, J. Zhang, D.E. Poulain, and J.P. Barton, "Scattering of incident KrF laser radiation resulting from the laser induced breakdown of H<sub>2</sub>O droplets," Optics Letters, Vol. 14, pp. 548-550, 1989.

J.) D.R. Alexander, J.P. Barton, S.A. Schaub, and G.M. Holtmeier, "Nonlinear interactions of KrF laser radiation with small water droplets," submitted to Applied Optics, October, 1989.

K.) S.A. Schaub, D.R. Alexander, D.E. Poulain, and J.P. Barton, "Measurement of hypersonic velocities resulting from the laser induced breakdown of aerosols using an excimer laser imaging system," Review of Scientific Instruments, Vol. 60, pp. 3688-3691, 1989.

L.) S.A. Schaub, J.P. Barton, and D.R. Alexander, "Simplified scattering coefficient expressions for a spherical particle located on the propagation axis of a fifth-order Gaussian beam," Applied Physics Vol. 55, pp. 2709-2711, 1989.

- M.) D.E. Poulain, D.R. Alexander, J.P. Barton, S.A. Schaub, and J. Zhang, "Interactions of intense ultraviolet laser radiation with solid aerosols," *Journal of Applied Physics*, Vol. 67, 1990.
- N.) S.A. Schaub, D.R. Alexander, and J.P. Barton, "Theoretical model for the image formed by a spherical particle in a coherent imaging system: comparison to experiment," *Optical Engineering*, Vol. 28, pp. 565-571, 1989.
- O.) S.A. Schaub, D.R. Alexander, J.P. Barton, and M.A. Emanuel, "Focused laser beam interactions with methanol droplets: effects of relative beam diameter," *Applied Optics*, Vol. 28, pp. 1666-1669, 1989.
- P.) G.M. Holtmeier, D.R. Alexander, and J.P. Barton, "High intensity ultraviolet laser interaction with a metallic filament," submitted to the *Journal of Applied Physics*, August, 1990.
- Q.) S.A. Schaub, D.R. Alexander, and J.P. Barton, "Theoretical model of the laser imaging of small aerosols: applications to aerosol sizing," submitted to *Applied Optics*, May, 1990.
- R.) S.A. Schaub, D.R. Alexander, and J.P. Barton, "Modeling of a coherent imaging system," *Proceedings of the 2nd International Congress on Optical Particle Sizing*, Tempe, Arizona, 1990.
- S.) J.P. Barton, D.R. Alexander, and S.A. Schaub, "Electromagnetic field calculations for a tightly-focused laser beam incident upon a spherical particle," presentation at the 1989 U.S. Army CRDEC Scientific Conference on Obscuration and Aerosol Research, Aberdeen, Maryland, June 27-30, 1989.
- T.) D.R. Alexander, J.P. Barton, and S.A. Schaub, "Laser induced breakdown of H<sub>2</sub>O droplets and solid wires," presentation at the 1989 U.S. Army CRDEC Scientific Conference on Obscuration and Aerosol Research, Aberdeen, Maryland, June 27-30, 1989.
- U.) J.P. Barton, W. Ma, S.A. Schaub, and D.R. Alexander, "Theoretical determination of the electromagnetic fields for a laser beam incident upon two adjacent spherical particles of arbitrary arrangement," presentation at the 2nd International Congress on Optical Particle Sizing, Tempe, Arizona, March 5-8, 1990.
- V.) D.R. Alexander, S.A. Schaub, and J.P. Barton, "Modeling of a coherent imaging system: Application to focus determination in aerosol sizing," presentation at the 2nd International Congress on Optical Particle Sizing, Tempe, Arizona, March 5-8, 1990.

## ABSTRACT

Experimental results are presented on the time dependent material ejection dynamics associated with focused excimer laser beams interacting with a small diameter wire. Copper wire 75  $\mu\text{m}$  in diameter was illuminated with a KrF excimer laser at an irradiance of 80 GW/cm<sup>2</sup>. Interaction dynamics were recorded using both real time and double strobed ultraviolet laser imaging techniques. Temporal evolutions of both vaporous and molten material are reported for the laser beam/wire interactions. Material observed during 2-D shadow imaging on the shadow side of the wire was shown to originate from the illuminated surface without spallation of material on the shadow surface. Material emission velocities are reported utilizing two different imaging techniques. A maximum velocity of 1500 m/s was obtained for material ejected in a direction toward the illuminating laser. The elastically scattered incident radiation (ESIR) for both solid copper wires and H<sub>2</sub>O drops show a distinct two-peak structure which is dependent on the incident energy. Broad band plasma emission for copper starts at  $6.5 \pm 1.4$  ns after the pulse arrival as compared to  $11 \pm 0.36$  ns for water drops. Future work will include the use of a femtosecond laser to investigate laser interactions at higher irradiances (200 GW/cm<sup>2</sup>) and associated nonlinear behavior.

## I. INTRODUCTION

Excimer laser interaction with metals has been widely investigated utilizing generally flat targets with beam intensities near the optical breakdown thresholds<sup>1-4</sup> and at intensities above the breakdown thresholds.<sup>5,6</sup> Limited work appears in the literature on the interaction of a high intensity laser beam with metallic aerosols or small filaments. Armstrong *et al.*<sup>7</sup> performed a theoretical investigation of the propagation of a high-energy laser beam through metallic aerosols. Poulain *et al.*<sup>8</sup> performed experimental work on high intensity KrF excimer laser interaction with solid aerosols and reported interesting interaction dynamics and material breakdown thresholds for several types of solid aerosol particles. In order to overcome some of the experimental difficulties reported by Poulain *et al.*<sup>8</sup> and to better understand interaction dynamics phenomena associated with a high-energy laser beam interacting with solid aerosols, the present investigation utilized a thin metallic wire instead of solid aerosol particles in the laser beam probe volume. Thus, in this investigation, interaction dynamics of a high intensity (80 GW/cm<sup>2</sup>) KrF excimer laser beam with a 75  $\mu$ m diameter copper wire were studied under atmospheric illumination conditions.

Alexander *et al.*<sup>9</sup> has previously studied the time history of ESIR and broadband emission for a water droplet illuminated by KrF laser pulse. The present work reports differences in plasma formation from copper wire targets and water droplets, i.e. time dependent plasma formations and ESIR. In this paper we present comparative data from the two distinct types of plasmas for incident laser beam irradiance ranging from 1-100 GW/cm<sup>2</sup>.

## II. EXPERIMENTAL SETUP

A schematic of the experimental setup is shown in Figure 1. A high-energy beam was produced by a KrF excimer laser (Questek model 2860,  $\lambda = 248$  nm, pulse duration = 17 ns FWHM) using unstable optics and was focused by a plano-convex lens ( $d = 50$  mm,  $f = 250$  mm). The cross sectional dimensions of the high-energy beam were determined experimentally by translating a knife-edge through the focused beam.<sup>8</sup> A second method verified the cross sectional dimensions by measuring the illuminated damage area of a polished nickel plate placed in the focused probe volume. Dimensions of the focused high-energy beam were approximately  $110 \times 135 \mu$ m for this investigation. A second excimer laser, identical to the first with the exception of using stable resonator optics, was used to produce an imaging beam incident in a direction orthogonal to both the high-energy pulse and the copper wire. Laser pulses used for imaging were synchronized with the high-energy pulses illuminating the targets using an analog/digital delay unit, Questek model 9200 Laser Sync Unit (LSU). Sync signals from the camera control unit (Cohu model 8000) were sent to a pulse generator (HP model 8015A) which subsequently provided the trigger pulse for the LSU. Pulses from both lasers were simultaneously monitored using a fast photodiode (Hamamatsu model C1083) and digitizing oscilloscope (Hewlett Packard model 54200A). Analog delay controls on the LSU were used to calibrate arrival of the imaging pulse to be coincident with the high-energy pulse (defined as 0 ns image delay in this investigation). Jitter for the system was approximately  $\pm 7$  ns. The digital delay on the LSU made it possible to delay the image pulse arrival with respect to the high-energy pulse from 0-100  $\mu$ s in increments of 10 ns.

Real time images of the laser beam interacting with the wire were obtained with a UV sensitive vidicon camera. Thus, the image is integrated over the laser pulse duration of 17 ns FWHM. Images were stored on an optical disk recorder (Panasonic model TQ-2023F) and processed with a digital image processing system<sup>10</sup> for subsequent analysis. The probe volume of the high-energy illuminating pulse was positioned in the image plane by observing the plasma formed during air

breakdown with the vidicon camera. Wire targets were positioned in the same imaging probe volume and centered by observing the maximum visible emission from the illuminated wire. Location of the 75  $\mu\text{m}$  diameter copper wire within the same probe volume was maintained by feeding the wire from a spool through two glass micro-capillaries with an inside diameter of 127  $\mu\text{m}$ . A mass equal to 17.5 g was connected to the bottom of the wire to keep the wire taut. A stepping motor was used to rotate the spool to feed new wire into the probe volume for each laser pulse/wire interaction. The experimental setup used in the current work for interacting  $\text{H}_2\text{O}$  droplets with the excimer laser beam and detecting the plasma emission is described in Reference 9.

### III. INTERACTION DYNAMICS

Experimental work to visualize the interaction dynamics was performed using a pulsed real time video imaging system to record the dynamics associated with the high-energy laser interaction with a small diameter wire. An ArF excimer laser imaging system was operated at  $\lambda=193\text{ nm}$  to provide high resolution images as well as to eliminate scattered 248 nm emission from the high-energy pulse by using a 193 nm bandpass filter in line with the imaging optics. Dynamic interactions were observed for a single 80  $\text{GW}/\text{cm}^2$  pulse ( $\lambda = 248\text{ nm}$ , pulse duration = 17 ns) incident on a 75  $\mu\text{m}$  diameter copper wire. For comparative purposes, images of the wire were recorded before the high-energy pulse interaction and after the high-energy pulse interaction as shown in Figure 2. The illuminating pulse was incident from right to left in Figure 2 and produced a crater-shaped region at the illuminated surface as a result of material removal. The term crater in this work refers to the volumetric region at the illuminated surface of the wire where material has been removed as a result of the interaction. Images recorded at various time delays during the laser beam/wire interaction process are shown in Figures 3-5. Delay time given under each photograph is the delay of the image beam ( $\pm 7\text{ ns}$ ) with respect to the arrival of the high-energy pulse. Dark regions on the left of the images were characteristic of the imaging system used and were primarily due to the optical effects associated with the bandpass filter.

The first noticeable evidence of any laser beam/wire interaction dynamics was at 10 ns image delay as shown in Figure 3. A cloud of material is visible at the illuminated (front) surface of the wire but not at the shadow (rear) surface. At 40 ns image delay, material emission is evident at the shadow surface of the wire and a crater like depression is clearly forming at the illuminated surface of the wire as a result of the material removal at approximately the location of the probe volume. Scanning electron microscope (SEM) images of the samples showed no physical material removal from the shadow surface of the wire. Thus, ejected material appearing at the shadow surface of the wire was removed from the illuminated surface of the wire and propagated around the sides of the wire. At 60 ns delay, a crater on the illuminated surface of the wire is clearly defined with an opaque lip forming at the edge of the probe volume region. In addition, no cloud of material is apparent above and below the probe volume region as shown at 40 ns image delay. Lifetime of the visible plasma emission from the laser beam/wire interaction was determined to have an average value of 62 ns (FWHM). The cloud of material appearing at the illuminated surface of the wire prior to 60 ns image delay is thought to be a dense plasma. At 100 ns delay, a dark region appears directly in front of the probe volume on the illuminated side. The material is thought to be plasma or vapor and is evident from 80-120 ns. This material in front of the probe volume was not evident in the images prior to 80 ns image delay since sufficient quantities do not exist to be detected by the imaging system. After 120 ns delay, this material moves out of the field of view of the imaging system.

Images at longer time delays ranging from 170 ns to 600 ns are shown in Figure 4. From these images, it is evident that material has traveled from the illuminated front wire surface to form diffuse fans behind the shadow surface of the wire. These series of photographs show material moving along the illuminated surface away from the crater region in a lateral direction parallel to the wire surface. This lateral moving material has moved out of the field of view of the imaging system after 800 ns delay as shown in Figure 5. Material having individual particle characteristics is evident behind the shadow surface of the wire for time delays of 800 ns and longer. Particles could be observed in the photographs for time delays up to 4.5  $\mu$ s and were shown to be in a molten state by collecting them onto polished nickel plates.

SEM images are shown in Figure 6 revealing a side view (top) and a shadow surface view (bottom) of copper wire samples after illumination by a KrF laser pulse ( $\lambda = 248$  nm) at 80 GW/cm<sup>2</sup>. The side view clearly shows where material removal occurred and the crater formed. In addition, molten material flow has occurred as demonstrated by the relatively smooth surface above and below the crater followed by a rough surface region where solidification of the material occurred. The top photograph in Figure 6 further shows material flowed in all directions from the crater region. The bottom photograph in Figure 6 provides evidence that no material was removed from the shadow surface. Further examination of the photograph shows that a lip has formed on the side of the wire from molten material exploding away from the illuminated surface as a result of high pressures.

High magnification SEM images taken of solidified material located in the rough surface region on the front of the wire are shown in Figure 7. Particles that solidified before "pinching off" a wave surface can be identified in the top photograph. Solidification waves traveling from the front surface of the wire to the sides are evident in the bottom photograph of Figure 7. Particles ejected at the sides of the wire are smaller than particles forming from the surface waves formed near the front surface of the wire. Surface tension and the height of the surface waves are important parameters in determining the size of particles formed.

#### IV. VELOCITY MEASUREMENTS

Velocity measurements of emitted materials from the laser beam/wire interactions were performed using single pulse ( $\lambda = 193$  nm) images similar to those shown in Figures 3-5 and also by a dual pulse imaging method described in previous work by Schaub *et al.*<sup>11</sup> Dual pulse imaging is performed by splitting the laser pulse used for imaging into two separate pulses as shown in Figure 1. One part of the imaging pulse travels directly to the imaging system while the second part travels over an additional 17.1 m (56 ft) of optical path length. Thus, two 17 ns pulses ( $\lambda = 248$  nm) optically delayed by 56 ns enter the imaging system providing a double exposure image on the vidicon camera of the emitted material produced from the laser beam/wire interaction. Velocity of the emitted material was determined by measuring the distance the molten material moved during the 56 ns time interval. The time interval separating the dual imaging pulses is fixed by the optical path length, however, the time delay of the first imaging pulse with respect to the high-energy pulse can be adjusted with the LSU previously described.

Figure 8 is a typical dual pulse image obtained of emitted material with the first image pulse delayed 500 ns after the arrival of the high-energy pulse (80 GW/cm<sup>2</sup>) which was incident from right to left. Samples were positioned to appear beyond the right edge of the monitor screen to eliminate scattered 248 nm emission from the laser beam/wire interaction which saturates the vidicon camera. Average velocities of materials emitted in a direction away from the illuminating laser were 570 m/s at 300 ns image delay and 460 m/s at 500 ns delay. Dual pulse images were

not obtained for image delays shorter than 300 ns since the material was not dense enough to be picked up by the imaging system and for image delays longer than 500 ns as a result of material expanding in diffuse fans covering the complete field of view. Figure 9 is a typical dual pulse image obtained at image delays of 1500 ns and longer of individual particles traveling in a direction away from the illuminating laser (right to left). Particles are approximately  $10\text{ }\mu\text{m}$  in diameter and move less than  $5\text{ }\mu\text{m}$  in 56 ns time delay which corresponds to a velocity less than 90 m/s.

The velocity of emitted material was also determined by utilizing a single imaging pulse and measuring the material movement for a known time delay relative to the arrival of the ablation pulse. A similar technique was used by Alexander *et al.*<sup>12</sup> to determine interaction velocities when an excimer laser beam interacted with a water droplet. For the current work, it is assumed that ejected material originates from the front of the crater region and emission starts at 0 ns image delay. Velocity calculations for ejected materials from the dual and single imaging pulse techniques are presented in Figure 10. Data plotted in the graphs differ only by the scale of the time (horizontal) axis. The top graph has been expanded to emphasize the acceleration and deceleration during the laser pulse. Each data point on the graphs represents the average of approximately five velocity calculations for each time frame. An estimated error associated with the material emission velocity calculations is  $\pm 20\%$  and is primarily due to the uncertainties in properly identifying the exact starting and ending of material boundaries.

Material emission velocities in a direction towards the illuminating laser were calculated by measuring the material movement on the illuminated (front) surface of the wire and in a direction perpendicular to the wire. The starting position of the front wire surface was located by comparing wire images before the high-energy pulse illumination with the delayed images during illumination of the samples. Measurements of emitted material movement toward the illuminating laser could generally be made for time delays longer than 30 ns since material boundaries could not be clearly identified. However, the emission velocity was calculated for material shown in front of the probe volume at 100 ns delay in Figure 3. The average velocity of spatially emitted material toward the laser is shown to increase from 1300 m/s at 10 ns time delay to 1500 m/s at 20 ns. The corresponding acceleration is from the 17 ns (FWHM) high-energy pulse still depositing energy into the interaction region. A subsequent deceleration of material occurs after the end of high-energy laser pulse. Material emission velocities in a direction away from the illuminating laser were calculated by the same procedure used to measure material movement on the illuminated surface of the wire. In order to obtain velocity calculations in a direction away from the illuminating laser, single pulse imaging was used up to 70 ns, i.e., until material boundaries were no longer distinguishable and dual pulse imaging was used from 300–500 ns.

Lateral material emission is defined in this work as emitted material at the illuminated surface of the wire moving out of the crater region in a direction parallel to the wire. Lateral emission velocities were obtained only up to 800 ns image delay since material moves out of the field of view of the imaging system as shown in Figure 4 and 5. As shown in Figure 10, lateral emission velocities remain constant at approximately 800 m/s until 130 ns image delay when deceleration to 270 m/s occurs at 300 ns delay. Deceleration occurs after the emitted material crosses the smooth interaction surface region located above and below the crater and enters the rough surface region shown in Figure 6. Molten material is cooling and solidifying in the rough surface region on the illuminated wire surface causing deceleration. The velocity of the lateral material emission at 300 ns image delay is comparable to the speed of sound at atmospheric conditions.

As shown in Figure 5, emitted particles appear behind the shadow surface of the wire at a time delay of  $4.5\text{ }\mu\text{s}$ . An explanation for particles emitted microseconds after a 17 ns pulse interaction is

provided by examining the thermal diffusion time and the material emission velocities. For metals interacting with an excimer laser pulse, Jervis *et al.*<sup>13</sup> report that the thermal diffusion length ( $\delta$ ) is given by

$$\delta = 2\sqrt{\chi\tau} \quad (1)$$

where  $\chi$  is the thermal diffusivity and  $\tau$  is the beam pulse width. For copper and a 17 ns pulse width (FWHM),  $\delta = 2.2 \mu\text{m}$ . Penetration depth ( $d$ ) of the incident beam ( $\lambda = 248 \text{ nm}$ ) into copper is calculated to be 11 nm. Since  $\delta \gg d$ , depth of energy distribution over the 17 ns pulse width is determined by thermal diffusion as opposed to the laser penetration depth. Therefore, thermal diffusion cannot be neglected for this investigation. Particles emitted during long time delays originated from rough surface regions of the wire shown in Figure 7. SEM analysis of cross sections of interacted specimens revealed that the molten material in the rough surface regions can exceed  $8 \mu\text{m}$  in thickness. By rearranging Eq. (1), a convenient order-of-magnitude estimation for the thermal diffusion time ( $t$ ) through a metal surface is given by Ready<sup>14</sup> as

$$t = \frac{D^2}{4\chi} \quad (2)$$

where  $D$  is the desired penetration thickness. For  $D = 8 \mu\text{m}$ , thermal diffusion time ( $t$ ) would be 200 ns. Single pulse imaging revealed molten material moving over the rough surface region of the wire at approximately  $1 \mu\text{s}$  image delay. Emitted particles from this zone were previously reported to have velocities less than 90 m/s. Since these particles originate from the front wire surface and are imaged behind the shadow surface, total distance traveled is over  $75 \mu\text{m}$  (wire diameter) and the corresponding travel time would be over  $1.0 \mu\text{s}$  for a velocity under 90 m/s. Therefore, thermal diffusion time and material velocities across the wire surface account for microsecond delays of particle emission from the laser beam/wire interaction.

## V. COPPER AND H<sub>2</sub>O DROPLET PLASMA EMISSION

For our experiments at  $\lambda = 248 \text{ nm}$ , one photon is needed to ionize copper while three are required for water and air. As shown in Figure 11 the onset of ionization and plasma formation for copper starts approximately 4 ns earlier than plasma formation in a water droplet. Several mechanisms contribute to the observed differences. Before ionization occurs in water, the molecules of H<sub>2</sub>O will breakup into H<sub>2</sub> and O which initially delays the plasma. The ionization potential for H<sub>2</sub> and O is three times greater than the ionization potential for copper. After initial electron formation by multiphoton ionization (MPI), cascade breakdown occurs. For cascade ionization to occur, electrons are needed with an energy greater than the material ionization potential. During the cascade ionization (CAI) process, energy losses such as electron diffusion, attachment to oxygen, and excitation all alter the plasma formation processes. In Figure 11, the plasma emission times for both copper and water plasma are shown. The delay in the start of the copper plasma can be explained by the  $4s^1-3d^{10}$  transition.

The time history of ESIR behavior for copper is similar to the water case as shown in Figure 12. Figure 12 is a plot of the arbitrary intensity of the incident pulse and ESIR as a function of time for  $75 \mu\text{m}$  diameter copper wire illuminated by a KrF laser pulse at  $1-100 \text{ GW/cm}^2$ . The arrival of the incident pulse is defined as the time when the intensity reaches  $1/e^2$  of its maximum value and is used to reference all other delay times. The delay times  $P_{t1}$  and  $P_{t2}$  are taken from the incident pulse arrival to the first and second peak of ESIR, respectively.  $V_t$  is the delay time from the incident pulse arrival to the first minimum of the ESIR. As expected, the first ESIR starts as

the incident pulse arrives. In Figure 12(a), one observes that the first ESIR is rapidly increasing within 6 ns after the incident laser pulse reaches the surface of the copper wire. ESIR peaks and then decreases as a result of the plasma formation on the surface of the material which absorbs the incident pulse energy. As the time is increased, the density of the resulting electrons and ions increase such that a dense plasma reflects the incident pulse until it reaches the peak,  $P_{t2}$ . At the irradiance of 100 GW/cm<sup>2</sup>, the intensity of the second ESIR peak is higher than  $P_{t1}$ . This indicates that the higher input energy results in a higher frequency plasma as well as a more dense plasma. At the input energy of 50 GW/cm<sup>2</sup>, the first ESIR appears to be dominant. At lower input energies, there is no distinct second ESIR peak which implies only a low density plasma on the surface of the copper wire. Examination of the wire surface using a stereo microscope revealed oxidation and no material removal for the lower input energies.

The delay times,  $P_{t1}$ ,  $P_{t2}$  and  $V_t$  for the copper and water can be compared and are shown in Figure 13. In Figure 13, subscripts c and w refer to the copper and the water, respectively. As shown in Figure 13, there is a general trend for the delay times of the copper to be higher than for water. However, the standard deviation for the copper wire results is much higher than  $P_{t2}$  and  $V_t$  due to the plasma instability in time, even though the  $P_{t1}$  is quite stable. As the input irradiance is increased, the delay time for plasma formation for both materials remains essentially constant. The spectral distribution of the ESIR and plasma emission in the spectral range of 440-520 nm is shown in Figure 14. The second harmonic of the ESIR is approximately 496 nm and serves as a reference wavelength. At 26 ns after the incident pulse arrival, the ESIR is less than the continuum radiation. The copper line (510.5 nm) and nitrogen (510 nm) line are both very evident in the plasma emission spectrum.

## VI. SUMMARY

High intensity ultraviolet laser interaction with a metallic filament and with H<sub>2</sub>O droplets has been investigated. A 2-D shadow imaging system showed both vaporous and molten material emitted from the laser beam/wire interaction. Material was shown to be emitted in every direction from the probe volume as a result of a high pressure region at the surface of the wire. Emitted material imaged at the shadow surface of the wire originated from the illuminated surface and propagated around the sides of the wire. A maximum material velocity of approximately 1500 m/s was calculated for ablated material in a direction back toward the illuminating laser. Emitted particles were evident 4.5  $\mu$ s after arrival of the high-energy pulse. It was concluded that this delay was the resultant combination of the thermal diffusion time and material emission velocities. Particles ejected at these later times were shown to have a velocity of under 90 m/s.

The ESIR of copper wire plasma also has a two distinct peak structure which is dependent on the input energy and, except for differences in initiation times, is similar to plasma formation in H<sub>2</sub>O droplets. Plasma formation of the copper wire started 4 ns earlier as a result of the dissociation times of H<sub>2</sub>O. In addition, the ionization potential of copper is around three times smaller than H<sub>2</sub> and O. However, the rise time in the copper plasma was not as fast as that observed in plasma emitted from water droplets as a result of interband transition.

## ACKNOWLEDGMENTS

This work was supported in part by the Army Research Office under Contract No. DAAL03-87-K-0182 and was performed in the Center for Electro-Optics at the University of Nebraska at Lincoln.



## REFERENCES

1. Viswanathan, R. and Ingo Hussla, "Ablation of Metal Surfaces by Pulsed Ultraviolet Lasers Under Ultrahigh Vacuum," *J. Opt. Soc. Am. B*, Vol. 3, No. 5, p. 796, May 1986.
2. Ursu, I., I.N. Mihailescu, Al. Popa, A.M. Prokhorov, V.P. Ageev, A.A. Gorbunov and V.I. Konov, "Studies of the Change of a Metallic Surface Microrelief as a Result of Multiple-Pulse Action of Powerful UV Laser Pulses," *J. Appl. Phys.*, Vol. 58, No. 10, p. 3909, 15 November 1985.
3. Kelly, Roger and Joshua E. Rothenberg, "Laser Sputtering Part III. The Mechanism of the Sputtering of Metals at Low Energy Densities," *Nuclear Instruments and Methods in Physics Research B*, Vol. 7/8, p. 755, 1985.
4. Rosen, D.I., D.E. Hastings and G.M. Weyl, "Coupling of Pulsed 0.35- $\mu$ m Laser Radiation to Titanium Alloys," *J. Appl. Phys.*, Vol. 53, No. 8, p. 5882, August 1982.
5. Offenberger, A.A., R. Fedosejevs, P.D. Gupta, R. Popil and Y.Y. Tsui, "Experimental Results for High Intensity KrF Laser/Plasma Interaction," *Laser and Particle Beams*, Vol. 4, Parts 3 and 4, p. 329, 1986.
6. Panchenko, A.N. and V.F. Tarasenko, "Experiments on Plasma Production and Expansion During UV-Laser Irradiation of Metals," *Sov. J. Plasma Phys.*, Vol. 14, No. 6, p. 450, June 1988.
7. Armstrong, Robert L. and Andrew Zardecki, "Propagation of High Energy Laser Beams through Metallic Aerosols," *Applied Optics*, Vol. 29, No. 12, p. 1786, 20 April 1990.
8. Poulain, D.E., D.R. Alexander, J.P. Barton, S.A. Schaub and J. Zhang, "Interactions of Intense Ultraviolet Laser Radiation with Solid Aerosols," *J. Appl. Phys.*, Vol. 67, No. 5, p. 2283, 1 March 1990.
9. Alexander, D.R., S.A. Schaub, J.Zhang, D.E. Poulain and J.P. Barton, "Scattering of Incident KrF Radiation Resulting From the Laser-Induced Breakdown of H<sub>2</sub>O Droplets," *Opt. Lett.*, Vol. 14, p. 548, 1989.
10. Ahlers, K.D. and D.R. Alexander, "Microcomputer Based Digital Image Processing System Developed to Count and Size Laser- Generated Small Particle Images," *Opt. Eng.*, Vol. 24, No. 6, p. 1060, 1985.
11. Schaub, S.A., D.R. Alexander, D.E. Poulain and J.P. Barton, "Measurement of Hypersonic Velocities Resulting from the Laser-Induced Breakdown of Aerosols Using an Excimer Laser Imaging System," *Rev. Sci. Instrum.*, Vol. 60, No. 12, p. 3688, December 1989.
12. Alexander, D.R., J.P. Barton, S.A. Schaub and G.M. Holtmeier, "Nonlinear Interactions of KrF Laser Radiation with Small Water Droplets," *Appl. Optics*, accepted for publication, 5 February 1990.
13. Jervis, T.R., M. Nastasi and T.G. Zocco, "Excimer Laser Mixing of Titanium Layers on AISI 304 Stainless Steel," *Mat. Res. Soc. Symp. Proc.*, Materials Research Society, Vol. 100, p. 621, 1988.
14. Ready, J.F., *Effects of High-Power Laser Radiation*, Academic Press, New York, 1971.

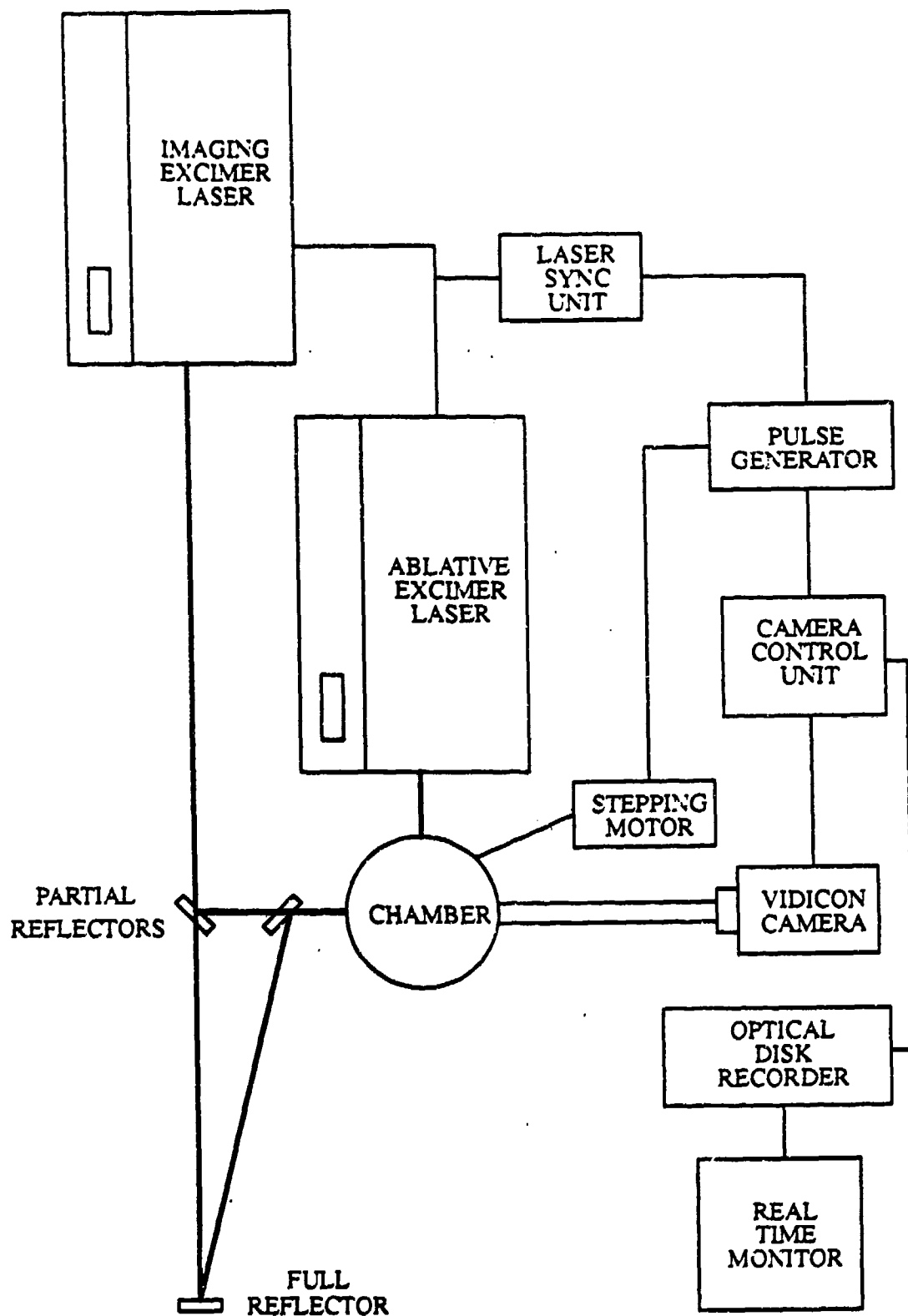


Figure 1. Schematic of the experimental setup.

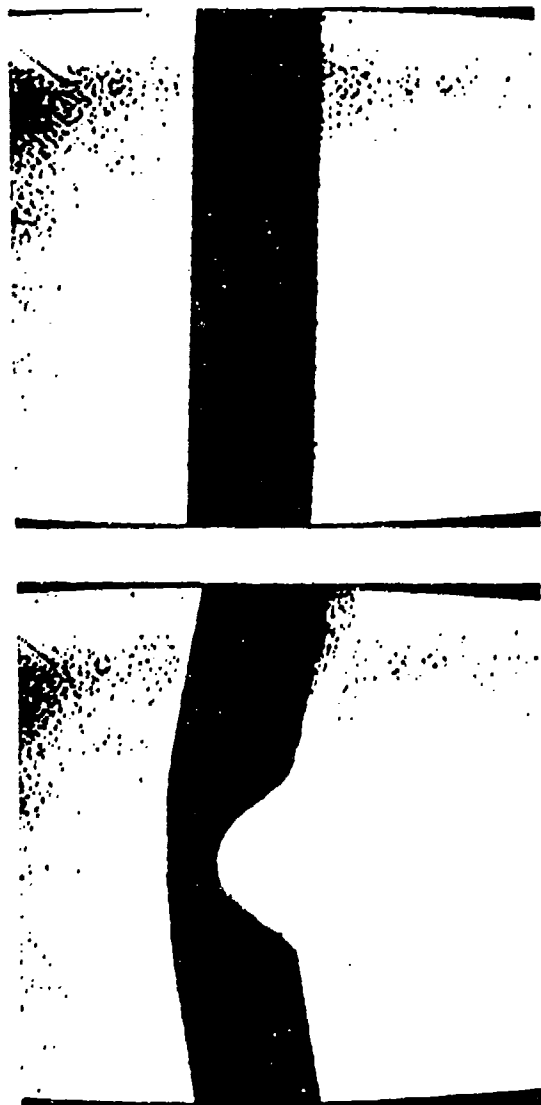
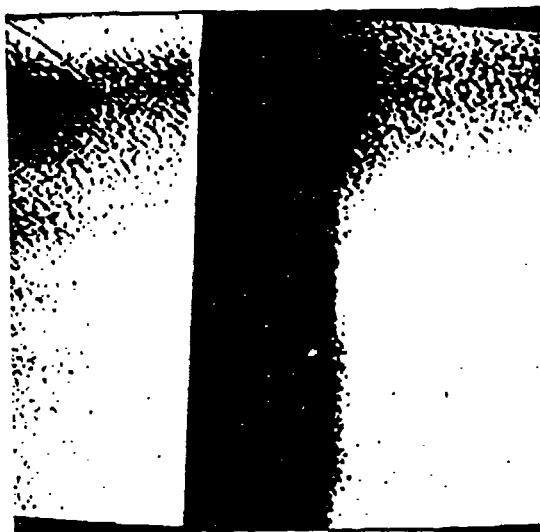
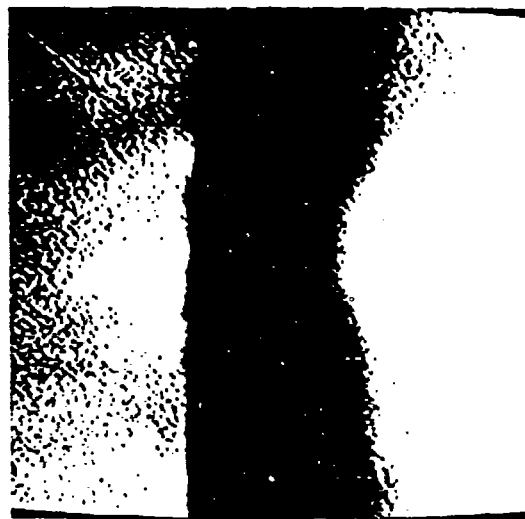


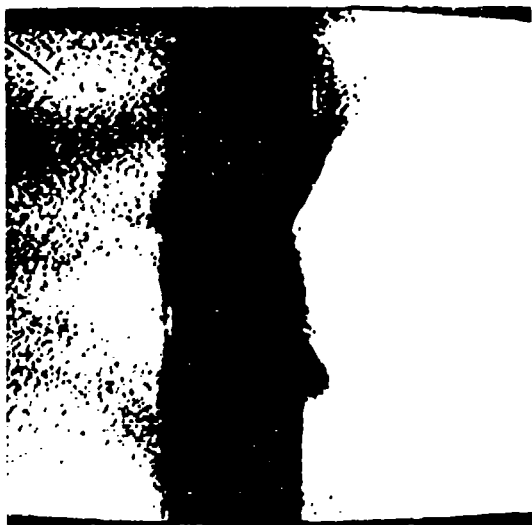
Figure 2. Images of 75  $\mu\text{m}$  diameter copper wire before high-energy illumination (top) and after illumination (bottom). Irradiation was 80 GW/cm<sup>2</sup> using a KrF pulse ( $\lambda = 248$  nm). Beam propagation was from right to left.



10 ns



40 ns



60 ns

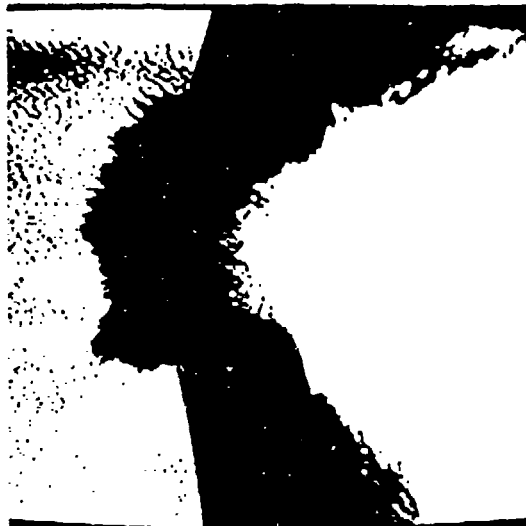


100 ns

Figure 3. Interaction of KrF laser ( $\lambda \approx 248$  nm) with a  $75 \mu\text{m}$  diameter copper wire at  $80 \text{ GW}/\text{cm}^2$ . Time given under each photograph is the delay of the image beam with respect to the arrival of the high-energy laser pulse. Beam propagation is from right to left.



170 ns



300 ns



400 ns



600 ns

Figure 4. Interaction of KrF laser ( $\lambda = 248$  nm) with a  $75\ \mu\text{m}$  diameter copper wire at  $80\ \text{GW}/\text{cm}^2$ . Time given under each photograph is the delay of the image beam with respect to the arrival of the high-energy laser pulse. Beam propagation is from right to left.

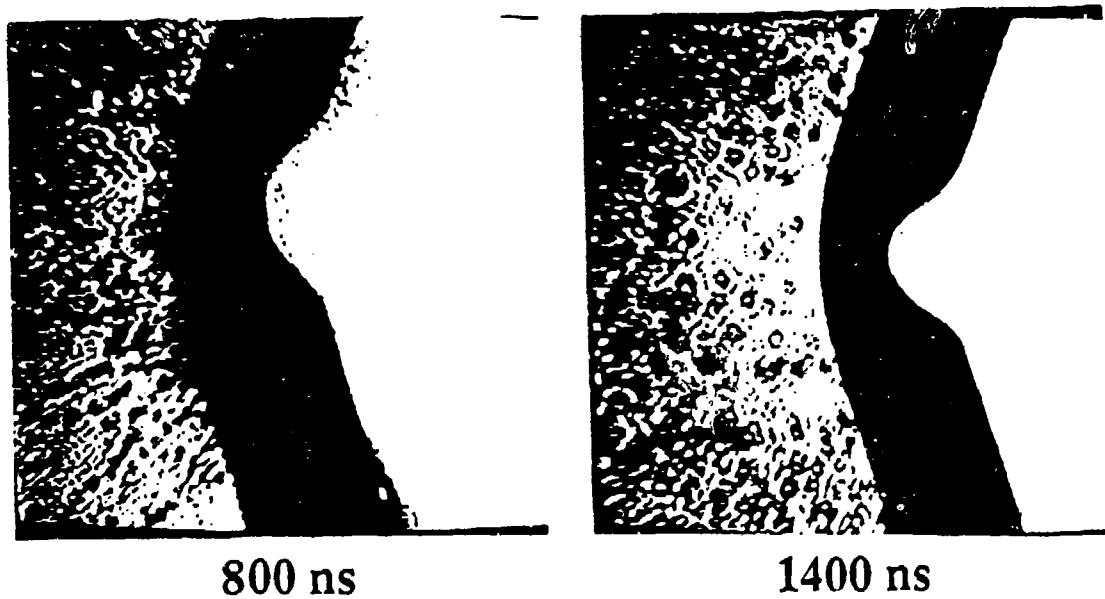


Figure 5. Interaction of KrF laser ( $\lambda = 248$  nm) with a  $75\ \mu\text{m}$  diameter copper wire at  $80\ \text{GW}/\text{cm}^2$ . Time given under each photograph is the delay of the image beam with respect to the arrival of the high-energy laser pulse. Beam propagation is from right to left.

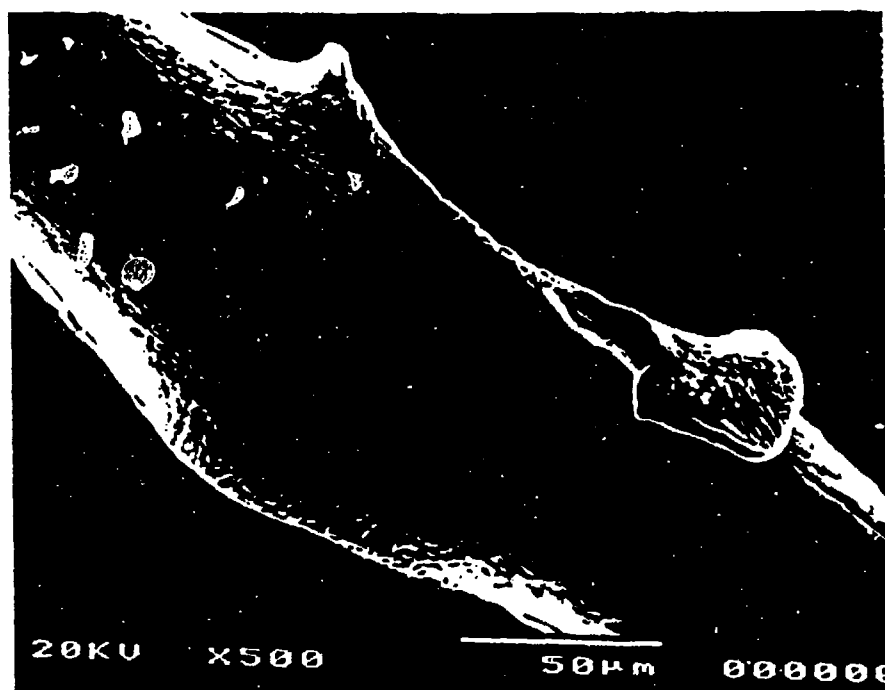
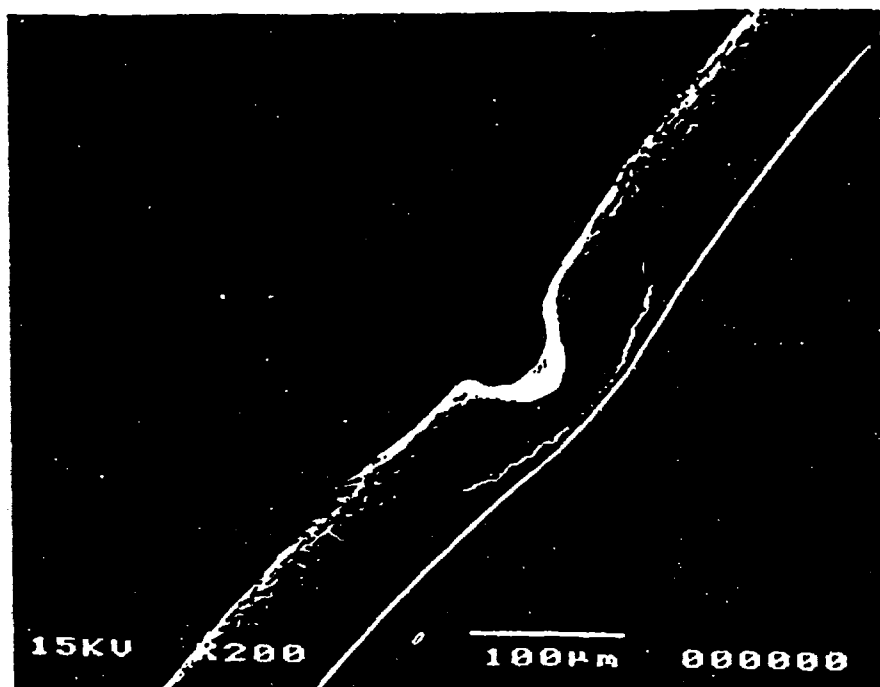


Figure 6. Photomicrographs of side view (top) and shadow surface (bottom) of an illuminated 75  $\mu\text{m}$  diameter copper wire. Irradiation was 80  $\text{GW}/\text{cm}^2$  by a KrF pulse ( $\lambda = 248 \text{ nm}$ ).

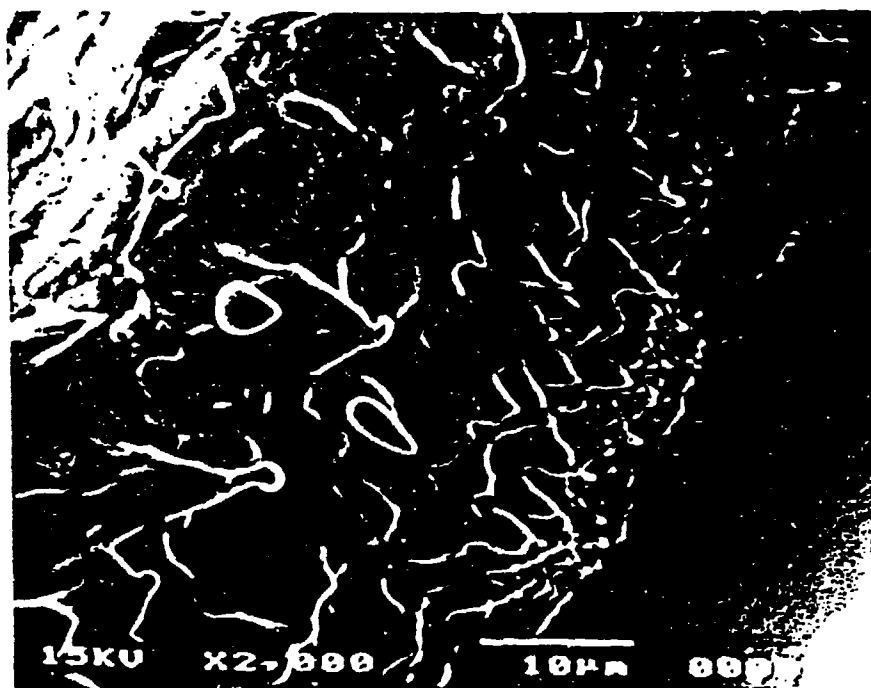


Figure 7. Photomicrographs of typical waves and particle formations on the front surface of an illuminated 75  $\mu\text{m}$  diameter copper wire. Irradiation was 80  $\text{GW}/\text{cm}^2$  by a KrF pulse ( $\lambda = 248 \text{ nm}$ ).



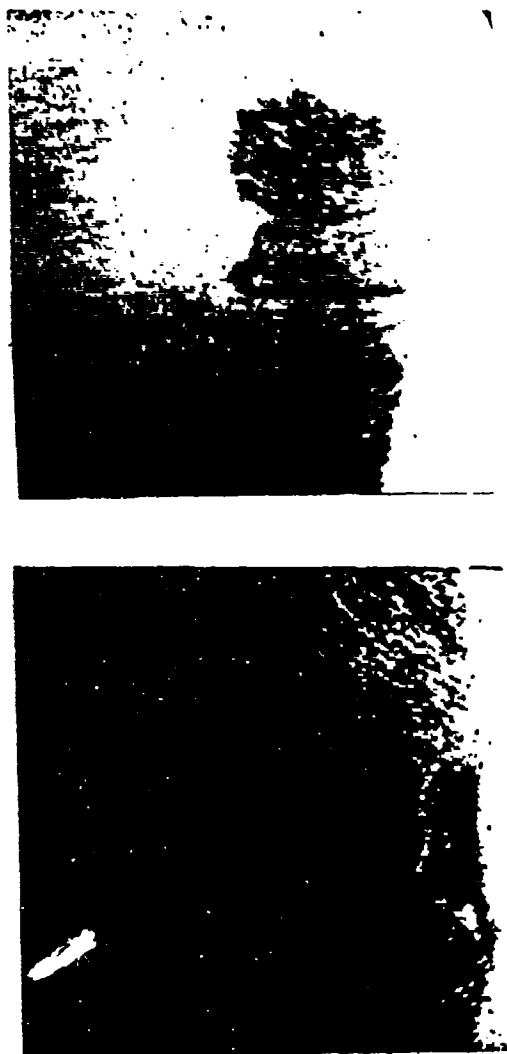


Figure 8. Typical dual pulse images of emitted material traveling from right to left away from the ablation area. Time delay between each imaging pulse is 56 ns providing a double exposure image. First image pulse delayed 500 ns after arrival of high-energy pulse. Irradiation was 80 GW/cm<sup>2</sup> by a KrF pulse ( $\lambda = 248$  nm). Image dimensions are 280  $\mu$ m square.

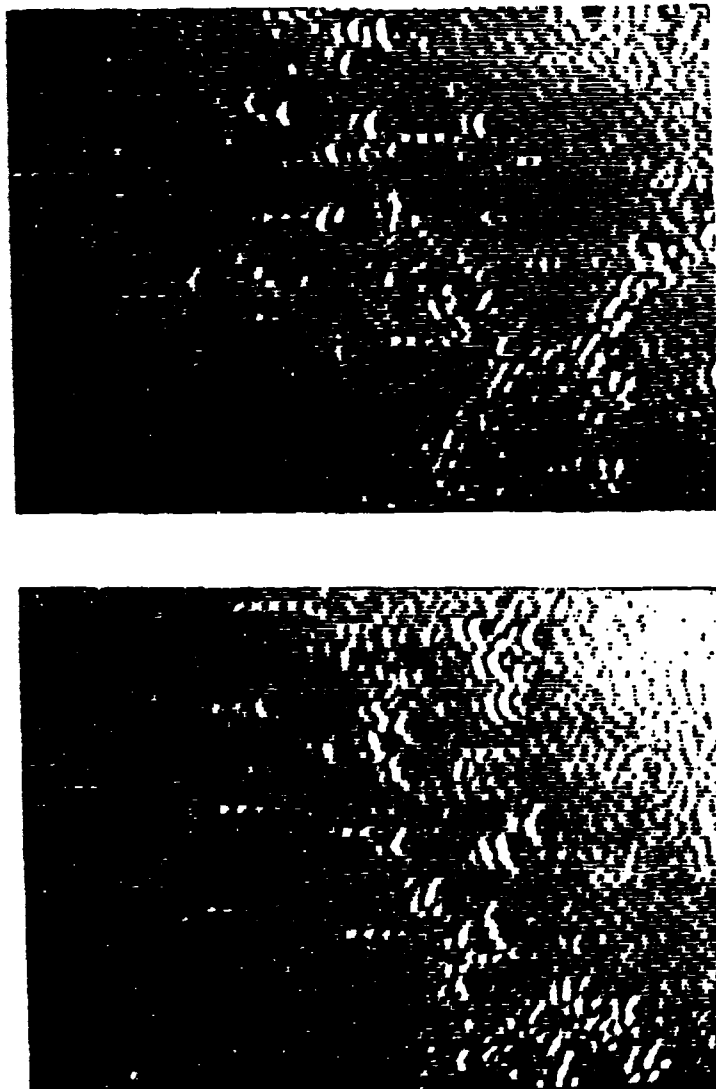


Figure 9. Typical dual pulse images of emitted copper particles traveling from right to left away from the ablation area. Time delay between each imaging pulse is 56 ns providing a double exposure image. First image pulse delayed 1500 ns after arrival of high-energy pulse. Irradiation was 80 GW/cm<sup>2</sup> by a KrF pulse ( $\lambda = 248$  nm). Image dimensions are 165  $\times$  230  $\mu$ m.

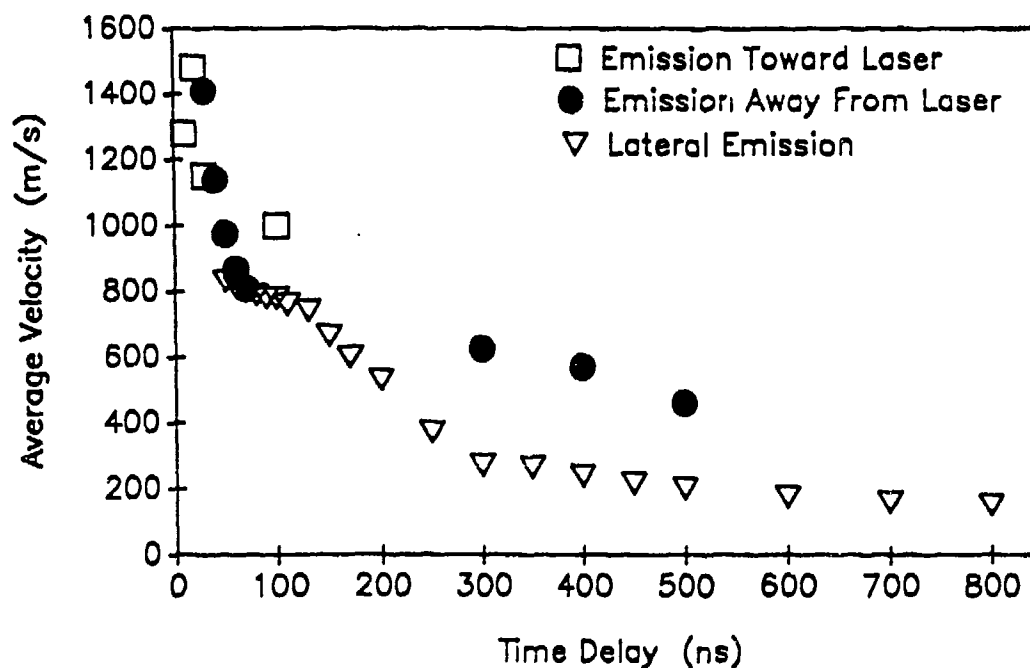
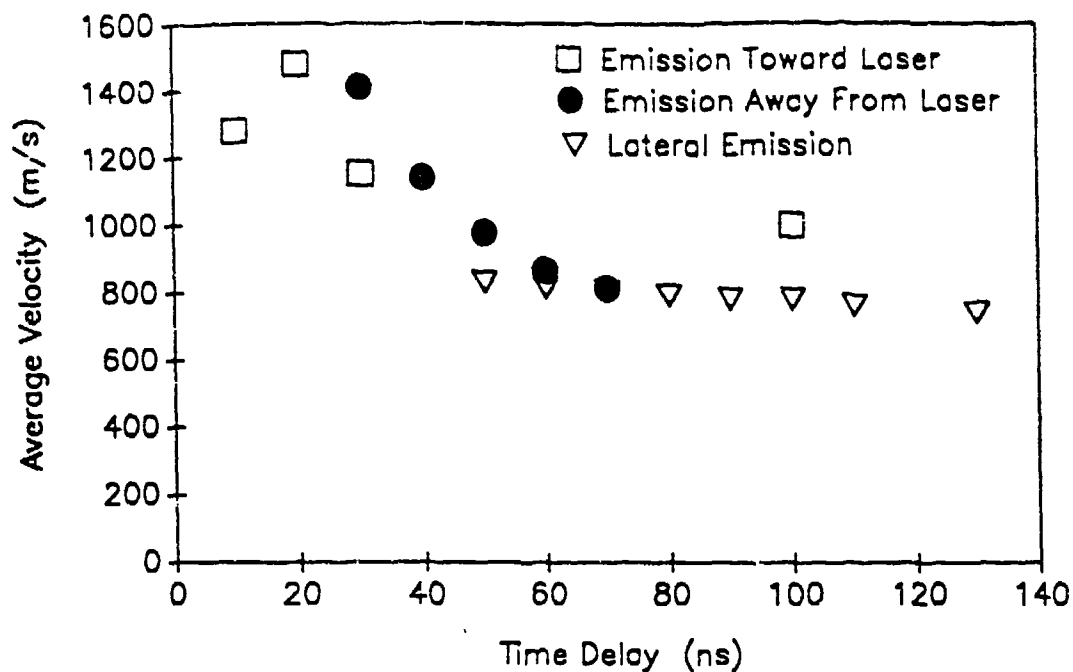


Figure 10. Average velocities of emitted materials from interactions of KrF laser radiation at 80 GW/cm<sup>2</sup> with 75  $\mu$ m diameter copper wire as a function of the image time delay. Top graph has been expanded to emphasize the acceleration during the laser pulse and the subsequent deceleration.

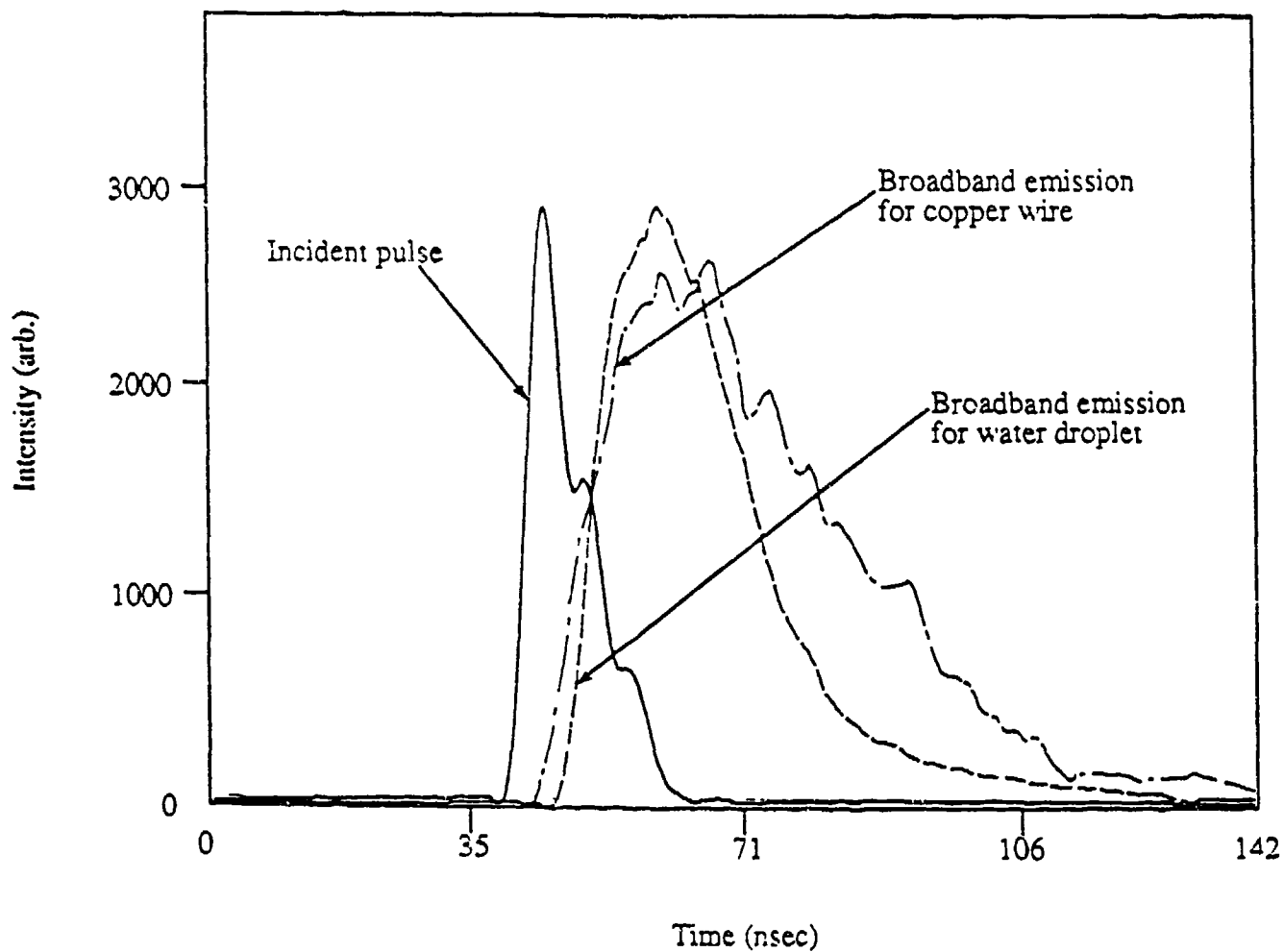


Figure 11. Intensities as a function of time for the incident pulse, the broadband emissions of copper wire ( $75\ \mu\text{m}$  dia.) and water droplet ( $75\ \mu\text{m}$  dia.) illuminated by a  $100\ \text{GW}/\text{cm}^2$  KrF laser pulse.

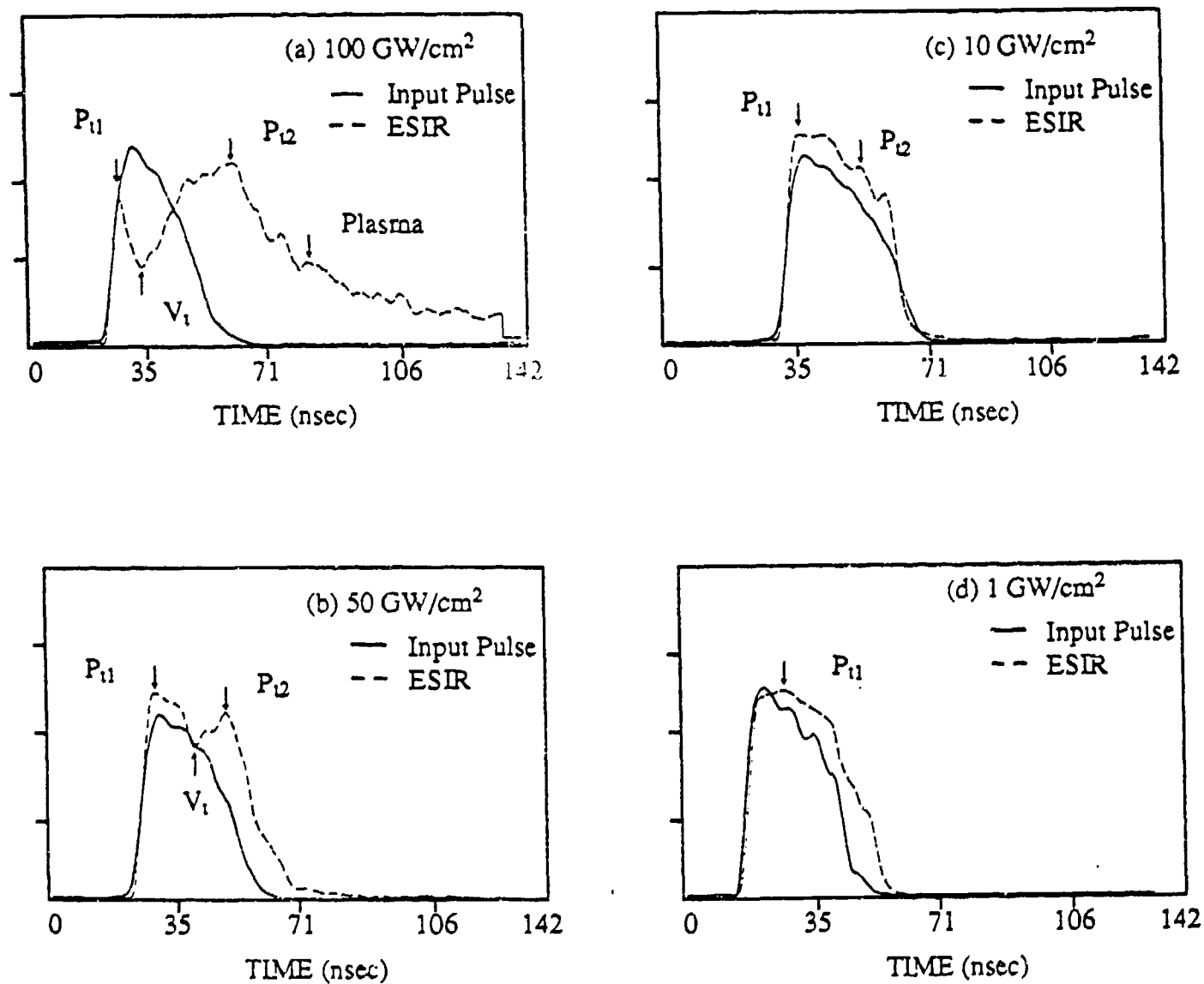


Figure 12. Intensities of the incident pulse (solid curves) and the ESIR (dashed curves) as a function of time for 75  $\mu\text{m}$  diameter copper wire illuminated by a KrF laser pulse of 1-100  $\text{GW}/\text{cm}^2$ . The vertical scale is in arbitrary intensity units.

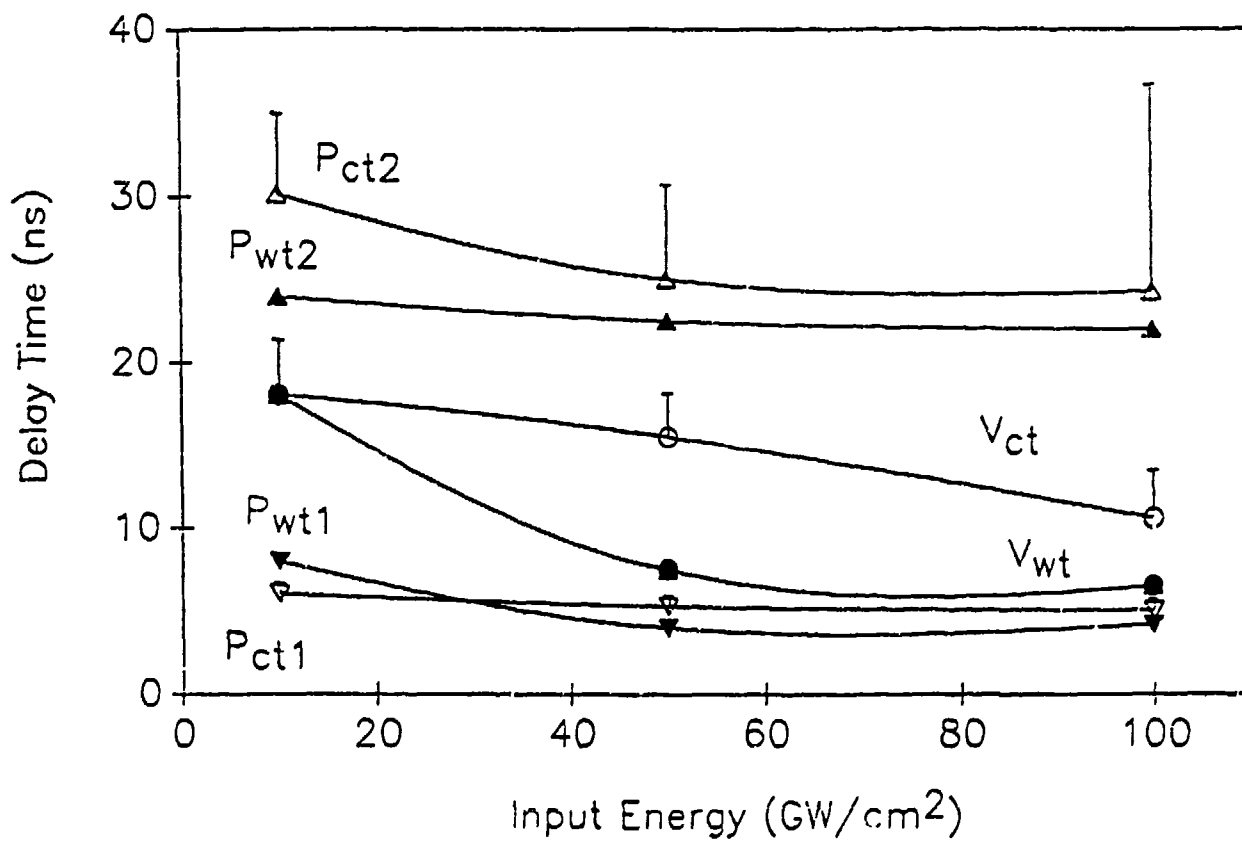


Figure 13. Delay time between the incident pulse and  $P_{t1}$ ,  $P_{t2}$  and  $V_t$  for 75  $\mu\text{m}$  dia. water droplet and 75  $\mu\text{m}$  dia. copper wire.

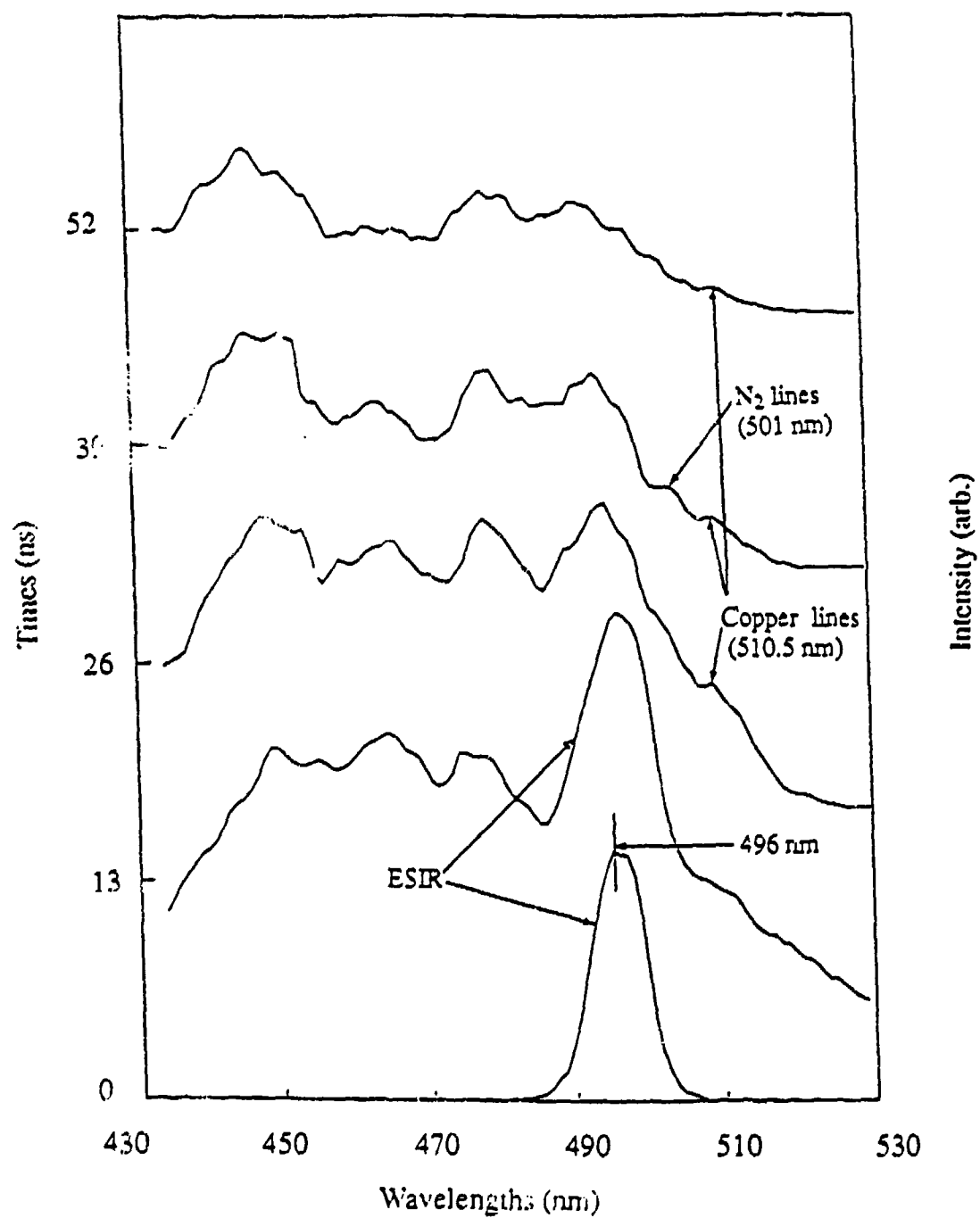


Figure 14. Spectral distributions of ESIR and plasma.

BLANK



## WAVE PROPAGATION FROM LASER-INDUCED PLASMAS IN DROPLETS

J. C. CARLS AND J. R. BROCK  
Chemical Engineering Department  
University of Texas  
Austin, Texas 78712

### RECENT PUBLICATIONS, SUBMITTALS FOR PUBLICATION AND PRESENTATIONS

- Wave propagation from laser-induced plasmas in droplets" *Proceedings of the 1990 CRDEC Scientific Conference on Obscuration and Aerosol Research*, CRDEC, U. S. Army, 1990 (with J. Carls)
- "Aerosol jet etching", *Aerosol Sci. Tech.*, 12, 842-856 (1990) (with Y. L. Chen and I. Trachtenberg)
- "A study of low pressure impaction processes", *J. Aerosol Science* 20, 560, 1989. (with B. Jurcik and I. Trachtenberg)
- "Laser-induced breakout and detonation waves in droplets: II. Model", *J. Optical Soc. America B*, In Press, 1990. (with J. C. Carls and Y. Seo)
- "Distributions for moment simulation of aerosol evaporation", *In Press Journal of Aerosol Science* 1990 (with Y. Seo)
- "Comparison between theory and experiment for laser-induced plasma and shock waves in droplets", *Proceedings of the 1989 CRDEC Scientific Conference on Obscuration and Aerosol Research*, CRDEC, U. S. Army, In Press, 1990 (with J. Carls)
- "Statistical properties of windows in atmospheric plumes", *Proceedings of the 1990 CRDEC Scientific Conference on Obscuration and Aerosol Research*, CRDEC, U. S. Army, In Press, 1990
- "Alkane oligomerization and graphite fiber formation in an electrocatalytic system", *Proceedings of the 1990 CRDEC Scientific Conference on Obscuration and Aerosol Research*, CRDEC, U. S. Army, In Press, 1990
- "Particle formation by homogeneous nucleation in expanding flows", *Proceedings of the 1990 CRDEC Scientific Conference on Obscuration and Aerosol Research*, CRDEC, U. S. Army, In Press, 1990 (with B. Jurcik)
- "A finite element solution of the Maxwell equations for absorption and scattering of electromagnetic radiation by a sphere" *Proceedings of the 1990 CRDEC Scientific Conference on Obscuration and Aerosol Research*, CRDEC, U. S. Army, In Press, 1990 (with L. Liebmann)
- "Aerosol jet etching of  $Hg_{1-x}Cd_xTe$ ", *Applied Physics Letters* 56 1682-1685 (1990) (with B. J. Jurcik and I. Trachtenberg)
- Particle formation by homogeneous nucleation in expanding flows" Submitted for publication (1990) (with B. J. Jurcik)
- "Theory and experiment on laser assisted etching of silicon", *In Press, AIChE Symposium Series*, 1990.
- "A new process for graphite fiber formation from alkane vapors", Submitted for publication, 1990.

### ABSTRACT

A computer model is used to study laser-induced plasma formation and explosion of single droplets. The model accounts for the evolutions of the plasma and the resulting fluid flow. The model shows all the qualitative features of experiments, including laser-supported detonation waves. In addition quantitative agreement with measured wave velocities is obtained to within better than 50%. Results are presented here for wave velocities as a function of average laser intensity.

### INTRODUCTION

The problem of laser-induced breakdown (LIB) of small droplets has been the subject of many recent studies<sup>e.g. 1-10</sup>. Chang and coworkers have developed experimental techniques<sup>e.g. 1-6</sup> permitting detailed study of laser-induced breakdown (LIB) of small droplets. Most recently, they have reported a new diagnostic technique<sup>6</sup> which gives both temporal and spatial information on LIB-generated plasma at two selectable wavelengths. In this Journal, they have reported new results<sup>8</sup> using this technique for LIB of a single water droplet containing Na salts exposed to single

and multiple laser pulses. In this manner, they have been able to compare propagation speeds of H and Na in the exploding droplet and to obtain information on cooling rates of the plasma at various positions. Such information is essential in formulating models for the LIB processes in particles.

#### THE MODEL

We have previously described<sup>7</sup> theoretical results from a one dimensional model that describes the evolution of the LIB plasma and the resulting fluid flow. The model agreed well with the experimental results, giving all the qualitative features of an experiment of Hsieh et al<sup>5</sup>, including laser-supported detonation waves. In addition, the model gave quantitative agreement with measured fluid velocities<sup>5</sup> to within around 50%.

We have used the model to examine the most recent experiments of Zheng et al<sup>8</sup> on LIB of small droplets. Here we give the wave velocities as a function of average laser intensity and compared with some of the available experimental data<sup>8</sup>. We begin by briefly describing the model, the equation of state data base, and the calculation procedures employed for the plasma properties; a more extensive discussion of the model may be found in Carls and Brock<sup>9</sup>; a detailed discussion of the model is contained in the dissertation of Carls<sup>11</sup>.

All experiments on LIB of small droplets by visible lasers have been carried out in the geometrical optics regime. Thus, due to focussing by the droplet, any heating is non-uniform and so the resulting fluid flow is two dimensional. Nonetheless, we have shown previously that a one dimensional model of the flow illustrates many of the features of the flow that are observed during LIB<sup>7</sup>. The reason for the success of the 1-d model is that, at very high irradiance, the laser forces a very directional (planar) response of the fluid. Also, because the shock waves are strong, they are very narrow and minimize distortions of the planar shocks by the droplet geometry. Thus, during the laser pulse the most important hydrodynamic flows occur down the laser axis. Two dimensional effects come to dominate the flow at later times or after the laser pulse ends.

The system we simulate<sup>8</sup> consists of a water droplet, surrounded by air and irradiated by a laser at 532 nm. The one dimensional Cartesian model represents the droplet as a region of high density (the liquid water) surrounded on either side by regions of low density (air). The model does not include prediction of the initiation of breakdown. Instead, a small region of plasma is initially assumed to have formed. In the model, this region is represented as a thin slab located close to the shadowed side of the "droplet," as observed in the experiments<sup>8</sup>. The model predicts the subsequent growth and evolution of the plasma during the laser pulse as well as the evolution of nonionized regions, including the breakdown of initially nonionized material. Coupling of the plasma to the laser radiation is included explicitly.

The plasma is assumed to be at local thermodynamic equilibrium (LTE) and thus, as the plasma heats or cools, its properties change according to its equation of state. The model does not include an explicit breakdown mechanism but allows formation and recombination of plasma as the local equilibrium result of compressional or radiative heating or cooling due to expansion. LTE is a reasonable assumption in this case because the high fluid densities (0.1 - 1 g/cm<sup>3</sup>) yield very high collision rates and short relaxation times. The pressures are sufficiently high that ionization can occur by the pressure mechanism.

The laser beam is assumed to propagate (largely unattenuated) into the droplet until reaching the plasma. There, part reflects from the plasma/liquid interface and the rest is transmitted or absorbed. (The assumption that there is a distinct interface is justified later in the paper.) Because of the high temperature of the initial plasma region (30000 K), its pressure is very high (~500000 atm). Thus at  $t > 0$  this region literally explodes into the surrounding regions. The resulting fluid flow changes the plasma optical properties. In addition, as the plasma heats, it drives the fluid flow. Thus, absorption varies with time and position. This nonlinear coupling between the droplet and the laser beam is an essential feature of the LIB process after plasma initiation.

The fluid flow of both the nonionized and the plasma regions is described by the Euler equations:

$$\partial p / \partial t + \partial (\rho v) / \partial z = 0 \quad (1)$$

$$\partial(\rho v)/\partial t + \partial(\rho v v)/\partial z = -\partial P/\partial z \quad (2)$$

$$\partial(\rho E)/\partial t + \partial(\rho v(E + P))/\partial z = S_{rad}(z) \quad (3)$$

Here, for the one dimensional model,  $t$  is time and  $z$  is the direction defined by the laser beam.  $\rho$  is the mass density,  $v$  the  $z$  component of the fluid velocity,  $p$  the fluid pressure,  $E$  is the combined specific kinetic and internal energy, and  $S_{rad}(z)$  is the energy absorption rate from the laser per unit volume.

Equations (1), (2), and (3) were solved using the Flux Corrected Transport (FCT) method pioneered by Boris and Book<sup>12</sup>. This technique is a stable, conservative method for solving hyperbolic partial differential equations, and is especially effective in the calculation of flows containing shock waves. We used an FCT algorithm having higher order phase accuracy that computes blast waves more effectively than the original version<sup>13</sup>. The calculation was explicit in time.

The gradient of the pressure,  $\partial P/\partial z$ , drives fluid motion through the momentum equation (2). The extent to which the pressure is reliably predicted for a substance determines, in part, how well the hydrodynamic simulation corresponds to observed behavior. For LIB, the fluid states must include plasma states. By assuming local thermodynamic equilibrium for the plasma and the other fluid states, the pressure can be obtained through an equation of state (EOS) solely as a function of the mass density and internal energy of the fluid. Thus, an EOS that reliably predicts the equilibrium properties of the liquid, vapor, supercritical and plasma states of water over a very wide range of temperatures and densities is necessary.

For the liquid, vapor and supercritical states of water, the EOS of Kestin et al<sup>14</sup> and Haar et al<sup>15</sup> have been used. These authors give Helmholtz free energy as a function of density and temperature [  $A = A(\rho, T)$  ]. For the plasma state, the EOS compiled by Ree<sup>16</sup> was used. This plasma EOS is a combination of experimental data where available, and theoretical predictions where necessary. Ree's EOS was used in the range of densities between 1 - 4 g/cm<sup>3</sup>, and temperatures between 3000 - 120000 K. The most extreme conditions encountered in the simulations were densities somewhat more than twice the normal liquid density (2.2 g/cm<sup>3</sup>), and temperatures around 50000 K. The various EOS had to be lapped together consistently at their boundaries to provide a smooth transition from one EOS to the next.

The next step in modelling the LIB system is to specify the source term,  $S_{rad}(z)$ . This term accounts for heating of the fluid by absorption of laser radiation, and requires knowledge of the interaction of the fluid with the laser radiation. The most important of these is the plasma's interaction with the light since nonionized regions are essentially transparent. The model presented for this interaction is simple yet still represents the essential features of the plasma. To model the plasma/laser interactions one must describe the optical properties of the plasma. Of course, these properties vary as a function of position and time because of fluid flow and nonuniform heating. The model accounts for spatial variations of the plasma properties. The complete optical properties of a material are described by its dielectric function,  $\epsilon = \epsilon' + i\epsilon''$ , composed of its real and imaginary parts. The Drude model<sup>17</sup> was used to determine the dielectric function of the plasma in this calculation.

#### PLASMA WAVE VELOCITIES

An experimental observable in many investigations is the wave velocity. We report here average wave velocities as a function of average laser intensity (for a 50 nsec pulse). Fig. 1 shows the three waves studied--namely, the shadow side blast wave, the illuminated side liquid shock and the illuminated side blast wave. The calculation in our model begins with a plasma layer imbedded in the droplet, close to the shadow side of the droplet, as indicated in Fig. 1. Immediately, two identical compression waves erupt from the plasma region. The two waves form when the high pressure initial plasma region explodes in both directions, compressing and ionizing the adjacent liquid. At early times these two waves are nearly identical, but the wave nearest the shadow face

quickly leaves the droplet, causing rapid decompression and heating the surrounding gas. The shock accelerates into a blast wave as it enters the gas phase, forming the shadow side blast wave.

The second shock, moving through the droplet and toward the laser, also compresses, heats, and ionizes the liquid that it traverses. The shock strength determines the initial degree of ionization. As the liquid ionizes, it absorbs radiation, leading to further ionization. With sufficient ionization, the liquid becomes a plasma and absorbs strongly. Thus two ionization mechanisms are in operation-- so-called pressure ionization and laser heating. Strong laser heating can only occur after pressure ionization has ionized the liquid sufficiently. At very high laser intensities, the high intensity causes the shocked ionized liquid to absorb more energy than it uses compressing. The resultant higher ionization leads to higher absorption; the flow becomes self-accelerating. The shock grows strong enough to ionize the liquid completely, and so the liquid absorbs strongly, immediately after the shock passes, without any laser-assisted ionization. This is an optical detonation wave (ODW).

As the illuminated side liquid shock reaches the gas-liquid interface, it breaks out of the droplet, accelerates to high velocities, and strongly compresses the surrounding gas, forming the illuminated side blast wave. At sufficiently high laser intensities this illuminated side blast wave may become an ODW.

Fig. 2 shows a plot of illuminated side average blast wave speed as a function of average laser intensity. The 50 nsec pulse actually is modulated<sup>6</sup>; this modulation is simulated in our calculations. The modulation results in a decreasing slope of the wave speed vs intensity curve. The modulation also tends to inhibit development of a strong ODW. Fig. 3 shows the illuminated side liquid shock speed as a function of average laser intensity. The two experimental points are from the study of Chang et al.<sup>6</sup> and represent the difference between the experimental speeds derived from following the Na emissions and the H $\alpha$  emissions. The movement of the maximum in these emissions is identified with the actual wave movement, although the relation of the peaks in the emissions to any of the fluid waves discussed here has not yet been established. Fig. 4 shows the shadow side blast wave speed as a function of the average laser intensity. This curve shows some interesting detail. At low intensities, the intensity is too low to produce much ionization of the illuminated side liquid shock. Even though the illuminated side waves do not absorb strongly, the radiation is too weak and the degree of ionization of the shadow side blast wave too low to increase the shadow side blast wave speed. Somewhere in the vicinity of 2 GW/cm<sup>2</sup> this all changes. The laser intensity becomes high enough to increase the shadow side blast wave speed, more than compensating for the energy this wave uses in compressing. Finally, at intensities higher than around 10 GW/cm<sup>2</sup>, the illuminated side liquid shock and blast waves are highly ionized and absorb a large fraction of the laser radiation. This causes the shadow side blast wave speed to level off. Additional increases in laser intensity merely ionize more strongly the illuminated side waves, allowing only a decreasing fraction of the increasing total energy to reach the shadow side blast wave to compensate for energy used in compressing. The apparent agreement between experiment<sup>6</sup> and our model results may be regarded as fortuitous for reasons discussed above. Additional experimental measurements would be desirable to explore the interesting behavior indicated in Fig. 4.

As we develop our code for solution of the nonlinear Maxwell's equation for scattering and absorption of laser radiation by particles of arbitrary shape, it would at that time be desirable to extend our code to axisymmetric flows to explore the fascinating new field known as electrohydrodynamics where there is close, nonlinear coupling of Maxwell's equations to hydrodynamics. This is a subject that has hardly been explored as yet either experimentally or theoretically.

#### ACKNOWLEDGMENTS

This work has been supported by CRDEC, U. S. Army. Authors acknowledge with thanks many useful discussions with Professor Richard K. Chang, initiated with the aid of Dr. Ed Stuebing and the CRDEC Scientific Conferences on Obscuration and Aerosol Research.

## REFERENCES

1. S.-X. Qian, J. B. Snow, H.-M. Tzeng, and R. K. Chang, *Science* **231** 486 (1986).
2. W. F. Hsieh, J. H. Eickmans, and R. K. Chang, *J. Opt. Soc. Am.* **B4** 1816 (1987).
3. J. H. Eickmans, W. F. Hsieh, and R. K. Chang, *Appl. Opt.* **26** 3721 (1987).
4. J.-Z. Zhang, J. K. Lam, C. F. Wood, B. T. Chu and R. K. Chang, *Appl. Opt.* **26** 4731 (1987).
5. W. F. Hsieh, J.-B. Zheng, C. F. Wood, B. T. Chu and R. K. Chang, *Opt. Lett.* **12** 575 (1987).
6. J. B. Zheng, W. F. Hsieh, S.-C. Chen and R. K. Chang, *Opt. Lett.* **13** 559 (1988).
7. J. C. Carls and J. R. Brock, *Opt. Lett.* **13** 273 (1988).
8. J.-B. Zheng, W. F. Hsieh, Shu-Chi Chen and R. K. Chang, *This Journal*.
9. P. Chylek, M. Jarzembski, N. Chou, and R. Pinnick, *Appl. Phys. Lett.* **49**, 1475 (1986).
10. R. Pinnick, P. Chylek, M. Jarzembski, E. Creegan, V. Srivastava, G. Fernandez, J. Pendleton and A. Biswas, *Appl. Opt.* **27**, 987 (1988).
11. J. C. Carls, *Nonlinear Interactions between Lasers and Single Small Droplets*, Ph. D. Dissertation, University of Texas, Austin, 1988.
12. J. Kestin, J. V. Sengers, B. Kamar-Parisi, and J. M. H. Levelt-Sengers, *J. Phys. Chem. Ref. Data*, **13** 175 (1984).
13. L. Haar, J. S. Gallagher, and G. S. Kell in J. V. Sengers, Ed. *Proceedings of 8th Symposium of Thermophysical Properties of Water*, vol II, p. 298, A.S.M.E., N.Y., 1982.
14. F. H. Ree, *Equation of State of Water*, Lawrence Livermore National Laboratory, JCRL-52190, 1976.
15. J. D. Jackson *Classical Electrodynamics*, 2nd ed. Wiley, N.Y., 1975.
16. Y.T. Lee and R. M. More, *Phys. Fluids* **27** 1273 (1987).
17. G. A. Lyzenga and T. J. Ahrens *J. Chem. Phys.* **76** 6282 (1982).

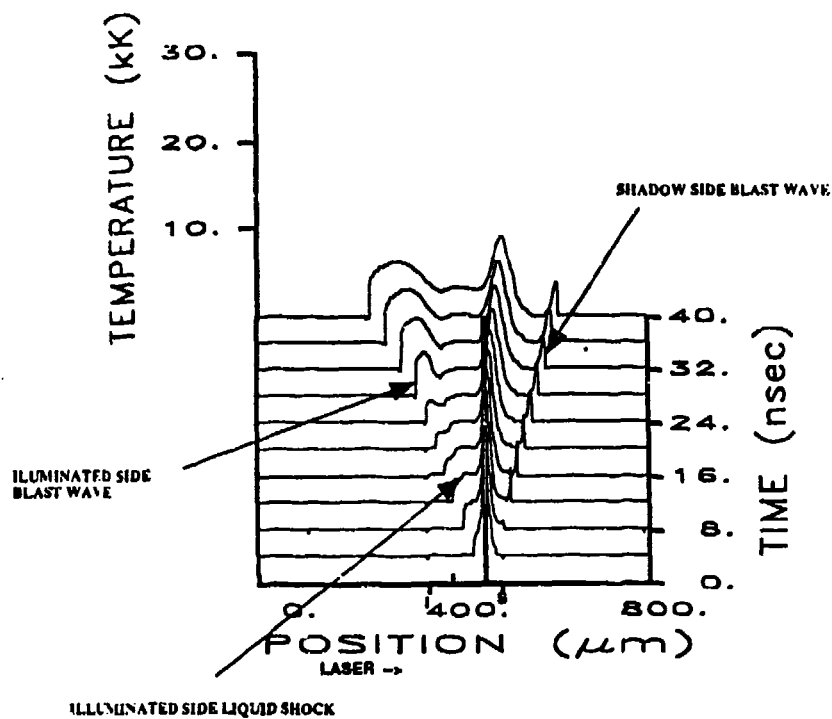


Fig. 1. The three waves whose velocities are studied in this paper.

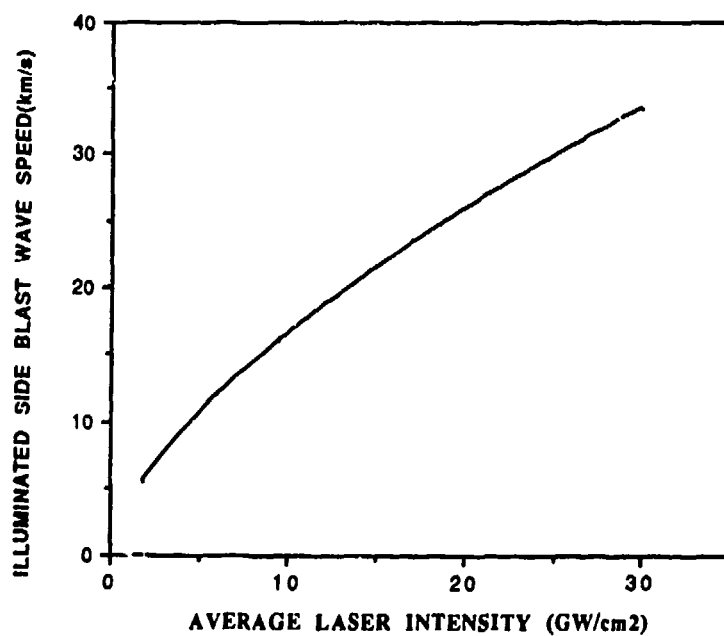


Fig. 2. Illuminated side average blast wave speed as function of average laser intensity.

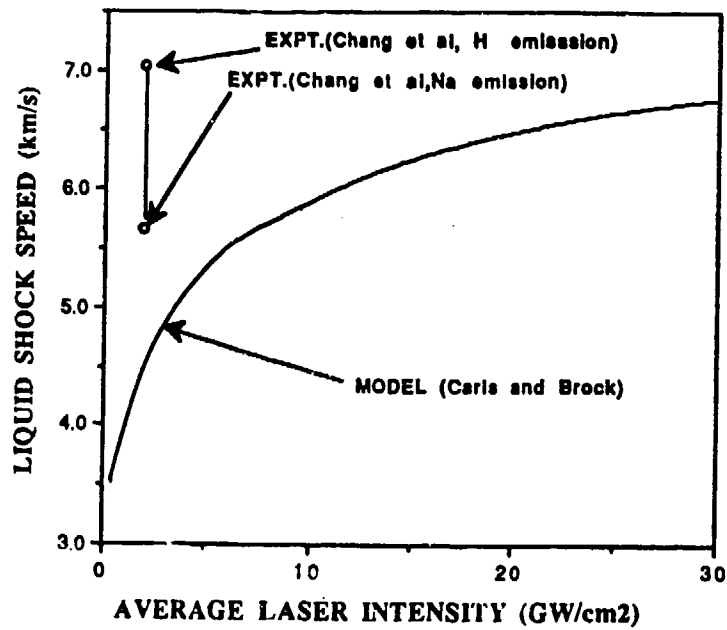


Fig. 3. Illuminated side liquid shock speed as function of average laser intensity.

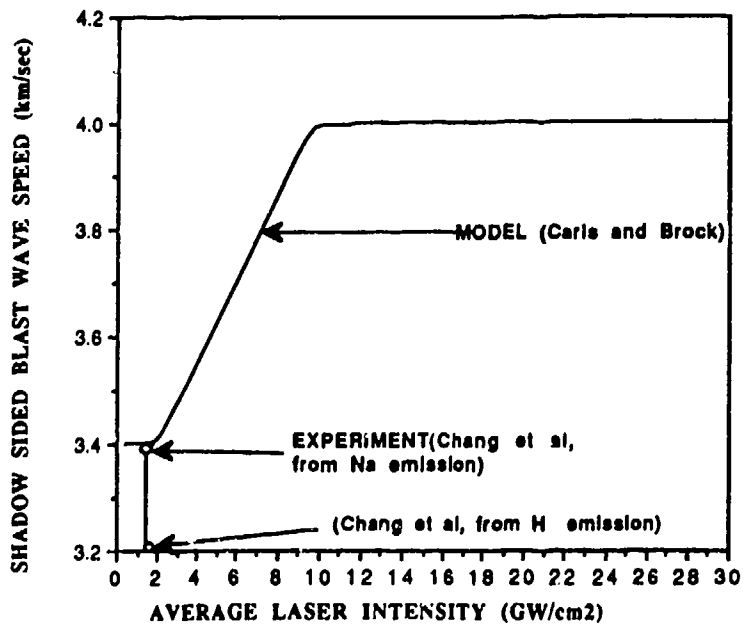


Fig. 4. Shadow side average blast wave speed as function of average laser intensity.

BLANK



## V. OPTICAL PROPERTIES OF AEROSOLS

### A FINITE ELEMENT SOLUTION OF THE MAXWELL EQUATIONS FOR ABSORPTION AND SCATTERING OF ELECTROMAGNETIC RADIATION BY A SPHERE

L. Liebman and J. Brock  
Chemical Engineering Department  
University of Texas, Austin, Texas 78712

#### RECENT PUBLICATIONS, SUBMITTALS FOR PUBLICATION AND PRESENTATIONS

Wave propagation from laser-induced plasmas in droplets"

*Proceedings of the 1990 CRDEC Scientific Conference on Obscuration and Aerosol Research*, CRDEC, U. S. Army, 1990 (with J. Carls)

"Aerosol jet etching", *Aerosol Sci. Tech.*, 12, 842-856 (1990) (with Y. L. Chen and I. Trachtenberg)

"A study of low pressure impaction processes", *J. Aerosol Science* 20, 560, 1989. (with B. Jurcik and I. Trachtenberg)

"Laser-induced breakout and detonation waves in droplets: II. Model", *J. Optical Soc. America B*, In Press, 1990. (with J. C. Carls and Y. Seo)

"Distributions for moment simulation of aerosol evaporation", *In Press Journal of Aerosol Science* 1990 (with Y. Seo)

"Comparison between theory and experiment for laser-induced plasma and shock waves in droplets", *Proceedings of the 1989 CRDEC Scientific Conference on Obscuration and Aerosol Research*, CRDEC, U. S. Army, In Press, 1990 (with J. Carls)

"Statistical properties of windows in atmospheric plumes", *Proceedings of the 1990 CRDEC Scientific Conference on Obscuration and Aerosol Research*, CRDEC, U. S. Army, In Press, 1990

"Alkane oligomerization and graphite fiber formation in an electrocatalytic system", *Proceedings of the 1990 CRDEC Scientific Conference on Obscuration and Aerosol Research*, CRDEC, U. S. Army, In Press, 1990

"Particle formation by homogeneous nucleation in expanding flows", *Proceedings of the 1990 CRDEC Scientific Conference on Obscuration and Aerosol Research*, CRDEC, U. S. Army, In Press, 1990 (with B. Jurcik)

"A finite element solution of the Maxwell equations for absorption and scattering of electromagnetic radiation by a sphere" *Proceedings of the 1990 CRDEC Scientific Conference on Obscuration and Aerosol Research*, CRDEC, U. S. Army, In Press, 1990 (with L. Liebmann)

"Aerosol jet etching of  $Hg_{1-x}Cd_xTe$ ", *Applied Physics Letters* 56 1682-1685 (1990) (with B. J. Jurcik and I. Trachtenberg)

Particle formation by homogeneous nucleation in expanding flows" Submitted for publication (1990) (with B. J. Jurcik)

"Theory and experiment on laser assisted etching of silicon", In Press, AIChE Symposium Series, 1990.

"A new process for graphite fiber formation from alkane vapors", Submitted for publication, 1990.

"Wave propagation from laser-induced plasmas in droplets", Submitted for publication, 1990.

#### ABSTRACT

The problem of scattering and absorption of electromagnetic radiation by particles can be solved analytically for only the simplest cases, but numerical methods allow a straightforward extension to particles with arbitrary inhomogeneities and arbitrary shapes. In this paper a recently developed frequency domain method involving CFD techniques is reviewed and applied to the problem of a dielectric sphere. Numerical results indicating the promise of finite element methods are given and recommendations for further investigations are presented.

#### INTRODUCTION

Mie theory exactly describes the absorption and scattering of a plane electromagnetic wave by a dielectric sphere of arbitrary size and refractive index (van de Hulst, 1957; Kerker, 1969). This conceptually simple analytical solution is well known, but it involves cumbersome computations. Since the advent of high-speed computers, which utilize parallel and vector processing, much effort has been made to improve the analytical scattering

Previously a finite difference method was applied to the problem of a linearly polarized plane electromagnetic wave scattered by a perfectly conducting sphere (Ling, 1988). The results demonstrated the applicability of computational fluid dynamics (CFD) methods to the basic scattering problem. CFD methods offer geometrical flexibility, allowing generalization to more complex shapes and inhomogeneous particles. In this presentation, the investigation is broadened by using a finite element method to model scattering by a dielectric sphere; preliminary results confirm that CFD methods are a promising technique. The objectives of further studies are discussed in the final section.

## THEORY

The problem to be solved consists of a plane polarized wave incident on a dielectric particle; only linear scattering is considered. Assuming  $\exp(i\omega t)$  dependence for all fields, the electric and magnetic fields must satisfy the vector wave equation both inside and outside the particle:

$$\nabla^2 \mathbf{E} + k^2 \mathbf{E} = 0 \qquad \nabla^2 \mathbf{H} + k^2 \mathbf{H} = 0 \qquad (1,2)$$

where  $k^2 = \omega^2 \epsilon \mu$ . Additionally, the boundary conditions:

$$(\mathbf{E}_{\text{out}} - \mathbf{E}_{\text{in}}) \times \hat{\mathbf{n}} = 0 \qquad (\mathbf{H}_{\text{out}} - \mathbf{H}_{\text{in}}) \times \hat{\mathbf{n}} = 0 \qquad (3,4)$$

require that the tangential components of  $\mathbf{E}$  and  $\mathbf{H}$  must be continuous across the surface of the particle (Bohren and Huffman, 1983) and the Sommerfeld radiation condition (Stratton, 1941) requires that the scattered fields represent divergent traveling waves as  $r \rightarrow \infty$ .

By introducing two auxiliary scalar functions, the electric and magnetic Debye potentials,  ${}^e\Pi$  and  ${}^m\Pi$  (Kerker, 1969; Born and Wolf, 1959), it is possible to reduce the vector equations (1) and (2) to a set of uncoupled scalar wave equations:

$$\nabla^2 {}^e\Pi + k^2 {}^e\Pi = 0 \qquad \nabla^2 {}^m\Pi + k^2 {}^m\Pi = 0. \qquad (5,6)$$

The field quantities then can be deduced from the potentials as follows:

$$\mathbf{E} = \nabla \times [\nabla (r {}^e\Pi) \times \hat{\mathbf{r}}] + i\omega\mu \nabla \times (r {}^m\Pi) \qquad (7)$$

$$\mathbf{H} = \nabla \times [\nabla (r {}^m\Pi) \times \hat{\mathbf{r}}] + i\omega\epsilon \nabla \times (r {}^e\Pi). \qquad (8)$$

Since the field variables are oscillatory in nature over the infinite domain it is advantageous to reformulate the problem once again, this time in terms of a generalized amplitude function which eliminates the oscillations due to the incident field (Ling, 1987). By making use of the superposition property of the fields, the Debye potentials outside the particle can be decomposed into incident and scattered components. The scattered components then are written as:

$${}^e\Pi_s = \frac{\cos \phi \sin \theta}{k^2} f_1(r, \theta) \frac{e^{ikr}}{r} \qquad (9)$$

$$m\Pi_s = \sqrt{\frac{\epsilon}{\mu}} \frac{\sin \phi \sin \theta}{k^2} f_2(r, \theta) \frac{e^{ikr}}{r} \quad (10)$$

where  $f(r, \theta)$  is a Debye amplitude function. Similar expressions can be written for the potentials inside the particle. It should be noted that the formulation of equations (9) and (10) inherently restrict one to the consideration of only axisymmetric problems. For asymmetric cases the  $\phi$  dependence of the Debye potentials can not be factored out explicitly and one must solve for  $f(r, \theta, \phi)$ .

By substituting equation (9) into (5) and equation (10) into (6) it can be shown that the problem to be solved becomes:

$$\frac{e^{ikr}}{k^2} \left[ \frac{\partial^2 f_1}{\partial r^2} + 2ik \frac{\partial f_1}{\partial r} + \frac{3}{r^2} \cot \theta \frac{\partial f_1}{\partial \theta} + \frac{1}{r^2} \frac{\partial^2 f_1}{\partial \theta^2} - \frac{2}{r^2} f_1 \right] = 0 \quad (11)$$

$$\sqrt{\frac{\epsilon}{\mu}} \frac{e^{ikr}}{k^2} \left[ \frac{\partial^2 f_2}{\partial r^2} + 2ik \frac{\partial f_2}{\partial r} + \frac{3}{r^2} \cot \theta \frac{\partial f_2}{\partial \theta} + \frac{1}{r^2} \frac{\partial^2 f_2}{\partial \theta^2} - \frac{2}{r^2} f_2 \right] = 0 \quad (12)$$

The boundary conditions (3) and (4) are, in terms of  $f_1$  and  $f_2$ :

$$\frac{\omega^{II} \epsilon^{II} e^{ik^{II}a}}{(k^{II})^2} f_1^{II}(a, \theta) - \frac{\omega^I \epsilon^I e^{ik^I a}}{(k^I)^2} f_1^I(a, \theta) = \frac{\omega^I \epsilon^I}{(k^I)^2 \sin \theta} W(a, \theta) \quad (13)$$

$$\frac{e^{ik^{II}a}}{k^{II}} f_2^{II}(a, \theta) - \frac{e^{ik^I a}}{k^I} f_2^I(a, \theta) = \frac{1}{k^I \sin \theta} W(a, \theta) \quad (14)$$

$$\frac{e^{ik^{II}a}}{(k^{II})^2} \left[ ik^{II} f_1^{II} + \frac{\partial f_1^{II}}{\partial r} \right]_{r=a} - \frac{e^{ik^I a}}{(k^I)^2} \left[ ik^I f_1^I + \frac{\partial f_1^I}{\partial r} \right]_{r=a} = \frac{1}{(k^I)^2 \sin \theta} \frac{\partial W}{\partial r} \Big|_{r=a} \quad (15)$$

$$\sqrt{\frac{\epsilon^{II}}{\mu^{II}}} \frac{e^{ik^{II}a}}{(k^{II})^2} \left[ ik^{II} f_2^{II} + \frac{\partial f_2^{II}}{\partial r} \right]_{r=a} - \sqrt{\frac{\epsilon^I}{\mu^I}} \frac{e^{ik^I a}}{(k^I)^2} \left[ ik^I f_2^I + \frac{\partial f_2^I}{\partial r} \right]_{r=a} = \sqrt{\frac{\epsilon^I}{\mu^I}} \frac{1}{(k^I)^2 \sin \theta} \frac{\partial W}{\partial r} \Big|_{r=a} \quad (16)$$

where:

$$W(r, \theta) = \frac{e^{ikr \cos \theta}}{\sin \theta} - \cot \left( \frac{\theta}{2} \right) \frac{e^{ikr}}{2} - \tan \left( \frac{\theta}{2} \right) \frac{e^{-ikr}}{2} \quad (17)$$

and the radiation condition can be expressed as:

$$\lim_{r \rightarrow \infty} \frac{\partial f_1}{\partial r} = 0 \quad \lim_{r \rightarrow \infty} \frac{\partial f_2}{\partial r} = 0. \quad (18)$$

Equations (13) through (16) are formulated for a spherical particle, where "a" is the radius of the sphere, "I" denotes quantities outside the sphere, and "II" denotes quantities inside

the sphere. For the general asymmetric problem, equations (13) through (16) must be satisfied at all  $(x,y)$  on the particle surface and the partial derivatives are given by  $\nabla f \cdot n$ .

## FINITE ELEMENT METHOD AND CURRENT RESULTS

The system of equations is solved numerically on a Cray X-MP by a finite element method with 9-node Lagrange quadrilaterals (Becker, et al., 1981) that utilizes a frontal solver to invert the matrix (Irons and Ahmad, 1980). A multiplier method (Carey and Oden, 1984) is used to enforce the jump in solution across the particle boundary, which must coincide with element boundaries. The radiation boundary condition is imposed at a finite artificial surface,  $r < \infty$ , using an operator to annihilate the first two terms of the analytical solution (Bayliss, et al., 1982). Both the radiation boundary condition and the jump in flux condition are incorporated into the weak formulation of the differential equation.

Initial investigations have been performed for a spherical water droplet with a  $2 \mu\text{m}$  radius irradiated by a plane wave having  $\lambda = 10.591 \mu\text{m}$ . The refractive index of the particle was  $1.179 + 0.071i$  and the size

parameter was 1.19. To test the validity of the numerical code, the Debye amplitude functions were calculated for the external region alone so that the difficulties encountered in handling the jump conditions could be avoided. Results for this study were compared to the analytical solution and are shown in Fig. 1. As can be seen, excellent agreement was obtained using a  $4 \times 8$  grid and 0.33 sec. of CPU time.

Current studies are focusing on solving the complete problem over the internal and external regions. At this time the jump conditions are being modelled successfully but a numerical problem as  $r \rightarrow 0$  must be resolved. However, results indicate that once this is done the complete problem for this spherical droplet can be obtained accurately with an  $8 \times 8$  grid and approximately 2 sec. of CPU time.

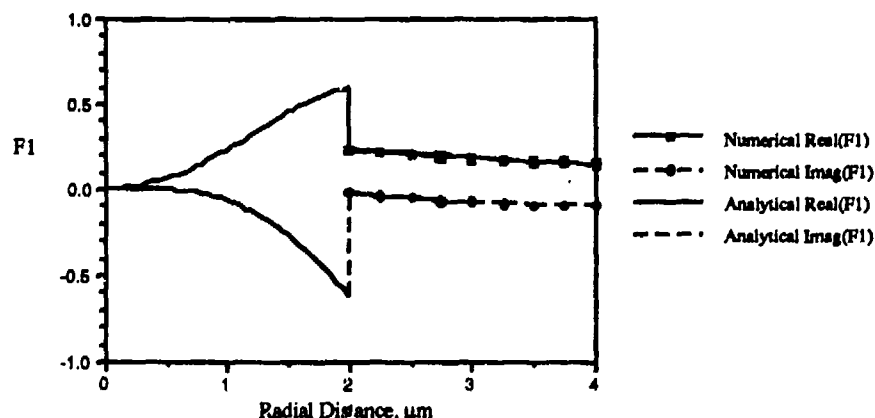


Figure 1. Debye amplitude function  $F1$  along centerline of particle at  $\theta=0$  (forward scattering). Particle radius =  $2 \mu\text{m}$ , wavelength =  $10.591 \mu\text{m}$ , and refractive index =  $1.179 + 0.071i$ .

Another point worth noting concerns far-field solutions, which are often the desired result of the calculations. The complete problem (internal and external regions) was studied for a larger, spherical water droplet (radius of 20  $\mu\text{m}$ ) having a

size parameter of 11.8. For this particle forward scattering was much stronger than backward scattering and field oscillations were present inside the particle. Fig. 2 compares the numerical results for the external region (forward direction) to the analytical ones. Even though inadequate internodal distances in the internal region caused oscillations in the near-external region, the far-field numerical solution was in excellent agreement with the analytical one. Hence it was not necessary to use mesh refinement and completely capture the internal characteristics to obtain accurate far-field solutions. The results in Fig. 2 were obtained in 33.6 CPU sec. using a uniform  $64 \times 16$  mesh.

Summarizing, current results imply that the above finite element, frequency domain (FE-FD) method is a promising technique. Thus far computation times have been low; therefore larger, more arbitrarily shaped particles can be handled with the FE-FD method.

## RECOMMENDATIONS FOR CONTINUED INVESTIGATIONS

Following is a list of recommendations for further investigations; a short description of necessary requirements accompanies each suggestion.

- (1) Consider multilayer spheres  
This is a minor modification which involves adding a second set of jump conditions at the material interface within the spherical particle.
- (2) Consider arbitrarily-shaped axisymmetric particles  
A grid generation routine that allows the user to define an arbitrary surface of revolution must be added.
- (3) Add postprocessor  
For practical applications the results may be needed in terms of the Mueller scattering matrix, normalized source function, or efficiency factors. A postprocessor would calculate the desired quantities from the Debye amplitude functions.
- (4) Improve current algorithm  
To date no time has been spent on code vectorization, implementing a more efficient solver, or utilizing localized grid refinement or adaptive grid techniques. These modifications can reduce CPU time significantly, and may be necessary to obtain accurate results in 3-dimensions.
- (5) Extend the calculations to asymmetric cases

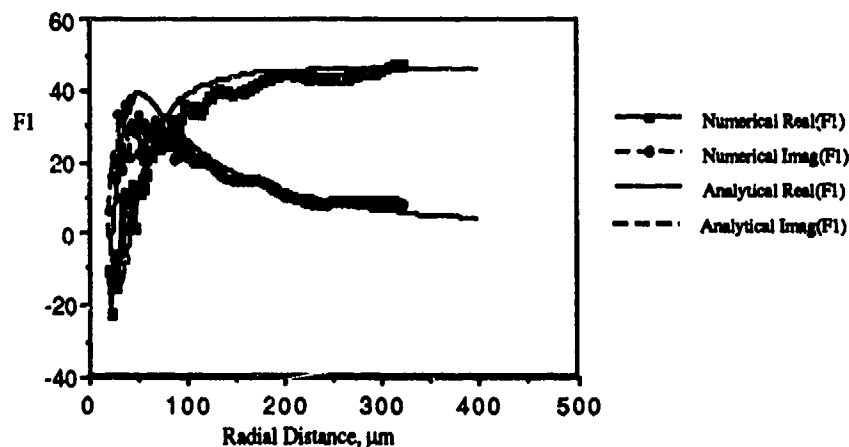


Figure 2. Debye amplitude function  $F1$  along centerline of particle at  $\theta=0$  (forward scattering). Particle radius = 20  $\mu\text{m}$ , wavelength = 10.591  $\mu\text{m}$ , and refractive index =  $1.179 + 0.071i$ .

The Debye amplitude functions must be determined as functions of  $r$ ,  $\theta$ , and  $\phi$ . This involves a straightforward but nontrivial extension to three-dimensional finite elements.

(6) Consider nonlinearities

Considering nonlinear materials where the polarization is a nonlinear function of the electric fields will result in a different, nonlinear differential equation for the Debye amplitude functions. The finite element code must be modified to handle nonlinear equations.

#### ACKNOWLEDGMENTS

This work was supported by CRDEC, U.S. Army. We wish to thank Drs. R. Ling, M. Lax, I. Sindoni and E. Stuebing for helpful discussions on this problem.

#### REFERENCES

- Bayliss, A., M. Gunzburger, and E. Turkel, 1982. *SIAM J. Appl. Math.*, **42**, 430.  
Becker, E. B., G. F. Carey, and J. T. Oden, 1981. *Finite Elements: An Introduction (Vol. I)*, Prentice-Hall, Englewood Cliffs, New Jersey.  
Bohren, C. F., and D. R. Huffman, 1983. *Absorption and Scattering of Light by Small Particles*, Wiley, New York.  
Born, M., and E. Wolf, 1959. *Principles of Optics*, Pergamon, London.  
Carey, G. F., and J. T. Oden, 1984. *Finite Elements: Computational Aspects (Vol. II)*, Prentice-Hall, Englewood Cliffs, New Jersey.  
Irons, B., and S. Ahmad, 1980. *Techniques of Finite Elements*, Ellis Horwood, Chichester.  
Kerker, M., 1969. *The Scattering of Light and Other Electromagnetic Radiation*, Academic, New York.  
Ling, R. T., 1987. *AIAA J.*, **25**, 560.  
Ling, R. T., 1988. *J. Appl. Phys.*, **64**, 3785.  
Stratton, J. A., 1941. *Electromagnetic Theory*, McGraw-Hill, New York.  
van de Hulst, H. C., 1957. *Light Scattering by Small Particles*, Wiley, New York.  
Wiscombe, W. J., 1979. National Center for Atmospheric Research Tech. Note, NCAR TN-140+STR.  
Wiscombe, W. J., 1980. *Appl. Opt.*, **19**, 1505.

# AN APPROXIMATION TO EXTINCTION EFFICIENCY FOR RANDOMLY ORIENTED SPHEROIDS

by

G.R. Fournier and B.T.N. Evans  
Defense Research Establishment Valcartier  
Courcelette, Quebec G0A 1R0 Canada

## RECENT/SUBMITTED PUBLICATIONS

- A) B.T.N. Evans and G.R. Fournier, "Simple Approximation to Extinction Efficiency Valid Over All Size Parameters", *Applied Optics*, to be published 1 Nov. 1990.
- B) G.R. Fournier and B.T.N. Evans, "An Approximation to Extinction Efficiency for Randomly Oriented Spheroids", submitted to *Applied Optics*.
- C) B.T.N. Evans and G.R. Fournier, "A Procedure for Obtaining An Algebraic Approximation to Certain Integrals", to be submitted to *J. Comp. Phys.*

## ABSTRACT

A semi-empirical approximation to the extinction efficiency,  $Q_{ext}$ , for randomly oriented spheroids, based on an extension of the anomalous diffraction formula, is given. Using this formula,  $Q_{ext}$  can be evaluated over  $10^4$  times faster than by previous methods. This approximation has been verified for complex refractive indices  $m = n - ik$ , where  $1.01 \leq n \leq 2.00$  and  $0 \leq k \leq 1$  and aspect ratios from .5 - 4. The approximation is uniformly valid over all size parameters and aspect ratios.

## 1. INTRODUCTION

The calculation of the extinction efficiency for randomly oriented spheroids by either spheroidal functions<sup>1</sup>, the T-matrix method<sup>2</sup> or other more general techniques is computationally expensive. Furthermore, all these techniques are limited in both aspect ratio and size. The approximation presented here is over  $10^4$  times faster and has no limitations in aspect ratio or size.

We know of only two approximations to the extinction efficiency for randomly oriented spheroids  $Q_{ext}$ , the Rayleigh for small particles and the anomalous diffraction (or Eikonal) theory<sup>3</sup> for all sizes. The former gives excellent results for minor axis size parameters typically less than 0.5 whereas the latter always underestimates  $Q_{ext}$  outside the Rayleigh region.

We have previously used<sup>4</sup> the Eikonal approximation in conjunction with edge effect terms (or Fock theory) to develop a simple approximation to  $Q_{ext}$  for spheres for medium to large size parameters (Eikonal-Fock region). Small sizes were handled by the Rayleigh theory. A 'bridging' function was used to smoothly transfer from the Rayleigh region to the Eikonal-Fock region. The same general approach will be used in this report. We found it necessary to modify the Eikonal approximation for spheroids with large aspect ratios ( $> 4$ ) and in addition appropriate expressions for the Fock terms for oblique incidence had to be derived.

## 2. DEVELOPMENT OF THE EXTINCTION FORMULA

### 2.1 Extended Eikonal Approximation

The Eikonal formula is derived by assuming that the incident plane wave is not significantly skewed in passing through the scattering object and that, to first order, the effect of the scatterer is to locally

retard the phase of the wave and attenuate its amplitude<sup>5</sup>. The strict limit of validity of the formula is therefore the region where  $(n - 1) \ll 1$ . The scattering object is in effect treated as an irregular disc normal to the incident wave and possessing a spatially dependent phase and amplitude. The Fraunhofer pattern at infinity is then derived and  $Q_{ext}$  evaluated from the standard relations. For a spheroidal scatterer, this procedure leads immediately to the following formula<sup>6</sup>:

$$Q_v = \text{Re} \left\{ 2 + 4 \frac{e^{-\omega}}{\omega} + 4 \frac{(e^{-\omega} - 1)}{\omega^2} \right\} \quad [1]$$

where  $\omega$  is given by

$$\omega = i\Delta\psi, \quad \Delta\psi = 2(m - 1) \frac{rb}{p} \quad [2]$$

and

$$p = \sqrt{\cos^2 \theta + r^2 \sin^2 \theta}, \quad a = 2\pi\alpha/\lambda, \quad b = 2\pi\beta/\lambda, \quad m = n - ik. \quad [3]$$

Where  $r = a/b$  is the aspect ratio (for prolates  $r > 1$  and for oblates  $r < 1$ ),  $\alpha$  is the length of the semi-axis of rotation,  $\beta$  is the other axis of the spheroid,  $\theta$  is the angle between the incident radiation and the  $\alpha$  or  $a$  axis,  $\lambda$  is the wavelength of the scattered radiation and  $m$  is the complex index of refraction. Hence  $a$  and  $b$  are the two size parameters associated with the spheroid and  $p$  can be considered a projection operator of the penumbral ellipse (the ellipse defined by the shadow line on the surface of the spheroid) onto the plane perpendicular to the direction of the incoming radiation.

Equation 1 has the same form as that for the sphere but with a variable change. The radius of the sphere has been replaced by half the distance covered by the ray that traverses the spheroid through its centre. This similarity in form is due to the fact that the spheroid is an affine transformation of the sphere. However  $\Delta\psi$ , the phase difference through the particle is not correct. For large aspect ratios and indices much different from one the phase of the diffraction peaks for randomly oriented spheroids becomes incorrect when compared with exact results. A similar effect was noticed by Stephens<sup>6</sup> for infinite cylinders.

As a result of the above discussion we have slightly modified the Eikonal approximation. Now the deviation of the central ray is taken into account when computing its phase difference. This new  $\Delta\psi$  replaces the Eikonal  $\Delta\psi$ . Figure 1 shows this modification. Strictly speaking, the form of equation 1 should also be modified since, in accounting for the ray deviations, the affine transformation is no longer valid. However, since this is a second order effect we have chosen to keep the form of equation 1 but use instead the new  $\Delta\psi$  as the variable.

After some straightforward but tedious algebra the new  $\Delta\psi$  is found to be

$$\begin{aligned} \omega = i\Delta\psi &= ib \left\{ \frac{2r}{p} \left[ \frac{p^2 \cos(\phi) + s \sin(\phi)}{p^2 \cos^2(\phi) + q^2 \sin^2(\phi) + 2s \cos(\phi) \sin(\phi)} \right] \right\} (m - \cos(\phi)) \\ \cos(\phi) &= \frac{s^2 + p^2 \Delta}{m(p^4 + s^2)} \\ \sin(\phi) &= \frac{s^2(p^2 - \Delta)^2}{m^2(p^4 + s^2)^2} \\ \Delta &= [m^2(p^4 + s^2) - s^2]^{1/2} \\ s &= p^2 q^2 - r^2 \\ q &= [r^2 \cos^2(\theta) + \sin^2(\theta)]^{1/2} \end{aligned} \quad [4]$$

In the limiting cases of  $r \rightarrow \infty$  for prolates or  $r \rightarrow 0$  for oblates  $\Delta\psi$  becomes:

$$\Delta\psi = 2b\{(m^2 - \cos^2 \theta)^{1/2} - \sin \theta\} \quad \text{for prolates} \quad [5]$$

$$\Delta\psi = 2a\{(m^2 - \sin^2 \theta)^{1/2} - \cos \theta\} \quad \text{for oblates} \quad [6]$$

These expressions give good results when  $Q_{ext}$  is evaluated for randomly oriented spheroids. They are not always good for oriented spheroids however. The orientations for which the expressions do



poorly are strongly weighted against in the angular averaging process. The angular averaging is carried out as follows:

$$\overline{Q_v} = \frac{\int_0^{\pi/2} Q_v p \sin \theta d\theta}{\int_0^{\pi/2} p \sin \theta d\theta} \quad [7]$$

## 2.2 Edge Effects

Equation 7 gives by itself a remarkably close fit to  $Q_{ext}$  for randomly oriented spheroids considering the rather crude assumptions involved in its derivation. Equation 7 however approaches the large particle asymptotic limit of 2 from below, and it is well known that  $Q_{ext}$  approaches that same limit from above. The reason for this discrepancy is the neglect of edge effects. Jones<sup>7</sup> has shown how to estimate these edge effects for three dimensional convex bodies. As he clearly explains, near a glancing point the body will behave approximately like a cylinder with its axis perpendicular to the surface normal (at the glancing point) and the direction of propagation of the incident wave. The scattering and absorption from all such cylindrical sections can be integrated around the projection of the penumbral curve to give the total contribution of the edge effects to the extinction cross section. The projection is on to the plane normal to the incident ray direction. The energy scattered per unit length of the cylinder by region on its surface around the glancing point is proportional to  $c_{TE}R^{1/3}$  for the TE mode and  $c_{TM}R^{1/3}$  for the TM mode, where  $R$  is the radius of curvature of the cylinder. The constants  $c_{TE}$  and  $c_{TM}$  are the first order Fock terms. It can be shown that, for convex bodies, randomly oriented or illuminated by a randomly polarized beam,  $(c_{TE} + c_{TM})/2 = c_0$  where  $c_0$  is a universal constant. Since for the sphere  $c_0 = 0.996193$ , as derived by Nussenneig and Wiscombe<sup>8</sup>, this value can be used for any convex body. Therefore the edge contribution to the extinction efficiency of the body is

$$Q_{edge} = \frac{c_0}{S} \int_P R^{1/3} ds \quad [8]$$

where  $S$  is the projected area of the body on a plane normal to the direction of propagation of the incident wave and  $s$  is the arc length along the projection of the shadow boundary  $P$  on that same plane.

From basic solid geometry for the spheroid the terms in [8] can be shown to be as follows:

$$S = \pi b^2 p, \quad ds = bq' d\chi \quad \text{and} \quad R = \frac{br^2 q'}{p^3} \quad [9]$$

where  $q' = \sqrt{\sin^2 \chi + p^2 \cos^2 \chi}$

and  $\chi$  is the parametric angle of the penumbral ellipse. Thus substituting into [8] and using equation 13.1.9 from<sup>9</sup> we obtain

$$Q_{edge} = \frac{4}{\pi} \frac{c_0 r^{2/3}}{b^{2/3} p^2} \int_0^{\pi/2} q'^{4/3} d\chi \quad [10]$$

$$= \frac{2c_0 r^{2/3}}{b^{2/3} p^2} {}_2F_1(-2/3, 1/2; 1; (1 - 1/p^2)) \quad (\text{prolates}) \quad [11]$$

$$= \frac{2c_0 r^{2/3}}{b^{2/3} p^2} {}_2F_1(-2/3, 1/2; 1; (1 - p^2)) \quad (\text{oblates}) \quad [12]$$

Jones<sup>7</sup> derived a similar result but only for normal incidence. The hypergeometric function in the above equations is readily approximated<sup>10</sup> with relative error of less than  $5.3 \times 10^{-5}$  by

$${}_2F_1(-2/3, 1/2; 1; z) = \frac{.999947 - 2.19081z + 1.51871z^2 - .325449z^3}{1 - 1.85884z + .947705z^2 - .0847327z^3}, \quad |z| \leq 1. \quad [13]$$

The large particle limit for the spheroid is

$$Q_{ext} \rightarrow 2 + Q_{edge}. \quad [14]$$

We now wish to produce a term  $T$  which, when it multiplies [1], gives the same limit as [14] without diverging as the size parameter goes to zero. An adequate expression for our purposes is:

$$T = 2 - e^{-Q_{edge}/2} \quad [15]$$

We used the same form of  $T$  for the sphere<sup>4</sup>.

### 2.3 Bridging Function

If we expand [1] in powers of  $\omega$ , we obtain the following result<sup>5</sup>

$$Q_v = 4\text{Re}\left\{\frac{\omega}{3} - \frac{\omega^2}{8} + \frac{\omega^3}{30} - \frac{\omega^4}{144} + \dots\right\}. \quad [16]$$

The linear and cubic terms are only present when the scatterer has finite absorption. The first-order pure scattering term is quadratic in the  $Q_v$  formula as opposed to quartic in the Rayleigh formula. Adjustments of the constants will not bring about an asymptotic match. As in the case of spheres<sup>4</sup> the approach taken to this problem was to directly use the Rayleigh approximation<sup>11</sup>, and assure an explicit bridging of our expression from  $Q_{ray}$  to  $Q_v T$  as the size parameter increased. We found by repeated trial and error that the most satisfactory formulation is given by:

$$Q_{app} = \frac{Q_{ray}}{\left[1 + \left(\frac{Q_{ray}}{Q_v T}\right)^\mu\right]^{1/\mu}} \quad [17]$$

where  $\mu$  is the following function of size parameter

$$\mu = \alpha + \frac{\gamma}{x}. \quad [18]$$

where  $x = \Delta\psi/(m - \cos\phi)$  and  $\alpha$  and  $\gamma$  are adjustable parameters discussed below.

When  $x$  tends to 0 ( $b \rightarrow 0$ ),  $\mu$  goes to infinity and  $Q_{app}$  becomes equal to the Rayleigh formula. As the size parameter increases,  $Q_{ray}$  usually grows to very large values and  $Q_{ext}$  approaches  $Q_v T$ . Note that our formula satisfies both asymptotes simultaneously. The behaviour of our approximation in the transition region between the Rayleigh limit and the extended Eikonal-Fock limit is completely controlled by the values of  $\alpha$  and  $\gamma$  in [18]. These are, in general, functions of both the complex and real part of the index of refraction. We have found that the same expressions for  $\alpha$  and  $\gamma$  as those we obtained for spheres<sup>4</sup> were adequate for randomly oriented spheroids:

$$\alpha = \frac{1}{2} + [(n-1) - \frac{2}{3}\sqrt{k} - \frac{k}{2}] + [(n-1) + \frac{2}{3}(\sqrt{k} - 5k)]^2 \quad [19]$$

and

$$\gamma = \left[\frac{3}{5} - \frac{3}{4}(n-1)^{1/2} + 3(n-1)^4\right] + \frac{5}{\frac{6}{5} + \frac{(n-1)}{k}}. \quad [20]$$

Finally for randomly oriented spheroids we must integrate [17] over all orientations. This gives

$$\overline{Q_{app}} = \frac{\int_0^{\pi/2} Q_{app} p \sin\theta d\theta}{\int_0^{\pi/2} p \sin\theta d\theta} \quad [21]$$

It should be pointed out that the bridging function is not necessary if  $Q_{ext}$  is only required outside the transition region. In this case  $Q_{app} = Q_{ray}$  or  $Q_{app} = Q_v T$  according to the region of interest.

### 3. RESULTS

Figure 2 shows the comparison between our approximate formula and the T-matrix calculation for the approximate index of glass in the visible,  $n = 1.5$  and aspect ratio  $r = 2$ . There is an excellent general agreement over the complete range of  $b$ . The differences are mainly caused by the surface wave resonances<sup>12</sup> which are not included in the approximation. However this effect is much less pronounced than it is for the sphere,  $r = 1$ .

Another physically interesting case, but this time with a large absorption coefficient is shown in Fig. 3. This case is with  $m = 1.5 - 0.1i$  and  $r = 2$ . The strong absorption and the relatively small value  $n$  combine to completely damp the surface wave resonances. Consequently the fit is excellent everywhere. In this case our largest relative error is located in the transition region between the Rayleigh limit and the extended Eikonal-Fock limit. This occurs at the smaller values of  $b$ , typically  $< 1$ . This effect cannot be seen in Fig. 3 because of the scale used.

Figures 4 and 5 contain examples where the T-matrix method as coded by P. Barber begins to show numerical instabilities because of ill conditioning. For large values of  $k$  the internal field is very small and therefore it is difficult to achieve accurate boundary matching conditions. Large values of  $r$  also create ill conditioning due to the excessive curvature of the surface of the spheroid. Figure 4 is for  $m = 1.5 - 1.0i$  and  $r = 2$  and Fig. 5 is for  $m = 1.5$  and  $r = 4$ . For the sake of clarity, the large oscillations due to ill conditioning, which occur beyond  $b \approx 7$ , are not shown in Fig. 4. More modest but still serious oscillations are shown in Fig. 5. Additional confirmation that the T-matrix code is unstable at this point was obtained by analysis of the backscatter efficiency. Up to the point where the T-matrix code is deemed valid our approximation is very good.

A case of large aspect ratio is shown in Fig. 6 and is compared with the randomly oriented cylinders<sup>13</sup>. Here  $m = 1.5$  for both cases and  $r = 100$  for the spheroids (larger aspect ratios e.g.  $r = 10^4$  make no essential difference). It is interesting to note that the phase of the diffraction peaks are not well matched and the magnitudes of the peaks and troughs are quite different. The spheroid shows a very strong damping as a function of size parameter. Most of the contribution to  $Q_{ext}$  occurs at normal incidence for both infinite cylinders and spheroids of very high aspect ratio. The location of the diffraction peaks is therefore insensitive to  $a$  and depends only on the semi-minor axis of the spheroid  $b$  or the radius of the cylinder. The damping of the diffraction peaks is weaker and their location is different for infinite cylinders than prolate spheroids because the phase difference is constant along the cylinder axis but varies from a maximum to zero along the axis of the spheroid. This gives rise to the engaging possibility of easily distinguishing the extinction of randomly oriented long cylinders from that of high aspect ratio randomly oriented prolate spheroids. The insensitivity of  $Q_{ext}$  to sufficiently large aspect ratios implies that it is also insensitive to the length distribution. We do not know of any experimental or theoretical values with which to compare this type of result and thus we consider it new.

Figure 7 is a contour plot of the maximum percent error between the approximate formula  $\overline{Q_{app}}$  and  $Q_{ext}$  as calculated by the T-matrix method for the semi-major axis size parameter  $a$  varying from 0.1–30, in steps of 0.1. The real part of the index ranges from 1.0 to 2.0 and the imaginary part of the index ranges from  $10^{-8}$  to .1 and  $r = 2$ . For  $n \geq 1.05$ , errors greater than 5% occur due to resonances. For  $n < 1.05$ , the large percentage errors are caused by the transition region. Similar results can be obtained for other aspect ratios.

All our approximate  $Q_{ext}$  results in this section were produced at a rate of greater than  $10^4$  times faster than by the T-matrix code. If larger size parameters or larger refractive indices were requested a much larger speed-up factor would be obtained.

### 4. LIMITATIONS

The formula for  $Q_{ext}$ , [21], has no limitations in terms of size parameter or aspect ratio. In its current form the formula has refractive index limitations. These fall under three categories:

- Very large  $n$  (i.e.  $n > 10$ );
- Very large  $k$  (i.e.  $k > 1$ );
- For  $n > 2$  and values of  $b$  in the transition region (approximately between the Rayleigh region and the first diffraction peak).

For very large  $n$  the physics in  $Q_{ext}$  must be modified. In particular the first Fock constant changes towards its value at  $n = \infty$  ( $c_0 = .0659708$ ) as  $n$  increases due to changing boundary conditions<sup>8,14</sup> and the Rayleigh scattering coefficients are increased from 8/3 to 10/3<sup>12</sup> due the increasing magnetic dipole contributions.

As in the case of spheres, for spheroids in the Rayleigh limit with very large  $k$ , the equation for  $Q_{abs}$ , must include a complicated cubic term<sup>5</sup>.

The restriction in item 3. above is due to the fitting of  $\alpha$  and  $\gamma$  over a restricted range of  $n$ <sup>4</sup>. This restriction is not present outside the transition region in which case only  $Q_v T$  or  $Q_{ray}$  needs to be computed.

### CURRENT AND FUTURE WORK

The limitations, as mentioned in the last section have or are being overcome by additional physics. Additionally, the numerical integrations that are required in the randomizing process have been replaced by approximate analytic expressions that will retain the essential physics, avoid numerical problems that occur from highly oscillatory kernels and allows for the extinction efficiency to be computed and additional 6 times faster. Work is currently focussing also on the absorption efficiency. All this work will be reported in forthcoming papers.

### 6. ACKNOWLEDGEMENT

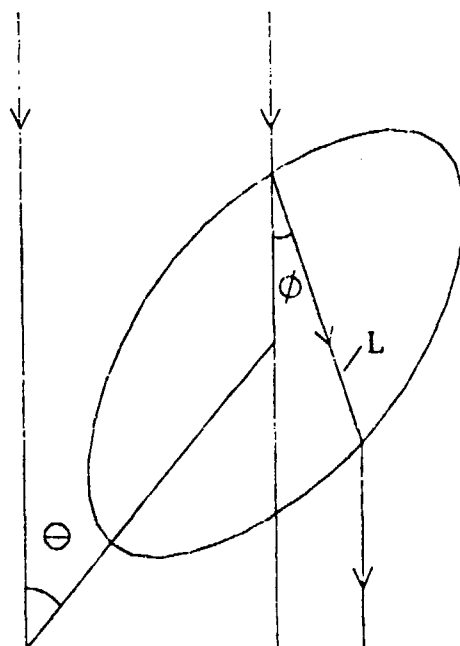
The authors would like to thank Dr. Peter Barber for generously making available his T-matrix spheroid code without which this work could not have been carried out.

### 7. REFERENCES

1. Asano, S. and Yamamoto, G., "Light Scattering by a Spheroidal Particle", *Applied Optics*, 14, 29, 1975.
2. Barber, P.W., Hill, S.C. and Hill, A.C., "Light Scattering by Size/Shape Distributions of Soil Particles and Spheroids", *Applied Optics*, 23, 1025, 1984.
3. Greenberg, J.M. and Meltzer, A.S., "The Effect of Orientation of Non-Spherical Particles on Interstellar Extinction", *Astrophys. J.*, 132, 667, 1960.
4. Evans, B.T.N. and Fournier, G.R., "A Simple Approximation to Extinction Efficiency Valid Over All Size Parameters," *Applied Optics*, 1 Nov., 1990.
5. Van de Hulst, H.C., "Light Scattering by Small Particles," Wiley, New York, 1957.
6. Stephens, G.L., "Scattering of Plane Waves by Soft Obstacles: Anomalous Diffraction Theory for Circular Cylinders," *Applied Optics*, 23, 954, 1984.
7. Jones, D.S., "High-Frequency Scattering of Electromagnetic Waves," *Proc. Roy. Soc. A*240, 206, 1957.
8. Nussenzveig, H.M. and Wiscombe, W.J., "Efficiency Factors in Mie Scattering", *Phys. Rev. Lett.*,

45, 1490, 1980.

9. Erdélyi, A., Magnus, W., Oberhettinger, F., and Tricomi, F.G., "Tables of Integral Transforms, Vol. II", McGraw-Hill, New York, 1954.
10. Wolfram, S., "Mathematica: A System for Doing Mathematics by Computer", Addison-Wesley, New York, 1989.
11. Wang, R.T., "Extinction Signatures by Randomly Oriented, Axisymmetric Particles", Proc. of the CSL Conference on Obscuration and Aerosol Research, June, 1983.
12. M. Kerker, M., "The Scattering of Light and Other Electromagnetic Radiation," Academic Press, New York, 1969.
13. Evans, B.T.N., "An Interactive Program for Estimating Extinction and Scattering Properties of Most Particulate Clouds," Materials Research Laboratory, Melbourne, Victoria, Australia, MRL-R-1123, June 1988.
14. Beckmann, V.P. and Franz, W., "Berechnung der Streuquerschnitte von Kugel und Zylinder unter Anwendung einer modifizierten Watson-Transformation," Z. Naturforschg., 12a, 533, 1957.



## EXTENDED EIKONAL RAY PATHS

Fig.1 Schematic diagram of the extended Eikonal approach.  $\Delta\phi$ , the phase difference is given by  $L(m - \cos\phi)$ . Where  $\phi$  is the deflection angle of the central ray and  $\theta$  is the spheroid orientation angle.

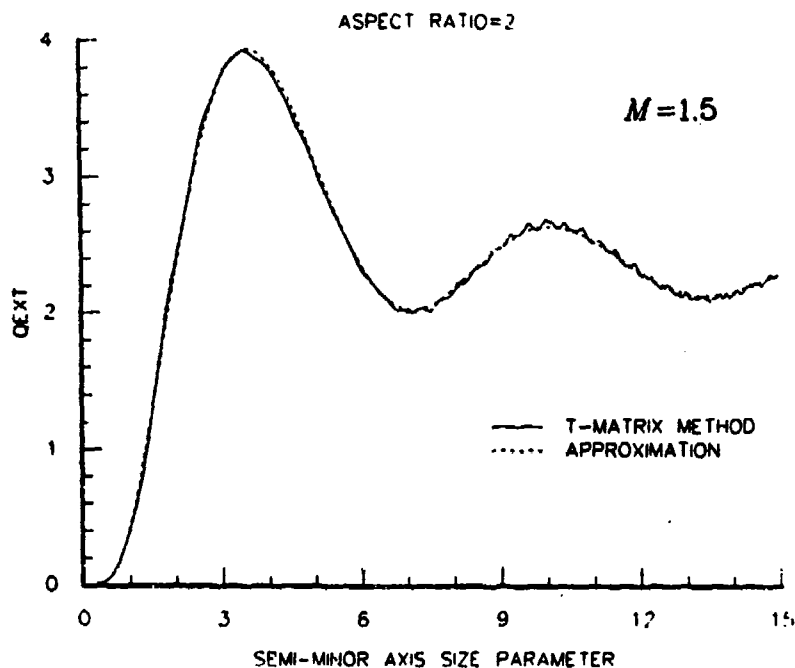


Fig.2 Comparison between approximation and T-matrix method for an index of 1.5 and an aspect ratio of 2.

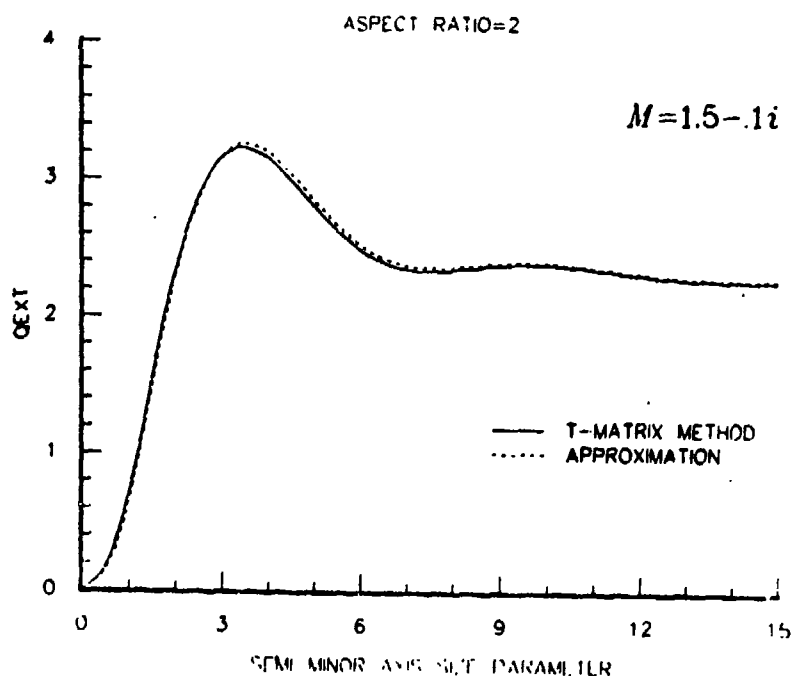


Fig.3 Comparison between approximation and T-matrix method for an index of  $1.5 - .1i$  and an aspect ratio of 2. Surface waves are damped by absorption. Maximum error occurs in transition region.

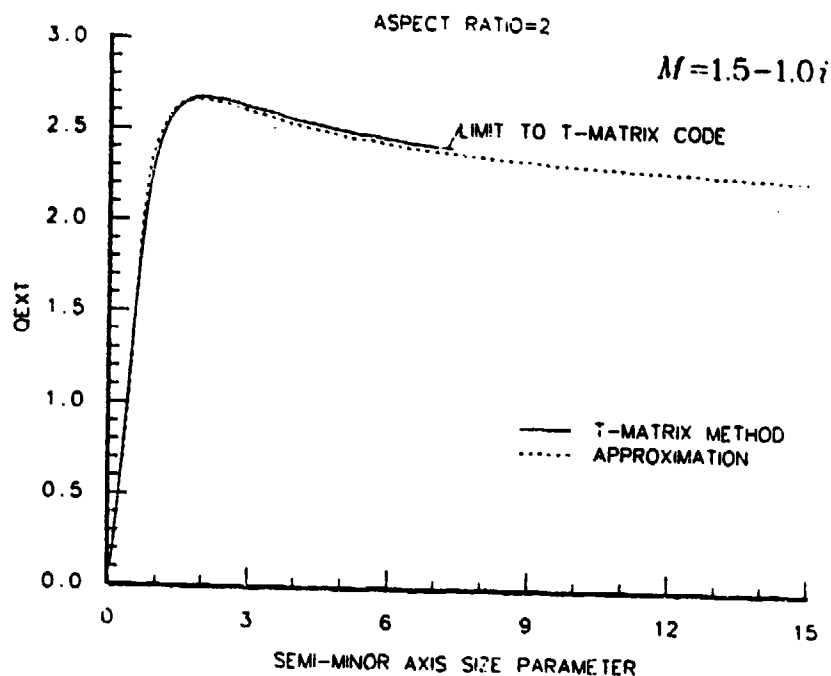


Fig.4 Comparison between approximation and T-matrix method for an index of  $1.5 - 1i$  and an aspect ratio of 2. Numerical instabilities appearing in T-matrix code.

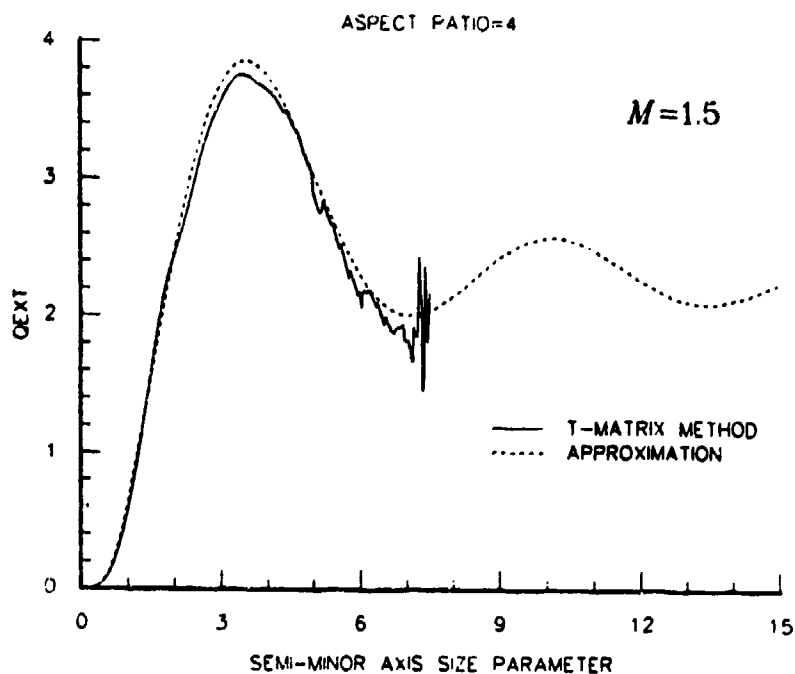


Fig.5 Comparison between approximation and T-matrix method for an index of 1.5 and an aspect ratio of 4. Numerical instabilities appearing in T-matrix code.

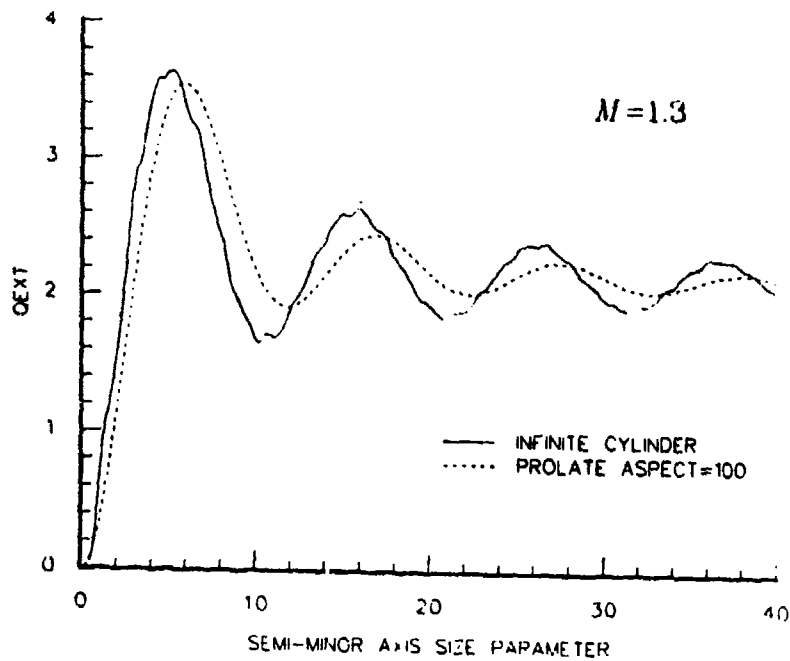


Fig.6 Comparison between randomly oriented infinite cylinders and randomly oriented spheroids with aspect ratio 100 and index of 1.3.

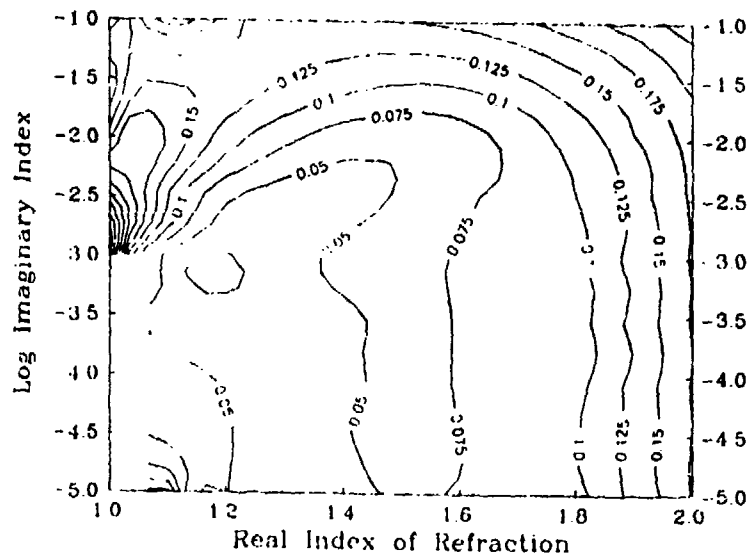


Fig.7 Contour plot of maximum percent error between approximation and T-matrix code for aspect ratio 2.



## **ELECTROMAGNETIC FIELDS FOR A BEAM INCIDENT UPON A NONSPHERICAL PARTICLE**

J.P. Barton and D.R. Alexander  
Center for Electro-Optics  
College of Engineering  
University of Nebraska  
Lincoln, Nebraska 68588-0656

### **RECENT PUBLICATIONS, SUBMITTALS FOR PUBLICATION, AND PRESENTATIONS:**

- A.) J.P. Barton, D.R. Alexander, and S.A. Schaub, "Electromagnetic field calculations for a tightly-focused laser beam incident upon a spherical particle," Proceedings of the 1989 U.S. Army CRDEC Scientific Conference on Obscuration and Aerosol Research, Aberdeen, Maryland, 1989.
- B.) D.R. Alexander, J.P. Barton, and S.A. Schaub, "Laser induced breakdown of H<sub>2</sub>O droplets and solid wires at 0.248  $\mu\text{m}$ ," Proceedings of the 1989 U.S. Army CRDEC Scientific Conference on Obscuration and Aerosol Research, Aberdeen, Maryland, 1989.
- C.) J.P. Barton, D.R. Alexander, and S.A. Schaub, "Theoretical determination of net radiation force and torque for a spherical particle illuminated by a focused laser beam," Journal of Applied Physics, Vol. 66, pp. 4594-4602, 1989.
- D.) J.P. Barton and D.R. Alexander, "Fifth-order corrected electromagnetic field components for a fundamental Gaussian beam," Journal of Applied Physics, Vol. 66, pp. 2800-2802, 1989.
- E.) J.P. Barton, D.R. Alexander, and S.A. Schaub, "Internal fields of a spherical particle illuminated by a tightly-focused laser beam: focal point positioning effects at resonance," Journal of Applied Physics, Vol. 65, pp. 2900-2906, 1989.
- F.) J.P. Barton, W. Ma, S.A. Schaub, and D.R. Alexander, "Theoretical determination of the electromagnetic fields for a laser beam incident upon two adjacent spherical particles of arbitrary arrangement," Proceedings of the 2nd International Congress on Optical Particle Sizing, Tempe, Arizona, 1990.
- G.) J.P. Barton, W. Ma, S.A. Schaub, and D.R. Alexander, "Electromagnetic fields for a beam incident upon two adjacent spherical particles," submitted to Applied Optics, May, 1990.
- H.) J.P. Barton and D.R. Alexander, "Electromagnetic fields for an irregularly-shaped, near-spherical particle illuminated by a focused laser beam," submitted to the Journal of Applied Physics, August, 1990.
- I.) D.R. Alexander, S.A. Schaub, J. Zhang, D.E. Poulain, and J.P. Barton, "Scattering of incident KrF laser radiation resulting from the laser induced breakdown of H<sub>2</sub>O droplets," Optics Letters, Vol. 14, pp. 548-550, 1989.
- J.) D.R. Alexander, J.P. Barton, S.A. Schaub, and G.M. Holtmeier, "Nonlinear interactions of KrF laser radiation with small water droplets," submitted to Applied Optics, October, 1989.
- K.) S.A. Schaub, D.R. Alexander, D.E. Poulain, and J.P. Barton, "Measurement of hypersonic velocities resulting from the laser induced breakdown of aerosols using an excimer laser imaging system," Review of Scientific Instruments, Vol. 60, pp. 3688-3691, 1989.
- L.) S.A. Schaub, J.P. Barton, and D.R. Alexander, "Simplified scattering coefficient expressions for a spherical particle located on the propagation axis of a fifth-order Gaussian beam," Applied Physics Letters, Vol. 55, pp. 2709-2711, 1989.
- M.) D.E. Poulain, D.R. Alexander, J.P. Barton, S.A. Schaub, and J. Zhang, "Interactions of intense ultraviolet laser radiation with solid aerosols," Journal of Applied Physics, Vol. 67, 1990.
- N.) S.A. Schaub, D.R. Alexander, and J.P. Barton, "Theoretical model for the image formed by a spherical particle in a coherent imaging system: comparison to experiment," Optical Engineering, Vol. 28, pp. 565-571, 1989.
- O.) S.A. Schaub, D.R. Alexander, J.P. Barton, and M.A. Emanuel, "Focused laser beam interactions with methanol droplets: effects of relative beam diameter," Applied Optics, Vol. 28, pp. 1666-1669, 1989.

- P.) G.M. Holtmeier, D.R. Alexander, and J.P. Barton, "High intensity ultraviolet laser interaction with a metallic filament," submitted to the Journal of Applied Physics, August, 1990.
- Q.) S.A. Schaub, D.R. Alexander, and J.P. Barton, "Theoretical model of the laser imaging of small aerosols: applications to aerosol sizing," submitted to Applied Optics, May, 1990.
- R.) S.A. Schaub, D.R. Alexander, and J.P. Barton, "Modeling of a coherent imaging system," Proceedings of the 2nd International Congress on Optical Particle Sizing, Tempe, Arizona, 1990.
- S.) J.P. Barton, D.R. Alexander, and S.A. Schaub, "Electromagnetic field calculations for a tightly-focused laser beam incident upon a spherical particle," presentation at the 1989 U.S. Army CRDEC Scientific Conference on Obscuration and Aerosol Research, Aberdeen, Maryland, June 27-30, 1989.
- T.) D.R. Alexander, J.P. Barton, and S.A. Schaub, "Laser induced breakdown of H<sub>2</sub>O droplets and solid wires," presentation at the 1989 U.S. Army CRDEC Scientific Conference on Obscuration and Aerosol Research, Aberdeen, Maryland, June 27-30, 1989.
- U.) J.P. Barton, W. Ma, S.A. Schaub, and D.R. Alexander, "Theoretical determination of the electromagnetic fields for a laser beam incident upon two adjacent spherical particles of arbitrary arrangement," presentation at the 2nd International Congress on Optical Particle Sizing, Tempe, Arizona, March 5-8, 1990.
- V.) D.R. Alexander, S.A. Schaub, and J.P. Barton, "Modeling of a coherent imaging system: Application to focus determination in aerosol sizing," presentation at the 2nd International Congress on Optical Particle Sizing, Tempe, Arizona, March 5-8, 1990.

## ABSTRACT

A theoretical procedure has been developed for the determination of the internal and external electromagnetic fields for a monochromatic beam incident upon a homogeneous particle of arbitrarily-defined shape. The procedure is best suited for the analysis of near-spherical particles (i.e., particles which deviate from a sphere by plus-or-minus a few tenths of a radii). Verification and demonstration calculations are presented. Also presented are calculations investigating the effect of particle shape on internal heating distributions for CO<sub>2</sub> laser heated water droplets, and calculations investigating the effect of surface deformation on resonance excitation within an otherwise spherical particle. Future work will include consideration of modifications of the theoretical procedure that would allow solutions for elongated particles, and the comparison of theoretical calculations with corresponding experimental measurements.

## I. INTRODUCTION

In an earlier work,<sup>1</sup> equations were derived for the theoretical determination of the internal and external electromagnetic fields for a *beam* incident upon a homogeneous *spherical* particle. A procedure has been developed that now permits the determination of the electromagnetic fields for a *beam* incident upon a homogeneous particle of *arbitrarily-defined shape*. This new approach, to be referred to as the irregularly-shaped particle/arbitrary beam theory, appears to be most applicable for the analysis of near-spherical particles (i.e., particles which deviate from a sphere by plus-or-minus a few tenths of a radii). The theory could be used, for example, to determine the electromagnetic fields for a laser beam incident upon a small liquid droplet that has been deformed in shape due to aerodynamic, thermal, or electromagnetic stresses.

Previously, Yeh, Colak, and Barber,<sup>2</sup> have also considered the beam incident upon an irregularly-shaped particle problem. In the approach of Yeh, Colak, and Barber,<sup>2</sup> the incident field is expanded in a plane wave spectrum and a superposition of plane wave solutions, obtained using the extended boundary condition method (EBCM),<sup>3</sup> is performed. In our theoretical development, the incident field is utilized directly, and a superposition of solutions is not necessary. In addition, the primary emphasis of the work of Yeh, Colak, and Barber<sup>2</sup> concerned the determination of far-field scattering patterns. In our paper, the primary emphasis is the determination of the internal and near-surface electromagnetic field distributions.

## II. THEORETICAL DEVELOPMENT

Only a general description of the irregularly-shaped particle/arbitrary beam theory will be presented here. Detailed equations are given in Ref. 4.

The specific problem considered is that of a monochromatic electromagnetic beam within an infinite, nonabsorbing, dielectric medium incident upon a particle of arbitrarily-defined shape. The particle and the surrounding medium are each homogeneous, linear, isotropic, and nonmagnetic ( $\mu = 1$ ). The geometrical arrangement is shown in Fig. 1. The coordinate system origin is located within (and near the center) of the particle. The particle has an associated characteristic radius,  $a$ , and all spatial quantities are nondimensionalized (as indicated by a tilde) relative to this characteristic radius. Though the theoretical development is applicable for any incident beam for which a mathematical description is known, for the calculations presented in this paper, a focused, linearly-polarized, Gaussian-profiled (TEM<sub>00</sub> mode) beam will be assumed. A fifth-order corrected mathematical description of the electromagnetic field components for the Gaussian beam, as previously presented in Ref. 5, is utilized for the analysis. All electromagnetic quantities are nondimensionalized relative to an electric field magnitude characteristic of the incident beam,  $E_0$ . For the Gaussian beam,  $E_0$  is the electric field magnitude at the focal point, which can be related to the beam power by an expression given in Ref. 5.

The input parameters of the analysis are as follows: (1) the particle shape function,  $\hat{r}(\theta, \phi)$  (A nondimensionalized single-valued function of the spherical coordinate angles that defines the surface of the particle. For a centered sphere, this function would equal to one.), (2) the particle size parameter,  $\alpha = 2\pi a/\lambda_{ext}$  ( $\lambda_{ext}$  is the wavelength within the surrounding medium.), (3) the complex relative refractive index of the particle,  $\bar{n} = \sqrt{\epsilon_{int}/\epsilon_{ext}}$ , (4) the nondimensionalized beam focal point coordinates,  $(\tilde{x}_0, \tilde{y}_0, \tilde{z}_0)$  (The location of the focal point of the incident beam relative to the particle.), (5) the nondimensionalized beam waist radius,  $\tilde{w}_0$ , (6) the beam propagation direction angle,  $\theta_{bd}$  (The beam is assumed to propagate parallel to the x-z plane.  $\theta_{bd}$  is the angle of beam propagation relative to the y-z plane.), and (7) the beam polarization orientation angle,  $\phi_{bd}$  (For  $\phi_{bd} = 0^\circ$ , the beam electric field polarization is parallel to the x-z plane. For  $\phi_{bd} = 90^\circ$ , the beam electric field polarization is perpendicular to the x-z plane.).

The procedure for determining the electromagnetic fields for a beam incident upon a particle of arbitrarily-defined shape is a generalization of the beam incident upon a spherical particle development presented in Ref. 1. The electromagnetic field is divided into three parts: the incident field (the field that would exist in the absence of the particle), the scattered field (the difference between the external particle field and the incident field), and the internal field (the field within the particle). The external field is the sum of the incident field (assumed known) and the scattered field:  $\vec{E}^{ext} = \vec{E}^{(i)} + \vec{E}^{(s)}$  and  $\vec{H}^{ext} = \vec{H}^{(i)} + \vec{H}^{(s)}$ . The scattered field and the internal field are to be determined. The solution is formulated in spherical coordinates,  $(r, \theta, \phi)$ .

The electromagnetic field components of the unknown scattered and internal fields are expressed in the form of general series expansions (obtained from a separation-of-variables solution of Maxwell's equations) involving products of radial-dependent Riccati-Bessel functions ( $\psi_l, \chi_l$ ) and angularly-dependent spherical harmonic functions ( $Y_{lm}$ ), as were derived in Ref. 1. It is assumed, even though the particle is not spherical, that the scattered field is appropriately expressed in terms of outgoing spherical waves ( $\xi_l^{(1)} = \psi_l - i\chi_l$ ) and the internal field is appropriately expressed in terms of standing waves ( $\psi_l$  only). The validity of these assumptions will be discussed in Sec. III. The series expansions for the electromagnetic field components are each of the form of double summations over the indexes  $l$  and  $m$ . If  $L$  is the maximum value of the index  $l$  required for series convergence, there will then be

$$N = \sum_{l=1}^L (2l + 1) \quad (1)$$

terms in each series expansion. (N equals the number of  $l$  and  $m$  combinations for a given L.)

The series coefficients for the scattered field ( $a_{lm}, b_{lm}$ ) and the series coefficients for the internal field ( $c_{lm}, d_{lm}$ ) are determined by applying the four boundary conditions associated with the fact

that the tangential electric and magnetic field fields are continuous across the particle surface. Evaluating the four boundary conditions at a particular angular position  $(\theta, \phi)$  and then expanding these equations in spherical harmonics ( $Y_{lm}$ ) provides a set of  $4N$  linear, algebraic equations for the determination of the  $4N$  values of the series coefficients ( $a_{lm}, b_{lm}, c_{lm}, d_{lm}$ ). Once the series coefficients for the scattered and internal fields are known, the series expansions can be used to determine the electromagnetic field anywhere internal or external to the particle.

If the particle is axisymmetric [ $\hat{r}(\theta)$ , independent of  $\phi$ ], then major simplifications in the solution procedure occur. In particular, the series coefficients for each index  $m$  can be determined by solving a set of  $4(L - |m| + 1)$  linear, algebraic equations (two sets of  $2(L + 1)$  equations for  $m = 0$ ). Thus, for the axisymmetric case, it is required to solve  $(L + 2)$  "small" sets of linear, algebraic equations, instead of a single "large"  $4N$  set of linear, algebraic equations, as is necessary for the general case.

### III. APPLICABILITY

As previously mentioned, it is assumed that the scattered field is appropriately expressed in terms of outgoing spherical waves ( $\xi_l^{(1)} = \psi_l - i\chi_l$ ) and the internal field is appropriately expressed in terms of standing waves ( $\psi_l$  only). These assumptions are sometimes referred to as the "Rayleigh hypothesis." Even though the validity of the assumptions associated with the Rayleigh hypothesis can be questioned for the case of the irregularly-shaped particle, Chew<sup>6</sup> has recently shown that, on a fundamental level, the Rayleigh hypothesis approach and the extended-boundary-condition-method (EBCM) are essentially equivalent. For both of these methods, the resultant matrix for the solution of the series coefficients describing the fields becomes ill-conditioned (small changes in the terms of the coefficient matrix may produce large changes in the solution vector) for the analysis of elongated particles. The irregularly-shaped particle/arbitrary beam theory, similar to the EBCM, is best suited for the analysis of near-spherical particles. A further discussion of the applicability of the theory is presented in Ref. 4. All calculations in this paper, with the exceptions of Figs. 6 and 7, represent fully converged solutions.

### IV. VERIFICATION CALCULATIONS

The irregularly-shaped particle/arbitrary beam theory was verified by making direct comparisons with known solutions. Calculations were performed for a spherical particle displaced from the origin. If the sphere is displaced along the  $z$ -axis, then the particle shape function is a function of the polar angle,  $\hat{r}(\theta)$ , and the axisymmetric irregularly-shaped particle/arbitrary beam theory can be applied. However, if plane wave illumination is assumed, the electromagnetic field distribution should be identical to that of plane wave Lorenz-Mie theory.

As an example, Fig. 2 presents a plot of the normalized source function ( $S = |\vec{E}|^2/E_0^2$ ) distribution in the  $x$ - $z$  plane for a  $30^\circ$  angle of incidence plane wave incident upon a centered sphere of  $\alpha = 8.0$  and  $\bar{n} = 1.2 + 0.02i$ . Figure 2 is the Lorenz-Mie theory solution rotated  $30^\circ$  about the origin in the  $x$ - $z$  plane in order to account for the angle of incidence of the plane wave. Figure 3 was generated using the axisymmetric theory for identical conditions as Fig. 2, except that the sphere has been displaced along the  $z$ -axis by a distance of  $\Delta\bar{z} = +0.25$ . A comparison of Figs. 2 and 3 shows that the normalized source function distribution of the displaced sphere (Fig. 3) calculated using the axisymmetric theory is identical to the normalized source function distribution of the centered sphere (Fig. 2) calculated using Lorenz-Mie theory, except that the entire solution of Fig. 3 (both internal and near-field) has been shifted along the  $z$ -axis by a distance of  $\Delta\bar{z} = 0.25$ , as would be expected.

A similar approach was used to confirm the general irregularly-shaped particle/arbitrary beam theory, except the sphere is now displaced along the  $x$ -axis so that the particle shape function is a function of both the polar and azimuthal angles,  $\hat{r}(\theta, \phi)$ . Figure 4 shows the normalized source function distribution for a  $30^\circ$  angle of incidence plane wave incident upon a centered sphere of  $\alpha = 2.0$  and  $\bar{n} = 1.2 + 0.02i$  as determined using Lorenz-Mie theory. Figure 5 provides the normalized source function distribution calculated using the general theory for conditions identical to those of

Fig. 4, except that the sphere has been displaced along the x-axis by a distance of  $\Delta\tilde{x} = 0.1$ . A comparison of Figs. 4 and 5 shows that the normalized source function distribution of Fig. 5 is identical to that of Fig. 4, except that the entire solution has been shifted along the x-axis by a distance of  $\Delta\tilde{x} = +0.1$ , as would be expected.

Another confirmation of the arbitrarily-shaped particle theory was obtained by making comparisons with an existing nonspherical, regular geometry solution. Asano and Yamamoto<sup>7</sup> have developed an analytical solution for the determination of the electromagnetic fields for a plane wave incident upon a spheroidal particle. In Ref. 7, far-field scattering patterns for a  $0^\circ$  angle of incidence plane wave incident upon prolate and oblate spheroids of various size parameters and various axis ratios are presented. Asano and Yamamoto<sup>7</sup> plotted far-field normalized scattering intensity,

$$S_r = \lim_{\tilde{r} \rightarrow \infty} \alpha^2 \tilde{r}^2 \frac{\frac{c}{8\pi} \text{Re}(\vec{E} \times \vec{H}^*)_r}{\frac{c}{8\pi} |E_0|^2}, \quad (2)$$

versus scattering angle ( $\theta$ ) in the plane of incident electric field polarization and in the plane perpendicular to the incident electric field polarization. This was done for size parameters,  $c$ , of 1 through 7, where the  $c$  size parameter of Asano and Yamamoto<sup>7</sup> is related to the size parameter,  $\alpha$ , of this paper by

$$\alpha = \frac{c(a/b)}{\sqrt{(a/b)^2 - 1}}, \quad (3)$$

where  $a/b$  is the major to minor axis ratio. An index of refraction of  $\bar{n} = 1.33 + 0.00i$  was assumed.

The axisymmetric irregularly-shaped particle/arbitrary beam theory was used to calculate far-field scattering patterns using parameters consistent with those used in Asano and Yamamoto.<sup>7</sup> Figure 6 presents the far-field scattering patterns for a  $0^\circ$  angle of incidence plane wave incident upon a prolate spheroid of  $a/b = 2$  axis ratio as calculated using the axisymmetric theory. Figure 6 can be directly compared with Fig. 3 of Asano and Yamamoto.<sup>7</sup> Figure 6 is a vertically-unscaled, semi-log plot with each vertical division representing a factor of ten difference in normalized scattering intensity. The forward-scattered ( $\theta = 0^\circ$ ) and the back-scattered ( $\theta = 180^\circ$ ) normalized scattering intensity values are shown for each size parameter. The scattering patterns generated using the axisymmetric theory agreed within a few percent with those of Asano and Yamamoto.<sup>7</sup> For the prolate spheroid, the forward-scattered values agreed with an average deviation of 0.3% and the back-scattered values agreed with an average deviation of 3.2%.

The far-field scattering patterns for an oblate spheroid of  $a/b = 2$  axis ratio, calculated using the axisymmetric theory, are given in Fig. 7. Figure 7 can be directly compared with Fig. 5 of Asano and Yamamoto.<sup>7</sup> Again, the two results were in general agreement. The back-scattered values agreed with an average deviation of 1.1% and the forward-scattered values agreed with an average deviation of 6.1%.

As was previously discussed, the theoretical procedure developed in this paper is best suited for the analysis of near-spherical particles. The far-field scattering calculations for the  $a/b=2$  axis ratio prolate/oblate spheroids of Figs. 6 and 7 were not fully converged solutions. For each case,  $L$  was increased until the algebraic equations became too ill-conditioned to permit accurate numerical solution. For the maximum permissible value of  $L$ , the far-field scattering intensities were still changing by plus or minus a few percent for each increment in  $L$ . This lack of full convergence may explain the slight difference of the results of Figs. 6 and 7 with the comparable results of Asano and Yamamoto.<sup>7</sup>

## V. TIGHTLY-FOCUSED BEAM ON AN OBLATE SPHEROID

In order to demonstrate the ability to determine the electromagnetic fields for a focused beam incident upon a nonspherical particle, calculations were performed for a tightly-focused beam incident upon an oblate spheroid of axis ratio  $a/b = 1.2$ ,  $\alpha = 15.0$ , and  $\bar{n} = 1.3 + 0.01i$ . The angle of incidence ( $\theta_{bd}$ ) was held at  $0^\circ$  and the incident electric field polarization was in the x-z plane

( $\phi_{bd} = 0^\circ$ ). Figure 8 shows the internal normalized source function distribution in the x-z plane for an incident plane wave ( $\tilde{w}_0 \Rightarrow \infty$ ). Only the internal field distribution is presented (the near-field values were artificially set to zero) so as to clearly show the nonspherical shape of the particle.

Figure 9 is for the same conditions as Fig. 8, but instead of plane wave incidence, a beam ( $\tilde{w}_0 = 0.667$ ) is focused at the center of the particle ( $\tilde{x}_0 = \tilde{y}_0 = \tilde{z}_0 = 0.0$ ). The normalized source function distribution for beam illumination is distinctly different than that for plane wave illumination, as can be seen by comparing Figs. 8 and 9. Figure 10 is for the same incident beam conditions as Fig. 9, except that the focal point of the beam has been moved up the x-axis to a position halfway along the major axis of the oblate spheroid ( $\tilde{x}_0 = 0.5, \tilde{y}_0 = \tilde{z}_0 = 0.0$ ). Figure 11 shows the normalized source function distribution with the beam focused at the edge of the particle ( $\tilde{x}_0 = 1.0, \tilde{y}_0 = \tilde{z}_0 = 0.0$ ).

## VI. CO<sub>2</sub> LASER HEATING OF SPHEROIDAL WATER DROPLETS

As an application of the axisymmetric irregularly-shaped particle/arbitrary beam theory, the effect of nonsphericity on the spatial heating distribution within a water droplet heated by a CO<sub>2</sub> laser beam ( $\lambda = 10.6\mu m, \bar{n} = 1.179 + 0.072i$ ) was investigated. The heating rate per unit volume within the droplet is directly proportional to the normalized source function,  $S$ . Equal volume prolate/oblate spheroidal water droplets ( $\alpha_{sphere} = 8.0, d_{sphere} \approx 27\mu m$ ) of major to minor axis ratios ( $a/b$ ) of 1.1 and 1.2 were analyzed. Plane wave incidence ( $\tilde{w}_0 \Rightarrow \infty$ ) was assumed and three particle orientations were considered: (Case A:  $\theta_{bd} = 0^\circ, \phi_{bd} = 0^\circ$ ), (Case B:  $\theta_{bd} = 90^\circ, \phi_{bd} = 0^\circ$ ), and (Case C:  $\theta_{bd} = 90^\circ, \phi_{bd} = 90^\circ$ ).

For the spherical particle ( $a/b=1$ ), Cases A, B, and C are indistinguishable, and the maximum normalized source function value within the spherical droplet was determined to be  $S_{max} = 1.019$ . The effect of particle shape and orientation on maximum source function is summarized in Table 1. For orientation A, the prolate shape results in an increased value of  $S_{max}$  (relative to that of an equal volume sphere) while for orientation C, the oblate shape results in an increased value of  $S_{max}$ . As an example of the effect of particle shape on the spatial distribution of normalized source function (heating), Fig. 12 gives the normalized source function in the y-z plane for orientation A for a.) a sphere, b.) a prolate spheroid with  $a/b = 1.1$ , and c.) a prolate spheroid with  $a/b = 1.2$ .

## VII. EFFECTS OF SURFACE DEFORMATION AT RESONANCE

The beam incident upon an arbitrarily-shaped particle theory permits electromagnetic field determinations for particles of irregular geometry. As an example of an application, the axisymmetric theory was used to investigate the effect of a surface deformation on resonance excitation within an otherwise spherical particle. (The effect of focal point positioning on resonance excitation was investigated in Ref. 8.) The particle is assumed spherical except for an axisymmetric surface deformation located within the polar angle interval  $\pi/8 < \theta < 3\pi/8$ :

$$\hat{r}(\theta) = \begin{cases} 1 & \text{for } \theta < \pi/8 \\ 1 + \epsilon/2(1 + \cos[8(\theta - \pi/8) - \pi]) & \text{for } \pi/8 < \theta < 3\pi/8 \\ 1 & \text{for } \theta > 3\pi/8 \end{cases} \quad (4)$$

The height of the deformation,  $\epsilon$ , can be either positive (protrusion), negative (depression), or zero (perfect sphere). Plane wave illumination with a  $0^\circ$  angle of incidence is assumed which provides a degenerate condition such that all series coefficients except  $m = \pm 1$  are identically zero. In

addition, the  $m = \pm 1$  terms can be combined so that the double summation electromagnetic field component expansions reduce to single summations over the radial index,

$$\sum_{l=1}^L \quad (5)$$

with the associated single index series coefficients:  $a_l, b_l, c_l, d_l$ .

Assuming an index of refraction of  $\bar{n} = 1.334 + 1.2 \times 10^{-9}i$  (0.5145  $\mu\text{m}$  wavelength argon-ion laser incident upon water),<sup>9</sup> a spherical particle resonance was located. The resonance chosen was the 34th mode, 1st order magnetic wave (TE mode) resonance which occurs at  $\alpha = 29.285$ . At this size parameter, the magnitude of the 34th radial index magnetic wave internal field series coefficient ( $|d_{34}|$ ) attains a peak value, as shown in Fig. 13.

The effect of a surface deformation on the excitation of this resonance was investigated by determining  $|d_{34}|$  as a function of  $\epsilon$  and  $\alpha$ . In Fig. 14,  $|d_{34}|$  is plotted versus size parameter for  $\epsilon = 0.00, \pm 0.01$ , and  $\pm 0.02$ , and in Fig. 15,  $|d_{34}|$  is plotted versus size parameter for  $\epsilon = 0.00$  and  $\pm 0.05$ . As can be seen in Figs. 14 and 15, the presence of the surface deformation shifts the resonance to smaller size parameters for protrusions ( $\epsilon > 0$ ) and to larger size parameters for depressions ( $\epsilon < 0$ ). Surface deformations also decrease the quality of the resonance with protrusions ( $\epsilon > 0$ ) having a greater effect than depressions ( $\epsilon < 0$ ) (for these particular conditions).

For small deformations,  $|\epsilon| < 0.02$ , resonance is apparently retained when the circumference of the deformed particle matches the circumference of the corresponding resonant spherical particle. This observation is illustrated by the results presented in Table 2.

## VIII. CONCLUSION

A theoretical procedure has been developed for the determination of the internal and external electromagnetic fields for a monochromatic beam incident upon a homogeneous particle of arbitrarily-defined shape. The procedure is apparently best suited for the analysis of near-spherical particles and, for example, could be used to analyze laser beams interactions with liquid droplets that have been slightly distorted in shape due to aerodynamic, thermal, or electromagnetic stresses. Future work will include consideration of modifications of the theoretical procedure that would allow solutions for elongated particles, and the comparison of theoretical calculations with corresponding experimental measurements.

## ACKNOWLEDGEMENT

This work has been supported, in part, by the U.S. Army Research Office under contract No. DAAL03-87-K-0138.

## REFERENCES

1. J.P. Barton, D.R. Alexander, and S.A. Schaub, "Internal and near-surface electromagnetic fields for a spherical particle irradiated by a focused laser beam," *J. Appl. Phys.* **64**, 1632 (1988).
2. C. Yeh, S. Colak, and P. Barber, "Scattering of sharply focused beams by arbitrarily shaped dielectric particles: an exact solution," *Appl. Opt.* **21**, 4426 (1982).
3. P. Barber and C. Yeh, "Scattering of electromagnetic waves by arbitrarily shaped dielectric bodies," *Appl. Opt.* **14**, 2864 (1975).
4. J.P. Barton and D.R. Alexander, "Electromagnetic fields for an irregularly-shaped, near-spherical particle illuminated by a focused laser beam," submitted to the *Journal of Applied Physics*, August, 1990.
5. J.P. Barton and D.R. Alexander, "Fifth-order corrected electromagnetic field components for a fundamental Gaussian beam," *J. Appl. Phys.* **66**, 2800 (1989).
6. W.C. Chew, *Waves and Fields in Inhomogeneous Media*, pp. 463, Van Nostrand Reinhold, New York, 1990.
7. S. Asano and G. Yamamoto, "Light scattering by a spheroidal particle," *Appl. Opt.* **14**, 29 (1975).
8. J.P. Barton, D.R. Alexander, and S.A. Schaub, "Internal fields of a spherical particle illuminated by a tightly-focused laser beam: focal point positioning effects at resonance," *J. Appl. Phys.* **65**, 2900 (1989).
9. G.M. Hale and M.R. Querry, "Optical constants of water in the 200-nm to 200- $\mu\text{m}$  wavelength region," *Appl. Opt.* **12**, 555 (1973).

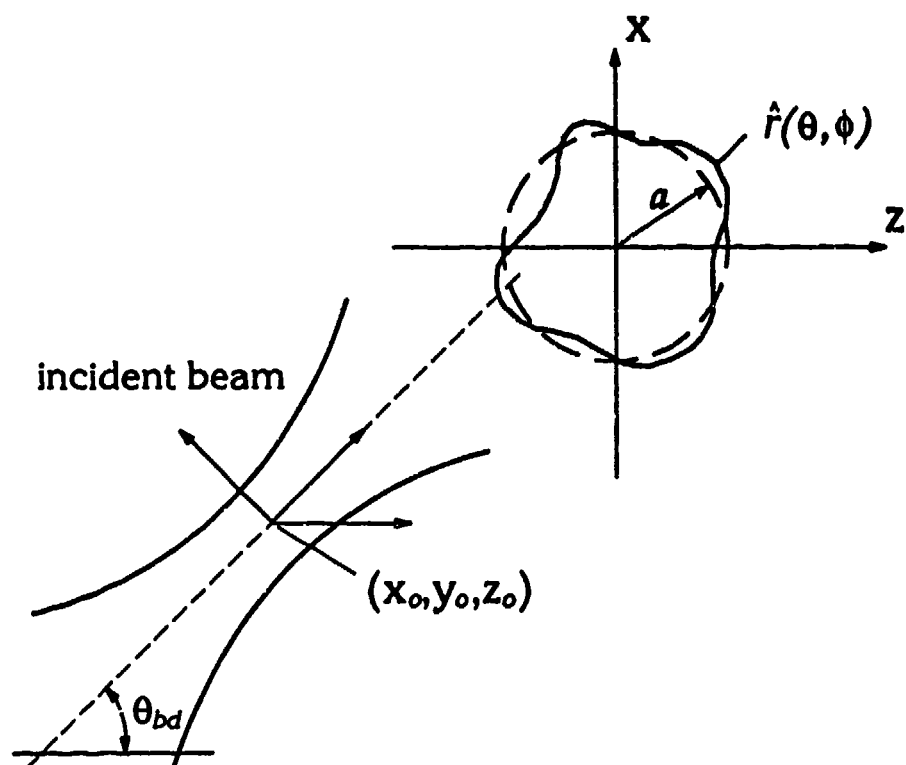


FIG 1. Geometrical arrangement for beam incident upon an arbitrarily-shaped particle analysis. The beam propagates parallel to the  $x$ - $z$  plane.



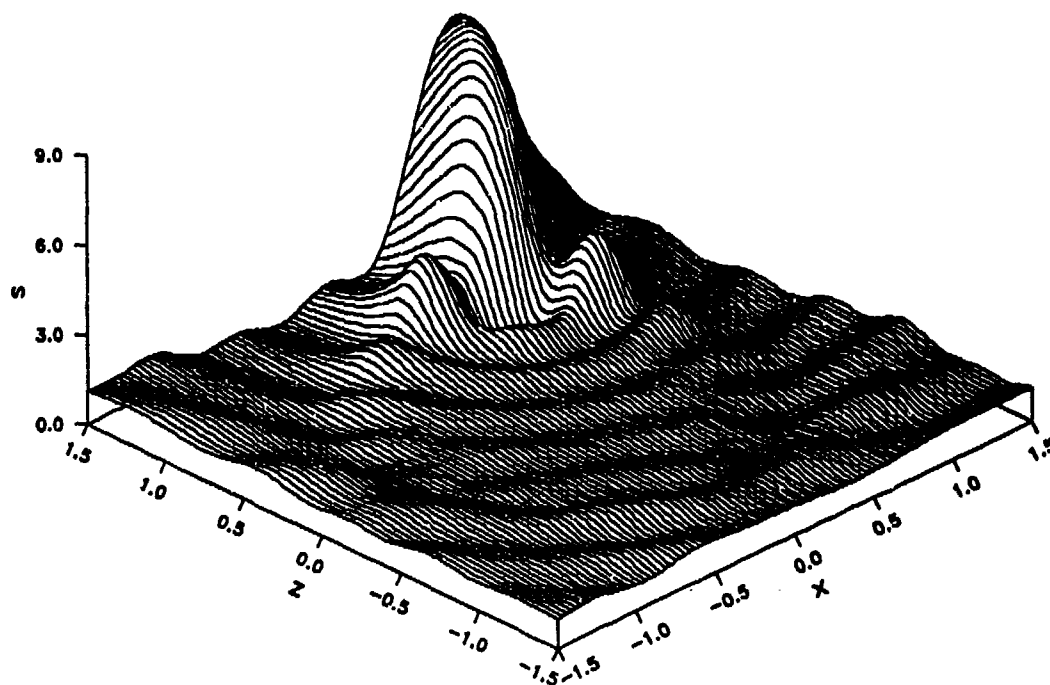


FIG 2. Normalized source function distribution in the  $x$ - $z$  plane for a  $30^\circ$  angle of incidence plane wave incident upon a centered sphere.  $\alpha = 8.0$ ,  $\bar{n} = 1.2 + 0.02i$ ,  $\bar{w}_0 = \infty$  (plane wave),  $\theta_{bd} = 30^\circ$ , and  $\phi_{bd} = 90^\circ$ .

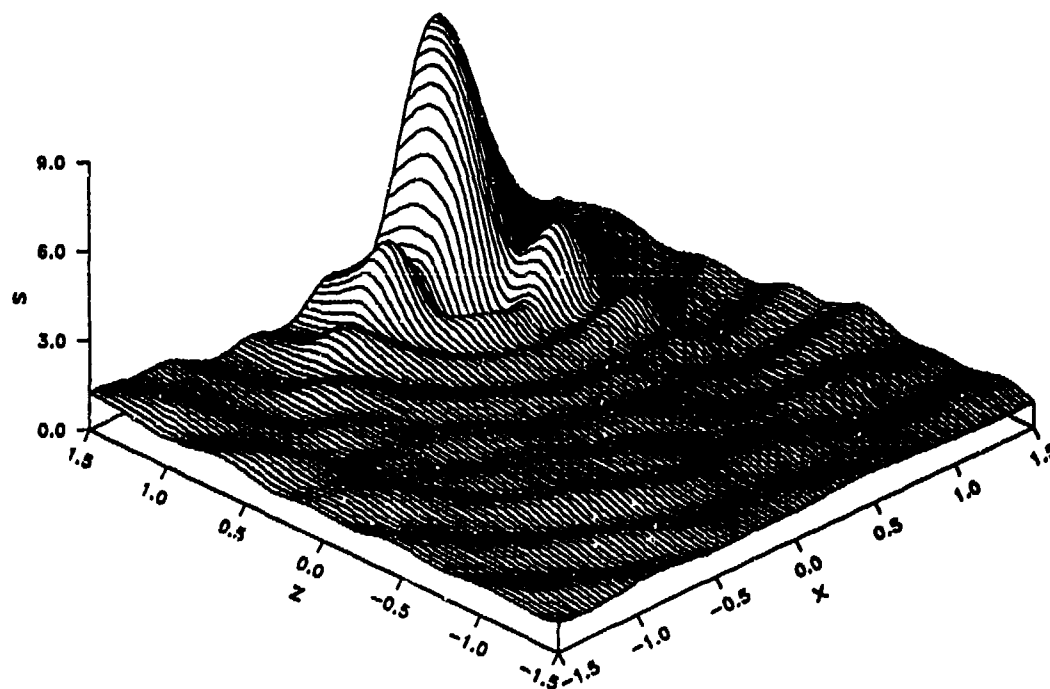


FIG 3. Normalized source function distribution in the  $x$ - $z$  plane for a  $30^\circ$  angle of incidence plane wave incident upon a sphere displaced along the  $z$ -axis by  $\Delta\bar{z} = +0.25$ .  $\alpha = 8.0$ ,  $\bar{n} = 1.2 + 0.02i$ ,  $\bar{w}_0 = \infty$  (plane wave),  $\theta_{bd} = 30^\circ$ , and  $\phi_{bd} = 90^\circ$ .

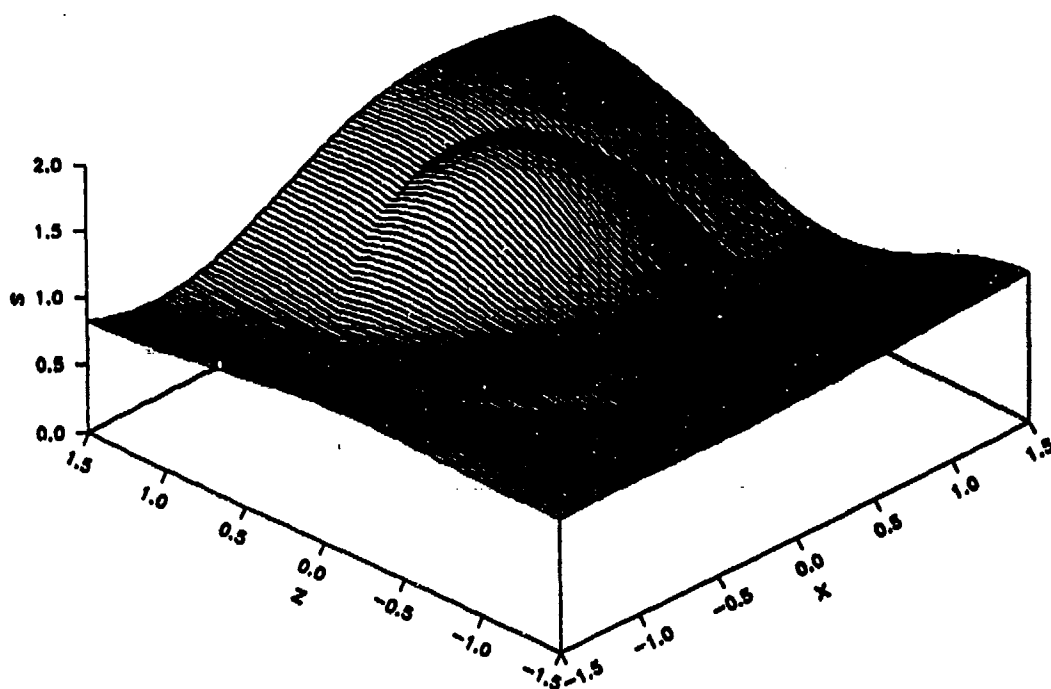


FIG 4. Normalized source function distribution in the x-z plane for a  $30^\circ$  angle of incidence plane wave incident upon a centered sphere.  $\alpha = 2.0$ ,  $\bar{n} = 1.2 + 0.02i$ ,  $\bar{w}_0 = \infty$  (plane wave),  $\theta_{bd} = 30^\circ$ , and  $\phi_{bd} = 90^\circ$ .

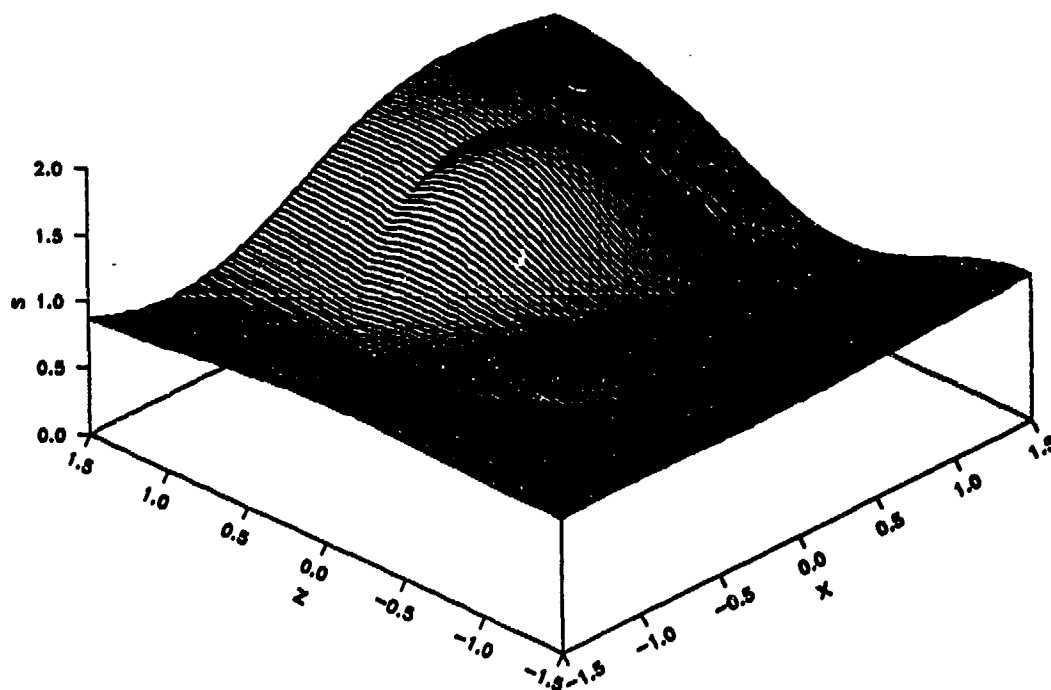


FIG 5. Normalized source function distribution in the x-z plane for a  $30^\circ$  angle of incidence plane wave incident upon a sphere displaced along the x-axis by  $\Delta\bar{x} = +0.10$ .  $\alpha = 2.0$ ,  $\bar{n} = 1.2 + 0.02i$ ,  $\bar{w}_0 = \infty$  (plane wave),  $\theta_{bd} = 30^\circ$ , and  $\phi_{bd} = 90^\circ$ .

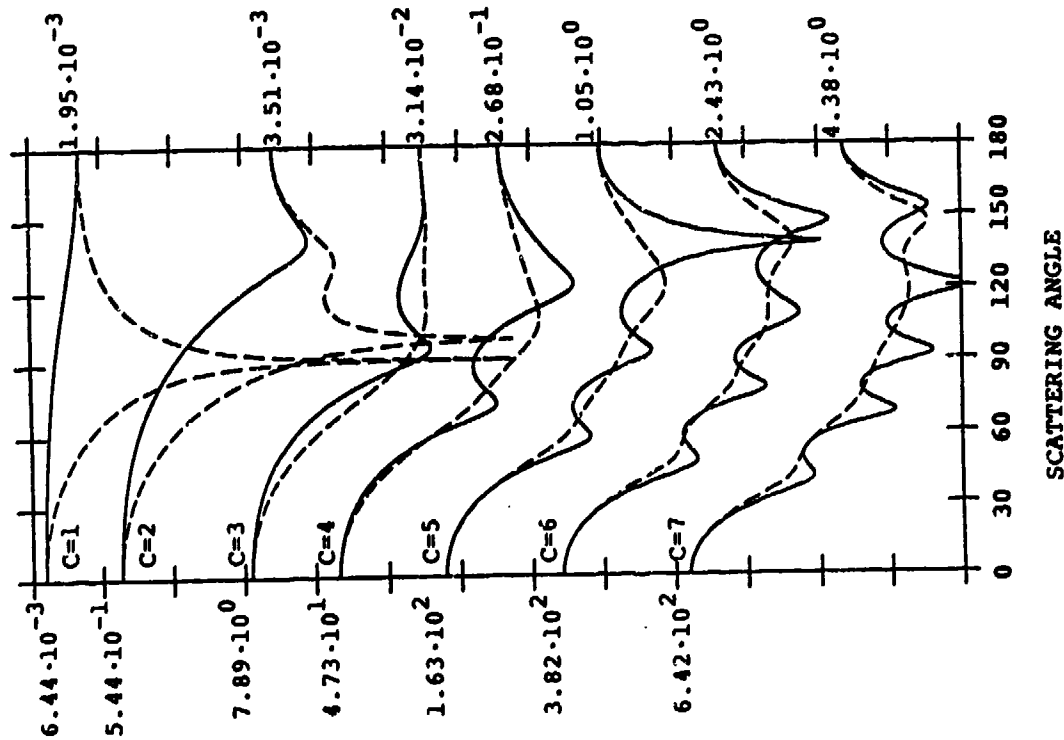


FIG 6. Far-field normalized scattering intensity for a  $0^\circ$  angle of incidence plane wave incident upon a  $a/b = 2$  axis ratio prolate spheroid. Solid line:  $y-z$  plane. Dashed line:  $x-z$  plane.  $\alpha = 1.155c$ ,  $\bar{n} = 1.33 + 0.00i$ ,  $\bar{u}_0 = \infty$  (plane wave),  $\theta_M = 0^\circ$ , and  $\phi_M = 0^\circ$ . Compare with Fig. 3 of Asano and Yamamoto.<sup>7</sup>

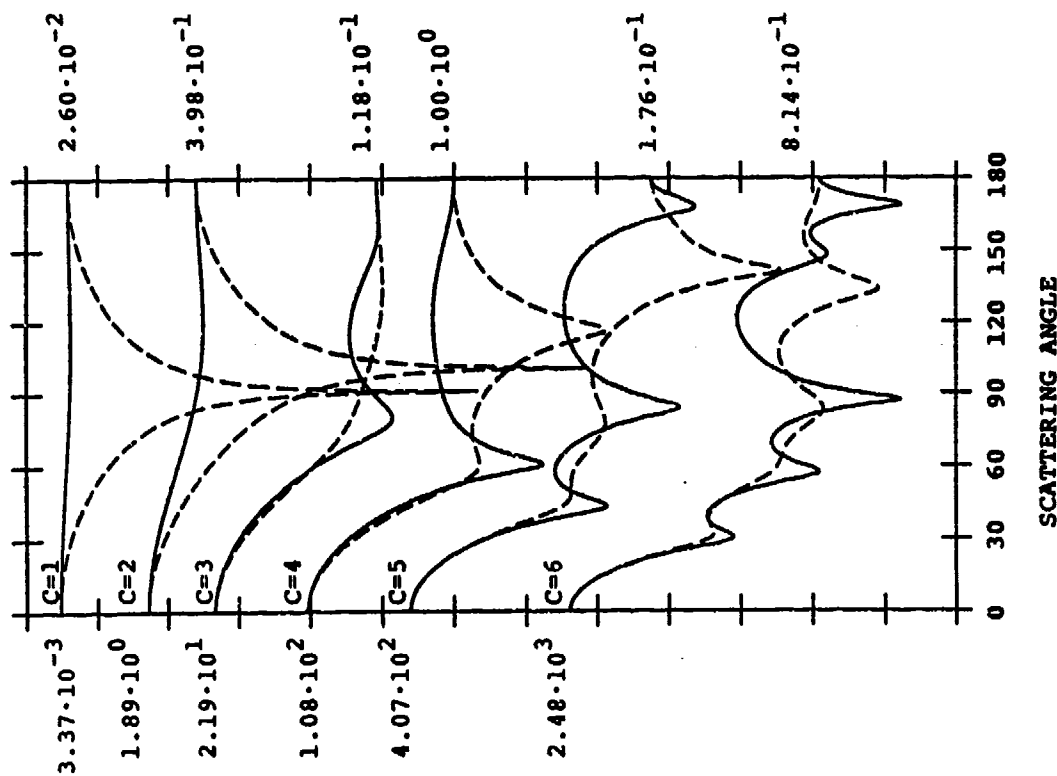


FIG 7. Far-field normalized scattering intensity for a  $0^\circ$  angle of incidence plane wave incident upon a  $a/b = 2$  axis ratio oblate spheroid. Solid line:  $y-z$  plane. Dashed line:  $x-z$  plane.  $\alpha = 1.155c$ ,  $\bar{n} = 1.33 + 0.00i$ ,  $\bar{u}_0 = \infty$  (plane wave),  $\theta_M = 0^\circ$ , and  $\phi_M = 0^\circ$ . Compare with Fig. 5 of Asano and Yamamoto.<sup>7</sup>

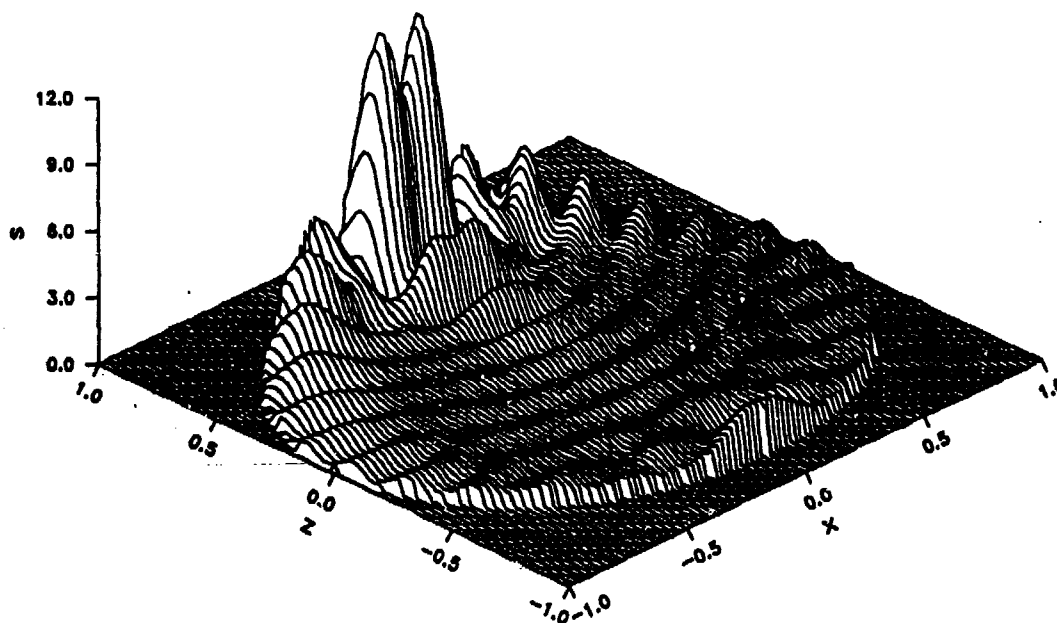


FIG 8. Internal normalized source function distribution in the  $x$ - $z$  plane for a  $0^\circ$  angle of incidence plane wave incident upon an oblate spheroid of axis ratio  $a/b = 1.2$ .  $\alpha = 15.0$ ,  $\bar{n} = 1.33 + 0.00i$ ,  $\bar{w}_0 \Rightarrow \infty$  (plane wave),  $\bar{x}_0 = \bar{y}_0 = \bar{z}_0 = 0.0$ ,  $\theta_{bd} = 0^\circ$ , and  $\phi_{bd} = 0^\circ$ .

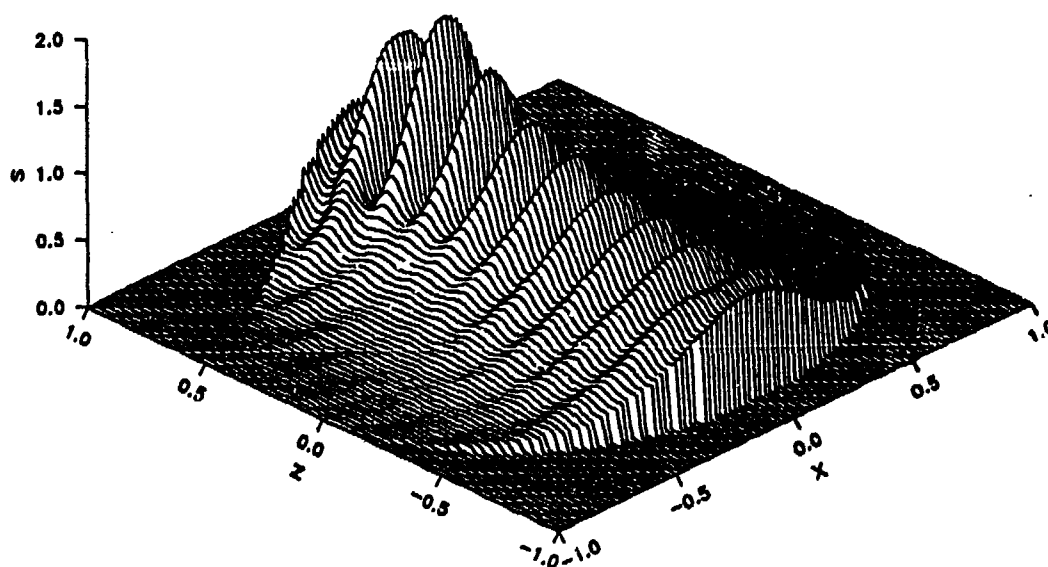


FIG 9. Internal normalized source function distribution in the  $x$ - $z$  plane for a  $0^\circ$  angle of incidence focused beam incident upon an oblate spheroid of axis ratio  $a/b = 1.2$ . On-center focal point positioning.  $\alpha = 15.0$ ,  $\bar{n} = 1.33 + 0.00i$ ,  $\bar{w}_0 = 0.667$ ,  $\bar{x}_0 = \bar{y}_0 = \bar{z}_0 = 0.0$ ,  $\theta_{bd} = 0^\circ$ , and  $\phi_{bd} = 0^\circ$ .

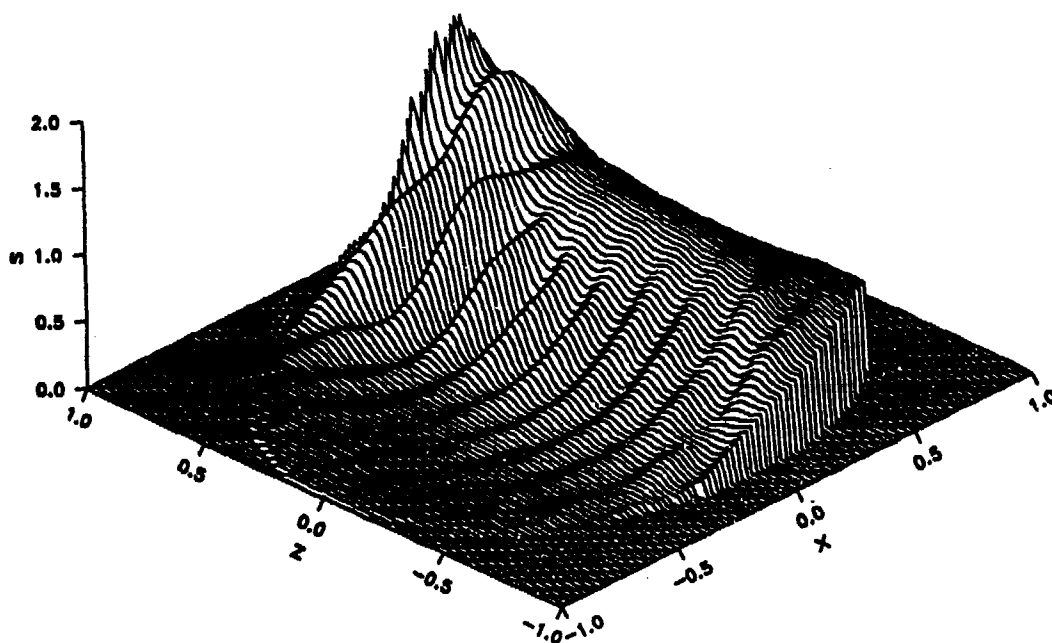


FIG 10. Internal normalized source function distribution in the x-z plane for a  $0^\circ$  angle of incidence focused beam incident upon an oblate spheroid of axis ratio  $a/b = 1.2$ . Mid-axis focal point positioning.  $\alpha = 15.0$ ,  $\bar{n} = 1.33 + 0.00i$ ,  $\tilde{w}_0 = 0.667$ ,  $\tilde{x}_0 = 0.5$ ,  $\tilde{y}_0 = \tilde{z}_0 = 0.0$ ,  $\theta_{bd} = 0^\circ$ , and  $\phi_{bd} = 0^\circ$ .

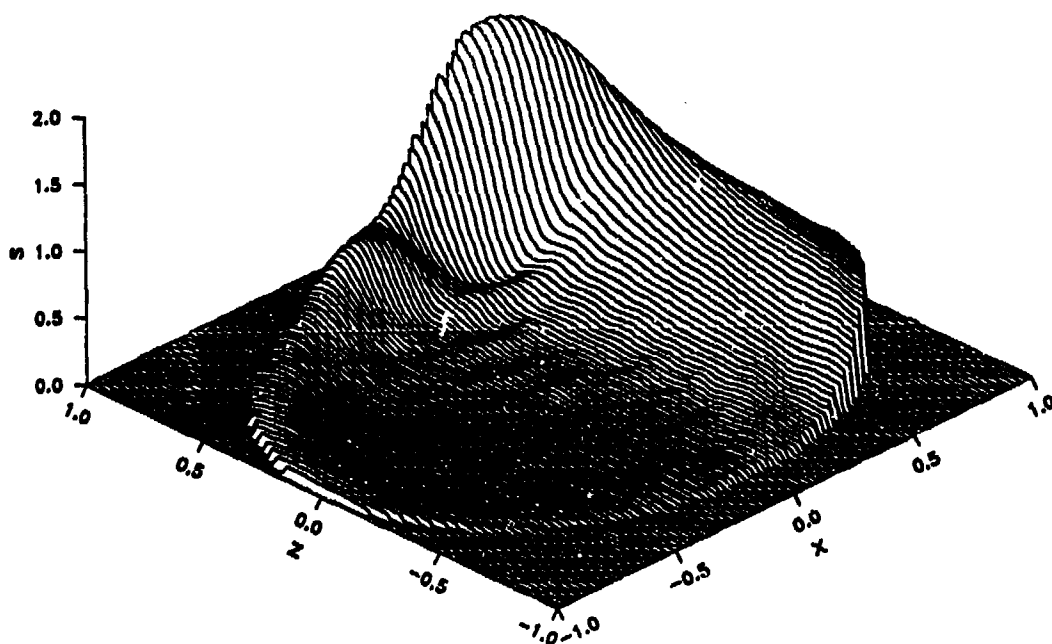


FIG 11. Internal normalized source function distribution in the x-z plane for a  $0^\circ$  angle of incidence focused beam incident upon an oblate spheroid of axis ratio  $a/b = 1.2$ . On-edge focal point positioning.  $\alpha = 15.0$ ,  $\bar{n} = 1.33 + 0.00i$ ,  $\tilde{w}_0 = 0.667$ ,  $\tilde{x}_0 = 1.0$ ,  $\tilde{y}_0 = \tilde{z}_0 = 0.0$ ,  $\theta_{bd} = 0^\circ$ , and  $\phi_{bd} = 0^\circ$ .

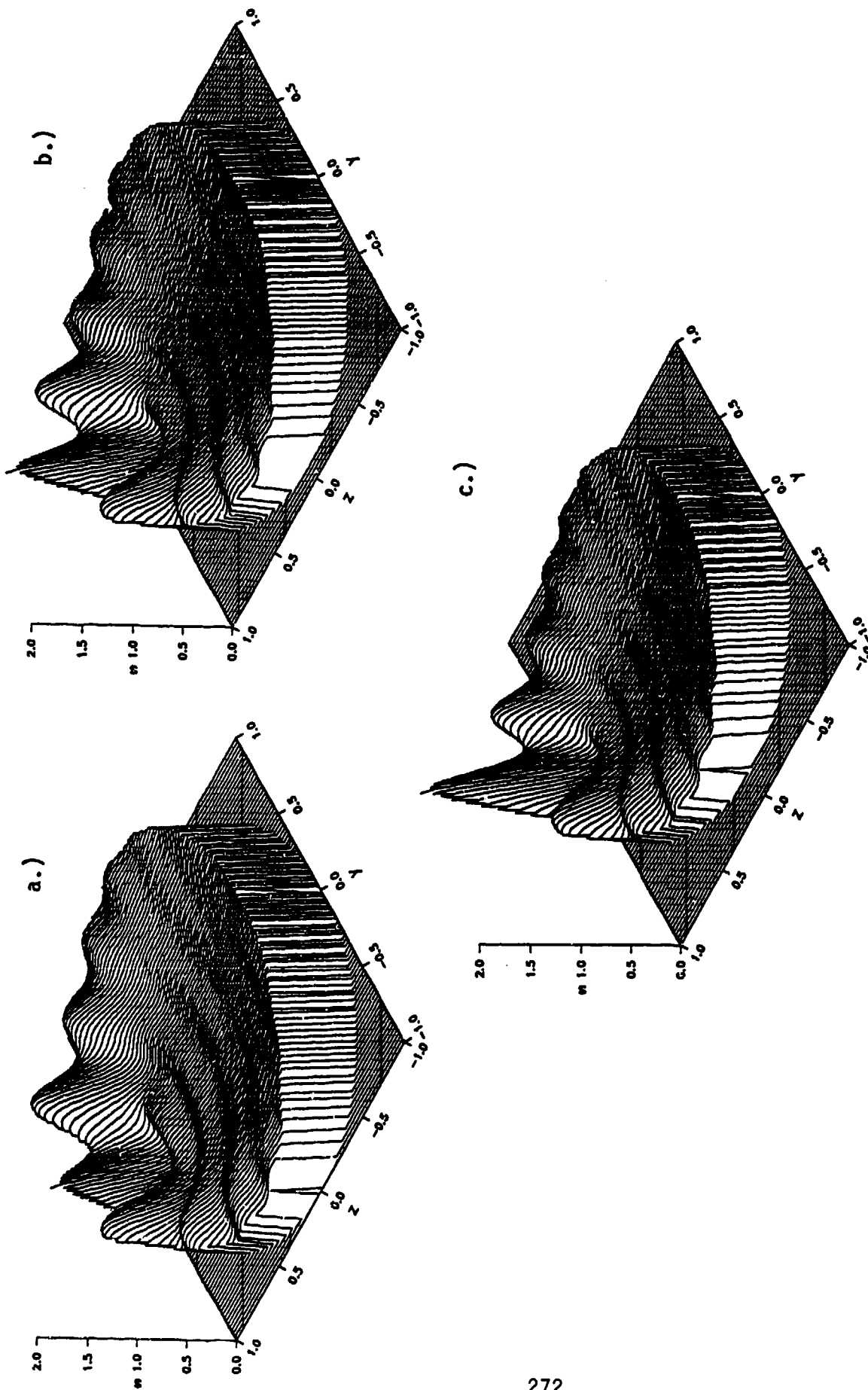


FIG 12. Internal normalized source function distribution in the y-z plane for a  $0^\circ$  angle of incidence plane wave incident upon equal volume a.) sphere, b.) 1.1 axis ratio prolate spheroid, and c.) 1.2 axis ratio prolate spheroid. ( $\text{CO}_2$  laser incident upon a water droplet, Case A orientation.)  $\alpha_{\text{sphere}} = 8.0$ ,  $\bar{n} = 1.179 + 0.072i$ ,  $\bar{w}_0 \Rightarrow \infty$ ,  $\bar{x}_0 = \bar{y}_0 = \bar{z}_0 = 0.0$ ,  $\theta_{bd} = 0^\circ$ , and  $\phi_{bd} = 0^\circ$ .

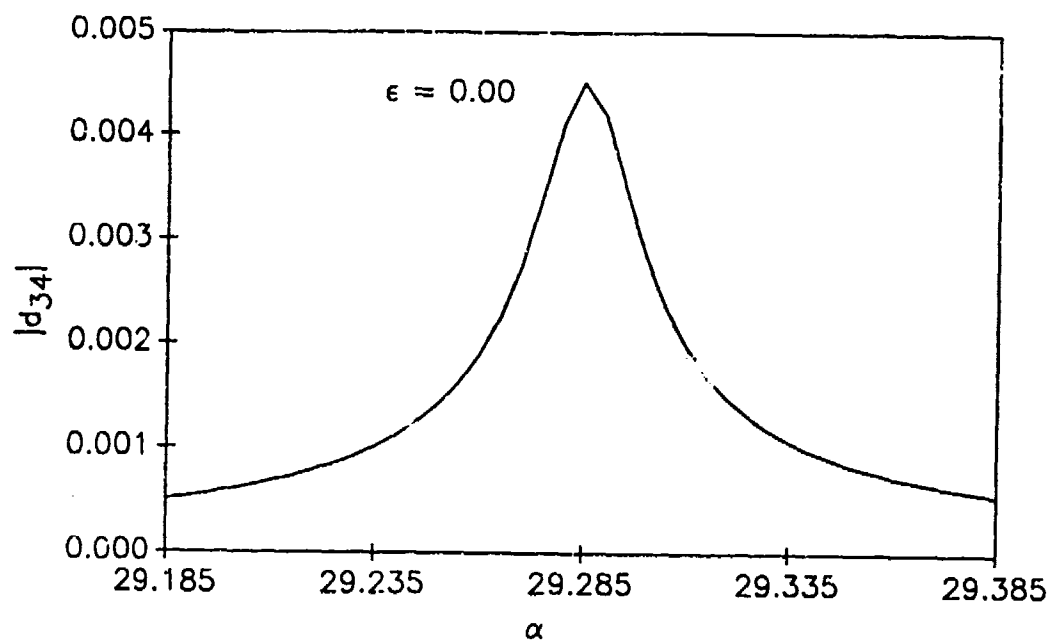


FIG 13.  $|d_{34}|$  versus  $\alpha$  for a spherical particle ( $\epsilon = 0.00$ ).  $\bar{n} = 1.334 + 1.2 \times 10^{-9}i$ .

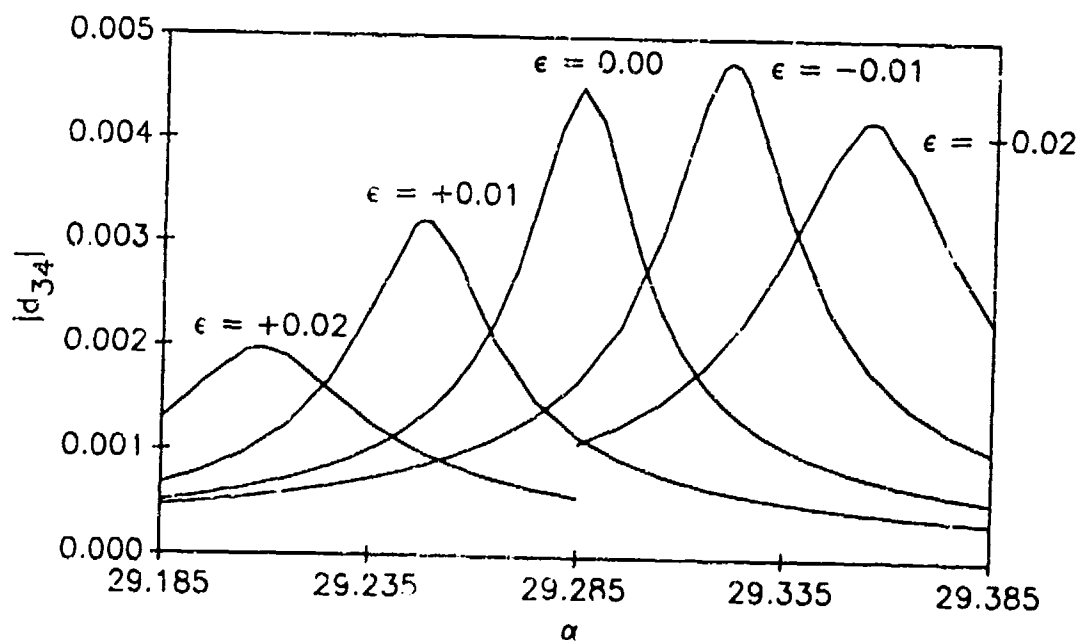


FIG 14.  $|d_{34}|$  versus  $\alpha$  for spherical particle with surface deformations of  $\epsilon = 0.00, \pm 0.01$ , and  $\pm 0.02$ .  $\bar{n} = 1.334 + 1.2 \times 10^{-9}i$ .

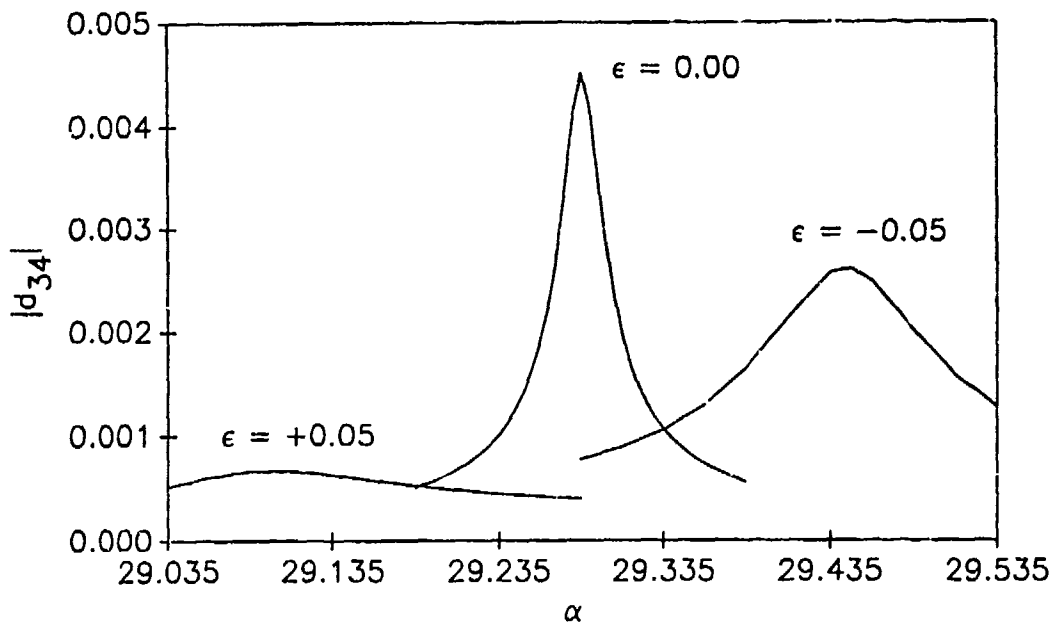


FIG 15.  $|d_{34}|$  versus  $\alpha$  for spherical particle with surface deformations of  $\epsilon = 0.00$  and  $\pm 0.05$ .  $\bar{n} = 1.334 + 1.2 \times 10^{-9}i$ .

	A	B	C
prolate) <sub>1.1</sub>	1.405 (+38%)	0.919 (-10%)	1.029 (+1%)
prolate) <sub>1.2</sub>	1.731 (+70%)	0.889 (-13%)	1.043 (+2%)
oblate) <sub>1.1</sub>	0.981 (-4%)	1.098 (+8%)	1.280 (+26%)
oblate) <sub>1.2</sub>	0.969 (-5%)	1.128 (+11%)	1.448 (+42%)

TABLE 1. Maximum normalized source function value (and % difference from spherical particle maximum value) for equal volume prolate/oblate spheroids of major to minor axis ratios of 1.1 and 1.2 and of orientations A, B, and C for plane wave incidence. Parameters are for a CO<sub>2</sub> laser incident upon a water droplet.  $\alpha_{sphere} = 8.0$  and  $\bar{n} = 1.179 + 0.072i$ .



$\epsilon$	Circumference [ $\lambda_{ext}$ ] at $\alpha = 29.285$	$\alpha_{res}$	Circumference [ $\lambda_{ext}$ ] at $\alpha_{res}$
-0.02	29.212	29.355	29.282
-0.01	29.248	29.321	29.284
0.00	29.285	29.285	29.285
+0.01	29.322	29.248	29.285
+0.02	29.358	29.208	29.281

TABLE 2. Circumference (in units of  $\lambda_{ext}$ ) for spherical particle with surface deformation at the 34th, 1st order magnetic wave resonance for  $\epsilon = 0.00, \pm 0.01$ , and  $\pm 0.02$ .  $\bar{n} = 1.334 + 1.2 \times 10^{-9}i$ .

BLANK

## **Light Scattering at Zero Degrees by Particulate Suspensions**

**Edward S. Fry and G. G. Padmabandu**  
**Department of Physics, Texas A & M University**  
**College Station, TX 77843**

### **RECENT PUBLICATIONS AND SUBMITTALS FOR PUBLICATION:**

- A) "Scattering of Femtosecond Laser Pulses," W. E. White, C. Wang, and E. S. Fry, Submitted to the Proceedings of the 1989 CRDEC Scientific Conference on Obscuration and Aerosol Research.
- B) "Absorption Measurements Using an Integrating Cavity," R. M. Pope, E. S. Fry, and R. L. Montgomery, Submitted to the Proceedings of the 1989 CRDEC Scientific Conference on Obscuration and Aerosol Research.
- C) "Scattering of Femtosecond Laser Pulses," W. E. White, Ph. D Thesis, Texas A&M University, December 1989.
- D) "Measurement of Light Scattering at  $0^\circ$  by Small Particle Suspensions," G. G. Padmabandu, and E. S. Fry, Submitted to the SPIE Proceedings, Ocean Optics X, April 1990.
- E) "Time Averaged Scattering of Femtosecond Laser Pulses by a Single Dielectric Sphere," William E. White, Edward S. Fry, and Ching Wang, Submitted to Applied Optics, October 1990.
- F) "Light Scattering at Zero Degrees by Particulate Suspensions," Edward S. Fry and G. G. Padmabandu, Submitted to the Proceedings of the 1990 CRDEC Scientific Conference on Obscuration and Aerosol Research. (This Paper)

### **ABSTRACT**

Light scattering at  $0^\circ$  by small particles has generally not been studied because of the difficulties associated with separating the

scattered beam from the main beam. The importance of this phenomenon will be discussed and an experimental resolution of the difficulties will be described. Data for 11  $\mu\text{m}$  polystyrene spheres suspended in water will be presented for scattering over the angular range,  $-0.5^\circ$  to  $05^\circ$ , with a resolution of  $0.01^\circ$ . These data will also be presented for scattering at  $0^\circ$  as a function of particle concentration.

This work will be extended to obtain absolute scattering amplitudes and phases over a wider range of angles centered at zero degrees. Work is also continuing on Mueller matrix measurements of sphere aggregates; femtosecond time resolved scattering from single levitated particles; and interactions of ultra high power, low energy laser pulses with aerosols.

## 1. INTRODUCTION

The focus of this paper is to investigate the light scattering by small particles at and near an angle of zero degrees. Light scattering by small particles has been the subject of intense investigations for many decades but all experimental work to date has been limited to angles from the near forward direction<sup>1-3</sup> to the back scattering direction. The limiting experimental factor in the forward direction,  $\theta = 0^\circ$ , is the unscattered plane wave which is superimposed on the scattered spherical wave.<sup>4,5</sup> As Van de Hulst<sup>6</sup> stated, "An experiment by which this spherical wave can be observed is impossible. . . . ." Actually it is not impossible, but there has, in fact, been little previous experimental success in attempts to separate the two waves in the forward direction.

Nevertheless, small angle scattering is extremely important. Because of its sheer magnitude at small angles, it significantly affects light propagation through dust, smokes, haze, and the atmosphere in general. It thus plays a critical role in imaging, laser propagation, etc.

Zero degree scattering may also be extremely useful in providing a classification scheme for all particles via their symmetries. Specifically, the Mueller matrix elements at a scattering angle of zero degrees

provide six symmetry classes for particles, including the class of particles with no symmetries.<sup>7</sup>

Measurements of scattering at zero degrees are especially important because of their fundamental relation to extinction via the optical theorem.<sup>1</sup> Specially the total extinction cross section  $C_{\text{EXT}}$  is given by,

$$C_{\text{EXT}} = \frac{4\pi}{k^2} \text{Re}[S(0^\circ)]$$

where,  $S(0^\circ)$  is the forward scattering amplitude and  $k$  is the wave vector of the incident wave. Thus, a measurement of the forward scattering amplitude gives the extinction cross section.

Next, there should be a coherent scattering effect at zero degrees from monodisperse suspensions of identical particles<sup>1</sup>. Observations of this effect have not been reported, but it should produce a pronounced peak in the scattering function at zero degrees; its amplitude is proportional to the square of the number of particles. For example, consider the forward scattering from a suspension of identical particles in a cylindrical volume of radius  $R$  as in Fig. 1

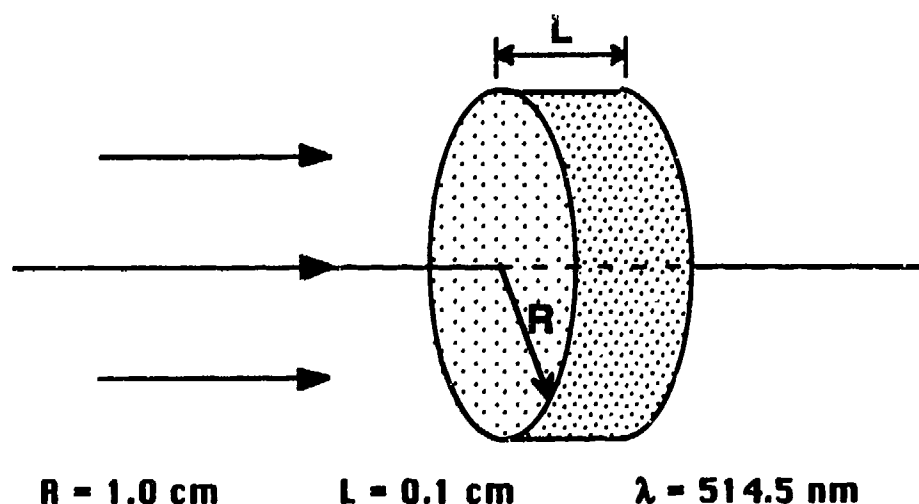


Fig. 1. Scattering geometry for forward scattering

Assuming the particle distribution is uniform and that the light propagation is along the axis of the cylinder, the angular width (FWHM) of this forward scattered peak, shown in Fig. 2, can be written as,

$$\Delta\theta_{\text{FWHM}} = 1.12 \frac{\lambda}{R}$$

where  $\lambda$  is the wavelength of light. Note that this is slightly over twice the angular width (FWHM) of the diffraction maximum of a circular aperture of the same radius.

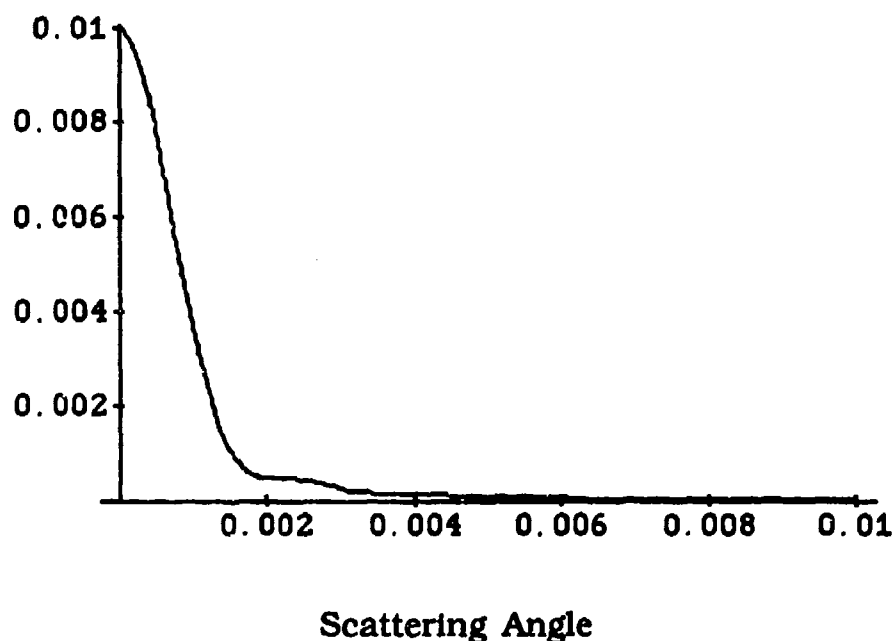


Fig. 2. Forward scattered intensity vs scattering angle for a collection of monodisperse particles.

Finally, since the strong forward scattering is coincident with the direct beam, it can produce erroneous results in experimentally measured optical extinction coefficients. Several algorithms have been developed to overcome these difficulties.<sup>8</sup> A precise measurement of the scattering at zero degrees will provide a direct test of these computations. The need for a measurement of scattering at and near zero degrees is obvious.

The only measurement of the forward scattering at zero degrees from isolated Mie spheres was reported in 1989<sup>9</sup>. This nice experiment took advantage of the Guoy phase shift at the waist of a focused Gaussian beam. However, it neglected the scattering phase shift and thus it is applicable only to very small particles. By contrast, the present work is directed towards all particles including larger ones for which there is a significant scattering phase shift

The identifying characteristic of the light scattered at zero degree is its shift in phase. Due to the Brownian motion, this phase shift has a spatial time dependence when light is scattered from a suspension of particles. However, linear interferometric techniques to separate the scattered light from the unscattered have been unsuccessful due to systematic problems. Our new technique, which takes the advantage of the time varying phase shift, will measure light scattering at zero degrees from particle suspensions as well as from isolated scatterers. The approach is based on the transient energy coupling between coherent light beams<sup>10-12</sup> in a photorefractive BaTiO<sub>3</sub> crystal.

### **LIGHT BEAM COUPLING IN BaTiO<sub>3</sub>**

Two beam coupling in BaTiO<sub>3</sub> has been discussed by several authors<sup>13,14</sup> and its application to the present work has been previously discussed<sup>15</sup>. Briefly, two coherent light beams  $I_{10}$  and  $I_{20}$  interfering in a BaTiO<sub>3</sub> crystal produce a space charge field due to charge migration (see Fig. 3). This periodic space charge field modulates the refractive index of the medium through the electro-optic interaction, producing an index grating. For BaTiO<sub>3</sub>, in the absence of an external electric field, this index grating is  $\pi/2$  phase shifted from the interference pattern<sup>13,14</sup>. The grating can diffract light from the beams which create it and thus energy is coupled between the two beams. As a result, one beam ( $I_2$ ) emerges from the crystal with a greater intensity, while the other beam ( $I_1$ ) is attenuated. For our experiment  $I_{10}$  is referred to as the object beam, and  $I_{20}$  as the reference beam. With correctly chosen parameters, greater than 99% of the energy from the object beam  $I_{10}$

can be coupled into the transmitted beam  $I_2$  by using a  $0^\circ$  cut  $\text{BaTiO}_3$  crystal.

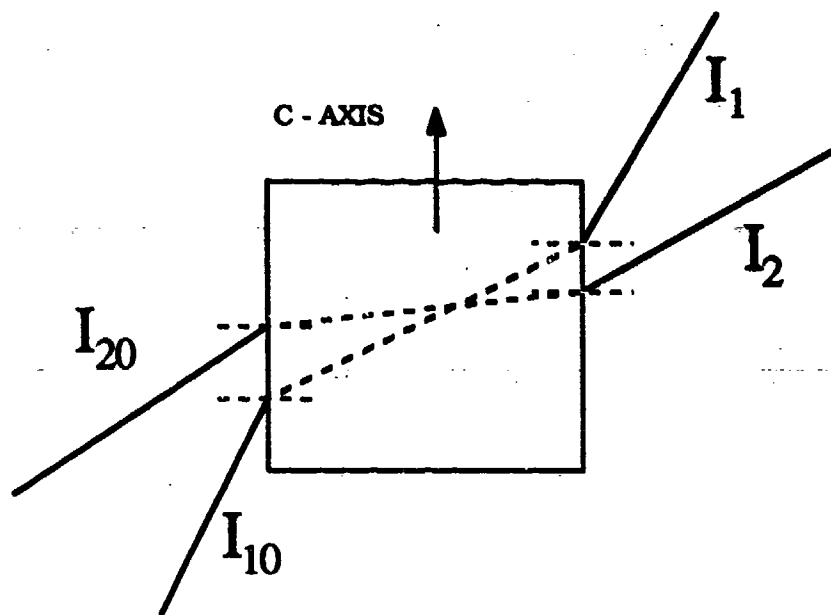


Fig. 3. Beam coupling in  $\text{BaTiO}_3$

The transient nature of the coupling comes from the finite response time  $\tau$  of the crystal. The formation and the erasure of the index grating requires this finite time  $\tau$  which is inversely proportional to the total light intensity<sup>14</sup>. In  $\text{BaTiO}_3$  the value of  $\tau$  ranges from a few seconds at very low light intensities ( $\text{mW}/\text{cm}^2$ ) down to nanoseconds at high intensities ( $\text{MW}/\text{cm}^2$ ). If one beam changes its position or phase rapidly compared with  $\tau$ , a phase mismatch between the light interference pattern and the grating occurs causing a sudden change in the steady state intensities of the two transmitted beams. This is known as transient energy coupling (TEC). Any changing part of the transmitted object beam  $I_1$  is highlighted in a dark background. The amount of energy that couples in a sudden phase mismatch depends on the reference beam intensity.

Due to Brownian motion, small particles in a solution move several wavelengths in a millisecond. Consequently, the light scattered from these particles undergoes a time varying phase change and thus, it can



be separated from the unscattered light by using transient energy coupling. Furthermore, since this is a real time holographic technique which continuously subtracts the previous picture from the current, the scattering from stationary parts of the instrument is removed from the object beam. For example, scattering from imperfections in the cell windows is not transmitted.

### 3. THE EXPERIMENT

A schematic of our experiment for measuring forward light scattering is shown in Fig. 4. The cw Ar<sup>+</sup> laser (514.5 nm) is polarized in the plane of incidence and the c- axis of the crystal is as shown. The incident laser beam is split into a reference beam and an object beam.

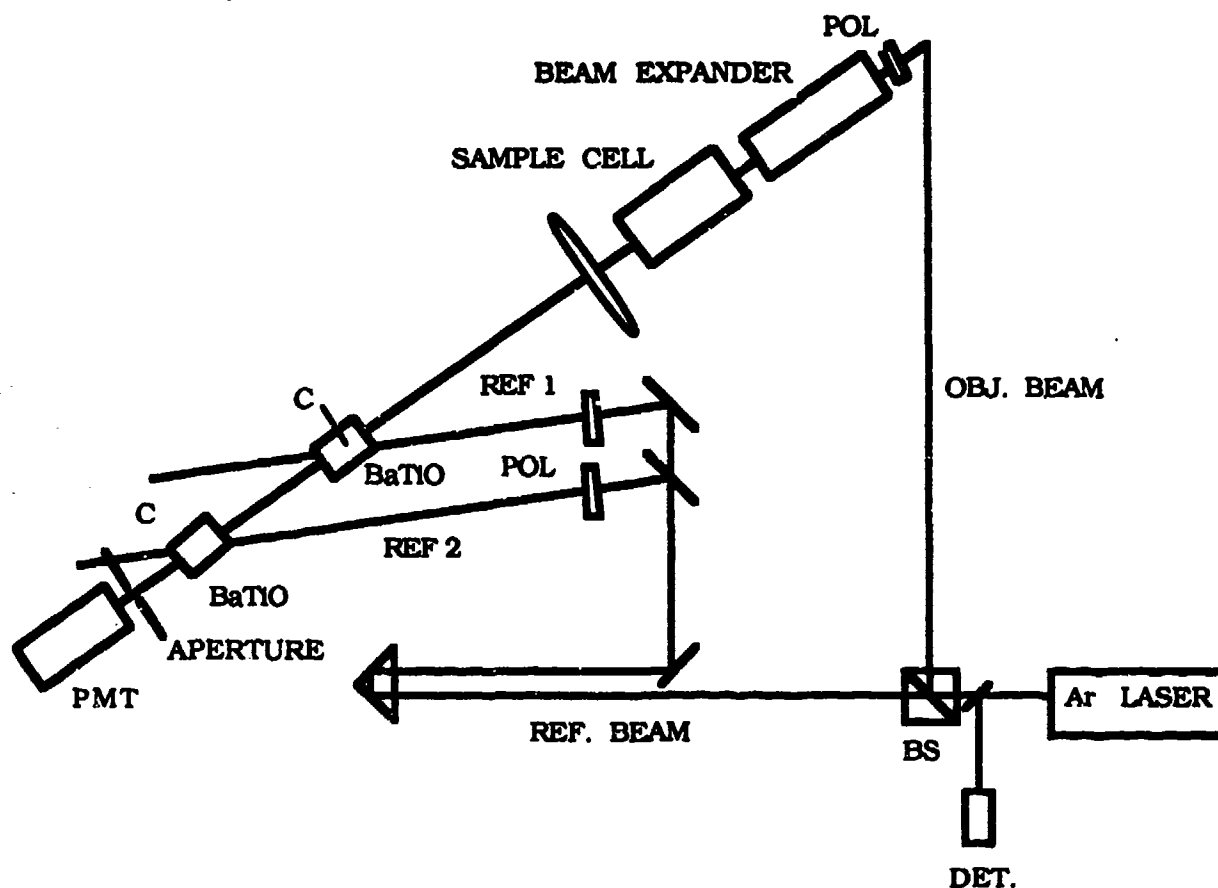


Fig. 4. Experimental set up to measure forward scattering

The reference beam is then split again. The object and reference beams follow equal optical paths before they are mixed again in BaTiO<sub>3</sub> crystals. The object beam is expanded and collimated to a 33 mm diameter to reduce the beam divergence to 0.001°. This beam is then passed through a 15 cm long, 7.5 cm diameter quartz cell, which contains a water based suspension of polystyrene spheres. The average diameter of the spheres was 11  $\mu\text{m}$  and the standard deviation was 1.9  $\mu\text{m}$ . The laser power incident on the sample cell was 7 mW. The light transmitted through the sample (scattered + unscattered) was collected and focused onto two successive BaTiO<sub>3</sub> crystals as in Fig.3. Inside the two crystals, the two reference beams (REF 1 and REF 2) couple with the object beam and the unscattered portion of the object beam is filtered out via photorefractive coupling.

A 5 mm BaTiO<sub>3</sub> single crystal cut parallel to crystal axes can produce 99% extinction of the object when large incidence angles are used. This extinction is not sufficient for scattering measurements since the scattered component of the beam is weak compared to the unscattered component. By using two BaTiO<sub>3</sub> crystals in series we achieved about 99.9% extinction of the object beam or 1000:1 extinction ratio. The two crystals were oriented so that each one produced approximately 97% extinction of the object beam intensity.

The use of two crystals instead of one longer crystal has several advantages. In one long crystal a long interaction length cannot be appropriately maintained since the two beams follow slightly curved paths when they couple through the index grating. In addition, a uniform grating cannot be maintained along the crystal since it depends on the ratio of the intensities of the two coupling beams. These problems are not present in the two crystal scheme since each crystal is short and two separate reference beams are used. The two crystal scheme can also suppress the crystal generated scattering noise. The strong object beam can undergo scattering in the crystal and send some light in the forward direction. Since the phase of this scattered light is constant in time, the second crystal conveniently subtracts it from the object beam when two crystals are used. However, there is a significant

loss of the signal due to large Fresnel reflections at the four faces of the two crystals.

After filtering through the two crystals, the object beam consisted mainly of the forward scattered light from the moving polystyrene spheres in the sample cell. This light is focused onto a 70  $\mu\text{m}$  pinhole and is detected in a photomultiplier tube (PMT). For one measurement, the PMT signal was recorded as a function of a increasing concentration of scatterers in the cell. For the second, the pinhole-PMT assembly was scanned across the object beam using a fine translational stage and the angular dependance of the signal was recorded for the range from  $-0.2^\circ$  to  $0.2^\circ$ .

Fig.5 shows the the results for the scattered intensity at  $0^\circ$  as a function of the concentration of scatterers in the suspension. The error bars represent the statistical fluctuations of each data point. For low concentrations, the signal increased monotonically with the concentration, indicating increased scattering as more particles were

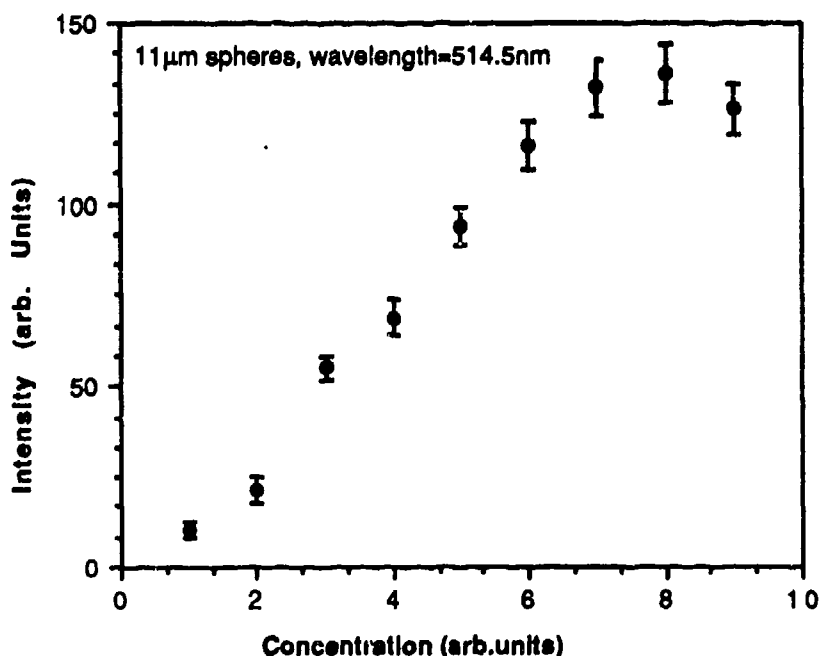


Fig. 5. Forward Scattering vs Particle Concentration

added. This is positive evidence to confirm that the photorefractive crystal has separated the scattered light from the unscattered. Note that the total intensity transmitted by the sample decreases as the concentration of scatterers increases but that the scattering at zero degrees should increase as we observed. However, for very large concentrations, a decrease in the signal is observed that is believed to be due to multiple scattering in the polystyrene suspension and has been discussed in detail.<sup>15</sup>

Fig. 6 shows the variation of the forward scattered intensity as a function of the angle measured from the  $\theta = 0^\circ$  direction.. The angular resolution for this measurement was  $0.01^\circ$ . From the graph it is clear that scattered light is detected in the angular region from  $-0.05^\circ$  to  $+0.05^\circ$ . The sharp fall of the detected signal between  $0.05^\circ$  and  $0.1^\circ$  and the loss of the signal beyond  $0.1^\circ$  is not real. In order to get a large extinction ratio from the crystal, it was necessary to use a large angle of incidence for the object beam. This reduced the useable aperture of the crystal, and the light scattered at angles greater than  $0.05^\circ$  did not clear the crystal aperture. This problem can be avoided by using a  $45^\circ$  cut  $\text{BaTiO}_3$  crystal which can produce a very large coupling efficiencies at near normal incidence<sup>16</sup>.

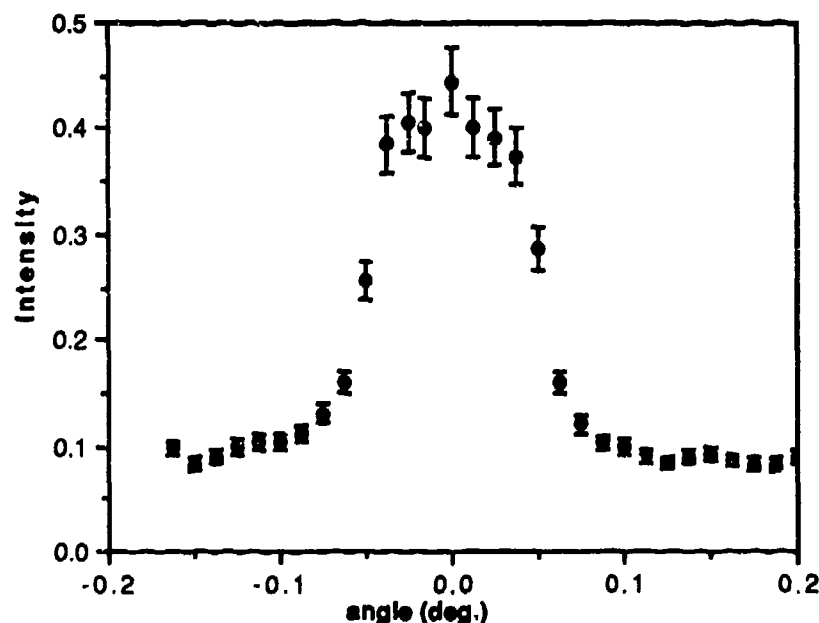


Fig. 6. Forward scattering as a function of angle

#### 4. CONCLUSION

In conclusion, we have successfully used the photorefractive technique to isolate the forward scattered light from polystyrene spheres suspended in water. This novel technique may be used to measure forward scattering from aerosols as well as isolated particles such as fibers and spheres. Aerosols are in constant Brownian motion and they will produce a time dependent phase in the scattered light so that the transient energy coupling can isolate the scattered light from the unscattered. For a single sphere or a fiber however, a time dependent phase should be introduced by applying a small mechanical vibration to the particle. This approach is still in its infancy and further investigation is needed to fully exploit it.

#### 5. ACKNOWLEDGMENTS

This material is based in part upon work supported by the Office of Naval Research under contract N00014-89-J-1466 and by the Texas Advanced Technology Program under Grant No. 3239.

#### 6. REFERENCES

1. C. F. Bohren and D. R. Huffman, Absorption and scattering of light by small particles. p69, (Wiley Interscience, New York 1981) .
2. B. W. Bell and W. S. Bickel, "Single fiber scattering matrix", Appl. Opt., 20 3874 (1981).
3. P. Chylek, J. T. Kiehl and M. W. Ko, "Narrow resonance structures in the Mie scattering characteristics", Appl. Opt. 17 3019 (1978).
4. T. J. Petzold, "Volume Scattering Function for Selected Ocean Waters", Scripps Institute of Oceanography, Ref.72-78 October (1972).
5. R. W. Spinrad, "Measurements of the volume scattering function near forward angles for suspended oceanic particulates", SPIE vol.60, Ocean optics V 18 (1978).

6. H. C. Van de Hulst, Light Scattering by Small Particles, p30 (Dover NY 1981)
7. Chia-Ren Hu, G. W. Kattawar, M. E. Parkin and P. Herb, "Symmetry theorems on the forward and Backward Scattering Mueller Matrices for Light Scattering from a Nonspherical Dielectric Scatterer", *Appl. Opt.* **26**, 4159 (1987).
8. A. Deepak and M. A. Box, "Forward Scattering Corrections for Optical Extinction Measurements in Aerosol Media: 1. Monodispersion", *Appl. Opt.* **17**, 2900-2908 (1978); *Appl. Opt.* **17**, 3169-3176 (1978).
9. J. S. Batchelder and M. A. Taubenbatt, "Interferometric Detection of Forward Scattered Light from Small Particles", *Appl. Phys. Lett.*, **55** 215 (1989).
10. D. Z. Anderson, D. M. Lininger and J. Feinberg, "Optical tracking novelty filter", *Opt. Lett.* **12** 123 (1987).
11. N. S. Kwong, Y. Tamita and A. Yariv, "Optical tracking Filter using transient energy coupling", *J. Opt. Soc. Am. B* **5** 1788 (1988).
12. R. S. Cudney, R. M. Pierce and J. Feinberg, "Transient Detection Microscope", *Nature* **332** 424 (1988)
13. J. Feinberg and R. W. Hellwarth, "Photorefractive effects and light induced charge migration in  $\text{BaTiO}_3$ ", *Opt. Lett.* **5**, 519 (1980).
14. J. Feinberg and K. R. McDonald in "Photorefractive Materials and Their Applications, vol.II", P. Gunter and J. P. Huignard ed. (Springer-Verlag 1988)
15. G. G. Padmabandu and E. S. Fry "Measurement of Light Scattering at  $0^\circ$  by Small particle Suspensions", Submitted to be published in SPIE proceedings, Ocean Optics X (1990)
16. J. E. Ford, Y. Fainmann and S. H. Lee, "Enhanced Photorefractive Performance from  $45^\circ$  cut  $\text{BaTiO}_3$ ", *Appl. Opt.* **28** 4808 (1989).

# RAPID MATRIX INVERSION

D. K. Cohoon

September 14, 1990

## 1 INTRODUCTION

We consider the problem of solving linear equations where the coefficients and unknowns may be members of  $\mathbb{Q}$ ,  $\mathbb{R}$ , or  $\mathbb{C}$ . The dramatic difference between an  $N^{2+\epsilon}$  matrix inversion method and the traditional method which requires  $N^3$  steps to invert an  $N$  by  $N$  matrix can be seen by conceiving of a computer that could perform ten billion operations per second. If one had a model of a man or some other scatterer in a radiation divided into a million small subunits in which one approximates electric and magnetic fields components by polynomials of degree two, then roughly 1000 human lifetimes would be required to solve for these unknowns once the matrix was created using the traditional method, whereas only one hour would be needed for the method requiring  $N^{2+\epsilon}$  steps, if  $\epsilon$  is sufficiently small.

We describe an order  $N^{2+\epsilon}$  algorithm for inverting a class of dense matrices. Part of our algorithm is based on rapid multiplication. The first algorithm which gave an order smaller than  $N^3$  for multiplying matrices was due to Strassen ([6]). This algorithm was based on reducing the problem using 2 by 2 submatrices and the multiplication scheme

$$\begin{pmatrix} a_{(1,1)} & a_{(1,2)} \\ a_{(2,1)} & a_{(2,2)} \end{pmatrix} \begin{pmatrix} b_{(1,1)} & b_{(1,2)} \\ b_{(2,1)} & b_{(2,2)} \end{pmatrix} = \begin{pmatrix} c_{(1,1)} & c_{(1,2)} \\ c_{(2,1)} & c_{(2,2)} \end{pmatrix} \quad (1.1)$$

where

$$c_{(1,1)} = p_1 + p_6 - p_5 + p_7 \quad (1.2)$$

$$c_{(1,2)} = p_3 + p_5 \quad (1.3)$$

$$c_{(2,1)} = p_2 + p_6 \quad (1.4)$$

$$c_{(2,2)} = p_1 - p_2 + p_3 + p_4 \quad (1.5)$$

and the functions  $p_j$  for

$$j \in \{1, 2, 3, 4, 5, 6, 7\}$$

are defined by the equations

$$p_1 = (a_{(1,1)} + a_{(1,2)})(b_{(1,1)} + b_{(2,2)}) \quad (1.6)$$

and

$$p_2 = (a_{(2,1)} + a_{(2,2)})b_{(1,1)} \quad (1.7)$$

$$p_3 = a_{(1,1)}(b_{(1,2)} - b_{(2,2)}) \quad (1.8)$$

$$p_4 = (-a_{(1,1)} + a_{(2,1)})(b_{(1,1)} + b_{(1,2)}) \quad (1.9)$$

$$p_5 = (a_{(1,1)} + a_{(1,2)})b_{(1,1)} \quad (1.10)$$

$$p_6 = a_{(1,1)}(-b_{(1,1)} - b_{(2,1)}) \quad (1.11)$$

$$p_7 = (a_{(1,2)} - a_{(2,2)})(b_{(2,1)} + b_{(2,2)}) \quad (1.12)$$

Here there are 7 multiplications and 18 additions and subtractions. We consider a  $2^N$  by  $2^N$  matrix. For this size of matrix we suppose that  $A(N)$  is the number of additions and that  $M(N)$  is the number of multiplications. Then the number of multiplications is

$$M(N+1) = 7M(N) \quad (1.13)$$

and the number of additions is

$$A(N+1) = 18(2^N)(2^N) + 7A(N) \quad (1.14)$$

since there are

$$4^N = (2^N)(2^N) \quad (1.15)$$

entries in a  $2^N$  by  $2^N$  matrix. We now make use of the following lemma.

**Lemma 1.1** *The solution of the difference equation*

$$y_{n+1} = A[R^n] + \lambda y_n$$

*that satisfies  $y_0 = 0$  is when  $R$  is distinct from  $\lambda$  given by*

$$y_n = \left( \frac{A}{\lambda - R} \right) (\lambda^n - R^n)$$

Solving the difference equation we see that since a general solution is

$$A(N) = C(7^N) - 6(4^N) \quad (1.16)$$

since a particular solution is, upon using  $A = 18$  and  $\lambda = 7$  and  $R = 4$  in the Lemma, given by

$$P(N) = -6(4^N) \quad (1.17)$$

As a check note that

$$-6(4)(4^N) = 18(4^N) + 7(-6)(4^N). \quad (1.18)$$

Since

$$A(0) = 0 \quad (1.19)$$

as no additions are required for multiplying 1 by 1 matrices, we see that

$$C = 6 \quad (1.20)$$



We can then see that the total number of operations for multiplying a  $2^N$  by  $2^N$  matrix is estimated by the inequality

$$A(N) + M(N) < 6 \cdot 7^N + 7^N \quad (1.21)$$

Thus, since the number of rows is

$$M = 2^N \quad (1.22)$$

we see an exponent  $\alpha$  such that

$$M^\alpha = 2^{\alpha N} < 7^{N+1} \quad (1.23)$$

or applying  $\log_2$  to both sides of inequality (1.23) we see that the order  $\alpha$  is estimated by the inequality,

$$\alpha N < \log_2(7) + N \{\log_2(7)\} \quad (1.24)$$

or upon dividing all terms of equation (1.24) by  $N$  and letting  $N$  go to infinity, we see that asymptotically the order  $\alpha$  is estimated by

$$\alpha < \log_2(7) = 2.807 \quad (1.25)$$

which means that the number of operations for multiplying two  $M$  by  $M$  matrices is about  $M^{2.807}$ .

The number of steps required for matrix inversion can in many circumstances be shown to be equivalent, except for multiplication by a constant independent of the number of rows, to the number of operations required for matrix multiplication.

**Proposition 1.1** *If the nonsingular  $N$  by  $N$  matrix  $A$  can be expressed in the form  $A = D - P$ , where  $D$  is an invertible diagonal matrix, and if  $D^{-1}P$  has  $\ell_\infty$  matrix norm less than 1, then for every number  $n$  of significant digits, there is a number  $M_n$ , independent of the number  $N$  of rows in the matrix, such that the entries of the inverse  $A^{-1}$  of  $A$  can be determined to at least  $n$  significant digits by the sum,*

$$A_n^{-1} = D^{-1} [I + (D^{-1}P) + (D^{-1}P)^2 + \dots + (D^{-1}P)^{M_n}] \quad (1.26)$$

which means that the number of operations for computing the inverse is equal to

$$C(A^{-1}) = (M_n - 1)C_N + \{M_n + 1\}N^2 \quad (1.27)$$

where  $C_N$  denotes the number of operations required for matrix multiplication.

**Proof.** Observe that since if  $r$  is equal to the norm of  $D^{-1}P$  that the norm of the remainder can be made arbitrarily small simply by making  $M_n$  large enough, since the remainder terms involve sums of powers of  $D^{-1}P$  and

$$\| (D^{-1}P)^{M_n} \| \leq r^{M_n} < 10^{-n} \| D^{-1} \| \quad (1.28)$$

that then  $A_n^{-1}$  agrees with  $A^{-1}$  to  $n$  decimal places. Since  $D$  is diagonal,  $N^2$  operations are required for the computation of  $D^{-1}P$ . Let us suppose that  $C_N$  operations are required for matrix multiplication. Then by performing the calculations in succession we see that exactly  $C_N$  operations are required for each of the computations  $(D^{-1}P)^2, (D^{-1}P)^3, \dots$ , and  $(D^{-1}P)^{M_n}$  giving a total of  $(M_n - 1)C_N$  operations. There are  $M_n N^2$  summation operations followed by  $N^2$  operations for the multiplication of the sum by  $D^{-1}$ . This argument proves equation (1.27).

**Proposition 1.2** *If  $A$  is any endomorphism of  $\mathbb{R}^n$ , then there is a*

$$\lambda_0 \in \mathbb{C} - \{0\}$$

*such that*

$$T_0 = \lambda_0 I - A \quad (1.29)$$

*is invertible and*

$$R_0 = (-T_0)^{-1} \quad (1.30)$$

*is known. Then there is an open connected set  $\Omega$  containing  $\lambda_0$  such that*

$$R_\lambda = (\lambda I - T_0)^{-1} \quad (1.31)$$

*exists and*

$$\frac{dR_\lambda}{d\lambda} = -R_\lambda^2 \quad (1.32)$$

*with*

$$R_0 = (-T_0)^{-1} \quad (1.33)$$

*giving the initial condition for the Ricatti equation (1.32).*

**Proof.** We use a classical theory of resolvents of operators (e.g. Friedman [3], pp 194-195). To find a  $\lambda_0$  such that the  $\ell_\infty$  norm of the matrix  $\lambda_0^{-1}A$  is smaller than 1 and use the result of the previous proposition.

**Definition 1.1** *We say that a  $\lambda \in \mathbb{C}$  is in the resolvent set of  $T_0$  if*

$$R_\lambda = (\lambda I - T_0)^{-1} \quad (1.34)$$

*exists.*

Note that we can consider the component of the complex plane  $\mathbb{C}$  containing  $\lambda_0$  such that the matrix  $R_\lambda$  defined by equation (1.34) exists. We know that  $T_0$  is invertible, and that if  $\lambda$  is in the resolvent set of  $T_0$ , then

$$\text{Det}(\lambda I - T_0) \neq 0 \quad (1.35)$$

and that the set of all  $\lambda$  satisfying equation (1.35) is, since the determinant function  $\text{Det}$  is continuous, an open set  $U$  containing  $\lambda_0$ . We simply choose  $\Omega$  to be a convex open subset of the component of  $U$  containing  $\lambda_0$ . We then write

$$\begin{aligned} R_\lambda - R_\mu &= (\lambda I - T_0)^{-1} - (\mu I - T_0)^{-1} \\ &= (\lambda I - T_0)^{-1} [(\mu I - T_0) - (\lambda I - T_0)] (\mu I - T_0)^{-1} \\ &= (\mu - \lambda) (\lambda I - T_0)^{-1} (\mu I - T_0)^{-1} \\ &= (\mu - \lambda) R_\lambda R_\mu \end{aligned} \quad (1.36)$$

Dividing both sides of equation (1.36) by  $\lambda - \mu$  and taking the limit as  $\mu$  approaches  $\lambda$  we see that equation (1.32) is valid in  $\Omega$  since for all choices of  $\lambda$  and  $\mu$  in  $\Omega$  the straight line joining  $\lambda$  and  $\mu$  is also contained in  $\Omega$ . This completes the proof of the proposition.

A contour integration method can also be used to calculate the inverse of  $A$ . One method is described by the following theorem.

**Theorem 1.1** *If  $C$  is a simple closed curve in the complex plane which contains  $\lambda_0$  but does not cross or contain within its interior any of the points  $\lambda$  where  $R_\lambda$  does not exist, then*

$$A^{-1} = \frac{1}{2\pi i} \int_C \frac{R_\lambda}{\lambda - \lambda_0} d\lambda \quad (1.37)$$

A variety of identities similar to that of equation (1.36) are found in Cohoon ([1]). We note that ([1]) if we introduce the operator,

$$R_a f(x) = \int_0^\infty \exp(a(x-s)) f(s) ds, \quad (1.38)$$

we can systematically solve ordinary differential equations of the form,

$$\left[ \left( \frac{d}{dx} - \lambda_1 \right)^{n_1} \left( \frac{d}{dx} - \lambda_2 \right)^{n_2} \cdots \left( \frac{d}{dx} - \lambda_r \right)^{n_r} \right] u(x) = f(x), \quad (1.39)$$

where  $f(x)$  is any member of  $C^\infty(\mathbb{R})$ . A solution of the general nonhomogeneous linear ordinary differential equation (1.39) with constant coefficients is given by

$$u(x) = [R_{\lambda_1}^{n_1} R_{\lambda_2}^{n_2} \cdots R_{\lambda_r}^{n_r}] f(x) \quad (1.40)$$

where the latter iterated integral expression can be reduced to a sum of single integrals by realizing that the identity

$$R_\lambda R_\mu = \frac{R_\lambda - R_\mu}{\lambda - \mu} \quad (1.41)$$

is identical to the expansion by partial fractions relation

$$X_\lambda X_\mu = \frac{X_\lambda - X_\mu}{\lambda - \mu} \quad (1.42)$$

where  $X_\lambda$  and  $X_\mu$  are defined by

$$X_\lambda = \frac{1}{x - \lambda} \quad (1.43)$$

Iterative methods have been suggested by many authors for overcoming computational complexity in electromagnetic interaction computations and most of these developments required that the scattering body be diaphanous or have nearly the properties of free space. However, a way of obtaining discretizations that use lower order matrices and use manipulations of these matrices to improve the accuracy of the solution have been developed by Cohoon ([2]); this paper describes a computerizable finite rank integral equation whose solution is exactly the projection onto the space of approximates of the solution of the original infinite rank integral equation. These methods of obtaining discretizations of integral equations that, upon solution, give accurate solutions of scattering problems, coupled with the potentially rapid methods of multiplying and inverting matrices give some promise of being able to develop realistic electromagnetic radiation dosimetry models as well as solving much larger matrix modeling problems of all types.

## 2 THE MATRIX INVERSION ALGORITHM

We now produce a method of finding the inverse of a general matrix  $A$  using these ideas.

**Theorem 2.1** *If  $A$  is an automorphism of  $C^N$  or  $R^N$  and  $\lambda$  is a complex number such that*

$$R_\lambda = (\lambda I - T_0)^{-1}$$

*exists, then we can find a connected, convex open set containing both  $\lambda_0$  and  $\lambda = 0$  such that if the  $R_\lambda$  defined by equation (2.1) exists, then we can obtain  $A^{-1}$  by solving the ordinary differential equation*

$$F'(s) = \frac{dR_\lambda}{d\lambda} \frac{d\lambda}{ds} \quad (2.1)$$

*along a curve*

$$\lambda : [0, 1] \rightarrow C \quad (2.2)$$

*joining  $\lambda = 0$  to  $\lambda = \lambda_0$  where*

$$F(0) = R_0 = (-T_0)^{-1} \quad (2.3)$$

*is the initial condition for equation (2.1).*

**Proof.** We just have to pick a curve  $\lambda = \lambda(s)$  which does not pass through any points of the spectrum, where

$$\text{Det}(\lambda I - T_0) = 0 \quad (2.4)$$

and since there are only a finite number of these points, we could with the proper choice of  $\lambda_0$  find a straight line

$$\lambda(s) = s\lambda_0 \quad (2.5)$$

which has this property. Then the differential equation (2.1) has the form,

$$F'(s) = \frac{dR_\lambda}{d\lambda} \frac{d\lambda}{ds} = -R_\lambda^2 \lambda_0 \quad (2.6)$$

This completes the proof of the theorem.

A variant of the ideas of this theorem can be used to treat a class of infinite matrices arising in several areas, including electromagnetic scattering theory.

**Theorem 2.2** *If  $L$  is a Fredholm integral operator given by*

$$LE(q) = \int_{\Omega} \mathcal{G}(p, q) E(q) d\nu(q) \quad (2.7)$$

*associated with the Fredholm integral equation*

$$E(p) - E^i(p) = \lambda(LE)(p) \quad (2.8)$$

where  $E^i$  is known and we are seeking the function  $E$ , and  $\mathcal{R}_\lambda$  is the resolvent kernel defined by

$$\frac{d\mathcal{R}}{d\lambda} = \int_{\Omega} \mathcal{R}_\lambda(p, w) \mathcal{R}_\lambda(w, q) d\nu(w) \quad (2.9)$$

with the initial condition being,

$$\mathcal{R}_0 = \mathcal{G}(p, q) \quad (2.10)$$

then the solution of equation (2.8) is given by

$$E = E^i + \lambda \mathcal{R}_\lambda E^i \quad (2.11)$$

where

$$\mathcal{R}_\lambda(p) E^i(p) = \int_{\Omega} \mathcal{R}_\lambda(p, q) E^i(q) d\nu(q) \quad (2.12)$$

**Proof:** The differential equation (2.9) is derived by expressing the inverse integral operator as a Born series assuming that  $\lambda$  is small and then analytically continuing the solution.

### 3 RAPID MATRIX INVERSION

In the previous sections we have related matrix inversion speed to matrix multiplication speed for a class of dense matrices. We shall use the lines for extending the matrix multiplication speed improvement for 2 by 2 matrices in our introductory section.

Assume that we have developed a matrix multiplication method for two  $m$  by  $m$  matrices that uses  $p$  multiplications and  $q$  additions.

**Theorem 3.1 (Fast Matrix Multiplication)** Suppose that  $A$  is a matrix with  $M = m^N$  rows and the same number of columns. Suppose that  $A(N)$  is the number of additions and  $\mathcal{M}(N)$  is the number of multiplications required for multiplying two matrices of this size. Then

$$\mathcal{M}(N+1) = p\mathcal{M}(N) \quad (3.1)$$

and

$$A(N+1) = q(m^N)(m^N) + pA(N) \quad (3.2)$$

and if  $\alpha$  is an exponent such that the matrix multiplication requires  $M^\alpha$  steps for multiplying two  $M$  by  $M$  matrices, then

$$\alpha < \text{Log}_m(p) \quad (3.3)$$

which means to get the desired result the number of multiplications required for the matrix multiplication just has to get down to

$$p = m^{2+\epsilon} \quad (3.4)$$

proof: To derive the difference equations for the number of multiplications and additions, we simply subdivide two  $m^{N+1}$  by  $m^{N+1}$  matrices into  $m$  submatrices each of which are  $m^N$  by  $m^N$  matrices. Treating the submatrices as members of an algebra, we see that the number of additions required to carry out the multiplications is  $q$  times the number of entries,  $m^{2N}$  plus the number of multiplications  $p$  of submatrices times the number  $A(N)$  of additions used in each of these multiplications. The number of multiplications is simply  $p$  times the number  $M(N)$  of multiplications required for multiplying two of the submatrices. These arguments constitute a derivation of the difference equations (3.1) and (3.2).

We now give the solution of the difference equations (3.1) and (3.2) and an estimate of  $A(N) + M(N)$ . Thinking of particular solutions plus general solutions of the homogenous equation associated with equation (3.2), we see that one solution of equation (3.2) is  $Dm^{2N}$  and that substitution into equation (3.2) implies that

$$Dm^{2(N+1)} - pDm^{2N} = qm^{2N} \quad (3.5)$$

which implies that

$$m^{2N} \{ Dm^2 - pD - q \} = 0, \quad (3.6)$$

which tells us that

$$D = \frac{q}{m^2 - p} \quad (3.7)$$

Thus, the most general solution of equation (3.2) is

$$A(N) = Cp^N + \left( \frac{q}{m^2 - p} \right) m^{2N} \quad (3.8)$$

We can solve for the constant  $C$  by considering a matrix with one row and column, the case  $N = 0$ , which would since no additions are required, tell us that

$$0 = A(N) = C + \left( \frac{q}{m^2 - p} \right) \quad (3.9)$$

or that

$$C = \frac{q}{p - m^2} \quad (3.10)$$

As a check on this work, we also consider the situation where the number of rows is  $M = m^1$  which means that  $N = 1$ . We know that in this case

$$q = A(1) = Cp + \left( \frac{q}{m^2 - p} \right) m^2 \quad (3.11)$$

which implies that

$$C = \frac{1}{p} \left[ q + \left( \frac{q}{p - m^2} \right) m^2 \right] \quad (3.12)$$

which after some manipulation is seen to be identical to that given by equation (3.10). The number of multiplications is easily seen to be

$$M(N) = p^N \quad (3.13)$$

We now estimate the total number of operations required to carry out the matrix multiplication. Observe that

$$A(N) + M(N) = \left( \frac{q}{p - m^2} \right) [p^N - m^{2N}] + p^N \quad (3.14)$$

From equation (3.14) we see that

$$A(N) + M(N) < \left[ \frac{q}{p - m^2} + 1 \right] p^N \quad (3.15)$$

Observe that if  $M = m^N$  is the number of rows and if the number of operations for matrix multiplication is  $M^\alpha$ , then equation (3.15) implies that

$$M^\alpha = m^{\alpha N} < \left[ \frac{q}{p - m^2} + 1 \right] p^N \quad (3.16)$$

Taking the logarithm to the base  $m$  of both sides of equation (3.16) we deduce that

$$\alpha N \text{Log}_m(m) < \text{Log}_m \left[ 1 + \frac{q}{p - m^2} \right] + N \text{Log}_m(p) \quad (3.17)$$

Dividing all terms of equation (3.17) by  $N$  and taking the limit as  $N$  approaches infinity we see that asymptotically we need

$$\alpha < \text{Log}_m(p) \quad (3.18)$$

If we could carry out the operations with  $p = m^{2+\epsilon}$ , then we would have

$$M^\alpha = M^{2+\epsilon} \quad (3.19)$$

as an estimate of the number of operations required to multiply two  $M$  by  $M$  matrices. The number of additions used in the multiplication of the submatrices apparently makes no difference the the asymptotic computational complexity of the matrix multiplication of the large matrices. Our discussion in the previous section then gives us a class of dense matrices that can also be inverted in this number of operations.

## References

- [1] Cohoon, D. K. "Free commutative semi-groups of right invertible operators with decomposable kernels" *Journal of Mathematical Analysis and Applications*, Vol 19, Number 2 (August, 1967) pp 274-281.
- [2] Cohoon, D. K. "An exact formula for the accuracy of a class of computer solutions of integral equation formulations of electromagnetic scattering problems" *Electromagnetics Volume 7, Number 2* (1987) pp 153-165.

- [3] Friedman, Avner. *Foundations of Modern Analysis* New York: Holt, Reinhart, and Winston (1970)
- [4] Kronsjo, Lydia. *Algorithms: Their Complexity and Efficiency, Second Edition* New York: John Wiley (1979)
- [5] Pan, Victor. "How can we speed up matrix multiplication" *SIAM Review*. Volume 26, Number 3 (July, 1984) pp 393-415.
- [6] Strassen, Volker. "Gaussian Elimination is not Optimal" *Numerical Math. Vol 13* (1969) pp 184-204.
- [7] Whittaker, E. T. and G. N. Watson. *A Course of Modern Analysis* London: Cambridge University Press (1986).



# THE RESPONSE OF A CLASS OF N LAYER ELECTROMAGNETICALLY BIANISOTROPIC SPHERES TO SPATIALLY AND TEMPORALLY COMPLEX WAVES

D. K. Cohoon

West Chester University

West Chester, PA 19383

July 30, 1990

We consider the problem of determining the response of a class of  $N$  layer electromagnetically bianisotropic spheres to a possibly transient and spatially heterogeneous radiation source (Barton [8], Chevaillier [19] [18], Chylek [20] Schaub [42], Tsai [46], Yeh [56]) when these spheres are placed in an ambient medium with material properties such that if  $\Omega$  is an open set in the ambient medium and

$$\int_{\Omega} \text{div}(\vec{E} \times \vec{H}^*) dv = 0,$$

then  $\vec{E}$  and  $\vec{H}$  are both zero in  $\Omega$

In this paper we describe the exact solution to the problem of describing the interaction of electromagnetic radiation with an  $N$  layer structure whose regions of continuity of

tensorial electromagnetic properties are separated by concentric spheres. We assume that each of the layers are bianisotropic.

Bianisotropic materials have used (Ferencz [25], Gamo [26], Hebenstreit [29], Shiozawa, [44] and Yeh [55]) in modeling a medium moving through an electromagnetic field. We consider also the possibility of an electromagnetic field whose spatial distribution would suggest a complex source that would include an off center laser beam interaction with a droplet or a radar beam sweeping across a stationary structure. By considering a layered spherically symmetric structure whose core may be metallic and with outer layers having complex material properties or containing sources of radiation, we may be able to predict the level of the hazard experienced by an individual with a metallic bone replacement or clamp who is placed in such a field.

The source of internal power density distribution for a bianisotropic structure exposed to external sources is distinct from anisotropic materials, since terms involving the product of the electric vector  $\vec{E}$  and the magnetic vector  $\vec{H}$  appear in the internal power density distribution. Using the concepts contained in this paper, a solution of an energy equation with a tensor conductivity can be obtained by an exact formula when the electromagnetic properties do not change during the exposure process. Using the derived energy density distribution as a source term, a more general nonlinear heat equation, taking into account radiative conductivity concepts can be derived. Several authors (Barton [8], Chylek [22], Schaub [42]) simply assume that the power density depends on the square of the length of the electric vector times the conductivity. In a bianisotropic material, however, there is a power density contribution from the coupling of the electric and magnetic vectors (see equation (4.6)).

## Contents

1	A Mie Like Solution for Bianisotropic Sphere Scattering	3
1.1	Problem Definition . . . . .	4
1.2	Spherical Harmonics and Orthogonality Relations . . . . .	4
1.3	Radial Functions and Field Representations . . . . .	6

<b>2 Expansion Coefficient Relations</b>	<b>17</b>
<b>3 Spatially Complex Sources</b>	<b>28</b>
3.1 An Exterior Complex Source . . . . .	31
3.2 Interior Sources . . . . .	31
<b>4 Energy Balance</b>	<b>36</b>
4.1 Computer Output . . . . .	38
4.2 Thermal Response to Radiation . . . . .	41
<b>5 References</b>	<b>42</b>
<b>6 Acknowledgements</b>	<b>47</b>

# 1 A Mie Like Solution for Bianisotropic Sphere Scattering

Although it is possible to develop an integral equation formulation of the problem of describing the scattering of electromagnetic radiation by a bounded three dimensional body (Jones [33], pp 528-529), the only bounded body for which a truly exact solution has been obtained to the problem for describing its response to electromagnetic radiation have been those with spherical symmetry. It is possible to give a representation (Jones [33], pp 490 to 495) of the fundamental Green's tensor  $\bar{\bar{\Gamma}}$  satisfying

$$\text{curl}(\text{curl}(\bar{\bar{\Gamma}})) - k^2 \bar{\bar{\Gamma}} = \bar{\bar{I}} \delta \quad (1.1)$$

in terms of vector spherical harmonics and to use these to develop a concise derivation of the solution of the problem of describing scattering by a sphere (Jones [33] pp 496-526). Some earlier work on anisotropic sphere scattering ([28] [32]), [48], [52]) have extended the classical result of Mie ([34] 1908) which is believed to have been first obtained by Clebsch ([23] 1863). We describe, here, an exact Mie like solution that is applicable to a class of bianisotropic spheres.

## 1.1 Problem Definition

We assume that  $\vec{\epsilon}$  and  $\vec{\mu}$  are tensors defining the permeability and permittivity that are functions of the spatial variables and the frequency  $\omega$  of the radiation. Here Maxwell's equations have the form

$$\text{curl}(\vec{E}) = -i\omega\vec{\mu}\vec{H} - \vec{\alpha}\vec{E} \quad (1.2)$$

and

$$\text{curl}(\vec{H}) = i\omega\vec{\epsilon}\vec{E} + \vec{\sigma}\vec{E} + \vec{\beta}\vec{H} \quad (1.3)$$

In the ambient medium we assume that the tensors  $\vec{\alpha}$  and  $\vec{\beta}$  are the zero tensor  $\vec{0}$ . In this paper the energy balance is described which enables us to validate a computer code for describing the interaction of radiation with an N layer bianisotropic sphere where the layers may be separated by impedance sheets. The inner core may be penetrable or perfectly conducting.

## 1.2 Spherical Harmonics and Orthogonality Relations

The basic idea of the code is that the induced and scattered electric and magnetic vectors can be expressed in terms of

$$\vec{A}_{(m,n)} = \left[ im \frac{P_n^m(\cos(\theta))}{\sin(\theta)} \vec{e}_\theta - \frac{d}{d\theta} P_n^m(\cos(\theta)) \vec{e}_\phi \right] \exp(im\phi), \quad (1.4)$$

$$\vec{B}_{(m,n)} = \left[ \frac{d}{d\theta} P_n^m(\cos(\theta)) \vec{e}_\theta + im \frac{P_n^m(\cos(\theta))}{\sin(\theta)} \vec{e}_\phi \right] \exp(im\phi), \quad (1.5)$$

and

$$\vec{C}_{(m,n)} = P_n^m(\cos(\theta)) \exp(im\phi) \vec{e}_r, \quad (1.6)$$

where  $\vec{e}_r$ ,  $\vec{e}_\theta$ , and  $\vec{e}_\phi$  are the unit vectors perpendicular, respectively, to the  $r = 0$ ,  $\theta = 0$ , and  $\phi = 0$ , coordinate planes, and where  $P_n(\cos(\theta))$  is the ordinary Legendre function defined by Rodrigues's formula

$$P_n(z) = \frac{1}{2^n n!} \left( \frac{d}{dz} \right)^n (z^2 - 1)^n \quad (1.7)$$

The associated Legendre functions  $P_n^m$  are given by

$$P_n^m(z) = (1 - z^2)^{m/2} \left( \frac{d}{dz} \right)^m P_n(z) \quad (1.8)$$

It is obvious that even without integrating over a sphere that the dot product of either of  $\vec{A}_{(m,n)}$  or  $\vec{B}_{(m,n)}$  with  $\vec{C}_{(m,n)}$  is zero. The orthogonality of the functions  $\exp(im\phi)$  and  $\exp(i\tilde{m}\phi)$  on the unit circle for  $m \neq \tilde{m}$  show that if as in ([11]) we define the inner product of two vector valued functions  $\vec{U}(\theta, \phi)$  and  $\vec{V}(\theta, \phi)$  defined on the unit sphere by,

$$\langle \vec{U}, \vec{V} \rangle = \int_0^{2\pi} \int_0^\pi \vec{U}(\theta, \phi) \cdot \vec{V}(\theta, \phi)^* \sin(\theta) d\theta d\phi \quad (1.9)$$

with two different values of  $m$  are orthogonal. If we take the dot product of two distinct members of the collection

$$S = \{ \vec{A}_{(m,n)}, \vec{B}_{(m,n)}, \vec{C}_{(m,n)} : m \in \mathbb{Z}, \text{ and } n \in \{|m|, |m| + 1, \dots\} \}, \quad (1.10)$$

with the same values of  $m$  and make use of ([2], p 333) the negative index relationship

$$P_\nu^{-\mu}(z) = \frac{\Gamma(\nu - \mu + 1)}{\Gamma(\nu + \mu + 1)} \left[ P_\nu^\mu(z) - \frac{2}{\pi} \exp(-i\mu\pi) \sin(\mu\pi) Q_\nu^\mu(z) \right] \quad (1.11)$$

we find that any two members with different values of  $n$  are orthogonal with respect to the inner product defined by equation (??). For example, to see that

$$\langle \vec{A}_{(m,n)}, \vec{B}_{(m,r)} \rangle = 0 \quad (1.12)$$

for all  $n$  and  $r$  we note that this dot product reduces to

$$im(2\pi) \int_0^\pi \frac{d}{d\theta} [P_n^m(\cos(\theta)) P_r^m(\cos(\theta))] d\theta = im(2\pi) \int_{-1}^1 \frac{d}{dx} \{P_n^m(x) P_r^m(x)\} dx \quad (1.13)$$

The details of the remaining orthogonality relations are found in ([11]) or can be derived from properties of the Legendre functions described in Jones ([33]).

Plane waves in free space can be represented using the functions described above by carrying out the expansion (Bell, [10] page 51 and Jones [33], page 490, equation 94)

$$\exp(-ik_0 r \cos(\theta)) = \sum_{n=0}^{\infty} a_n P_n(\cos(\theta)) j_n(k_0 r) \quad (1.14)$$

where the expansion coefficients  $a_n$  are given by (see Jones [33], page 490)

$$a_n = (-i)^n (2n + 1). \quad (1.15)$$

These coefficients are determined by letting  $z = k_0 r$ , carrying out a Taylor series expansion in  $z$ , and making use of the orthogonality relationships

$$\int_0^\pi P_n(\cos(\theta)) P_m(\cos(\theta)) \sin(\theta) d\theta = \begin{cases} 2/(2n+1) & \text{if } n = m \\ 0 & \text{if } n \neq m \end{cases} \quad (1.16)$$

This equation is based on the relation (Bell [10], page 61)

$$\int_{-1}^1 (z^2 - 1)^n dz = \int_{-1}^1 (z - 1)^n (z + 1)^n dz = \frac{2^{2n+1} (n!)^2}{(2n+1)!} \cdot (-1)^n \quad (1.17)$$

which follows from integration by parts in the left side of equation (1.16). This relationship can be proven using the Rodrigues definition (equation 1.7). By using the notion that the algebraic structure formed by linearly combining these vector fields in a ring of radial functions is invariant under the curl operation also enables one to get an exact solution to the scattering problem for bianisotropic spheres.

### 1.3 Radial Functions and Field Representations

We assume that if  $\vec{V}$  is a vector, then

$$\begin{aligned} \text{curl}(\vec{V}) = & \frac{1}{r \sin(\theta)} \left[ \frac{\partial}{\partial \theta} (\sin(\theta) V_\phi) - \frac{\partial V_\theta}{\partial \phi} \right] \vec{e}_r + \\ & \frac{1}{r} \left[ \frac{1}{\sin(\theta)} \left( \frac{\partial V_r}{\partial \phi} \right) - \frac{\partial}{\partial r} (r V_\phi) \right] \vec{e}_\theta + \\ & \frac{1}{r} \left[ \frac{\partial}{\partial r} (r V_\theta) - \frac{\partial}{\partial \theta} V_r \right] \vec{e}_\phi \end{aligned} \quad (1.18)$$

We then find that if we define vector fields  $\vec{A}$ ,  $\vec{B}$ ,  $\vec{C}$  by the rules

$$\vec{A} = F(r) \vec{A}_{(m,n)} \quad (1.19)$$

$$\vec{B} = F(r) \vec{B}_{(m,n)} \quad (1.20)$$

$$\vec{C} = F(r) \vec{C}_{(m,n)} \quad (1.21)$$

that then

$$\text{curl}(\vec{A}) = n(n+1) \frac{F(r)}{r} \vec{C}_{(m,n)} +$$

$$\frac{1}{r} \frac{\partial}{\partial r} (r F(r)) \vec{B}_{(m,n)}(\theta, \phi) \quad (1.22)$$

$$\text{curl}(\vec{C}) = \frac{F(r)}{r} \vec{A}_{(m,n)} \quad (1.23)$$

and

$$\text{curl}(\vec{B}) = -\frac{1}{r} \frac{\partial}{\partial r} (r F(r)) \vec{A}_{(m,n)} \quad (1.24)$$

We assume that there are three radial functions that are used in representing the induced fields. The induced electric vector has the form,

$$\begin{aligned} \vec{E} = \sum_{(m,n) \in I} \left\{ a_{(m,n)} Z_n^{(a)}(r) \vec{A}_{(m,n)}(\theta, \phi) + \right. \\ \left. c_{(m,n)} \frac{Z_n^{(c)}(r)}{kr} \vec{C}_{(m,n)}(\theta, \phi) + \right. \\ \left. \frac{b_{(m,n)}}{kr} \left( - \left( \frac{\partial}{\partial r} \right) (r Z_n^{(b)}(r)) \right) \vec{B}_{(m,n)}(\theta, \phi) \right\} \end{aligned} \quad (1.25)$$

We now begin to develop the consequences of Maxwell's equations by noting that  $\text{curl}(\vec{E})$  is given by

$$\begin{aligned} \text{curl}(\vec{E}) = \\ \sum_{(m,n) \in I} \left\{ a_{(m,n)} \left[ n(n+1) \frac{Z_n^{(a)}(r)}{r} \vec{C}_{(m,n)} + \frac{1}{r} \frac{\partial}{\partial r} (r Z_n^{(a)}(r)) \vec{B}_{(m,n)} \right] \right. \\ \left. c_{(m,n)} \frac{Z_n^{(c)}(r)}{kr^2} \vec{A}_{(m,n)} + b_{(m,n)} \frac{1}{r} \left( \frac{\partial}{\partial r} \right)^2 (r Z_n^{(b)}(r)) \vec{A}_{(m,n)} \right\} = \\ -\bar{\alpha} \left[ \sum_{(m,n) \in I} \left\{ a_{(m,n)} Z_n^{(a)}(r) \vec{A}_{(m,n)} + c_{(m,n)} \frac{Z_n^{(c)}(r)}{kr} \vec{C}_{(m,n)} + \right. \right. \\ \left. \left. \frac{b_{(m,n)}}{kr} \left( - \left( \frac{\partial}{\partial r} \right) (r Z_n^{(b)}(r)) \right) \vec{B}_{(m,n)} \right\} \right] - i\omega \bar{\mu} \vec{H} \end{aligned} \quad (1.26)$$

In a class of special cases the scattering of radiation by a bianisotropic N layer spherical structure has a particularly simple solution. Solving equation (1.26) for  $\bar{\mu} \vec{H}$ , we see that in general if we simply assume that  $\bar{\alpha}$  is a diagonal tensor whose action on a vector represented in spherical coordinates is defined by,

$$\bar{\alpha} \cdot \vec{E} = \begin{pmatrix} \alpha_r & 0 & 0 \\ 0 & \alpha & 0 \\ 0 & 0 & \alpha \end{pmatrix} \begin{pmatrix} E_r \\ E_\theta \\ E_\phi \end{pmatrix} \quad (1.27)$$

that then making use of equation (1.27)

$$\begin{aligned}
 -i\omega\bar{\mu}\vec{H} = & \sum_{(m,n) \in I} \left\{ \left[ a_{(m,n)} n(n+1) \frac{Z_n^{(a)}(r)}{r} + \alpha_r c_{(m,n)} \frac{Z_n^{(c)}(r)}{kr} \right] \vec{C}_{(m,n)} \right. \\
 & + \left[ a_{(m,n)} \frac{1}{r} \frac{\partial}{\partial r} (r Z_n^{(a)}(r)) - \alpha b_{(m,n)} \left( \frac{1}{kr} \right) \left( \frac{\partial}{\partial r} \right) (r Z_n^{(b)}(r)) \right] \vec{B}_{(m,n)} + \\
 & \left. \left[ c_{(m,n)} \frac{Z_n^{(c)}(r)}{kr^2} + b_{(m,n)} \frac{1}{kr} \left( \frac{\partial}{\partial r} \right)^2 (r Z_n^{(b)}(r)) + \alpha a_{(m,n)} Z_n^{(a)}(r) \right] \vec{A}_{(m,n)} \right\} \quad (1.28)
 \end{aligned}$$

While coupled systems of equations can be obtained for the radial functions for more general tensors, we assume that the bianisotropy coupling tensors  $\bar{\alpha}$  and  $\bar{\beta}$  and the permeability tensors are all diagonal, having a form similar to equation (1.21),

With these assumptions, we see that for a bianisotropic material, the magnetic vector will then have the form

$$\begin{aligned}
 \vec{H} = & \sum_{(m,n) \in I} \left[ \frac{i}{\omega\mu_r} \left\{ a_{(m,n)} \frac{Z_n^{(a)}(r) n(n+1)}{r} + \alpha_r c_{(m,n)} \frac{Z_n^{(c)}(r)}{kr} \right\} \vec{C}_{(m,n)} \right. \\
 & + \frac{i}{\omega\mu} \left\{ a_{(m,n)} \frac{1}{r} \frac{\partial}{\partial r} (r Z_n^{(a)}(r)) - \alpha b_{(m,n)} \frac{1}{kr} \left( \frac{\partial}{\partial r} \right) (r Z_n^{(b)}(r)) \right\} \vec{B}_{(m,n)} + \\
 & \left. b_{(m,n)} \left( \frac{1}{kr} \right) \left( \frac{\partial}{\partial r} \right)^2 (r Z_n^{(b)}(r)) + \alpha a_{(m,n)} Z_n^{(a)}(r) \right\} \vec{A}_{(m,n)} \quad (1.29)
 \end{aligned}$$

Applying the *curl* operation to both sides of equation 1.29 we obtain an expanded form of the final Maxwell equation given by,

$$\begin{aligned}
 \text{curl}(\vec{H}) = & \left( \frac{i}{\omega\mu_r} \right) \frac{1}{r} \left\{ a_{(m,n)} \frac{Z_n^{(a)}(r) n(n+1)}{r} + \alpha_r c_{(m,n)} \frac{Z_n^{(c)}(r)}{kr} \right\} \vec{A}_{(m,n)} + \\
 & \left( \frac{i}{\omega\mu} \right) \left( \frac{-1}{r} \frac{\partial}{\partial r} \right) \left( r \left\{ a_{(m,n)} \frac{1}{r} \frac{\partial}{\partial r} (r Z_n^{(a)}(r)) \right. \right. \\
 & \left. \left. - \alpha b_{(m,n)} \frac{1}{kr} \frac{\partial}{\partial r} (r Z_n^{(b)}(r)) \right\} \right) \vec{A}_{(m,n)} + \\
 & \left( \frac{i}{\omega\mu} \right) \frac{n(n+1)}{r} \left\{ c_{(m,n)} \frac{Z_n^{(c)}(r)}{kr^2} + \right. \\
 & \left. b_{(m,n)} \frac{1}{kr} \left( \frac{\partial}{\partial r} \right)^2 (r Z_n^{(b)}(r)) + \alpha a_{(m,n)} Z_n^{(a)}(r) \right\} \vec{C}_{(m,n)} +
 \end{aligned}$$



$$\begin{aligned}
& \left( \frac{i}{\omega\mu} \right) \frac{1}{r} \frac{\partial}{\partial r} \left( r \left\{ c_{(m,n)} \frac{Z_n^{(c)}(r)}{kr^2} + \right. \right. \\
& \left. \left. b_{(m,n)} \frac{1}{kr} \left( \frac{\partial}{\partial r} \right)^2 (r Z_n^{(b)}(r)) + \alpha a_{(m,n)} Z_n^{(a)}(r) \right\} \right) \bar{B}_{(m,n)} \\
& = (i\omega\bar{\epsilon} + \bar{\sigma}) \bar{E} + \bar{\beta} \bar{H}
\end{aligned} \tag{1.30}$$

To make use of the second Maxwell equation (1.30) we need to develop an expression for  $(i\omega\bar{\epsilon} + \bar{\sigma})\bar{E} + \bar{\beta}\bar{H}$ . We find that

$$\begin{aligned}
& (i\omega\bar{\epsilon} + \bar{\sigma})\bar{E} + \bar{\beta}\bar{H} = \\
& \sum_{(m,n) \in I} \left\{ \left[ (i\omega\epsilon + \sigma) a_{(m,n)} Z_n^{(a)}(r) + \frac{i\beta}{\omega\mu} \left\{ \frac{c_{(m,n)}}{kr^2} Z_n^{(c)}(r) + \right. \right. \right. \\
& \left. \left. \frac{b_{(m,n)}}{kr} \left( \frac{\partial}{\partial r} \right)^2 (r Z_n^{(b)}(r)) + \alpha a_{(m,n)} Z_n^{(a)}(r) \right\} \right] \bar{A}_{(m,n)}(\theta, \phi) + \\
& \left[ (i\omega\epsilon + \sigma) \frac{b_{(m,n)}}{kr} \left( -\frac{\partial}{\partial r} \right) (r Z_n^{(b)}(r)) + \right. \\
& \left. \left[ \frac{i\beta}{\omega\mu} \left\{ a_{(m,n)} \frac{1}{r} \frac{\partial}{\partial r} (r Z_n^{(a)}(r)) + \frac{\alpha b_{(m,n)}}{kr} \left( -\frac{\partial}{\partial r} (r Z_n^{(b)}(r)) \right) \right\} \right] \right] \bar{B}_{(m,n)}(\theta, \phi) \\
& + \left[ (i\omega\epsilon_r + \sigma_r) c_{(m,n)} \frac{Z_n^{(c)}(r)}{kr} + \right. \\
& \left. \frac{i\beta_r}{\omega\mu_r} \left\{ a_{(m,n)} Z_n^{(a)}(r) \frac{n(n+1)}{r} + \alpha_r \frac{c_{(m,n)} Z_n^{(c)}(r)}{kr} \right\} \right] \bar{C}_{(m,n)}(\theta, \phi)
\end{aligned} \tag{1.31}$$

The solution of the electromagnetic interaction problem is then obtained by relating coefficients on both sides of equation (1.30) and making use of orthogonality relations to get differential equations for the, a priori unknown, radial functions.

Equation (1.30) coupled with equation (1.31) is the key to the development of a system of ordinary differential equations satisfied by the radial functions. Using orthogonality properties of the vector functions  $\bar{A}_{(m,n)}$  and  $\bar{B}_{(m,n)}$  we see that we may equate their coefficients on both sides of equation (1.30). Equating coefficients of  $\bar{A}_{(m,n)}$  on both sides of equation (1.30) we find that

$$\left[ \left( \frac{i}{\omega\mu_r} \right) \frac{1}{r} \left\{ a_{(m,n)} \frac{Z_n^{(a)}(r) n(n+1)}{r} + \alpha_r c_{(m,n)} \frac{Z_n^{(c)}(r)}{kr} \right\} + \right.$$

$$\begin{aligned}
& \left( \frac{i}{\omega\mu} \right) \left( \frac{-1}{r} \frac{\partial}{\partial r} \right) \left( r \left\{ a_{(m,n)} \frac{1}{r} \frac{\partial}{\partial r} (r Z_n^{(a)}(r)) \right. \right. \\
& \quad \left. \left. - \alpha b_{(m,n)} \frac{1}{kr} \frac{\partial}{\partial r} (r Z_n^{(b)}(r)) \right\} \right) = \\
& \left[ (i\omega\epsilon + \sigma) a_{(m,n)} Z_n^{(a)}(r) + \frac{i\beta}{\omega\mu} \left\{ \frac{c_{(m,n)}}{kr^2} Z_n^{(c)}(r) + \right. \right. \\
& \quad \left. \left. \frac{b_{(m,n)}}{kr} \left( \frac{\partial}{\partial r} \right)^2 (r Z_n^{(b)}(r)) + \alpha a_{(m,n)} Z_n^{(a)}(r) \right\} \right] \quad (1.32)
\end{aligned}$$

We can see the consistency of this equation with the equations obtained for the special case of anisotropic spherical structures. If in equation (1.32) we set  $\bar{\alpha}$  and  $\bar{\beta}$  equal to the zero tensor, we obtain

$$\begin{aligned}
& \left[ \left( \frac{i}{\omega\mu_r} \right) \frac{1}{r} \left\{ a_{(m,n)} \frac{Z_n^{(a)}(r) n(n+1)}{r} \right\} + \right. \\
& \left. \left( \frac{i}{\omega\mu} \right) \left( \frac{-1}{r} \frac{\partial}{\partial r} \right) \left( r \left\{ a_{(m,n)} \frac{1}{r} \frac{\partial}{\partial r} (r Z_n^{(a)}(r)) \right\} \right) \right] = [(i\omega\epsilon + \sigma) a_{(m,n)} Z_n^{(a)}(r)] \quad (1.33)
\end{aligned}$$

or upon multiplying both sides of equation (1.33) by  $-i\omega\mu$  we find that if we let

$$k_a^2 = \omega^2 \mu \epsilon - i\omega \mu \sigma \quad (1.34)$$

that then  $Z_n^{(a)}$  satisfies,

$$\left( \frac{\mu}{\mu_r} \right) Z_n^{(a)}(r) \frac{n(n+1)}{r^2} - k^2 Z_n^{(a)}(r) = \frac{1}{r} \left( \frac{\partial}{\partial r} \right)^2 (r Z_n^{(a)}(r)) \quad (1.35)$$

which is exactly the equation satisfied by the radial function  $Z_n^{(a)}$  for an anisotropic sphere.

We can also, in a similar fashion, relate coefficients of  $\vec{B}_{(m,n)}$  on both sides of equation (1.30) to obtain the relationship.

$$\begin{aligned}
& \left( \frac{i}{\omega\mu} \right) \frac{1}{r} \frac{\partial}{\partial r} \left( r \left\{ c_{(m,n)} \frac{Z_n^{(c)}(r)}{kr^2} + \right. \right. \\
& \quad \left. \left. b_{(m,n)} \frac{1}{kr} \left( \frac{\partial}{\partial r} \right)^2 (r Z_n^{(b)}(r)) + \alpha a_{(m,n)} Z_n^{(a)}(r) \right\} \right) = \\
& \left[ (i\omega\epsilon + \sigma) \frac{b_{(m,n)}}{kr} \left( -\frac{\partial}{\partial r} \right) (r Z_n^{(b)}(r)) + \right. \\
& \quad \left. \left[ \frac{i\beta}{\omega\mu} \left\{ a_{(m,n)} \frac{1}{r} \frac{\partial}{\partial r} (r Z_n^{(a)}(r)) + \frac{\alpha b_{(m,n)}}{kr} \left( -\frac{\partial}{\partial r} (r Z_n^{(b)}(r)) \right) \right\} \right] \right] \quad (1.36)
\end{aligned}$$

If in equation (1.36) we equate the differentiated terms, then this equation is implied by the simpler relation,

$$\begin{aligned} & \left( \frac{i}{\omega\mu} \right) \left\{ c_{(m,n)} \frac{Z_n^{(c)}(r)}{kr^2} + \right. \\ & \left. b_{(m,n)} \frac{1}{kr} \left( \frac{\partial}{\partial r} \right)^2 (r Z_n^{(b)}(r)) + \alpha a_{(m,n)} Z_n^{(a)}(r) \right\} = \\ & \left[ (i\omega\epsilon + \sigma) \frac{b_{(m,n)}}{kr} (Z_n^{(b)}(r)) + \right. \\ & \left. \left[ \frac{i\beta}{\omega\mu} \left\{ a_{(m,n)} (Z_n^{(a)}(r)) - \frac{\alpha b_{(m,n)}}{k} ((Z_n^{(b)}(r))) \right\} \right] \right] \end{aligned} \quad (1.37)$$

Equating coefficients of  $\tilde{C}_{(m,n)}$  on both sides of equation (1.30) reveals that

$$\begin{aligned} & \left( \frac{-i}{\omega\mu} \right) \frac{n(n+1)}{r} \left\{ c_{(m,n)} \frac{Z_n^{(c)}(r)}{kr^2} + \right. \\ & \left. b_{(m,n)} \frac{1}{kr} \left( \frac{\partial}{\partial r} \right)^2 (r Z_n^{(b)}(r)) + \alpha a_{(m,n)} Z_n^{(a)}(r) \right\} = \\ & + \left[ (i\omega\epsilon_r + \sigma_r) c_{(m,n)} \frac{Z_n^{(c)}(r)}{kr} + \right. \\ & \left. \frac{i\beta_r}{\omega\mu_r} \left\{ a_{(m,n)} Z_n^{(a)}(r) \frac{n(n+1)}{r} + \alpha_r \frac{c_{(m,n)} Z_n^{(c)}(r)}{kr} \right\} \right] \end{aligned} \quad (1.38)$$

To compare equation (1.37) and equation (1.38) we multiply both sides of equation (1.37) by  $r/(n(n+1))$  and we find that

$$\begin{aligned} & \left( \frac{i}{\omega\mu} \right) \left\{ \frac{c_{(m,n)}}{kr^2} Z_n^{(c)}(r) + b_{(m,n)} \left( \frac{1}{kr} \right) \left( \frac{\partial}{\partial r} \right)^2 (r Z_n^{(b)}(r)) + \alpha a_{(m,n)} Z_n^{(a)}(r) \right\} = \\ & \left( \frac{i\omega\epsilon_r + \sigma_r}{n(n+1)} \right) c_{(m,n)} \frac{Z_n^{(c)}(r)}{k} + \\ & \beta_r \frac{i}{\omega\mu_r} a_{(m,n)} Z_n^{(a)}(r) + \left( \frac{\alpha_r \beta_r}{n(n+1)} \right) \left( \frac{i}{\omega\mu_r} c_{(m,n)} \right) \frac{Z_n^{(c)}(r)}{k} \end{aligned} \quad (1.39)$$

We have consistency between equation (1.39) and equation (1.37) provided that

$$\begin{aligned} & (i\omega\epsilon + \sigma)(-b_{(m,n)} Z_n^{(b)}(r)) + \\ & \left( \frac{i\beta}{\omega\mu} \right) k a_{m,n} Z_n^{(a)}(r) - \left( \frac{i\beta\alpha}{\omega\mu} \right) b_{(m,n)} Z_n^{(b)}(r) = \end{aligned}$$

$$\left(\frac{i\omega\epsilon_r + \sigma_r}{n(n+1)}\right) c_{(m,n)} Z_n^{(c)}(r) + \frac{i\beta_r k}{\omega\mu_r} a_{(m,n)} Z_n^{(a)}(r) + \frac{\alpha_r \beta_r}{n(n+1)} \left(\frac{i}{\omega\mu_r}\right) c_{(m,n)} Z_n^{(n)}(r) \quad (1.40)$$

We note that the consistency relation given by equation (1.40) specializes for the case of the ordinary anisotropic sphere, where the coupling tensors  $\bar{\alpha}$  and  $\bar{\beta}$ , are both equal to the zero tensor by

$$(i\omega\epsilon + \sigma)(-b_{(m,n)}) Z_n^{(b)}(r) = \left(\frac{i\omega\epsilon_r + \sigma_r}{n(n+1)}\right) c_{(m,n)} Z_n^{(c)} \quad (1.41)$$

We note that equation (1.41) is satisfied if

$$Z_n^{(c)}(r) = Z_n^{(b)}(r) \quad (1.42)$$

and

$$c_{(m,n)} = -n(n+1) \left(\frac{i\omega\epsilon + \sigma}{i\omega\epsilon_r + \sigma_r}\right) b_{(m,n)} \quad (1.43)$$

We, however, now collect the terms multiplying the coefficients  $a_{(m,n)}$ ,  $b_{(m,n)}$ , and  $c_{(m,n)}$  in equation (1.32) we have

$$\begin{aligned} & \left[ \left(\frac{i}{\omega\mu_r}\right) \left(\frac{1}{r}\right) Z_n^{(a)}(r) \frac{n(n+1)}{r} - (i\omega\epsilon + \sigma) Z_n^{(a)}(r) \right. \\ & \left. - \frac{i\beta}{\omega\mu} \alpha Z_n^{(a)}(r) - \frac{i}{\omega\mu} \frac{1}{r} \left(\frac{\partial}{\partial r}\right)^2 (r Z_n^{(a)}(r)) \right] a_{(m,n)} + \\ & \left[ \left(\frac{-i}{\omega\mu}\right) \frac{\alpha}{k} - \frac{i\beta}{\omega\mu k} \right] \left\{ \frac{1}{r} \left(\frac{\partial}{\partial r}\right)^2 (r Z_n^{(b)}(r)) \right\} b_{(m,n)} + \\ & \left[ \frac{i\alpha_r}{\omega\mu_r} - \frac{i\beta}{\omega\mu} \frac{1}{kr^2} Z_n^{(c)}(r) \right] c_{(m,n)} = 0 \end{aligned} \quad (1.44)$$

Collecting the coefficients of  $a_{(m,n)}$ ,  $b_{(m,n)}$ , and  $c_{(m,n)}$  in equation (1.37) we have

$$\begin{aligned} & \left[ \left(\frac{i}{\omega\mu}\right) \alpha Z_n^{(a)}(r) - \frac{i\beta}{\omega\mu} Z_n^{(a)}(r) \right] a_{(m,n)} \\ & + \left[ \frac{i}{\omega\mu} \left(\frac{1}{kr}\right) \left(\frac{\partial}{\partial r}\right)^2 (r Z_n^{(b)}(r)) + \frac{\sigma + i\omega\epsilon}{k} Z_n^{(b)}(r) \right. \\ & \left. + \frac{i\beta\alpha}{\omega\mu k} Z_n^{(b)}(r) \right] b_{(m,n)} + \frac{i}{\omega\mu} \left(\frac{1}{kr^2}\right) Z_n^{(c)} c_{(m,n)} = 0 \end{aligned} \quad (1.45)$$

Equation (1.45) yields the relationship

$$\begin{aligned}
 & b_{(m,n)} \frac{i}{\omega\mu} \frac{1}{kr} \left( \frac{\partial}{\partial r} \right)^2 (r Z_n^{(b)}(r)) = \\
 & - \left[ \frac{i}{\omega\mu} \alpha Z_n^{(a)}(r) - \frac{i\beta}{\omega\mu} Z_n^{(a)}(r) \right] a_{(m,n)} - \\
 & \left[ \frac{\sigma + i\omega\epsilon}{k} Z_n^{(b)} + \frac{i\beta\alpha}{\omega\mu k} Z_n^{(b)}(r) \right] b_{(m,n)} \\
 & - \frac{i}{\omega\mu} \frac{1}{kr^2} Z_n^{(c)}(r) c_{(m,n)}
 \end{aligned} \tag{1.46}$$

Equation (1.38) yields the relationship

$$\begin{aligned}
 & \frac{n(n+1)}{r} \left\{ b_{(m,n)} \frac{i}{\omega\mu} \frac{1}{kr} \left( \frac{\partial}{\partial r} \right)^2 (r Z_n^{(b)}(r)) \right\} \\
 & = \left\{ \frac{-n(n+1)}{r} \left( \frac{i}{\omega\mu} \frac{1}{kr^2} Z_n^{(c)}(r) \right) + \beta_r \left( \frac{i}{\omega\mu_r} \right) \frac{\alpha_r}{kr} Z_n^{(c)} \right. \\
 & \quad \left. + \frac{i\omega\epsilon_r + \sigma_r}{kr} Z_n^{(c)}(r) \right\} c_{(m,n)} + \\
 & a_{(m,n)} \left\{ \frac{-i}{\omega\mu} \frac{n(n+1)}{r} \alpha Z_n^{(a)}(r) + \beta_r \left( \frac{i}{\omega\mu_r} \right) Z_n^{(a)}(r) \frac{n(n+1)}{r} \right\}
 \end{aligned} \tag{1.47}$$

Multiplying all terms of equation (1.47) by  $r/(n(n+1))$  we find that

$$\begin{aligned}
 & \left\{ b_{(m,n)} \frac{i}{\omega\mu} \frac{1}{kr} \left( \frac{\partial}{\partial r} \right)^2 (r Z_n^{(b)}(r)) \right\} = \\
 & \left\{ - \left[ \frac{i}{\omega\mu} \frac{1}{kr^2} Z_n^{(c)}(r) \right] + \left( \frac{i\alpha_r\beta_r}{\omega\mu_r} \right) \frac{1}{kn(n+1)} Z_n^{(c)} \right. \\
 & \quad \left. + \frac{i\omega\epsilon_r + \sigma_r}{kn(n+1)} Z_n^{(c)}(r) \right\} c_{(m,n)} + \\
 & \left\{ \frac{-i}{\omega\mu} \alpha Z_n^{(a)}(r) + \left( \frac{i\beta_r}{\omega\mu_r} \right) Z_n^{(a)}(r) \right\} a_{(m,n)}
 \end{aligned} \tag{1.48}$$

Solving for the term

$$U = \frac{i}{\omega\mu} \frac{1}{kr} \left( \frac{\partial}{\partial r} \right)^2 (r Z_n^{(b)}(r)) b_{(m,n)} \tag{1.49}$$

in equations (1.48) and (1.46) we find that

$$- \left[ \alpha \frac{i}{\omega\mu} Z_n^{(a)}(r) - \frac{i\beta}{\omega\mu} Z_n^{(a)}(r) \right] a_{(m,n)}$$

$$\begin{aligned}
& - \left[ \frac{\sigma + i\omega\epsilon}{k} Z_n^{(b)}(r) + \frac{i\beta}{\omega\mu} \frac{\alpha}{k} Z_n^{(b)}(r) \right] b_{(m,n)} \\
& - c_{(m,n)} \left( \frac{i}{kr^2\omega\mu} \right) Z_n^{(c)}(r) = \\
& - \left[ \frac{i\alpha}{\omega\mu} Z_n^{(a)}(r) - \frac{i\beta_r}{\omega\mu_r} Z_n^{(a)}(r) \right] a_{(m,n)} - \\
& \left[ \left( \frac{i}{\omega\mu} \right) \frac{1}{kr^2} Z_n^{(c)}(r) - \frac{i\omega\epsilon_r + \sigma_r}{kn(n+1)} Z_n^{(c)}(r) \right. \\
& \left. - \left( \frac{\alpha_r\beta_r}{k\omega\mu_r n(n+1)} \right) Z_n^{(c)}(r) \right] c_{(m,n)} \quad (1.50)
\end{aligned}$$

Equation (1.50) implies, after subtracting identical terms from both sides of the equation, that

$$\begin{aligned}
& \left[ -\frac{i\omega\epsilon_r + \sigma_r}{kn(n+1)} - \frac{\beta_r\alpha_r}{k\omega\mu_r n(n+1)} \right] c_{(m,n)} Z_n^{(c)}(r) = \\
& - \left( \frac{i\beta}{\omega\mu} - \frac{i\beta_r}{\omega\mu_r} \right) Z_n^{(a)}(r) a_{(m,n)} + \\
& \left[ \frac{\sigma + i\omega\epsilon}{k} + \frac{i\beta\alpha}{\omega\mu k} \right] Z_n^{(b)}(r) b_{(m,n)} \quad (1.51)
\end{aligned}$$

Solving equation (1.40) for  $c_{(m,n)} Z_n^{(c)}(r)$  we find that

$$\begin{aligned}
& \left\{ \frac{i\omega\epsilon_r + \sigma_r}{n(n+1)} + \frac{i\alpha_r\beta_r}{\omega\mu_r n(n+1)} \right\} c_{(m,n)} Z_n^{(c)}(r) = \\
& \left\{ -(i\omega\epsilon + \sigma) - \frac{i\beta\alpha}{\omega\mu} \right\} b_{(m,n)} Z_n^{(b)}(r) + \\
& \left( \frac{i\beta k}{\omega\mu} - \frac{i\beta_r k}{\omega\mu_r} \right) a_{(m,n)} Z_n^{(a)}(r) \quad (1.52)
\end{aligned}$$

For a simple chiral sphere where

$$\frac{\beta}{\mu} = \frac{\beta_r}{\mu_r}, \quad (1.53)$$

equation (1.52) has the form

$$c_{(m,n)} Z_n^{(c)}(r) = -n(n+1) \left( \frac{i\omega\epsilon + \sigma + i\beta\alpha/(\omega\mu)}{(i\omega\epsilon_r + \sigma_r) + (i\alpha_r\beta_r)/(\omega\mu_r)} \right) b_{(m,n)} Z_n^{(b)}(r) \quad (1.54)$$

If we assume that equation (1.52) is satisfied, and equation (1.53) is valid so that equation (1.54) is valid and, furthermore, that

$$\frac{i\alpha}{\omega\mu} = \frac{i\beta}{\omega\mu}, \quad (1.55)$$

then equation (1.37) will be of the form

$$\begin{aligned} \frac{i}{\omega\mu} \left[ -n(n+1) \left( \frac{i\omega\epsilon + \sigma + i\beta\alpha/(\omega\mu)}{(i\omega\epsilon_r + \sigma_r) + (i\alpha_r\beta_r)/(\omega\mu_r)} \right) \right] b_{(m,n)} \frac{Z_n^{(b)}(r)}{kr^2} \\ \left( \frac{i}{\omega\mu} \right) b_{(m,n)} \left( \frac{1}{kr} \left( \frac{\partial}{\partial r} \right)^2 \right) (rZ_n^{(b)}(r)) = \\ \frac{\sigma + i\omega\epsilon}{k} b_{(m,n)} (-Z_n^{(b)}(r)) - \frac{i\beta\alpha}{\omega\mu k} b_{(m,n)} Z_n^{(b)}(r) \end{aligned} \quad (1.56)$$

If we also impose the condition

$$\frac{i\alpha_r}{\omega\mu_r} = \frac{i\beta}{\omega\mu} \quad (1.57)$$

then equation (1.32) takes on the form

$$\begin{aligned} \left( \frac{in(n+1)}{\omega\mu_r r^2} \right) Z_n^{(a)}(r) + \left( \frac{-i}{\omega\mu} \right) \frac{1}{r} \left( \frac{\partial}{\partial r} \right)^2 (rZ_n^{(a)}(r)) = \\ (i\omega\mu + \sigma) Z_n^{(a)}(r) + \frac{i\beta\alpha}{\omega\mu} Z_n^{(a)}(r) \end{aligned} \quad (1.58)$$

Multiplying all terms of equation (1.58) by  $i\omega\mu$  and defining

$$k^2 = \omega^2\mu\epsilon - i\omega\mu\sigma \quad (1.59)$$

we see that

$$\begin{aligned} -\frac{\mu n(n+1)}{\mu_r r^2} Z_n^{(a)} + \frac{1}{r} \left( \frac{\partial}{\partial r} \right)^2 (rZ_n^{(a)}(r)) = \\ -k^2 Z_n^{(a)}(r) - \alpha\beta Z_n^{(a)}(r) \end{aligned} \quad (1.60)$$

or if we introduce the variable

$$\zeta_a = \frac{\mu}{\mu_r} \quad (1.61)$$

the ordinary differential equation (1.60) satisfied by  $Z_n^{(a)}$  is

$$\frac{1}{r} \left( \frac{\partial}{\partial r} \right)^2 (rZ_n^{(a)}(r)) + \left[ (k^2 + \alpha\beta) - \zeta_a \frac{n(n+1)}{r^2} \right] Z_n^{(a)}(r) = 0 \quad (1.62)$$

The spherical Bessel function is defined as

$$\Psi_\nu(z) = \frac{\sqrt{\pi} J_{\nu+1/2}(z)}{\sqrt{2}\sqrt{z}} \quad (1.63)$$

where  $\Psi_\nu(z)$  satisfies

$$\frac{1}{z} \left( \frac{\partial}{\partial z} \right)^2 (z \Psi_\nu(z)) + \left[ 1 + \frac{\nu(\nu+1)}{z^2} \right] \Psi_\nu(z) = 0 \quad (1.64)$$

Dividing all terms of equation (1.60) by

$$k^2 + \alpha\beta = \omega^2 \mu \epsilon + \beta\alpha - i\omega\mu\sigma \quad (1.65)$$

we have with the definition

$$z^2 = (k^2 + \beta\alpha)r^2 \quad (1.66)$$

the fact that equation (1.62) implies

$$\frac{1}{z} \left( \frac{\partial}{\partial z} \right)^2 (z \Psi_\nu(z)) + \left[ 1 - \frac{\zeta_a n(n+1)}{z^2} \right] \Psi_\nu = 0 \quad (1.67)$$

where

$$\nu(\nu+1) = \zeta_a n(n+1) \quad (1.68)$$

We can find a simple formula for the index  $\nu$  of the form

$$\nu = \frac{-1 + \sqrt{1 + 4\zeta_a n(n+1)}}{2} \quad (1.69)$$

Equation (1.56) gives the second equation which implies that

$$\begin{aligned} \frac{i}{\omega\mu} \left\{ \frac{1}{kr^2} \right\} \left[ -n(n+1) \left( \frac{i\omega\epsilon + \sigma + i\beta\alpha/(\omega\mu)}{(i\omega\epsilon_r + \sigma_r) + (i\alpha_r\beta_r)/(\omega\mu_r)} \right) \right] Z_n^{(b)}(r) \\ \left( \frac{i}{\omega\mu} \right) \left( \frac{1}{kr} \left( \frac{\partial}{\partial r} \right)^2 \right) (r Z_n^{(b)}(r)) = \\ \frac{\sigma + i\omega\epsilon}{k} (-Z_n^{(b)}(r)) - \frac{i\beta\alpha}{\omega\mu k} Z_n^{(b)}(r) \end{aligned} \quad (1.70)$$

Multiplying all terms of equation (1.70) by  $-i\omega\mu kr^2$  and using equation (1.59) we deduce from equation (1.70) that

$$\begin{aligned} \left( \frac{1}{r} \left( \frac{\partial}{\partial r} \right)^2 \right) (r Z_n^{(b)}(r)) + (k^2 + \alpha\beta) Z_n^{(b)}(r) - \\ \frac{1}{r^2} \left[ -n(n+1) \left( \frac{i\omega\epsilon + \sigma + i\beta\alpha/(\omega\mu)}{(i\omega\epsilon_r + \sigma_r) + (i\alpha_r\beta_r)/(\omega\mu_r)} \right) \right] Z_n^{(b)}(r) = 0 \end{aligned} \quad (1.71)$$



Letting  $\zeta_b$  be defined by

$$\zeta_b = \left( \frac{i\omega\epsilon + \sigma + i\beta\alpha/(\omega\mu)}{(i\omega\epsilon_r + \sigma_r) + (i\alpha_r\beta_r)/(\omega\mu_r)} \right) \quad (1.72)$$

Substituting equation (1.72) into equation (1.54) we deduce that

$$c_{(m,n)} Z_n^{(c)} = -n(n+1)\zeta_b Z_n^{(b)} b_{(m,n)} \quad (1.73)$$

The equation (1.72) is substituted into equation (1.71) to yield the equation,

$$\begin{aligned} & \left( \frac{1}{r} \left( \frac{\partial}{\partial r} \right)^2 \right) (r Z_n^{(b)}(r)) \\ & + \left[ (k^2 + \alpha\beta) - \frac{n(n+1)\zeta_b}{r^2} \right] Z_n^{(b)}(r) = 0 \end{aligned} \quad (1.74)$$

Combinations of solutions of equations (1.62) and (1.74) and their derivatives are used to represent the electric and magnetic fields induced inside an N layered sphere where each layer has nontrivial magnetic properties and the electric and magnetic properties are coupled in the sense that the layers are bianisotropic.

## 2 Expansion Coefficient Relations

Substituting equation (1.54) into (1.25) and making use of the relation defined by equation (1.72) we see that

$$\begin{aligned} \vec{E} = \sum_{(m,n) \in I} & \left\{ a_{(m,n)} Z_n^{(a)}(r) \vec{A}_{(m,n)}(\theta, \phi) + \right. \\ & [-n(n+1)\{\zeta_b\}] b_{(m,n)} \frac{Z_n^{(b)}(r)}{kr} \vec{C}_{(m,n)}(\theta, \phi) + \\ & \left. \frac{b_{(m,n)}}{kr} \left( - \left( \frac{\partial}{\partial r} \right) (r Z_n^{(b)}(r)) \right) \vec{B}_{(m,n)}(\theta, \phi) \right\} \end{aligned} \quad (2.1)$$

Now making use of a form of the relation (1.74) given by

$$\left( \frac{1}{r} \left( \frac{\partial}{\partial r} \right)^2 \right) (r Z_n^{(b)}(r)) =$$

$$+ \left[ \frac{n(n+1)\zeta_b}{r^2} - (k^2 + \alpha\beta) \right] Z_n^{(b)}(r) \quad (2.2)$$

we see that

$$\begin{aligned} \text{curl}(\vec{E}) = \sum_{(m,n) \in I} \left\{ \right. \\ a_{(m,n)} \left[ n(n+1) \frac{Z_n^{(a)}(r)}{r} \vec{C}_{(m,n)} + \frac{1}{r} \frac{\partial}{\partial r} (r Z_n^{(a)}(r)) \vec{B}_{(m,n)} \right] + \\ (-n(n+1)\zeta_b) b_{(m,n)} \frac{Z_n^{(b)}(r)}{kr^2} \vec{A}_{(m,n)} + \\ \left. b_{(m,n)} \frac{1}{kr} \left( \frac{\partial}{\partial r} \right)^2 (r Z_n^{(b)}(r)) \vec{A}_{(m,n)} \right\} \quad (2.3) \end{aligned}$$

Substituting equation (2.2) into equation (2.3) we see that

$$\begin{aligned} \text{curl}(\vec{E}) = \\ \sum_{(m,n) \in I} \left\{ a_{(m,n)} \left[ n(n+1) \frac{Z_n^{(a)}(r)}{r} \vec{C}_{(m,n)} + \frac{1}{r} \frac{\partial}{\partial r} (r Z_n^{(a)}(r)) \vec{B}_{(m,n)} \right] + \right. \\ (-n(n+1)\zeta_b) b_{(m,n)} \frac{Z_n^{(b)}(r)}{kr^2} \vec{A}_{(m,n)} + \\ \left. b_{(m,n)} \frac{1}{kr} \left[ \frac{n(n+1)\zeta_b}{r^2} - (k^2 + \alpha\beta) \right] Z_n^{(b)}(r) \vec{A}_{(m,n)} \right\} \quad (2.4) \end{aligned}$$

Some telescoping in the right side of equation (2.4) yields the reduced form,

$$\begin{aligned} \text{curl}(\vec{E}) = \\ \sum_{(m,n) \in I} \left\{ a_{(m,n)} \left[ n(n+1) \frac{Z_n^{(a)}(r)}{r} \vec{C}_{(m,n)} + \frac{1}{r} \frac{\partial}{\partial r} (r Z_n^{(a)}(r)) \vec{B}_{(m,n)} \right] + \right. \\ \left. -b_{(m,n)} \frac{1}{r} [(k^2 + \alpha\beta)] Z_n^{(b)}(r) \vec{A}_{(m,n)} \right\} \\ = i\omega \bar{\mu} \vec{H} - \bar{\beta} \vec{E} \quad (2.5) \end{aligned}$$

Defining a new function  $W_n^{(a)}$  by the rule

$$W_n^{(a)}(r) = \frac{1}{kr} \left( \frac{\partial}{\partial r} \right) (r Z_n^{(a)}(r)) \quad (2.6)$$

or equivalently by

$$W_n^{(a)}(r) = \lim_{z \rightarrow kr} \left( \frac{1}{z} \right) \frac{\partial}{\partial z} (z \Psi_n^{(a)}(z)) \quad (2.7)$$

where  $\Psi_y^{(a)}$  is defined by (1.67) and where  $\zeta_a$  is related to the parameter  $\nu$  in equation (2.7) by equation (1.61). We define  $W_n^{(b)}(r)$  by changing  $a$  to  $b$  in equation (2.7).

Using the new function  $W_n^{(a)}$  defined by equation (2.7) we define

$$\begin{aligned} \text{curl}(\vec{E}) = & \sum_{(m,n) \in I} \left\{ a_{(m,n)} \left[ n(n+1) \frac{Z_n^{(a)}(r)}{r} \vec{C}_{(m,n)} + a_{(m,n)} k W_n^{(a)}(r) \vec{B}_{(m,n)} \right] + \right. \\ & \left. - b_{(m,n)} \frac{1}{r} [(k^2 + \alpha\beta)] Z_n^{(b)}(r) \vec{A}_{(m,n)} \right\} \\ & = i\omega \bar{\mu} \vec{H} - \bar{\beta} \vec{E} \end{aligned} \quad (2.8)$$

In terms of the function  $W_n^{(a)}(r)$  we express the function  $\vec{H}$  by the rule,

$$\begin{aligned} i\omega \bar{\mu} \vec{H} = & \sum_{(m,n) \in I} \left\{ a_{(m,n)} \left[ n(n+1) \frac{Z_n^{(a)}(r)}{r} \vec{C}_{(m,n)} + a_{(m,n)} k W_n^{(a)}(r) \vec{B}_{(m,n)} \right] + \right. \\ & \left. - b_{(m,n)} \frac{1}{r} [(k^2 + \alpha\beta)] Z_n^{(b)}(r) \vec{A}_{(m,n)} \right\} + \\ & \sum_{(m,n) \in I} \left\{ a_{(m,n)} \beta Z_n^{(a)}(r) \vec{A}_{(m,n)}(\theta, \phi) + \right. \\ & \left. \beta_r [-n(n+1) \{\zeta_b\}] b_{(m,n)} \frac{Z_n^{(b)}(r)}{kr} \vec{C}_{(m,n)}(\theta, \phi) + \right. \\ & \left. \beta \frac{b_{(m,n)}}{kr} \left( - \left( \frac{\partial}{\partial r} \right) (r Z_n^{(b)}(r)) \right) \vec{B}_{(m,n)}(\theta, \phi) \right\} \end{aligned} \quad (2.9)$$

Collecting terms we find that equation (1.54) which relates the function  $c_{(m,n)} Z_n^{(a)}$  to the function  $Z_n^{(b)}$  can be used to derive the relationship,

$$\begin{aligned} -i\omega \bar{\mu} \vec{H} = & \sum_{(m,n) \in I} \left\{ \left[ a_{(m,n)} n(n+1) \frac{Z_n^{(a)}(r)}{r} + \alpha_r c_{(m,n)} \frac{Z_n^{(c)}(r)}{kr} \right] \vec{C}_{(m,n)} \right. \\ & + \left[ a_{(m,n)} \frac{1}{r} \frac{\partial}{\partial r} (r Z_n^{(a)}(r)) - \alpha b_{(m,n)} \left( \frac{1}{kr} \right) \left( \frac{\partial}{\partial r} \right) (r Z_n^{(b)}(r)) \right] \vec{B}_{(m,n)} + \\ & \left. \left[ c_{(m,n)} \frac{Z_n^{(a)}(r)}{kr^2} + b_{(m,n)} \frac{1}{kr} \left( \frac{\partial}{\partial r} \right)^2 (r Z_n^{(b)}(r)) + \alpha a_{(m,n)} Z_n^{(a)}(r) \right] \vec{A}_{(m,n)} \right\} \end{aligned} \quad (2.10)$$

Let us develop the full theory using the functions,

$$W_{(n,p)}^{(a,j)}(r) = \frac{1}{k_p r} \left( \frac{\partial}{\partial r} \right) (r Z_{(n,p)}^{(a,j)}(r)) \quad (2.11)$$

where  $Z_{(n,p)}^{(a,j)}(r)$  is the singular solution if  $j = 3$  and the solution with the integrable singularity at  $r = 0$  corresponds to  $j = 1$ .

The expansion coefficients in layer  $p$  associated with the functions,  $Z_{(n,p)}^{(a,1)}(r)$  and  $W_{(n,p)}^{(a,1)}(r)$  with the integrable singularity will be denoted by  $a_{(m,n)}^{(p)}$  and  $b_{(m,n)}^{(p)}$  and the coefficients and  $\alpha_{(m,n)}^{(p)}$  and  $\beta_{(m,n)}^{(p)}$  of the functions  $Z_{(n,p)}^{(a,3)}(r)$  and  $W_{(n,p)}^{(a,3)}(r)$  which are singular at  $r = 0$ . The electric vector with general representation given by equation (1.25) is in the  $p$ th layer of the multilayer bianisotropic sphere represented by

$$\begin{aligned} \vec{E}_p = & \sum_{(m,n) \in I} \left\{ [a_{(m,n)}^{(p)} Z_{(n,p)}^{(a,1)}(r) + \alpha_{(m,n)}^{(p)} Z_{(n,p)}^{(a,3)}(r)] \vec{A}_{(m,n)}(\theta, \phi) + \right. \\ & [-n(n+1) \{\hat{S}_b\}] b_{(m,n)}^{(p)} \frac{Z_{(n,p)}^{(a,1)}(r)}{kr} \vec{C}_{(m,n)}(\theta, \phi) + \\ & [-n(n+1) \{\hat{S}_b\}] \beta_{(m,n)}^{(p)} \frac{Z_{(n,p)}^{(a,3)}(r)}{kr} \vec{C}_{(m,n)}(\theta, \phi) + \\ & \left. [-b_{(m,n)}^{(p)} W_{(n,p)}^{(b,1)}(r) - \beta_{(m,n)}^{(p)} W_{(n,p)}^{(b,3)}(r)] \vec{B}_{(m,n)}(\theta, \phi) \right\} \quad (2.12) \end{aligned}$$

Using our previous expression for the magnetic field vector but using the definitions (2.11) and the fact that  $k_p$  is the propagation constant in the  $k$ th layer, we see that

$$\begin{aligned} \vec{H} = & \sum_{(m,n) \in I} \left[ \frac{i}{\omega \mu_r} \left\{ a_{(m,n)}^{(p)} \frac{Z_{(n,p)}^{(a,1)}(r) n(n+1)}{r} + \alpha_r c_{(m,n)}^{(p)} \frac{Z_{(n,p)}^{(c,1)}(r)}{kr} \right\} \vec{C}_{(m,n)} \right. \\ & + \frac{i}{\omega \mu} \left\{ a_{(m,n)}^{(p)} k W_{(n,p)}^{(a,1)}(r) + \alpha b_{(m,n)}^{(p)} \frac{1}{kr} \left( -\frac{\partial}{\partial r} \right) (r Z_{(n,p)}^{(b,1)}(r)) \right\} \vec{B}_{(m,n)} + \\ & \left. \left( \frac{i}{\omega \mu} \right) \left\{ c_{(m,n)}^{(p)} \frac{Z_{(n,p)}^{(c,1)}(r)}{k_p r^2} + \right. \right. \end{aligned}$$

$$b_{(m,n)}^{(p)} \left( \frac{1}{kr} \right) \left( \frac{\partial}{\partial r} \right)^2 \left( r Z_{(n,p)}^{(b,1)}(r) \right) + \alpha a_{(m,n)}^{(p)} Z_{(n,p)}^{((a,1))}(r) \left\{ \bar{A}_{(m,n)} \right\} \quad (2.13)$$

Now using equation (1.74) and equation (1.43) we see equation (2.13), and making use the telescoping of terms or specifically the relation that is derivable from equations (1.43) and (1.74) and given by

$$\begin{aligned} & c_{(m,n)}^{(p)} \frac{Z_{(n,p)}^{(c,1)}(r)}{k_p r^2} + \\ & b_{(m,n)}^{(p)} \left( \frac{1}{kr} \right) \left( \frac{\partial}{\partial r} \right)^2 \left( r Z_{(n,p)}^{(b,1)}(r) \right) = \\ & b_{(m,n)}^{(p)} \left[ -\frac{(k^2 + \alpha\beta)}{k} \right] Z_{(n,p)}^{(b,1)}(r) \end{aligned} \quad (2.14)$$

we see that the magnetic vector in the core of the multilayer spherical structure corresponding to  $p = 1$  is given by

$$\begin{aligned} \vec{H} = & \sum_{(m,n) \in I} \left[ \frac{i}{\omega \mu_r^{(p)}} \left\{ a_{(m,n)}^{(p)} \frac{Z_{(n,p)}^{(a,1)}(r) n(n+1)}{r} - \alpha_r \zeta_b n(n+1) b_{(m,n)}^{(p)} \frac{Z_{(n,p)}^{(b,1)}(r)}{kr} \right\} \vec{C}_{(m,n)} \right. \\ & + \frac{i}{\omega \mu^{(p)}} \left( \left\{ a_{(m,n)}^{(p)} k_p W_{(n,p)}^{(a,1)}(r) + \alpha b_{(m,n)}^{(p)} (-W_{(n,p)}^{(b,1)}(r)) \right\} \vec{B}_{(m,n)} + \right. \\ & \left. \left. \left\{ b_{(m,n)}^{(p)} \left[ -\frac{(k^2 + \alpha\beta)}{k} \right] Z_{(n,p)}^{(b,1)}(r) + \alpha^{(p)} a_{(m,n)}^{(p)} Z_{(n,p)}^{((a,1))}(r) \right\} \bar{A}_{(m,n)} \right) \right] \end{aligned} \quad (2.15)$$

We now consider the representation of the magnetic vector in an interior layer of a multilayer sphere that does not contain the center of the sphere. The magnetic vector has the representation in terms of functions  $Z_{(n,p)}^{(a,1)}(r)$  which have integrable singularities and the functions  $Z_{(n,p)}^{(a,3)}$  whose representation, in the case considered here involves Hankel functions with complex index. The magnetic vector representation in a penetrable shell is given by

$$\begin{aligned} \vec{H} = & \sum_{(m,n) \in I} \left[ \left( \frac{i}{\omega \mu_r} \right) \left\{ a_{(m,n)}^{(p)} \frac{Z_{(n,p)}^{(a,1)}(r) n(n+1)}{r} + \right. \right. \\ & \left. \left. \alpha_{(m,n)}^{(p)} \frac{Z_{(n,p)}^{(a,3)}(r) n(n+1)}{r} + (-1) \left( \alpha_r^{(p)} \zeta_b n(n+1) b_{(m,n)}^{(p)} \frac{Z_{(n,p)}^{(b,1)}(r)}{kr} + \right. \right. \right. \end{aligned}$$

$$\begin{aligned}
& \left. \alpha_r^{(p)} \Omega_b n(n+1) \beta_{(m,n)}^{(p)} \frac{Z_{(n,p)}^{(b,3)}(r)}{kr} \right) \} \tilde{C}_{(m,n)} + \\
& \frac{i}{\omega \mu^{(p)}} \{ a_{(m,n)}^{(p)} k_p W_{(n,p)}^{(a,1)}(r) + \alpha_{(m,n)}^{(p)} k_p W_{(n,p)}^{(a,3)}(r) \} \tilde{B}_{(m,n)} + \\
& \left( \frac{-i}{\omega \mu^{(p)}} \right) \{ \alpha^{(p)} b_{(m,n)}^{(p)} (W_{(n,p)}^{(b,1)}(r)) + \alpha^{(p)} \beta_{(m,n)}^{(p)} (W_{(n,p)}^{(b,3)}(r)) \} \tilde{B}_{(m,n)} + \\
& \left( \frac{i}{\omega \mu^{(p)}} \right) \left[ -\frac{(k^2 + \alpha \beta)}{k} \right] \{ b_{(m,n)}^{(p)} Z_{(n,p)}^{(b,1)}(r) + \beta_{(m,n)}^{(p)} Z_{(n,p)}^{(b,3)}(r) \} \tilde{A}_{(m,n)} + \\
& \left( \frac{i}{\omega \mu^{(p)}} \right) \{ \alpha^{(p)} a_{(m,n)}^{(p)} Z_{(n,p)}^{(a,1)}(r) + \alpha^{(p)} \alpha_{(m,n)}^{(p)} Z_{(n,p)}^{(a,3)}(r) \} \tilde{A}_{(m,n)} \Big] \quad (2.16)
\end{aligned}$$

We now consider the representation of the electric vector in the core region  $p = 1$  of the multilayer, spherically symmetric bianisotropic structure. Making use of equation (1.74) we deduce from equation (1.25) that

$$\begin{aligned}
\vec{E}_p = \sum_{(m,n) \in I} & \left\{ a_{(m,n)} Z_n^{(a)}(r) \tilde{A}_{(m,n)}(\theta, \phi) + \right. \\
& [-n(n+1) \{ \Omega_b \}] b_{(m,n)} \frac{Z_n^{(b)}(r)}{kr} \tilde{C}_{(m,n)}(\theta, \phi) + \\
& \left. \frac{b_{(m,n)}}{kr} \left( - \left( \frac{\partial}{\partial r} \right) (r Z_n^{(b)}(r)) \right) \tilde{B}_{(m,n)}(\theta, \phi) \right\} \quad (2.17)
\end{aligned}$$

Equating tangential components of  $\vec{E}$  across the shell  $r = R_p$  equation (2.12), the representation of the electric vector in a shell region, implies that equating coefficients of  $\tilde{A}_{(m,n)}(\theta, \phi)$  leads to

$$\begin{aligned}
& [a_{(m,n)}^{(p)} Z_{(n,p)}^{(a,1)}(r) + \alpha_{(m,n)}^{(p)} Z_{(n,p)}^{(a,3)}(r)] \\
& = [a_{(m,n)}^{(p+1)} Z_{(n,p+1)}^{(a,1)}(r) + \alpha_{(m,n)}^{(p+1)} Z_{(n,p+1)}^{(a,3)}(r)] \quad (2.18)
\end{aligned}$$

Multiplying both sides of equation (2.12) by  $\tilde{B}_{(m,n)}$  and integrating over the sphere, we deduce that

$$\begin{aligned}
& [b_{(m,n)}^{(p)} Z_{(n,p)}^{(b,1)}(r) + \beta_{(m,n)}^{(p)} Z_{(n,p)}^{(b,3)}(r)] \\
& = [b_{(m,n)}^{(p+1)} Z_{(n,p+1)}^{(b,1)}(r) + \beta_{(m,n)}^{(p+1)} Z_{(n,p+1)}^{(b,3)}(r)] \quad (2.19)
\end{aligned}$$

We now set up the differential equations which state that the tangential components of the magnetic vector are continuous across the boundary of a sphere separating regions

of continuity of tensorial electric properties. Equation (2.16) implies, upon equating tangential components  $\vec{H}$ , on each side of the boundary  $r = R_p$ , that

$$\begin{aligned} & \frac{i}{\omega\mu^{(p)}} \left\{ a_{(m,n)}^{(p)} k_p W_{(n,p)}^{(a,1)}(r) + \alpha_{(m,n)}^{(p)} k_p W_{(n,p)}^{(a,3)}(r) \right\} + \\ & \left( \frac{-i}{\omega\mu^{(p)}} \right) \left\{ \alpha_{(m,n)}^{(p)} b_{(m,n)}^{(p)} (W_{(n,p)}^{(b,1)}(r)) \alpha_{(m,n)}^{(p)} \beta_{(m,n)}^{(p)} (W_{(n,p)}^{(b,3)}(r)) \right\} = \\ & \frac{i}{\omega\mu^{(p+1)}} \left\{ a_{(m,n)}^{(p+1)} k_{p+1} W_{(n,p+1)}^{(a,1)}(r) + \alpha_{(m,n)}^{(p+1)} k_{p+1} W_{(n,p+1)}^{(a,3)}(r) \right\} + \\ & \left( \frac{-i}{\omega\mu^{(p+1)}} \right) \left\{ \alpha_{(m,n)}^{(p+1)} b_{(m,n)}^{(p+1)} (W_{(n,p+1)}^{(b,1)}(r)) \alpha_{(m,n)}^{(p+1)} \beta_{(m,n)}^{(p+1)} (W_{(n,p+1)}^{(b,3)}(r)) \right\} \end{aligned} \quad (2.20)$$

Using equation (2.16) and equating coefficients of the vector  $\vec{A}$  on both sides of the spherical shell  $r = R_p$  we have

$$\begin{aligned} & \left( \frac{i}{\omega\mu^{(p)}} \right) \left[ -\frac{(k_p^2 + \alpha^{(p)}\beta^{(p)})}{k_p} \right] \left\{ b_{(m,n)}^{(p)} Z_{(n,p)}^{(b,1)}(r) + \beta_{(m,n)}^{(p)} Z_{(n,p)}^{(b,3)}(r) \right\} \\ & \left( \frac{i}{\omega\mu^{(p)}} \right) \left\{ \alpha_{(m,n)}^{(p)} a_{(m,n)}^{(p)} Z_{(n,p)}^{(a,1)}(r) + \alpha_{(m,n)}^{(p)} \alpha_{(m,n)}^{(p)} Z_{(n,p)}^{(a,3)}(r) \right\} = \\ & \left( \frac{i}{\omega\mu^{(p+1)}} \right) \left\{ b_{(m,n)}^{(p+1)} \left[ -\frac{(k_{p+1}^2 + \alpha^{(p+1)}\beta^{(p+1)})}{k_{p+1}} \right] Z_{(n,p+1)}^{(b,1)}(r) \right. \\ & \quad \left. + \beta_{(m,n)}^{(p+1)} \left[ -\frac{(k_{p+1}^2 + \alpha^{(p+1)}\beta^{(p+1)})}{k_{p+1}} \right] Z_{(n,p+1)}^{(b,3)}(r) \right\} \\ & \left( \frac{i}{\omega\mu^{(p+1)}} \right) \left\{ \alpha_{(m,n)}^{(p+1)} a_{(m,n)}^{(p)} Z_{(n,p+1)}^{(a,1)}(r) + \alpha_{(m,n)}^{(p+1)} \alpha_{(m,n)}^{(p+1)} Z_{(n,p+1)}^{(a,3)}(r) \right\} \end{aligned} \quad (2.21)$$

We now attempt to develop transition matrices which will relate expansion coefficients in one layer to expansion coefficients in another layer. We start with equation (2.20); we find, after multiplying both sides of this equation by  $\mu^{(p)}$  and dividing both sides of equation (2.20) by  $k_p$ , that

$$\begin{aligned} & \left\{ a_{(m,n)}^{(p)} W_{(n,p)}^{(a,1)}(r) + \alpha_{(m,n)}^{(p)} W_{(n,p)}^{(a,3)}(r) \right\} + \\ & \left\{ \left( -\frac{\alpha^{(p)}}{k_p} \right) b_{(m,n)}^{(p)} (W_{(n,p)}^{(b,1)}(r)) \left( -\frac{\alpha^{(p)}}{k_p} \right) \beta_{(m,n)}^{(p)} (W_{(n,p)}^{(b,3)}(r)) \right\} = \\ & \left( \frac{\mu^{(p)} k_{p+1}}{\mu^{(p+1)} k_p} \right) \left\{ a_{(m,n)}^{(p+1)} W_{(n,p+1)}^{(a,1)}(r) + \alpha_{(m,n)}^{(p+1)} W_{(n,p+1)}^{(a,3)}(r) \right\} + \end{aligned}$$

$$\left( \frac{-\mu^{(p)} \alpha^{(p+1)}}{\mu^{(p+1)} k_p} \right) \left\{ b_{(m,n)}^{(p+1)}(W_{(n,p+1)}^{(b,1)}(r)) \beta_{(m,n)}^{(p+1)}(W_{(n,p+1)}^{(b,3)}(r)) \right\} \quad (2.22)$$

Multiplying both sides of equation (2.16) by  $\vec{A}_{(m,n)}(\theta, \phi)$  and observing that

$$\begin{aligned} \lim_{r \rightarrow R_0^-} \int_{S_p(r)} \vec{H} \cdot \vec{A}_{(m,n)}(\theta, \phi) dA = \\ \lim_{r \rightarrow R_p^+} \int_{S_p(r)} \vec{H} \cdot \vec{A}_{(m,n)}(\theta, \phi) dA \end{aligned} \quad (2.23)$$

we derive equation (2.21). From this, after multiplying all terms by  $-i\omega\mu^{(p)}k_p$  and dividing all terms by  $(k_p^2 + \alpha^{(p)}\beta^{(p)})$ , we derive the relation that

$$\begin{aligned} & \left( \frac{k_p \alpha^{(p)}}{(k_p^2 + \alpha^{(p)}\beta^{(p)})} \right) \left\{ a_{(m,n)}^{(p)} Z_{(n,p)}^{(a,1)}(r) + \alpha_{(m,n)}^{(p)} Z_{(n,p)}^{(a,3)}(r) \right\} + \\ & \left\{ b_{(m,n)}^{(p)} Z_{(n,p)}^{(b,1)}(r) + \beta_{(m,n)}^{(p)} Z_{(n,p)}^{(b,3)}(r) \right\} = \\ & \left( \frac{\mu^{(p)} k_p \alpha^{(p+1)}}{\mu^{(p+1)} (k_p^2 + \alpha^{(p)}\beta^{(p)})} \right) \left\{ a_{(m,n)}^{(p)} Z_{(n,p+1)}^{(a,1)}(r) + \alpha_{(m,n)}^{(p+1)} Z_{(n,p+1)}^{(a,3)}(r) \right\} + \\ & \left[ -\frac{(\mu^{(p)} k_p) (k_{p+1}^2 + \alpha^{(p+1)}\beta^{(p+1)})}{(\mu^{(p+1)} k_{p+1}) k_p^2 + \alpha^{(p)}\beta^{(p)}} \right] \cdot \left\{ b_{(m,n)}^{(p+1)} Z_{(n,p+1)}^{(b,1)}(r) + \beta_{(m,n)}^{(p+1)} Z_{(n,p+1)}^{(b,3)}(r) \right\}. \end{aligned} \quad (2.24)$$

We now define parameters which appear in the matrix relating expansion coefficients in one layer to those in an adjacent layer. We obtain these by considering terms appearing in equation (2.24)

$$\rho_{(b,3)}^{(p+1)} = \left( \frac{\mu^{(p)} k_p}{\mu^{(p+1)} k_{p+1}} \right) \left[ -\frac{(k_{p+1}^2 + \alpha^{(p+1)}\beta^{(p+1)})}{k_p^2 + \alpha^{(p)}\beta^{(p)}} \right] \quad (2.25)$$

Also

$$\rho_{(a,3)}^{(p+1)} = \left( \frac{\mu^{(p)} k_p \alpha^{(p+1)}}{\mu^{(p+1)} (k_p^2 + \alpha^{(p)}\beta^{(p)})} \right) \quad (2.26)$$

A similar term appearing in the inner shell matrix is

$$\rho_{(a,3)}^{(p)} = \left( \frac{k_p \alpha^{(p)}}{k_p^2 + \alpha^{(p)}\beta^{(p)}} \right) \quad (2.27)$$

A term in the second row of the outer shell matrix is

$$\rho_{(a,2)}^{(p+1)} = \left( \frac{\mu^{(p)} k_{p+1}}{\mu^{(p+1)} k_p} \right) \quad (2.28)$$



Another term appearing in second row of the matrix is

$$\rho_{(b,2)}^{(p+1)} = \left( \frac{-\mu^{(p)} \alpha^{(p+1)}}{\mu^{(p+1)} k_p} \right) \quad (2.29)$$

The corresponding term in the inner shell matrix is

$$\rho_{(b,2)}^{(p)} = \left( \frac{-\alpha^{(p)}}{k_p} \right) \quad (2.30)$$

With the special functions  $Z_{(n,p)}^{(a,j)}$  and  $Z_{(n,p)}^{(b,j)}$  and the derivative terms defined by equation (2.11) being evaluated at the separating spherical boundary  $r = R_p$ , we see that the matrix equation relating expansion coefficients in layer  $p$  to those in layer  $p + 1$  is given by

$$\begin{bmatrix} Z_{(n,p)}^{(a,1)}(R_p) & Z_{(n,p)}^{(a,3)}(R_p) & 0 & 0 \\ W_{(n,p)}^{(a,1)}(R_p) & W_{(n,p)}^{(a,3)}(R_p) & \rho_{(b,2)}^{(p)} W_{(n,p)}^{(b,1)}(R_p) & \rho_{(b,2)}^{(p)} W_{(n,p)}^{(b,3)}(R_p) \\ \rho_{(a,3)}^{(p)} Z_{(n,p)}^{(a,1)}(R_p) & \rho_{(a,3)}^{(p)} Z_{(n,p)}^{(a,3)}(R_p) & Z_{(n,p)}^{(b,1)}(R_p) & Z_{(n,p)}^{(b,3)}(R_p) \\ 0 & 0 & W_{(n,p)}^{(b,1)}(R_p) & W_{(n,p)}^{(b,3)}(R_p) \end{bmatrix} \begin{bmatrix} a_{(m,n)}^{(p)} \\ \alpha_{(m,n)}^{(p)} \\ b_{(m,n)}^{(p)} \\ \beta_{(m,n)}^{(p)} \end{bmatrix} = \begin{bmatrix} Z_{(n,p+1)}^{(a,1)} & Z_{(n,p+1)}^{(a,3)} & 0 & 0 \\ W_{(n,p+1)}^{(a,1)} & W_{(n,p+1)}^{(a,3)} & \rho_{(b,2)}^{(p+1)} W_{(n,p+1)}^{(b,1)} & \rho_{(b,2)}^{(p+1)} W_{(n,p+1)}^{(b,3)} \\ \rho_{(a,3)}^{(p+1)} Z_{(n,p+1)}^{(a,1)} & \rho_{(a,3)}^{(p+1)} Z_{(n,p+1)}^{(a,3)} & \rho_{(b,3)}^{(p+1)} Z_{(n,p+1)}^{(b,1)} & \rho_{(b,3)}^{(p+1)} Z_{(n,p+1)}^{(b,3)} \\ 0 & 0 & W_{(n,p+1)}^{(b,1)} & W_{(n,p+1)}^{(b,3)} \end{bmatrix} \begin{bmatrix} a_{(m,n)}^{(p+1)} \\ \alpha_{(m,n)}^{(p+1)} \\ b_{(m,n)}^{(p+1)} \\ \beta_{(m,n)}^{(p+1)} \end{bmatrix} \quad (2.31)$$

This equation can be written more compactly in the form

$$T_n^{(p)}(R_p) \begin{bmatrix} a_{(m,n)}^{(p)} \\ \alpha_{(m,n)}^{(p)} \\ b_{(m,n)}^{(p)} \\ \beta_{(m,n)}^{(p)} \end{bmatrix} = T_n^{(p+1)}(R_p) \begin{bmatrix} a_{(m,n)}^{(p+1)} \\ \alpha_{(m,n)}^{(p+1)} \\ b_{(m,n)}^{(p+1)} \\ \beta_{(m,n)}^{(p+1)} \end{bmatrix} \quad (2.32)$$

Wronskian relations will show that we can define a new matrix  $Q_n^{(p)}$  by the rule

$$Q_n^{(p)} = T_n^{(p)}(R_p)^{-1} T_n^{(p+1)}(R_p). \quad (2.33)$$

Using equations (2.32) and (2.33) we see that the expansion coefficients in the core are related to the expansion coefficients in the outer shell by the rule,

$$\begin{bmatrix} a_{(m,n)}^{(1)} \\ 0 \\ b_{(m,n)}^{(1)} \\ 0 \end{bmatrix} = Q_n^{(1)} Q_n^{(2)} \dots Q_n^{(N)} \begin{bmatrix} a_{(m,n)}^{(N+1)} \\ \alpha_{(m,n)}^{(N+1)} \\ b_{(m,n)}^{(N+1)} \\ \beta_{(m,n)}^{(N+1)} \end{bmatrix} \quad (2.34)$$

This gives us four equations in four unknowns, since we assume that the expansion coefficients  $\alpha_{(m,n)}^{(N+1)}$  and  $\beta_{(m,n)}^{(N+1)}$  are determined; these expansion coefficients could define a complex source such as a radar or laser beam in the near field (Barton [8] and [9], Pinnick [39] and [37]). Solving equation (2.34) we find values of  $a_{(m,n)}^{(1)}$  and  $b_{(m,n)}^{(1)}$  and assuming that  $\alpha_{(m,n)}^{(1)}$  and  $\beta_{(m,n)}^{(1)}$  are both zero, we can easily obtain the expansion coefficients in every layer of the structure. If we define the matrix  $\mathcal{R}_n^{(p)}$  by the rule,

$$\mathcal{R}_n^{(p)} = T_n^{(p+1)}(R_p)^{-1} T_n^{(p)}(R_p) \quad (2.35)$$

We see that

$$\mathcal{R}_n^{(p)} \begin{bmatrix} a_{(m,n)}^{(p)} \\ \alpha_{(m,n)}^{(p)} \\ b_{(m,n)}^{(p)} \\ \beta_{(m,n)}^{(p)} \end{bmatrix} = \begin{bmatrix} a_{(m,n)}^{(p+1)} \\ \alpha_{(m,n)}^{(p+1)} \\ b_{(m,n)}^{(p+1)} \\ \beta_{(m,n)}^{(p+1)} \end{bmatrix} \quad (2.36)$$

These computations are facilitated by the fact that we have exact formulas for the determinant and inverses of the 4 by 4 matrices  $T_n^{(p)}$ . Let the determinant of  $T_n^{(p)}$  be defined by

$$\begin{aligned} \Delta_p &= Z_{(n,p)}^{(a,1)}(R_p) W_{(n,p)}^{(a,3)}(R_p) \\ &\quad \{ Z_{(n,p)}^{(b,1)}(R_p) W_{(n,p)}^{(b,3)}(R_p) - W_{(n,p)}^{(b,1)}(R_p) Z_{(n,p)}^{(b,3)}(R_p) \} + \\ &\quad (-1) [ Z_{(n,p)}^{(a,3)}(R_p) W_{(n,p)}^{(a,1)}(R_p) ] \\ &\quad \{ Z_{(n,p)}^{(b,1)}(R_p) W_{(n,p)}^{(b,3)}(R_p) - W_{(n,p)}^{(b,1)}(R_p) Z_{(n,p)}^{(b,3)}(R_p) \} \end{aligned} \quad (2.37)$$

which means that the determinant  $\Delta_p$  is the product of two Wronskians  $\mathcal{W}_{(n,p)}^{(a)}$  and  $\mathcal{W}_{(n,p)}^{(b)}$  where

$$\mathcal{W}_{(n,p)}^{(b)} = Z_{(n,p)}^{(b,1)}(R_p) W_{(n,p)}^{(b,3)}(R_p) - W_{(n,p)}^{(b,1)}(R_p) Z_{(n,p)}^{(b,3)}(R_p) \quad (2.38)$$

We find that

$$\mathcal{W}_{(n,p)}^{(a)}(R_p) = \frac{-i}{(k_p R_p)^2} \quad (2.39)$$

This enables us to get exact formulas for the entries of the inverse of this matrix. If  $(T_n^{(p)}(R_p)^{-1})_{(i,j)}$  denotes the entry in the  $i$ th row and  $j$ th column of the inverse of the matrix  $T_n^{(p)}$ , then the entry in row 1 and column 1 of the inverse is

$$(T_n^{(p)}(R_p)^{-1})_{(1,1)} = W_{(n,p)}^{(a,3)}(R_p) \mathcal{W}_{(n,p)}^{(b)}(R_p) / \Delta_p, \quad (2.40)$$

The (1,2) entry is

$$(T_n^{(p)}(R_p)^{-1})_{(1,2)} = -W_{(n,p)}^{(a,1)}(R_p) \mathcal{W}_{(n,p)}^{(b)}(R_p) / \Delta_p, \quad (2.41)$$

The (1,3) term is

$$(T_n^{(p)}(R_p)^{-1})_{(1,3)} = W_{(n,p)}^{(b,3)}(R_p) \rho_{(a,3)}^{(p)} \mathcal{W}_{(n,p)}^{(b)}(R_p) / \Delta_p, \quad (2.42)$$

The (1,4) term is

$$(T_n^{(p)}(R_p)^{-1})_{(1,4)} = -W_{(n,p)}^{(b,1)}(R_p) \rho_{(a,3)}^{(p)} \mathcal{W}_{(n,p)}^{(a)}(R_p) / \Delta_p, \quad (2.43)$$

The entry in row 2 and column 1 of the inverse is

$$(T_n^{(p)}(R_p)^{-1})_{(2,1)} = -Z_{(n,p)}^{(a,3)}(R_p) \rho_{(a,3)}^{(p)} \mathcal{W}_{(n,p)}^{(b)}(R_p) / \Delta_p, \quad (2.44)$$

The entry in row 2 and column 2 of the inverse is

$$(T_n^{(p)}(R_p)^{-1})_{(2,2)} = -Z_{(n,p)}^{(a,3)}(R_p) \rho_{(a,3)}^{(p)} \mathcal{W}_{(n,p)}^{(b)}(R_p) / \Delta_p, \quad (2.45)$$

The entry in row 2 and column 3 of the inverse is

$$(T_n^{(p)}(R_p)^{-1})_{(2,3)} = 0 \quad (2.46)$$

The entry in row 2 and column 4 of the inverse is

$$(T_n^{(p)}(R_p)^{-1})_{(2,4)} = 0 \quad (2.47)$$

The (3,1) entry is

$$(T_n^{(p)}(R_p)^{-1})_{(3,1)} = 0 \quad (2.48)$$

The (3,2) entry is

$$(T_n^{(p)}(R_p)^{-1})_{(3,2)} = 0 \quad (2.49)$$

The (3,3) entry is

$$(T_n^{(p)}(R_p)^{-1})_{(3,3)} = W_{(n,p)}^{(b,3)}(R_p) \mathcal{W}_{(n,p)}^{(a)}(R_p) / \Delta_p, \quad (2.50)$$

The (3,4) entry is

$$(T_n^{(p)}(R_p)^{-1})_{(3,4)} = W_{(n,p)}^{(b,1)}(R_p) \mathcal{W}_{(n,p)}^{(a)}(R_p) / \Delta_p, \quad (2.51)$$

The (4,1) entry is given by

$$(T_n^{(p)}(R_p)^{-1})_{(4,1)} = -Z_{(n,p)}^{(a,3)}(R_p) \mathcal{W}_{(n,p)}^{(b)}(R_p) / \Delta_p, \quad (2.52)$$

The (4,2) entry is

$$(T_n^{(p)}(R_p)^{-1})_{(4,2)} = Z_{(n,p)}^{(a,1)}(R_p) \mathcal{W}_{(n,p)}^{(b)}(R_p) / \Delta_p, \quad (2.53)$$

The (4,3) entry is

$$(T_n^{(p)}(R_p)^{-1})_{(4,3)} = -Z_{(n,p)}^{(b,3)}(R_p) \mathcal{W}_{(n,p)}^{(a)}(R_p) / \Delta_p, \quad (2.54)$$

Finally, the (4,4) entry of the inverse of  $T_n^{(p)}$  is

$$(T_n^{(p)}(R_p)^{-1})_{(4,4)} = Z_{(n,p)}^{(b,1)}(R_p) \mathcal{W}_{(n,p)}^{(a)}(R_p) / \Delta_p, \quad (2.55)$$

We have therefore obtained round-off error free expressions for the entries of the inverse of  $T_n^{(p)}(R_p)$ . Thus, except for the expression relating the expansion coefficients in equation (2.34), all computations are carried out by exact formulas. The matrix inverse computation requires no subtractions or additions and consequently there is no round off error if the Bessel and Hankel functions of complex index and their derivatives can be computed precisely.

### 3 Spatially Complex Sources

We provide the user with an analysis of the response of an  $N$  layer structure to spatially and temporally complex sources of electromagnetic radiation. Let  $\vec{E}(x, y, z, t)$  and  $\vec{H}(x, y, z, t)$  be the electric and magnetic fields of a complex source with Fourier transforms  $\hat{\vec{E}}(x, y, z, \omega)$  and  $\hat{\vec{H}}(x, y, z)$ . We suppose that this radiation source exists in layer

$$p \in \{2, 3, \dots, N + 1\}.$$

where  $N$  is the number of layers in the spherical structure. Let us suppose that this energy source in layer  $p$  has an electric vector (see equation 2.1) given by

$$\vec{E} = \sum_{(m,n) \in I} \left\{ \tilde{a}_{(m,n)} Z_{(n,p)}^{(a,1)}(r) \vec{A}_{(m,n)}(\theta, \phi) + \right.$$

$$\begin{aligned} & [-n(n+1) \{ \zeta_b^{(p)} \} ] \tilde{b}_{(m,n)} \frac{Z_{(n,p)}^{(b,1)}(r)}{kr} \tilde{C}_{(m,n)}(\theta, \phi) + \\ & \frac{\tilde{b}_{(m,n)}}{k_p r} \left( - \left( \frac{\partial}{\partial r} \right) (r Z_{(n,p)}^{(b,1)}(r)) \right) \tilde{B}_{(m,n)}(\theta, \phi) \Big\} \end{aligned} \quad (3.56)$$

Observe that the coefficients  $\tilde{a}_{(m,n)}^{(p)}$  are determined for every  $p > 1$  by the relation,

$$\begin{aligned} & \lim_{r \rightarrow R_{p-1}} \left[ \frac{\int \int_{C(r)} \hat{\tilde{E}}_p(x, y, z, \omega) \cdot \tilde{A}_{(m,n)}(\theta, \phi)^* \sin(\theta) d\theta d\phi}{\int \int_{C(r)} \tilde{A}_{(m,n)}(\theta, \phi) \cdot \tilde{A}_{(m,n)}(\theta, \phi)^* \sin(\theta) d\theta d\phi} \right] \\ & = \tilde{a}_{(m,n)}^{(p)} Z_{(n,p)}^{(a,1)}(R_{p-1}) \end{aligned} \quad (3.57)$$

where

$$C(r) = \{ (x, y, z) : x^2 + y^2 + z^2 = r^2 \} \quad (3.58)$$

Thus, equation (3.57) gives us the expansion coefficients for the representation of  $\tilde{E}$  just outside the sphere  $C(R_{p-1})$  defined by equation (3.58). The coefficients  $\tilde{b}_{(m,n)}^{(p)}$  are determined by the equation,

$$\begin{aligned} & \lim_{r \rightarrow R_{p-1}} \left[ \frac{\int \int_{C(r)} \hat{\tilde{E}}_p(x, y, z, \omega) \cdot \tilde{B}_{(m,n)}(\theta, \phi)^* \sin(\theta) d\theta d\phi}{\int \int_{C(r)} \tilde{B}_{(m,n)}(\theta, \phi) \cdot \tilde{B}_{(m,n)}(\theta, \phi)^* \sin(\theta) d\theta d\phi} \right] \\ & = \tilde{b}_{(m,n)}^{(p)} (-W_{(n,p)}^{(b,1)}(R_{p-1})) \end{aligned} \quad (3.59)$$

where, using the definition (see equation 2.11),

$$W_{(n,p)}^{(b,j)}(r) = \frac{1}{k_p r} \left( \frac{\partial}{\partial r} \right) (r Z_{(n,p)}^{(b,j)}(r)) \quad (3.60)$$

and the functions  $\tilde{A}_{(m,n)}(\theta, \phi)$  and  $\tilde{B}_{(m,n)}(\theta, \phi)$  are given by equations (1.4) and (1.5). We will show that the integrals in the denominators in equations (3.57) and (3.59) can be determined by an exact formula. To exactly evaluate the integrals appearing in the denominators, we use the equation (see Bell [10], equation 11 and equation 18) which states that

$$\begin{aligned} & \int_{-\pi}^{\pi} \int_0^{\pi} \left\{ \left( \frac{d}{d\theta} P_n^m(\cos(\theta)) \right)^2 + m^2 \frac{P_n^m(\cos(\theta))^2}{\sin^2(\theta)} \right\} \sin(\theta) d\theta d\phi = \\ & = \left( \frac{2}{2n+1} \right) \left( \frac{(n+m)!}{(n-m)!} \right) n(n+1) \end{aligned} \quad (3.61)$$

where the functions  $P_n^m(x)$  are defined by

$$P_n^m(x) = \frac{(1-x^2)^{m/2}}{2^n n!} D^{n+m}(x^2-1)^n \quad (3.62)$$

of the associated Legendre function.

We use the basic definition

$$P_n^m(x) = \left( \frac{(1-x^2)^{m/2}}{2^n n!} \right) D^{n+m}(x^2-1)^n \quad (3.63)$$

of the associated Legendre function. If

$$x = \cos(\theta) \quad (3.64)$$

then

$$d\theta = -\frac{dx}{\sqrt{1-x^2}} \quad (3.65)$$

and

$$\begin{aligned} \int_0^\pi P_n^m(\cos(\theta))^2 \sin(\theta) d\theta = \\ \frac{1}{2^{2n}(n!)^2} \int_{-1}^{+1} (1-x^2)^m (D^{n+m}(x^2-1)^n)^2 dx = \frac{2(n+m)!}{(2n+1)(n-m)!} \end{aligned} \quad (3.66)$$

The orthogonality relationship follows from the fact that

$$\frac{d}{d\theta} = \frac{dx}{d\theta} \frac{d}{dx} = -\sin(\theta) \frac{d}{dx} \quad (3.67)$$

implies that

$$\begin{aligned} A_{(n,r)}^m &= \int_0^\pi \left[ \frac{d}{d\theta} P_n^m(\cos(\theta)) \right] \left[ \frac{d}{d\theta} P_r^m(\cos(\theta)) \right] \sin(\theta) d\theta \\ &= \int_{-1}^1 (1-x^2) \frac{d}{dx} P_n^m(x) \frac{d}{dx} P_r^m(x) dx \end{aligned} \quad (3.68)$$

The derived identity then follows from an integration by parts and a use of the differential equation relationship,

$$\begin{aligned} (1-x^2) \left[ \left( \frac{d}{dx} \right)^2 P_n^m(x) \right] + (-2x) \frac{d}{dx} P_n^m(x) = \\ \left[ -n(n+1) + \frac{m}{1-x^2} \right] P_n^m(x) \end{aligned} \quad (3.69)$$

Details of the analysis can be found in ([11]) and the basic properties of  $P_n^m$  are found in ([51])

### 3.1 An Exterior Complex Source

We now define intralayer relationships that give us the induced field when there are no sources in layers indexed by

$$p \in \{2, 3, \dots, N\}$$

where  $N$  is the number of layers in the sphere. The intralayer relationship yields, for a penetrable core,

$$\begin{bmatrix} a_{(m,n)}^{(1)} \\ 0 \\ b_{(m,n)}^{(1)} \\ 0 \end{bmatrix} = S_N \begin{bmatrix} \tilde{a}_{(m,n)}^{(N+1)} \\ \alpha_{(m,n)}^{(N+1)} \\ \tilde{b}_{(m,n)}^{(N+1)} \\ \beta_{(m,n)}^{(N+1)} \end{bmatrix} \quad (3.70)$$

We can separate the four, a priori unknown coefficients, from the known expansion coefficients of the known external source by rewriting equation (3.70) in the form

$$\begin{bmatrix} a_{(m,n)}^{(1)} \\ 0 \\ b_{(m,n)}^{(1)} \\ 0 \end{bmatrix} - S_N \begin{bmatrix} 0 \\ \alpha_{(m,n)}^{(N+1)} \\ 0 \\ \beta_{(m,n)}^{(N+1)} \end{bmatrix} = S_N \begin{bmatrix} \tilde{a}_{(m,n)}^{(N+1)} \\ 0 \\ \tilde{b}_{(m,n)}^{(N+1)} \\ 0 \end{bmatrix} \quad (3.71)$$

Thus, relating the a priori unknown coefficients to the known expansion coefficients  $\tilde{a}_{(m,n)}^{(N+1)}$  and  $\tilde{b}_{(m,n)}^{(N+1)}$  reduces to the problem of finding the inverse of the matrix

$$\tau = \bar{I} - S_N \quad (3.72)$$

### 3.2 Interior Sources

We now suppose that there are interior sources in the layers. This could be important in assessing the impact of a sweeping radar on a person living near the radar who has one or more metallic implants to replace broken bones or clamps to hold them in place. The potentially serious nature of this can be seen from the fact that ([54] p 40) has used this concept to postulate a design for an electromagnetic missile.

With interior sources, the expansion coefficients in the free space surrounding the N layer sphere and the expansion coefficients in the inner core will be shown to be related by affine transformations rather than linear transformations.

We model complex sources in a layer by allowing an arbitrary representation of a source in terms of an expansion in a Hilbert space of vector valued functions. We assume that if the shell containing the source lies between  $r = R_p$  and  $r = R_{p+1}$  and represent the expansion coefficients of the electric field due to this source in the inner shell in terms of expansion coefficients  $\tilde{a}_{(m,n)}^{(p)}$ ,  $\tilde{b}_{(m,n)}^{(p)}$ . We assume that these are given and represent a source located at a point  $r = \tilde{R}_p$  that is between  $r = R_p$  and  $r = R_{p+1}$ . These are obtained by assuming that the source is unaffected by the medium and that the currents, say in a dipole source, are used to represent an electric vector  $\tilde{\vec{E}}_p$ . This electric vector is then represented on the inner shell by the relations,

$$\begin{aligned} \lim_{r \rightarrow R_p} \left[ \frac{\int \int_{C(r)} \tilde{\vec{E}}_p(x, y, z, \omega) \cdot \vec{A}_{(m,n)}(\theta, \phi)^* \sin(\theta) d\theta d\phi}{\int \int_{C(r)} \vec{A}_{(m,n)}(\theta, \phi) \cdot \vec{A}_{(m,n)}(\theta, \phi)^* \sin(\theta) d\theta d\phi} \right] \\ = \tilde{a}_{(m,n)}^{(p)} Z_{(n,p)}^{(a,1)}(R_p) \end{aligned} \quad (3.1)$$

The values of the expansion coefficients  $\tilde{b}_{(m,n)}^{(p)}$  of this source field on the shell  $r = R_p$  are given by

$$\begin{aligned} \lim_{r \rightarrow R_p} \left[ \frac{\int \int_{C(r)} \tilde{\vec{E}}_p(x, y, z, \omega) \cdot \vec{B}_{(m,n)}(\theta, \phi)^* \sin(\theta) d\theta d\phi}{\int \int_{C(r)} \vec{B}_{(m,n)}(\theta, \phi) \cdot \vec{B}_{(m,n)}(\theta, \phi)^* \sin(\theta) d\theta d\phi} \right] \\ = \tilde{b}_{(m,n)}^{(p)} (-W_{(n,p)}^{(b,1)}(R_p)) \end{aligned} \quad (3.2)$$

Thus, we know the electric field due to the isolated source at this point on the shell  $r = R_p$ . However, unlike the source in the space surrounding the N layer spherical structure we cannot assume that the field is represented by these expansion coefficients and the expansion coefficients  $\alpha_{(m,n)}^{(p)}$  and  $\beta_{(m,n)}^{(p)}$  used to represent the radiation emanating from the inner shell, as there may be additional sources coming from beyond  $r = R_p$  that are due to external sources and reflections of these sources from the layer  $r = R_p$ . Instead we approximate the representation of this source by a finite linear combination of vector spherical wave functions and assume that at some point  $r = \tilde{R}_p$  possibly just slightly smaller than the location of the actual source, so that value of the field at the point considered



would not be singular, we impose essentially an impedance boundary condition (Wu [54]) at  $r = R_p$  which will give us a relationship between the general expansion coefficients  $\alpha_{(m,n)}^{(p,-)}$  and  $\beta_{(m,n)}^{(p,-)}$  and  $a_{(m,n)}^{(p,-)}$  and  $b_{(m,n)}^{(p,-)}$  used to represent the fields when  $r < \tilde{R}_p$  and the expansion coefficients  $\alpha_{(m,n)}^{(p,+)}$  and  $\beta_{(m,n)}^{(p,+)}$  and  $a_{(m,n)}^{(p,+)}$  and  $b_{(m,n)}^{(p,+)}$  that are used to represent the fields when  $r > \tilde{R}_p$ . We suppose that the magnetic vector just outside  $r = \tilde{R}_p$  is denoted by  $\vec{H}_p^+$  and that the magnetic vector just inside  $r = \tilde{R}_p$  is given by  $\vec{H}_p^-$  and that the boundary conditions used to relate the expansion coefficients  $\alpha_{(m,n)}^{(p,-)}$  and  $\beta_{(m,n)}^{(p,-)}$  and  $a_{(m,n)}^{(p,-)}$  and  $b_{(m,n)}^{(p,-)}$  for  $R_p < r < \tilde{R}_p$  to the expansion coefficients  $\alpha_{(m,n)}^{(p,+)}$  and  $\beta_{(m,n)}^{(p,+)}$  and  $a_{(m,n)}^{(p,+)}$  and  $b_{(m,n)}^{(p,+)}$  for  $R_{p+1} > r > \tilde{R}_p$  are continuity of tangential components of  $\vec{E}$  and the nonhomogeneous impedance boundary condition

$$\vec{n} \times (\vec{H}_p^+ - \vec{H}_p^-) = (i\omega\epsilon + \sigma)(\vec{\tilde{E}}_p - (\vec{\tilde{E}}_p \cdot \vec{e}_r)\vec{e}_r) \quad (3.3)$$

Taking the dot product of both sides of equation (3.3) with respect to the vector  $\vec{B}_{(m,n)}(\theta, \phi)$  and integrating over the sphere  $r = \tilde{R}_p$  we see that

$$\begin{aligned} & \frac{i}{\omega\mu^{(p)}} \left\{ a_{(m,n)}^{(p,+)} k_p W_{(n,p)}^{(a,1)}(\tilde{R}_p) + \alpha_{(m,n)}^{(p,+)} k_p W_{(n,p)}^{(a,3)}(\tilde{R}_p) \right\} + \\ & \left( \frac{-i}{\omega\mu^{(p)}} \right) \left\{ \alpha^{(p)} b_{(m,n)}^{(p,+)} (W_{(n,p)}^{(b,1)}(\tilde{R}_p)) + \alpha^{(p)} \beta_{(m,n)}^{(p,+)} (W_{(n,p)}^{(b,3)}(\tilde{R}_p)) \right\} = \\ & \frac{i}{\omega\mu^{(p)}} \left\{ a_{(m,n)}^{(p,-)} k_p W_{(n,p)}^{(a,1)}(\tilde{R}_p) + \alpha_{(m,n)}^{(p,-)} k_p W_{(n,p)}^{(a,3)}(\tilde{R}_p) \right\} + \\ & \left( \frac{-i}{\omega\mu^{(p)}} \right) \left\{ \alpha^{(p)} b_{(m,n)}^{(p,-)} (W_{(n,p)}^{(b,1)}(\tilde{R}_p)) + \alpha^{(p)} \beta_{(m,n)}^{(p,-)} (W_{(n,p)}^{(b,3)}(\tilde{R}_p)) \right\} + \\ & (i\omega\epsilon^{(p)} + \sigma^{(p)}) [-\tilde{b}_{(m,n)}^{(p)} W_{(n,p)}^{(b,1)}(\tilde{R}_p) - \tilde{\beta}_{(m,n)}^{(p)} W_{(n,p)}^{(b,3)}(\tilde{R}_p)] \end{aligned} \quad (3.4)$$

Taking the dot product of both sides of equation (3.3) with respect to the vector  $\vec{A}_{(m,n)}(\theta, \phi)$  and integrating over the sphere  $r = \tilde{R}_p$  we see that

$$\begin{aligned} & \left( \frac{i}{\omega\mu^{(p)}} \right) \left[ -\frac{(k^2 + \alpha\beta)}{k} \right] \left\{ b_{(m,n)}^{(p,+)} Z_{(n,p)}^{(b,1)}(\tilde{R}_p) + \beta_{(m,n)}^{(p,+)} Z_{(n,p)}^{(b,3)}(\tilde{R}_p) \right\} = \\ & \left( \frac{i}{\omega\mu^{(p)}} \right) \left\{ \alpha^{(p)} a_{(m,n)}^{(p,+)} Z_{(n,p)}^{(a,1)}(\tilde{R}_p) + \alpha^{(p)} \alpha_{(m,n)}^{(p,+)} Z_{(n,p)}^{(a,3)}(\tilde{R}_p) \right\} + \\ & (i\omega\epsilon^{(p)} + \sigma^{(p)}) [\tilde{a}_{(m,n)}^{(p)} Z_{(n,p)}^{(a,1)}(\tilde{R}_p) + \tilde{\alpha}_{(m,n)}^{(p)} Z_{(n,p)}^{(a,3)}(\tilde{R}_p)] \end{aligned} \quad (3.5)$$

Using the fact that  $\tilde{\alpha}_{(m,n)}^{(p)} = 0$  and  $\tilde{\beta}_{(m,n)}^{(p)} = 0$  and that the coefficients  $\tilde{a}_{(m,n)}^{(p)}$  and  $\tilde{b}_{(m,n)}^{(p)}$  are completely known gives us a simple relationship between the expansion coefficients (see equation 2.12)

$$\begin{aligned} & [a_{(m,n)}^{(p,+)} Z_{(n,p)}^{(a,1)}(\tilde{R}_p) + \alpha_{(m,n)}^{(p,+)} Z_{(n,p)}^{(a,3)}(\tilde{R}_p)] \\ & = [a_{(m,n)}^{(p,-)} Z_{(n,p)}^{(a,1)}(\tilde{R}_p) + \alpha_{(m,n)}^{(p,-)} Z_{(n,p)}^{(a,3)}(\tilde{R}_p)] \end{aligned} \quad (3.6)$$

and multiplying both sides of the relationship

$$\vec{E}_p^+(\tilde{R}_p) \cdot \vec{e}_r = \vec{E}_p^-(\tilde{R}_p) \cdot \vec{e}_r \quad (3.7)$$

by  $\tilde{B}_{(m,n)}(\theta, \phi)$  and integrating over the sphere  $r = \tilde{R}_p$  we see that

$$\begin{aligned} & [-b_{(m,n)}^{(p,+)} W_{(n,p)}^{(b,1)}(\tilde{R}_p) - \beta_{(m,n)}^{(p,+)} W_{(n,p)}^{(b,3)}(\tilde{R}_p)] \\ & = [-b_{(m,n)}^{(p,-)} W_{(n,p)}^{(b,1)}(\tilde{R}_p) - \beta_{(m,n)}^{(p,-)} W_{(n,p)}^{(b,3)}(\tilde{R}_p)] \end{aligned} \quad (3.8)$$

We define

$$\xi_{(m,n)}^{(p,2)} = 0 = \xi_{(m,n)}^{(p,4)} \quad (3.9)$$

and

$$\xi_{(m,n)}^{(p,1)} = (i\omega\epsilon^{(p)} + \sigma^{(p)}) \tilde{a}_{(m,n)}^{(p)} Z_{(n,p)}^{(a,1)}(\tilde{R}_p) \quad (3.10)$$

and finally,

$$(i\omega\epsilon^{(p)} + \sigma^{(p)}) \xi_{(m,n)}^{(p,3)} = -\tilde{b}_{(m,n)}^{(p)} W_{(n,p)}^{(a,1)}(\tilde{R}_p) \quad (3.11)$$

The expansion coefficients on opposite sides of the sphere  $r = \tilde{R}_p$  are in view of equations (3.5), (3.4), (3.6) and (3.8) and equations (3.9), (3.10), and (3.11) are related by

$$\begin{bmatrix} a_{(m,n)}^{(p,-)} \\ \alpha_{(m,n)}^{(p,-)} \\ b_{(m,n)}^{(p,-)} \\ \beta_{(m,n)}^{(p,-)} \end{bmatrix} = \begin{bmatrix} a_{(m,n)}^{(p,+)} \\ \alpha_{(m,n)}^{(p,+)} \\ b_{(m,n)}^{(p,+)} \\ \beta_{(m,n)}^{(p,+)} \end{bmatrix} - S_{(n,p)}^{-1} \begin{bmatrix} \xi_{(m,n)}^{(p,1)} \\ \xi_{(m,n)}^{(p,2)} \\ \xi_{(m,n)}^{(p,3)} \\ \xi_{(m,n)}^{(p,4)} \end{bmatrix} \quad (3.12)$$

To complete the determination of the relationship between expansion coefficients in one layer to those in the next one we use equation (2.32) and equation (2.33) to write

$$\begin{bmatrix} a_{(m,n)}^{(p,-)} \\ \alpha_{(m,n)}^{(p,-)} \\ b_{(m,n)}^{(p,-)} \\ \beta_{(m,n)}^{(p,-)} \end{bmatrix} = Q_n^{(p)} \begin{bmatrix} a_{(m,n)}^{(p+1,-)} \\ \alpha_{(m,n)}^{(p+1,-)} \\ b_{(m,n)}^{(p+1,-)} \\ \beta_{(m,n)}^{(p+1,-)} \end{bmatrix} - S_{(n,p)}^{-1} \begin{bmatrix} \xi_{(m,n)}^{(p,1)} \\ \xi_{(m,n)}^{(p,2)} \\ \xi_{(m,n)}^{(p,3)} \\ \xi_{(m,n)}^{(p,4)} \end{bmatrix} \quad (3.13)$$

Now as there are no sources in the core region we have for the simplest structure with a source in a single shell the relationship

$$\begin{bmatrix} a_{(m,n)}^{(1,+)} \\ 0 \\ b_{(m,n)}^{(1,+)} \\ 0 \end{bmatrix} = Q_n^{(1)} Q_n^{(2)} \begin{bmatrix} a_{(m,n)}^{(3,-)} \\ \alpha_{(m,n)}^{(3,-)} \\ b_{(m,n)}^{(3,-)} \\ \beta_{(m,n)}^{(3,-)} \end{bmatrix} - Q_n^{(1)} S_{(n,2)}^{-1} \begin{bmatrix} \xi_{(m,n)}^{(2,1)} \\ \xi_{(m,n)}^{(2,2)} \\ \xi_{(m,n)}^{(2,3)} \\ \xi_{(m,n)}^{(2,4)} \end{bmatrix} \quad (3.14)$$

where the known field representation coefficients  $\xi_{(m,n)}^{(p,1)}$ ,  $\xi_{(m,n)}^{(p,2)}$  and  $\xi_{(m,n)}^{(p,4)}$  and  $\xi_{(m,n)}^{(p,3)}$  are given by equations (3.10), (3.9), and (3.11) respectively. The general relationship is given by

$$\begin{bmatrix} a_{(m,n)}^{(1,+)} \\ 0 \\ b_{(m,n)}^{(1,+)} \\ 0 \end{bmatrix} = Q_n^{(1)} Q_n^{(2)} \dots Q_n^{(N)} \begin{bmatrix} a_{(m,n)}^{(N+1,-)} \\ \alpha_{(m,n)}^{(N+1,-)} \\ b_{(m,n)}^{(N+1,-)} \\ \beta_{(m,n)}^{(N+1,-)} \end{bmatrix} - \sum_{p=1}^{N-1} Q_n^{(1)} Q_n^{(2)} \dots Q_n^{(p)} S_{(n,p+1)}^{-1} \begin{bmatrix} \xi_{(m,n)}^{(p,1)} \\ \xi_{(m,n)}^{(p,2)} \\ \xi_{(m,n)}^{(p,3)} \\ \xi_{(m,n)}^{(p,4)} \end{bmatrix} \quad (3.15)$$

As before, if the expansion coefficients  $a_{(m,n)}^{(N+1,-)}$  and  $b_{(m,n)}^{(N+1,-)}$  of the external source are known, then we have a system of 4 equations in 4 unknowns connecting the expansion coefficients in the source free core and the expansion coefficients  $\alpha_{(m,n)}^{(N+1,-)}$  and  $\beta_{(m,n)}^{(N+1,-)}$  of the radiation scattered by the N layer bianisotropic structure.

## 4 Energy Balance

In this section we consider the unusual energy balance relationships associated with the interaction of radiation with a bianisotropic material ([13]). The energy balance analysis for an isotropic sphere is carried out in great detail in (Bell [11]). An interchange of dot product and cross product in the triple scalar product implies that the total absorbed power  $P_a$  is given by

$$\begin{aligned} P_a &= (1/2) Re \int \int_{C(R_N)} (\vec{E}_{N+1} \times \vec{H}_{N+1})^* \cdot \vec{n} dA \\ &= (1/2) Re \int \int_{C(R_N)} [(\vec{E}_N \times \vec{H}_{N+1}^*) \cdot \vec{n}] dA \end{aligned} \quad (4.1)$$

where we have used the fact that on the spherical boundary  $r = R_N$  we have

$$\vec{n} \times \vec{E}_{N+1} = \vec{n} \times \vec{E}_N \quad (4.2)$$

because tangential components of  $\vec{E}$  are assumed to be continuous across boundaries separating regions of continuity of tensorial electromagnetic properties. We next make use of

the fact that for an impedance boundary condition on the surface of the scattering body that

$$(\vec{H}_{N+1}^* - \vec{H}_N^*) \times \vec{n} = \sigma_s (\vec{E}_N^* - (\vec{E}_N^* \cdot \vec{n})\vec{n}) \quad (4.3)$$

where  $\sigma_s$  is the impedance sheet conductivity. From equations (4.3) and (4.1) we see that

$$P_a = (1/2)Re \int \int_{C(R_N)} (\vec{E}_N \times \vec{H}_N)^* \cdot \vec{n} dA + \\ (1/2)Re \int \int_{C(R_N)} [\vec{E}_N \cdot (\sigma_s (\vec{E}_N^* - (\vec{E}_N^* \cdot \vec{n})\vec{n}))] dA \quad (4.4)$$

Using this and the fact that

$$div(\vec{E} \times \vec{H}^*) = \vec{H}^* \cdot curl(\vec{E}) - \vec{E} \cdot curl(\vec{H}^*) \quad (4.5)$$

we derive a formula for the internal energy density. For a sweeping beam or a stationary beam interacting with a bianisotropic body or a stationary beam interacting with a moving body (Hebenstreit [29]) there may be unusual couplings of the electromagnetic energy with the structure. For a general one layer structure covered by an impedance sheet the internal energy density is given in terms of the bilinear form

$$b(\vec{E}, \vec{H}) = \\ \int_{V_2} \{ (\vec{E}_2^* \cdot (i\omega\vec{\epsilon} + \vec{\sigma})\vec{E}_2) + (\vec{E}_2 \cdot (-i\omega\vec{\epsilon}^* + \vec{\sigma}^*)\vec{E}_2^*) \} dv + \\ \int_{V_2} \{ (\vec{E}_2^* \cdot (\vec{\alpha})\vec{H}_2) + (\vec{E}_2 \cdot (\vec{\alpha}^*)\vec{H}_2^*) \} dv + \\ - \int_{V_2} \{ (\vec{H}_2 \cdot (i\omega\vec{\mu}^*)\vec{H}_2^*) + (\vec{H}_2^* \cdot (-i\omega\vec{\mu})\vec{H}_2) \} dv + \\ \int_{V_2} \{ (\vec{H}_2 \cdot \vec{\beta}^*\vec{E}_2^*) + (\vec{H}_2^* \cdot \vec{\beta}\vec{E}_2) \} dv + \\ \int_{S_2} (\sigma_s^* + \sigma_s) \{ (\vec{E}_2 \cdot \vec{E}_2^*) - (\vec{E}_2 \cdot \vec{n})(\vec{E}_2^* \cdot \vec{n}) \} da \quad (4.6)$$

where  $S_2$  is the bounding surface and  $V_2$  is the interior volume. This can be used as a source term for the heat equation and can be used to predict the response of the structure to a sweeping beam or the response of a moving structure to a stationary beam (Ferencz [25], Gamo [26], Hebenstreit [29], and Shiozawa, [44]). Energy balance computations were carried out in (Bell, Cohoon, and Penn [10], [11]) for isotropic structures and in (Cohoon

[15]) for anisotropic structures. These energy balance computations involve comparing the total energy entering the structure minus the total energy reflected from the structure to the sum of the integrals of the power density distributions in the impedance sheets and in the layers themselves.

## 4.1 Computer Output

Electromagnetic Energy Deposition in a Concentric Layered Sphere.

Frequency = 1.000E+03 MHz.

Field Strength = 1.00 V/M    Number of Regions = 1

### Layer 1

-----

Relative Permittivity (Radial): ( 4.00E+01, 0.00E+00)

Relative Permittivity (Angular): ( 3.00E+01, 0.00E+00)

Relative Permeability (Radial): ( 1.00E+00, 0.00E+00)

Relative Permeability (Angular): ( 1.00E+00, 0.00E+00)

Conductivity (Mho/M) (Radial): ( 5.00E-03, 0.00E+00)

Conductivity (Mho/M) (Angular): ( 5.00E-03, 0.00E+00)

Impedance Sheet Cond. (Mho/M): ( 0.00E+00, 0.00E+00)

Surface Boundaries (cm) = 3.0000E+00

Average Absorbed Power Density

obtained by integration of the Poynting vector

over the surface and dividing by the volume  
of the sphere is = 1.22227D-03 W/M\*\*3

Total Absorbed Power

by integrating the Poynting vector over the surface  
is = 1.38235819D-07 Watts.

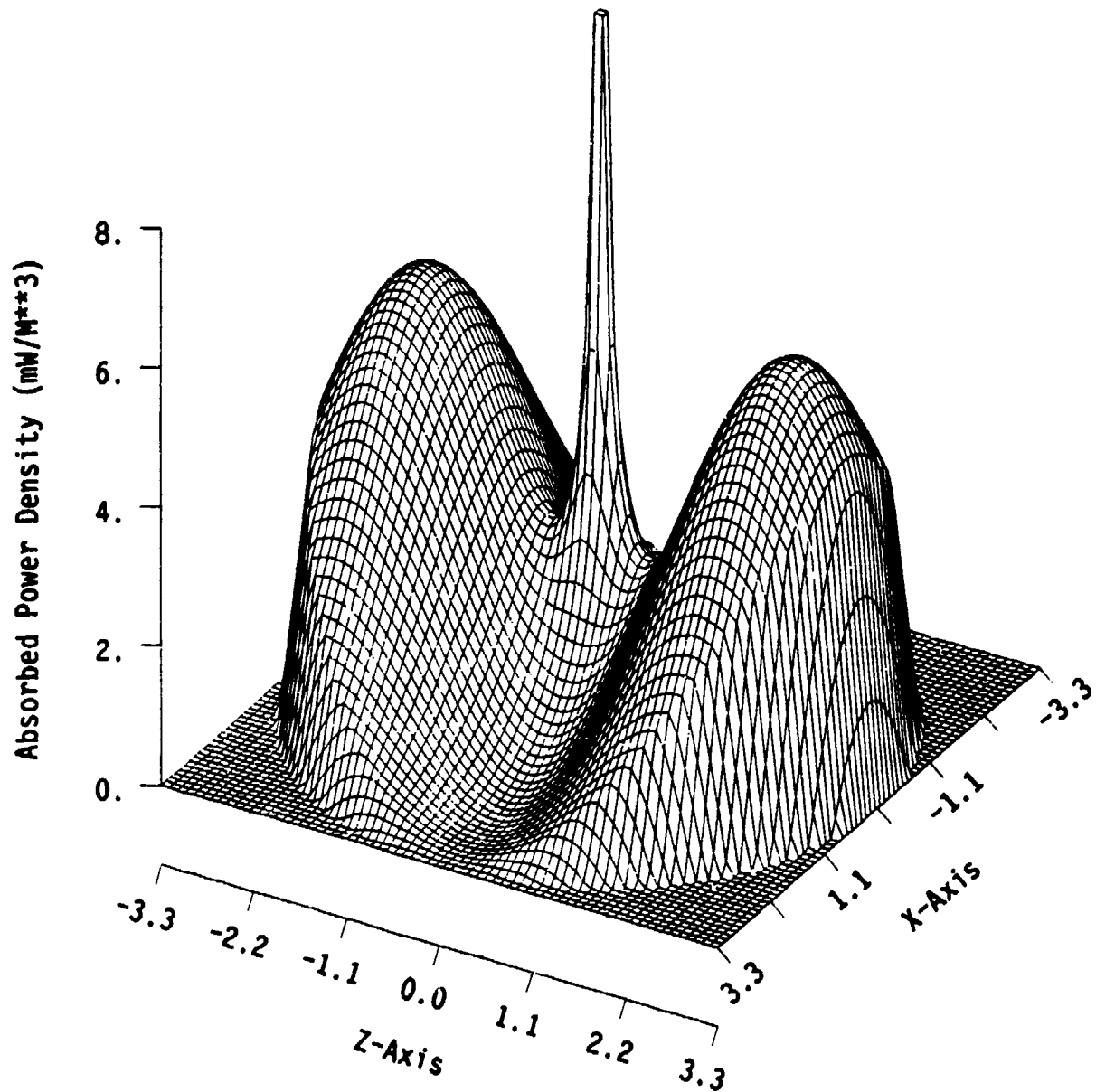
Total Absorbed Power by Volume Integration Method = 1.38235800D-07 Watts.

The fact that the last two numbers nearly coincide represents a confirmation of the correctness of the coding implementing the solution for an anisotropic sphere. The determination of the total absorbed power by the Poynting vector method is described in (Jones [33]) and in full detail in (Bell, [11]). For the plane wave problem described in Jones ([33]) we can give exact formulas for the total absorbed power in terms of the total power entering the sphere minus the total power scattered away from the sphere ([33], page 504, equation 126). We let  $\alpha_{(n,N+1)}$  and  $\beta_{(n,N+1)}$  denote the expansion coefficients of the scattered radiation and by carrying out an energy balance book keeping on the boundary we observe that the total absorbed power is

$$P_a = \frac{\pi |E_0|^2}{k_0^2} \sqrt{\frac{\epsilon_0}{\mu_0}} \left[ \operatorname{Re} \sum_{n=1}^{\infty} (2n+1) (\alpha_{(n,N+1)} + \beta_{(n,N+1)}) \right] \\ - \frac{\pi |E_0|^2}{k_0^2} \sqrt{\frac{\epsilon_0}{\mu_0}} \left[ \sum_{n=1}^{\infty} (2n+1) (|\alpha_{(n,N+1)}|^2 + |\beta_{(n,N+1)}|^2) \right] \quad (4.7)$$

This is referred to as the Poynting vector method in the computer output; the last number is the result of numerically integrating the power density distribution over the interior of the sphere. The difficulty of this numerical integration is evident from the following plot of the internal power density distribution for an anisotropic structure with a radial permittivity that is higher than the tangential permittivity.

# Absorbed Power Density in an Anisotropic Sphere





## 4.2 Thermal Response to Radiation

The absorption of radiation results in a temperature increase. An energy equation describing this change of state is given by

$$\rho \frac{De}{Dt} = \left( \frac{\partial}{\partial t} \right) Q_{in} + \left( \frac{\partial}{\partial t} \right) Q_{out} + (-p \text{div}(\vec{v})) + \text{div}(\bar{\bar{K}} \text{grad}(T)) + \Phi, \quad (4.8)$$

where  $e$  is equal to  $c_v T$  with  $T$  denoting the temperature, and  $c_v$  denoting the specific heat at constant volume,  $\Phi$  is the viscous dissipation function (Anderson, Tannehill and Pletcher [1], pages 188-189),  $\vec{v}$  is the fluid velocity,  $\rho$  is the density,  $p$  is the pressure,  $\bar{\bar{K}}$  is the tensor thermal conductivity, the term representing the transfer by radiation from one part of the fluid to another is given by (Siegel and Howell [43], page 689)

$$\left( \frac{\partial}{\partial t} \right) Q_{out} = \text{div} \left( \frac{16\sigma_e T^3}{3a_R} \cdot \text{grad}(T) \right), \quad (4.9)$$

where the internal radiative conductivity is given by

$$k_r = \frac{16\sigma_e T^3}{3a_R}, \quad (4.10)$$

where  $a_R$  is the Rosseland mean absorption coefficient (Siegel [43], p 504 and Rosseland [41]) and where  $\sigma_e$  (Siegel [43], page 25) is the hemispherical total emissive power of a black surface into vacuum having a value of

$$\sigma_e = 5.6696 \times 10^{-8} \text{ Watts / (meters}^2 \text{ } ^\circ K), \quad (4.11)$$

and where if  $\mathcal{B}(\vec{E}, \vec{H})$  represents the absorbed electromagnetic energy per unit volume, whose integral is, (after conversion from cgs units) equal to the  $b(\vec{E}, \vec{H})$  given by equation (4.6) then

$$\left( \frac{\partial}{\partial t} \right) Q_{in} = \mathcal{B}(\vec{E}, \vec{H}). \quad (4.12)$$

In general solving equation (4.8) requires the simultaneous solution of the Maxwell, continuity, and momentum equations (see Jones [33], p 775). However, for low levels of radiation the energy equation (4.8) reduces to a simple heat equation with a source term which can be solved by dovetailing ([12], [14]) it to the solution of the Maxwell equations. The experimental verification of the latter procedure is described in ([12]) and in ([14]).

## 5 References

### References

- [1] Anderson, Dale A., John C. Tannehill, and Richard H. Pletcher *Computational Fluid Mechanics and Heat Transfer* New York: McGraw Hill (1984)
- [2] Abramowitz, Milton, and Irene Stegun. *Handbook of Mathematical Functions with Formulas, Graphs and Mathematical Tables. NBS Applied Math Series 55* Washington, D.C.: U.S. Government Printing Office (1972)
- [3] Altman, C., A. Schatzberg, and K. Suchy. "Symmetries and scattering relations in plane stratified anisotropic, gyrotropic, and bianisotropic media" *Applied Physics B (Germany)* Vol B26, No. 2 (1981) pp 147-153
- [4] Altman, C. and A. Schatzberg. "Reciprocity and equivalence in reciprocal and nonreciprocal media through reflection transformations of the current distributions" *Applied Physics B (Germany)* Volume B28, No 4 (August, 1982) pp 327-333
- [5] Altman, C., Schatzberg, K. Suchy. "Symmetry transformations and time reversal of currents and fields in bounded bianisotropic media" *IEEE Transactions on Antennas and Propagation. Vol. AP 32, No. 11* (November, 1984) pp 1204-1210
- [6] Altman, C., A. Schatzberg, and K. Suchy. "Symmetries and scattering relations in plane stratified anisotropic, gyrotropic, and bianisotropic media" *Applied Physics B. (Germany)* Volume B26, No. 2 (1981) pp 147-153
- [7] Avdeev, V. B., A. V. Demin, Yu A. Kravtsov, M. V. Tinin, A. P. Yarygin. "The interferential integral method" *Radiophys. Quantum Electronics. Vol 31, No. 11* (1988) pp 907-921
- [8] Barton, J. P., D. R. Alexander, and S. A. Schaub. "Internal fields of a spherical particle illuminated by a tightly focused laser beam: focal point positioning effects at resonance." *Journal of Applied Physics. Volume 65 No. 8* (April 15, 1989) pp 2900-2906

- [9] Barton, J. P., D. R. Alexander, and S. A. Schaub. "Internal and near surface electromagnetic fields for a spherical particle irradiated by a focused laser beam" *Journal of Applied Physics*. Volume 64, no 4 (1988) pp 1632-1639.
- [10] Bell, Earl L., David K. Cohoon, and John W. Penn. *Mie: A FORTRAN program for computing power deposition in spherical dielectrics through application of Mie theory*. SAM-TR-77-11 Brooks AFB, Tx 78235: USAF School of Aerospace Medicine (RZ) Aerospace Medical Division (AFSC) (August, 1977)
- [11] Bell, Earl L., David K. Cohoon, and John W. Penn. *Electromagnetic Energy Deposition in a Concentric Spherical Model of the Human or Animal Head* SAM-TR-79-6 Brooks AFB, Tx 78235: USAF School of Aerospace Medicine (RZ) Aerospace Medical Division (AFSC) (December, 1982).
- [12] Burr, John G., David K. Cohoon, Earl L. Bell, and John W. Penn. Thermal response model of a Simulated Cranial Structure Exposed to Radiofrequency Radiation. *IEEE Transactions on Biomedical Engineering*. Volume BME-27, No. 8 (August, 1980) pp 452-460.
- [13] Cohoon, D. K. "Uniqueness of electromagnetic interaction problems associated with bianisotropic bodies covered by impedance sheets" (to appear in *Heritage of Gauss*)
- [14] Cohoon, D. K., J. W. Penn, E. L. Bell, D. R. Lyons, and A. G. Cryer. *A Computer Model Predicting the Thermal Response to Microwave Radiation* SAM-TR-82-22 Brooks AFB, Tx 78235: USAF School of Aerospace Medicine. (RZ) Aerospace Medical Division (AFSC) (December, 1982).
- [15] Cohoon, D. K. "An exact solution of Mie Type for Scattering by a Multilayer Anisotropic Sphere" *Journal of Electromagnetic Waves and Applications*, Volume 3, No. 5 (1989) pp 421-448
- [16] Cohoon, D. K. and R. M. Purcell. An exact formula for the interaction of radiation with an N layer anisotropic sphere and its computer implementation. *Notices of the American Mathematical Society* (January, 1989).

- [17] Chen, H. C. "Electromagnetic wave propagation in bianisotropic media—a coordinate free approach." *Proceedings of the 1985 International Symposium on Antennas and Propagation, Japan— A Step to New Radio Frontiers. Kyoto, Japan 1985* Volume 1 Tokyo: Institute of Electronic Commun. Eng. (1985) pp 253-256.
- [18] Chevaillier, Jean Phillippe, Jean Fabre, and Patrice Hamelin. "Forward scattered light intensities by a sphere located anywhere in a Gaussian beam" *Applied Optics, Vol. 25, No. 7* (April 1, 1986) pp 1222-1225.
- [19] Chevaillier, Jean Phillippe, Jean Fabre, Gerard Grehan, and Gerard Gousbet. "Comparison of diffraction theory and generalized Lorenz-Mie theory for a sphere located on the axis of a laser beam." *Applied Optics, Vol 29, No. 9* (March 20, 1990) pp 1293-1298.
- [20] Chylek, Petr, J. D. Pendleton, and R. G. Pinnick. "Internal and near surface scattered field of a spherical particle at resonant conditions" *Applied Optics, Volume 24, No. 23* (December 1, 1985) pp 3940-3943
- [21] Chylek, Petr, Maurice A. Jarzembski, Vandana Srivastava, and Ronald G. Pinnick. "Pressure dependence of the laser induced breakdown thresholds of gases and droplets" *Applied Optics, Volume 29, No. 15* (May 20, 1990) pp 2303-2306
- [22] Chylek, Petr, Maurice A. Jarzembski, Vandana Srivastava, R. G. Pinnick, J. David Pendleton, and John P. Cruncleton. "Effect of spherical particles on laser induced breakdown of gases" *Applied Optics. Volume 26, No. 5* (March 1, 1987) pp 760-762
- [23] Clebsch, R. F. A. "Über die Reflexion an einer Kugelfläche" *Crelle's Journal, Volume 61* (1863) p 195.
- [24] Daniele, V. "Electromagnetic properties of Rotating Bodies" *Alta Freq. Vol 52, No. 3* (May-June, 1983) pp 146-148.
- [25] Ferencz, C. "Geometric questions of electromagnetic wave propagation in moving media" *Acta Tech. Acad. Sci. Hungary. Volume 100, no 3-4* (1987) pp 195-205

- [26] Gamo, H. "A generalized reciprocity theorem for electromagnetic optics in the moving media" Ensenada, Mexico: Conference on optics in four dimensions *AIP Conference Proceedings (USA) No. 65* (1980) pp 106-122
- [27] Garcia, C. B. and W. I. Zangwill. Pathways to Solutions, Fixed Points, and Equilibria. Englewood Cliffs, NJ: Prentice Hall(1981)
- [28] Holoubek, J. "A simple representation of small angle light scattering from an anisotropic sphere," *Journal of Polymer Science, Part A-2, Volume 10* (1972) pp 1094-1099.
- [29] Hebenstreit, H. "Constitutive relations for moving plasmas" *Z. Naturforsch. A. Volume 34A, No. 2* (1979) pp 147-154
- [30] Hochstadt, Harry. *The Functions of Mathematical Physics*. New York: Dover(1986).
- [31] Hormander, Lars. *Linear Partial Differential Operators* New York: Academic Press (1963)
- [32] Hovhannessian, S. S., and V. A. Baregamian. "The diffraction of a plane electromagnetic wave on an anisotropic sphere," *Isdateleva Akad. Nauk of Armenia. S. S. R. Physics Volume 16* (1981) pp 37-43
- [33] Jones, D. S. *Theory of Electromagnetism* Oxford: Pergamon Press(1964)
- [34] Mie, G. "Beiträge zur Optik trüber Medien speziell kolloidaler Metallösungen," *Ann. Phys. 25* (1908) p 377.
- [35] Mrozowski, M. and J. Mazur. "Coupled mode analysis of waveguiding structures containing bianisotropic media". *IEEE Trans. Magn. (USA) Vol. 24, No. 2, pt. 2* (1988) pp 1975-1977
- [36] Mrozowski, M. "General solutions to Maxwell's equations in a bianisotropic medium: a computer oriented spectral domain approach" *Arch. Elektron. and Uebertragungstech (Germany) Vol. 40, No. 3* (May-June, 1986) pp 195-197.

- [37] Pinnick, R. G. and J. D. Pendleton. *Applied Optics*. Vol 29 (1990) page 918
- [38] Mugnai, Alberto and Warren J. Wiscombe. "Scattering from Nonspherical Chebyshev Particles. I: Cross Sections, Single Scattering Albedo, Asymmetry Factor, and Backscattered Radiation" *Applied Optics*, Volume 25, No. 7 pp 1235-1244.
- [39] Pinnick, R. G., P. Chylek, M. Jarzembski, E. Creegan, and V. Srivastava, G. Fernandez, J. D. Pendleton, and A. Biswas. "Aerosol induced laser breakdown thresholds wavelength dependence" *Applied Optics*. Vol 27, No. 5 (March 1, 1988) pp 987-996
- [40] Richardson, C. B., R. L. Hightower, and A. L. Pigg. "Optical measurement of the evaporation of sulfuric acid droplets" *Applied Optics*. Volume 25, No. 7 (April 1986) pp 1226-1229
- [41] Rosseland, S. *Theoretical Astrophysics: Atomic Theory and the Analysis of Stellar Atmospheres and Envelopes*. Oxford, England: Clarendon Press (1936).
- [42] Schaub, Scott A., Dennis R. Alexander, John P. Barton, and Mark A. Emanuel. "Focused Laser Beam Interactions with Methanol Droplets: Effects of Relative Beam Diameter" *Applied Optics*. Volume 28, No. 9 (May 1, 1989) pp 1666-1669
- [43] Siegel, Robert, and John R. Howell. *Thermal Radiation Heat Transfer* New York: Hemisphere Publishing Company (1981)
- [44] Shiozawa, T. "Electrodynamics of rotating relativistic electron beams" *Proceedings of the IEEE*. Volume 66, No. 6 (June, 1978) pp 638-650
- [45] Suchy, K., C. Altman, A. Schatzberg. "Orthogonal mappings of time-harmonic electromagnetic fields in inhomogeneous bianisotropic media" *Radio Science(USA)* Vol. 20, No. 2 (March-April, 1985) pp 149-160.
- [46] Tsai, Wen-Chung, and Ronald J. Pogorzelski. "Eigenfunction solution of the scattering of beam radiation fields by spherical objects." *Journal of the Optical Society of America*. Volume 63, No. 12 (December, 1975) pp 1457-1463

- [47] Waggoner, Alan P. and Lawrence F. Radke. "Enhanced cloud clearing by pulsed  $CO_2$  lasers." *Applied Optics*. Volume 28, No. 15 (August 1, 1989) pp 3039-3043
- [48] Wang, R. T. and J. M. Greenberg. "Scattering by spheres with nonisotropic refractive indices" *Applied Optics*, Volume 15 (1976) p 1212
- [49] Weiglhofer, W. "Isotropic chiral media and scalar Hertz potentials" *Journal of Physics A. Math. Gen.* Vol. 21, no. 9 (May 7, 1988) pp 2249-2251
- [50] Weiglhofer, W. "Scalarization of Maxwell's equations in general homogeneous bianisotropic media" *IEE Proc. H (GB)* Vol. 134, No. 4 (1987) pp 357-360
- [51] Whittaker, E. T. and G. N. Watson. *A Course of Modern Analysis* London: Cambridge University Press (1986).
- [52] Wolff, I. "A description of the spherical three layer resonator with an anisotropic dielectric material. *IEEE MTT-S Digest* (1987) pp 307-310
- [53] Wu, Tai Tsun, Ronald W. P. King, and Hao-Ming Shin. "Circular cylindrical lens as a line source electromagnetic missile launcher" *IEEE Transactions on Antennas and Propagation* Volume 37. Number 1 (January, 1989) pages 39-44
- [54] Wu, Tai Tsur, Ronald W. P. King, and Hao-Ming Shin. "Spherical lens as a launcher of electromagnetic missiles" *Journal of Applied Physics*. Volume 62, Number 10 (November 15, 1987) pp 4036-4040
- [55] Yeh, C. "Scattering of Obliquely Incident Microwaves by a Moving Plasma Column" *Journal of Applied Physics*, Volume 40, Number 13 (December, 1966) pp 5066-5075.
- [56] Yeh, C. S. Colak, and P. Barber. "Scattering of sharply focused beams by arbitrarily shaped dielectric particles" *Applied Optics*. Vol. 21, No. 24 (December 15, 1982) pp 4426-4433.

## 6 Acknowledgements

The author wishes to thank Dr. J. W. Frazer for reading the manuscript and correcting errors.

BLANK



# The Response of a Cylinder with a Thin High Index of Refraction Bianisotropic Coating to Electromagnetic Radiation

D. K. Cohoon

Department of Mathematics  
West Chester University  
West Chester, PA 19383

July 5, 1990

Some new methods of developing the response of a thinly coated metallic cylinder to electromagnetic radiation have been developed. In contrast to theories developed by (Cohen [16], Wait [42], and Yeh [47]) the representation of the fields in the thin coating uses no Bessel or Hankel functions. This method eliminated a severe round off error that was incurred when using the traditional solutions (Bussey [11]).

# 1 VECTOR FIELDS IN CYLINDERS

The vector fields in the interior of a penetrable layer and outside the cylinder are represented in terms of the vector fields

$$\vec{A}_{(m,h)} = \exp(im\theta)\exp(-ihz)\vec{e}_r, \quad (1.1)$$

$$\vec{B}_{(m,h)} = \exp(im\theta)\exp(-ihz)\vec{e}_\theta, \quad (1.2)$$

and

$$\vec{C}_{(m,h)} = \exp(im\theta)\exp(-ihz)\vec{e}_z. \quad (1.3)$$

where in terms of the unit vectors  $\vec{e}_x$ ,  $\vec{e}_y$ , and  $\vec{e}_z$  of the cartesian coordinate system we have

$$\vec{e}_r = \cos(\theta)\vec{e}_x + \sin(\theta)\vec{e}_y, \quad (1.4)$$

and

$$\vec{e}_\theta = \left(\frac{\partial}{\partial\theta}\right)\vec{e}_r = -\sin(\theta)\vec{e}_x + \cos(\theta)\vec{e}_y, \quad (1.5)$$

and

$$\vec{e}_z = \vec{e}_z. \quad (1.6)$$

Thus, in terms of the unit vectors of cylindrical coordinates after multiplying both sides of equation (1.4) by  $\cos(\theta)$  and multiplying both sides of equation (1.5) by  $-\sin(\theta)$  and adding we obtain

$$\vec{e}_x = \cos(\theta)\vec{e}_r - \sin(\theta)\vec{e}_\theta \quad (1.7)$$

and similarly

$$\vec{e}_y = \sin(\theta)\vec{e}_r + \cos(\theta)\vec{e}_\theta \quad (1.8)$$

Hence, if an arbitrary vector is represented in Cartesian coordinates as

$$\vec{V} = V_x \vec{e}_x + \vec{V}_y + \vec{V}_z \quad (1.9)$$

then

$$\begin{aligned} \vec{V} &= (\cos(\theta)V_x + \sin(\theta)\vec{V}_y)\vec{e}_r + \\ &(-\sin(\theta)V_x + \cos(\theta)\vec{V}_y)\vec{e}_\theta + \vec{V}_z \end{aligned} \quad (1.10)$$

and more importantly if a vector  $\vec{V}$  has radial, theta and z components given by  $V_r$ ,  $V_\theta$  and  $V_z$  respectively, then

$$\begin{aligned} \text{vec } V &= (V_r \cos(\theta) - V_\theta \sin(\theta))\vec{e}_x + \\ &(V_r \sin(\theta) + V_\theta \cos(\theta))\vec{e}_y + V_z \vec{e}_z \end{aligned} \quad (1.11)$$

If the electric field is represented in terms of cylindrical coordinates, then

$$\begin{aligned} \text{curl}(V_r \vec{e}_r + V_\theta \vec{e}_\theta + V_z \vec{e}_z) &= \\ \left( \frac{1}{r} \frac{\partial V_z}{\partial \theta} - \frac{\partial V_\theta}{\partial z} \right) \vec{e}_r + \left( \frac{\partial V_r}{\partial z} - \frac{\partial V_z}{\partial r} \right) \vec{e}_\theta \\ \frac{1}{r} \left( \left( \frac{\partial}{\partial r} \right) (r V_\theta) - \frac{\partial V_r}{\partial \theta} \right) \vec{e}_z \end{aligned} \quad (1.12)$$

We will represent the internal and external fields as a linear combination, with coefficients in a ring of functions of the radial variable, of the vector fields defined by equations (1.1), (1.2), and (1.3). The identities

$$\begin{aligned} \text{curl}(F(r)\vec{C}_{(m,n)}) &= \\ im \frac{F(r)}{r} \vec{A}_{(m,h)} + ih F(r) \vec{B}_{(m,h)} \end{aligned} \quad (1.13)$$

$$\begin{aligned} \text{curl}(F(r)\vec{A}_{(m,n)}) = \\ -ihF(r)\vec{A}_{(m,h)} + \left(\frac{-F(r)}{r}\right)im\vec{C}_{(m,h)} \end{aligned} \quad (1.14)$$

$$\begin{aligned} \text{curl}(F(r)\vec{B}_{(m,n)}) = \\ ihF(r)\vec{A}_{(m,h)} + \left(\frac{1}{r}\left(\frac{\partial}{\partial r}\right)(rF(r))\right)\vec{C}_{(m,h)} \end{aligned} \quad (1.15)$$

## 2 COORDINATE FRAMES

Following Ariel Cohen ([16]) we describe coordinate frames which are used to represent incoming, internal, and scattered fields in laboratory, absorber, and detector coordinate frames. We let  $\vec{e}_z$  denote the unit vector along the  $z$ -axis of the laboratory frame. We suppose that  $\text{vece}_{x_a}$  is the unit vector along the axis of a cylinder which passes through the origin of the original coordinate system. We suppose that

$$\vec{e}_{x_a} = \sin(\theta_a)\cos(\phi_a)\vec{e}_x + \sin(\theta_a)\sin(\phi_a)\vec{e}_y + \cos(\theta_a)\vec{e}_z \quad (2.1)$$

We define the  $x_a$  axis by the cross product,

$$\vec{e}_{x_a} = (\vec{e}_{z_a} \times \vec{e}_z)/\sin(\theta_0) \quad (2.2)$$

so that

$$\vec{e}_{x_n} = \sin(\phi_a)\vec{e}_x - \cos(\phi_a)\vec{e}_y \quad (2.3)$$

$$\vec{e}_{y_a} = \cos(\theta_a)\cos(\phi_a)\vec{e}_x + \cos(\theta_a)\sin(\phi_a)\vec{e}_y - \sin(\theta_a)\vec{e}_z \quad (2.4)$$

We see that we can describe the electric vector of the incoming radiation by the rule,

$$\vec{E}^i = E_0 \exp(-ik_0 x + i\omega t) \vec{e}_x \quad (2.5)$$

### 3 MAXWELL EQUATIONS

We assume that the coating material is bianisotropic, a material more general than a chiral material. The Maxwell equations are, for time harmonic radiation, given by

$$\text{curl}(\vec{E}) = -i\omega \vec{\mu} \vec{H} - \vec{\alpha} \vec{E} \quad (3.1)$$

and

$$\text{curl}(\vec{H}) = (i\omega \vec{\epsilon} + \vec{\sigma}) \vec{E} + \vec{\beta} \vec{H} \quad (3.2)$$

The radiation source term which gives the power density is given by

$$\begin{aligned} \left( \frac{\partial}{\partial t} \right) Q_{in} = \\ (1/2) \text{Re} \left\{ \vec{E}^* \cdot (i\omega \vec{\epsilon} + \vec{\sigma}) \vec{E} + \vec{E} \cdot \vec{\alpha} \vec{H}^* - \right. \\ \left. \vec{H} \cdot (i\omega \vec{\mu} \vec{H}^*) + \vec{H} \cdot (\vec{\beta} \vec{E}^*) + \right. \\ \left. \chi_{\partial\Omega}(r) \sigma_s |\vec{E}_{\text{tangential}}|^2 \right\} \end{aligned} \quad (3.3)$$

where if  $\partial\Omega$  is the surface containing the impedance sheet, then

$$\int_{\Omega} \chi_{\partial\Omega} \sigma_s |\vec{E}_{\text{tangential}}|^2 dv = \int_{\partial\Omega} \sigma_s |\vec{E}_{\text{tangential}}|^2 dA \quad (3.4)$$

is the characteristic function of the surface supporting the impedance sheet.

We consider non plane wave sources such as tightly focused laser beams

interacting with these structures ([12], [36], [25], [6], [5]) and use the energy densities as a source term in the energy equation to determine the future state of the cylinder.

## 4 Cross Products

The numerical problem associated with scattering of radiation by thinly coated perfect conductors reduces to the problem of evaluating the cross products of Bessel and Neuman functions (Abramowitz and Stegun [1], page 361 formula 9.1.32),

$$p_\nu = J_\nu(a)Y_\nu(b) - J_\nu(b)Y_\nu(a), \quad (4.1)$$

$$q_\nu = J_\nu(a)Y'_\nu(b) - J'_\nu(b)Y_\nu(a), \quad (4.2)$$

$$r_\nu = J'_\nu(a)Y_\nu(b) - J_\nu(b)Y'_\nu(a), \quad (4.3)$$

and

$$s_\nu = J'_\nu(a)Y'_\nu(b) - J'_\nu(b)Y'_\nu(a), \quad (4.4)$$

Observe that the recursion relation is

$$J_{\nu+1}(z)Y_\nu(z) - J_\nu(z)Y_{\nu+1}(z) = \frac{2}{\pi z} \quad (4.5)$$

If  $\mathcal{G}_\nu(z)$  is one of  $J_\nu(z)$  or  $Y_\nu(z)$  then we see that

$$\mathcal{G}_{\nu+1}(z) = -\mathcal{G}'_\nu(z) + \frac{\nu}{z}\mathcal{G}_\nu(z) \quad (4.6)$$

We see that equations (4.5) and (4.6) imply that

$$-J'_\nu(z)Y_\nu(z) - J_\nu(z)Y'_\nu(z) = \frac{2}{\pi z} \quad (4.7)$$

We expand the Neuman function and obtain

$$Y_\nu(b) = Y_\nu(a) + Y'_\nu(a)(b-a) + \sum_{j=2}^{\infty} \left\{ (F_{(j,\nu)}Y'_\nu(a) + G_{(j,\nu)}Y_\nu(a)) \left( \frac{(b-a)^j}{j!} \right) \right\} \quad (4.8)$$

The function  $\mathcal{G}_\nu(z)$  satisfies Bessel's differential equation,

$$z^2 \mathcal{G}_\nu''(z) + z \mathcal{G}_\nu'(z) + (z^2 - \nu^2) \mathcal{G}_\nu(z) = 0 \quad (4.9)$$

Dividing all terms by  $z^2$  we see that

$$\mathcal{G}_\nu''(z) = -\frac{1}{z} \mathcal{G}_\nu'(z) + \left( \frac{\nu^2}{z^2} - 1 \right) \mathcal{G}_\nu(z) \quad (4.10)$$

Differentiating all terms of equation (4.10) we see that

$$\begin{aligned} \mathcal{G}_\nu^{(3)}(z) &= \left\{ \frac{2 + \nu^2}{z^2} - 1 \right\} \mathcal{G}_\nu'(z) \\ &+ \left\{ -\frac{3\nu^2}{z^3} + \frac{1}{z} \right\} \mathcal{G}_\nu(z) \end{aligned} \quad (4.11)$$

Differentiating both sides of equation (4.11) and using equation (4.10) to remove the second derivative terms we find that

$$\mathcal{G}_\nu^{(4)}(z) = \left[ \left( \frac{-6\nu^2 - 6}{z^3} \right) + \frac{1}{z} \right] \mathcal{G}_\nu'(z)$$

$$\left[ \frac{11\nu^2 + \nu^4}{z^4} - \left( \frac{1 + 2\nu^2}{z^2} \right) + 1 \right] \mathcal{G}_\nu(z) \quad (4.12)$$

We see that there are two forms for the derivatives given by

$$\begin{aligned} \mathcal{G}_\nu^{(2n)}(z) &= \sum_{k=1}^n \left( \frac{a_k^{(2n)}}{z^{2k-1}} \right) \mathcal{G}'_\nu(z) + \\ &\quad \sum_{k=0}^n \left( \frac{b_k^{(2n)}}{z^{2k}} \right) \mathcal{G}_\nu(z) \end{aligned} \quad (4.13)$$

and by

$$\begin{aligned} \mathcal{G}_\nu^{(2n+1)}(z) &= \sum_{k=1}^n \left( \frac{c_k^{(2n+1)}}{z^{2k}} \right) \mathcal{G}'_\nu(z) + \\ &\quad \sum_{k=0}^n \left( \frac{d_k^{(2n+1)}}{z^{2k+1}} \right) \mathcal{G}_\nu(z) \end{aligned} \quad (4.14)$$

Substituting the expansions into the expression for  $q_\nu$  we see that

$$\begin{aligned} q_\nu &= J_\nu(a)Y'_\nu(b) - J_\nu(b)Y'_\nu(a) = \\ &\quad J_\nu(a) \left\{ Y'_\nu(a) + \right. \\ &\quad \left. \sum_{j=2}^{\infty} [F_{(j,\nu)} Y'_\nu(a) + G_{(j,\nu)} Y_\nu(a)] \left( \frac{(b-a)^{j-1}}{(j-1)!} \right) \right\} \\ &\quad - Y_\nu(a) \left\{ J'_\nu(a) + \right. \\ &\quad \left. \sum_{j=2}^{\infty} [F_{(j,\nu)} J'_\nu(a) + G_{(j,\nu)} J_\nu(a)] \left( \frac{(b-a)^{j-1}}{(j-1)!} \right) \right\} \end{aligned}$$

The Wronskian relation implies that

$$q_\nu = \frac{2}{2\pi} +$$



$$\sum_{j=2}^{\infty} F_{(j,\nu)} \left( \frac{2}{2\pi} \right) \left( \frac{(b-a)^{j-1}}{(j-1)!} \right) \quad (4.15)$$

In this expression there are no Bessel functions and no round off error.

## References

- [1] Abramowitz, Milton, and Irene Stegun (Editors). *Handbook of Mathematical Functions* New York: Dover (1972)
- [2] Armstrong, Robert L. and Andrew Zardecki. "Propagation of High Energy Laser Beams Through Metallic Aerosols" *Applied Optics. Volume 29, Number 12* (April 20, 1990) pp 1786-1792
- [3] Barton, J. P., D. R. Alexander, and S. A. Schaub. "Internal fields of a spherical particle illuminated by a tightly focused laser beam: focal point positioning effects at resonance." *Journal of Applied Physics. Volume 65 No. 8* (April 15, 1989) pp 2900-2906
- [4] Barton, J. P., D. R. Alexander, and S. A. Schaub. "Internal and near surface electromagnetic fields for a spherical particle irradiated by a focused laser beam" *Journal of Applied Physics. Volume 64, no 4* (1988) pp 1632-1639.
- [5] Barton, J. P., D. R. Alexander, and S. A. Schaub. "Internal fields of a spherical particle illuminated by a tightly focused laser beam: focal point positioning effects at resonance." *Journal of Applied Physics. Volume 65 No. 8* (April 15, 1989) pp 2900-2906

- [6] Barton, J. P., D. R. Alexander, and S. A. Schaub. "Internal and near surface electromagnetic fields for a spherical particle irradiated by a focused laser beam" *Journal of Applied Physics. Volume 64, no 4* (1988) pp 1632-1639.
- [7] Belts, V. A., O. A. Volkovitsky, A. F. Dobrovolksy, E. V. Ivanov, Y. V. Nasedkin, L. N. Pavlova. "Intensive  $CO_2$  laser pulse transmission through droplet and ice crystal fogs" *IN Kaye, A. S. and A. C. Walker. Gas flow and chemical lasers. 1984. Proceedings of the Fifth International Symposium Oxford, England: Gas Flow and Chemical Laser Symposium (August, 1984) pp 20-24*
- [8] Biswas, A., H. Latifi, R. L. Armstrong, and R. G. Pinnick. "Time resolved spectroscopy of laser emission from dye doped droplets" *Optics Letters. Volume 14, No. 4* (February 15, 1989) pp 214-216
- [9] Bloembergen, N. *Nonlinear Optics* New York: W. A. Benjamin (1965)
- [10] Borison, S. L. "Bistatic cross section of a randomly oriented dipole" *IEEE Transactions on Antennas and Propagation* (March, 1967) pp 320-321
- [11] Bussey, Howard E. and Jack H. Richmond. "Scattering by a lossy dielectric circular cylindrical multilayer, Numerical Values" *IEEE Transactions on Antennas and Propagation. Volume 23* (1975) pp 723-725

- [12] Caledonia, G. E. and J. D. Teare. "Laser beam hygroscopic aerosol interactions" *Transactions of the ASME Journal of Heat Transfer*. Vol 99 (May, 1977) pp 281-286.
- [13] Chow, S. N., J. Mallet-Paret, and J. A. Yorke. Finding zeros of maps: homotopy methods that are constructive with probability one. *Math. Comp. Volume 32* (1978) pp 887-889.
- [14] Chevaillier, Jean Phillippe, Jean Fabre, and Patrice Hamelin. "Forward scattered light intensities by a sphere located anywhere in a Gaussian beam" *Applied Optics*, Vol. 25, No. 7 (April 1, 1986) pp 1222-1225.
- [15] Chevaillier, Jean Phillippe, Jean Fabre, Gerard Grehan, and Gerard Gousbet. "Comparison of diffraction theory and generalized Lorenz-Mie theory for a sphere located on the axis of a laser beam." *Applied Optics*, Vol 29, No. 9 (March 20, 1990) pp 1293-1298.
- [16] Cohen, Ariel, Richard D. Haracz, and Leonard D. Cohen. "Asymmetry factors for randomly oriented infinite cylinders" *Journal of Applied Physics*, Volume 58, Number 3 (August, 1985) pp 1135-1140.
- [17] English, William J. "Vector variational solutions of inhomogeneously loaded cylindrical waveguide structures" *IEEE Transactions of Microwave Theory and Techniques Volume MTT 19* (January, 1971) pp 9 -18

- [18] Flory, E. "Boundary value for a stratified anisotropic ionosphere" *Arch. Elektron. and Uebertragungstech. Volume 34, Number 12* (December, 1980) pp 506-513
- [19] Garcia, C. B. and V. I. Zangwill. *Pathways to Solutions, Fixed Points, and Equilibria*. Englewood Cliffs, NJ: Prentice Hall(1981)
- [20] Hammond, W. S. and M. A. K. Hamid. "Diffraction by an infinite dielectric cylinder due to a normally incident cylindrical wave" *Electronics Letters. Volume 6, No. 26* (December 27, 1969) pp 675-676)
- [21] Ho, Henry S. "Dose rate distribution in triple layered dielectric cylinder with irregular cross section irradiated by plane wave sources" *Journal of Microwave Power Volume 10. Number 4* (1975) pp 421-432
- [22] Hochstadt, Harry. *The Functions of Mathematical Physics*. New York: Dover(1986).
- [23] Hörmander, Lars. *Linear Partial Differential Operators* New York: Academic Press (1963)
- [24] Kogelnik, H. and T. Li. "Laser beams and resonators" *Applied Optics. Volume 5, Number 10* (October, 1966) pp 1550-1566
- [25] Kozaki, Shogo. "Scattering of a Gaussian Beam by a Homogeneous Dielectric Cylinder" *Journal of Applied Physics. Volume 53. No. 11* (November, 1982) pp 7195-7200
- [26] Liou, K. N., S. C. Ou Takano, A. Heymsfield, and W. Kreiss. "Infrared transmission through cirrus clouds: a radiative model for target

- detection" *Applied Optics. Volume 29, Number 13* (May 1, 1990) pp 1886-1896
- [27] Mackowski, D. W., R. A. Altenkirch, and M. P. Menguc. "Internal absorption cross sections in a stratified sphere" *Applied Optics, Volume 29, Number 10* (April 1, 1990) pp 1551-1559
- [28] Maystre, D. and P. Vincent. "Diffraction d'une onde electromagnetique plane par un objet cylindrique non infiniment conducteur de section arbitraire" *Optics Communications Volume 5, Number 5* (August, 1972) pp 327-330.
- [29] Miyazaki, Y. "Scattering and Diffraction of Electromagnetic Waves by an Inhomogeneous Dielectric Cylinder" *Radio Science. Volume 16, Number 6* (November December, 1981) pp 1009-1014
- [30] Mugnai, Alberto and Warren J. Wiscombe. "Scattering from nonspherical Chebyshev Particles. I. Cross Sections, Single Scattering Albedo, Asymmetry factor, and backscattered fraction" *Applied Optics, Volume 25, Number 7* (April 1, 1986) pp 1235-1244.
- [31] Park, Bae-Sig, A. Biswas, and R. L. Armstrong. "Delay of explosive vaporization in pulsed laser heated droplets" *Optics Letters. Volume 15, No. 4* (February 15, 1990) pp 206-208
- [32] Pinnick, R. G., Abhijit Biswas, Robert L. Armstrong, S. Gerard Jennings, J. David Pendleton, and Gilbert Fernandez. "Micron size

- droplets irradiated with a pulsed  $CO_2$  laser: Measurement of Explosion and Breakdown Thresholds" *Applied Optics. Volume 29, No. 7* (March 1, 1990) pp 918-925
- [33] Pinnick, R. G., S. G. Jennings, Petr Chylek, Chris Ham, and W. T. Grandy. "Backscatter and Extinction in Water Clouds" *Journal of Geophysical Research. Vol 88, No. C11* (August 20, 1983) pp 6787-6796
- [34] Richardson, C. B., R. L. Hightower, and A. L. Pigg. "Optical measurement of the evaporation of sulfuric acid droplets" *Applied Optics. Volume 25, Number 7* (April 1, 1986) pp 1226-1229
- [35] Rosseland, S. *Theoretical Astrophysics: Atomic Theory and the Analysis of Stellar Atmospheres and Envelopes* Oxford, England: Clarendon Press (1936)
- [36] Schaub, S. A., D. R. Alexander, J. P. Barton, and M. A. Emanuel. "Focused laser beam interactions with methanol droplets: effects of relative beam diameter" *Applied Optics. Volume 28, No. 9* (May 1, 1989) pp 1666-1669
- [37] Schiffer, Ralf. "Perturbation approach for light scattering by an ensemble of irregular particles of arbitrary material" *Applied Optics, Volume 29, Number 10* (April 1, 1990) pp 1536-1550
- [38] Tsai, Wen Chung and Ronald J. Pogorzelski. "Eigenfunction solution of the scattering of beam radiation fields by spherical objects" *Journal*

- of the Optical Society of America. Volume 65. Number 12 (December, 1975) pp 1457-1463.*
- [39] Trefl, J. S. *Introduction to the Physics of Fluids and Solids* New York: Pergamon Press, Inc. (1975)
  - [40] Tzeng, H. M., K. F. Wall, M. B. Long, and R. K. Chang. "Laser emission from individual droplets at wavelengths corresponding to morphology dependent resonances" *Optics Letters. Volume 9, Number 11 (1984) pp 499-501*
  - [41] Volkovitsky, O. A. "Peculiarities of light scattering by droplet aerosol in a divergent  $CO_2$  laser beam" *Applied Optics. Volume 26, Number 24 (December 15, 1987) pp 5307-5310*
  - [42] Wait, James R. *Electromagnetic Radiation from Cylindrical Structures* New York: Pergamon Press (1959)
  - [43] Wait, James R. and David A. Hill. "Electromagnetic Surface Fields Produced by a Pulse Excited Loop Buried in the Earth." *Journal of Applied Physics. Volume 43, Number 10 (October, 1972) pp 3988-3989*
  - [44] Wasow, Wolfgang. *Asymptotic Expansions for Ordinary Differential Equations* New York: John Wiley (1965)
  - [45] Whittaker, E. T. and G. N. Watson. *A Course of Modern Analysis* London: Cambridge University Press (1986).

- [46] Wu, Le Kao, and Leonard L. Tsai. "Scattering by Arbitrarily Cross section layered lossy dielectric cylinders" *IEEE Transactions Antennas and Propagation*
- [47] Yeh, C. and P. K. C. Wang. "Scattering of obliquely incident waves by inhomogenous fibers" *Journal of Applied Physics, Volume 43, No. 10* (October, 1972) pp 3999 - 4006.



THE THERMAL RESPONSE  
OF AN N LAYER  
ELECTROMAGNETICALLY AND  
THERMALLY ANISOTROPIC  
SPHERE  
TO ELECTROMAGNETIC RADIATION  
BY AN EXACT FORMULA

D. K. Cohoon

Department of Mathematics

West Chester University

West Chester, PA 19383

June 23, 1990

An exact formula for the thermal response of an N layer spherically symmetric structure to electromagnetic radiation has been determined. The thermal conductivity, K, the permittivity,  $\epsilon$ , the magnetic permeability,  $\mu$ , and the electromagnetic conductivity,  $\sigma$ , are assumed to be tensors.

## 1 INTRODUCTION

In this paper we extend previous results ([1],[2]) and give an exact solution to the problem of describing by exact formula the thermal response to low energy electromagnetic radiation of an N layer electromagnetically anisotropic structure, or said differently a spherically symmetric structure where the permittivity  $\epsilon$  and magnetic permeability,  $\mu$ , and the complex electromagnetic conductivity  $\sigma$  are tensors, and which is also thermally anisotropic in the sense that the thermal conductivity, K, is also a tensor. The heat transfer equation is written in the form,

$$\begin{aligned} \rho c \frac{\partial u}{\partial t} = & \frac{1}{r^2} \left( \frac{\partial}{\partial r} \right) \left( r^2 K_r \frac{\partial u}{\partial r} \right) + \\ & \frac{1}{r \sin(\theta)} \left( \frac{\partial}{\partial \theta} \right) \left( K_\theta \frac{\sin(\theta)}{r} \frac{\partial u}{\partial \theta} \right) + \\ & \frac{1}{r \sin(\theta)} \left( \frac{\partial}{\partial \phi} \right) \left( K_\phi \frac{1}{r \sin(\theta)} \frac{\partial u}{\partial \phi} \right) - bu + S \end{aligned} \quad (1.1)$$

where if the magnetic permeabilities  $\mu$  and the permittivities  $\epsilon$ , and the electromagnetic conductivity  $\sigma$  are diagonal tensors in the spherical coordinate system and their  $\epsilon$  and  $\theta$  components are equal, then the source term has the form

$$\begin{aligned}
S = F_0[\omega \text{Im}(\mu)(|H_\theta|^2 + |H_\phi|^2) + \omega \text{Im}(\mu_r)(|H_r|^2) + \\
\omega \text{Im}(\epsilon)(|E_\theta|^2 + |E_\phi|^2) + \omega \text{Im}(\epsilon_r)(|E_r|^2) + \\
\text{Re}(\sigma)(|E_\theta|^2 + |E_\phi|^2)]
\end{aligned} \tag{1.2}$$

where  $F_0$  is a factor for converting MKS energy densities to centimeter gram second(cgs) units of calories per gram degree Centigrade that is given by,

$$F_0 = \frac{1}{2 \times 10^6 \times 4.184} \tag{1.3}$$

In order to make use of Legendre functions with integer index in our solution we assume that

$$K = K_\theta \tag{1.4}$$

and

$$K = K_\phi \tag{1.5}$$

We will make use of the Legendre functions  $P_n^m(\cos(\theta))$  and note that they satisfy the ordinary differential equation

$$\begin{aligned}
\frac{1}{\sin(\theta)} \frac{d}{d\theta} P_n^m(\cos(\theta)) = \\
\frac{m^2}{\sin^2(\theta)} P_n^m(\cos(\theta)) - n(n+1) P_n^m(\cos(\theta))
\end{aligned} \tag{1.6}$$

which is equivalent to

$$\frac{d}{dz} \left( (1-z^2) \frac{dW}{dz} \right) + \left( n(n+1) - \frac{m^2}{1-z^2} \right) W = 0 \tag{1.7}$$

where

$$z = \cos(\theta) \quad (1.8)$$

since (1.7) implies that

$$\frac{dv}{d\theta} = \frac{dv}{dz} \frac{dz}{d\theta} \quad (1.9)$$

which implies that

$$\frac{dv}{d\theta} = -\sin(\theta) \frac{dv}{dz} \quad (1.10)$$

(Hochstadt [3], page 164). To see this more clearly note that

$$\begin{aligned} \frac{d}{dz} \left( (1 - z^2) \frac{dW}{dz} \right) = \\ -2\cos(\theta) \left( \frac{-1}{\sin(\theta)} \frac{dW}{d\theta} \right) + \sin^2(\theta) \left\{ \frac{-\cos(\theta)}{\sin^3(\theta)} \right\} + \frac{d^2W}{d\theta^2} \end{aligned} \quad (1.11)$$

Therefore, we see that

$$\frac{d}{dz} \left( (1 - z^2) \frac{dW}{dz} \right) = \frac{\cos(\theta)}{\sin(\theta)} \frac{dW}{d\theta} + \frac{d^2W}{d\theta^2} \quad (1.12)$$

This implies that

$$\frac{d}{dz} \left( (1 - z^2) \frac{dW}{dz} \right) = \frac{1}{\sin\theta} \frac{d}{d\theta} \left( \sin(\theta) \frac{dW}{d\theta} \right) \quad (1.13)$$

Having developed this understanding of the formulation of Legendre's differential equation we proceed to define the finite Legendre transform (not the integral over the index) by the rule,

$$\mathcal{L}_n^m v = (2n + 1) \frac{(n - m)!}{(n + m)!} \int_0^\pi v(\theta) P_n^m(\cos(\theta)) \sin(\theta) d\theta \quad (1.14)$$

for  $m$  being positive and further restricted by the relation,

$$m \in \{0, 1, \dots, n\} \cup \{-1, -2, \dots, -n\} \quad (1.15)$$

and

$$\mathcal{L}_n^0 v = \left( \frac{2n+1}{2} \right) \int_0^\pi v(\theta) P_n(\cos(\theta)) \sin(\theta) d\theta \quad (1.16)$$

In carrying out the simplification of the heat transfer equation we need in addition to the finite Legendre transform, a finite cosine transform defined by the rule,

$$C_m u = \frac{1}{\pi} \int_{-\pi}^{\pi} \cos(m\phi) u(\phi) d\phi \quad (1.17)$$

A calculation shows that

$$\begin{aligned} \frac{1}{\pi} \int_{-\pi}^{\pi} \cos(m\phi) \frac{\partial^2 u}{\partial \phi^2}(\phi) d\phi &= \frac{m}{\pi} \int_{-\pi}^{\pi} \sin(m\phi) \frac{\partial u}{\partial \phi} d\phi \\ &= -m^2 C_m u \end{aligned} \quad (1.18)$$

We now develop a formula that enables us to simplify the energy equation by successive application of the finite cosine transform  $C_m$  and the finite Legendre transform  $\mathcal{L}_m^n$ . Using Legendre's differential equation and integration by parts we find that

$$\begin{aligned} &\mathcal{L}_n^m C_m \left( \frac{1}{r \sin(\theta)} \frac{\partial}{\partial \theta} \left( K \sin(\theta) \frac{1}{r} \frac{\partial u}{\partial \theta} \right) \right) + \\ &\mathcal{L}_n^m C_m \left( \frac{1}{r \sin(\theta)} \frac{\partial}{\partial \phi} \left( K \frac{1}{r \sin(\theta)} \frac{\partial u}{\partial \phi} \right) \right) = \frac{-n(n+1)}{r^2} K \mathcal{L}_n^m C_m u \end{aligned} \quad (1.19)$$

since the terms involving  $m^2$  cancel out if the two tangential components of the thermal conductivity tensor are equal.

We now apply the combined finite Legendre and finite cosine transforms to all terms of the energy equation,

$$\begin{aligned} \rho c \frac{\partial}{\partial t} (\mathcal{L}_n^m \mathcal{C}_m u) &= \frac{1}{r^2} \frac{\partial}{\partial r} \left( r^2 K_r \frac{\partial}{\partial r} (\mathcal{L}_n^m \mathcal{C}_m u) \right) + \\ &\quad \frac{-n(n+1)}{r^2} K \mathcal{L}_n^m \mathcal{C}_m u - \mathcal{L}_n^m \mathcal{C}_m b u + \mathcal{L}_n^m \mathcal{C}_m S \end{aligned} \quad (1.20)$$

We simplify the writing of the above equation by introducing the variables

$$U_{(m,n)} = \mathcal{L}_n^m \mathcal{C}_m u \quad (1.21)$$

and

$$S_{(m,n)} = \mathcal{L}_n^m \mathcal{C}_m S \quad (1.22)$$

we, therefore, see that the original energy equation may be transformed into the relation,

$$\begin{aligned} \rho c \frac{\partial}{\partial t} (U_{(m,n)}) &= \frac{1}{r^2} \frac{\partial}{\partial r} \left( r^2 K_r \frac{\partial}{\partial r} (U_{(m,n)}) \right) + \\ &\quad \frac{-n(n+1)}{r^2} K U_{(m,n)} - b U_{(m,n)} + S_{(m,n)} \end{aligned} \quad (1.23)$$

We create another finite transform with respect to the radial variable by making use of the oscillation theorem to select a series of radial eigenfunctions,  $Z_{(n,k)}(r)$ , satisfying

$$(\lambda_{(n,k)} r^2 \rho c - K n(n+1) - b r^2) Z_{(n,k)} + \frac{d}{dr} \left( r^2 K_r(r) \frac{d}{dr} Z_{(n,k)}(r) \right) = 0. \quad (1.24)$$

the regularity conditions that state that

$$K_r \frac{d}{dr} Z_{(n,k)}(r) \in \mathcal{C} \quad (1.25)$$

and

$$Z_{(n,k)} \in \mathcal{C} \quad (1.26)$$

where  $\mathcal{C}$  denotes the space of continuous functions on the real line with the origin removed. We now multiply all terms of our transformed equation (1.24) by  $Z_{(n,k)}$  and integrate from 0 to  $R_N$ , which is the radius of the outermost sphere in our  $N$  layer structure. Upon doing so we obtain the relation,

$$\begin{aligned} & \int_0^{R_N} Z_{(n,k)}(r) \frac{\partial}{\partial t} (U_{(m,n)}) \rho c r^2 dr = \\ & \int_0^{R_N} Z_{(n,k)}(r) \frac{\partial}{\partial r} \left( r^2 K_r \frac{\partial}{\partial r} U_{(m,n)} \right) dr - \int_0^{R_N} Z_{(n,k)}(r) K n(n+1) U_{(m,n)}(r) dr \\ & - \int_0^{R_N} b U_{(m,n)} r^2 Z_{(n,k)}(r) dr + \int_0^{R_N} r^2 S_{(m,n)}(r, t) Z_{(n,k)}(r) dr \quad (1.27) \end{aligned}$$

We use integration by parts to simplify equation (1.27), and we find that

$$\begin{aligned} & \int_0^{R_N} Z_{(n,k)}(r) \frac{\partial}{\partial r} \left( r^2 K_r \frac{\partial}{\partial r} U_{(m,n)}(r, t) \right) dr = \\ & Z_{(n,k)}(R_N) R_N^2 K_r(R_N) \frac{\partial}{\partial r} U_{(m,n)}(R_N, t) - \\ & \int_0^{R_N} r^2 K_r \frac{\partial}{\partial r} U_{(m,n)} \left( \frac{d}{dr} Z_{(n,k)}(r) \right) dr \\ & = Z_{(n,k)}(R_N) R_N^2 K_r(R_N) \frac{\partial}{\partial r} U_{(m,n)}(R_N, t) \\ & - R_N^2 K_r(R_N) Z_{(n,k)}^{(1)}(R_N) U_{(m,n)}(R_N, t) \\ & + \int_0^{R_N} U_{(m,n)}(r, t) \frac{d}{dr} \left( r^2 K_r \frac{d}{dr} Z_{(n,k)} \right) dr \quad (1.28) \end{aligned}$$

Observe that the functions  $V = U_{(m,n)}$  or  $V = Z_{(n,k)}$  satisfy exactly the same boundary condition, namely the Newton cooling law constraint given by

$$K_r V^{(1)}(R_N) + H V(R_N) = 0 \quad (1.29)$$

and upon replacing the derivative terms by using this Newton cooling law relation we see that

$$\begin{aligned} & Z_{(n,k)}(R_N) R_N^2 K_r(R_N) U_{(m,n)}^{(1)}(R_N, t) - \\ & R_N^2 K_r(R_N) Z_{(n,k)}^{(1)}(R_N) U_{(m,n)}(R_N, t) \\ & = Z_{(n,k)}(R_N) R_N^2 (-H U_{(m,n)}) \\ & - R_N^2 (-H Z_{(n,k)})(R_N) U_{(m,n)} = 0 \end{aligned} \quad (1.30)$$

Thus, we find that

$$\begin{aligned} & \int_0^{R_N} Z_{(n,k)}(r) \frac{\partial}{\partial r} \left( r^2 K_r \frac{\partial}{\partial r} U_{(m,n)}(r, t) \right) dr \\ & = \int_0^{R_N} U_{(m,n)}(r, t) \frac{d}{dr} \left( r^2 K_r \frac{d}{dr} Z_{(n,k)}(r) \right) dr \end{aligned} \quad (1.31)$$

Substituting equation (1.25) into this relationship yields

$$\begin{aligned} & \int_0^{R_N} Z_{(n,k)}(r) \frac{\partial}{\partial r} \left( r^2 K_r \frac{\partial}{\partial r} U_{(m,n)}(r, t) \right) dr = \\ & \int_0^{R_N} U_{(m,n)} \{ K n(n+1) + b r^2 - \lambda_{(n,k)} r^2 \rho c \} Z_{(n,k)}(r) dr \end{aligned} \quad (1.32)$$

Using these relationships in equation (1.28) we find that

$$\int_0^{R_N} \frac{\partial}{\partial t} U_{(m,n)}(r, t) Z_{(n,k)}(r) \rho c r^2 dr =$$



$$\begin{aligned}
& -\lambda_{(n,k)} \int_0^{R_N} U_{(m,n)}(r,t) Z_{(n,k)}(r) \rho c r^2 dr \\
& + \int_0^{R_N} S_{(m,n)}(r,t) Z_{(n,k)}(r) r^2 dr
\end{aligned} \tag{1.33}$$

Thus, if we define the finite radial transform,  $\mathcal{T}$

$$\mathcal{T}_{(n,k)}(f) = \frac{\int_0^{R_N} f(r) Z_{(n,k)}(r) \rho c r^2 dr}{\int_0^{R_N} Z_{(n,k)}(r)^2 \rho c r^2 dr} \tag{1.34}$$

then if we let

$$b_k^{(m,n)}(t) = \mathcal{T}_{(n,k)} \mathcal{L}_n^m C_m \left( \frac{S}{\rho c} \right) (t) \tag{1.35}$$

we see that

$$\frac{d}{dt} \mathcal{T}_{(n,k)} U_{(m,n)} + \lambda_{(n,k)} \mathcal{T}_{(n,k)} U_{(m,n)} = b_k^{(m,n)}(t) \tag{1.36}$$

so that if we define the expansion coefficient by the rule,

$$a_k^{(m,n)}(t) = \mathcal{T}_{(n,k)} \mathcal{L}_n^m C_m u \tag{1.37}$$

then the problem reduces to that of solving the ordinary differential equation

$$\frac{d}{dt} a_k^{(m,n)}(t) + \lambda_{(n,k)} a_k^{(m,n)}(t) = b_k^{(m,n)}(t) \tag{1.38}$$

The solution of this differential equation is given by

$$a_k^{(m,n)}(t) = \int_0^t \exp(\lambda_{(n,k)}(t - \tau)) b_k^{(m,n)}(\tau) d\tau \tag{1.39}$$

where the term  $b_k^{(m,n)}$  is defined by equations (1.2) and (1.35).

For a variety of pulsed heating schemes ([2]), this integral has been evaluated exactly. In doing so we have made use of the dramatic difference in the time scales of conductive and radiative transfer in the materials being irradiated.

## 2 THE RADIAL FUNCTIONS

We have seen that the radial functions satisfy the ordinary differential equation,

$$\frac{d}{dr} \left( r^2 \frac{d}{dr} Z_{(n,k)} \right) + \left\{ \frac{\lambda_{(n,k)} \rho c - b}{K_r} - \frac{n(n+1)K}{K_r} \right\} Z_{(n,k)} = 0 \quad (2.1)$$

We let

$$z^2 = \left( \frac{\lambda_{(n,k)} \rho c - b}{K_r} \right) r^2 \quad (2.2)$$

in each layer. Then (2.1) and (2.2) imply that if

$$W(z) = Z_{(n,k)}(r) \quad (2.3)$$

that then

$$z^2 W^{(2)}(z) + \frac{2}{z} W^{(1)}(z) + \left( 1 - \frac{n(n+1)K}{z^2 K_r} \right) W = 0 \quad (2.4)$$

Rearranging the terms involving the derivative we find that

$$\frac{1}{z} \left( \frac{d}{dz} \right)^2 (zW(z)) + \left( 1 - \frac{n(n+1)K}{z^2 K_r} \right) W \quad (2.5)$$

Thus, the radial functions are given by

$$W = \Psi_\nu(z) = \frac{\sqrt{\pi} J_{\nu+1/2}(z)}{\sqrt{2}\sqrt{z}} \quad (2.6)$$

where

$$\nu = -1/2 + \sqrt{\frac{1}{4} + \frac{n(n+1)K}{K_r}} \quad (2.7)$$

### 3 EIGENVALUE DETERMINATION

We are seeking by computer algorithm a solution of an ordinary differential equation,

$$\frac{d}{dr} \left( r^2 \frac{d}{dr} Z_{(n,k)} \right) + \left\{ \frac{\lambda_{(n,k)} \rho c - b}{K_r} - \frac{n(n+1)K}{K_r} \right\} Z_{(n,k)} = 0 \quad (3.1)$$

which has a singular point at  $r = 0$ , and piecewise smooth coefficients with the additional property that one of the coefficients depends on a parameter which we have denoted by  $\lambda_{(n,k)}$ , where the solution,  $Z_{(n,k)}(r)$  and the product of the radial conductivity  $K_r$  and the derivative of  $Z_{(n,k)}$  are continuous and

$$\lim_{r \rightarrow \infty} \left( K_r(r) \frac{d}{dr} Z_{(n,k)}(r) + H Z_{(n,k)}(r) \right) = 0 \quad (3.2)$$

These eigenvalues and eigenfunctions are obtained by a shooting method by defining  $Z(r, \lambda)$  to be the solution of the ordinary differential equation.

$$\frac{d}{dr} \left( r^2 \frac{d}{dr} Z(r, \lambda) \right) + \left\{ \frac{\lambda \rho c - b}{K_r} - \frac{n(n+1)K}{K_r} \right\} Z(r, \lambda) = 0 \quad (3.3)$$

which has an integrable singularity at  $r = 0$  and which satisfies the regularity conditions and the Newton cooling law boundary conditions at the outer boundary of the sphere.

## 4 RADIATIVE HEATING

Because of orthonormality of the transformations we find that the difference  $u$  between the induced thermal excursion and the ambient temperature in the irradiated solid is given by

$$u(r, \theta, \phi, t) = \sum_{k=1}^{\infty} \sum_{n=0}^{\infty} \sum_{m=0}^n a_k^{(m,n)}(t) P_n^m(\cos(\theta)) \cos(m\phi) Z_{(n,k)}(r) \quad (4.1)$$

where the expansion coefficients are determined by equation (1.39), and the heat source term is given by (1.2). In the computer code the expansion coefficients are precomputed and saved. Once the expansion coefficients are known, the microwave induced thermal excursion can be computed at thousands of points for a modest computer cost. The entire code runs on a personal computer.

In the following sample computation, which gives a comparison of radiation induced temperature increases measured with a Vitek non field perturbing thermal probe and predictions of the computer program, a dielectric ball was enclosed in styrofoam. The calculation is for an isotropic muscle equivalent spherical structure with a radius of 3.3 centimeters exposed to 1.2 Gigahertz continuous wave radiation with a power of 70 milliwatts per square centimeter. The time of exposure for figure 1 was 30 seconds. In Figure 2 which follows the Vitek probe was placed at the center of the structure and the the power was turned off after 5.5 minutes.

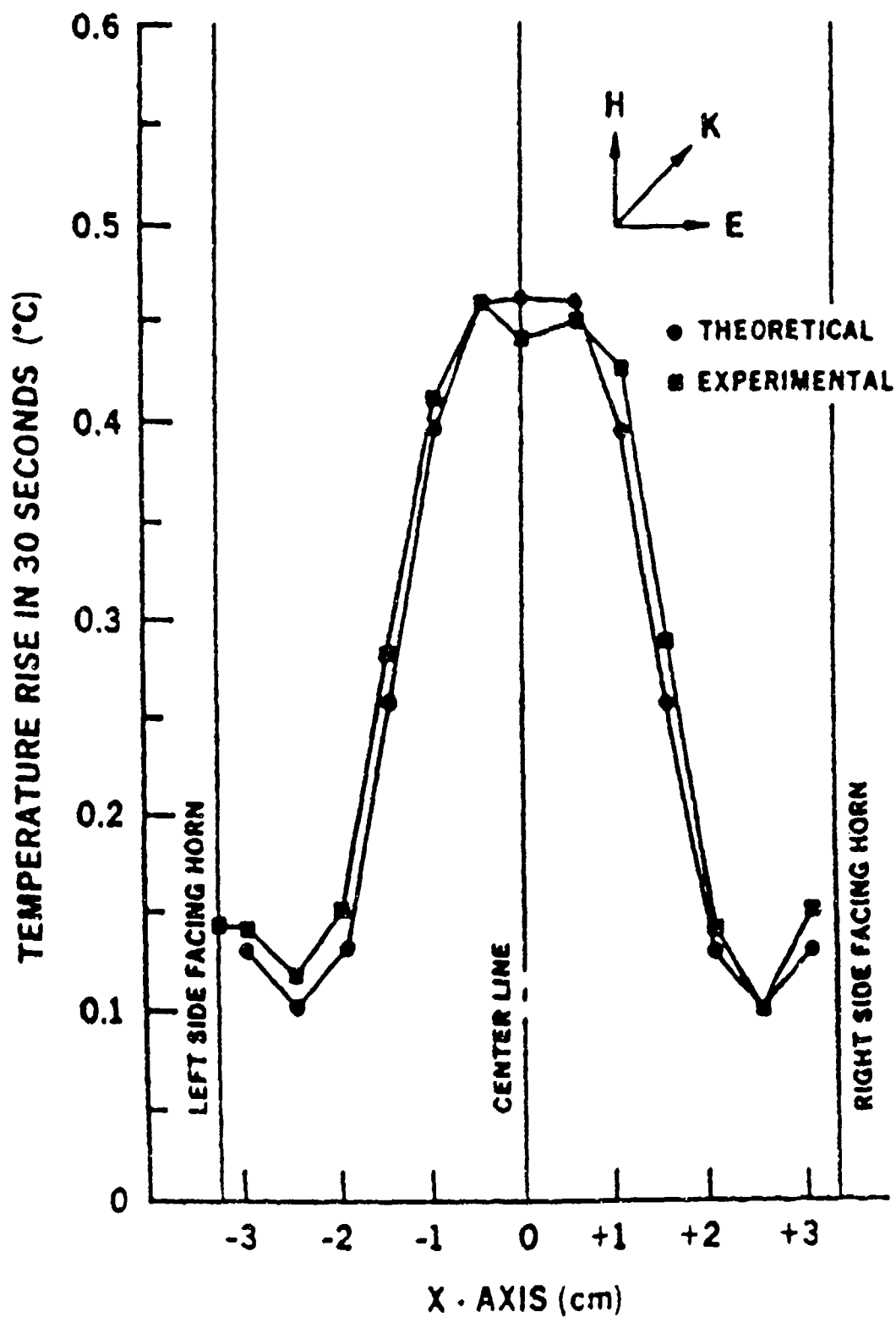


Figure 1. A 3.3 centimeter radius spherical structure exposed to 1.2 Gigahertz with a power of 70 milliwatts per square centimeter for 30 seconds. The structure is isotropic and the relative permittivity is 50.4 and the electromagnetic conductivity is 1.52 mhos per meter. The specific heat is .94 calories per gram degree Centigrade. The thermal conductivity in calories per centimeter per second per degree Centigrade is .0012.

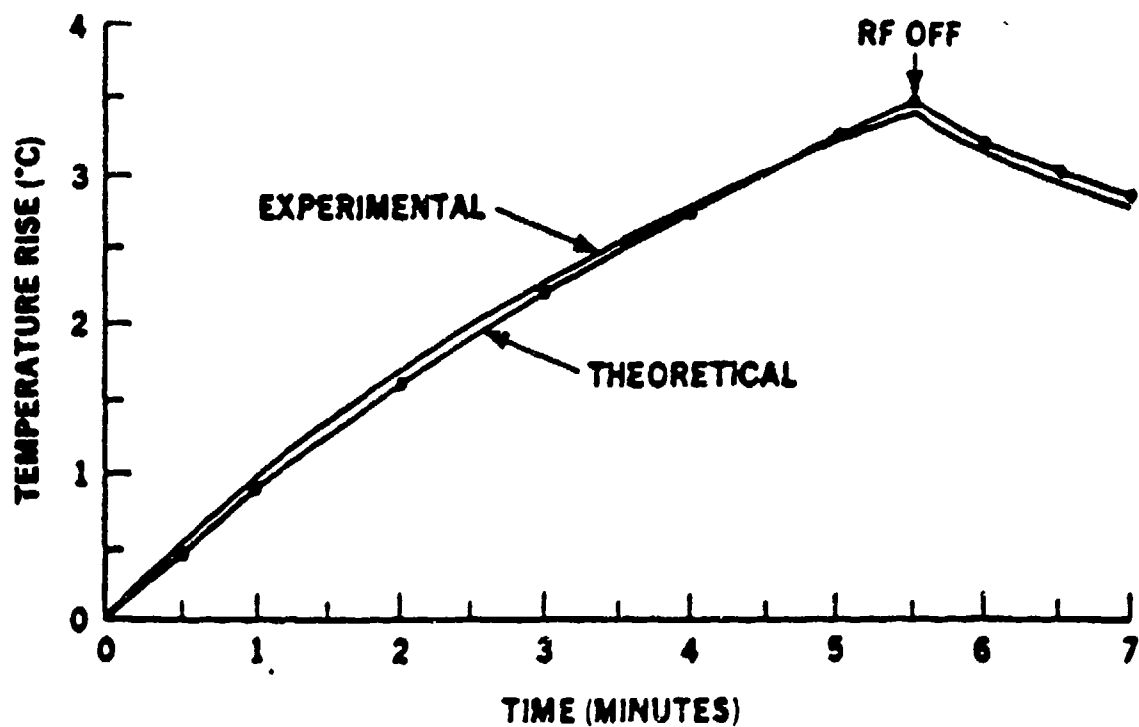


Figure 2. The temperature at the center of a 3.3 centimeter radius spherical structure exposed to 1.2 Gigahertz radiation with a power of 70 milliwatts per square centimeter as a function of time. The power was turned off after 5.5 minutes. The thermal and electromagnetic parameters are the same as those of Figure 1. The Newton cooling law constant used at the surface is

$$H = 5.722 \times 10^{-5} \text{ calories/cm}^2/\text{degree}^{\circ}\text{C}/\text{second}$$

## References

- [1] Bell, Earl L., David K. Cohoon, and John W. Penn. *Mie: A FORTRAN program for computing power deposition in spherical dielectrics through application of Mie theory. SAM-TR-77-11* Brooks AFB, Tx 78235: USAF School of Aerospace Medicine (RZ) Aerospace Medical Division (AFSC) (August, 1977)
- [2] Bell, Earl L., David K. Cohoon, and John W. Penn. *Electromagnetic Energy Deposition in a Concentric Spherical Model of the Human or Animal Head SAM-TR-79-6* Brooks AFB, Tx 78235: USAF School of Aerospace Medicine (RZ) Aerospace Medical Division (AFSC) (December, 1982).
- [3] Burr, John G., David K. Cohoon, Earl L. Bell, and John W. Penn. Thermal response model of a Simulated Cranial Structure Exposed to Radiofrequency Radiation. *IEEE Transactions on Biomedical Engineering. Volume BME-27, No. 8* (August, 1980) pp 452-460.
- [4] Cohoon, D. K., J. W. Penn, E. L. Bell, D. R. Lyons, and A. G. Cryer. *A Computer Model Predicting the Thermal Response to Microwave Radiation SAM-TR-82-22* Brooks AFB, Tx 78235: USAF School of Aerospace Medicine. (RZ) Aerospace Medical Division (AFSC) (December, 1982).
- [5] Hochstadt, Harry. *The Functions of Mathematical Physics*. New York: Dover(1986).

- [6] Whittaker, E. T. and G. N. Watson. *A Course of Modern Analysis*  
London: Cambridge University Press (1986).



## **Multiple Scattering of Electromagnetic Waves from Coated Rough Surfaces**

**Ezekiel Bahar  
S. Mark Haugland**  
Electrical Engineering Department, University of Nebraska-Lincoln,  
209N WSEC, Lincoln, NE 68588-0511

### **RECENT PUBLICATIONS**

- A) E. Bahar, "Physical Interpretation of the Full Wave Solutions for the Electromagnetic Fields Scattered from Irregular Stratified Media," *Radio Science*, vol. 23, no. 5, pp 749-759, September-October 1988.
- B) E. Bahar and G. Huang, "Transmission Scattering and Depolarization Across Rough Surfaces - Full Wave Solutions," 1989 CRDEC Scientific Conference on Obscuration and Aerosol Research, Aberdeen, MD, June 26-30, 1989.
- C) E. Bahar, "Physical Models of Nonspecular Scattering in Irregular Stratified Media," *URSI International Symposium on Electromagnetic Theory at the Royal Institute of Technology, Stockholm, Sweden*, August 14-17, 1989.
- D) E. Bahar and M. A. Fitzwater, "Full Wave Physical Models of Nonspecular Scattering in Irregular Stratified Media," *IEEE Trans. on A. and P.*, vol. 37, no. 12, pp 1609-1615, December, 1989.
- E) E. Bahar and G. Huang, "Scattering and Depolarization Across Rough Surfaces - Full Wave Solution," *URSI Meeting, University of Colorado, Boulder, CO*, January 3-5, 1990.

### **ABSTRACT**

Full wave solutions for the like and cross polarized scattered electromagnetic fields from an irregular stratified structure consisting of three distinct media are derived. Two surfaces (boundaries) described by a continuous function and first derivative separate the three media. The upper boundary (first encountered by the incident wave) is assumed to be a flat plane. The lower boundary is a two-dimensionally rough surface. Both the like and cross polarized scattered radiation fields are expressed as double infinite sums. Each term in the sum is identified as a wave reflected by the two interfaces several times before and after being nonspecularly scattered by an element of the rough surface. These solutions have been shown to satisfy the reciprocity relationships in electromagnetic theory (without artificially enforcing this property). In the high frequency limit, the full wave solutions reduce to the physical optics solutions provided that the major contributions to the scattered fields come from the neighborhood of the stationary phase (specular) points on the rough surface. The full wave analysis agrees with Rice's perturbation solutions for surfaces with very small height and negligible slope. The full wave solutions also reduce to the well known geometric optics solution when both boundaries are flat and parallel. This analysis is used to remotely sense layers of liquid coating deposited on rough terrain.

### **FUTURE WORK**

The analysis presented in this manuscript is used to compute the Mueller matrix elements that completely characterize light scattered from liquid coated terrain. This analysis provides the first

phase for the solution to the general problem in which both interfaces are rough.

## 1. INTRODUCTION

Electromagnetic wave propagation in irregular stratified media is an important problem in remote sensing and communications. In this paper, scattering and depolarization of electromagnetic waves in a structure consisting of three distinct media is considered using a full wave approach. The upper boundary is the  $y=0$  plane, separating free space (medium 0) from the coating layer (medium 1). The lower boundary is the two-dimensionally rough surface  $y=h(x,z)$  which separates medium 1 from the background material (medium 2). The rough boundary  $y=h$  can be regarded as a continuum of differential surface elements of arbitrary height and slope.

The full wave solutions have been shown to satisfy reciprocity relationships in electromagnetic theory [3]-[4]. These results reduce to the perturbation solution for surfaces with  $kh_{rms} \ll 1$  ( $k$  is the wavenumber and  $h_{rms}$  is the rms height) and negligible slope. They reduce to the physical optics solution in the high frequency limit when the major contributions to the scattered field come from regions around the specular points. When both interfaces are flat and parallel, the double infinite sum for the like polarized scattered field reduces to the well known geometric optics solution [4], and the cross polarized field vanishes. Each term in the double infinite sum is identified as a multiply reflected incident and scattered wave between the  $y=0$  plane and the rough boundary  $y=h$ .

## 2. FORMULATION OF THE PROBLEM

Generalized field transforms [1] are used to obtain full wave solutions for the like and cross polarized electromagnetic fields scattered by the irregular layered structure. These are used to express the electromagnetic fields in terms of a complete spectrum of radiation fields, lateral waves, and surface waves. In this work, only the radiation fields are considered since both the transmitter and the receiver are assumed to be far from the surface. The transform pairs are given by

$$\bar{E}_T(x, y, z) = \sum_v \int_{-\infty}^{+\infty} [E^V(x, v, w) \bar{e}_T^V + E^H(x, v, w) \bar{e}_T^H] dw \quad (1a)$$

$$\bar{H}_T(x, y, z) = \sum_v \int_{-\infty}^{+\infty} [H^V(x, v, w) \bar{h}_T^V + H^H(x, v, w) \bar{h}_T^H] dw \quad (1b)$$

where

$$E^P(x, v, w) = \int_{-\infty}^{+\infty} \int_{-\infty}^{+\infty} \bar{E}_T(x, y, z) \cdot (\bar{h}_P^T \times \bar{a}_x) dy dz \quad (2a)$$

$$H^P(x, v, w) = \int_{-\infty}^{+\infty} \int_{-\infty}^{+\infty} \bar{H}_T(x, y, z) \cdot (\bar{a}_x \times \bar{e}_P^T) dy dz \quad (2b)$$

in which the vector wavenumber is given by

$$\bar{k}_i = u \bar{a}_x + v \bar{a}_y + w \bar{a}_z \quad (3)$$

$$|\bar{k}_i| = \omega \sqrt{\mu_i \epsilon_i} \quad i=0, 1, 2 \quad (4)$$

for each of the 3 media in the layered structure. The radian frequency of the electromagnetic field is  $\omega$

and the complex permeability and permittivity of medium  $i$  are  $\mu_i$  and  $\epsilon_i$  respectively. Since an  $e^{i\omega t}$  time dependence is assumed here,  $\text{Im}(\mu_i) < 0$  and  $\text{Im}(\epsilon_i) < 0$ . The transverse (y and z) components of the electric and magnetic fields are  $\bar{E}_T$  and  $\bar{H}_T$  respectively. The field transforms  $E^P$  and  $H^P$  depend on polarization ( $P=H$  for horizontal and  $P=V$  for vertical). In (1),  $\bar{e}_T^P$  and  $\bar{h}_T^P$  are the basis functions, and in (2)  $\bar{e}_P^T$  and  $\bar{h}_P^T$  are the reciprocal basis functions. These field transforms are substituted into

Maxwell's equations and upon applying the exact boundary conditions at each interface and using Green's theorem (to avoid interchanging the order of integration and differentiation), the following

differential equations for the forward and backward wave amplitudes  $a^P$  and  $b^P$  respectively are obtained [2]:

$$-\left(\frac{d}{dx} + i u\right) a^P(x, v, w) = \sum_Q \int_0^{+\infty} \int_{-\infty}^{+\infty} [S_{PQ}^{BA}(v, v', w, w') a^Q(x, v', w') + S_{PQ}^{BB}(v, v', w, w') b^Q(x, v', w')] dw' dv'_0 - A^P \quad (5a)$$

$$-\left(\frac{d}{dx} - i u\right) b^P(x, v, w) = \sum_Q \int_0^{+\infty} \int_{-\infty}^{+\infty} [S_{PQ}^{AA}(v, v', w, w') a^Q(x, v', w') + S_{PQ}^{AB}(v, v', w, w') b^Q(x, v', w')] dw' dv'_0 + B^P \quad (5b)$$

The wave amplitudes are related as follows to the field transforms

$$E^P = a^P - b^P \quad (6a)$$

$$H^P = a^P + b^P \quad (6b)$$

Equations (5) are referred to as the generalized telegraphist's equations. The coupling coefficients  $S_{PQ}^{\alpha\beta}$  are associated with forward scattering ( $\alpha \neq \beta$ ), and backward scattering ( $\alpha = \beta$ ). For the like polarized scattered field  $P=Q$ , and for the cross polarized field ( $P \neq Q$ ). In (5),  $A^P$  and  $B^P$  are source transforms. The generalized telegraphist's equations can be solved using numerical techniques. To gain physical insight an iterative procedure is pursued here. To obtain the first order iterative solution, the scattering coefficients  $S_{PQ}^{\alpha\beta}$  are ignored in equation (5). The first order solutions for  $a^P$  and  $b^P$  are then substituted into the right hand side of (5) and the differential equations are integrated yielding the second order iterative solution [2]. On substituting the second order solution for the wave amplitudes into the transform expressions for the fields (1) yields the following expressions for the cross polarized and the co polarized scattered radiation fields:

$$E_S^{PQ} = \frac{E_0^{Q_i}}{(2\pi i)^2} \int_{-\infty}^{+\infty} \int \int \int C_1^i F_{11}^{PQ} \frac{T_{10}^{Q_i} T_{10}^P \exp(i\bar{k}_d \cdot \bar{F}_s) \exp(-i\bar{k}_0 \cdot \bar{F})}{[1 - R_{01}^{Q_i} R_{21}^{Q_i} \exp(iv_1^i h)][1 - R_{01}^P R_{21}^P \exp(iv_1 h)]} \times \frac{(C_1 + C_1^i)}{S_1 C_\phi - S_1^i C_\phi^i} N \frac{dh}{dx_s} dx_s dz_s \frac{k_1}{u} dv_0 dw \quad (7)$$

where the rough surface scattering coefficient  $F_{11}^{PQ}$  depends on the polarization of the incident and scattered waves ( $P=H$  for horizontal,  $P=V$  for vertical,  $Q=V, H$ ), the electromagnetic parameters of the layered medium, and the directions of the incident and scattered radiation field [5]. For simplicity in (7) it is assumed that  $h=h(x)$ . The solution for the two-dimensional surface  $h(x, z)$  can be obtained in a straightforward manner [6]. The vector wavenumber  $\bar{k}_d$  is defined as follows

$$\bar{k}_d = \bar{k}_1 - \bar{k}_1^i \quad (8)$$

where  $\bar{k}$  is in the direction of the scattered wave

$$\bar{k}_1 = k_1 (\sin\theta_1 \cos\phi \bar{a}_x + \cos\theta_1 \bar{a}_y + \sin\theta_1 \sin\phi \bar{a}_z) = k_1 (S_1 C_\phi \bar{a}_x + C_1 \bar{a}_y + S_1 S_\phi \bar{a}_z) \quad (9)$$

and  $\bar{k}^i$  is in the direction of the incident wave

$$\bar{k}_1^i = k_1 (\sin\theta_1^i \cos\phi^i \bar{a}_x + \cos\theta_1^i \bar{a}_y + \sin\theta_1^i \sin\phi^i \bar{a}_z) = k_1 (S_1^i C_\phi^i \bar{a}_x + C_1^i \bar{a}_y + S_1^i S_\phi^i \bar{a}_z) \quad (10)$$

The complex sines and cosines of the angles in equations (9) and (10) for each medium are determined using Snell's law

$$k_0 S_0 = k_1 S_1 = k_2 S_2 \quad (11a)$$

$$C_j = \sqrt{1 - S_j^2} ; \text{Im}(k_j C_j) < 0 \quad (11b)$$

Also in (7), the normalization constant is

$$N = \begin{cases} \eta_{r1} & P = Q = V \\ 1 & P \neq Q \\ 1/\eta_{r1} & P = Q = H \end{cases} \quad (12)$$

where

$$\eta_{r1} = \sqrt{\frac{\mu_1 \epsilon_0}{\mu_0 \epsilon_1}}$$

The Fresnel reflection coefficient  $R_{ij}^P$  is for waves incident upon medium  $j$  from medium  $i$  with

polarization  $P$ . The corresponding transmission coefficient is  $T_{ij}^P = 1 + R_{ij}^P$ . The position vector  $\bar{r}_s$  is

from the origin to the point  $(x_s, z_s)$  on the rough surface  $y=h$  and the vector position vector  $\bar{r}$  is from the origin to the field point.

On expressing the denominator of (7) in an infinite geometric series, each term in the resulting double infinite sum can be integrated by parts. A steepest descent integration of these expressions with respect to  $dv_0 dw$  results in the following expressions for the scattered radiation fields.

$$E_{S1}^{PQ} = E_0^{Qi} G_0 \sum_{p,q} \int_{-L}^{+L} \int_{-L}^{+L} C_1^i F_{11}^{PQ} T_{10}^{Pf} T_{10}^{Qi} N [R_{01}^{Pf} R_{21}^{Pf} \exp(i2v_1^f h)]^p [R_{01}^{Qi} R_{21}^{Qi} \exp(i2v_1^i h)]^q \times \frac{C_1^f + C_1^i}{(2p+1)C_1^f + (2q+1)C_1^i} \exp\{i(\vec{k}_1^f - \vec{k}_1^i) \cdot \vec{r}_s\} dx_s dz_s \quad (13)$$

where

$$G_0 = -ik_0 \frac{e^{-ik_0 r^f}}{2\pi r^f} \quad (14)$$

and  $r^f$  is the distance from the origin to the field point. In (13), the superscript  $f$  means to evaluate a given quantity using the scattered angle  $\theta^f$  and the scattered azimuth angle  $\phi^f$ . The vector wave number  $\vec{k}_1^f$  is in the direction of the position vector  $\vec{r}$ .

$$\vec{k}_1^f = k_1 (\sin\theta_1^f \cos\phi^f \vec{a}_x + \sin\theta_1^f \sin\phi^f \vec{a}_y + \cos\theta_1^f \vec{a}_z) \quad (15)$$

The variables  $x$  and  $z$  extend over the radar foot print ( $-L \leq x \leq L, -L \leq z \leq L$ ).

The expression for the like polarized field reduces to the well known exact solution when

$h = \text{constant}$ ,  $l \rightarrow \infty$ , and  $L \rightarrow \infty$  [4]. The cross polarized field vanishes whenever  $\vec{k}^f, \vec{k}^i$ , and the normal to the surface  $\vec{n}$  are coplanar [5].

### 3. PHYSICAL INTERPRETATION of RESULTS

Each term in the double infinite sum (13) can be identified as a scattered wave that undergoes multiple reflection between the interfaces  $y=0$  and  $y=h(x,z)$ . To simplify the notation in (13), let

$$R^{Qi} = R_{01}^{Qi} R_{21}^{Qi} \exp(i2v_1^i h) \quad (16a)$$

$$R^{Pf} = R_{01}^{Pf} R_{21}^{Pf} \exp(i2v_1^f h) \quad (16b)$$

Thus  $R^{Qi}$  and  $R^{Pf}$  account for reflection and propagation of a wave making one round trip in medium 1 ( $\mu_1, \epsilon_1$ ) at the incident and scattered angles respectively. Thus (13) can be expressed as follows

$$E_{S1}^{PQ} = E_0^{Qi} G_0 \sum_{p,q} \int_{-L}^{+L} \int_{-L}^{+L} T_{10}^{Qi} [R^{Qi}]^q C_1^i F_{11}^{PQ} [R^{Pf}]^p T_{10}^{Pf} N \times \frac{C_1 + C_1^i}{(2p+1)C_1 + (2q+1)C_1^i} \exp\{i(\vec{k}_1^f - \vec{k}_1^i) \cdot \vec{r}_s\} dx_s dz_s \quad (17)$$

The term in (17) with  $p=m$  and  $q=n$  represents a wave that enters ( $T_{10}^{Qi}$ ) the layered structure from above structure with polarization  $Q$  at the incident angle  $\theta^i$ , makes ( $[R^{Qi}]^n$ )  $n$  round trips in

medium 1 at the incident angle with polarization  $Q$ , ( $C_1^i F_{11}^{PQ}$ ) is scattered at the angle  $\theta_1^f$  by the surface element  $dx_s dz_s$  on  $h(x,z)$ , makes  $m$  round trips in medium 1 at the scattered

angle  $\theta_1^f$  with polarization  $P$  ( $[R^{Pf}]^m$ ), and is finally transmitted through the boundary  $y=0$  at the

scattered angle ( $T_{10}^{Pf}$ ). The full wave solutions are completely reciprocal [4].

#### 4. CONCLUSIONS

Each term in the double infinite sum representing the full wave like and cross polarized scattered radiation field is identified as a multiply reflected electromagnetic wave between the 2 interfaces of the layered structure. The absolutely convergent double infinite sum for the scattered field can be truncated for practical purposes. An efficient way to do so (while maintaining reciprocity) is to retain all the terms in the sum for which  $p+q=N$ , where  $N$  is determined by the accuracy desired.

The full wave solution reduces to the physical optics solution in the high frequency limit when the major contributions to the scattered field come from the neighborhood of the stationary phase points. It reduces to the perturbation solution where  $kh_{rms} \ll 1$  and the slopes are negligible. These solutions inherently satisfy duality and reciprocity relationships in electromagnetic theory. The Mueller matrix elements characterizing light scattered from liquid coated terrain can be computed using the analysis presented here. The matrix elements, in turn, can be used to facilitate remote identification of various coating materials.

#### ACKNOWLEDGMENT

This work was sponsored by the CRDEC contract DAAD05-90-P-4363.

#### REFERENCES

- [1] E. Bahar, "Depolarization of Electromagnetic Waves Excited by Distributions of Electric and Magnetic Sources in Inhomogeneous Multilayered Structures of Arbitrarily Varying Thickness. Generalized Field Transforms," J. Math Phys., Vol. 14, No. 11, pp 1502-1509, Nov. 1973.
- [2] E. Bahar, "Depolarization of Electromagnetic Waves Excited by Distributions of Electric and Magnetic Sources in Inhomogeneous Multilayered Structures of Arbitrarily Varying Thickness. Full Wave Solutions," J. Math Phys., Vol. 14, No. 10, pp 1510-1515, Nov. 1973.
- [3] E. Bahar, and M. A. Fitzwater, "Full Wave Physical Models of Nonspecular Scattering in Irregular Stratified Media," IEEE Trans. on A. and P., Vol. 37, No. 12, pp 1609-1615, Dec. 1989.
- [4] E. Bahar, "Physical Interpretation of the Full Wave Solutions for the Electromagnetic Fields Scattered from Irregular Stratified Media," Radio Sci., Vol. 23, No. 5, pp 749-759, Sept.-Oct. 1988.
- [5] E. Bahar, "Full Wave Solutions for the Depolarization of the Scattered Radiation Fields by Rough Interfaces of Arbitrary Slope," IEEE Trans. on A. and P., Vol. AP-29, No. 3, pp 443-454, May 1981.
- [6] E. Bahar, "Review of the Full Wave Solutions for Rough Surface Scattering and Depolarization: Comparisons with Geometric and Physical Optics, Perturbation, and Two-Scale Hybrid Solutions," Journal of Geophysical Research, Vol. 92, No. C5, pp 5209-5224, May 15, 1987.

**Density dependence of the absorption coefficient of a dispersion of  
spherical metal particles †**

**E. Fucile \*, O. I. Sindoni \*\*, F. Borghese \*, P. Denti \*, R. Saija \***

*\*Universita' di Messina, Istituto di Struttura della Materia*

*Salita Sperone 31, 98100 S. Agata-Messina,*

*Italy*

*\*\*Chemical Research Development and Engineering Center*

*Aberdeen Proving Ground, Maryland 21010-5423*

*USA*

**ABSTRACT**

An assesment to what extent and down to what densities the multiple scattering processes may effect the extinction coefficient of a dispersion of identical spherical scatterers. The whole dispersion is considered as made of compound nonisotropic scatterers with random orientation. An application of the theory to a dispersion of spherical metal particles is shown.

---

† Based on work supported in part by the US ARMY E.R.O. through contract

## 1. Introduction

Multiple scattering processes are known to be of prime importance in determining the optical behavior of a dispersion of scatterers. An exact evaluation of the effect of these processes would require, however, the knowledge of the position of all the scatterers and would result in the solution of a system of linear non-homogeneous equations with an order proportional to the number of the particles [1]. Since this kind of approach is clearly impracticable, several approximations have been devised such as *e. g.* the *quasicrystalline approximation* of Lax [2], that has been used by Varadan, Brongi and Varadan [3] to describe the propagation through a moderate-density dispersion of ellipsoidal scatterers.

The multiple scattering processes occurring within a high-density dispersion can be accounted for, in an average sense, through the *effective medium theory*. This approach, according to the topology of the dispersion, yields the Maxwell-Garnet or Bruggeman mixing rules [4], that are based on so severe approximations, however, as to be applicable only to particles with very small size parameter. This limitation also applies to the improvements to the Bruggeman mixing rule proposed by Stroud and Pan [5] - to include magnetic effects - and by Chylek and Srivastava [6] - to include the possibility of polydispersion - whereas the approach proposed by Borghese *et al.* is applicable to bigger particles up to the limit of validity of the dielectric description of a granulated medium.

When the dispersion has a low density the multiple scattering processes are unlikely to occur and are, therefore, usually neglected. As a consequence, the (complex) matrix of the refractive index of the dispersion, and the related macroscopic optical constants as well, can be calculated by simple superposition of the normalized forward-scattering amplitudes of the individual scatterers [8]. Unfortunately, the meaning of the expression *low-density dispersion* is based only on estimates such as those given by van de Hulst [9] and by Bayvel and Jones [10]. It is just for this reason that we determined to assess to what extent and down to what densities the multiple scattering processes may effect the extinction coefficient of a dispersion of identical spherical scatterers.

To accomplish our task we considered each sphere as forming a binary aggregate with any other sphere in the dispersion, the separation of the pairs being distributed according to the pair correlation function appropriate for the

---

DAJA45-86-C-0003 and in part by the Consiglio Nazionale delle Ricerche through the GNSM.



density at hand. This amounts to considering the whole dispersion as made of compound nonisotropic scatterers with random orientation. Now, as shown in our preceding papers [11-13], the only quantity we need to calculate the macroscopic optical constants of such a dispersion, taking into full account the multiple scattering processes that may occur within each pair, is the forward-scattering amplitude of one of the pairs averaged over the orientations and possibly over the separations. As our approach takes full advantage of the transformation properties of the scattered field to produce an analytical average over the orientations of the forward-scattering amplitude, the result of our calculations is a quantity that still depends only on the separation of the pairs. Therefore, we must perform numerically the required average over the separations using as a weight function the appropriate pair correlation function. The ultimate result of all our calculations is the forward-scattering amplitude of a sphere *dressed* by the effect of the two-body multiple scattering processes. It is this dressed amplitude we use to write the matrix of the refractive index and thus to calculate the macroscopic optical constants of the dispersion. Since it turns out that the dressed amplitude and the customary one differ by terms proportional to the square of the density of the dispersion, we are able to put an upper limit to the range in which a dispersion can be considered of low density.

The details of the theory outlined above will be expounded in section 2, while in section 3 we will show an application to a dispersion of spherical metal particles and will discuss the results.

## 2. Theory

The optical properties of a low-density dispersion of scatterers are entirely contained in the (complex) matrix of the refractive index

$$N_{\eta'\eta} = \delta_{\eta'\eta} + \frac{2\pi}{k^2} \sum_i f_{i,\eta'\eta} ; \quad (1)$$

where

$$f_{i,\eta'\eta} = f_{i,\eta} \doteq \hat{e}_{\eta'}^* ,$$

$f_{i,\eta}$  being normalized forward-scattering amplitude of the  $i$ -th scatterer when the polarization vector of the incident radiation is  $\hat{e}_{\eta}$ . In fact, the refractive index and the extinction coefficient of the dispersion are related to the diagonal elements of  $N$  through the equations

$$n_\eta = \text{Re}[N_{\eta\eta}] , \quad \alpha_\eta = 2k\text{Im}[N_{\eta\eta}] , \quad (2)$$

respectively. As equation (1) stems from the assumption that for sufficiently low density only single scattering processes may occur, the  $f_{i\eta}$ 's are those of the independent scatterers. However, if the effect of the multiple scattering processes is non negligible, equation (1) still applies but the  $f_{i\eta}$ 's are to be modified to account of the presence of all the other scatterers. We will show how this can be done with reference to a low-density dispersion of identical spherical particles.

In the absence of multiple scattering processes the amplitude  $f$  of one of the spheres, say the  $i$ -th, is given by

$$f_{i,\eta\eta'} = - \frac{i}{4\pi k} \sum_p \sum_{lm} |W_{\eta'lm}^{(p)}|^2 R_{lm}^{(p)} , \quad (3)$$

where the  $W_{\eta'lm}^{(p)}$ 's are the multipole amplitudes of the incident plane wave and the  $R_{lm}^{(p)}$ 's are the customary Mie amplitudes for a single sphere: the superscript  $p$  is a parity index that distinguishes the magnetic multipoles ( $p = 1$ ) from the electric ones ( $p = 2$ ).

Let us now assume that another sphere, say the  $j$ -th, happens to be at the vector distance  $\mathbf{R}_{ji}$  from the  $i$ -th. All the multiple scattering processes that may occur between these two scatterers can be fully accounted for by considering the two particles as a single compound scatterer of the kind we studied in our preceding papers [11,12]. As a consequence, characterizing with a prime the quantities associated with the  $i$ -th particle in the presence of the  $j$ -th, eq. (3) can be rewritten as

$$f'_{i,\eta\eta'} = - \frac{i}{4\pi k} \sum_p \sum_{lm} W_{\eta'lm}^{(p)*} A_{\eta lm}^{(p)ij} , \quad (4)$$

where the  $A_{\eta lm}^{(p)ij}$ 's are the multipole amplitudes of the field scattered by the  $i$ -th particle, considered as part of an aggregate, and are given in ref. [11,12]. It may be useful to emphasize that the amplitudes  $A_{\eta lm}^{(p)ij}$  depend on the separation of the spheres as well as on the orientation of the aggregate with respect to the incident field, but need not be calculated in practice as will be shown below.

We now define the effective scattering amplitude of the  $i$ -th particle in the presence of all the other particles in the dispersion as

$$f_{i,\eta\eta'}^{\text{eff}} = \sum_{j \neq i} f_{ij,\eta\eta'} , \quad (5)$$

and rewrite eq. (1) as

$$N_{\eta\eta'} = \delta_{\eta\eta'} + \frac{2\pi}{k^2 V} \sum_i f_{i,\eta\eta'}^{\text{eff}} ;$$

Till now, we operated as if we knew the vector positions of all the spheres in the dispersion. Since this is not true, we can perform an average over the distribution of the particles through the method of the reduced distribution functions [14]. Let us, indeed rewrite  $f_{i,\eta\eta'}^{\text{eff}}$  as

$$f_{i,\eta\eta'}^{\text{eff}} = f_{i,\eta\eta'} + \sum_{j \neq i} \Delta f'_{ij,\eta\eta'} , \quad (6)$$

with

$$\Delta f'_{ij,\eta\eta'} = f'_{ij,\eta\eta'} - f_{i,\eta\eta'} . \quad (7)$$

Now, if  $g(\mathbf{R}_{12})$  is the pair correlation function appropriate to the density at hand, the averaged effective amplitude of the dispersion turns out to be

$$\langle f_{\eta\eta'}^{\text{eff}} \rangle = \rho \int f_{1,\eta\eta'} d\mathbf{r}_1 + \rho^2 \int \int \Delta f'_{12,\eta\eta'}(\mathbf{R}_{12}) g(\mathbf{R}_{12}) d\mathbf{r}_1 d\mathbf{r}_2 , \quad -(8)$$

where we define

$$f_{\eta\eta'}^{\text{eff}} = \sum_i f_{i,\eta\eta'}^{\text{eff}}$$

and the argument  $\mathbf{R}_{12}$  has been added to  $\Delta f'_{12,\eta\eta'}$  to recall that this quantity depends on the relative position of the  $i$ -th particle with respect to the  $j$ -th. Furthermore, we notice that  $f_{1,\eta\eta'}$  does not depend on the position of the particle 1 and that, since  $g(\mathbf{R}_{12})$  depends only on the magnitude  $\mathbf{R}_{12}$ , the double integral in eq. (8) is equivalent to two separate averages, one over the separation and the other over the orientation of the pairs. We are able to perform this

latter average analytically as explained in full detail in ref. [13] and get, as a result, an amplitude that is still in the form of eq.(4) but for the substitution of the  $A'_{\eta m}^{(p)ij}$ 's with their averages. Indicating the quantities averaged over the orientations with  $\bar{J}'_{12,\eta\eta'}(R)$  we arrive at the final result

$$N_{\eta\eta'} = \delta_{\eta\eta'} \left\{ 1 + \frac{2\pi}{k^2} \rho \left[ f'_{\eta\eta'} + \frac{1}{2} \rho \int_{r_0}^{\infty} \Delta \bar{J}'_{12,\eta\eta'}(R) g(R) R^2 dR \right] \right\} . \quad (9)$$

As anticipated in section 1 and in agreement with the general results of statistical mechanics[14], equation (9) shows at once that, in the presence of two-body multiple scattering processes, the effective scattering amplitude of the particles contain a correction that depends on the square of the density.

### 3. Application to metal particles

We will now apply the theory of the preceeding section to a dispersion of spherical metal particles. As our aim is to show that the correction term in eq. (9) produce visible effects we choose for the dielectric function of the particles the free-electron Drude form

$$\epsilon = 1 - \frac{\omega_p^2}{\omega(\omega + i\Gamma\omega_p)}$$

The parameters of our calculation are those appropriate for silver particles ( $\omega_p = 5.7 \div 10^{15} \text{ sec}^{-1}$ ,  $\Gamma = 0.01$ ) with radius  $r_0 = 5 \div 10^{-8} \text{ m}$  and a size parameter  $kr_0 = 0.01$ ; thus the wavenumber of the incident radiation  $k = 2 \div 10^6 \text{ m}^{-1}$  and the ratio  $\frac{\omega}{\omega_p} \sim 0.01$ . In fig 1 we report the function  $\text{Im}[\Delta \bar{J}'_{12,\eta\eta'}]$ , hereafter referred to as  $\Delta f$  for short, as a function of the separation of the spheres. It is apparent that  $\Delta f$ , though small, is quite comparable with  $f$  itself for small separations. The figure also shows that, as expected,  $\Delta f$  becomes very small for an interparticle separation of the order of  $10^{-5} \text{ m}$ . In practice we were able to extend our calculations only up to an interparticle distance of  $R_i = 0.146 \div 10^{-4} \text{ m}$  i.e. up to  $292 r_0$ , because for larger distances some numerical instabilities start to occur. Now, according to eq. (9),  $\Delta f$  must be integrated to infinity after multiplication by the pair correlation function. This latter, in the range of densities we are interested in, can be taken as

$$g(r) = \begin{cases} 1 & r \geq r_0 \\ 0 & r < r_0 \end{cases}$$

so that, for the convergence of the integral,  $\Delta f$  must go to zero faster than  $R^{-2}$ . To clarify this point we attempted an extrapolation of the computed results on the assumption of a dependence on  $R$  of the form  $a \exp(bR)$ , starting from the last 5 calculated points before the appearance of the instabilities. We found that when  $a = -2.8 \cdot 10^6$  and  $b = 2.64 \cdot 10^{27}$  the correlation coefficient equals 1. This results allows us to state that the integral from  $R$ , to  $\infty$  is quite negligible and that we can confidently rely on the calculated values. Therefore, we report in Fig. 2 the correction to the extinction coefficient as a function of the packing fraction of the dispersion in the form

$$\Delta\alpha_\eta = \frac{\alpha_\eta}{\alpha_\eta^{(V)}} - 1 = \frac{\rho}{2} \frac{\text{Im} \left\{ \int_{r_0}^{\infty} \Delta T'_{12,\eta\eta}(R) R^2 dR \right\}}{\text{Im} \left\{ f_{1,\eta\eta} \right\}} = A\rho \quad (10)$$

i.e. as a ratio to the extinction coefficient of a dispersion of independent spheres with the same density. Fig. 2 shows that the influence of the two-body multiple scattering effects on the extinction coefficient may be considerable and is, in any event, non-negligible except at very low densities. This may seem surprising on account of the asymptotic behavior of  $\Delta f$  that goes to zero, with increasing separation, faster than  $R^{-2}$ . This asymptotic behaviour is necessary to ensure the convergence of the integral in eq. (10) and confirms that the interparticle effects become negligible for separations  $\sim 50r_0$ . Nevertheless, when  $R$  increases, the number of the particles that may interact with a given one increases even more thus yielding the results of fig. 2.

In conclusion, although the method presented in this paper may appear as an heuristic one, it can be shown to be equivalent to a truncation of *Twersky's* equation to the term including pair interactions. It is to be emphasized, however, that our method is based on the imposition of the correct boundary conditions at the surface of both the components of the pair. Therefore, all the multiple scattering processes that can arise between two bodies are included in our calculations, although these processes are of an order higher than the second order term that is actually included in the *Twersky* series. More precisely, our approach includes all the even order terms involving two bodies. It is just this limitation that restricts the applicability of our approach to low-density dispersions. Extension of our procedure to higher densities, would require the inclusion

of the three-body terms, at least, and would thus an undue - and perhaps impractical - increase of the computational effort.

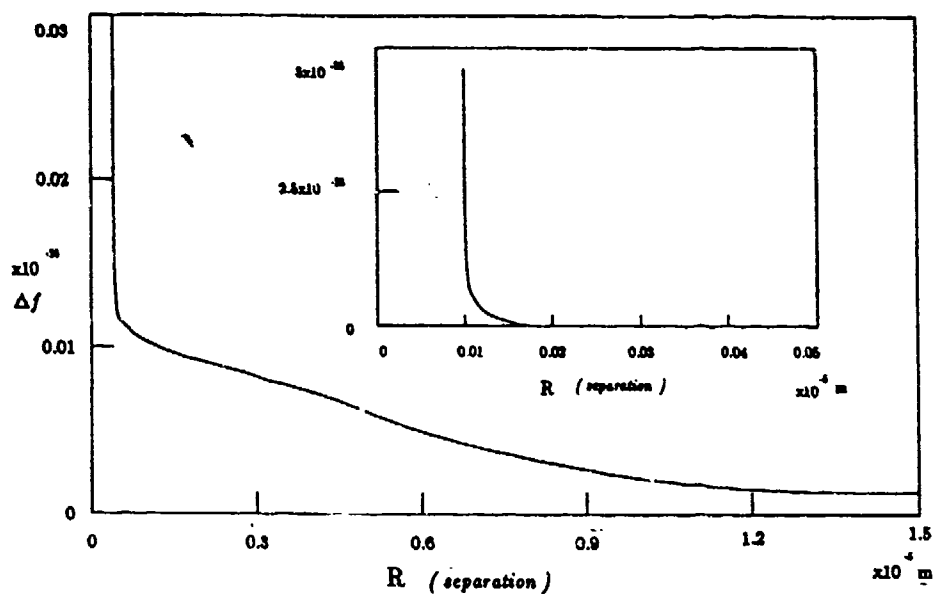


figure 1: Dependence of  $\Delta f$  on  $R$  for a pair of silver particles

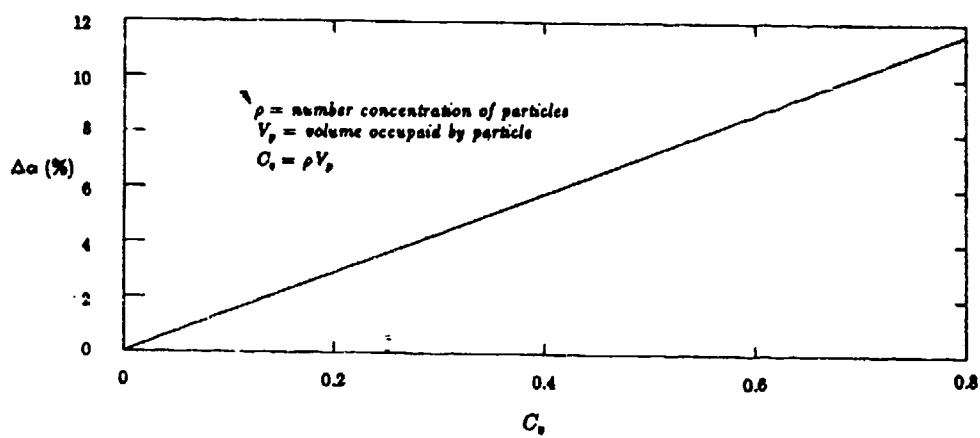


figure 2: Correction to the extinction coefficient  $\Delta\alpha$

## References

- [1] W. Lamb, D. M. Wood and N. W. Ashcroft: *Long-wavelength electromagnetic propagation in heterogeneous media*, Phys. Rev. B **21**, 2248-2266 (1980)
- [2] M. Lax: *Multiple scattering of waves*, Rev. Mod. Phys. **23**, 287-310 (1951)
- [3] V.K. Varadan, V. N. Bringi and V. V. Varadan: *Coherent electromagnetic wave propagation through randomly distributed dielectric scatterers*, Phys. Rev. D **19**, 2480-2489 (1979)
- [4] G. A. Niklason, C. G. Grandqvist and O. Hunderi: *Effective medium models for the optical properties of inhomogeneous materials*, Appl. Opt. **20**, 26-30 (1981)
- [5] D. Stroud and F. P. Pan: *Self-consistent approach to electromagnetic wave propagation in composite media: Application to model granular metals*, Phys. Rev. B **17**, 1602-1610 (1978)
- [6] P. Chylek and V. Srivastava: *Dielectric constant of a composite inhomogeneous medium*, Phys. Rev. B **27**, 5098-5106 (1983)
- [7] F. Borghese, P. Denti, R. Saija and O. I. Sindoni: *An enhanced Bruggeman model and the percolation threshold of a dispersion of metal particles*, Submitted to JOSA (1990)
- [8] R. G. Newton: *Scattering theory of waves and particles* (Mc Graw-hill, New York, 1966)

- [9] H. C. van de Hulst: *Light scattering by small particles* ( Wiley, New York 1957 )
- [10] L. P. Bayvel, A. R. Jones, *Electromagnetic scattering and Its applications* ( Applied Science, London 1981 )
- [11] F. Borghese, P. Denti, R. Saija, G. Toscano and O. I. Sindoni: *Multiple electromagnetic scattering from a cluster of spheres. I. Theory*, Aerosol Sci. Technol. **3** , 227-235 (1984)
- [12] O. I. Sindoni, F. Borghese, P. Denti, R. Saija, G. Toscano: *Multiple electromagnetic scattering from a cluster of spheres. II. Symmetrization*, Aerosol Sci. Technol. **3** , 237-243 (1984)
- [13] F. Borghese, P. Denti, R. Saija, G. Toscano and O. I. Sindoni: *Macroscopic optical constants of a cloud of randomly oriented nonspherical scatterers*, Nuovo Cimento **81** , 29-50 (1984)
- [14] R. Balescu: *Equilibrium and non equilibrium statistical mechanics*, ( Wiley, New York, 1975 )



# AEROSOL SIZE DISTRIBUTION INFERRED FROM LIDAR MULTIPLE SCATTERING MEASUREMENTS

Avishai Ben-David  
Science and Technology Corporation  
Edgewood, MD 21040 U.S.A.

Yair Benayahu and Shlomo Fastig  
Soreq Nuclear Research Center  
Yavne, 70600 Israel

Ariel Cohen  
Hebrew University  
Jerusalem, 91904 Israel

## ABSTRACT

Inversion of multiwavelength backscattering lidar signals can, in theory, provide the aerosol size distribution. However, the inversion results are restricted to a very thin optical medium for which a single-scattering approximation is valid, and it is extremely difficult to measure simultaneously backscattered lidar signals of more than a few wavelengths. A method for measuring lidar multiple scattering with a simple geometry is presented. In this method a detector measures alternately the total scattering (single and multiple) and the multiple scattering alone. The single wavelength range-resolved measurements (when the multiple scattering is approximated as double scattering) contain information about the aerosol size distribution through the double scattering phase function. A method to recover the aerosol double scattering phase function and its aerosol size distribution is shown.

## 1. INTRODUCTION

In optically dense media, such as clouds and fogs, multiple scattering makes a significant contribution to the measured backscattered lidar signal. While the presence of multiple scattering in lidar measurements causes difficulties in the interpretation of the lidar backscattered signal (which is based on a single-scattering approximation), it does provide an additional piece of information, when it can be separated from the single-scattering contribution. An example of this difficulty is the fact that the coefficient deduced from the single scattering lidar equation is much smaller than the true extinction coefficient (Pal and Carswell, 1976). However, depolarization due to multiple scattering (Pal and Carswell, 1976; Cohen, 1975; and Allen and Platt, 1977) can give information on the phase of the cloud particles.

Information about the aerosol size distribution is important in many different areas of the atmospheric sciences (Prospero et al., 1983; Herman et al., 1971; and Toon and Pollack, 1976). Most methods used in the last decade for inferring aerosol size distributions as a local property of a scattering volume involved spectral backscattered and extinction measurements obtained by a monostatic lidar (Capps et al., 1982; Ben-David et al. 1988; Zuev and Natts, 1983; Ben-David and Herman, 1985; and Reagan and Herman, 1972).

Multiwavelength backscattered measurements contain much information (Dave, 1971; and Twomey and Howell, 1967) about the aerosol size distribution. For multiwavelength measurements, several detectors, amplifiers, wavelength-dependent

optics, and the exact energy calibration for each wavelength, are needed. Therefore, in practice it is extremely difficult to measure simultaneously the backscattered lidar return of more than a few wavelengths, and those are usually restricted to a relatively narrow range of wavelength.

In this paper, we present a method for measuring range resolved single and multiple scattering in one wavelength with one detector. We show how these measurements can be used to obtain the double scattering phase function of the aerosols from which the aerosol size distribution function can be inferred.

## 2. MULTIPLE SCATTERING MEASUREMENTS

Experimentally, few measurements have been made of the multiple-scattering contribution to the backscattered signal of a pulsed lidar system (Allen and Platt, 1977; Ryan, et al., 1979; Carswell and Pal, 1980; and Pal and Carswell, 1985). In these measurements, spatial filters in the focal plane of the receiver were used to block the receiver field of view (FOV) corresponding to the diverging transmitted beam. Consequently, the measured signal was a result of multiple-scattering effects originating from the spatial volume outside the blocked FOV only. The multiple scattered measured signal contained contributions of multiple-scattered photons that were scattered in all scattering angles, the last scattering event of which was within the unblocked spatial volume.

Our measuring technique makes it possible to simultaneously measure total (single and multiple) scattering and multiple scattering alone, and by controlling the geometry of the system we can determine the multiple-scattering region. The main parts of the measuring system are given in Fig. 1a. The laser transmits a pulse within a divergence angle  $\alpha$  in two directions  $\phi_1$  and  $\phi_2$  at time  $t$  and  $t + \Delta t$  respectively ( $\Delta t$  depends on the laser pulse repetition rate). The angle  $\phi_1$  must be within the telescope FOV  $S$ . The angle  $\phi_2$  can be outside the telescope FOV. In the following description, we will assume the more general situation where  $\phi_2$  is within the telescope FOV. The two directions are set by the rotation range of the prism which deflects the laser pulses. In the focal plane of the telescope (i.e., the receiver), there is an aluminum plate with two holes,  $s_1$  and  $s_2$ . The FOV of each hole is  $s$  and the angular distance between the centers of  $s_1$  and  $s_2$  is  $d$  such that  $\alpha < s < d$ . The locations of the holes  $s_1$  and  $s_2$  are set such that at a time  $t$  (laser position at  $\phi_1$  [Fig. 1b]), the photon multiplier (PM), which is viewing the hole  $s_1$  only, will detect a signal. The signal consists of single-scattering contributions within the laser beam divergence  $\alpha$  and a multiple-scattering contribution from the spatial volume determined by the FOV of hole  $s_1$  around the laser beam divergence  $s > \alpha$ . The signal detected at the time  $t$  is noted as the signal  $g_1$  (single and multiple scattering). At time  $t + \Delta t$  (laser position at  $\phi_2$  [Fig. 1c]), the single-scattered photons will go through hole  $s_1$ . The multiple-scattered photons detected by the PM will be only those that were redirected from direction  $\phi_2$  into the FOV  $s$  of hole  $s_1$ , which is an angular distance  $d$  away from  $\phi_2$ . The signal detected at time  $t + \Delta t$  is noted as a multiple-scattered signal  $g_2$ , because there must be at least two scattering events to redirect photons from direction  $\phi_2$  into the FOV of  $s_1$ . In practice it is difficult to restrict the FOV of the PM to  $s$  around  $s_1$ , therefore hole  $s_2$  is kept closed. In this way, the PM will view only photons passing through hole  $s_1$ .

If a homogeneous and steady state scattering medium for the measuring time scale is assumed, we can regard the measured signal as a time sequence of

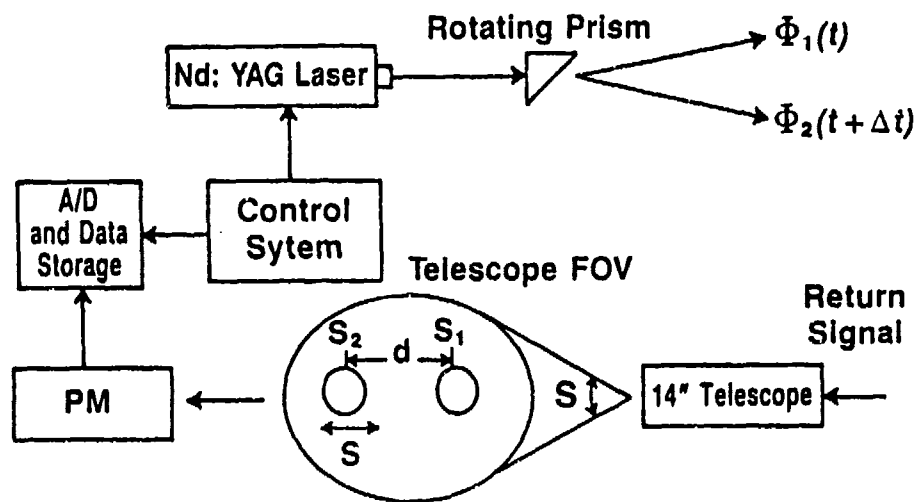


Fig. 1-a. Schematic of the lidar system for multiple scattering measurements.

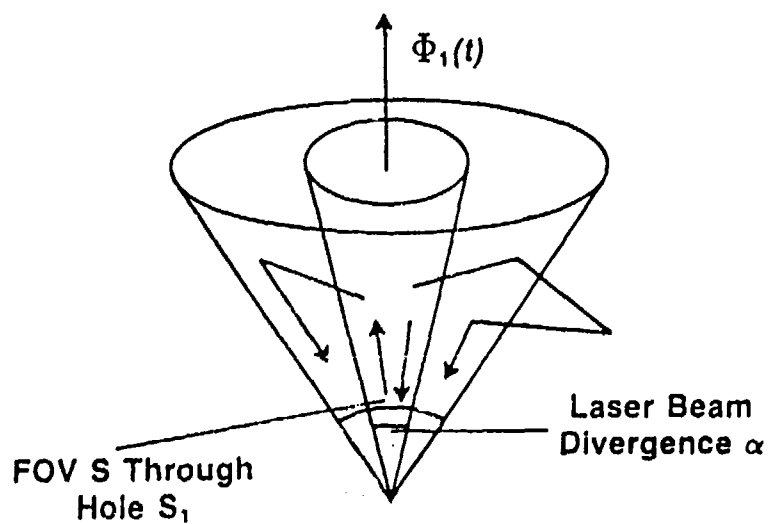


Fig. 1-b. The lidar system at time  $t$ , pointing at direction  $\Phi_1$ .

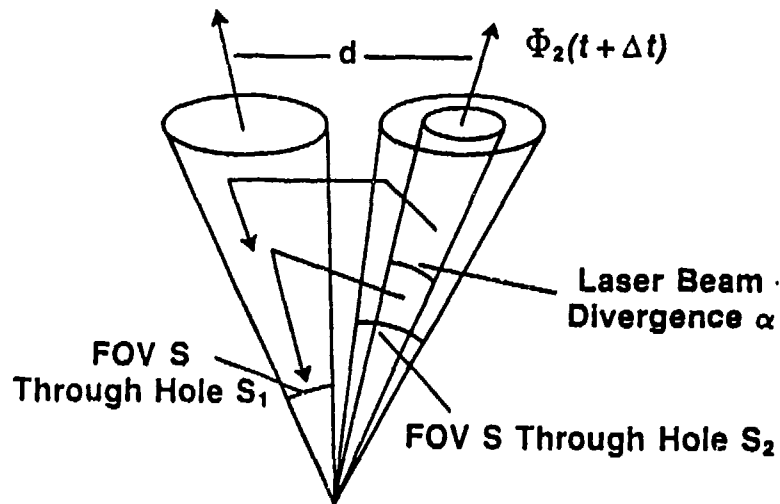


Fig. 1-c. The lidar system at time  $t + \Delta t$ , pointing at direction  $\Phi_2$ .

signal  $g_1$ , consisting of both single scattering and multiple scattering, and  $g_2$ , consisting of multiple scattering only. The multiple-scattering component measured at laser position  $\Phi_1$  is different from the multiple-scattered component measured at laser position  $\Phi_2$  because of the different geometry (scattering angles) for the two. However, if the FOV  $s$  is not much larger than the beam divergence  $\alpha$ , it is expected that the multiple-scattered contribution for laser position  $\Phi_1$  will be much smaller than the multiple-scattered contribution detected in the measured signal for laser position  $\Phi_2$ .

In the experiment the laser beam divergence  $\alpha$  and the FOV  $s$  of the hole  $s_1$  are small compared to the distance between the directions  $\Phi_1$  and  $\Phi_2$  (Fig. 1-a) at a distance  $R_0$  from the laser, so that the geometry of the lidar system can be greatly simplified, as shown in Fig. 2. In this figure, the spatial volumes of holes  $s_1$  and  $s_2$  are shown as two narrow cylinders separated by the distance  $D = dR_0$ . At a time  $t + \Delta t$  (position  $\Phi_2$  of the laser), the laser pulse propagates along the left-hand cylinder and the detector will measure the return signal along the right-hand cylinder. The height location  $R_0 + Z_{ss}$  is the height where a single-scattering event took place when the laser was directed at direction  $\Phi_1$  (i.e., the laser beam was in the FOV of the detector). The time corresponding to this scattering event is  $t' = 2(R_0 + Z_{ss})/c$  where  $c$  is the speed of light. In this figure, the detector at  $s_1$  will measure scattering events of the order 2 (double scattering) and higher. In the case of double scattering, the first scattering event, scattering angle  $\theta_1$ , will take place at height  $R_0 + Z_1$ , along the left-hand cylinder. The second scattering event, scattering angle  $180 - \theta_1$  back to the PM, will take place at a height  $R_0 + Z_2$  along the right-hand cylinder. From the lidar measurements  $g_1(t')$  and  $g_2(t')$  for each laser position  $\Phi_1$  and  $\Phi_2$  (where  $t' < \Delta t$  is a time between laser pulses before the laser changes its position), we can obtain the total return signal  $g_1(t')$  from location  $R_0 + Z_{ss}$  and the multiple scattering (mainly double scattering for the range of the

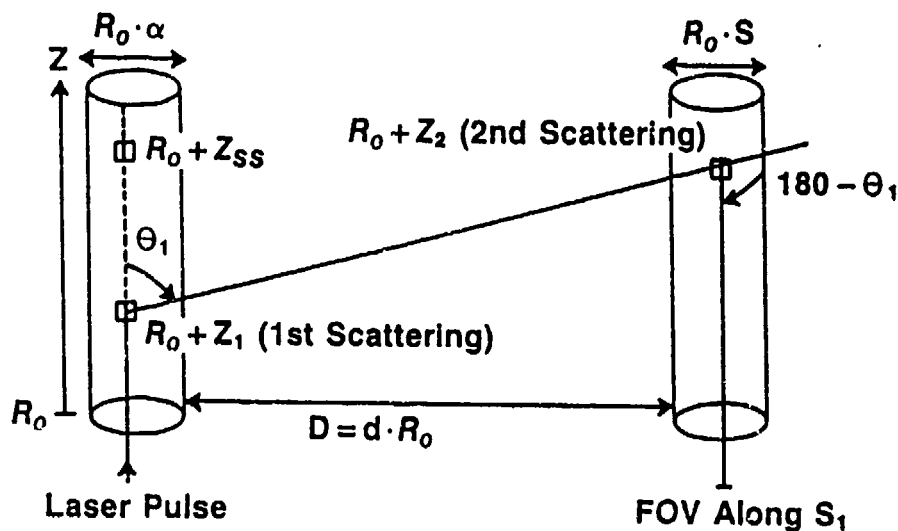


Fig. 2. A simplified geometry for the lidar system at position  $\phi_2$ .

optical depth of interest) signal,  $g_2(t')$ , for the first scattering event at height  $R_0 + Z_1 < R_0 + Z_{ss}$  and the second scattering event at  $R_0 + Z_2 = R_0 + Z_1 + D/\tan(\theta_1)$  along the right-hand cylinder. The scattering angle  $\theta_1$  as a function of  $Z_{ss}$  and  $D$  (for all  $Z_1 < Z_{ss}$ ), for which  $t' = 2(R_0 + Z_{ss})/c$  is given by:

$$\theta_1 = 2 \tan^{-1} \left( \frac{D}{2(Z_{ss} - Z_1)} \right) \quad (1)$$

For  $\theta_1 > 90^\circ$ ,  $Z_1$  must be  $Z_1 < -D/\tan(\theta_1) < Z_{ss}$  (i.e., the second scattering will occur above  $R_0$ ). As the laser pulse penetrates the scattering medium (as  $Z_{ss}$  increases), the range of  $Z_1$  that can contribute to the double scattering measured at lidar position  $\phi_2$  will increase as will the range of scattering angles  $\theta_1$  that will contribute to double scattering for which  $t' = 2(R_0 + Z_{ss})/c$ . The range of  $\theta_1$  as a function of single scattering location  $Z_{ss}$  within the scattering medium for a constant  $D = 10$  m is shown in Fig. 3.

The same experiment can be made without a rotating prism if the laser is directed at direction  $\phi_1$ , and two PMs, two amplifiers, and two A/Ds are used to detect the received signal through the two holes  $s_1$  and  $s_2$ . In our experiment we chose to use a rotating prism (rotating back and forth) and therefore used only one PM, amplifier, and A/D, which received the return signal through hole  $s_1$  while hole  $s_2$  remained closed.

Figure 4 shows preliminary measurements for the geometry  $d = 1$  mrad,  $\alpha = 0.5$  mrad, and  $R_0 = 6$  km. The lidar pulse width is 10 nsec; the pulse repetition rate is 20 Hz (i.e.,  $\Delta t = 50$  msec) and the electronic integration time is 150 nsec. The measurements were averaged over 6 sec (i.e., 60 pulses in each direction  $\phi_1$  and  $\phi_2$ ). The first curve (square symbols), in relative

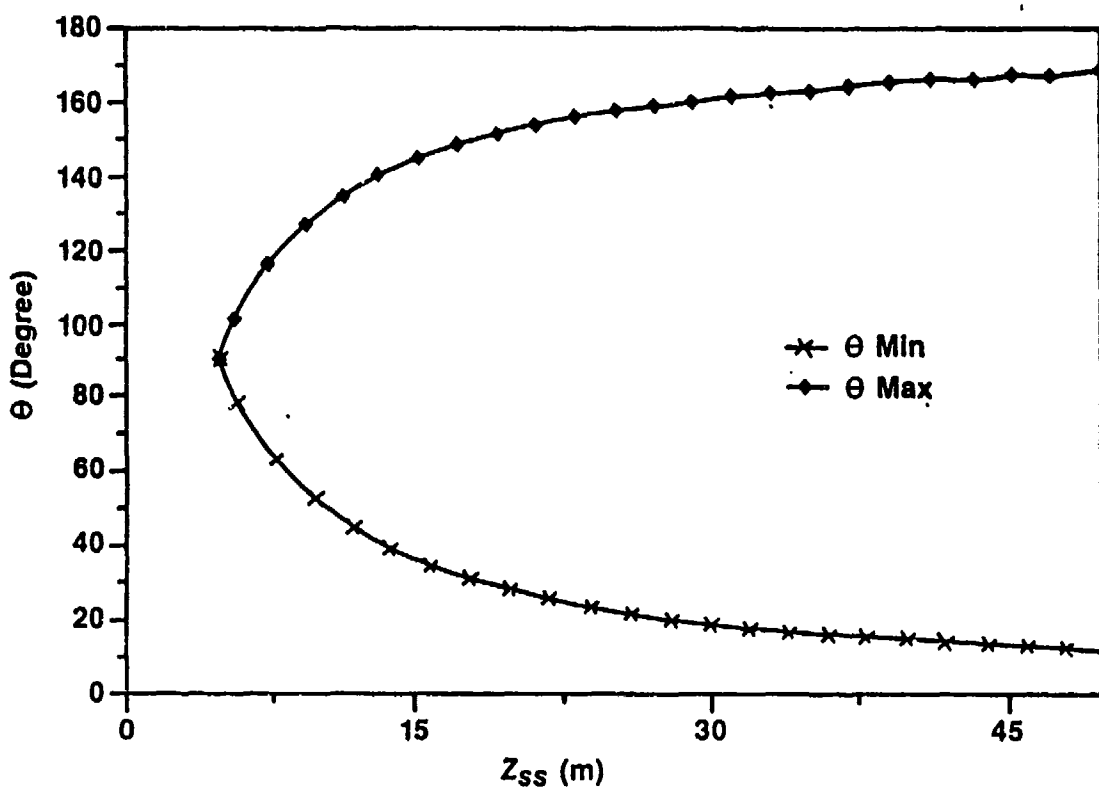


Fig. 3. The range of scattering angles (all angles between  $\theta_{\text{min}}$  and  $\theta_{\text{max}}$ ) that contribute to double scattering returns as a function of single scattering location  $Z_{ss}$  for  $D = 10$  m.

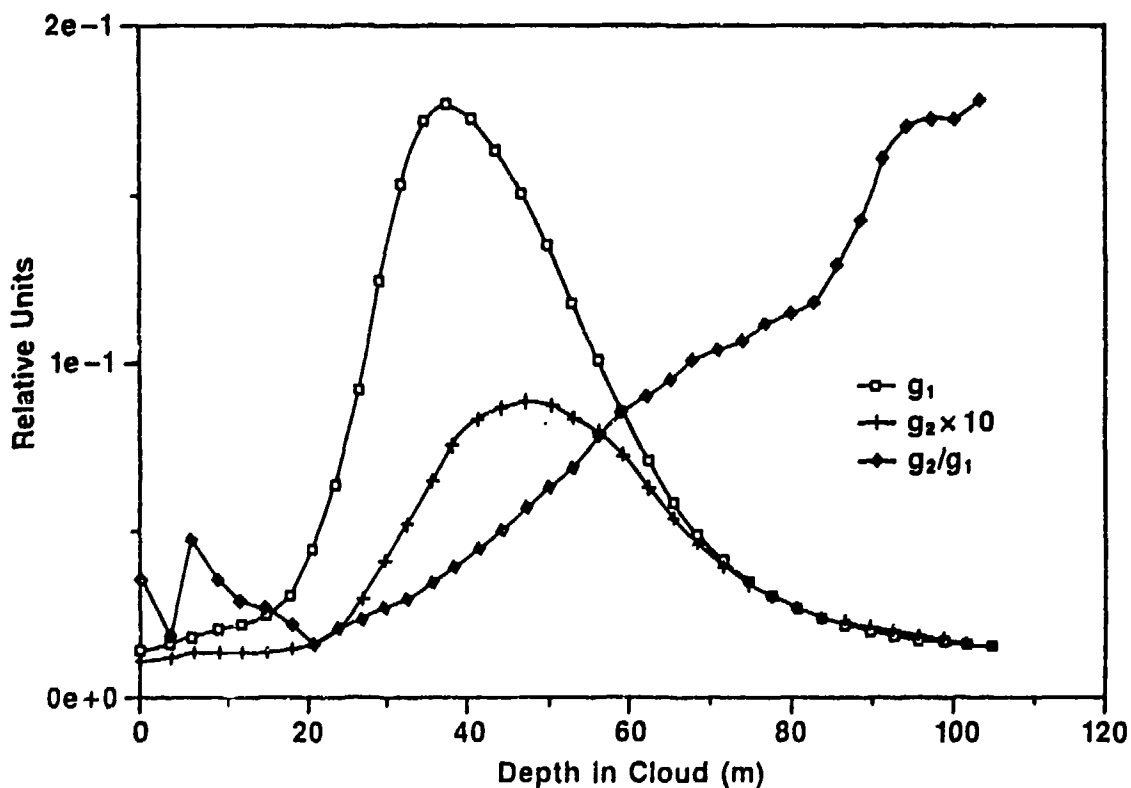


Fig. 4. Measurements for lidar position  $\Phi_1$  and  $\Phi_2$  ( $g_1$  and  $g_2$ ), taken on 10-30-88 at 17:08 for a cloud at  $R_0 = 6$  km as a function of penetration depth within the cloud.

units, is the measured signal  $g_1$ , when the lidar was pointing at  $\phi_1$ . If the cloud edge was well defined and the cloud was a homogeneous scattering medium, the signal would have dropped off monotonically as a function of  $R_0 + Z_{ss}$ . However, in our experiment, the cloud edge was not well defined and the integration time of the system corresponded to about 20 m. Therefore, the total scattering curve  $g_1$  increases with penetration depth until  $Z_{ss} = 40$  m and then falls off with increasing  $Z_{ss}$ . The second curve (plus symbols), in the same relative units times 10, shows the multiple-scattering signal  $g_2$  measured when the laser was directed in the  $\phi_2$  direction. This curve shows that the multiple scattering increases as the pulse penetrates the cloud. For  $Z_{ss} > 50$  m, the two-way attenuation dominates the contribution of the multiple scattering and the measured signal decreases with increased penetration depth. The third curve (diamond symbols) shows the interesting effect of the increased contribution of the multiple scattering, representing the ratio between the multiple scattering for laser position  $\phi_2$  to the total scattering for laser position  $\phi_1$  (i.e.,  $g_2/g_1$ ) as a function of penetration depth in the cloud. In the first 20 m, the multiple-scattering signal is very weak and therefore the signal-to-noise ratio is poor as reflected by the oscillations in this curve.

A set of measurements was conducted in order to ensure that, when the lidar is pointing at  $\phi_2$ , there is no single scattering measured by the detector which is only 1 mrad away from  $s_2$  (the angular distance between the center of  $s_1$  and the center of the laser beam). It was concluded that less than 1% of the single scattering from direction  $\phi_2$  will be measured by the detector. Therefore, the second curve of Fig. 4 ( $g_2$ ) contains, at most, a 1% contribution due to the laser beam cross-section profile (which is not zero at angular distances larger than  $\alpha$ ).

### 3. AEROSOL SIZE DISTRIBUTION AS INFERRED FROM DOUBLE-SCATTERING MEASUREMENTS

One of the main possible applications for our method is in deducing the aerosol size distribution of a dense homogeneous scattering medium. The aerosol size distribution can be deduced from a double scattering phase function that can be obtained from measurements  $g_2(t')$ . The double-scattering contribution to the multiple-scattering measurements for different locations of  $Z_{ss}$  can be written as:

$$g_2(t' = 2(R_0 + Z_{ss})/c) = \int_{\theta_{\min}(Z_{ss})}^{\theta_{\max}(Z_{ss})} K(Z_{ss}, \theta) P(\theta) P(180 - \theta) d\theta \quad (2)$$

where  $\theta_{\max}$  and  $\theta_{\min}$  can be taken from Fig. 3, and  $P(\theta)$  is the phase function for the medium. From Eq. (2) we can see that the range of integration over  $\theta$  is a function of the penetration depth  $Z_{ss}$  (i.e., a function of  $t'$ ) in the cloud. Therefore, from the measurements  $g_2(Z_{ss})$ , we can, in principle, obtain the double scattering phase function  $P(\theta) P(180 - \theta)$ , which contains information about the average aerosol size distribution in the cloud as shown below.  $K(Z_{ss}, \theta)$  is a weighting function for the path travelled by a photon, which was scattered at an angle  $\theta$  from the first scattering event and at an angle  $(180 - \theta)$  after the second scattering event, and accounts for the relative sizes of the scattering volumes involved. We note that when the penetration depth into the cloud is small, the double-scattering contribution to the multiple-scattering measurements is dominant. The phase function is given by:

$$P(\theta) = \int_r Q_s(r, \theta) n(r) dr \quad (3)$$

where  $Q_s(r, \theta)$  is the differential scattering cross section at an angle  $\theta$  for an aerosol of radius  $r$ , and  $n(r)$  is the aerosol number density distribution function.

The quantity  $P(\theta) P(180 - \theta)$  describes the nonlinear interaction of single scattering from a particle of radius  $r_1$  at a scattering angle  $\theta$ , with a second scattering at an angle  $(180 - \theta)$  from a particle of radius  $r_2$ . This process is given in Eq. (4):

$$P(\theta) P(180 - \theta) = \int_{r_1} \int_{r_2} Q_s(r_1, \theta) Q_s(r_2, 180 - \theta) n(r_1) n(r_2) dr_1 dr_2 \quad (4)$$

This equation can be used to solve for the aerosol number density  $n(r)$  distribution by using Newton Raphson's iterative technique (Courant and Hilbert, 1953).

Based on Eq. (2), a mathematical inversion technique can now be used in order to compute an average value of  $P(\theta) P(180 - \theta)$  for different scattering angles  $\theta$ ; for  $Z_{ss} = D/2$  ( $= 5$  m in Fig. 3) the multiple-scattering measurements  $g_2(Z_{ss})$  will consist of double scattering arising only from the  $\theta = 90$  at the cloud base,  $R_0$  (i.e.,  $Z_1 = 0$ ). As a result, we can compute from  $g(Z_{ss} = D/2)$  of Eq. (2) an average value  $\bar{P}(90)^2$  for  $P(90)^2$ . For the next  $Z_{ss}$ , such as  $Z_{ss} = 7.5$  m in Fig. 3, the double scattering events will spread over the range of  $\theta$  between approximately 80 and 100. The measurements  $g(Z_{ss} = 7.5)$  can thus be approximated with Eq. (2) to give:

$$g_2(Z_{ss} = 7.5) = K(Z_{ss}, 90) \bar{P}(90)^2 2\Delta + \int_{80}^{90-\Delta} K(Z_{ss}, \theta) P(\theta) P(180 - \theta) d\theta \\ + \int_{90+\Delta}^{100} K(Z_{ss}, \theta) P(\theta) P(180 - \theta) d\theta \quad (5)$$

where  $\Delta$  is the angular range for which  $P(\theta) = P(90)$  for  $(90 - \Delta < \theta < 90 + \Delta)$ . Equation (5) can be solved for an average value for  $P(85) P(95)$  using  $P(90)^2$  from the measurements  $g(Z_{ss} = D/2)$  using Eq. (6):

$$g(Z_{ss} = 7.5) = \bar{P}(90)^2 K(Z_{ss}, 90) 2\Delta \\ + P(85) P(95) \left[ \int_{80}^{90-\Delta} K(Z_{ss}, \theta) d\theta + \int_{90+\Delta}^{100} K(Z_{ss}, \theta) d\theta \right] \quad (6)$$

By using this process, we can find average values for  $P(\theta) P(180 - \theta)$  from the multiple-scattering measurements as a function of  $Z_{ss}$ .

The numerical technique for obtaining the double scattering phase function can be greatly simplified analytically by using the symmetry of the geometry of Fig. 2. For an arbitrary single-scattering location  $Z_{ss}$ , the scattering angle  $\theta_1$  at  $Z_1 = 0$  is equal to the scattering angle  $\pi - \theta_1$  for the location  $Z_1 = Z_{max}$ . The scattering angle  $\theta$  is given by:

$$\theta = 2 \tan^{-1} \left[ \frac{D}{2(Z_{ss} - Z_1)} \right] \bigg|_{Z_1=Z_{max}} = \pi - 2 \tan^{-1} \left[ \frac{D}{2(Z_{ss} - Z_1)} \right] \bigg|_{Z_1=0} \quad (7)$$



$Z_{\max}$  is the farthest location on the left-hand cylinder (Fig. 2) from which a double-scattered photon will arrive at the detector at the same time as a backscattered photon from a location  $Z_{ss}$ , and is given by:

$$Z_{\max} = \frac{D}{\tan \left[ 2 \tan^{-1} \left( \frac{D}{2 Z_{ss}} \right) \right]} \quad (8)$$

The double-scattering signal  $g_2(Z_{ss})$  that arrives at the detector at the same time as a backscattered signal from height  $Z_{ss}$  can be written as:

$$g_2(Z_{ss}) = A e^{-2\sigma Z_{ss}} \int_0^{Z_{\max}} P(\theta) P(180 - \theta) \frac{\sin^2(\theta)}{D^2} dZ_1 \quad (9)$$

where  $D / \sin(\theta)$  is the radial distance between  $Z_1$  and  $Z_2$  of Fig. 2;  $A$  is a constant that includes the factor  $1 / R_0^2$  and other system parameters; and  $\sigma$  is the volume extinction coefficient of the medium.

Multiplying Eq. (9) by  $e^{+2\sigma Z_{ss}}$ , taking a derivative with respect to  $Z_{ss}$ , and using the identity  $\frac{\partial f(\theta)}{\partial Z_{ss}} = -\frac{\partial f(\theta)}{\partial Z_1}$  from Eq. (1) we obtain:

$$\begin{aligned} \frac{\partial}{\partial Z_{ss}} \left[ g_2(Z_{ss}) e^{+2\sigma Z_{ss}} \right] = & - \int_0^{Z_{\max}} \frac{\partial}{\partial Z_1} \left[ P(\theta) P(180 - \theta) \frac{\sin^2(\theta)}{D^2} \right] dZ_1 \\ & + P(\theta) P(180 - \theta) \frac{\sin^2(\theta)}{D^2} \frac{\partial Z_{\max}}{\partial Z_{ss}} \bigg|_{Z_1=Z_{\max}} \end{aligned} \quad (10)$$

The first integral of the right-hand side of Eq. (9) is zero as can be shown by using the symmetry between  $\theta_{\min}$  and  $\theta_{\max}$  (i.e.,  $\theta_{\min}$  at  $Z_1 = 0$  is  $180 - \theta_{\min} = \theta_{\max}$  at  $Z_1 = Z_{\max}$ ).

Rearranging Eq. (10) and noting that  $Z_{\max}$  is a continuous function of  $Z_{ss}$  (Eq. (8)) as is  $\theta$  (Eq. (7)), we can write the double scattering phase function as:

$$\begin{aligned} & P \left[ \theta(Z_{ss} - Z_{\max}) \right] P \left[ 180 - \theta(Z_{ss} - Z_{\max}) \right] \\ & = \frac{\frac{\partial}{\partial Z_{ss}} \left[ g_2(Z_{ss}) e^{+2\sigma Z_{ss}} \right] D_2}{\sin^2 \left[ \theta(Z_{ss} - Z_{\max}) \right] \frac{\partial Z_{\max}}{\partial Z_{ss}} \bigg|_{Z_1=Z_{\max}}} \end{aligned} \quad (11)$$

Thus given the double-scattering measurements  $g_2(Z_{ss})$  and the volume extinction coefficient  $\sigma$ , the double scattering phase function of the scattering medium can be computed.

In our experiment, the cloud was not homogeneous (Fig. 4) and therefore the inferred double scattering phase function contained large errors, as did the recovered aerosol size distribution through the Newton Raphson iterative algorithm. In Fig. 5 we present results of the inferred aerosol size distribution functions, as obtained from simulated double scattering phase function of a homogeneous cloud model  $C_1$  (Deirmendjian, 1969) with  $\sigma = 17 \text{ km}^{-1}$ , wavelength of  $1.06 \mu\text{m}$ , and a real refractive index of 1.34. The phase function was averaged over 10-degree intervals. This figure shows the inferred aerosol size distribution for various rms errors in the simulated measurements. We can see that the main features of the aerosol size distribution function were recovered reasonably well.

#### 4. SUMMARY

In this paper, we have presented a method for measuring simultaneously multiple and total scattering (mainly single scattering) with a monostatic one wavelength lidar system and one detector. This method is relatively simple and can be used to contribute to the few multiple-scattering measurements of an optically dense medium. The multiple-scattering measurements (when approximated as double scattering) contain information about the aerosol size distribution through the double scattering phase function. The double scattering phase function can be computed from the range resolved multiple-scattering measurements. A Newton Raphson iterative algorithm is used to recover the aerosol size distribution function from the double scattering phase function. The main features of the distribution were recovered reasonably well for simulated rms errors up to 7%.

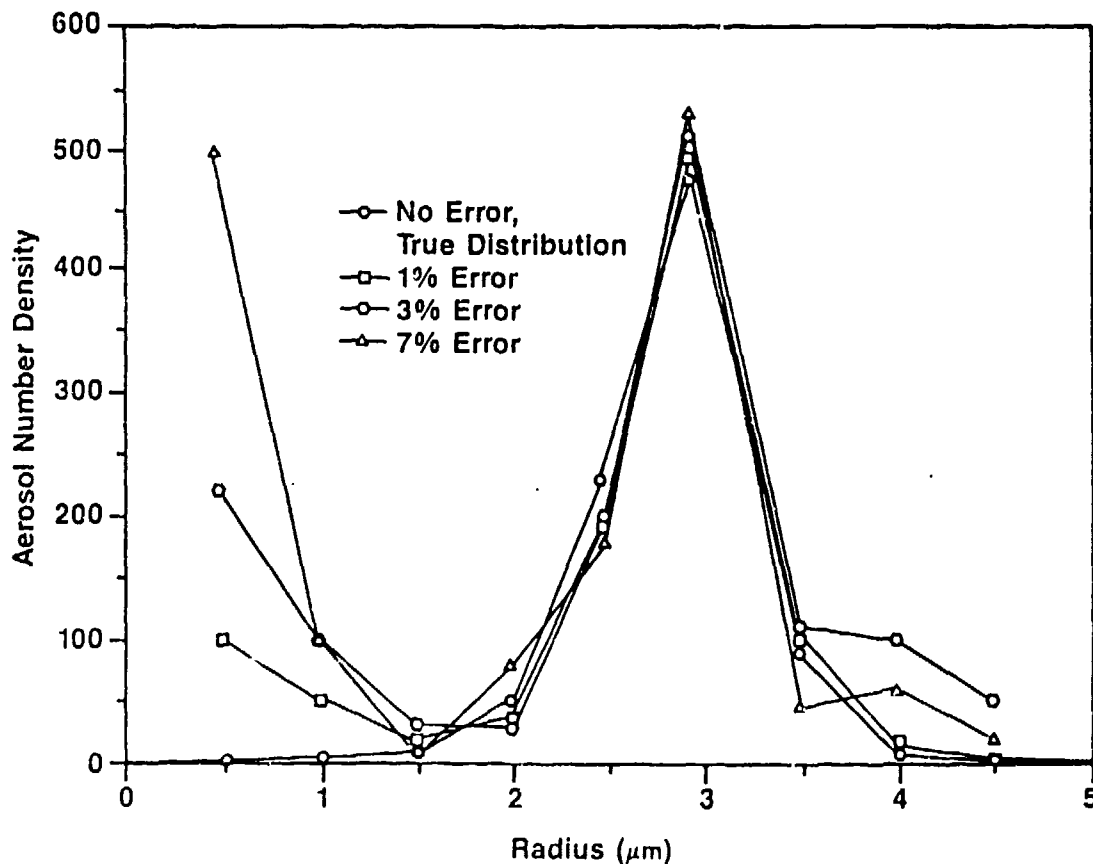


Fig. 5. Aerosol size distribution function as obtained from an inversion of simulated double scattering measurements of various rms errors.

## ACKNOWLEDGMENT

The authors thank A. Englander of Soreq Nuclear Research Center for his help in writing the programs for data acquisition.

## REFERENCES

- Allen, R.J., and C.M.R. Platt, 1977: "Lidar for Multiple Backscattered and Depolarization Observations," Appl. Opt. 16, 3193-3199.
- Ben-David, A., and B.M. Herman, 1985: "Method for Determining Particle Size Distributions by Nonlinear Inversion of Backscattered Radiation," Appl. Opt. 24, 1037-1042.
- Ben-David, A., B.M. Herman, and J.A. Regan, 1988: "Inversion Problem and the Pseudoempirical Orthogonal Function Method of Solution 2: Use," Appl. Opt. 27, 1243-1254.
- Capps, C.D., R.L. Henning, and G.M. Hess, 1982: "Analytic Inversion of Remote Sensing Data," Appl. Opt. 21, 3581-3587.
- Carswell, A.I., and S.R. Pal, 1980: "Polarization Anisotropy in Lidar Multiple Scattering from Clouds," Appl. Opt. 19, 4123-4126.
- Cohen, A., 1975: "Cloud-Base Water Measurement Using Single Wavelength Laser-Radar data," Appl. Opt. 14, 2873-2877.
- Courant, R., and D. Hilbert, 1953: Method of Mathematical Physics, Vol. 1, Interscience, New York, 561 pp.
- Dave, J.D., 1971: "Determination of Size Distribution of Spherical Poydispersion Using Scattered Radiation Data," Appl. Opt. 10, 2035-2044.
- Deirmendjian, D., 1969: Electromagnetic Scattering on Spherical Polydispersions, American Elsevier, New York, 240 pp.
- Herman, B.M., S.R. Browning, and J.K. Curran, 1971: "The Effect of Atmospheric Aerosols on Scattered Sunlight," J. Atmos. Sci. 28, 419-428.
- Pal, S.R., and A.I. Carswell, 1976: "Multiple Scattering in Atmospheric Clouds: Lidar Observation," Appl. Opt. 15, 1990-1995.
- Pal, S.R., and A.I. Carswell, 1985: "Polarization Anisotropy in Lidar Multiple Scattering from Atmospheric Clouds," Appl. Opt. 24, 3464-3471.
- Prospero, J.M., R.J. Charlson, V. Mohnen, R. Jaenicke, A.C. Delany, J. Moyers, W. Zoller, and K. Rahn, 1983: "The Atmospheric Aerosol System: An Overview," Rev. Geophys. Space Phys. 21, 1607-1629.
- Reagan, J.A., and B.M. Herman, 1972: "Three Optical Methods for Remotely Measuring Aerosol Size Distributions," AIAA 10, 1401-1407.
- Ryan, J.S., S.R. Pal, and A.I. Carswell, 1979: "Laser Backscattering from Dense Water Droplet Clouds," J. Opt. Soc. 69, 60-67.

Toon, O.B., and J.B. Pollack, 1976: "A Global Average Model of Atmospheric Aerosols for Radiative Transfer Calculations," J. Appl. Meteorol. 15, 225-246.

Twomey, S., and H.B. Howell, 1967: "Some Aspects of the Optical Estimation of Microstructure in Fog and Cloud," Appl. Opt. 6, 2125-2131.

Zuev, V.E., and I.E. Natts, 1983: Inverse Problems of Lidar Sensing of the Atmosphere, Springer-Verlag, Berlin, 260 pp.

## **FRACTAL ELECTRODYNAMICS: A NOVEL METHOD TO EXAMINE ROUGH SURFACE SCATTERING**

Xiaoguang Sun and Dwight L. Jaggard

Complex Media Laboratory  
Moore School of Electrical Engineering  
University of Pennsylvania  
Philadelphia, PA 19104-6390

### **RECENT PUBLICATIONS AND SUBMITTAL FOR PUBLICATIONS:**

- A) D. L. Jaggard and X. Sun, "Reflection from Fractal Multilayers," *Optics Lett.*, **16**, No. 24 (1990).
- B) D. L. Jaggard and X. Sun, "Fractal Surface Scattering: A Generalized Rayleigh Solution," *J. Appl. Phys.*, **68**, 5456-5462 (1990).
- C) D. L. Jaggard, "On Fractal Electrodynamics," in *Recent Advances in Electromagnetic Theory*, H. N. Kritikos and D. L. Jaggard, Editors, Springer-Verlag, New York (1990).
- D) X. Sun and D. L. Jaggard, "Scattering from Non-random Fractal Surfaces," *Optics Comm.*, **78**, 20-24 (1990).
- E) X. Sun and D. L. Jaggard, "Scattering from Fractally Fluted Cylinders," *J. Electromag. Waves Appl.*, **4**, 599-611 (1990).
- F) D. L. Jaggard and X. Sun, "Scattering from Fractally Corrugated Surfaces," *J. Opt. Soc. Am. A*, **7**, 1131-1139 (1990).
- G) D. L. Jaggard and X. Sun, "Scattering from Bandlimited Fractal Fibers," *IEEE Trans. Ant. Propag.*, **37**, 1591-1597 (1989).
- H) Y. Kim, H. Grebel and D. L. Jaggard, "Diffraction by Fractally Serrated Apertures," to appear in *J. Opt. Soc. Am. A* (1991).
- I) X. Sun and D. L. Jaggard, "Generalized Cantor Bar Fractal Multilayers: Reflection and Transmission," submitted for publication.
- J) D. L. Jaggard, Y. Kim and N. Cho, "Transients in a Fractal Slab," submitted for publication.

### **ABSTRACT**

We consider electromagnetic or optical wave scattering from fractal surfaces and structures. These surfaces are modelled by a continuous bandlimited fractal function, namely the roughness fractal function. Kirchhoff and generalized Rayleigh approaches are respectively used for scattering from rough fractal surfaces of a finite extend. Rayleigh-Gans approximation and perturbation expansions are used for scattering form fractally corrugated cylinders. Ongoing work concerns calculations of higher order and formulations valid in extended regimes of frequency and roughness.

## INTRODUCTION

The fractal concept was first popularized from the coastline problem [1]. In this problem, the length or perimeter of a rough coastline is measured by yardsticks of variable length. However, this perimeter increases as the measuring yardstick decreases due to the fact that increasingly fine structure of the coastline can be measured or "seen" as the yardstick becomes shorter. A fractal dimension is introduced [1] to quantify the roughness by the rate at which the perimeter increases with decreasing yardstick size.

In the problem of wave interaction with fractally rough surfaces, the wavelength of the incident wave acts as a yardstick which probes the fractal nature of the rough surfaces at different scales as its size is varied [C,G]. In this way, the increasingly fine structure of the rough objects can be "seen" as the wavelength becomes shorter. The fractal characteristics of these objects are embedded in the variation of their scattering properties as the wavelength is changed.

We consider the scattering of electromagnetic waves from a family of irregular rough objects characterized by bandlimited fractal functions such as the bandlimited Weierstrass function. This method provides a unified and realistic novel method for examining rough objects without the use of random functions and averaging techniques. In this manuscript, we first discuss various continuous fractal functions and their fractal dimensions. The Kirchhoff approach to scattering from fractally corrugated surfaces is then presented as an example. We explain the relations between the geometrical properties of multi-scaled fractal surfaces and its wave scattering properties through angular or frequency scattering pattern. More detailed analysis on this example is available in Ref. [F].

Fractal electrodynamics is a blend of electromagnetic theory with fractal geometry. Our work in wave interactions with fractal objects includes wave scattering from a family of canonical fractal objects such as fractally corrugated surfaces, fractally corrugated cylinders, and fractally fluted cylinders. The undisturbed incident field method is used in each case. In particular a generalized Rayleigh approach is used for scattering from fractally rough surfaces in Ref. [B] as a complement to the Kirchhoff approach used here. For cylindrical geometry, we studied wave scattering from fractally corrugated (longitudinal variation) cylinder in Ref. [G] using Rayleigh-Gans approximation while the scattering properties of fractally fluted (cross sectional variation) cylinders are treated in Ref. [E] through perturbation expansions. We found analytical expressions and carried out numerical calculations for these fractal scattering problems. In each investigation,

we relate the angular or frequency distribution of the scattering field to the fractal descriptors including the fractal dimension of these objects.

The work reported here and in Ref. [B,C,D,E,F,G] are concerned with continuous fractal models. Our recent work [A] considering the reflection and transmission properties of discrete fractal multilayers forms its complement. In the next section, different continuous fractal models are discussed and compared.

## FRactal Models

The *Weierstrass function* was discussed by Mandelbrot [1] and has the fractal properties of multiple scales and self-similarity. It is an infinite summation of weighted exponential terms and can be written as,

$$W(x) = \sum_{n=-\infty}^{\infty} b^{(D-2)n} (1 - e^{ib^n x}) . \quad (b > 1) \quad (1)$$

The real or imaginary part of (1), taken by itself, is also a self-similar fractal function. The self-similarity of the Weierstrass functions can be demonstrated by the relation,

$$W(bx) = b^{(2-D)} W(x) . \quad (2)$$

These Weierstrass functions are self-similar on all scales, from the infinitesimal to the infinitely large. This originates the unbounded nature of Weierstrass functions. It can be shown that the derivatives of Weierstrass functions are also unbounded, with the possible exception at some discrete points. In conclusion, these Weierstrass functions are everywhere continuous, almost everywhere unbounded, and almost nowhere differentiable.

Although the Weierstrass functions are mathematically interesting, their unbounded nature makes them impractical for use in modeling physical objects. Since every physical object has an inner and an outer scale. A *bandlimited Weierstrass function*, which truncates the summed terms to a finite number, was then introduced [2]. This modified version of the Weierstrass function is self-similar on a finite regime of size orders and bounded. After normalization with regard to the function variance, it reads,

$$W_B(x) = \eta \frac{\sqrt{2} [1 - b^{(2D-4)}]^{1/2}}{[b^{(2D-4)N_1} - b^{(2D-4)(N_2+1)}]^{1/2}} \sum_{n=N_1}^{N_2} b^{n(D-2)} \cos(2\pi s b^n x + \phi_n), \quad (3)$$

where  $s$  is the size scaling parameter,  $b$  ( $b > 1$ ) is the frequency scaling parameter, the  $\phi_n$  are randomly selected phases, and  $\eta$  is the standard deviation or rms height of the function defined by,

$$\eta^2 = \langle W_B(x)^2 \rangle = \lim_{L \rightarrow \infty} \frac{1}{2L} \int_{-L}^L W_B(x)^2 dx. \quad (4)$$

It can be shown that this bandlimited Weierstrass function (3) has zero mean, that is

$$\langle W_B(x) \rangle = \lim_{L \rightarrow \infty} \frac{1}{2L} \int_{-L}^L W(x) dx = 0. \quad (5)$$

The total number of tones or harmonics is  $N_2 - N_1 + 1$ .

We consider here an equivalent zero-mean bandlimited fractal function, denoted the *roughness fractal function* expressed as a weighted sum of periodic functions,

$$f_r(x) = \eta C \sum_{n=0}^{N-1} a^n \sin(\kappa b^n x + \phi_n) \quad (6)$$

where  $a$  ( $0 < a < 1$ ) is the amplitude scaling parameter,  $\kappa$  is the fundamental spatial wavenumber,  $b$  ( $> 1$ ) is the frequency scaling parameter, the  $\phi_n$  are arbitrary phases, and  $N$  is the number of tones.

The amplitude normalization factor,

$$C = \sqrt{\frac{2(1 - a^2)}{(1 - a^{2N})}} \quad (7)$$

is chosen so that the function (6) has a standard deviation or rms height  $\eta$  in the sense of (4). This function has a finite band of spatial frequencies and exhibits self-similarity over a corresponding finite range of resolution. The amplitude scaling parameter  $a$  in the function gives a measure of the surface roughness ranging from  $a = 0$  (smooth periodic curve) to  $a = 1$  (rough, area-filling curve). Note that the sine function in (6) can be replaced by other periodic functions. One of the discrete



fractal function is obtained by replacing the sine function by a periodic rectangular function. We discuss the fractal dimensions of these different fractal models in the following section.

## **FRACTAL DIMENSIONS**

In each one of the fractal functions discussed in the previous section, the periodic functions of increasing frequency in the summation produce the fine structure. As in the coastline problem, finer and finer structure of the function can be measured when the measuring "yardstick" becomes shorter and shorter. The rate at which the measured quantity increases as the measuring yardstick decreases is quantified by the fractal dimension, a measure of curve roughness. Usually several fractal dimensions are appropriate for a given fractal curve, each characterizing a different physical process.

We first discuss the fractal dimension of the Weierstrass functions. Traditionally, the parameter  $D$  ( $1 < D < 2$ ) in the Weierstrass functions (1) is denoted the *Weierstrass fractal dimension*. When  $D \rightarrow 2$ , weights for all exponential terms in the summation are unity. The corresponding curves are area-filling due to the large amplitude high frequency components. It coincides with our physical intuition. In the other limit  $D \rightarrow 1$ , however, a contradiction arises. At this limit, relation (2) reads,

$$W(bx) = b W(x), \quad (8)$$

which indicates the scaling on both horizontal and vertical axes are the same. Therefore, at  $D = 1$ , the Weierstrass functions do not reduce to smooth one-dimensional geometry, rather it has perfect self-similarity. The corresponding curve is still somewhat rough. Its measured perimeter will become longer and longer when shorter and shorter yardstick are used, hence from the yardstick concept we expect its fractal dimension to be larger than one. Note that Weierstrass functions (1) are well defined and do not have sudden changes on  $(-\infty < D < 2)$ . These functions become smooth as  $D \rightarrow -\infty$ .

A smooth curve is one-dimensional while an area is two dimensional in the sense of Euclidean dimension. Intuitively, we expect the fractal dimension as a measure of curve roughness to fill this gap, varying continuously from one-dimensional for smooth curves to two-dimensional for area-filling rough curves in the sense of fractal dimension. For the roughness fractal function (6), we use  $D_r (= 1 + a)$  as the *roughness fractal dimension* which varies from  $D_r = 1$  for smooth

sinusoidal to  $D_f = 2$  for area-filling rough. This fractal dimension provides a good measure for curve roughness and is suitable for the study of rough surface scattering. The Weierstrass fractal dimension  $D$  of function (6) is given by,

$$D = 2 + \frac{\log(a)}{\log(b)} \quad (9)$$

Although the *yardstick fractal dimension* for these fractal functions are not available analytically, numerically we have found that it's different from its corresponding Weierstrass fractal dimension [E]. Note that although different fractal dimensions take on different values for a given fractal function, a larger value in any fractal dimension always corresponds to increased curve roughness.

## SCATTERING FROM FRACTALLY CORRUGATED SURFACES

We consider here the scattering from perfectly-conducting fractally-corrugated rough surfaces. Shown in Fig. 1, the incident plane wave impinges on a one-dimensional rough surface characterized by fractal function  $f_r(x)$  extending from  $x = -L$  to  $x = L$ .

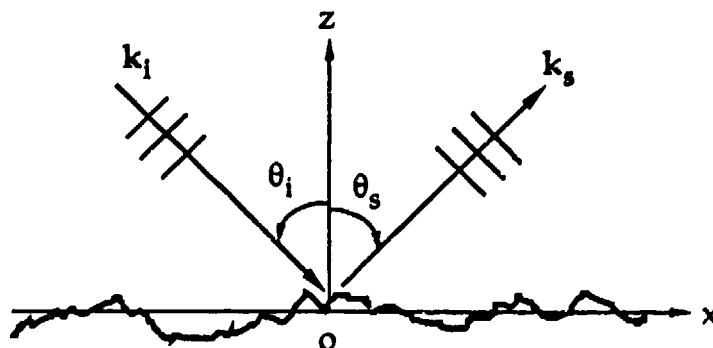


Fig. 1. The geometry of electromagnetic wave scattering in a plane from a rough surface where the subscripts i and s indicate parameters associated with incident and scattered waves, respectively. Here  $k$  represents the wavevector and  $\theta_i = 30^\circ$ .

This problem is formulated by the Kirchhoff approximation [3] with the assumption that the rough surfaces are locally flat. This is satisfied when the wavelength of the incident wave is small relative to the radius of curvature of the surface irregularities. After neglecting the edge effect

and using a Bessel function identity, the closed-form Kirchhoff solution for the scattering coefficient ( $E_{sc}/E_{sc0}$ ) is found to be,

$$\gamma^{\pm} = \pm \sec\theta_i \frac{1 + \cos(\theta_i + \theta_s)}{\cos\theta_i + \cos\theta_s} \times \quad (10)$$

$$\sum_{m_0, m_1, \dots, m_{N-1} = -\infty}^{+\infty} \exp\left(i \sum_{n=0}^{N-1} m_n \phi_n\right) \prod_{n=0}^{N-1} J_{m_n}[C(D-1)^n v_z \sigma] \operatorname{sinc}[(v_x + K_0 \sum_{n=0}^{N-1} m_n b^n)L].$$

where the wave vector projections are given by,

$$v_x = k(\sin\theta_i - \sin\theta_s) \quad (11)$$

$$v_z = -k(\cos\theta_i + \cos\theta_s) \quad (12)$$

and the superscripts + and - denote the perpendicular and parallel polarizations. The sinc function is defined as  $\operatorname{sinc}(x) = \sin(x)/x$ .

Consider large patch sizes ( $L \gg \Lambda_0 = 2\pi/K_0$ ). Expanding Bessel functions for small  $k\eta$ , the scattering coefficient of the fractal surface in the specular direction ( $\theta_i = \theta_s$ ) yields,

$$\gamma^{\pm} \approx \pm [1 - 2(k\eta)^2 \cos^2\theta_i] \quad (13)$$

This equation shows that the decrement in the specular scattering is proportional to the variance of the rough surface. Note that equation (13) is consistent with the result derived for the average scattering coefficient of random surfaces. This shows that only the relative rms height of the surface determines the scattering intensity in the specular direction whether the surface is fractal or random, in the low frequency regime.

We numerically calculate the scattering coefficient  $\gamma$  for different fractal dimensions. Plotted in logarithmic scale, Fig. 2 shows scattering patterns from fractal surfaces of several fractal dimensions with  $b = 2e/3 \approx 1.8122$ ,  $N = 6$ ,  $\theta_i = 30^\circ$ ,  $\eta = 0.05\lambda$ , and  $2L = 40\lambda$ . Each plot in Fig. 2 is the average result of ten members of the ensemble, each with a different set of  $\phi_n$  for  $f_r(x)$ . Two envelopes are indicated in the plots. The background envelope (slope  $\approx -1$ ) is due to the

finite patch size and consists of the specularly reflected main beam and its sidelobes. The coupling lobe envelope (variable slope) is due to surface coupling and consists of the first-order coupling of the surface harmonics. The slope of the coupling lobe envelope is indicative of surface roughness. These slopes are found to be  $-2.50$ ,  $-1.92$ ,  $-1.22$ , and  $-0.72$  for fractal dimensions  $D = 1.05$ ,  $1.30$ ,  $1.50$ , and  $1.70$ , respectively. This implies that the magnitude of slope for our continuous bandlimited fractal surfaces varies approximately as  $2.7(2 - D)$ . The spatial frequency parameter  $b$ , which determines the separation of the spatial frequency of the harmonics, controls the angular separation of the coupling beams in accordance with conservation of momentum.

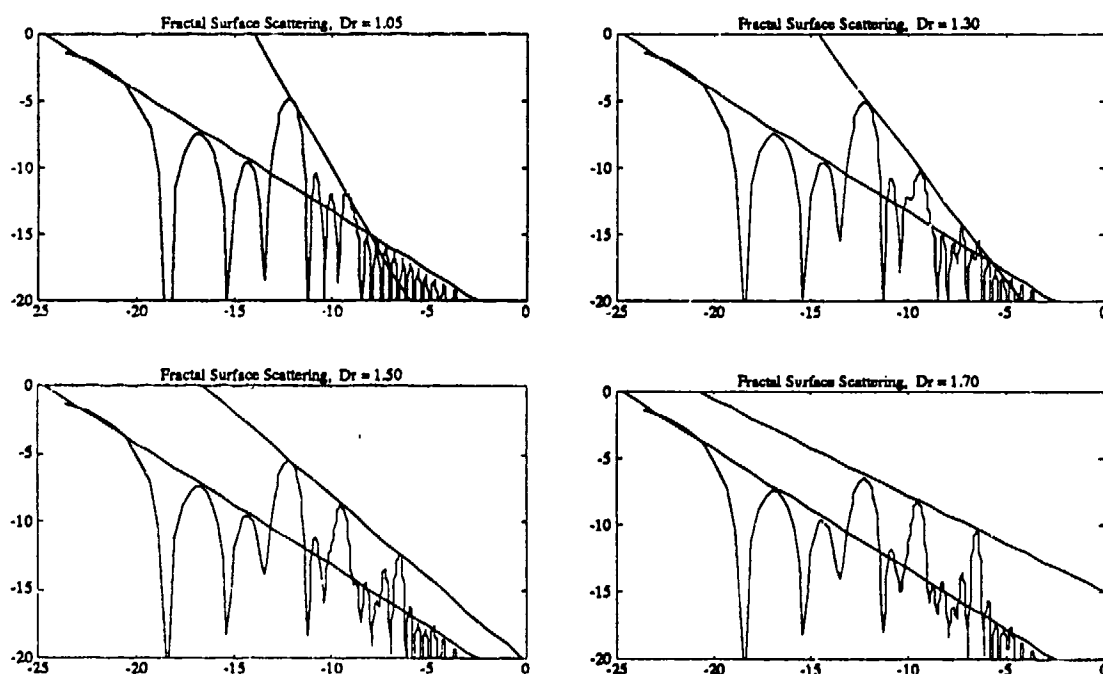


Fig. 2. The average differential scattering coefficient versus  $\sin[(\theta_s - 30^\circ)/2]$ , both in dB scales, for the roughness fractal dimensions  $D_r = 1.05$ ,  $1.30$ ,  $1.50$ , and  $1.70$ , respectively, from upper left to lower right. The envelope slopes of coupling sidelobes vary monotonically with the fractal dimension while the background slope is constant for varying  $D_r$ .

## CONCLUSION

We consider the blend of electromagnetic theory with fractal geometry, denoted *fractal electrodynamics* [C]. Here, we discuss different functions for fractal modelling, and techniques for exploring several problems in fractal electrodynamics. We relate the geometrical surface

roughness to the envelope slope value of scattering sidelobes via the roughness fractal dimension. Both mathematical and physical properties are discussed throughout the investigation.

We note that usually several fractal dimensions are appropriate for a given fractal curve, each characterizing a different physical process. Bandlimited fractal functions are suitable for physical modelling. The Kirchhoff approach for scattering from fractally corrugated surfaces is presented here. This electromagnetic calculation technique used here is a first order approximation applicable to high frequency regime. Low frequency interrogation will provide the average effect (specular reflection) of the scattering surface and is not of interest here. Our future work is on calculations of higher order and formulations of moderate frequency regime. Investigations using other approaches or for different continuous fractal configurations are available in Ref. [B,C,D,E,G,H,I,2,3,4,6]. Recently, wave interactions with discrete fractals are also considered elsewhere [A,I].

## REFERENCES

- [1] B. B. Mandelbrot, *The Fractal Geometry of Nature*, Freeman, San Francisco (1983).
- [2] D. L. Jaggard and Y. Kim, "Diffraction by Bandlimited Fractal Screens," *J. Opt. Soc. Am.*, **A4**, 1055-1062 (1987).
- [3] Y. Kim and D. L. Jaggard, "A Bandlimited Fractal Model of Atmospheric Refractivity Fluctuation," *J. Opt. Soc. Am.*, **A5**, 475-480 (1988).
- [4] Y. Kim and D. L. Jaggard, "Optical Beam Propagation in a Bandlimited Fractal Medium," *J. Opt. Soc. Am.*, **A5**, 1419-1426 (1988).
- [5] P. Beckmann and A. Spizzichino, *The Scattering of Electromagnetic Waves from Rough Surfaces*, Chap. 3, Pergamon, New York (1963).
- [6] X. Sun, "Electromagnetic Wave Scattering from Fractal Structures," *Ph.D. Thesis*, Univ. of Penn. (Dec. 1989), available from UMI International.

BLANK

INDEX A  
Index of Authors

D.R. ALEXANDER, 211, 259	S. FASTIG, 395
R.W. ALEXANDER, 99	L.M. FOLAN, 115
S. ARNOLD, 115, 139	G.R. FOURNIER, 249
E. BAHAR, 379	E.S. FRY, 277
J.P. BARTON, 211, 259	E. FUCILE, 385
R.J. BELL, 99	D.M. GOLDEN, 187
Y. BENAYAHU, 395	A. HADAD, 39
A. BEN-DAVID, 395	S.M. HAUGLAND, 379
F. BORGHESE, 385	G.M. HOLTMEIER, 211
K.H. BOWEN, 143	L.D. HINKLE, 163
H. BRENNER, 29	P. HU, 87
J.R. BROCK, 15, 23, 235, 243	A.L. HUSTON, 165
B.V. BRONK, 47, 139	P.L. JACOBSON, 59
A.J. CAMPILLO, 165, 173	D.L. JAGGARD, 407
J.C. CARLS, 235	R.G. JOHNSTON, 59
J.E. CERMAK, 39	B.J. JURCIK, 15
E.T. CHESWORTH, 131	B.R.F. KENDALL, 131, 163
A. COHEN, 395	L.H. KIDDER, 143
D.K. COHOON, 195, 289, 299, 347, 363	M. LAX, 87
B.P. CURRY, 51	K.H. LEONG, 51
P. DENTI, 385	L. LIEBMAN, 243
J.G. EATON, 143	H.-B. LIN, 165, 173
B.T.N. EVANS, 249	H. LITTMAN, 9
J.D. EVERSOLE, 165, 173	K.M. MCHUGH, 143

A.M. MIDDLEBROOK, 187  
M.H. MORGAN III, 9  
L. NEWQUIST, 99  
G.G. PADMABANDU, 277  
M. POREH, 39  
M.R. QUERRY, 99  
M.A. QUINLAN, 187  
J.M. RAMSEY, 139  
C.M. REIHS, 187  
R. SAIJA, 385  
H.W. SARKAS, 143  
M. SHAPIRO, 29  
O.I. SINDONI, 385  
K.-D. SONG, 211  
D.E. SPOCK, 115  
M. STANLEY, 47  
X. SUN, 407  
M.A. TOLBERT, 187  
W.P. VAN de MERWE, 47  
R. VANDIVER, 99  
J.F. WACKER, 125  
D. WIELSCZKA, 99  
R.T. WANG, 73  
W.B. WHITTEN, 139  
N.G. WIMER, 143



# INDEX B

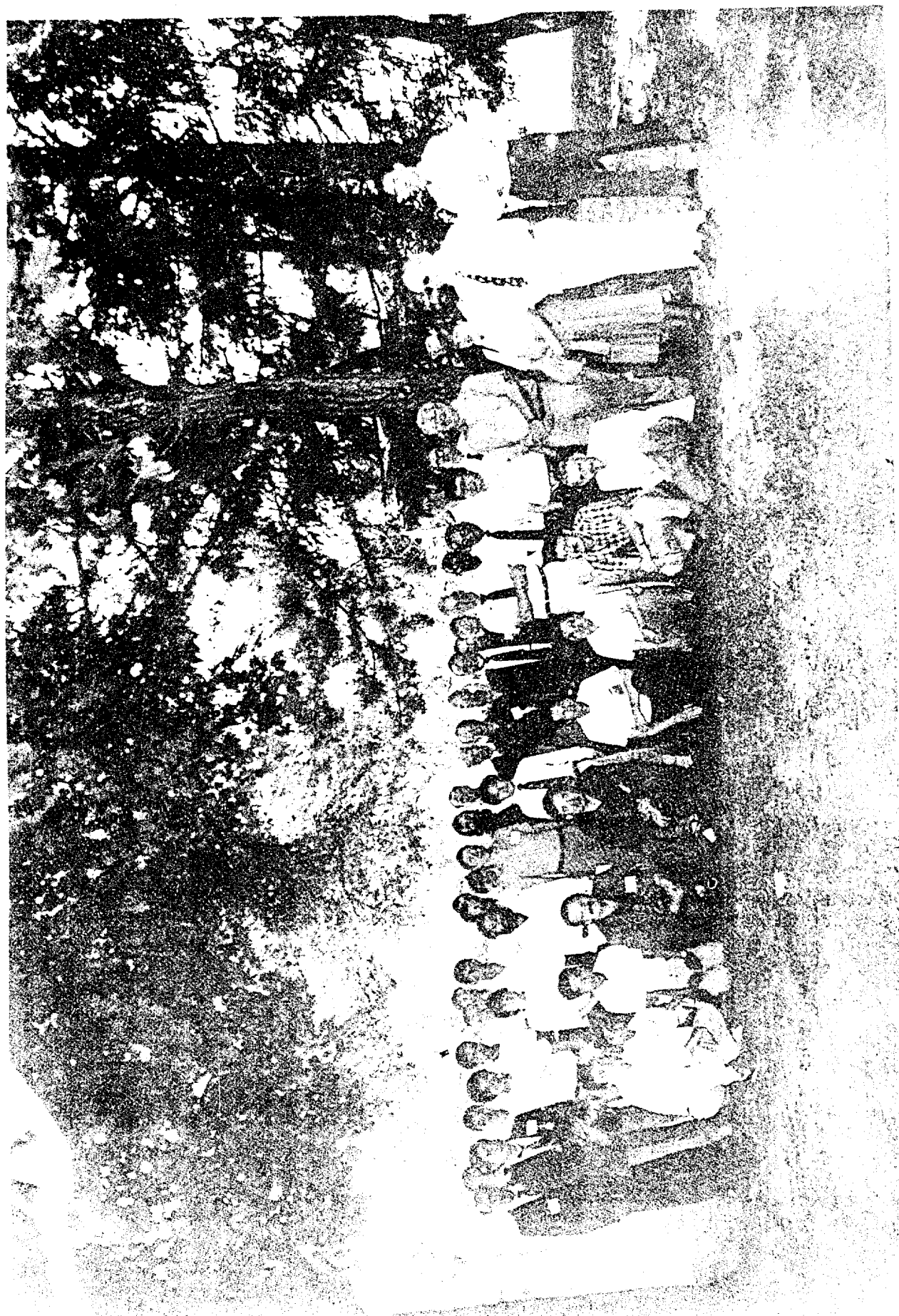
## Index of Authors' Organizations

Argonne National Laboratory	51
Battelle Pacific Northwest Laboratory	125
City College of New York Physics Department	87
Colorado State University	39
Defense Research Establishment Valcartier	249
Greenville College Department of Physics	59
Hebrew University	395
Institute for Space Science & Technology, Inc. Space Astronomy Laboratory	73
Israel Institute of Technology - Technion Faculty of Mechanical Engineering	29, 39
Los Alamos National Laboratory	59
Massachusetts Institute of Technology Department of Chemical Engineering	29
Naval Research Laboratory Optical Sciences Division	165, 173
Oak Ridge National Laboratory	139
Polytechnic Institute of New York	139
Polytechnic University Department of Physics	115
Potomac Photonics, Inc.	173
Rensselaer Polytechnic Institute	9
Science and Technology Corporation	395
Seven Mountains Scientific, Inc.	131
Soreq Nuclear Research Center	395
SRI International Department of Chemical Kinetics	187

Texas A&M University Department of Physics	277
The Aerospace Corporation Infrared Sciences Department	115
The Johns Hopkins University Department of Chemistry	143
The Pennsylvania State University Department of Physics	131, 163
Uniformed Services University of the Health Sciences	47
Universita di Messina Istituto di Struttura della Materia	385
University of Missouri-Rolla	99
University of Missouri-Kansas City Physics Department	99
University of Nebraska-Lincoln College of Engineering Center for Electro-Optics	211, 259
Electrical Engineering Department	379
University of Texas Chemical Engineering Department	15, 23, 235, 243
University of Pennsylvania Moore School of Electrical Engineering Complex Media Laboratory	407
U.S. Army Chemical Research, Development and Engineering Center	47, 139, 385
West Chester University Department of Mathematics	195, 289, 299, 347, 363

APPENDIX A

PHOTOGRAPH OF 1990 CONFERENCE ATTENDEES



1990 CRDEC SCIENTIFIC CONFERENCE ON  
OBSCURATION AND AEROSOL RESEARCH

Pictured from left to right are:

First Row

Maurice Jarzembski  
Vandana Srivastava  
Alfred Kwok  
Claude Phipps  
Steve Arnold  
Edward Stuebing  
Pao K. Wang  
Willem Van De Merwe  
Orazio I. Sindoni

Second Row

Wan Xian Wang  
Gang Chen  
Kim Juvan  
Avishai Ben-David  
Roger Johnston  
Xiaoguang Sun  
Howard Littman  
Madhav Ranade  
Burt Bronk  
Ru Wang  
Melvin Lax  
Louise Ann Liebman  
J. R. Brock

Third Row

John Barton  
Dennis Alexander  
Keng Leong  
Ali Serpenguzel  
Frank Poleski  
Jim Gillespie  
George Ritchie  
Lorcan Folan  
Tony Pluchino  
Kirk Fuller  
Ed S. Fry  
David K. Cohoon  
Robert Armstrong  
Ron Pinnick  
Blair Evans  
Morris Morgan, III  
John Wacker  
Ralph Alexander  
Marc Stanley  
Mark Seaver  
Dee W. Pack

Photo was taken on Wednesday, June 27, 1990

## APPENDIX B

### 1990 CRDEC SCIENTIFIC CONFERENCE ON OBSCURATION AND AEROSOL RESEARCH

#### ATTENDEES LIST

AKINYEMI, AGNES  
(301) 671-5744  
Commander  
US Army Chemical Research,  
Development and Engineering Center  
ATTN: SMCCR-DDT/A. Akinyemi  
APG, MD 21010

ALEXANDER, DENNIS  
(402) 472-3091  
University of Nebraska-Lincoln  
Center for Electro-Optics  
248 WSEC  
Lincoln, NE 68588-0656

ALEXANDER, JR., RALPH  
(314) 341-4781  
University of Missouri-Rolla  
Physics Department  
Rolla, MO 65401

ARMSTRONG, ROBERT L.  
(505) 646-3831  
New Mexico State University  
Dept. of Physics, 3D  
Las Cruces, NM 88003

ARNOLD, STEPHEN  
(718) 260-3085  
Polytechnic Institute of New York  
Dept. of Physics  
333 Jay Street  
Brooklyn, NY 11201

BARTON, JOHN P.  
(402) 472-5081  
University of Nebraska-Lincoln  
Center for Electro-Optics  
248 WSEC  
Lincoln, NE 68588-0656

BEN-DAVID, AVISHAI  
Commander  
US Army Chemical Research,  
Development and Engineering Center  
ATTN: SMCCR-RSL-S/A. Ben-David  
APG, MD 21010

BOWEN, KIT  
(301) 338-8425  
Johns Hopkins University  
Dept. of Chemistry  
Baltimore, MD 21218

BRENNER, HOWARD  
(617) 253-6687  
Massachusetts Institute of  
Technology  
Dept. of Chemical Engineering  
Cambridge, MA 02139

BROCK, JAMES R.  
(512) 471-3348  
University of Texas/Austin  
Dept. of Chemical Engineering  
Austin, TX 78712

BRONK, BURT  
(301) 671-2326  
Commander  
US Army Chemical Research,  
Development and Engineering Center  
ATTN: SMCCR-RSP-B  
APG, MD 21010-5423

BROZENA, ANN  
(301) 671-3833  
Commander  
US Army Chemical Research,  
Development and Engineering Center  
ATTN: SMCCR-RSC-P/A. Brozena  
APG, MD 21010

CAMPILLO, ANTHONY  
(202) 767-2057  
Naval Research Lab  
ATTN: Code 6546/A. Campillo  
Washington, D.C. 20375-5000

CARLON, HUGH  
(301) 671-4106/3058  
Commander  
US Army Chemical Research,  
Development and Engineering Center  
ATTN: SMCCR-RSP-P/H. Carlon  
APG, MD 21010-5423

CARPIN, JOHN  
(301) 671-4716  
Commander  
US Army Chemical Research,  
Development and Engineering Center  
ATTN: SMCCR-RST-E/J. Carpin  
APG, MD 21010-5423

CHANG, RICHARD  
(203) 432-4272  
Yale University  
Dept. of Applied Physics  
P.O. Box 2157, Yale Station  
New Haven, CT 06520

CHEN, GANG  
(203) 432-4235  
Yale University  
Dept. of Applied Physics  
P.O. Box 2157, Yale Station  
New Haven, CT 06520

CHESWORTH, THOMAS  
(814) 466-6559  
Seven Mountains Scientific, INC.  
P.O. Box 650  
Boalsburg, PA 16827

COHEN, ARIEL  
972-2-639003  
Hebrew University  
Dept. of Atmospheric Sciences  
Jerusalem  
Israel

COHOON, DAVID  
(215) 436-2641  
West Chester University  
Dept. of Mathematics  
West Chester, PA 19383

CURRY, WILLIAM  
(708) 972-7683  
Argonne National Lab  
9700 S. Cass Avenue  
Eng Bldg. 207  
Argonne, IL 60439-4841

DAUSER, EDWIN  
(301) 392-3300  
W.L. Gore & Associates  
P.O. Box 1100  
Elkton, MD 21921

DOHERTY, ROBERT  
(301) 671-2326  
Commander  
US Army Chemical Research,  
Development and Engineering Center  
ATTN: SMCCR-RSP-P/ R. Doherty  
APG, MD 21010-5423

EMBURY, JAY  
Commander  
US Army Chemical Research,  
Development and Engineering Center  
ATTN: SMCCR-RSP-B/J. Embury  
APG, MD 21010

ENGQUIST, ELMER  
(301) 676-0200  
Battelle Edgewood Operations  
2113 Emmorton Park Road  
Edgewood, MD 21040

EVANS, BLAIR  
(418) 844-4299  
Defense Research Establish, Valcarti  
2459, PIE XI Blvd., North  
P.O. Box 8800  
Courcelette, Quebec  
GOA, 1R0

EVERSOLE, JAY  
(202) 767-2057  
Naval Research Lab  
ATTN: Code 6546/J. Eversole  
Washington, D.C. 20375-5000

FLANNIGAN, DENNIS  
(301) 671-2760  
Commander  
US Army Chemical Research,  
Development and Engineering Center  
ATTN: SMCCR-RSP-B/ D. Flannigan  
APG, MD 21010-5423

FOLAN, LORCAN M.  
(718) 260-3381  
Polytechnic University  
Dept. of Physics  
333 Jay Street  
Brooklyn, NY 11201

FRICKEL, ROBERT  
Commander  
US Army Chemical Research,  
Development and Engineering Center  
ATTN: SMCCR-RSP-B/R. Fricke1  
APG, MD 21010-5423

FRY, EDWARD  
(409) 845-1910  
Texas A&M University  
Dept. of Physics  
College Station, TX 77843

FULLER, KIRK  
(505) 678-4078  
US Army Atmospheric Sciences Lab  
ATTN: SLCAS-AR-P/K. Fuller  
White Sands Missile Range, NM 88002

GILLESPIE, JAMES B.  
(505) 678-6609  
US Army Atmospheric Sciences Lab  
ATTN: SLCAS-AR-P/J. Gillespie  
White Sands Missile Range, NM 88002

HAUGLAND, S. MARK  
(402) 472-1966  
University of Nebraska-Lincoln  
Dept. of Electrical Engineering  
209N WSEC  
Lincoln, NE 68588-0511

HILL, STEVEN  
(315) 268-3804  
Clarkson University  
ECE Dept.  
Potsdam, NY 13676

HINKLE, LUKE  
(508) 975-2350  
MKS Instruments  
#6 Shattuck Road  
Andover, MA 01810

HU, PO  
(212) 690-6864  
City College of New York  
Dept. of Physics  
Convent Ave. & 138th Street  
New York, NY 10031

JARZEMBSKI, MAURICE  
(205) 544-0240  
NASA/Marshall Space Flight Center  
ES 43/NASA/MSFC  
Huntsville, AL 35812

JOHNSTON, ROGER  
(505) 667-7414  
Los Alamos National Lab  
MS M880  
Los Alamos, NM 87545

JOLLIFFE, ROBERT  
(301) 671-4285  
Commander  
US Army Chemical Research,  
Development and Engineering Center  
ATTN: SMCCR-RSP-P/R. Jolliffe  
APG, MD 21010

JONES, PAULETTE  
(301) 671-4252  
Commander  
US Army Chemical Research,  
Development and Engineering Center  
ATTN: SMCCR-RSP-P/P. Jones  
APG, MD 21010

JURCIK, BENJAMIN  
(512) 471-1328  
University of Texas/Austin  
Dept. of Chemical Engineering  
Austin, TX 78712

JUVAN, KIM  
Graduate Student  
Yale University  
Dept. of Applied Physics  
P.O. Box 2157, Yale Station  
New Haven, CT 06520

KWOK, ALFRED  
(203) 432-4231  
Yale University  
Dept. of Applied Physics  
P.O. Box 2157, Yale Station  
New Haven, CT 06520

LATHAM, JOHN  
061-200-3932  
Dept. of Pure & Applied Physics  
U.M.I.S.T.  
P.O. Box 88, Sackville Street  
Manchester, M60 1QD  
England

LEONG, KENG H.  
(708) 972-3254  
Argonne National Lab  
Eng Bldg 207  
9700 S. Cass Avenue  
Argonne, IL 60439-4841

LETTIERI, THOMAS R.  
(301) 975-3496  
National Institute of Standards and  
Met-A117  
Gaithersburg, MD 20899

LIEBMAN, LOUISE ANN  
(512) 471-1378  
University of Texas/Austin  
Dept. of Chemical Engineering  
Austin, TX 78712

LIN, H.B.  
(202) 757-2057  
Naval Research Lab  
ATTN: Code 6546/H.B. Lin  
Washington, D.C. 20375-5000

LITTMAN, HOWARD  
(518) 276-6039  
Rensselaer Polytechnic Institute  
Dept. of Chemical Engineering  
131 Ricketts Bldg.  
Troy, NY 12180-3590

LOCHNER, J. M.  
(301) 671-2730  
Commander  
US Army Chemical Research,  
Development and Engineering Center  
ATTN: SMCCR-RSL/J.M. Lochner  
APG, MD 21010-5423

LONG, RANDOLPH  
(301) 671-2437  
Commander  
US Army Chemical Research,  
Development and Engineering Center  
ATTN: SMCCR-RSL/R. Long  
APG, MD 21010

MARTIN, L. R.  
(213) 336-6920  
Aerospace Corporation  
M5-754  
P.O. Box 92957  
Los Angeles, CA 90009

METZGER, KRISTA  
(301) 671-5744  
Commander  
US Army Chemical Research,  
Development and Engineering Center  
ATTN: SMCCR-RSP-P/K. Metzger  
APG, MD 21010



MILHAM, MERRILL  
(301) 671-3854  
Commander  
US Army Chemical Research,  
Development and Engineering Center  
ATTN: SMCCR-RSP-B/M. Milham  
APG, MD 21010

MORGAN, MORRIS H.  
(518) 276-6059  
Rensselaer Polytechnic Institute  
Dept. of Chemical Engineering  
131 Ricketts Bldg.  
Troy, NY 12180-3590

PACK, DEE  
(213) 336-5645  
Aerospace Corporation  
Chemistry and Physics Laboratory  
M2/251  
P.O. Box 92957  
Los Angeles, CA 90009-2957

PARKER, MICHAEL A.  
Commander  
US Army Chemical Research,  
Development and Engineering Center  
ATTN: SMCCR-TD/M. Parker  
APG, MD 21010

PATERNO, DOROTHEA  
(301) 671-4466  
Commander  
US Army Chemical Research,  
Development and Engineering Center  
ATTN: SMCCR-BSP-P/D. Paterno  
APG, MD 21010-5423

PHIPPS, CLAUDE R.  
(505) 667-6956  
Los Alamos National Laboratory  
Chemistry and Laser Sciences  
Division  
MS E535  
Los Alamos, NM 87545

PINNICK, RONALD  
(505) 678-5634  
US Army Atmospheric Sciences Lab  
ATTN: SLCAS-AR/R. Pinnick  
White Sands Missile Range, NM 88002

POLESKI, FRANKLIN  
(803) 9807868  
Commander  
US Army Foreign Science and  
Technology Center  
ATTN: AIFRIB/F. Poleski  
220 Seventh St. NE  
Charlottesville, VA 22901

POREH, MICHAEL  
(303) 454-8204  
Colorado State University  
Engineering Research Center  
Fort Collins, CO 80523

RANADE, MADHAV  
(301) 454-0303  
Particle Technology, Inc.  
Bldg. 335  
Paint Branch Dr.  
College Park, Md 20742

RAY, ASIT  
(606) 257-7990  
University of Kentucky  
Dept of Chemical Engineering  
161 Anderson Hall  
Lexington, KY 40502

RIN, CHIN-HSUN  
(301) 671-2140  
Commander  
US Army Chemical Research,  
Development and Engineering Center  
ATTN: SMCCR-DDW/C.H. Rin  
APG, MD 21010-5423

RITCHIE, GEORGE  
(609) 895-5415  
345 South 25th Street  
Philadelphia, PA 19103

RUBEL, GLENN  
(301) 671-2395  
Commander  
US Army Chemical Research,  
Development and Engineering Center  
ATTN: SMCCR-RSP-B/G. Rubel  
APG, MD 21010-5423

SALEM, HARRY  
(301) 671-3034  
Commander  
US Army CRDEC RSCH DIR,  
Toxicology Div  
ATTN: SMCCR-RST/H. Salem  
APG, MD 21010

SCHUMACHER, CLIFFORD  
(301) 267-2893  
David Taylor Research Center  
Code 28-J  
Non-Metallics Division  
Annapolis, MD 21402

SEAVER, MARK  
(202) 767-9422  
Naval Research Lab  
ATTN: Code 6540/M. Seaver  
Washington, D.C. 20375-5000

SERPENGUZEL, ALI  
(203) 432-4235  
Yale University  
Dept. of Applied Physics  
P.O. Box 2157, Yale Station  
New Haven, CT. 06520

SINDONI, ORAZIO  
(301) 671-4404  
Commander  
US Army Chemical Research,  
Development and Engineering Center  
ATTN: SMCCR-RSP-B/O. Sindoni  
APG, MD 21010-5423

SNYDER, PETE  
(301) 671-3129]  
Commander  
US Army Chemical Research,  
Development and Engineering Center  
ATTN: SMCCR-RSL/P. Snyder  
APG, MD 21010

SRIVASTAVA, VANDANA  
(205) 544-0240  
NASA/Marshall Space Flight Center  
ES 43/NASA/USRA  
Huntsville, AL 35812

STANLEY, MARC  
(301) 295-5674  
Uniformed Services University  
of Health Sciences  
Laser Biophysics Center  
4301 Jones Bridge Road  
Bethesda, MD 20814-4799

STUEBING, EDWARD  
(301) 671-3089  
Commander  
US Army Chemical Research,  
Development and Engineering Center  
ATTN: SMCCR-RSP-B/E. Stuebing  
APG, MD 21010

STUEMPFLE, ARTHUR  
(301) 671-2651  
Commander  
US Army Chemical Research,  
Development and Engineering Center  
ATTN: SMCCR-RSP/A. Stuempfle  
APG, MD 21010

STURM, EDWARD  
(203) 355-2681  
ATM, Inc.  
520-B Danbury Rd.  
New Milford, CT 06776

SUN, XIAO GUANG  
(215) 898-3480  
University of Pennsylvania  
Moore School/ 6314  
Philadelphia, PA 19104-6390

TOLBERT, MARGARET  
(415) 859-4665  
SRI International  
333 Ravenswood Ave  
Menlo Park, CA 94025

VAN DE MERWE, WILLEM  
(301) 295-5674  
Uniformed Services University  
of Health Sciences  
Laser Biophysics Center  
4301 Jones Bridge Rd.  
Bethesda, MD 20814-4799

VARADAN, V. K.  
(814) 863-4210  
Pennsylvania State University  
Director, Center for the Engineering  
of Electronic and Acoustic Material  
University Park, PA 16802

VERVIER, JOSEPH  
(301) 671-4364  
Commander  
US Army Chemical Research,  
Development and Engineering Center  
ATTN: SMCCR-RS/J. Vervier  
APG, MD 21010

WACKER, JOHN  
(509) 376-1076  
Battelle Pacific Northwest  
Laboratory  
P.O. Box 999  
MS P7-07  
Richland, WA 99352

WANG, RU T.  
(904) 371-4778  
Institute of Space Science and Tech.  
Space Astronomy Lab  
1810 N.W. 6th Street  
Gainesville, FL 32609

WANG, PAO K.  
(608) 263-6479  
University of Wisconsin  
Dept. of Meteorology  
1225 West Dayton Street  
Madison, WI 53706

WANG, WAN-XIAN  
(904) 371-4778  
Institute for Space Science and  
Technology  
Space Astronomy Lab  
1810 N.W. 6th Street  
Gainesville, FL 32609

WHITE, JOHN R.  
Commander  
US Army Chemical Research,  
Development and Engineering Center  
ATTN: SMCCR-RSP-B/J. White  
APG, MD 21010

WHITTEN, WILLIAM  
(615) 574-4921  
Oak Ridge National Lab  
Analytical Chem. Division MS-6142  
P.O. Box 2008  
Oak Ridge, TN 37831

WILLIAMS, JOE  
(301) 671-2849  
Commander  
US Army Chemical Research,  
Development and Engineering Center  
ATTN: SMCCR-RS/J. Williams  
APG, MD 21010

WITRIOL, NORMAN  
(301) 278-7067  
Commander US Army  
Ballistic Research Laboratories  
ATTN: SLCBR-IB-I/N. Witriol  
APG, MD 21005-5066

BLANK

# APPENDIX C

## CONFERENCE AGENDA

### TECHNICAL AGENDA

MONDAY, 25 JUNE

#### I. AEROSOL DYNAMICS

MONDAY, 25 JUNE

#### B. Transport and Dispersion of Aerosols

9:00 Registration Opens

9:45 Opening of Conference

Edward W. Stuebing, Aerosol Science Coordinator

Welcome

Michael A. Parker, Technical Director, CNDEC

Administrative Announcements

Elmer Engquist, Conference Administrator

#### I. AEROSOL DYNAMICS

Moderator: Glenn Rubel

#### A. Fundamental Physicochemical Properties of Aerosols

10:10 Benjamin Jurek and James Brock (Univ. of TX/Austin), The Theory and Simulation of Particle Formation in Expanding Flows

10:30 P. Lin and James Brock (Univ. of TX/Austin), Investigations on Aerosol Dynamics

11:00 Mark Seaver (Naval Research Lab), Temperature Measurements in Evaporating Droplets

11:20 Asit Ray and J.L. Huckaby (Univ. of KY), Adsorption of Vapors on Single Droplets

11:50 LUNCH

1:10 Michael Shapiro and Howard Brenner (MIT), Interceptional and Diffusional Deposition and Dispersion of Fine Particles in Fibrous Filters

1:35 John Latham (UMIST), Field Studies of the Turbulent Mixing of Undersaturated Air into Volatile Aerosol Populations

1:55 Michael Poreh, A. Hadad, and J.E. Cernak (CO State Univ), Statistics of Vertical Integrated Concentration Fluctuations for Plumes from Point Sources in a Turbulent Boundary Layer

#### II. AEROSOL CHARACTERIZATION METHODS

Moderator: Durt Bronk

#### A. Physics, Characterization - Light Scattering & Inversion

2:15 Luke Hinkel and D.N.F. Kendall (MKS Instruments), An Instrument to Measure Pressure Dependent Damping of a Single Suspended Micron Sized Particle

2:35 BREAK

3:15 Po Hu and Melvin Lax (CCNY), Optical Inversion Decision Making

3:35 William Curry and Keng Leong (Argonne National Lab), Single Particle Inversion Method

3:55 Durt V. Bronk (CNDEC), Willem P. Van De Merwe, and Marc M. Stanley (USUHS), The Quest for Understanding the Relationship Between Physical Parameters of Bacteria and Features of the S(3,4)/S(1,1) Scattering Curve.

4:15 Roger Johnston (Los Alamos National Lab), S(3,4) and Magnetic Bacteria

TUESDAY, 26 JUNE

## II. AEROSOL CHARACTERIZATION METHODS

## B. Spectroscopy of Single Particles and Aerosols

8:30 Kit Downen (Johns Hopkins Univ.), S.T. Arnold, J.G. Eaton, H.W. Sarkas, L.H. Kidder, N. Winer (Polytechnic Univ.), Spectroscopy of Large Gas Phase Clusters: Large Cluster and Cluster Ions of Water, Ammonia and Metals

8:50 Steven Arnold, D.E. Spock, and L.M. Folan (Polytechnic Univ.), Electric Field Modulated Light Scattering Near a Morphological Resonance of a Trapped Aerosol Particle

9:10 Jay Eversole, H.D. Lin, and A.J. Campillo (Naval Research Lab), Cavity Mode Identification of Fluorescence and Lasing Modes in Micro Droplets

9:30 BREAK

## III. WORKSHOP: THE ROLE OF AEROSOLS IN ATMOSPHERIC CHEMISTRY

Moderator: Burt Brunk

10:00 L.R. Martin (Aerospace Corp.), Acidification of Aerosols in the Atmosphere

10:30 Mario J. Molina (MIT), Stratospheric Chemistry on Ice Particles

11:00 Margaret Tolbert (SRI International), Atmospheric Chemistry on Polar Stratospheric Cloud Particles

11:30 Discussion

12:00 LUNCH

TUESDAY, 26 JUNE

## II. AEROSOL CHARACTERIZATION METHODS - Part B Continued

1:15 Asit Ray (Univ. of KY), Physical and Chemical Characterization of Microparticles by Elastic and Inelastic Scattering

1:35 James B. Gillespie (ASL) and Marcelino Esslen (NMSU), Single Particle Fluorescence Spectroscopy of Atmospheric Aerosols

1:55 William B. Whitten (Oak Ridge National Lab), J.M. Ramsey, S.T. Arnold (Polytechnic Univ.), and D.V. Brunk (CRDEC), Progress in the Detection of Single Molecules in Levitated Droplets

## IV. NONLINEAR EFFECTS

Moderator: John White

## A. Nonlinear Optics

2:15 Robert Armstrong, A. Biswas (NMSU), and R.G. Pinnick (ASL), Stimulated Raman Scattering Threshold Behavior of Binary Mixture Micron-Sized Droplets

2:35 BREAK

3:15 Ali Serpenguzel, William Acker, Richard Chang, and Steven Hill (Yale University), One- and Two-Photon Absorption Effects on Stimulated Raman Scattering in Single Droplets

3:35 David Leach, William Acker, and Richard Chang (Yale University), Stimulated Anti-Stokes Raman Scattering from Monodispersed Droplets

3:55 Gang Chen, Richard Chang, and Steven Hill (Yale University), Angular Distribution of Stimulated Raman Scattering from Ethanol Droplets

WEDNESDAY, 27 JUNE

## VII. POSTER PROGRAM - Previews Continued

- II. Loran M. Folan and G. Keramidas (Polytechnic Univ. of NY), *An Angle Resolved Spectrometer for Single Levitated Particles*
- II. B.N.F. Kendall (Penn State Univ.) and E. Thomas Chesworth (Seven Mountains Scientific, Inc.), *Measuring the Temperature of Diamagnetically Suspended Micro Particles Using Magnetic Susceptibility*
- II. John Wacker (Battelle Northwest Lab), *Mass Spectrometry of Single Particles*
- II. James B. Gillespie, David L. Rosen, and Young Yee (ASL), *Chemical Identification of Atmospheric Aerosols by Fluorescence Lidar*
- II. Ralph W. Alexander, Lawrence Newquist, Robert J. Bell (Univ. of MO/Rolla), Marvin R. Querry, and David Wieliczka (Univ. of MO/Kansas City), *Optical Properties of Some Graphite Materials*
- IV. H.B. Lin, Jay Eversole, and A.J. Campillo (Naval Research Lab), *Mode Identification of Linear and Nonlinear Optical Processes in Micro Droplets*
- VI. David Colhoon (West Chester Univ.), *The Response of an N Layer Electromagnetically Anisotropic Cylinder to Obliquely Incident Electromagnetic Radiation - An Exact Solution*
- VI. David Colhoon (West Chester Univ.), *The Response of an N Layer Electromagnetically Anisotropic Cylinder to Obliquely Incident Electromagnetic Radiation - An Exact Solution*
- VI. G. Fournier and B.T.H. Evans (DRIEV), *Simple Analytic Approximations to the Extinction Efficiency for Randomly Oriented Spheroids and Discs*

## B. Poster Session

2:45 - 5:00 Posters Open (Seminar Center)

THURSDAY, 28 JUNE

## VI. OPTICAL PROPERTIES OF AEROSOLS - Part A Continued

- 8:10 B.T.H. Evans (DRIEV), *PHASE: Integrated Program Host for Absorption, Scattering and Extinction Calculations*
- 8:30 David Colhoon (West Chester Univ.), *The Response of a Sphere or Cylinder with a High Index of Refraction Confining to Electromagnetic Radiation*
- 8:50 E. Fucile (Univ. of Messina), Orazio Sindoni (CNDEC), F. Borghese, P. Denti, and R. Saija (Univ. of Messina), *Density Dependences of the Absorption Coefficient of a Dispersion of Spherical Scatterers*
- 9:10 Ru T. Yang (ISST-Space Astronomy Lab), *Nanobows and Particle Characterization*
- 9:30 E. Fry and G.G. Padmarabandu (Texas A&M Univ.), *Scattering at Zero Degrees by Particulate Suspensions*
- 9:50 BREAK
- 10:30 B. Multiple Scattering and Radiative Transfer
- 10:30 Avishai Ben-David, Yair Benayahu, Shlomo Faslig, and Ariel Cohen (Drexel Univ. and Hebrew Univ.), *Aerosol Size Distribution Inferred from Lidar Multiple Scattering Measurements*
- 10:50 Ezekiel Bahar and Mark Haugland (Univ. of NE/Lincoln), *Multiple Scattering of Electromagnetic Waves from Coated Rough Surfaces*
- 11:10 Xianguang Sun and Dwight Jaggar (Univ. of Penn), *Fractal Electrodynamics: A Novel Method for Examining Rough Surface Scattering*
- 11:30 Vijay K. Varadan, V.V. Varadan, and Yushih Ma (Penn. State Univ.), *Multiple Scattering by a Distribution of Chiral Particles*

ADJOURN

ADDENDUM TO THE AGENDA

Luke Hinkle's name was misspelled on page 2. The correct spelling is Hinkle.

## VII. POSTER PROGRAM

DELETED

- I. D.E. Hagen, M.B. Trueblood, and J. Podzimek (Univ. of MO/Rolla), Laboratory Measurements of Scavenging Rates for Combustion Aerosols in the Submicron Size Range

- I. Tate Tsang (Univ. of KY) and Kenneth Evans (CRDEC), Simulation of Smoke Clouds Using Supercomputer Technology

ADDITIONS

- I. Morris Morgan and Howard Littman (Rensselaer Polytechnic Institute), Drag and Wall Friction Coefficients in Dilute Phase Transport

- I. Howard Littman and Morris Morgan (Rensselaer Polytechnic Institute), Absorption of Toxic Vapors by Activated Carbon in a Transport Line

- VI. Ru T. Wang (ISST - Space Astronomy Lab), Rainbows and Particle Characterization

- VI. Wan-Xian Wang (ISST - Space Astronomy Lab), Electro-magnetic Wave Scattering by an Arbitrary Finite Cylinder